STRUCTURE, PROCESSING, AND PROPERTIES OF CARBON NANOTUBE COMPOSITES WITH POLYPROPYLENE

A Dissertation
Presented to
The Academic Faculty

by

Po-Hsiang Wang

In Partial Fulfillment
Of the Requirement for the Degree
Doctor of Philosophy in the
School of Materials Science and Engineering

Georgia Institute of Technology

May 2018

STRUCTURE, PROCESSING, AND PROPERTIES OF CARBON NANOTUBE COMPOSITES WITH POLYPROPYLENE

Dr. Satish Kumar, *Advisor*
School of Materials Science and Engineering
Georgia Institute of Technology

Dr. Naresh Thadhani
School of Materials Science and Engineering
Georgia Institute of Technology

Dr. Rosario Gerhardt
School of Materials Science and Engineering
Georgia Institute of Technology

Dr. Nikhil Verghese
Research Fellow
SABIC

Dr. Kyriaki Kalaitzidou
The G.W. Woodruff School of Mechanical Engineering
Georgia Institute of Technology

Dr. Donggang Yao
School of Materials Science and Engineering
Georgia Institute of Technology

Date Approved: November 14, 2017

ACKNOWLEDGEMENTS

First of all, I would like to thank my advisor, Dr. Satish Kumar, for the advice, knowledge, and williness to place the emphasis on my education as a scientist. I always feel that I have benefited greatly from his critical thinking and inquisitive mind. Also, his management style allows my own ideas and creativities flourish in my research field.

I am grateful for the support from SABIC for funding this study. I would like to thank Dr. Nikhil Verghese for his critical contribution of expertise and time in this work as well as being my thesis committee member. I would also like to thank the rest of the SABIC team: Dr. Ihab N. Odeh, Dr Devendra Bajaj, Mr. James Lowrey, and Mr. Saad Al Hussain for many valuable discussions.

I would like to thank Dr. Rosario Gerhardt, Dr. Kyriaki Kalaitzidou, Dr. Naresh Thadhani, and Dr. Donggang Yao for their service as my committee members as well as their time and effort on my dissertation. I appreciate the help from Dr. Naresh Thadhani and his student Dr. Rene Diaz for the training for conducting ballistic tests. I would like to thank Dr. Rosario Gerhardt for impedance measurements and for discussion of the test results. Also, I would to thank Dr. Kyriaki Kalaitzidou for generously allowing us to use her lab facilities including the microcompounder, injection molding machine, and DMA.

Many thanks to all my research group members: Dr. Prabhakar Gulgunje, Dr. Sushanta Ghoshal, and Dr. Sourangsu Sarkar, for their assistance in setting up equipment, help in conducting many experiments, in master batch preparation, and all the scientific discussions; Dr. An-Ting Chien, Dr. Bradley Newcomb, Dr. Amir Ahmad Bakhtiary Davijani, and Dr. Clive Liu, for their attentive mentorship and willingness to share their

strengths and experience. Mr. Huibin Chang and Mr. Jeffrey Luo, for their assistance and discussions in various experiments; Dr. Han Gi Chae, Dr. Yaodong Liu, and Dr. Kishor Gupta, for providing their suggestions and comments in the group meetings from professional perspectives.

I would like to acknowledge Dr. Radhakrishnaiah Parachuru and Dr. Jonathan Colton for providing access to their lab equipment for various types of mechanical testing. I would also like to acknowledge Dr. Yi-Feng Su at Florida State University for the TEM study, Dr. Sergei I. Nazarenko at the University of Southern Mississippi for doing the gas and moisture permeability tests, and Keystone Compliance, LCC for the measurement of EMI shielding effectiveness.

Finally, I would like to thank my family for their unceasing encouragement, support, understanding, and love. Special thanks to all my friends, who are always there during my ups and downs Without you, I can not accomplish this.

TABLE OF CONTENTS

CHAPTER 9 CONCLUSIONS AND RECOMMEDATIONS

LIST OF TABLES

LIST OF FIGURES

ABSTRACT

Having high aspect ratio and structural similarity to the macromolecular building blocks, carbon nanotubes (CNTs) have demonstrated their great potential in tailoring the physical properties, e.g. conformation, crystallization, rheological, electrical and thermal characteristics etc., of the polymers. However, achieving good CNT dispersion, while also achieving good interfacial properties, remains a challenge, especially in non-polar polymers such as polyethylene (PE) and polypropylene (PP). In this study, the CNT modified PP with an engineered interphase was manufactured using a co-solvent process where a homogeneous PP layer was bonded non-covalently on acid functionalized multiwall carbon nanotubes (f-MWNTs) (Figure 1 and Chapter 2). Unlike conventional melt blending, which simply compounds the neat polymer and pristine CNTs, or preparing the nanocomposite with covalently modified CNTs, e.g. via in-situ polymerization of macromolecules, this approach provides a practical way to obtain not only good CNT dispersion but also to alter the polymer physical properties by using small amount of CNTs (less than 1 wt% CNT in the polymer).

This research systematically investigates the polymer-CNT interaction when the interphase is tailored. Three types of interphase were studied: (i) The PP/f-MWNT system using co-solvent process. (ii) The maleic anhydride grafted polypropylene (MA-g-PP)/f-MWNT system using co-solvent process. (iii) The PP/pristine MWNT (p-MWNT) system using melt process. It was shown in this thesis work that CNTs serve as a strong nucleating agent for templated polymer crystal growth. With addition of 1 wt % f-MWNT, an 152 % increase in PP impact strength was achieved (Chapter 3). On the other hand, addition of

pristine (unmodified) MWNTs yielded no statistical difference between the impact strength of nanocomposite and the neat PP. In Chapter 4, strong adhesion between PP and f-MWNTs owing to the presence of interphase, was verified by Raman spectroscopy and SEM and was shown to be absent between PP and pristine MWNTs (p-MWNTs). The fracture toughening mechanism in PP/f-MWNT system is attributed to the following: (i) the nucleating ability of CNTs that reduces the spherulite size and thus, results in more tortuous crack propagation paths. (ii) CNTs' ability to act as connecting links between spherulites and in between interlamellar amorphous regions. This bridging effect, in contrast to CNT debonding and pull-out, potentially absorbs more shock and impact energy during material failure. Upon crack propagation, because of the high flexibility of CNTs (stain to failure of 10 % or more), the CNTs can extend over a distance on either side of the bridged crack, absorb fracture energy and promote local plastic deformation (as confirmed by SEM fractography). This process is generally unimportant in the traditional brittle fiber based composites, and most importantly, can only be achieved if the interfacial adhesion between CNTs and the matrix polymer is strong enough.

In Chapter 5, the influence of three types of polymer/MWNT interfaces, namely PP/f-MWNT, MA-g-PP/f-MWNT, and PP/p-MWNT, on the crystallization and melting behavior of the matrix polymer was investigated. Among all types of nanocomposites, sample containing 0.3 wt% f-MWNT prepared from PP/f-MWNT master batch showed the highest increase in crystal perfection along with a narrow crystal size distribution (as confirmed by the FWHM of melting peak in DSC). With the designed heating and cooling profile for polymer self-seeding and templated growth, columnar crystals surrounding f-MWNTs were observed under SEM. The span of this ordered crystalline layer was about

26 nm from the surface of f-MWNT. Melting peak maximum (T_p) of such polymer interphase was about 10 °C higher than the polymer that merely underwent isothermal crystallization in the unfilled PP sample.

In Chapter 6, from WAXD, aligned MWNTs increase the orientation of PP during injection molding. From dynamic shear rheological studies, an improved processability and melt homogeneity were observed in PP/f-MWNT, as compared with p-MWNT based nanocomposites. Presumably, the presence of CNT aggregations reduces the processability of PP/MWNT nanocomposite, especially at high MWNT concentration. Improved PP melt strength after melt annealing in the presence of low CNT concentration was observed. That is, the storage modulus (G') at 0.1 rad/s increased by two-order of magnitude in 1 wt% f-MWNT filled sample after annealing at 200 °C for 165 minutes. Similar effect can also be seen with only 0.1 wt% f-MWNT loading when annealing at 240 °C. Typically, in the literature, more than 3 wt% CNT has been reported to provide such effect. Such improved melt elasticity or melt strength can potentially broaden PP's application to blow molding, foam extrusion and similar processes, i.e. the structure can become strong enough to keep the extensional force without rupturing.

In Chapter 7, the thermal stability, moisture and gas barrier properties as well as electromagnetic interference (EMI) shielding effectiveness of the 1 wt% PP/MWNT nanocomposites was studied. It is observed that even with thermally unstable -COOH group on f-MWNTs, the thermal stability of the PP/f-MWNTs nanocomposite exhibits similar level of improvement to that of the PP/p-MWNT nanocomposite, both with about 95 °C higher temperature at maximum mass loss rate than that of the neat PP. Also, the introduction of hydrophilic -COOH group does not lower the oxygen barrier property of

PP as much as the p-MWNT nanocomposite does. Addition of 1 wt% polymer coated f-MWNTs has not yet effectively increased the dielectric constant and conductivity of the neat PP, neither the EMI shielding behavior.

In Chapter 8, the structure of PP/f-MWNT interphase was characterized by thermal analysis (DSC) and wide-angle X-ray diffraction. It was found that the polymer at the interphase exhibits higher melting points (up to 5 °C), enthalpy of melting (about 16 %), and crystallization temperature (up to 5 °C), suggesting higher crystal perfection and/or larger crystal with respect to the bulk polymer. The structure of the bonded polymer layer, with the thickness about 4 to 5 nm, was also characterized by removing the bulk and loosely bonded polymer with xylene. DSC based calculation suggests a more extended conformation in the interfacial polymer layer with respect to the bulk and loosely bonded polymer. Finally, abnormal temperature dependence of shear viscosity was observed when temperature of the polymer melt was increased from 190 °C to 220 °C.

In Chapter 9, the conclusions of the thesis work are provided along with some recommendations for future studies.

CHAPTER 1

INTRODUCTION

1.1 OVERVIEW

Carbon nanotubes (CNTs) [1], including multiwall carbon nanotubes (MWNT) have been incorporated into various polymer systems owing to their outstanding tensile modulus (270-950 GPa) [3], tensile strength (11-63 GPa) [3], as well as thermal (200-3000 W/m/K at 300 K) [4-6] and electrical conductivity (10^2-10^7 S/m at 300 K) [7]. While interfacial stress transfer from nanotubes to polymer accounts for mechanical reinforcement [8-10], it has also been demonstrated in many polymer/CNT composites that CNTs act as nucleating agent for polymer crystallization [11-14] as well as induce the formation of a highly ordered interphase polymer layer [15-21].

Polypropylene (PP) is a widely used commercial polymer due to its excellent chemical stability, physical and mechanical properties, processability and low cost. Numerous industrial applications of PP can be found in fibrous products, packaging, automotive components, and construction. Over the years, PP matrix has been reinforced with fibrous (e.g. carbon, glass, Kevlar, and natural fibers) and particulate (talc, mica, clay) fillers as well as by melt blending with other polymers [22] to enhance its mechanical properties.

Although the field of CNTs is about 25 years old and more than 20,000 papers on polymer/CNTs have been published, we are still asking one critical question to ourselves: Have CNT based nanocomposites performed to their utmost theoretical capability? Oftentimes the micromechanical models which assume strong filler-matrix interfacial

bonding fail to predict the mechanical properties of the nanocomposites [23]. This is most likely due to the weak interfacial interaction between polymer and CNTs, poor dispersion and curviness of CNTs, etc [24]. Having said that, CNTs potentially can serve as better reinforcing agent than carbon fibers due to higher tensile strength (11 to 63 GPa vs 3 to 7 GPa), tensile modulus (270 to 950 GPa vs 200 to 500 GPa), electrical conductivity (up to 10^7 S/m vs up to 10^6 S/m), thermal conductivity (200 to 3000 W/m/K vs up to 1000 W/m/K), and lower density (1.3 to 2 g/cm^3 vs 1.75 to 2 g/cm^3). Wichmann et al. [25] calculated and compared the pull-out energy of a carbon fiber, G_f, with that of an array of n CNTs, nG_{CNT} with a volume equivalent to that of a single fiber:

$$\frac{nG_{CNT}}{G_f} = \frac{nr_{CNT}\tau_{CNT}l_{c_{CNT}}^2}{r_f\tau_f l_{c_f}^2} = \frac{\sigma_{CNT}}{\sigma_f} \quad (1)$$

where r is the radius, l_c is the critical length, τ is the interfacial shear strength and σ is the tensile strength. The above ratio is anywhere between 1.5 to about 20, indicating CNT based nanocomposites can achieve same level of fracture toughness with much lower filler concentration as compared with the carbon fiber based composite. Also, Desai and Haque [26] proposed that as the dimension (size of the filler) goes down, the surface forces dominates. During filler debonding and pull-out upon fracturing, the friction force in the CNT/polymer system can be significantly higher than that in the carbon fiber/polymer system, contributing to higher fracture toughness. Also, CNTs have been shown to template polymer orientation and to act as nucleating agent for polymer crystallization. While PP is a widely-used commodity plastic, because of its low polarity, it is also one of the most challenging system for dispersing CNTs. Conventionally, chemical modification of PP (e.g. maleic anhydride grafting) or that of CNTs (e.g. by in-situ polymerization) is used for improving CNT dispersion. However, usually such treatment can deteriorate the interaction

between PP and pristine CNT surfaces, thus, resulting in poor performance. To this end, it is important to understand the role of CNT/PP interface and interphase on the structure, processing, and properties of the nanocomposite. Also, in order to obtain a system where CNTs are well-dispersed in PP, meanwhile, with tailored interface/interphase, a method for dispersing CNTs in PP has to be develop.

1.2 POLYPROPYLENE (PP)

Polypropylene (PP) is a widely used commercial polymer due to its good chemical stability, physical and mechanical properties, processability and low cost. Numerous industrial applications of PP can be found in textiles, medical devices, electronics, packaging, automotive components, construction, and consumer products. It is one of the fastest growing classes of commercial thermoplastics, with a market demand growth of 5-7 % per year and the PP market worldwide is expected to exceed US $130 billion by 2023 owning to the globally rising demand for lightweight vehicles [27]. Amongst various polymers, the volume of polypropylene produced is only exceeded by that of polyethylene (PE).

Polypropylene has several aspects similar to polyethylene. While the presence of methyl group in PP improves mechanical properties and thermal resistance, its chemical resistance is compromised as compared with PE [28]. The physical and chemical properties of PP depend on the molecular weight, molecular weight distribution, crystallinity, tacticity and polymorphism. Density of PP is between 0.89 to 0.92 g/cm^3, which is the lowest amongst commodity plastics [28]. It is normally tough and flexible, especially when copolymerized with ethylene or diene to form an ethylene/propylene copolymer or an ethylene/propylene/diene terpolymer. This allows the impact strength of polypropylene to

compete with that of engineering plastics such as polycarbonate (PC), acrylonitrile butadiene styrene (ABS), and polyether ether ketone (PEEK). Competing with these engineering polymers, however, PP is reasonably economical. PP is at room temperature resistant to almost all acids and bases, except nitric acid. At elevated temperature, PP can be dissolved in low polarity solvents, such as xylene, toluene, tetralin and decalin, etc. [29, 30]. The melting point of polymers, including that of PP occurs in a temperature range depending on the thickness and perfection of the crystalline lamella. Typically, differential scanning calorimetry (DSC) is used for determining the melting temperature. Commercial isotactic PP melts at about 160 °C while syndiotactic PP melts around 130 °C [31]. Manufacturing of PP is normally done by melt processing including thermoforming, extrusion and molding including, injection, compressing, and blow molding.

1.2.1 Chemical structure of polypropylene

Polypropylene is synthesized by polymerizing propylene monomer (Figure 1.1), in the presence of catalyst under controlled conditions. Propylene is an unsaturated hydrocarbon which can be derived as a gaseous byproduct during petroleum refining.

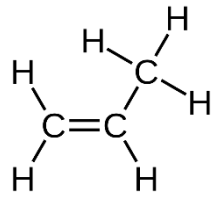

Figure 1.1. Molecular structure of propylene.

Since the propylene monomer is asymmetrical in shape because of a methyl group attached to one of the backbone carbons, three possible types of linkage, namely, "*head-to-head*", "*tail-to-tail*", and "*head-to tail*" can happen during polymerization (Figure 1.2).

While the most common insertion method is the "*head-to-tail*" fashion, however, occasionally there will be an insertion error and the monomers form a "*head-to-head*" or "*tail-to-tail*" linkage which disrupts the alternating arrangement of methyl groups in the polymer.

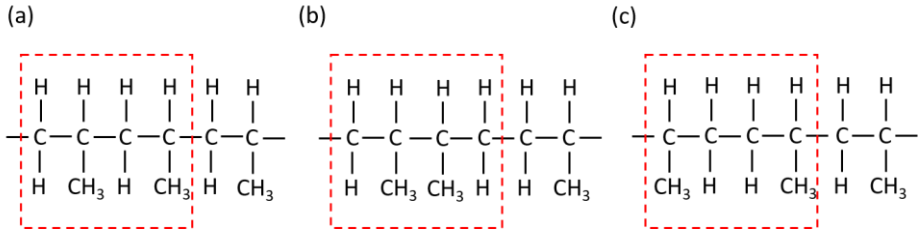

Figure 1.2. (a) *Head-to-tail* addition, (b) *head-to-head* addition, and (c) *tail-to-tail* addition.

If the pendant methyl groups are all in the same configuration and are on the same side of the polymer chain, they are referred to as in an "*isotactic*" arrangement. If the alternate pendant methyl groups are on opposite sides of the polymer backbone, with exactly opposite configurations with respect to the polymer chain, they are referred to as in a "*syndiotactic*" arrangement. A random arrangement of pendent groups along the chain provides little or no symmetry and the resulting polymer is termed as "*atactic*" polymer (Figure 1.3). Due to the regular repeating arrangement, isotactic PP (iPP) has a high degree of crystallinity. On the other hand, atactic PP (aPP) is an amorphous rubbery material.

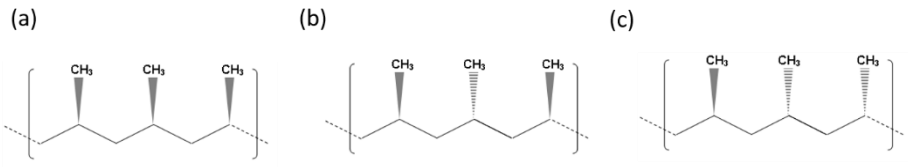

Figure 1.3. (a) isotactic polypropylene, (b) syndiotactic polypropylene, and (c) atactic polypropylene.

1.2.2 Polymorphism

One important characteristic of polypropylene is that it can form different crystal structures, depending on the crystallization conditions such as pressure, temperature, shear, and cooling rate, etc. [32-38]. While different forms can coexist, one form can also transfer into the other as conditions change [39, 40].

The most common crystalline form of isotactic PP (iPP), crystallized under atmospheric pressure, is the monoclinic α-form. The unit cell of the α-iPP contains four three-fold helical chains, with the lattice parameters a = 6.65 Å, b = 20.96 Å, c= 6.5 Å, and $\alpha = \gamma = 90°$, $\beta = 99.3°$ [41, 42]. The β-form of iPP has a hexagonal unit cell structure, with the lattice parameters $a = b$ = 11.03 Å, c= 6.49 Å, and $\alpha = \beta = 90°$, $\beta = 120°$ [43]. A high amount of β-form crystals can be produced under some special crystallization conditions [44, 45] and when selective β-nucleating agents [34, 46, 47] are present. Percentage of β-crystals (K_β) in a sample can be evaluated from wide-angle x-ray diffraction (WAXD) where the relative amount of the β crystals in the crystalline phase is calculated based on the following equation [48]:

$$K_\beta = \frac{I_{\beta 1}}{I_{\beta 1}+I_{\alpha 1}+I_{\alpha 2}+I_{\alpha 3}} \quad (2)$$

where $I_{\beta 1}$ is the integral intensity of (300) diffraction of the β-phase, and $I_{\alpha 1}$, $I_{\alpha 2}$, and $I_{\alpha 3}$ are the integral intensities of the (110), (040) and (130) diffraction of the α-phase, respectively. The γ-form of iPP is usually observed as a co-crystallized component within the α-form spherulites [41]. The crystal structure of γ-iPP is considered as a face-centered orthorhombic unit cell with lattice parameter a = 8.54 Å, b = 9.93 Å, and c= 42.41 Å [49]**.** They are generally observed under shear-controlled-orientation or under high pressure

crystallization [50, 51]. In addition to the above mentioned three crystalline forms, a mesomorphic or a smectic form of PP can also exist which is intermediate in order between crystalline and amorphous forms. Under fast quenching to low crystallization temperature (80 °C), a transition from α to (probably) sematic phase has been reported [52].

The structure of α and β spherulites is different, and therefore different mechanical properties. A lamellar branching specific to α-form iPP is normally called "cross-hatched" morphology which consistes of tangential lamellae connected to radial lamellae with a 100° branching angle. There is no cross-hatched texture in β-form of iPP, as only radial lamellae are presented in β type spherulites. The presence of the tangential lamellae in the α phase makes the spherulites more rigid and cause an increase in Young's modulus and yield stress with increase of α phase content. In addition, these tangential lamellae reduce the elongation at break of the spherulites and make PP more brittle [34, 35, 53]. On the other hand, β phase crystals are more ductile than the α phase ones. For example, the specimen containing 100 % α phase iPP versus the specimen containing 54-92 % of β phase iPP has a tensile modulus of 2.57 GPa versus 2.27 GPa, yield stress of 25.6 MPa versus 23.6 MPa, and elongation at break of 256 % versus 644 %, respectively [35]. Melting point of β phase iPP is reported to be in the range of 150 °C to 154 °C which is about 10 to 15 °C lower than that of the α phase [34, 54].

Table 1.1. Structural parameters of PP crystal forms from WAXD [13, 50]

2 θ value*	Crystal form	Corresponding crystal plane
14.1°	α-form	(110)
15.0°	γ-form	(113)
16.1°	β-form	(300)
16.9°	α-form	(040)
18.5°	α-form	(130)
20.2°	γ-form	(117)
21.2°	β-form	(301)
22.1°	α-form	(111)
22.2°	α-form	(041)

*2 θ value is based on x-ray wavelength of 0.154 nm

1.2.3. Maleic anhydride grafted polypropylene (MA-g-PP)

Compatibilizers, also referred as coupling agents, are additives added during melt extrusion for promoting the miscibility of the blend. One of the most successful techniques for compatibilization of PP is the use of maleic anhydride grafted copolymer. In the polymer blend or composite system where PP is one of the main components, maleic anhydride grafted PP (MA-g-PP) [55], Figure 1.4. and maleic anhydride grafted styrene-ethylene/butylene-styrene copolymer (MA-SEBS) [56] are two common compatibilizers.

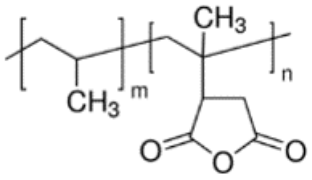

Figure 1.4. Molecular structure of maleic anhydride grafted polypropylene (MA-g-PP).

1.3 CARBON NANOTUBES (CNTs)

The field of carbon nanotubes (CNT) is about 25 years old and over 150,000 research publications in the CNT related area have been published to-date (Figure 1.5). The global CNT market is anticipated to witness growth in the nanomaterial applications in plastics, electronics, and energy storage, etc. owing to its outstanding properties and cost effectiveness. CNTs' use in polymers account for over 60 % of its market share in 2014 [57]. The use of CNTs in this area is fueled by the growth of polymer composite applications in the construction and automobile industries where lightweight materials with enhanced mechanical properties are required. Multiwall carbon nanotubes (MWNTs), which consists of from four up to about hundred walls, are cheaper as compared with single wall carbon nanotubes (SWNTs) and graphene. According to the price provided by cheaptubes.com (2017) [58], MWNTs cost \$0.6 – \$25 per gram while high purity (> 99 wt. %) SWNT and reduced graphene oxide is around \$125 - \$300 per gram and \$400 - \$450 per gram, respectively. The economic incentive along with its excellent mechanical performance compared with other conventional fillers have made MWNT a promising material in the composite industry. Comparison of MWNTs with glass and carbon fibers, two common fillers for reinforcing polymer used in the industry, are given in Table 1.2. Also, the emergence of CNTs has paved the way for new composite applications in other

field such as electromagnetic interference shielding [59, 60], enhanced oxygen barrier performance [61], improved dielectric performance [62], and for antistatic purposes [63].

Table 1.2. Properties of MWNT, carbon fibers, and glass fibers.

	CNT (MWNT)	Carbon fiber -PAN based [64]	Carbon fiber -pitch based [64]	Glass fiber [65]
Specific density	1.4 - 2.1 [66]	1.73 - 1.8	1.9 - 2.2	~2.5
Young's modulus (GPa)	270 - 950 [67]	200 - 500	160 - 900	80 - 90
Tensile strength (GPa)	11 - 63 [67]	3 - 5.5	1.4 - 3	2 - 4.7
Electrical conductivity (S/m)	10^2 - 10^7 [4-6]	10^4	Up to 10^6	10^{-23} - 10^{-22}
Thermal conductivity (W/m/K)	200 - 3000 [7]	10	Up to 1000	1.2 - 1.35

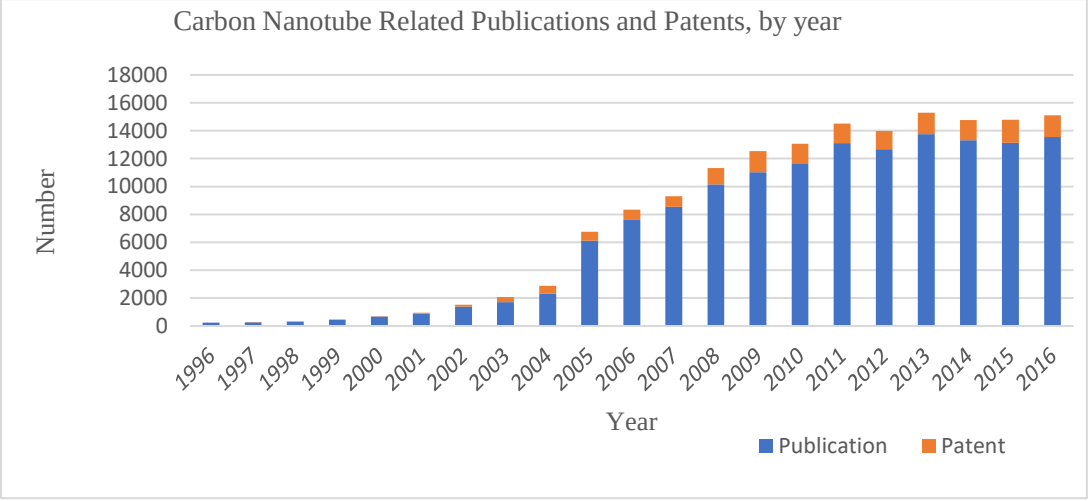

Figure 1.5. CNT related publications and patents, by year. Number of publication and patent are based on the search results from Web of Science.

CNTs can also introduce structural and morphological changes in the polymer matrix (Figure 1.6), e.g. templated graphitic layers at the surface of CNT [19], shish-kebab morphology formed under shear deformation [68], orientated crystallization [69], and the transcrystalline layer surrounding CNT fibers [70].

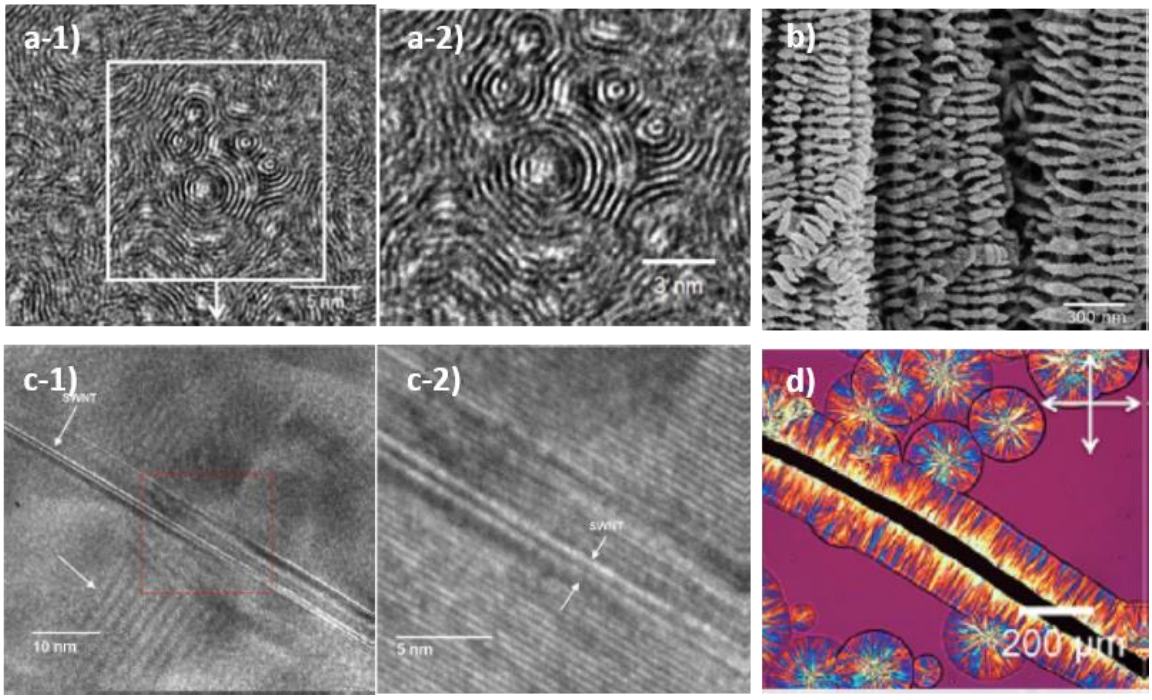

Figure 1.6. CNT induced structural and morphological changes at the polymer/CNT interfaces. (a-1 and a-2) templated graphitic structure in polyacrylonitrile (PAN)-based carbon fiber [19], (b) shish-kebab morphology of polyethylene (PE) on CNT [68], (c-1 and c-2) CNT templated oriented crystallization of polyvinyl alcohol (PVA) [69], and (d) transcrystalline morphology of PP on a CNT fiber [70].

1.3.1 **Structure of carbon nanotubes**

Carbon nanotubes are hollow cylindrical molecules composed of carbon atoms equivalent to a graphitic (graphene) sheet rolled into a seamless tube, capped or uncapped at the ends. The strong covalent in-plane σ bond binds the atoms in the plane and results in high stiffness and high strength of the CNTs. While the out-of-plane, delocalized π bonds contribute to a weaker interlayer interaction [1]. There are number of ways of rolling the

graphene sheet to form CNTs and depending on the chirality, they can be categorized as zigzag, armchair, and chiral (Figure 1.7). The electrical conductivity of a SWNT is also determined by its chirality [1, 71]. In general, a (n,m) carbon nanotube is metallic when n - m= 3q (q is an integer), and semiconducting when n - m ≠ 3q. Armchair (n,n) carbon nanotubes are always metallic and a zigzag (n,0) carbon nanotube are semi-metallic or metallic [1].

MWNT are made of concentric cylinders and have diameter between 5 to 100 nm with a 0.34 nm spacing between the layers [71]. These concentric cylinders can either consist of identical structure but different in diameter or a mixed type of chirality. Considering that the length of carbon nanotubes can reach several micrometers, the aspect ratio of MWNTs, thus can sometimes be greater than 10^4.

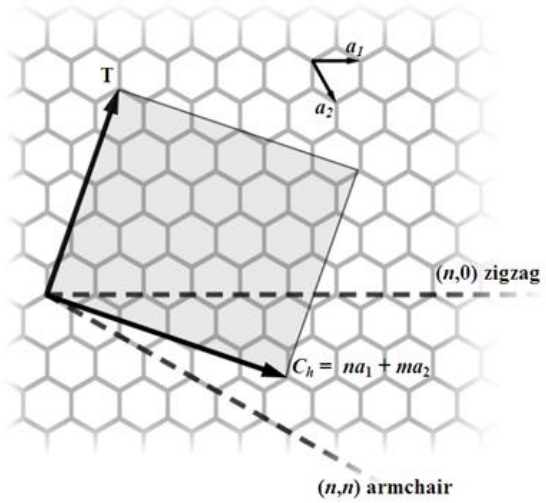

Figure 1.7. Schematic of the roll-up of a graphene sheet to form a SWNT structure. The chiral vector *(n,m)* determines whether a SWNT will be zigzag *(n,0)*, armchair *(n,n)* or chiral *(n,m)*.

1.3.2 Dispersion of carbon nanotubes in polypropylene

It is difficult to fully disperse CNTs into the polymer matrix, as CNTs tend to bundle together through van der Waals forces [72, 73]. In general, the partial disentanglement and exfoliation of CNTs in polymer/CNT nanocomposites can be achieved by mechanical and chemical means (Figure 1.8) [74, 75]. Typically, the mechanical approaches such as homogenization, ultra-sonication, and ball milling result in sacrificing CNT's structural integrity and length preservation which is not favorable for producing high performance nanocomposites. Chemical approaches include covalent and non-covalent functionalization of CNTs where the former also introduces defects on the outer layer of CNT and reduces direct polymer-CNT interaction. Thus, the preferable approach is through non-covalent wrapping or physical adsorption of polymer chains onto CNTs that prevents them from re-agglomeration.

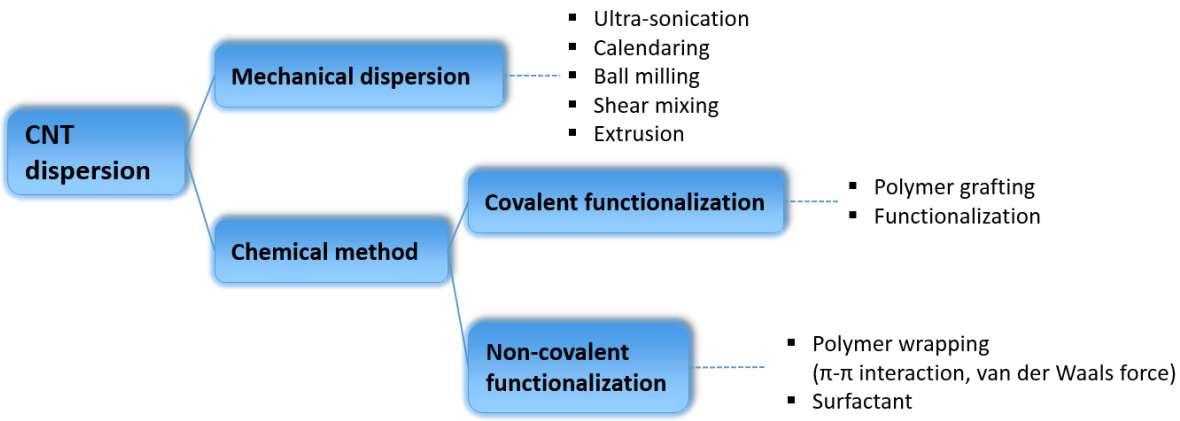

Figure 1.8. Currently used methods for improving CNT dispersion towards fabrication of high performance polymer/CNT nanocomposite.

1.3.2.1 CNT functionalization and polymer grafting

Chemical functionalization is based on the covalent linkage of functional entities onto the carbon scaffold of CNTs. This can be performed at the end or the sidewall of the nanotube [76, 77]. For example, to improve the solubility of CNT in polar solvents, a common practice of acid functionalized CNTs was adopted through the introduction of carboxylic acid (-COOH) or hydroxyl (-OH) groups by reflux reaction in concentrated HNO_3, H_2SO_4, and HCl or some combinations thereof [78-81].

There are two methodologies for the grafting of CNTs, namely, "grafting to" (Figure 1.9) and "grafting from". In the "grafting to" approach, a polymer with specific reactive group is attached to the surface of CNTs by addition or condensation reaction while the "grafting from" scheme involves growing of polymer from CNT surface via *in situ* polymerization of monomers [2, 76, 82-84].

In the polyolefin (PP and PE)/CNT system, the covalent modification of CNTs normally consists of functionalization of CNTs followed by grafting of alkyl chains (C1 to

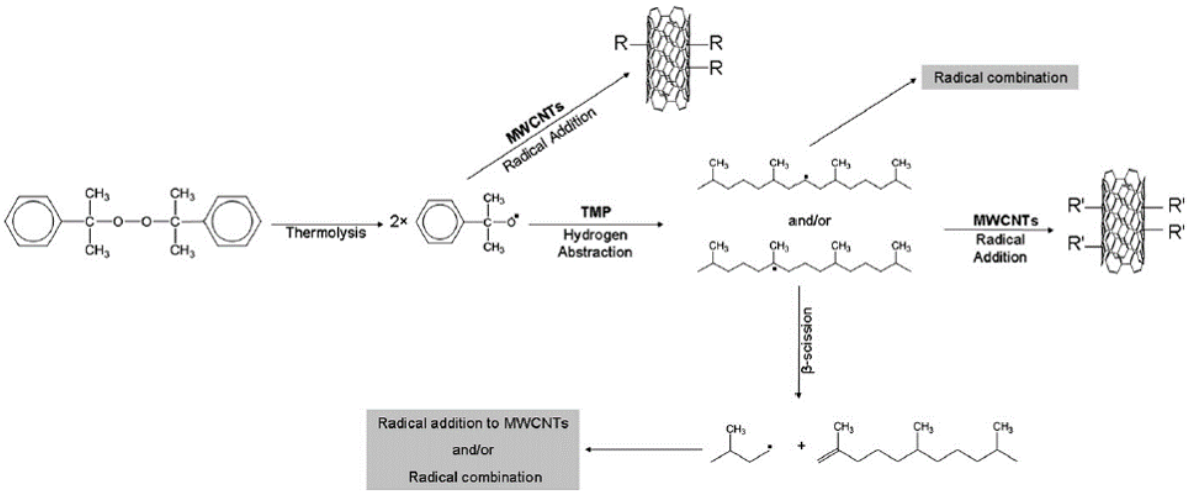

Figure 1.9. Grafting of 2,6,10,14-tetramethylpentadecane (TMP, $C_{19}H_{40}$), a long alkane chain, onto CNT [2].

C20) [2, 85], amine [86], PP [82-84], MA-g-PP [87], silane coupling agent [88], alkyl aryl amine having more than 9 carbon atoms in length (up to 50) [89], or ionic liquids with complex structure (1-docosanyl-3-methylimidazolium and 1-docosanyl-3-methylimidazolium hexafluorophosphate) [90] to enhance compatibility with the polyolefin matrix.

1.3.2.2 Non-covalent modification of CNTs by polymer

According to Smalley group [91], "What is needed is a procedure that detaches tubes from bundles by physical means, applies a non-perturbing coating to prevent re-aggregation, and then removes from the solution any remaining bundles". To this end, a method was developed to stabilize CNTs in aqueous solution via non-covalent association between nanotubes and poly(vinyl pyrrolidone) (PVP) [92]. These PVP wrapped CNTs can be further dispersed in other polymers, e.g. in PVA [93].

However, attaching PP on the sidewall of CNT through non-covalent modification can be challenging. First, according to the molecular dynamics simulation, PP exhibits a zigzag conformation on the CNT surface, instead of helical conformation as in crystal [94], which makes it unfavorable for the coating process comparing to the polymer chains that adopt helical conformation (e.g., PmPV, PPA and PPV) [94-96]. Second, noncovalent adsorption of polymer onto the sidewall of CNTs occurs most commonly through π-π interactions [97, 98], where the chosen polymer is an electron-rich chemical compound, e.g. compounds that are highly aromatic in nature. Having said that, interactions can also occur between carbon-hydrogen groups and π system [99-101]. CH-π interaction is relatively weak and is comparable to van der Waals forces [99], and it is about one-tenth the strength of the hydrogen bond [101]. Presence of CH-π interactions has been identified

through peak shifts in FTIR. Examples of these include shifts corresponding to CH stretching (3266 cm^{-1} in acetylene) [100] or CH bending (1450 cm^{-1} in polybutadiene) [101] vibration.

To the best of our knowledge, there are no literature reports prior to this study, where PP coating of CNTs has been achieved via non-covalent interactions. During crystallization in 1,2-Dichlorobenzene (DCB), Zhang *et al.* [102] found that MWNTs were wrapped by a homogenous coating of PE (Figure 1.10a), while PP coating was not observed in that process (Figure 1.10b). In another study, encapsulation of CNT with MA-g-PP via solution mixing approach using butanol and xylene was shown to be successful [55] (Figure 1.10c). It was also demonstrated that via ball milling approach, some MA-g-PP chains adsorbed onto the sidewall of MWNT while PP did not [103].

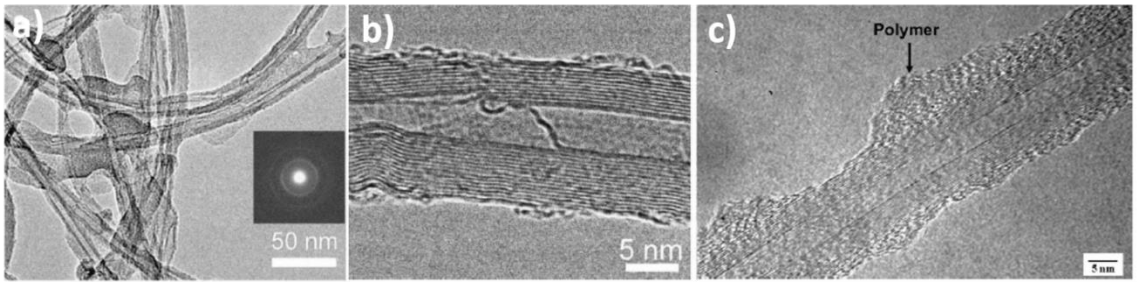

Figure 1.10. (a) PE coating on MWNTs via solution mixing [102], (b) much fewer PP chains adsorbed onto MWNT through the same process as compared with the PE coating in (a) [102], and (c) layer of MA-g-PP coating on MWNT [55].

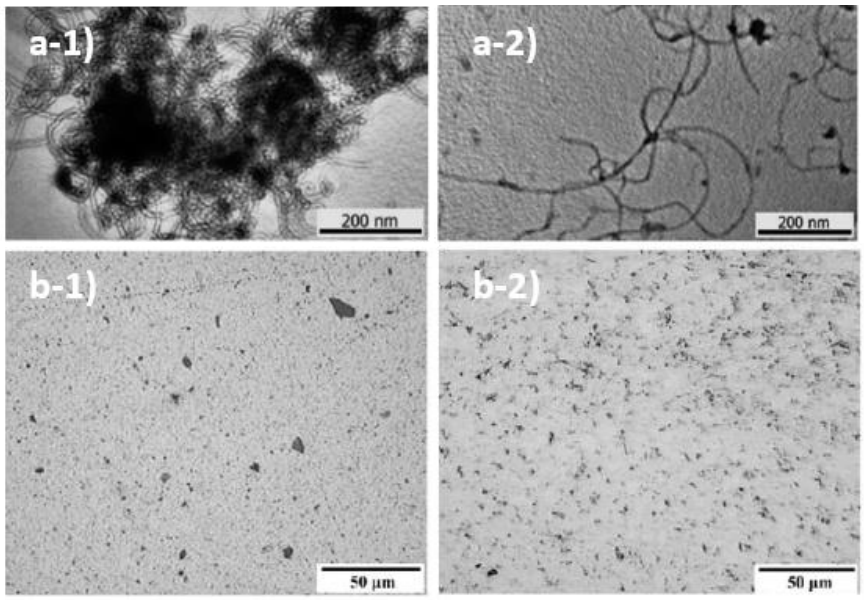

Figure 1.11. (a-1) TEM image of pristine MWNTs and (a-2) SDS-treated MWNTs [104], (b-1) Optical image of 1 wt. % pristine MWNT with PP and (b-2) 1 wt. % pristine MWNT/3 wt. % MA-g-PP with PP [72].

Incorporation of compatibilizer such as MA-g-PP [55, 72, 73, 103, 105] and maleic anhydride grafted styrene-ethylene/butylenes-styrene copolymer (MA-SEBS) [56], surfactants such as sodium dodecyl sulfate (SDS) and sodium dodecylbenzene sulfonate (NaDDBS) [104] can also improving the dispersion of CNTs in PP (Figure 1.11).

1.4 PP/CNT NANOCOMPOSITES

Generally, polypropylene can be blended with various types of fillers, additives and even with other polymers to meet the performance specifications and desired processing conditions for given applications (Figure 1.12). The effects of CNTs on the performance of PP have been studied in the following areas:

i. Mechanical reinforcement

ii. Dimensional stability

iii. Accelerating crystallization

iv. Rheology

v. Interphase developments and templated polymer orientation

vi. Tailored electrical and thermal properties

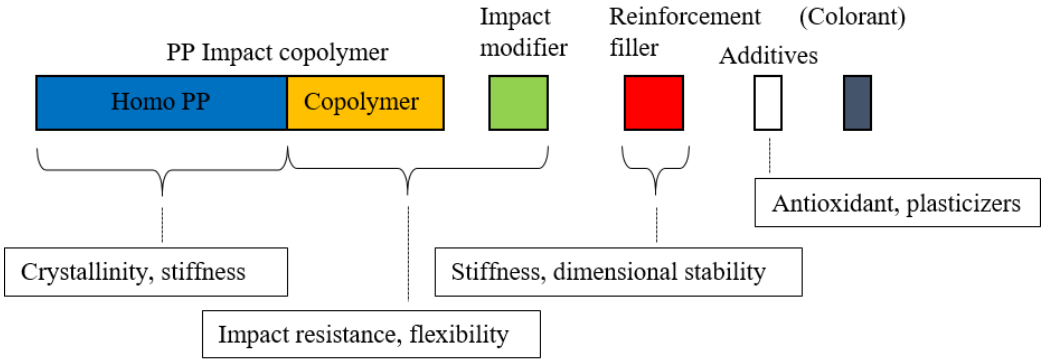

Figure 1.12. Common additives and their effects on polypropylene performance [106].

1.4.1 Processing of the polypropylene/carbon nanotube nanocomposites

Only a limited number of organic solvents, such as N,N-dimethylformamide (DMF), 1,2-dichlorobenzene (ODCB), N-methylpyrrolidinone (NMP), Tetrahydrofuran (THF) and chloroform etc. [107], are known to disperse CNTs to some extent. Many CNT incorporated nanocomposites were successfully produced via solution processing approach with conjugated polymers [108], aromatic polymers [109], and other polar polymers like pol(vinyl chloride) [110], polyacrylonitrile [17], poly(methyl methacrylate) [111], poly(vinyl alcohol) [93] and poly (ethylene oxide) [112], etc. Polypropylene, due to its non-polar nature, does not have sufficient solubility in these solvents. Therefore, the manufacturing of PP/CNT nanocomposite is mostly done through melt processing,

including extrusion, thermoforming, injection molding, blow molding, compression molding, die casting, etc.

1.4.2 Properties of the polypropylene/carbon nanotube nanocomposites

In this section, the mechanical properties and crystallization behavior of the PP/MWNT nanocomposite will be reviewed.

1.4.2.1 Mechanical properties

Although there are wide variations in CNT modification methods and in PP/CNT nanocomposite processing, some general observations and conclusions can still be drawn from the results reported in the literature (Table 1.3). Also, In Figure 1.13, % increase in impact strength in the thermoplastic composites having various type of fillers is given:

- Most of the literature studies have been conducted at CNT loading above 0.1 wt. %.
- The maximum percent increase in the impact strength is 56 % at 1 wt% MWNT.
- Tensile modulus and tensile strength can be improved by more than 100 %, but the material became brittle (low elongation at break) under these conditions.
- Addition of micro-size fillers such as carbon black, $CaCO_3$, talc, carbon fiber and glass fiber, requires relatively high loading of fillers (above 5 to 20 % or even more) to achieve intermediate level (10 to 100 %) of improvement in impact strength.

While α-type crystals predominantly exist in PP, under certain conditions, e.g. in the presence of β-nucleating agent, β crystals can form and co-exist with the α-phase. When comparing α crystalline PP to predominantly β crystalline PP, the latter has [34, 35, 53]:

- Lower young's modulus and yield stress.
- Higher elongation at yield and elongation at break and higher impact strength.

By treating graphene oxide grafted with octadecylamine (GO-D) with β–nucleating agent (GO-N), PP nanocomposites were manufactured [113]. At 0, 0.1, 0.2 and 0.5 wt. % GO-N loading, impact strength was 3.2, 7.5, 7.0 and 5.0 kJ/m^2, respectively. In this case, GO-D acts as a carrier of β–nucleating agent. The impact strength remained the same when adding 0.1 wt. % GO-D, as without GO-D. So, this is clearly the beta nucleating agent effect and not the effect of graphene oxide. Tordjeman et al. [114] studied the effect of α and β crystalline structure on the mechanical properties of polypropylene. β nucleating agent was added in molten state to obtain 80 % β crystal phase. Subsequently β-phase was reduced by heat treating the samples at 152 °C for different time periods. Tensile modulus of the sample containing 80% β-phase was ~1.75 GPa and that for the sample containing 40 % β-phase was 2.7 GPa. Strain to failure increased from ~15 % to ~45 % with increase in β-phase content from 40% to 80%. Essential work of fracture increased from 4 kJ/m^2 to 6 kJ/m^2 with increase in β-phase content from 40% to 80%.

Table 1.3. Mechanical properties of the PP/CNTs nanocomposites from literature studies. Numbers in the brackets are % increase (+)/decrease (-) from the neat PP. It is worth noting that, directly comparing the values between the literature data may not be possible as sample history, polymer molecular weights, and additives are not always specified.

CNT (wt.%)	Impact strength (KJ/m^2)	Tensile modulus (GPa)	Tensile strength/Yield stress (MPa)	ε_b (%)	Notes
1.5	N/A	1.61 (+108%)	60.7 (+141%)	10.7 (+49%)	Covalent MA-g-PP-grafted MWNT; hot-pressed [115]
1	2.8 (+24%)	1.62 (+27%)	33.2 (+18%)	436 (-30%)	Commercial master batch, compression molded [116]
1	5.5 (+33%)	1.62 (+53%)	32.0 (+16%)	227 (-57%)	p-MWNT, injection molded [117]
5	N/A	1.72 (+38%)	38.9 (+22%)	N/A	p-MWNT, injection molded [118]
0.6	26.5 (+47%)[1]	N/A	59 (+16%)	N/A	p-MWNT, dynamic packing injection molded [119]
1	4.2 (+56%)[2]	0.75 (+16%)	32.2 (+14%)	N/A	p-MWNT, compression molded [120]
1	N/A	1.7 (+36%)	36.5 (+9%)	350 (-59%)	Covalent MAO-grafted MWNT[3], hot-pressed [121]
0.6	N/A	2.2 (+47%)	40.7 (+19%)	12 (-95%)	Covalent ODA[4]-grafted MWNT, injection molded [122]
0.1	N/A	1.45 (+22%)	38.0 (+3%)	375 (-17%)	Covalent MAO-grafted MWNT[3], in situ polymerized [123]
0.5	18.5 (+27%)[1]	0.89 (+8%)	32.1 (+5%)	N/A	p-MWNT extruded with PP and injection molded [124]
2	4.47 (+25%)	N/A	N/A	N/A	p-MWNT extruded with PP [125]
0.3	N/A	2.1 (+34%)	35.9 (+17%)	>500	p-MWNT extruded with PP [126]

[1]The value of impact strength is unusually high, [2]In J/m, [3]MAO: methylaluminoxane, [4]ODA: octadecylamine.

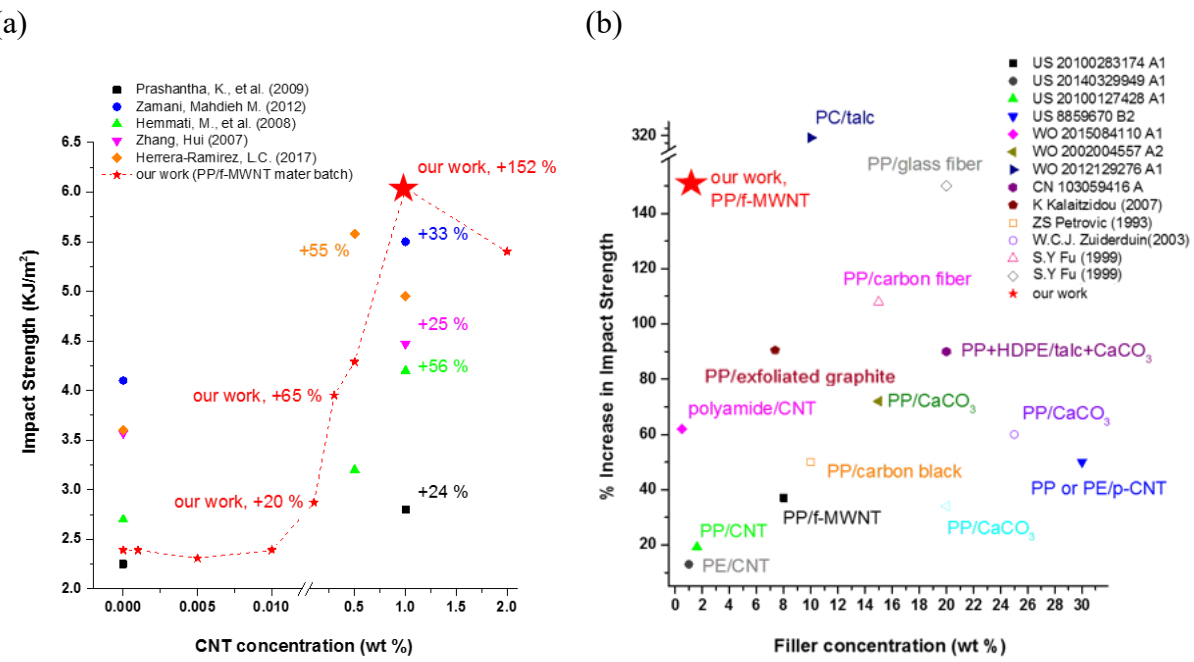

Figure 1.13. (a) Impact strength of PP/CNTs nanocomposites from the literature. (b) % increase in impact strength in the thermoplastic composites having various type of fillers.

1.4.2.2 Crystallization properties

In general, there are two mutually opposite effects of fillers on the crystallization behavior, namely, nucleation ability and growth retardation. Both of these are related to the filler concentration and dispersion quality. Various approaches have been undertaken to modify the surface of fillers in order to improve their dispersion quality [21, 82, 121, 127-139]. The effect of these surface modifications on the crystallization and melting behavior as compared with their unmodified counterparts are summarized in Table 1.4 and Table 1.5, and key observations and results are briefly summarized below:

- Incorporation of various types of nano-fillers results in up to 90% reduction in $t_{1/2}$ (crystallization half-time).

- Equilibrium melting temperature (T_m^0) decreases with the incorporation of CNT in PP.
- Incorporation of different types of nano-fillers result in up to 15 °C increase in crystallization temperature (T_c).
- Most of the literature studies show up to about 2 °C change in melting peak maximum (T_p) of PP in the nanocomposite, except one study where the increase was 8 °C.

These observations demonstrate that the incorporation of the fillers in the composites, in most cases, accelerates the crystallization process of matrix polymer but has little or even negative influence on the crystalline perfection. For example, the silane groups grafted on MWNT improved its dispersion in the matrix which compensated the negative effect of silane groups on the polymer crystallization nucleation. However, while the reduction of $t_{1/2}$ is similar between the silane grafted MWNT and p-MWNT containing composite, more dramatic decrease T_m^0 was found in the former which brought about 32 °C change with 1 wt. % MWNT loading [128].

Table 1.4. Literature results of the isothermal crystallization experiments on PP composites with various type of fillers.

Filler type	Filler concentration	Method	Crystallization behavior		Ref.
			Change of $t_{1/2}$ [1]	Change of T_m^0 [2]	
MA-g-PP grafted MWNT; p-MWNT	1 and 2 wt. %	Melt compounding	not reported	-15 °C at 1 wt. % grafted MWNT; -21 °C at 1 wt. % p-MWNT	[127]
Silane grafted MWNT	0.5 and 1 wt. %	Solution mixing	-90 % at 0.5 wt. %; -92 % at 1 wt.% (at 130 °C)	-21.4 °C at 0.5 wt. %; -32.2 °C at 1 wt. %	[128]
p-MWNT	0.5 and 1 wt. %	Solution mixing	-87 % at 0.5 wt. %; -92 % at 1 wt.% (at 130 °C)	-9.4 °C at 0.5 wt. %; -26.2 °C at 1 wt. %	[128]
p-MWNT	0.5 to 4 wt. %	Melt compounding	-44 % at 1 wt. %; -63 % at 4 wt.% (at 130 °C)	not reported	[129]
Reduced graphene oxide (rGO)	0.12 to 2 wt.%	In-situ polymerization	-80 % at 0.12 wt. %; -89 % at 0.63 and 2 wt.% (at 130 °C)	not reported	[130]
Cellulose nanocrystal (CNC)	1 wt. %	Melt compounding	-80 % at 1 wt. % (at 120 °C)	+5.5 °C	[131]
Elastomeric nano-particles (ENP)	5 wt. %	Melt compounding	-74 % (at 125 °C)	not reported	[132]
Montmorillonite (MMT)	2.5 to 8.1 wt.%	Intercalation polymerization	-62 % at 2.5 wt. %; -70 % at 8.1 wt.% (at 130 °C)	+4.7 °C at 2.5 wt. %; +11.4 °C at 8.1 wt. %	[133]

1 crystallization half time 2 equilibrium melting temperature; derived from linear Hoffman-Weeks plot

Table 1.5. Literature results of the non-isothermal crystallization experiments on PP composites with various type of fillers.

Filler type	Filler concentration	Method	Crystallization behavior		Ref.
			Change of T_c	Change of T_p[1]	
Octadecylamine grafted MWNT	0.1 and 0.6 wt. %	Melt compounding	+2.3 °C at 0.1 wt. %; +4.1 °C at 0.6 wt. %	-1 °C at 0.1 wt. %; -0.8 °C at 0.6 wt. %	[134]
MA-g-PP grafted MWNT	0.5 to 2 wt. %	Melt compounding	+7.6 °C at 0.5 wt. %; +9 °C at 1 wt. %	+2.1 °C at 0.5 wt. %; +2.2 °C at 1 wt. %	[135]
MAO[2]-grafted MWNT	0.1 to 7.5 wt.%	Hot-pressed	+12.3 °C at 0.1 wt. %; +11.4 °C at 0.5 wt. %	-1.6 °C at 0.1 wt. %; +0.5 °C at 0.5 wt. %	[121]
MAO[2]-grafted MWNT	0.1 to 3.5 wt.%	In situ polymerization	+3.8 °C at 0.1 wt. %; +7.3 °C at 0.9 wt. %	-0.3 °C at 0.1 wt. %; +1.9 °C at 0.9 wt. %	[82]
Acid treated MWNT	0.01 to 5 wt. %	Solution mixing	+4.5 °C at 0.01 wt. %; +7.1 °C at 1 wt. %	-0.4 °C at 0.01 wt. %; +2.1 °C at 2 wt. %	[136]
p-MWNT	0.05 to 2 wt.%	Latex mixing	+5 °C at 2 wt. %	+5 °C at 2 wt. %	[21]
p-MWNT	5 to 20 wt. %	Melt compounding	+5.8 °C at 5 wt. %; +14.2 °C at 20 wt. %	+2.3 °C at 5 wt. %; +2.2 °C at 20 wt. %	[137]
p-SWNT[3]	0.05 to 2 wt.%	Latex mixing	+15 °C at 2 wt. %	+8 °C at 2 wt. %	[21]
p-SWNT	5 to 20 wt. %	Melt compounding	+13.2 °C at 5 wt. %; +18.3 °C at 20 wt. %	-2.8 °C at 5 wt. %; -1 °C at 20 wt. %	[138]
graphite	2 to 45 wt. %	Melt compounding	+8.1 °C at 10 wt. %; +15.2 °C at 45 wt. %	+3 °C at 10 wt. %; +3.9 °C at 45 wt. %	[137]
rGO	5 to 20 wt. %	Melt compounding	+6.5 °C at 5 wt. %; +10.7 °C at 20 wt. %	-0.6 °C at 5 wt. %; +2.2 °C at 20 wt. %	[137]
$CaCO_3$	1.5 to 3 wt. %	Melt compounding	+7 °C at 1.5 wt. %; +6.3 °C at 3 wt. %	-0.6 °C at 1.5 wt. %; +0.3 °C at 3 wt. %	[139]

1 melting peak maximum 2 MAO: methylaluminoxane 3 SWNT: single wall carbon nanotube

1.4.2.3 Rheological properties

The shear viscosity of neat polymer has two characteristic regions, namely, the Newtonian region and the shear thinning region [140-142]. At low shear rate region, the Newtonian plateau is observed where the shear viscosity is independent of shear rate (Figure 1.14). Beyond the Newtonian region, as the shear rate increases, decreasing of

viscosity is observed (Figure 1.14) due to disentanglement and orientation of the polymer chains [143]. As for the polymer nanocomposites, complex viscosity increases with increasing filler content at low shear rate region because of the confined polymer chain motion by the filler [142]. When the filler content is above the rheological percolation concentration, a non-Newtonian behavior is observed (Figure 1.14) and the shear thinning phenomenon through the whole shear rate region indicates the breakdown of the filler network [142].

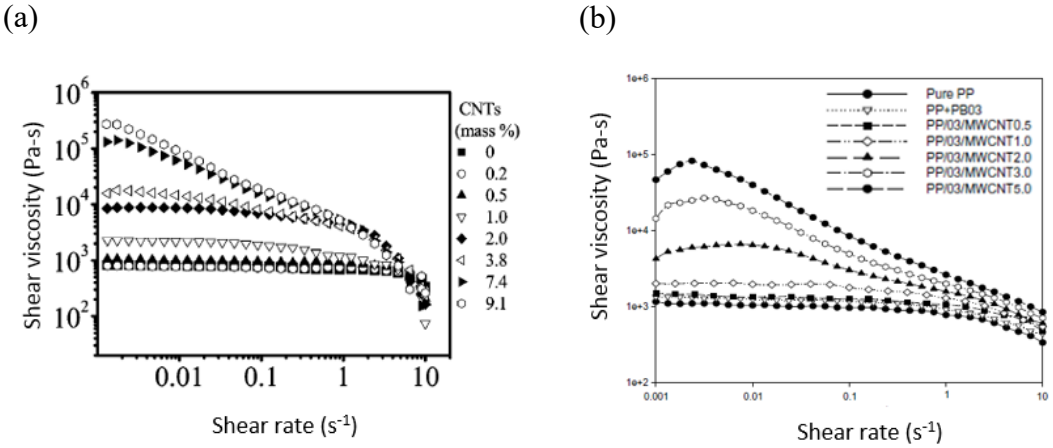

Figure 1.14. Viscosity of PP and PP/MWNT nanocomposites with different MWNT concentrations [141, 142]: (a) from 0.2 to 9.1 wt% CNTs in PP, and (b) from 0.5 to 5 wt% CNTs in PP in the presence of 3 wt% MA-g-PP.

The frequency dependence of loss tangent (tan δ) is measured for observing the liquid-solid transition of polymer composite melts (Figure 1.15a) in which fillers render strong restriction on polymer motion. As shown in Figure 1.15a, tan δ began to increase at low frequency at 7.4 wt. % CNT loading. The author referred this to a rheological symptom of physical gelation showing elastic character of the material [142]. Similarly, in Figure 1.15b, the magnitude of tan δ became smaller while its shape became relatively broad with

peak maximum shifting to higher shear rate region with higher MWNT incorporation. Such phenomenon was again attributed to the reduced polymer chain mobility due to the interconnected MWNT network [144].

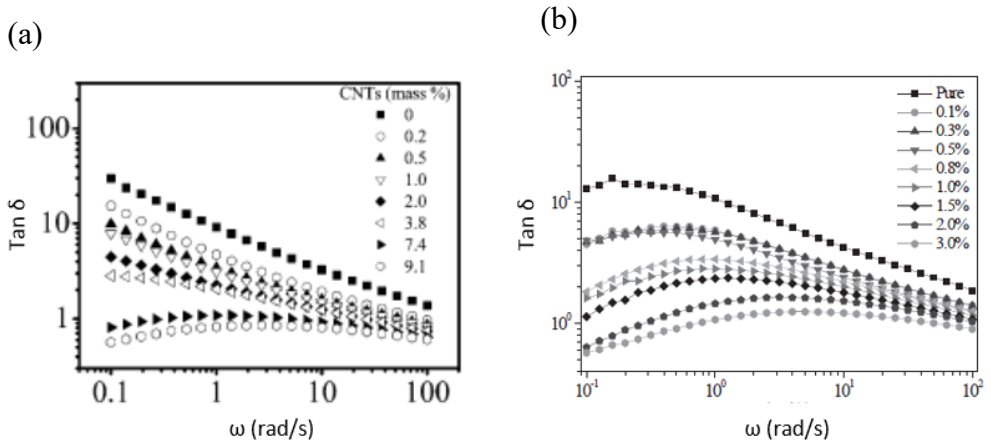

Figure 1.15. Tan δ as a function of angular frequency of PP and PP/MWNT nanocomposites with different MWNT concentrations [142, 144]: (a) from 0.2 to 9.1 wt% CNTs in PP, and (b) from 0.1 to 3 wt% CNTs in PP.

In contrast to neat PP where the terminal behavior at low shear rate region in which G'~ω^1 and G"~ω^2 imply full relaxation of polymer chains [144], with increasing nanotube content, the slope of elastic modulus (G') and loss modulus (G'') becomes less dependent on the shear rate that signifies the solid-liquid transition [144, 145] in the nanocomposite (Figure 1.16). It is also worth noting that G'' showed a relatively moderate increase comparing with G' as MWNT concentration increased. Du et al. [146] determined the rheological percolation threshold of PMMA/SWNT using the simple power law relationship: $G' \propto (m - m_{cG'})^{\beta_{G'}}$, where m is the SWNT mass fraction, $m_{cG'}$ is the rheological percolation threshold and $\beta_{G'}$ is the critical exponent.

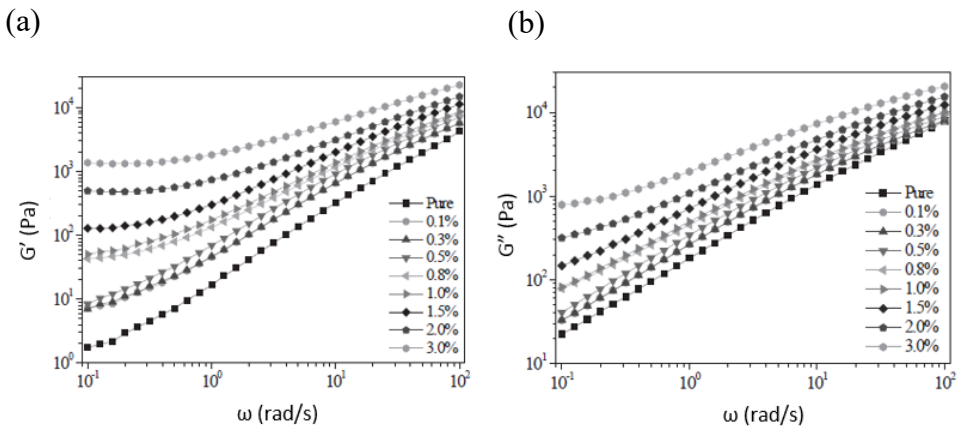

Figure 1.16. (a) Elastic modulus, G' and (b) loss modulus, G'' as a function of angular frequency of PP and PP/MWNT nanocomposites with different MWNT concentration from 0.1 to 3 wt% [144].

1.5 THESIS OBJECTIVES

In the previous sections of this chapter, it is shown that CNTs can act as a nucleating agent for polymer crystallization and as a template for polymer orientation. Potentially, CNT can be a good reinforcement filler for polymers even at low concentrations, owing to its high strength, high modulus, high aspect ratio and high surface area. Moreover, it is possible that the electrically conductive CNTs can alter the electric and dielectric characteristics of PP. However, the above-mentioned advantages can not be obtained unless we can achieve good CNT dispersion in PP.

The objectives of this study are to enhance PP performance through the incorporation of multiwall carbon nanotubes (MWNTs). We hypothesize that tailored CNT/polymer interphase is needed for achieving high performance nanocomposites. This can be done by modifying the CNT surface chemistry by a combination of covalent and non-covalent functionalization. To justify our hypothesis, following studies are carried out and reported in this thesis:

- Develop protocols for dispersing MWNTs in polypropylene (PP).
- Study the structure-property relationship, crystallization, rheological, and thermal behavior of PP/MWNT nanocomposites with various MWNT concentrations from 0.001 wt. % to 1 wt. %. Effect of different type of interphases, i.e. PP/pristine (p-MWNTs), PP/functionalized MWNTs (f-MWNTs), and MA-g-PP/f-MWNT, on these physical properties, will also be compared.
- Study the interfacial shear strength and interphase formation on various PP/MWNT systems. This includes PP containing p-MWNTs and f-MWNTs.
- Investigate the potential of PP/MWNT nanocomposites in electromagnetic interference shielding (EMI shielding) as well as its performance for O_2 and moisture barrier, etc.

1.6 REFERENCES

1. Sharmistha Basu-Dutt, Marilyn L Minus, Rahul Jain, Dhriti Nepal, and Satish Kumar, *Chemistry of carbon nanotubes for everyone.* Journal of Chemical Education, 2011. **89**(2): p. 221-229.

2. Gholamali Farzi, Sohaib Akbar, Emmanuel Beyou, Philippe Cassagnau, and Flavien Melis, *Effect of radical grafting of tetramethylpentadecane and polypropylene on carbon nanotubes' dispersibility in various solvents and polypropylene matrix.* Polymer, 2009. **50**(25): p. 5901-5908.

3. Min-Feng Yu, Oleg Lourie, Mark J Dyer, Katerina Moloni, Thomas F Kelly, and Rodney S Ruoff, *Strength and breaking mechanism of multiwalled carbon nanotubes under tensile load.* Science, 2000. **287**(5453): p. 637-640.

4. Qing Zhang, George Chen, SF Yoon, J Ahn, SG Wang, Q Zhou, Q Wang, and JQ Li, *Thermal conductivity of multiwalled carbon nanotubes.* Physical Review B, 2002. **66**(16): p. 165440.

5. H. Q. Xie, A. Cai, and X. W. Wang, *Thermal diffusivity and conductivity of multiwalled carbon nanotube arrays.* PHYSICS LETTERS A, 2007. **369**(1-2): p. 120-123.

6. M. K. Samani, N. Khosravian, G. C. K. Chen, M. Shakerzadeh, D. Baillargeat, and B. K. Tay, *Thermal conductivity of individual multiwalled carbon nanotubes.* International Journal of Thermal Sciences, 2012. **62**: p. 40-43.

7. TW Ebbesen, HJ Lezec, H Hiura, JW Bennett, HF Ghaemi, and T Thio, *Electrical conductivity of individual carbon nanotubes.* 1996.

8. Bradley A. Newcomb, Han Gi Chae, Prabhakar V. Gulgunje, Kishor Gupta, Yaodong Liu, Dmitri E. Tsentalovich, Matteo Pasquali, and Satish Kumar, *Stress transfer in polyacrylonitrile/carbon nanotube composite fibers.* Polymer, 2014. **55**: p. 2734-2743.

9. L. Xie, F. Xu, F. Qiu, H. Lu, and Y. Yang, *Single-walled carbon nanotubes functionalized with high bonding density of polymer layers and enhanced mechanical properties of composites.* Macromolecules, 2007. **40**(9): p. 3296-3305.

10. Rebekah D. Downes, Ayou Hao, Jin Gyu Park, Yi-Feng Su, Richard Liang, Benjamin D. Jensen, Emilie J. Siochi, and Kristopher E. Wise, *Geometrically constrained self-assembly and crystal packing of flattened and aligned carbon nanotubes.* Carbon, 2015. **93**: 953-966.

11. S. Zhang and S. Kumar, *Shaping polymer particles by carbon nanotubes.* Macromolecular Rapid Communications, 2008. **29**(7): p. 557-561.

12. A. R. Bhattacharyya, T. V. Sreekumar, Liu Tao, S. Kumar, L. A. Ericson, R. H. Hauge, and R. E. Smalley, *Crystallization and orientation studies in polypropylene/single wall carbon nanotube composite.* Polymer, 2003. **44**(8): p. 2373-2377.

13. Zhang Shanju, M. L. Minus, Zhu Lingbo, Wong Ching-Ping, and S. Kumar, *Polymer transcrystallinity induced by carbon nanotubes.* Polymer, 2008. **49**(5): p. 1356-1364.

14. K. A. Anand, U. S. Agarwal, and R. Joseph, *Carbon nanotubes induced crystallization of poly(ethylene terephthalate).* Polymer, 2006. **47**(11): p. 3976-3980.

15. M. L. Minus, H. G. Chae, and S. Kumar, *Polyethylene crystallization nucleated by carbon nanotubes under shear.* ACS Applied Materials and Interfaces, 2012. **4**(1): p. 326-330.

16. M. L. Minus, Chae Han Gi, and S. Kumar, *Single wall carbon nanotube templated oriented crystallization of poly(vinyl alcohol).* Polymer, 2006. **47**(11): p. 3705-3710.

17. S. Kumar, Chae Han Gi, and M. L. Minus, *Oriented and exfoliated single wall carbon nanotubes in polyacrylonitrile.* Polymer, 2006. **47**(10): p. 3494-3504.

18. Y. Y. Zhang, K. N. Song, J. S. Meng, and M. L. Minus, *Tailoring Polyacrylonitrile Interfacial Morphological Structure by Crystallization in the Presence of Single-Wall Carbon Nanotubes.* ACS APPLIED MATERIALS & INTERFACES, 2013. **5**(3): p. 807-814.

19. Bradley A. Newcomb, Lucille A. Giannuzzi, Kevin M. Lyons, Prabhakar Gulgunje, Kishor Gupta, Yaodong Liu, Manjeshwar Kamath, Kenneth McDonald, Jaeyun Moon, Bo Feng, G. P. Peterson, Han Gi Chae, and Satish Kumar, *High resolution transmission electron microscope study on polyacrylonitrile/carbon nanotube based carbon fibers and the effect of structure development on the thermal and electrical conductivities.* Carbon, 2015. **93**: p. 502-514

20. Y. Zhang, N. Tajaddod, K. Song, and M. L. Minus, *Low temperature graphitization of interphase polyacrylonitrile (PAN).* Carbon, 2015. **91**: p. 479-493.

21. H. E. Miltner, C. E. Koning, B. Van Mele, N. Grossiord, K. Lu, and J. Loos, *Isotactic polypropylene/carbon nanotube composites prepared by latex technology. Thermal analysis of camon nanotube induced nucleation.* Macromolecules, 2008. **41**(15): p. 5753-5762.

22. Harutun Karian, *Handbook of polypropylene and polypropylene composites, revised and expanded*. 2003: CRC press.

23. Stern, N., Marom, G., Zhang, L., & Hu, X. (2018). *Comprehensive Composite Materials II*.

24. R Andrews and MC Weisenberger, *Carbon nanotube polymer composites.* Current Opinion in Solid State and Materials Science, 2004. **8**(1): p. 31-37.

25. Malte HG Wichmann, Karl Schulte, and H Daniel Wagner, *On nanocomposite toughness.* Composites Science and Technology, 2008. **68**(1): p. 329-331.

26. AV Desai and MA Haque, *Mechanics of the interface for carbon nanotube–polymer composites.* Thin-walled structures, 2005. **43**(11): p. 1787-1803.

27. Sudip S. *Polypropylene Market to Reach US$133.3 bn by 2023 owing to Globally Rising Demand for Lightweight Vehicles*. 2015; Transparency Market Research.

28. Devesh Tripathi, *Practical guide to polypropylene*. 2002: iSmithers Rapra Publishing.

29. SCO Ugbolue and TC Uzomah, *Effect of exposure time on the mechanical properties of solvent vapor-treated polypropylene films.* Journal of applied polymer science, 1996. **62**(10): p. 1693-1698.

30. Alan S Michaels, Wolf R Vieth, and Haim H Alcalay, *The solubility parameter of polypropylene.* Journal of Applied Polymer Science, 1968. **12**(7): p. 1621-1624.

31. Clive Maier and Theresa Calafut, *Polypropylene: the definitive user's guide and databook*. 1998: William Andrew.

32. DR Norton and A Keller, *The spherulitic and lamellar morphology of melt-crystallized isotactic polypropylene.* Polymer, 1985. **26**(5): p. 704-716.

33. Guien Zhou, Zhiqun He, Jianmin Yu, Zhewen Han, and Guanyi Shi, *Studies on the β-form of isotactic polypropylene, 1. Characterization of the β-form and study of the β - α transition during heating by wide angle X - ray diffraction.* Die Makromolekulare Chemie, 1986. **187**(3): p. 633-642.

34. Ph Tordjeman, C Robert, G Marin, and P Gerard, *The effect of α, β crystalline structure on the mechanical properties of polypropylene.* The European Physical Journal E, 2001. **4**(4): p. 459-465.

35. SC Tjong, JS Shen, and RKY Li, *Mechanical behavior of injection molded β-crystalline phase polypropylene.* Polymer Engineering & Science, 1996. **36**(1): p. 100-105.

36. Andrew J Lovinger, Jaime O Chua, and Carl C Gryte, *Studies on the α and β forms of isotactic polypropylene by crystallization in a temperature gradient.* Journal of Polymer Science: Polymer Physics Edition, 1977. **15**(4): p. 641-656.

37. EJ Addink and J Beintema, *Polymorphism of crystalline polypropylene.* Polymer, 1961. **2**: p. 185-193.

38. Sergio Brückner, Stefano V Meille, Vittorio Petraccone, and Beniamino Pirozzi, *Polymorphism in isotactic polypropylene.* Progress in Polymer Science, 1991. **16**(2): p. 361-404.

39. J. X. Li and W. L. Cheung, *On the deformation mechanisms of β-polypropylene: 1. Effect of necking on β-phase PP crystals.* Polymer, 1998. **39**(26): p. 6935-6940.

40. J. Garbarczyk, T. Sterzynski, and D. Paukszta, *Influence of additives on the structure and properties of polymers. 4. Study of phase transition in isotactic polypropylene by synchrotron radiation.* Polymer communications Guildford, 1989. **30**(5): p. 153-157.

41. Xiaofeng Chen, *Study on crystallization of isotactic polypropylene: effect of stereotacticity defects and nanofillers*. 2007: ProQuest.

42. G Natta and P Corradini, *Structure and properties of isotactic polypropylene.* Il Nuovo Cimento (1955-1965), 1960. **15**: p. 40-51.

43. Stefano V Meille, Dino R Ferro, S Brückner, Andrew J Lovinger, and Frank J Padden, *Structure of. beta.-isotactic polypropylene: a long-standing structural puzzle.* Macromolecules, 1994. **27**(9): p. 2615-2622.

44. Weawkamol Leelapornpisit, Minh - Tan Ton - That, Florence Perrin - Sarazin, Kenneth C Cole, Johanne Denault, and Benoit Simard, *Effect of carbon nanotubes on the crystallization and properties of polypropylene.* Journal of Polymer Science Part B: Polymer Physics, 2005. **43**(18): p. 2445-2453.

45. Brian P Grady, Francisco Pompeo, Robert L Shambaugh, and Daniel E Resasco, *Nucleation of polypropylene crystallization by single-walled carbon nanotubes.* The Journal of Physical Chemistry B, 2002. **106**(23): p. 5852-5858.

46. Shicheng Zhao, Zhi Cai, and Zhong Xin, *A highly active novel β-nucleating agent for isotactic polypropylene.* Polymer, 2008. **49**(11): p. 2745-2754.

47. József Varga, István Mudra, and Gottfried W Ehrenstein, *Highly active thermally stable β-nucleating agents for isotactic polypropylene.* Journal of Applied Polymer Science, 1999. **74**(10): p. 2357-2368.

48. A Turner Jones, Jean M Aizlewood, and DR Beckett, *Crystalline forms of isotactic polypropylene.* Die Makromolekulare Chemie, 1964. **75**(1): p. 134-158.

49. Stefano Valdo Meille and Sergio Brückner, *Non-parallel chains in crystalline gamma-isotactic polypropylene.* Nature, 1989. **340**: p. 455-457.

50. Gürhan Kalay and Michael J Bevis, *Processing and physical property relationships in injection-molded isotactic polypropylene. 2. Morphology and crystallinity.* Journal of Polymer Science Part B: Polymer Physics, 1997. **35**(2): p. 265-291.

51. R Anderson Campbell, Paul J Phillips, and JS Lin, *The gamma phase of high-molecular-weight polypropylene: 1. Morphological aspects.* Polymer, 1993. **34**(23): p. 4809-4816.

52. Bernard Lotz, Bertrand Fillon, Annette Thierry, and Jean-Claude Wittmann, *Low T c growth transitions in isotactic polypropylene: β to α and α to smectic phases.* Polymer bulletin, 1991. **25**(1): p. 101-105.

53. M Aboulfaraj, C G'sell, B Ulrich, and A Dahoun, *In situ observation of the plastic deformation of polypropylene spherulites under uniaxial tension and simple shear in the scanning electron microscope.* Polymer, 1995. **36**(4): p. 731-742.

54. Rui-Ying Bao, Jun Cao, Zheng-Ying Liu, Wei Yang, Bang-Hu Xie, and Ming-Bo Yang, *Towards balanced strength and toughness improvement of isotactic polypropylene nanocomposites by surface functionalized graphene oxide.* Journal of Materials Chemistry A, 2014. **2**(9): p. 3190-3199.

55. Geon-Woong Lee, Sudhakar Jagannathan, Han Gi Chae, Marilyn L. Minus, and Satish Kumar, *Carbon nanotube dispersion and exfoliation in polypropylene and structure and properties of the resulting composites.* Polymer, 2008. **49**: p. 1831-1840.

56. Xing Ping Zhou, Xiao Lin Xie, Fandi Zeng, Robert Kwok Yiu Li, and Yiu Wing Mai. *Properties of polypropylene/carbon nanotube composites compatibilized by maleic anhydride grafted SEBS*. in *Key Engineering Materials*. 2006. Trans Tech Publ.

57. *Carbon Nanotubes (CNT) Market Analysis By Product (Single Walled Carbon Nanotubes (SWCNT), Multi Walled Carbon Nanotubes (MWCNT)), By Application (Polymers, Energy, Electrical & Electronics) And Segment Forecasts To 2022*, *ISBN 978-1-68038-393-5*. 2015.

58. Cheap Tubes.com (2017). Retrieved from https://www.cheaptubes.com/.

59. M. H. Al-Saleh and U. Sundararaj, *Electromagnetic interference shielding mechanisms of CNT/polymer composites.* Carbon, 2009. **47**(7): p. 1738-1746.

60. Kenichi Hayashida and Yoriko Matsuoka, *Electromagnetic interference shielding properties of polymer-grafted carbon nanotube composites with high electrical resistance.* Carbon, 2015. **85**: p. 363-371.

61. H. Ulbricht, G. Moos, and T. Hertel, *Physisorption of molecular oxygen on single-wall carbon nanotube bundles and graphite*. Physical Review B (Condensed Matter and Materials Physics), 2002. **66**(7): p. 075404/1-7.

62. Xiang Lin, Jie Wei Tian, Peng Hao Hu, Rohan Ambardekar, Glen Thompson, Zhi Min Dang, and Phil Coates, *Improved dielectric performance of polypropylene/multiwalled carbon nanotube nanocomposites by solid - phase orientation.* Journal of Applied Polymer Science, 2016. **133**(3).

63. Chensha Li, Tongxiang Liang, Weizhe Lu, Chunhe Tang, Xiaoqing Hu, Maosheng Cao, and Ji Liang, *Improving the antistatic ability of polypropylene fibers by inner antistatic agent filled with carbon nanotubes.* Composites Science and Technology, 2004. **64**: p. 2089-2096.

64. Marilyn MInus and Satish Kumar, *The processing, properties, and structure of carbon fibers.* Jom, 2005. **57**(2): p. 52-58.

65. E-Glass Fibre. Retrieved from https://www.azom.com/properties.aspx?ArticleID=764.

66. Young Ho Choi (2010), *Polyacrylonitrile/carbon nanotube composite fibers: effect of various processing parameters on fiber structure and properties.* (Doctoral dissertation, Georgia Institute of Technology).

67. Yu Min-Feng, O. Lourie, M. J. Dyer, K. Moloni, T. F. Kelly, and R. S. Ruoff, *Strength and breaking mechanism of multiwalled carbon nanotubes under tensile load.* Science, 2000. **287**(5453): p. 637-640.

68. Marilyn L Minus, Han Gi Chae, and Satish Kumar, *Polyethylene crystallization nucleated by carbon nanotubes under shear.* ACS applied materials & interfaces, 2011. **4**(1): p. 326-330.

69. Marilyn L Minus, Han Gi Chae, and Satish Kumar, *Single wall carbon nanotube templated oriented crystallization of poly (vinyl alcohol).* Polymer, 2006. **47**(11): p. 3705-3710.

70. John P Abdou, Karina J Reynolds, Michaela R Pfau, Justin van Staden, Gregory A Braggin, Navid Tajaddod, Marilyn Minus, Víctor Reguero, Juan J Vilatela, and Shanju Zhang, *Interfacial Crystallization of Isotactic Polypropylene Surrounding Macroscopic Carbon Nanotube and Graphene Fibers.* Polymer, 2016.

71. Chintamani Nagesa Ramachandra Rao, BC Satishkumar, A Govindaraj, and Manashi Nath, *Nanotubes.* ChemPhysChem, 2001. **2**(2): p. 78-105.

72. Yongzheng Pan, Lin Li, Siew Hwa Chan, and Jianhong Zhao, *Correlation between dispersion state and electrical conductivity of MWCNTs/PP composites prepared by melt blending.* Composites Part A, 2010. **41**: p. 419-426.

73. C. Q. Li, Q. N. Zhao, H. Deng, C. Chen, K. Wang, Q. Zhang, F. Chen, and Q. Fu, *Preparation, structure and properties of thermoplastic olefin nanocomposites containing functionalized carbon nanotubes.* POLYMER INTERNATIONAL, 2011. **60**(11): p. 1629-1637.

74. Kenan Song, Yiying Zhang, Jiangsha Meng, Emily C Green, Navid Tajaddod, Heng Li, and Marilyn L Minus, *Structural polymer-based carbon nanotube composite fibers: understanding the processing–structure–performance relationship.* Materials, 2013. **6**(6): p. 2543-2577.

75. Tsuyohiko Fujigaya and Naotoshi Nakashima, *Non-covalent polymer wrapping of carbon nanotubes and the role of wrapped polymers as functional dispersants.* Science and Technology of Advanced Materials, 2016. **16.2**: 024802.

76. Zdenko Spitalsky, Dimitrios Tasis, Konstantinos Papagelis, and Costas Galiotis, *Carbon nanotube–polymer composites: chemistry, processing, mechanical and electrical properties.* Progress in polymer science, 2010. **35**(3): p. 357-401.

77. Peng-Cheng Ma, Naveed A Siddiqui, Gad Marom, and Jang-Kyo Kim, *Dispersion and functionalization of carbon nanotubes for polymer-based nanocomposites: a review.* Composites Part A: Applied Science and Manufacturing, 2010. **41**(10): p. 1345-1367.

78. Maxim N Tchoul, Warren T Ford, Giulio Lolli, Daniel E Resasco, and Sivaram Arepalli, *Effect of mild nitric acid oxidation on dispersability, size, and structure of single-walled carbon nanotubes.* Chemistry of Materials, 2007. **19**(23): p. 5765-5772.

79. S Costa and E Borowiak-Palen, *Raman study on doped multiwalled carbon nanotubes.* Acta Physica Polonica-Series A General Physics, 2009. **116**(1): p. 32.

80. Iosif Daniel Rosca, Fumio Watari, Motohiro Uo, and Tsukasa Akasaka, *Oxidation of multiwalled carbon nanotubes by nitric acid.* Carbon, 2005. **43**(15): p. 3124-3131.

81. Yeon-Ran Shin, In-Yup Jeon, and Jong-Beom Baek, *Stability of multi-walled carbon nanotubes in commonly used acidic media.* Carbon, 2012. **50**(4): p. 1465-1476.

82. Anton A Koval'chuk, Alexander N Shchegolikhin, Vitaliy G Shevchenko, Polina M Nedorezova, Alla N Klyamkina, and Alexander M Aladyshev, *Synthesis and properties of polypropylene/multiwall carbon nanotube composites.* Macromolecules, 2008. **41**(9): p. 3149-3156.

83. Andreas Funck and Walter Kaminsky, *Polypropylene carbon nanotube composites by in situ polymerization.* Composites Science and Technology, 2007. **67**(5): p. 906-915.

84. Walter Kaminsky, *Metallocene based polyolefin nanocomposites.* Materials, 2014. **7**(3): p. 1995-2013.

85. Jacob Joseph Habeeb, *Functionalized carbon nanostructures which are soluble in hydrocarbons and method for preparation*. 2014, Google Patents.

86. Chen-Chi Martin Ma, Min-Chien Hsiao, Shu-Hang Liao, Jeng-Chih Weng, Shuo-Jen Lee, and Ay Su, *Fabrication of polymer grafted carbon nanotubes/polypropylene composite bipolar plates for fuel cell*. 2009, Google Patents.

87. Min-Chien Hsiao, Shu-Hang Liao, Yu-Feng Lin, Cheng-Chih Weng, Han Min Tsai, Chen-Chi M Ma, Shie-Heng Lee, Ming-Yu Yen, and Po-I Liu, *Polypropylene-grafted multi-walled carbon nanotube reinforced polypropylene composite bipolar plates in polymer electrolyte membrane fuel cells.* Energy & Environmental Science, 2011. **4**(2): p. 543-550.

88. Zhen Zhou, Shifeng Wang, Lan Lu, Yinxi Zhang, and Yong Zhang, *Functionalization of multi-wall carbon nanotubes with silane and its reinforcement on polypropylene composites.* Composites Science and Technology, 2008. **68**(7): p. 1727-1733.

89. Robert C Haddon and Jian Chen, *Solubilizing Single Walled Carbon Nanotubes by Direct Reaction with Amines and Alkylaryl Amines.* U.S. Patent No. 6,187,823. 13 Feb. 2001.`

90. Benjamin Chu, Benjamin S Hsiao, Hongyang Ma, and Nobuyuki Taniguchi, *Polyolefin nanocomposites with functional ionic liquids and carbon nanofillers*. 2012, Google Patents.

91. Michael J. O'Connell, Sergei M. Bachilo, Chad B. Huffman, Valerie C. Moore, Michael S. Strano, Erik H. Haroz, Kristy L. Rialon, Peter J. Boul, William H. Noon, Carter Kittrell, Jianpeng Ma, Robert H. Hauge, R. Bruce Weisman, and Richard E. Smalley, *Band Gap Fluorescence from Individual Single-Walled Carbon Nanotubes*. 2002, American Association for the Advancement of Science. p. 593.

92. M. J. O'Connell, P. Boul, L. M. Ericson, C. Huffman, Wang Yuhuang, E. Haroz, C. Kuper, J. Tour, K. D. Ausman, and R. E. Smalley, *Reversible water-solubilization of single-walled carbon nanotubes by polymer wrapping.* Chemical Physics Letters, 2001. **342**(3): p. 265-271.

93. Xiefei Zhang, Tao Liu, TV Sreekumar, Satish Kumar, Valerie C Moore, Robert H Hauge, and Richard E Smalley, *Poly (vinyl alcohol)/SWNT composite film.* Nano letters, 2003. **3**(9): p. 1285-1288.

94. Wei Liu, Chuan-Lu Yang, Ying-Tao Zhu, and Mei-shan Wang, *Interactions between single-walled carbon nanotubes and polyethylene/polypropylene/polystyrene/poly (phenylacetylene)/poly (p-phenylenevinylene) considering repeat unit arrangements and conformations: a molecular dynamics simulation study.* The Journal of Physical Chemistry C, 2008. **112**(6): p. 1803-1811.

95. Qingbin Zheng, Qingzhong Xue, Keyou Yan, Lanzhong Hao, Qun Li, and Xili Gao, *Investigation of molecular interactions between SWNT and*

polyethylene/polypropylene/polystyrene/polyaniline molecules. The Journal of Physical Chemistry C, 2007. **111**(12): p. 4628-4635.

96. Jihua Gou, Bob Minaie, Ben Wang, Zhiyong Liang, and Chuck Zhang, *Computational and experimental study of interfacial bonding of single-walled nanotube reinforced composites.* Computational Materials Science, 2004. **31**(3): p. 225-236.

97. Robert J Chen, Yuegang Zhang, Dunwei Wang, and Hongjie Dai, *Noncovalent sidewall functionalization of single-walled carbon nanotubes for protein immobilization.* Journal of the American Chemical Society, 2001. **123**(16): p. 3838-3839.

98. Jian Zhang, J-K Lee, Yue Wu, and Royce W Murray, *Photoluminescence and electronic interaction of anthracene derivatives adsorbed on sidewalls of single-walled carbon nanotubes.* Nano Letters, 2003. **3**(3): p. 403-407.

99. Seiji Tsuzuki, *CH/π interactions.* Annual Reports Section" C"(Physical Chemistry), 2012. **108**: p. 69-95.

100. Asuka Fujii, So-ichi Morita, Mitsuhiko Miyazaki, Takayuki Ebata, and Naohiko Mikami, *A molecular cluster study on activated CH/π interactions: Infrared spectroscopy of aromatic molecule-acetylene clusters.* The Journal of Physical Chemistry A, 2004. **108**(14): p. 2652-2658.

101. D. Baskaran, J. W. Mays, and M. S. Bratcher, *Noncovalent and nonspecific molecular interactions of polymers with multiwalled carbon nanotubes.* CHEMISTRY OF MATERIALS, 2005. **17**(13): p. 3389-3397.

102. Ling Zhang, Tao Tao, and Chunzhong Li, *Formation of polymer/carbon nanotubes nano-hybrid shish–kebab via non-isothermal crystallization.* Polymer, 2009. **50**: p. 3835-3840.

103. V. Ambrogi, G. Gentile, C. Ducati, M. C. Oliva, and C. Carfagna, *Multiwalled carbon nanotubes functionalized with maleated poly(propylene) by a dry mechano-chemical process.* Polymer, 2012. **53**(2): p. 291-299.

104. Henry Kuo Feng Cheng, Yongzheng Pan, Nanda Gopal Sahoo, Kahwei Chong, Lin Li, Siew Hwa Chan, and Jianhong Zhao, *Improvement in properties of multiwalled carbon nanotube/polypropylene nanocomposites through homogeneous dispersion with the aid of surfactants.* Journal of applied polymer science, 2012. **124**(2): p. 1117-1127.

105. K. Prashantha, J. Soulestin, M. F. Lacrampe, P. Krawczak, M. Claes, and G. Dupin, *Multi-walled carbon nanotube filled polypropylene nanocomposites based on masterbatch route: Improvement of dispersion and mechanical properties through PP-g-MA addition.* Express Polymer Letters, 2008. **2**(10): p. 735-745.

106. Satoru Moritomi, Tsuyoshi Watanabe, and Susumu Kanzaki, *Polypropylene compounds for automotive applications.* R&D Report, Sumimoto Kagaku, 2010. **2010**: p. 1-16.

107. Jeffrey L Bahr, Edward T Mickelson, Michael J Bronikowski, Richard E Smalley, and James M Tour, *Dissolution of small diameter single-wall carbon nanotubes in organic solvents?* Chemical Communications, 2001(2): p. 193-194.

108. E Kymakis and GAJ Amaratunga, *Single-wall carbon nanotube/conjugated polymer photovoltaic devices.* Applied Physics Letters, 2002. **80**(1): p. 112-114.

109. Rahul Jain, Young Ho Choi, Yaodong Liu, Marilyn L Minus, Han Gi Chae, Satish Kumar, and Jong-Beom Baek, *Processing, structure and properties of poly (ether ketone) grafted few wall carbon nanotube composite fibers.* Polymer, 2010. **51**(17): p. 3940-3947.

110. Briza Pérez-López, Joan Sola, Salvador Alegret, and Arben Merkoçi, *A carbon nanotube PVC based matrix modified with glutaraldehyde suitable for biosensor applications.* Electroanalysis, 2008. **20**(6): p. 603-610.

111. Jing Liu, Asif Rasheed, Marilyn L Minus, and Satish Kumar, *Processing and properties of carbon nanotube/poly (methyl methacrylate) composite films.* Journal of applied polymer science, 2009. **112**(1): p. 142-156.

112. M Shaheer Akhtar, Jung-Geun Park, Hyun-Cheol Lee, S-K Lee, and O-Bong Yang, *Carbon nanotubes–polyethylene oxide composite electrolyte for solid-state dye-sensitized solar cells.* Electrochimica Acta, 2010. **55**(7): p. 2418-2423.

113. R. Y. Bao, J. Cao, Z. Y. Liu, W. Yang, B. H. Xie, and M. B. Yang, *Towards balanced strength and toughness improvement of isotactic polypropylene nanocomposites by surface functionalized graphene oxide.* Journal of materials chemistry a, 2014. **2**(9): p. 3190-3199.

114. Ph Tordjeman, C. Robert, P. Gerard, and G. Marin, *The effect of α, β crystalline structure on the mechanical properties of polypropylene.* European Physical Journal E, 2001. **4**(4): p. 459-465.

115. Bing-Xing Yang, Jia-Hua Shi, K. P. Pramoda, and Suat Hong Goh, *Enhancement of the mechanical properties of polypropylene using polypropylene-grafted multiwalled carbon nanotubes.* Composites Science and Technology, 2008. **68**: p. 2490-2497.

116. K. Prashantha, J. Soulestin, M. F. Lacrampe, P. Krawczak, G. Dupin, and M. Claes, *Masterbatch-based multi-walled carbon nanotube filled polypropylene nanocomposites: assessment of rheological and mechanical properties.* Composites Science and Technology, 2009. **69**(11): p. 1756-1763.

117. M. M. Zamani, A. Fereidoon, and A. Sabet, *Multi-walled carbon nanotube-filled polypropylene nanocomposites: High velocity impact response and mechanical properties.* Iranian Polymer Journal (English Edition), 2012. **21**(12): p. 887-894.

118. Martin Ganß, Bhabani K. Satapathy, Mahendra Thunga, Roland Weidisch, Petra Pötschke, and Dieter Jehnichen, *Structural interpretations of deformation and fracture behavior of polypropylene/multi-walled carbon nanotube composites.* Acta Materialia, 2008. **56**: p. 2247-2261.

119. Xiao Yan, Zhang Xiaoqing, Cao Wen, Wang Ke, Tan Hong, Zhang Qin, Du Rongni, and Fu Qiang, *Dispersion and mechanical properties of polypropylene/multiwall carbon nanotubes composites obtained via dynamic packing injection molding.* Journal of Applied Polymer Science, 2007. **104**(3): p. 1880-1886.

120. M. Hemmati, G. H. Rahimi, A. B. Kaganj, S. Sepehri, and A. M. Rashidi, *Rheological and Mechanical Characterization of Multi-Walled Carbon Nanotubes/Polypropylene Nanocomposites.* Journal of Macromolecular Science: Physics, 2008. **47**(6): p. 1176-1187.

121. H. Deng, E. Bilotti, R. Zhang, and T. Peijs, *Effective reinforcement of carbon nanotubes in polypropylene matrices.* Journal of Applied Polymer Science, 2010. **118**(1): p. 30-41.

122. P. Liu, K. L. White, H. J. Sue, H. Sugiyama, J. Xi, T. Higuchi, T. Hoshino, R. Ishige, H. Jinnai, and A. Takahara, *Influence of trace amount of well-dispersed carbon nanotubes on structural development and tensile properties of polypropylene.* Macromolecules, 2013. **46**(2): p. 463-473.

123. A. A. Koval'chuk, P. M. Nedorezova, A. N. Klyamkina, A. M. Aladyshev, A. N. Shchegolikhin, and V. G. Shevchenko, *Synthesis and properties of polypropylene/multiwall carbon nanotube composites.* Macromolecules, 2008. **41**(9): p. 3149-3156.

124. Zuo-Jia Wang, Dong-Jun Kwon, Ga-Young Gu, Hak-Soo Kim, Dae-Sik Kim, Choon-Soo Lee, K. Lawrence DeVries, and Joung-Man Park, *Mechanical and interfacial evaluation of CNT/polypropylene composites and monitoring of damage using electrical resistance measurements.* Composites Science and Technology, 2013. **81**: p. 69-75.

125. H. Zhang and Z. Zhang, *Impact behaviour of polypropylene filled with multi-walled carbon nanotubes.* European Polymer Journal, 2007. **43**(8): p. 3197-3207.

126. S. P. Bao and S. C. Tjong, *Mechanical behaviors of polypropylene/carbon nanotube nanocomposites: the effects of loading rate and temperature.* Materials Science & Engineering: A (Structural Materials: Properties, Microstructure and Processing), 2008. **485**(1): p. 508-516.

127. Valerio Causin, Bing-Xing Yang, Carla Marega, Suat Hong Goh, and Antonio Marigo, *Nucleation, structure and lamellar morphology of isotactic polypropylene filled with polypropylene-grafted multiwalled carbon nanotubes.* European Polymer Journal, 2009. **45**(8): p. 2155-2163.

128. Zhen Zhou, Shifeng Wang, Lan Lu, Yong Zhang, and Yinxi Zhang, *Isothermal crystallization kinetics of polypropylene with silane functionalized multi-walled carbon nanotubes.* Journal of Polymer Science Part B: Polymer Physics, 2007. **45**(13): p. 1616-1624.

129. Pawan Verma and Veena Choudhary, *Polypropylene random copolymer/MWCNT nanocomposites: Isothermal crystallization kinetics, structural, and morphological interpretations.* Journal of Applied Polymer Science, 2015. **132**(13).

130. Songmei Zhao, Fenghua Chen, Yingjuan Huang, Jin-Yong Dong, and Charles C Han, *Crystallization behaviors in the isotactic polypropylene/graphene composites.* Polymer, 2014. **55**(16): p. 4125-4135.

131. Vahid Khoshkava, Hesam Ghasemi, and Musa R Kamal, *Effect of cellulose nanocrystals (CNC) on isothermal crystallization kinetics of polypropylene.* Thermochimica Acta, 2015. **608**: p. 30-39.

132. Manli Zhang, Yiqun Liu, Xiaohong Zhang, Jianming Gao, Fan Huang, Zhihai Song, Genshuan Wei, and Jinliang Qiao, *The effect of elastomeric nano-particles on the mechanical properties and crystallization behavior of polypropylene.* Polymer, 2002. **43**(19): p. 5133-5138.

133. Jisheng Ma, Shimin Zhang, Zongneng Qi, Ge Li, and Youliang Hu, *Crystallization behaviors of polypropylene/montmorillonite nanocomposites.* Journal of applied polymer science, 2002. **83**(9): p. 1978-1985.

134. Chien-Chia Chu, Kevin L White, Peng Liu, Xi Zhang, and Hung-Jue Sue, *Electrical conductivity and thermal stability of polypropylene containing well-dispersed multi-walled carbon nanotubes disentangled with exfoliated nanoplatelets.* Carbon, 2012. **50**(12): p. 4711-4721.

135. Bing-Xing Yang, Jia-Hua Shi, KP Pramoda, and Suat Hong Goh, *Enhancement of the mechanical properties of polypropylene using polypropylene-grafted multiwalled carbon nanotubes.* Composites Science and Technology, 2008. **68**(12): p. 2490-2497.

136. Parvathalu Kalakonda, Germano S Iannacchione, Michael Daly, Georgi Y Georgiev, Y Cabrera, R Judith, and Peggy Cebe, *Calorimetric study of nanocomposites of multiwalled carbon nanotubes and isotactic polypropylene polymer.* Journal of Applied Polymer Science, 2013. **130**(1): p. 587-594.

137. Cristhian Garzon, Manfred Wilhelm, Mahdi Abbasi, and Humberto Palza, *Effect of Carbon-Based Particles on the Mechanical Behavior of Isotactic Poly (propylene) s.* Macromolecular Materials and Engineering, 2016.

138. L Valentini, J Biagiotti, MA López-Manchado, S Santucci, and JM Kenny, *Effects of carbon nanotubes on the crystallization behavior of polypropylene.* Polymer Engineering & Science, 2004. **44**(2): p. 303-311.

139. Shihong Chen, Xiangdong Wang, Xiuqing Ma, and Kuisheng Wang, *Morphology and properties of polypropylene/nano-CaCO3 composites prepared by supercritical carbon dioxide-assisted extrusion.* Journal of Materials Science, 2016. **51**(2): p. 708-718.

140. Qinghua Zhang, Fang Fang, Xin Zhao, Yingzhi Li, Meifang Zhu, and Dajun Chen, *Use of dynamic rheological behavior to estimate the dispersion of carbon nanotubes in carbon nanotube/polymer composites.* The Journal of Physical Chemistry B, 2008. **112**(40): p. 12606-12611.

141. Seung Hwan Lee, Myung Wook Kim, Sung Ho Kim, and Jae Ryoun Youn, *Rheological and electrical properties of polypropylene/MWCNT composites prepared with MWCNT masterbatch chips.* European polymer journal, 2008. **44**(6): p. 1620-1630.

142. Dong-Hua Xu, Zhi-Gang Wang, and Jack F Douglas, *Influence of carbon nanotube aspect ratio on normal stress differences in isotactic polypropylene nanocomposite melts.* Macromolecules, 2008. **41**(3): p. 815-825.

143. Ali Rahmatpour and Jamal Aalaie, *Steady shear rheological behavior, mechanical properties, and morphology of the polypropylene/carbon nanotube nanocomposites.* Journal of Macromolecular Science, Part B, 2008. **47**(5): p. 929-941.

144. Yongzheng Pan, Xue Shuang Chan, and Lin Li, *Rheological Study on the Gel-like Behaviour of Carbon Nanotube/Polypropylene Composites: Effect of Interfacial Adhesion.* Nihon Reoroji Gakkaishi, 2013. **41**(3): p. 121-128.

145. K Prashantha, J Soulestin, MF Lacrampe, P Krawczak, G Dupin, and M Claes, *Masterbatch-based multi-walled carbon nanotube filled polypropylene nanocomposites: Assessment of rheological and mechanical properties.* Composites science and technology, 2009. **69**(11): p. 1756-1763.

146. Fangming Du, Robert C Scogna, Wei Zhou, Stijn Brand, John E Fischer, and Karen I Winey, *Nanotube networks in polymer nanocomposites: rheology and electrical conductivity.* Macromolecules, 2004. **37**(24): p. 9048-9055.

CHAPTER 2

POLYPROPYLENE NANOCOMPOSITES WITH POLYMER COATED MULTIWALL CARBON NANOTUBES

2.1 INTRODUCTION

For the ease of processing and to achieve performance, polymer coating of CNTs via non-covalent means is preferable than via covalent bonding. In this chapter, for the first time, we show that the non-covalent coating of PP can be achieved on the functionalized MWNTs (f-MWNTs). This follows a procedure similar to the process used for MA-g-PP coating of f-MWNTs [1]. To achieve this goal, f-MWNTs were dispersed in butanol and then a solution of PP/xylene or MA-g-PP/xylene was added to this dispersion dropwise at a controlled temperature. The solvent was subsequently removed by evaporation to prepare PP/f-MWNT or MA-g-PP/f-MWNT master batches. This approach allowed gradual adsorption of PP or MA-g-PP chains onto f-MWNTs sidewalls. PP coated f-MWNTs are found to be more effective nucleating agent for PP crystallization than MA-g-PP coated f-MWNTs. An attempt was also made to coat PP onto pristine MWNTs (p-MWNT), and the result is presented in Appendix A.

An important aspect for the full utilization of CNT's potentials in nanocomposites is achieving good interaction between the polymer matrix and the carbon nanotubes. Interfacial shear strength (IFSS) of CNT fiber/PP interface was reported to be 10.6 MPa [2], and this can be compared to that of CNT/polyacrylonitrile (13.1 to 44.3 MPa) [3], MWNT/polyetheretherketone (6-14 MPa) [4], and MWNT/polyethylene-butene (47 MPa)

[5]. Yang et al. [6] melt blended PP with 1.5 wt. % of MA-g-PP grafted MWNTs and found that during tensile testing MWNTs were broken instead of being pulled out of the matrix upon tensile failure. CNTs are effective nucleating agents for PP, result in reduced spherulite size, increase the onset of crystallization temperature, and enhanced crystallization rate [7-11]. However, although chemical modification of CNT or PP promotes CNT dispersion in the nanocomposite, it can also bring down the effectiveness of CNT as a nucleating agent for polymer crystallization [12]. PP can form oriented lamella perpendicular to the CNT length and these are termed as trans-crystalline layer [8, 9, 13]. This is different from the commonly encountered spherulitic crystal growth. In some studies, higher crystalline perfection or thicker crystal lamellae were also observed in the presence of CNT which brings about an increase in the melting peak maximum (T_p) [6, 9, 10]. While PP coating of CNTs has been reported via grafting of MA-g-PP [6, 14, 15] or PP [16], there are no literature reports of PP coating on CNT non-covalently. During crystallization in 1,2-Dichlorobenzene (DCB), Zhang *et al.* [17] found that MWNTs were wrapped by a homogenous coating of PE, while PP coating was not observed in that process. In another study, encapsulation of CNT with MA-g-PP via solution mixing approach using butanol and xylene was shown to be successful [1]. It was also demonstrated that via ball milling approach, some MA-g-PP chains adsorbed onto the sidewall of MWNT while PP did not [18]. To the best of our knowledge, there are no literature reports to-date where PP coating of CNTs has been achieved via non-covalent interactions.

2.2 EXPERIMENTAL

2.2.1 Materials

MWNTs (SMW200) used in this study were obtained from SouthWest NanoTechnologies, Inc. (SWeNT), OK. Average number of walls (9 to 10) and average diameter (12 ± 3 nm) were determined from full width at half maximum (FWHM) of 2θ~25.8° integrated peak from wide angle X-ray diffraction (WAXD) and scanning electron microscopy (SEM), respectively. Impurity content in MWNT is about 2 % as determined by thermogravimetric analysis (TGA) in air and length of the tubes is about 4 μm according to the supplier. For functionalization and dispersion of MWNTs, nitric acid (ACS reagent, 70% purchased from Sigma-Aldrich) and butanol (99.9 % purchased from Sigma-Aldrich) was used, respectively. Isotactic PP homopolymer (isotacticity: 97% and polydispersity index: 5) was provided by SABIC, Geleen, Netherlands. MA-g-PP (Epolene E-43 polymer, M_w ~9100 g/mole, acid number of 45 mg KOH/g) was purchased from Westlake Chemical Corporation, TX. Xylene (99.9 % purchased from Sigma-Aldrich) was used as solvent for the two polymers.

2.2.2 MWNT functionalization

Pristine MWNTs (p-MWNTs) were homogenized in deionized water (DI water) for 20 min at 7000 rpm followed by sonication (Branson bath sonicator 3510R-MT, 100 W, 42 kHz) in 10 M nitric acid for 30 min. The mixture was refluxed at 120 °C (oil-bath temperature) for 24 hours and then repeatedly centrifuged and washed in DI water until the pH value reached that of the DI water. The resulting f-MWNT suspension was filtered and washed using butanol followed by 48 hours of sonication at 5 mg/dl concentration.

2.2.3 Master batch preparation

f-MWNT/butanol dispersion (5 mg/dl) was heated to 60 °C while PP or MA-g-PP was dissolved in xylene at 120 °C (190 mg/dl) and added drop-wise into the former with final xylene to butanol ratio equaled to 1:2. The solution was dried at 60 °C under vacuum while stirring in the reactor to obtain PP/f-MWNT or MA-g-PP/f-MWNT master batches containing 5 wt. % f-MWNT. The two master batches were converted to powders using mortar and pestle.

2.2.4 Characterization

Scanning electron microscopy (SEM) was performed on Zeiss Ultra 60 FE-SEM at an accelerating voltage of 2 kV. Average diameter of p-MWNT and polymer coated MWNT was measured using ImageJ software from 40-50 measurements. For transmission electron microscopy (TEM), few drops of f-MWNT/polymer solution mixture slurry was put on the holey carbon coated copper grid. TEM images were obtained by Dr. Yi-Feng Su at Florida State University using a probe corrected scanning/transmission electron microscope JEOL JEM-ARM200cF (JEOL, Ltd, Tokyo, Japan) operated at 80kV. Polarized optical microscope (Leica, DM 2500P) equipped with Linkam THMS 600 heating stage was used to study the crystallization behavior. For this purpose, small pieces of the injection molded samples were heated at 200 °C for 5 minutes and then cooled to 135 °C at a rate of 20 °C/min, and then held at this temperature for monitoring crystallization behavior over a period of time. WAXD was performed using Rigaku MicroMax-002 beam generator (Cu Kα $\boldsymbol{\lambda}$= 0.1542 nm, operating voltage and current 45 kV and 0.65 mA) equipped with R-axis IV++ detector. Raman spectra were collected using a HORIBA XploRA ONE ($\boldsymbol{\lambda}$=785 nm) spectrometer. FTIR spectra of p-MWNT, f-MWNT,

PP, MA-g-PP, and the master batches mixed with potassium bromide (KBr) pellets were recorded using a PerkinElmer Spectrum One FTIR spectrometer with a resolution of 4 cm^{-1}. TGA study was carried out at a heating rate of 10 °C/min under nitrogen using TA Instrument Q500. For DSC study (using TA Instrument Q100), heating rate was 10 °C /min or 2.5 °C /min, and samples were heated from room temperature to 220 °C and then cooled and re-heated at the same rate. Crystallization temperature (T_c) and melt temperature (T_m) were derived from the 1st cooling cycle and the 2nd heating cycles, respectively. Crystallinity was calculated from enthalpy of melting assuming the enthalpy of melting for 100 % crystalline PP to be 207 J/g [1]. Baselines for integration under crystallization and melting peaks were chosen in the range of 90 to 140 °C and 105 to 180 °C, respectively.

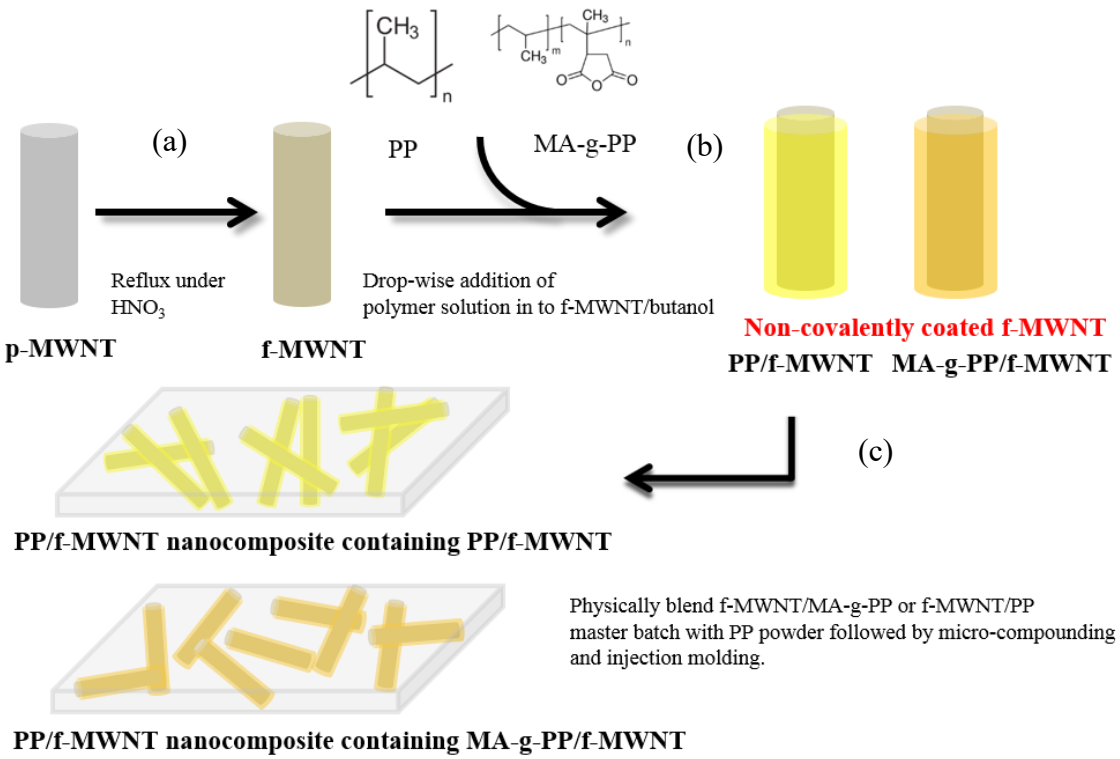

Figure 2.1. Schematic illustration of MWNT functionalization, master batch and nanocomposite preparation (will be discussed in Chapter 3). (a) p-MWNT was treated with 10 M HNO_3 at 120 °C for 24 hours. (b) f-MWNT was sonicated in butanol for 48 hours after which MA-g-PP/xylene or

PP/xylene solution was added drop-by-drop into the f-MWNT/butanol dispersion at 60 °C followed by drying. (c) f-MWNT master batch was physically mixed with PP. The mixture was then micro-compounded and injection molded.

2.3 RESULTS AND DISCUSSIONS

2.3.1 Dispersion of MWNTs and polymer coating

It has been well-documented that carboxyl groups (-COOH) can be introduced on the carbon nanotube surface through nitric acid treatment [1, 19] to promote its solubility in polar solvents such as butanol [1]. While increasing the treatment time, temperature, or other harsher reaction conditions can introduce more functional groups on MWNT [20], these nanotubes can also be fragmented [19, 21] or unzipped [22] under such treatment conditions. Relative degree of functionalization can be estimated by the intensity ratio of D-band (I_D) at ~1300 cm^{-1} (due to disorder in the carbon lattice) to that of the G-band (I_G) at ~1590 cm^{-1} (due to sp^2 longitudinal vibration of graphitic structure) in the Raman spectra (Figure 2.2). Higher Raman I_D/I_G ratio (Table 2.1) suggests a less perfect graphitic structure in f-MWNT compared to that of p-MWNT due to the presence of -COOH groups on f-

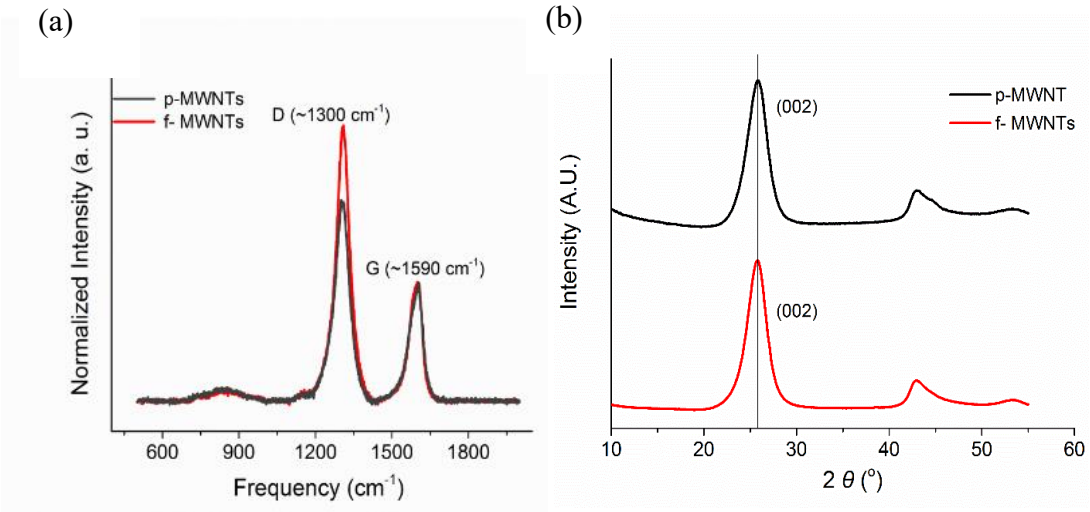

Figure 2.2. (a) Raman spectra and (b) WAXD of p-MWNT and f-MWNT.

MWNT side wall. The presence of carboxylic acid C=O (~1700 cm^{-1}) and OH stretch (~2800-3000 cm^{-1}) in f-MWNT also suggests the successful functionalization from nitric acid treatment (Figure 2.3).

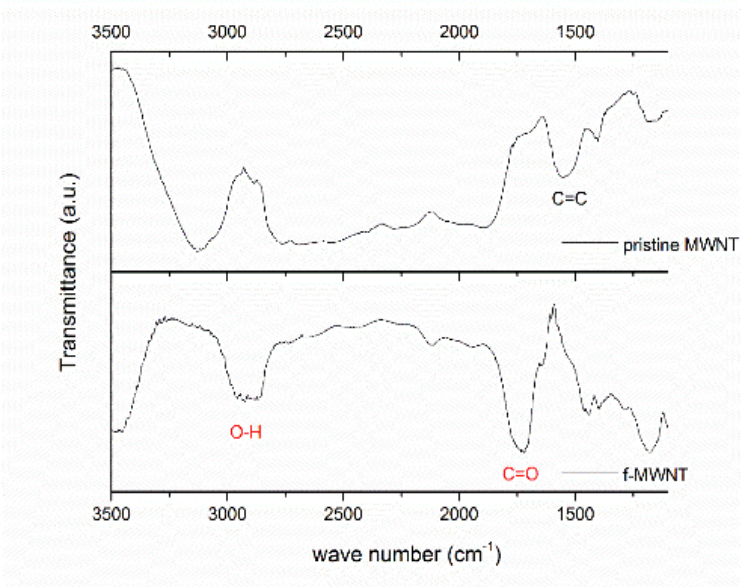

Figure 2.3. FTIR spectra of p-MWNT and f-MWNT.

Average number of walls in p-MWNT and f-MWNTs were determined from the WAXD (002) FWHM using the Scherrer equation (Figure 2.2 and Table 2.1) and the average number of walls in p-MWNTs and f-MWNTs were found to be the same within experimental error. This shows that the process of nitric acid treatment and the introduction of the functional groups in the current study have not destroyed even a single wall of the MWNTs. A comparison of the TEM images of p-MWNT (Figure 2.4a and 2.4b) to those of the f-MWNT (Figure 2.4c and 2.4d) also confirms that there is no significant damage on MWNT sidewall upon nitric acid treatment under conditions used in the current study. Sonicated f-MWNT/butanol dispersions (at 5 mg/dl) were found to be very stable (there was no noticeable phase separation), when kept at room temperature over several months

(Figure 2.4e). By comparison, similarly sonicated p-MWNT/butanol system did not exhibit good dispersion (Figure 2.4f).

Table 2.1. I_D/I_G values from Raman spectra, crystal sizes derived from WAXD (002) integrated peak using Scherrer equation, and the corresponding number of MWNT walls assuming 0.34 nm interlayer separation.

Sample	I_D/I_G (average of 5 different measurements)	(002) Crystal size (nm)	Number of walls
p-MWNT	1.69 ± 0.05	3.17	9.2
f-MWNT	2.32 ± 0.05	3.30	9.6

Figure 2.5 shows SEM images of f-MWNT, PP and MA-g-PP coated f-MWNTs. The average diameter of f-MWNT was 15 nm, PP coated f-MWNT was 23 nm, and that of MA-g-PP coated f-MWNT was 26 nm (Table 2.2). This represents an average PP coating thickness of ~4 nm and of ~5 nm for MA-g-PP. This coating is achieved while the solvent is slowly evaporated at a controlled temperature while stirring. TEM images (Figure 2.6) also confirm the presence of polymer coating on f-MWNTs and show that there is no gap between nanotubes and the polymer, and that f-MWNTs are fully wetted and encapsulated by the two polymers, PP or MA-g-PP, used in this study. The resulting master batches are black powder (Figure 2.4g). In an alternative procedure, when polymer (PP or MA-g-PP)/f-MWNT/butanol/xylene system was precipitated by introducing methanol (rather than removing the solvent by slow evaporation), f-MWNT and the polymers were phase separated. This could be easily seen by white powder (polymer) and black particles (f-MWNTs) (Figure 2.4h). Such coagulation precipitation is one of the common solution-based approaches for preparing PP composites [15, 23], however, the fast dissolution of

CNT-PP precipitants does not provide enough time for the development of PP layer on the CNT surface [23].

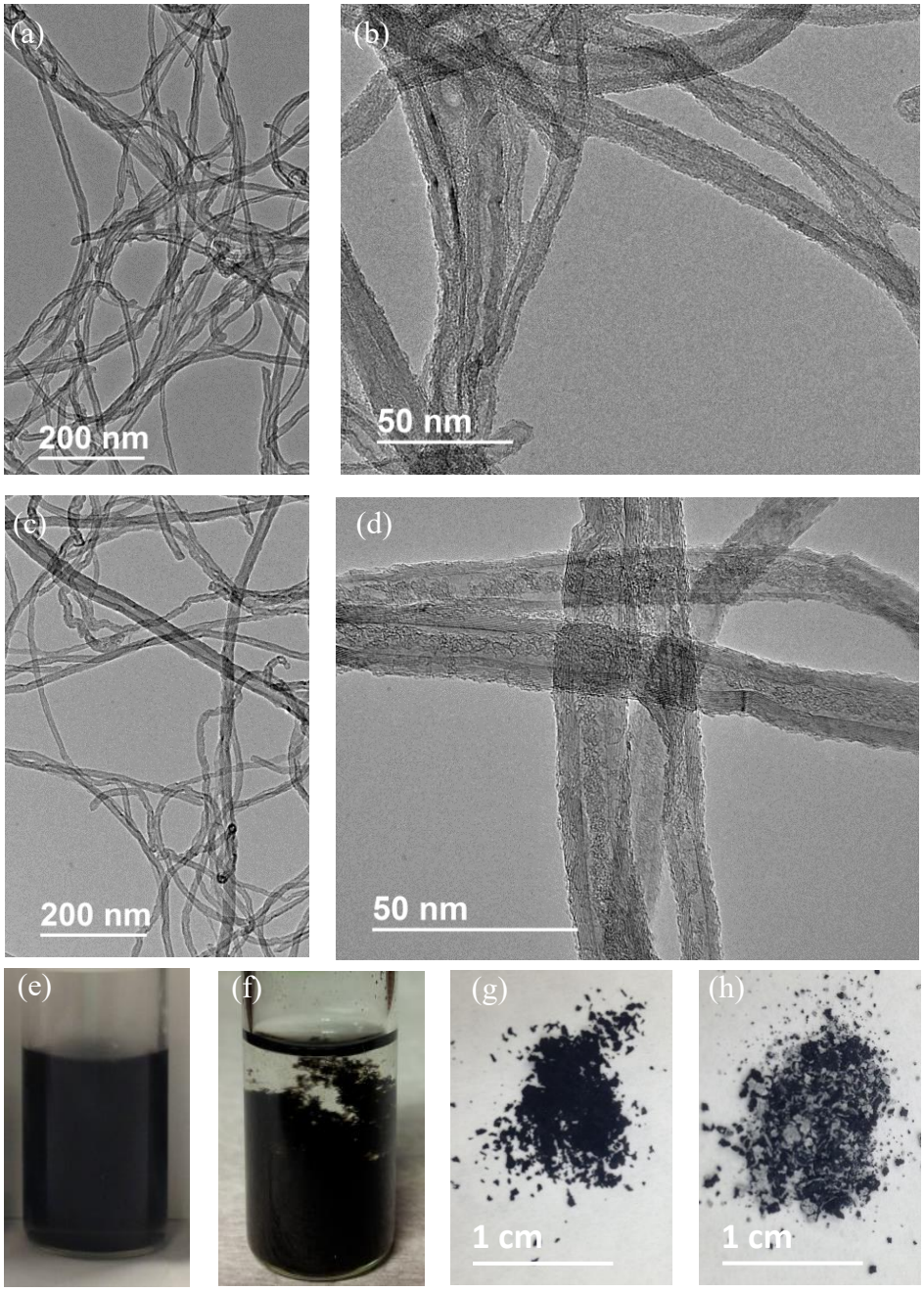

Figure 2.4. TEM images of (a,b) p-MWNTs, (c,d) f-MWNTs. Photographs of (e) f-MWNT/butanol, and (f) p-MWNT/butanol dispersions in vials after 48 hours of sonication. Photographs of PP/f-MWNT master batch prepared (g) via gradual evaporation of solvents (xylene and butanol) and (h) via precipitation using methanol.

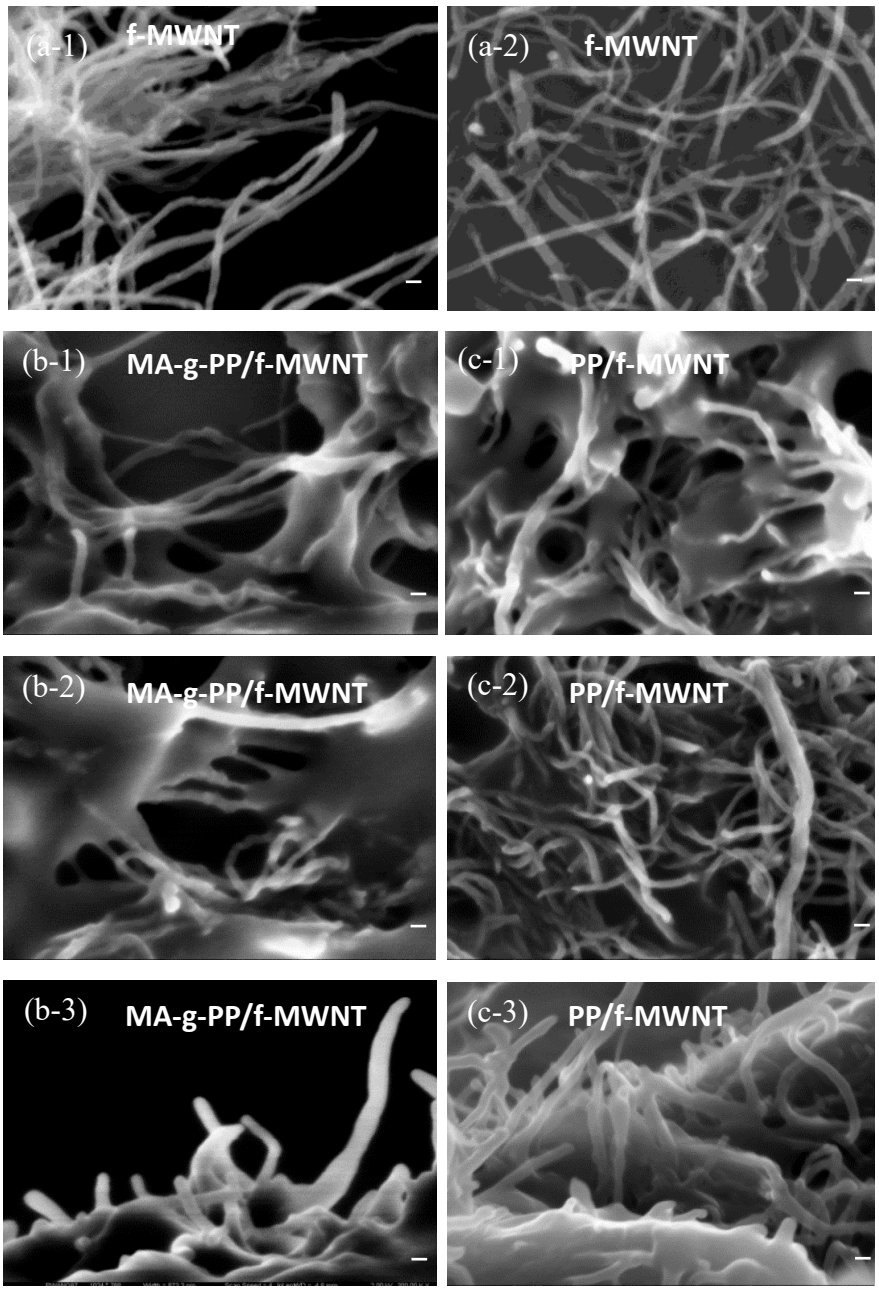

Figure 2.5. SEM images of f-MWNT (a-1) before and (a-2) after sonication in butanol, (b-c) MA-g-PP/f-MWNT and PP/f-MWNT master batches at various stages of solvent evaporation: (b-1) and (c-1) right after the mixing of polymer solution in f-MWNT dispersion (stage 1), (b-2) and (c-2) when 80% of the solvent had been removed by evaporation (stage 2), (b-3) and (c-3) when all solvent had been removed by evaporation (stage 3). Scale bar represents 30 nm. The solvent evaporation refers to the timing of when the sample was removed from the reactor. Of course, for SEM observation, ultimately all solvent was removed. However, after the sample removal from the reactor, the solvent removal was without any stirring. Thus, during stage 1 and stage 2, there is lower probability of polymer coating on the carbon nanotubes than during stage 3.

Table 2.2. Average MWNTs diameters at various stages.

Sample	Diameter (nm)	Sample	Diameter (nm)
p-MWNT	12 ±3		
PP/f-MWNT (stage1)	16 ± 6	MA-g-PP /f-MWNT (stage1)	20 ± 3
PP/f-MWNT (stage2)	19 ± 4	MA-g-PP /f-MWNT (stage2)	22 ± 4
PP/f-MWNT (stage3)	23 ± 5	MA-g-PP /f-MWNT (stage3)	26 ± 6

Note: Various sample stages as defined in the caption of Figure 2.5

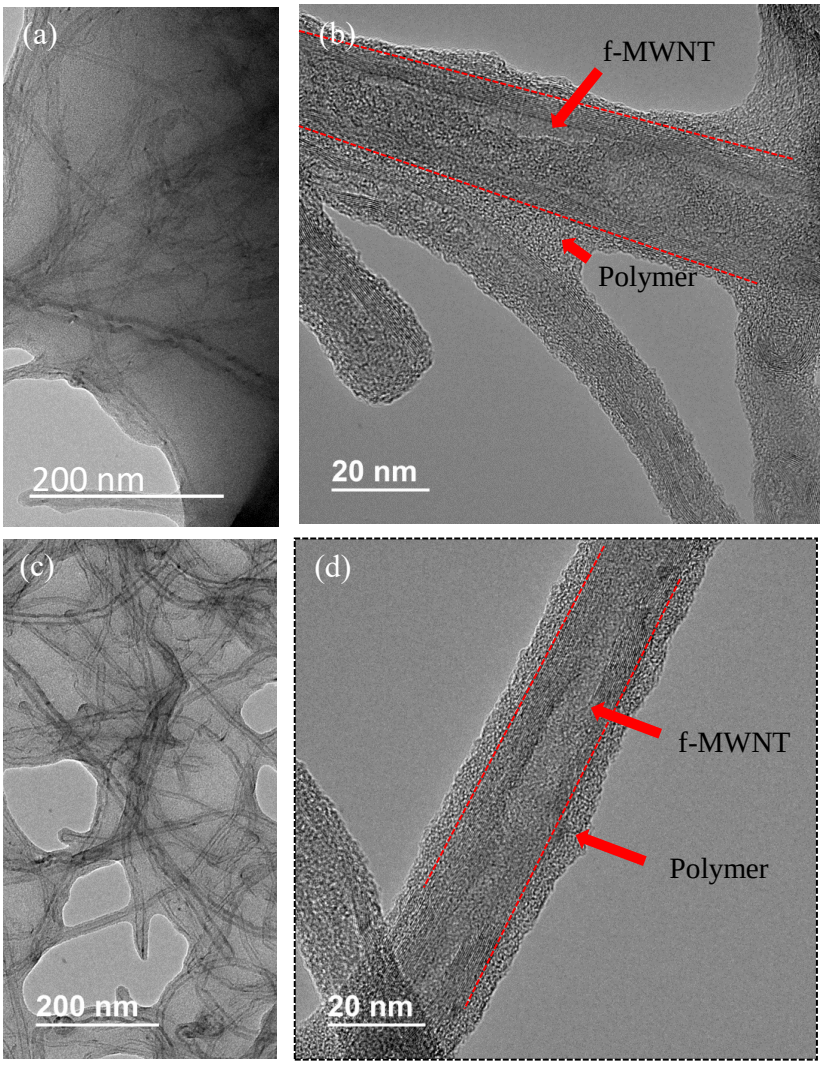

Figure 2.6. TEM images of (a,b) PP/f-MWNT and (c,d) MA-g-PP/f-MWNT master batches. Both PP and MA-g-PP form continuous coating on f-MWNTs, suggesting interaction between nanotubes and the polymers. There appears to be no gap between polymer and f-MWNTs. Images (a) and (c) as well as the arrow in (b) demonstrates the ability of polymer coating on separating vicinity MWNTs.

2.3.2 Stability of interfacial polymer layer on coated MWNT

Thermal stability of MWNTs and that of the two master batches was investigated by TGA in nitrogen (Figure 2.7 and 2.8). The weight loss from 150 to 550 ˚C in the case of f-MWNT is attributed to the loss of functional groups [24], and the loss of the nanotubes catalyzed by the loss of functional groups. Above 550 ˚C, degradation of f-MWNT is facilitated by the defects generation through breaking of the carbon double bonds [25]. Pristine PP and MA-g-PP powders samples, that underwent similar solution preparation and drying process as the two master batches, were used as the control samples for studying the thermal degradation behavior of the two master batches. The degradation temperature (T_d) of the pristine MA-g-PP and PP are at 341 and 331 ˚C, respectively (Figure 2.7a and Figure 2.7b). In the MA-g-PP/f-MWNT master batch, T_d is 21 ˚C higher (at 362 ˚C) than that in pristine MA-g-PP (Figure 2.7a). Similarly, enhancement in T_d was also observed in PP/f-MWNT master batch where a shoulder peak in the derivative plot is observed at 349 ˚C as compared to the peak degradation temperature of 331 ˚C for pristine PP (Figure 2.7b).

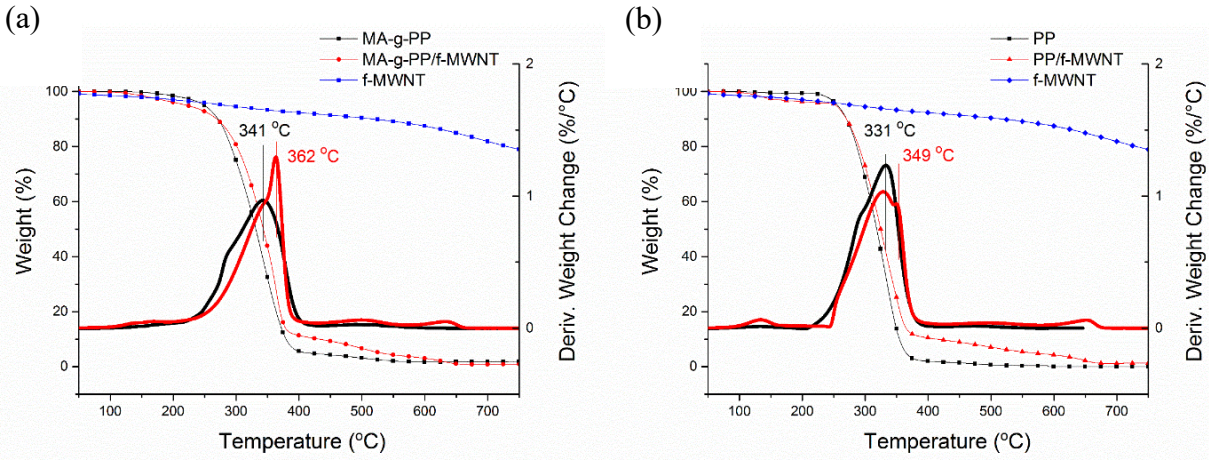

Figure 2.7. TGA under N_2 of (a) MA-g-PP and MA-g-PP/f-MWNT master batch, (b) PP and PP/f-MWNT master batch.

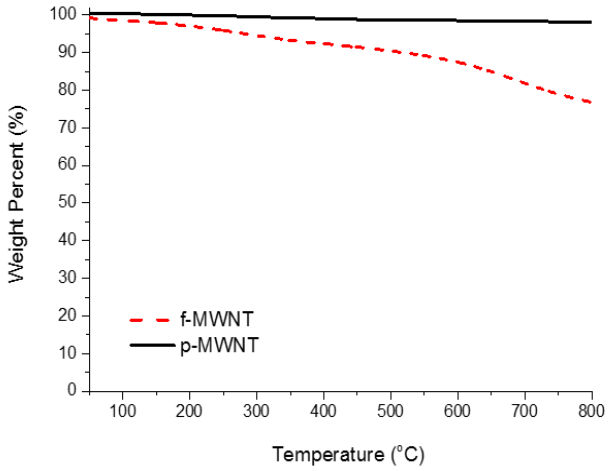

Figure 2.8. TGA under N_2 of f-MWNT and p-MWNT.

Increase in thermal stability of polymer-CNT composite can be attributed to number of factors. Firstly, the barrier effect of CNT network in the nanocomposite can hinder the diffusion of the degradation products from the bulk polymer to the gas phase [26]. Secondly, the interfacial interaction between CNT and polymer restricts the thermal motion of macromolecules that increases the degradation activation energy [26]. Thirdly, CNT demonstrates antioxidant effect due to its strong radical accepting ability that decelerates the degradation process [27]. Therefore, the enhanced T_d of PP/f-MWNT and MA-g-PP/f-MWNT compared with the control samples can be attributed to the combined effect of well dispersed f-MWNT in the polymer matrix as well as to the interphase polymer layer on f-MWNT.

The polymer chain adsorbed onto the f-MWNT sidewalls also demonstrates enhanced chemical stability. While PP is fully soluble in xylene above 70 ˚C, the PP/f-MWNT master batch has lower solubility than the control PP under the same treatment (Figure 2.9). After washing at 70 ˚C in xylene for two hours, dissolved polymer in the

master batch was filtered. The remaining weight of the master batch was about 69% of the original weight, suggesting that 31% polymer dissolved. From scanning electron micrographs, it was determined that the average f-MWNT diameter of PP/f-MWNT after 70 °C xylene washing and filtering, decreased from 23 nm to 20 nm (Table 2.3). The remaining sample, after washing in xylene at 70 °C showed further increase in T_d from 348 °C (before xylene treatment) to 380 °C (Figure 2.10). Similarly, for MA-g-PP/f-MWNT master batch, about 57 % residual weight was observed after 70 °C xylene washing for two hours. After treatment in xylene, the peak degradation temperature did not change significantly (Figure 2.10). When the xylene washing temperature was increased to 120 ° C, almost all PP in the PP/f-MWNTs and MA-g-PP in MA-g-PP/f-MWNT were washed away, and the average f-MWNT diameter decreased close to the value of the uncoated f-MWNT (Table 2.3).

Table 2.3. Average f-MWNTs diameters at various stages (nm).

Sample	Diameter (nm)
f-MWNTs	15 ±3
PP/f-MWNT master batch	23 ± 5
PP/f-MWNT master batch washed with xylene at 70 °C	20 ± 3
PP/f-MWNT master batch washed with xylene at 120 °C	17 ± 4

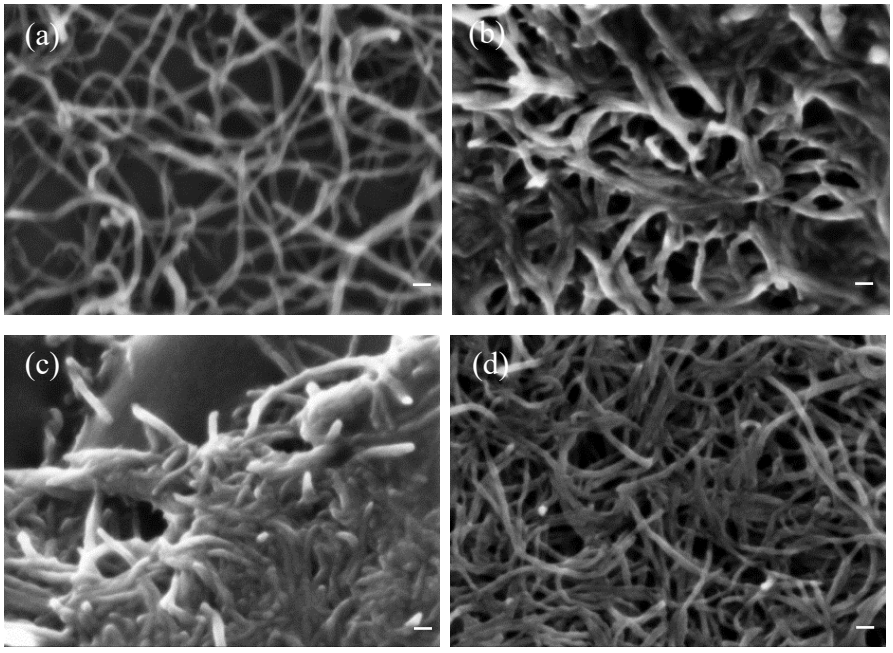

Figure 2.9. SEM images of (a) f-MWNT, (b) PP/f-MWNT master batch, (c) PP/f-MWNT master batch washed in xylene at 70 °C, and (d) PP/f-MWNT master batch washed in xylene at 120 °C. It is shown that the polymer chains adsorbed on MWNTs are not easily washed away. This supports the idea of good interaction between the polymer and f-MWNTs. Scale bar represents 30 nm.

2.3.3 Polymer/f-MWNT interaction

Noncovalent adsorption of electron-rich chemical compounds, e.g. compounds that are highly aromatic in nature, on the sidewall of CNT occurs most commonly through π-π interactions [28, 29]. Interactions can also occur between carbon-hydrogen groups and π system which has also been well studied [30-32]. Presence of CH-π interactions has been identified through peak shifts in FTIR. Examples of these include shifts corresponding to CH stretching (3266 cm^{-1} in acetylene) [31] or CH bending (1450 cm^{-1} in polybutadiene) [32] vibration. Figure 2.11 shows FTIR spectra of PP/f-MWNT and MA-g-PP/MWNT master batches and that for the two control polymers. While there is no change in resonance frequency of the CH_2, CH_3 asymmetry bending vibration (1460 cm^{-1}, 1458 cm^{-1}) [33], and

CH_2 wagging/CH_3 symmetry bending (1377 cm^{-1}) vibration [33] when either PP or MA-g-PP interact with the f-MWNT, slight upshift (from 1256 to 1262 cm^{-1}) in the CH_2 torsion motion is observed in both cases (Figure 2.11). This indicates the presence of intermolecular CH-π interaction between f-MWNT and PP as well as between f-MWNT and MA-g-PP. In addition, in MA-g-PP/f-MWNT, hydrogen bonding between anhydride

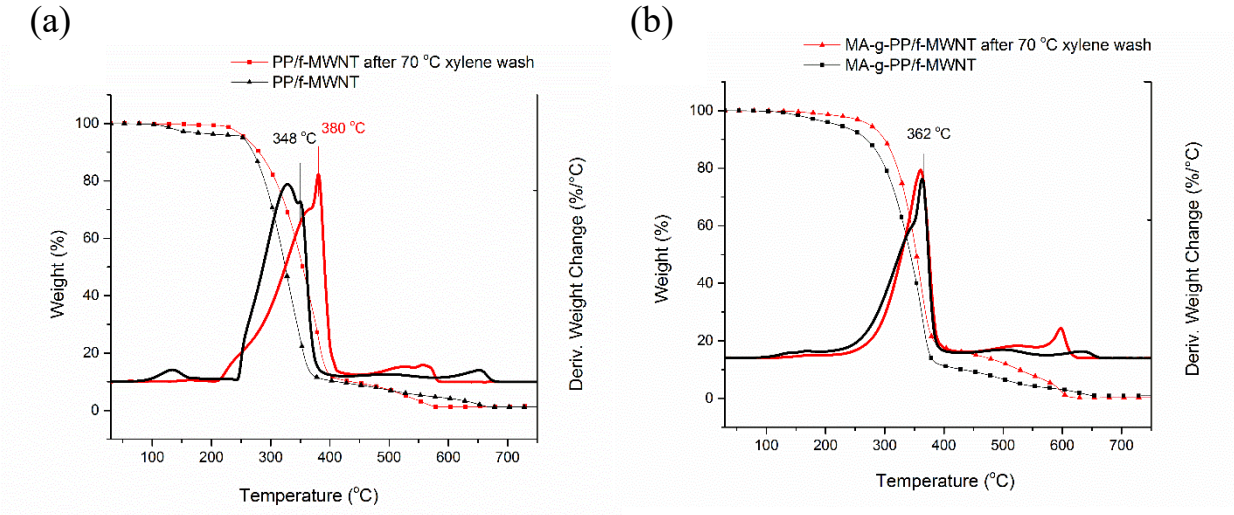

Figure 2.10. TGA under N_2 of (a) PP/f-MWNT, and (b) MA-g-PP/f-MWNT master batches before and after xylene wash at 70 ºC for two hours.

group in MA-g-PP and carbonyl groups in f-MWNT is also observed through down shift in anhydride stretch from 1783 to 1774 cm^{-1} (Figure 2.11) [1]. CH-π interaction is relatively weak and is comparable to van der Waals forces [30], and it is about one-tenth the strength of the hydrogen bond [32]. Thus, it can be concluded that MA-g-PP interacts more strongly (via the formation of hydrogen as well as CH-π interaction) with f-MWNT than PP which only forms CH-π interaction with f-MWNT. Thicker MA-g-PP coating observed on f-MWNTs than that of PP also demonstrates the difference of interaction in two polymers with f-MWNT (Table 2.2).

Figure 2.12 shows the Raman spectra of p-MWNT, f-MWNT, PP/f-MWNT and MA-g-PP/f-MWNT where a more pronounced peak shift is observed in D band rather than G and D* bands (Figure 2.13). After functionalization, the upshift of D band from 1301 to 1313 cm^{-1} is related to the direct electron charge transfer from the nanotube to acceptor carbonyl groups [34]. When f-MWNTs are encapsulated by the polymer sheath, strain is developed within the graphitic lattice that affects the vibration motion of C-C bond due to the CH-π interactions or hydrogen bonds. Downshift of D band from 1313 to 1307 cm^{-1} in both PP/f-MWNT and MA-g-PP/f-MWNT master batches suggests strain induced in the f-MWNTs (Figure 2.12). Similarly, downshift of both D and G bands in CNTs were also reported due to the stretching and weakening of carbon-carbon (C-C) bond in CNT during tensile deformation [3] or uniaxial bending [35]. Interestingly, although MA-g-PP interacts more strongly with f-MWNT through hydrogen bonds and CH-π interaction compared with

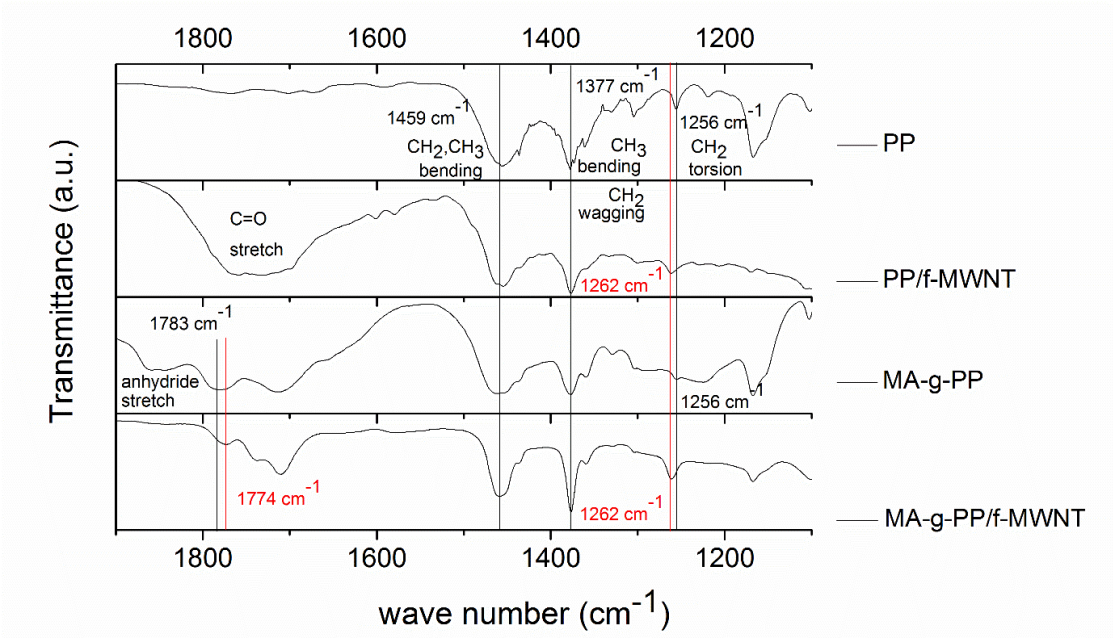

Figure 2.11. FTIR spectra of PP/f-MWNT and MA-g-PP/f-MWNT master batches. PP and MA-g-PP spectra are also given for comparison.

PP where only CH-π interaction exists, the D band resonance frequency exhibits the same shift of 6 cm^{-1} in f-MWNT coated with either PP or MA-g-PP.

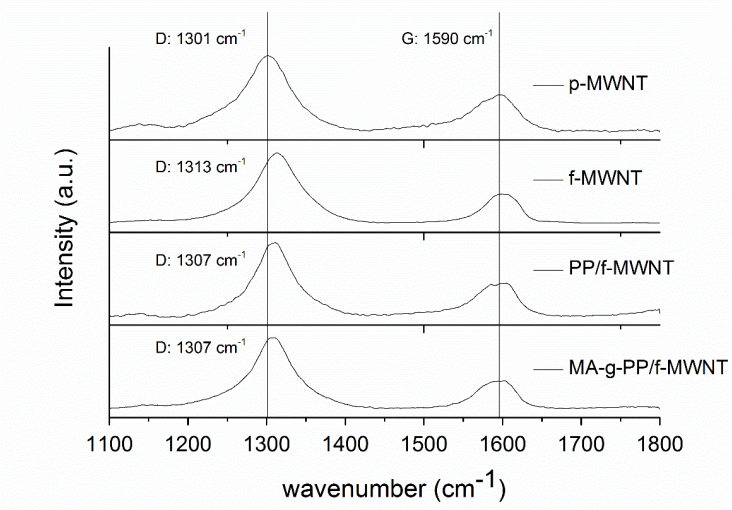

Figure 2.12. Raman spectra of p-MWNT, f-MWNT, PP/f-MWNT, & MA-g-PP/f-MWNT master batches.

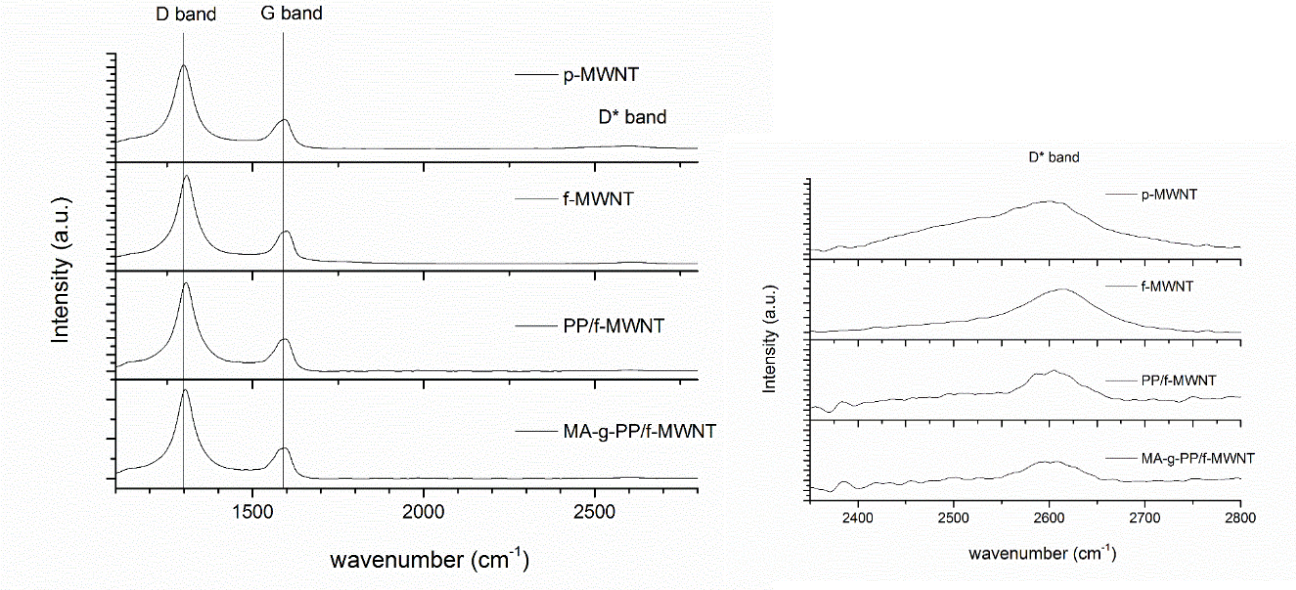

Figure 2.13. Raman spectra (D band, G band and D* band) of p-MWNT, f-MWNT, and PP/f-MWNT, MA-g-PP/f-MWNT master batches.

2.3.4 f-MWNT dispersion in the master batches

The f-MWNT dispersion in both PP and MA-g-PP based master batches was investigated under molten state using optical microscopy (Figure 2.14). Dark regions in PP/f-MWNT master batch in Figure 2.14a are regions with high f-MWNT concentration. As compared to PP/f-MWNT master batch, MA-g-PP/f-MWNT master batch exhibits greater homogeneity (Figure 2.14a and 2.14b) in terms of f-MWNT dispersion in the polymer matrix. This result is not surprising, as MA-g-PP is often used as a compatibilizer to achieve good CNT dispersion in PP/CNT nanocomposites [1, 18, 36, 37]. f-MWNT dispersion can be further improved by increasing shear rates during melt compounding (Figure 2.15).

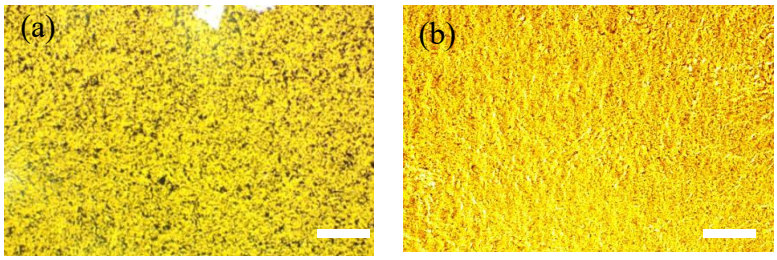

Figure 2.14. Optical micrographs of (a) PP/f-MWNT, and (b) MA-g-PP/f-MWNT master batches. Scale bar represents 100 μm.

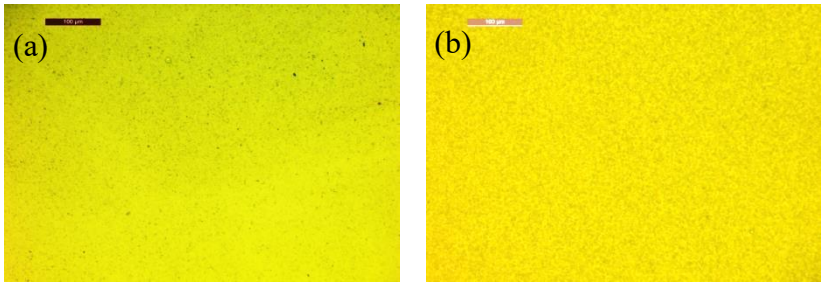

Figure 2.15. Optical micrographs of PP/f-MWNT (0.1 wt. %) nanocomposites containing MA-g-PP/f-MWNT master batch. (a) micro-compounding (using 15 cc micro-compounder from Xplore Instruments, Netherlands) at 200 rpm screw speed, and (b) compounded using twin screw extruder (Brabender KETSE 12/36 twin screw extruder, TSE) at 500 rpm screw speed. The latter shows much improved f-MWNT dispersion than the former. Scale bar represents 100 μm.

2.3.5 Melting and crystallization behavior of the master batches

Table 2.4 provides DSC melting and crystallization data of the two master batches and for the respective control samples. To ensure comparable control samples for the DSC study, PP and MA-g-PP samples were dissolved in xylene and then xylene was evaporated. The vacuum dried polymer samples were grounded using mortar and pestle. WAXD shows only α-form crystal in both PP/f-MWNT and MA-g-PP/f-MWNT master batches (Figure 2.16). Addition of f-MWNT resulted in increased crystallization temperature (T_c) and decreased FWHM of the crystallization peak as compared to that of the unfilled polymer in both PP and MA-g-PP systems. Increased crystallization temperature suggests enhanced nucleation rate while a decreased FWHM of the crystallization peak suggests narrower crystal size distribution [1, 7]. The effect is more evident in PP/f-MWNT where 4 $^{\circ}$C increase of T_c is observed as compared to 2 $^{\circ}$C increase in MA-g-PP/f-MWNT as compared to their respective control samples (Figure 2.17a and 2.17b, Table 2.4).

In the case of PP master batch, T_p shifted from 160 to 162 $^{\circ}$C (Table 2.4, Figure 2.17d), suggesting higher crystal perfection and/or larger crystals [9] in PP/f-MWNT containing sample than in the control. Double melting endotherm peak is observed in the MA-g-PP based samples (Figure 2.17c). Smaller and imperfect crystals melt at lower temperature, and then recrystallize into more perfect and/or larger crystals upon further heating. These more perfect or larger crystals melt at higher temperature and contribute to the double melting peaks in the DSC curve (Figure 2.17c) [38].

Table 2.4. DSC data of PP/f-MWNT, MA-g-PP/f-MWNT master batches at 10 °C/min ramping rate.

Sample	T_o[1] (°C)	T_c (°C)	FWHM of T_c peak	T_p (°C)	Crystallinity (%)
MA-g-PP	119.2	115.5	5.4	147/155	--[2]
MA-g-PP/f-MWNTs master batch	120.5	117.5	4.9	146/154	--[2]
PP	123.6	119.0	5.7	160	51
PP/f-MWNTs master batch	125.0	123.0	3.4	162	48

1 onset of crystallization temperature (T_o), Crystallization temperature ($T_{c)}$, and melting peak maximum (T_p)
2 Enthalpy of melting for 100% crystalline MA-g-PP was not available.

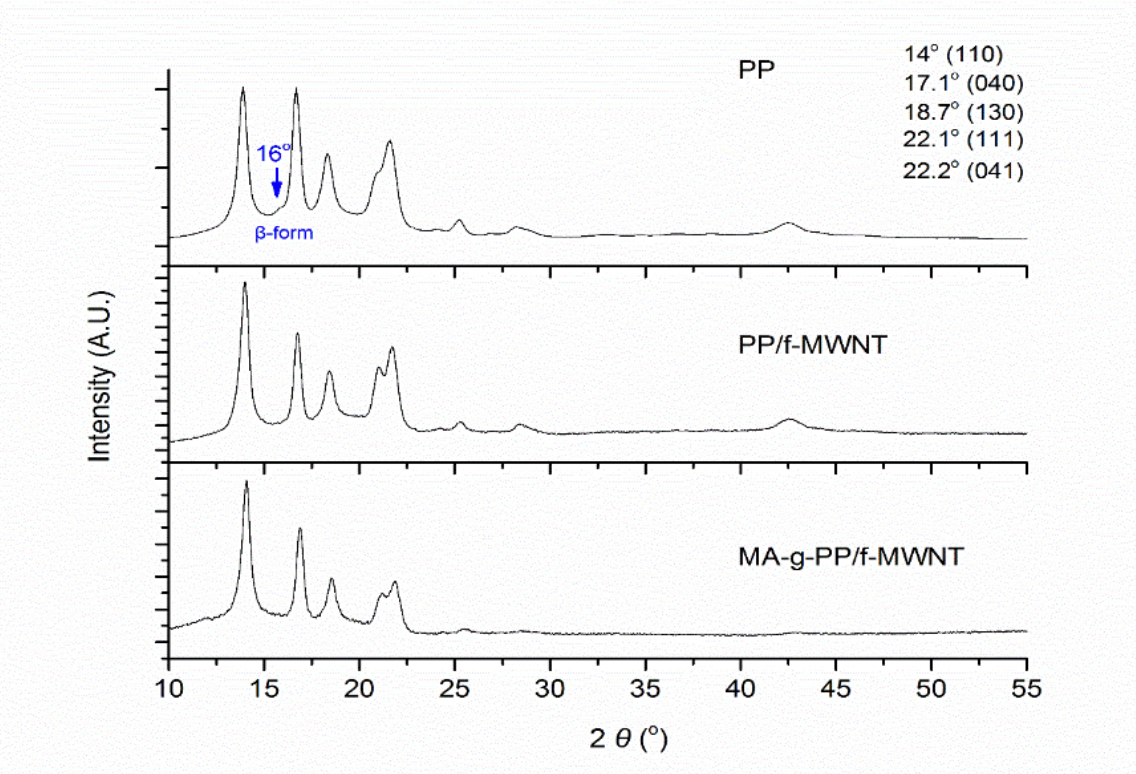

Figure 2.16. WAXD of control PP, PP/f-MWNT and MA-g-PP/f-MWNT master batches.

The crystallization and melting behavior of the PP/MWNT nanocomposites prepared from PP/f-MWNT and MA-g-PP/f-MWNT mater batches, as well as from the p-MWNT, will be studied and presented in Chapter 5.

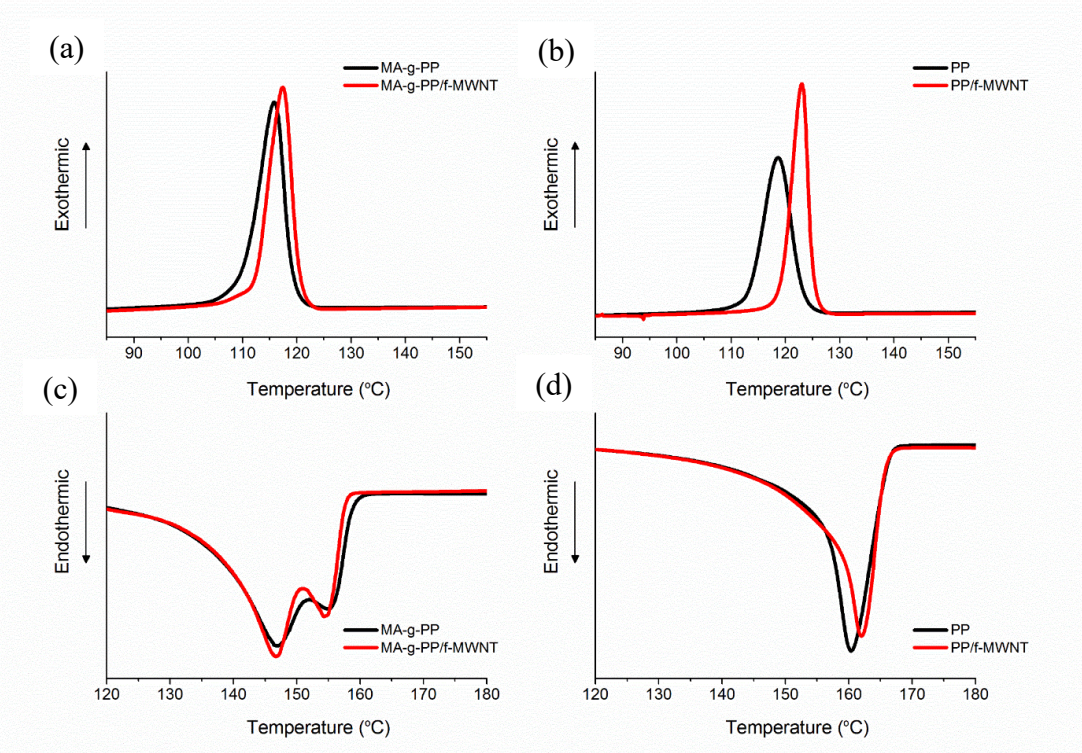

Figure 2.17. DSC plots of (a,c) first cooling cycles of MA-g-PP and MA-g-PP/f-MWNT master batch, and (b,d) second heating cycles of PP and PP/f-MWNT master batch at 10 °C/min ramping rate. T_c and T_p were measured from 1st cooling cycle and 2nd heating cycle, respectively.

2.4 CONCLUSIONS

Polypropylene (PP) or maleic anhydride grafted polypropylene (MA-g-PP) master batches containing 5 wt. % functionalized multiwall carbon nanotubes (f-MWNTs) were prepared in butanol/xylene solvent mixture. For this purpose, MWNTs were functionalized using nitric acid. Through SEM and TEM imaging, 4 to 5 nm thick layer of PP and MA-g-PP polymer coating is observed on the MWNT sidewall in the two master batches. As

compared to the control PP and MA-g-PP, the thermal degradation temperature of the two master batches was about 20 °C higher (under nitrogen atmosphere). After washing the PP/f-MWNT master batch in xylene at 70 °C, thermal degradation temperature of the remaining PP in this xylene washed sample was 50 °C higher than that of the control PP. The two master batches also exhibited better solvent resistance than the respective control polymers. These observations provide evidence of interaction between the interfacial polymers and the f-MWNTs. Evidence of CH_2-$\boldsymbol{\pi}$ interaction between PP and f-MWNTs, MA-g-PP and MWNTs, as well as hydrogen bonding between MA-g-PP and f-MWNTs was obtained via FTIR spectroscopy. More pronounced enhancement of both the crystallization (T_c) and melting (T_p) temperatures as compared to the respective control samples was observed in the PP/f-MWNTs master batch than in the MA-g-PP/f-MWNTs master batch, although f-MWNT dispersion was better in the latter case. Both master batches were effective in promoting PP crystallization, however in this regard PP/f-MWNT master batch proved to be more effective than MA-g-PP/f-MWNT master batch although superior f-MWNTs dispersion can be achieved using the MA-g-PP/f-MWNTs master batch.

2.5 REFERENCES

1. Geon-Woong Lee, Sudhakar Jagannathan, Han Gi Chae, Marilyn L. Minus, and Satish Kumar, *Carbon nanotube dispersion and exfoliation in polypropylene and structure and properties of the resulting composites.* Polymer, 2008. **49**: p. 1831-1840.

2. Yao Gao, Yi Wu, Maoqing Liang, and Qiang Fu, *Transcrystallinity and relevant interfacial strength induced by carbon nanotube fibers in a polypropylene matrix.* Journal of Applied Polymer Science, 2015. **132**(25).

3. Bradley A. Newcomb, Han Gi Chae, Prabhakar V. Gulgunje, Kishor Gupta, Yaodong Liu, Dmitri E. Tsentalovich, Matteo Pasquali, and Satish Kumar, *Stress transfer in polyacrylonitrile/carbon nanotube composite fibers.* Polymer, 2014. **55**: p. 2734-2743.

4. Terumasa Tsuda, Toshio Ogasawara, Fei Deng, and Nobuo Takeda, *Direct measurements of interfacial shear strength of multi-walled carbon nanotube/PEEK composite using a nano-pullout method.* Composites Science and Technology, 2011. **71**(10): p. 1295-1300.

5. Asa H Barber, Sidney R Cohen, and H Daniel Wagner, *Measurement of carbon nanotube–polymer interfacial strength.* Applied Physics Letters, 2003. **82**(23): p. 4140-4142.

6. Bing-Xing Yang, Jia-Hua Shi, K. P. Pramoda, and Suat Hong Goh, *Enhancement of the mechanical properties of polypropylene using polypropylene-grafted multiwalled carbon nanotubes.* Composites Science and Technology, 2008. **68**: p. 2490-2497.

7. A. R. Bhattacharyya, T. V. Sreekumar, Liu Tao, S. Kumar, L. A. Ericson, R. H. Hauge, and R. E. Smalley, *Crystallization and orientation studies in polypropylene/single wall carbon nanotube composite.* Polymer, 2003. **44**(8): p. 2373-2377.

8. Zhang Shanju, M. L. Minus, Zhu Lingbo, Wong Ching-Ping, and S. Kumar, *Polymer transcrystallinity induced by carbon nanotubes.* Polymer, 2008. **49**(5): p. 1356-1364.

9. H. E. Miltner, C. E. Koning, B. Van Mele, N. Grossiord, K. Lu, and J. Loos, *Isotactic polypropylene/carbon nanotube composites prepared by latex technology. Thermal analysis of camon nanotube induced nucleation.* Macromolecules, 2008. **41**(15): p. 5753-5762.

10. Anton A Koval'chuk, Alexander N Shchegolikhin, Vitaliy G Shevchenko, Polina M Nedorezova, Alla N Klyamkina, and Alexander M Aladyshev, *Synthesis and properties of polypropylene/multiwall carbon nanotube composites.* Macromolecules, 2008. **41**(9): p. 3149-3156.

11. Chien-Chia Chu, Kevin L. White, Peng Liu, Xi Zhang, and Hung-Jue Sue, *Electrical conductivity and thermal stability of polypropylene containing well-dispersed multi-walled carbon nanotubes disentangled with exfoliated nanoplatelets.* Carbon, 2012. **50**: p. 4711-4721.

12. George Z Papageorgiou, Maria Nerantzaki, Ifigeneia Grigoriadou, Dimitrios G Papageorgiou, Konstantinos Chrissafis, and Dimitrios Bikiaris, *Isotactic Polypropylene/Multi-Walled Carbon Nanotube Nanocomposites: The Effect of Modification of MWCNTs on Mechanical Properties and Melt Crystallization.* Macromolecular Chemistry and Physics, 2013. **214**(21): p. 2415-2431.

13. K. Lu, J. Loos, N. Grossiord, C. E. Koning, H. E. Miltner, and B. Van Mele, *Carbon nanotube/isotactic polypropylene composites prepared by latex technology: Morphology analysis of CNT-induced nucleation.* Macromolecules, 2008. **41**(21): p. 8081-8085.

14. M. C. Hsiao, C. C. Weng, H. M. Tsai, C. C. M. Ma, S. H. Lee, M. Y. Yen, P. I. Liu, S. H. Liao, and Y. F. Lin, *Polypropylene-grafted multi-walled carbon nanotube reinforced polypropylene composite bipolar plates in polymer electrolyte membrane fuel cells.* Energy and Environmental Science, 2011. **4**(2): p. 543-550.

15. Q. L. He, T. T. Yuan, X. R. Yan, D. W. Ding, Q. Wang, Z. P. Luo, T. D. Shen, S. Y. Wei, D. P. Cao, and Z. H. Guo, *Flame-Retardant Polypropylene/Multiwall Carbon Nanotube Nanocomposites: Effects of Surface Functionalization and Surfactant Molecular Weight.* MACROMOLECULAR CHEMISTRY AND PHYSICS, 2014. **215**(4): p. 327-340.

16. Gholamali Farzi, Sohaib Akbar, Emmanuel Beyou, Philippe Cassagnau, and Flavien Melis, *Effect of radical grafting of tetramethylpentadecane and polypropylene on carbon nanotubes' dispersibility in various solvents and polypropylene matrix.* Polymer, 2009. **50**: p. 5901-5908.

17. Ling Zhang, Tao Tao, and Chunzhong Li, *Formation of polymer/carbon nanotubes nano-hybrid shish–kebab via non-isothermal crystallization.* Polymer, 2009. **50**: p. 3835-3840.

18. V. Ambrogi, G. Gentile, C. Ducati, M. C. Oliva, and C. Carfagna, *Multiwalled carbon nanotubes functionalized with maleated poly(propylene) by a dry mechano-chemical process.* Polymer, 2012. **53**(2): p. 291-299.

19. M. N. Tchoul, W. T. Ford, G. Lolli, D. E. Resasco, and S. Arepalli, *Effect of mild nitric acid oxidation on dispersability, size, and structure of single-walled carbon nanotubes.* Chemistry of Materials, 2007. **19**(23): p. 5765-5772.

20. Shin Yeon-Ran, Jeon In-Yup, and Baek Jong-Beom, *Stability of multi-walled carbon nanotubes in commonly used acidic media.* Carbon, 2012. **50**(4): p. 1465-1476.

21. Iosif Daniel Rosca, Fumio Watari, Motohiro Uo, and Tsukasa Akasaka, *Oxidation of multiwalled carbon nanotubes by nitric acid.* Carbon, 2005. **43**(15): p. 3124-3131.

22. Biwei Xiao, Xifei Li, Xia Li, Biqiong Wang, Craig Langford, Ruying Li, and Xueliang Sun, *Graphene nanoribbons derived from the unzipping of carbon nanotubes: controlled synthesis and superior lithium storage performance.* The Journal of Physical Chemistry C, 2013. **118**(2): p. 881-890.

23. IN Mazov, NA Rudina, AV Ishchenko, VL Kuznetsov, AI Romanenko, OB Anikeeva, VI Suslyaev, and VA Zhuravlev, *Structural and physical properties of MWNT/polyolefine composites.* Fullerenes, Nanotubes and Carbon Nanostructures, 2012. **20**(4-7): p. 510-518.

24. Yasunori Tsukahara, Tomohisa Yamauchi, Tadashi Kawamoto, and Yuji Wada, *Functionalization of multi-walled carbon nanotubes realized by microwave-driven chemistry inducing dispersibility in liquid media.* Bulletin of the Chemical Society of Japan, 2008. **81**(3): p. 387-392.

25. Rike Yudianti, Holia Onggo, Y Saito Sudirman, Tadahisa Iwata, and Jun-ichi Azuma, *Analysis of functional group sited on multi-wall carbon nanotube surface.* Open Materials Science Journal, 2011. **5**: p. 242-247.

26. D Bikiaris, *Can nanoparticles really enhance thermal stability of polymers? Part II: an overview on thermal decomposition of polycondensation polymers.* Thermochimica Acta, 2011. **523**(1): p. 25-45.

27. PCP Watts, PK Fearon, WK Hsu, NC Billingham, HW Kroto, and DRM Walton, *Carbon nanotubes as polymer antioxidants.* Journal of Materials Chemistry, 2003. **13**(3): p. 491-495.

28. Robert J Chen, Yuegang Zhang, Dunwei Wang, and Hongjie Dai, *Noncovalent sidewall functionalization of single-walled carbon nanotubes for protein immobilization.* Journal of the American Chemical Society, 2001. **123**(16): p. 3838-3839.

29. Jian Zhang, J-K Lee, Yue Wu, and Royce W Murray, *Photoluminescence and electronic interaction of anthracene derivatives adsorbed on sidewalls of single-walled carbon nanotubes.* Nano Letters, 2003. **3**(3): p. 403-407.

30. Seiji Tsuzuki, *CH/π interactions.* Annual Reports Section" C"(Physical Chemistry), 2012. **108**: p. 69-95.

31. Asuka Fujii, So-ichi Morita, Mitsuhiko Miyazaki, Takayuki Ebata, and Naohiko Mikami, *A molecular cluster study on activated CH/π interactions: Infrared spectroscopy of aromatic molecule-acetylene clusters.* The Journal of Physical Chemistry A, 2004. **108**(14): p. 2652-2658.

32. D. Baskaran, J. W. Mays, and M. S. Bratcher, *Noncovalent and nonspecific molecular interactions of polymers with multiwalled carbon nanotubes.* CHEMISTRY OF MATERIALS, 2005. **17**(13): p. 3389-3397.

33. G Steiner and C Zimmerer, *Polypropylene (PP),* in *Polymer Solids and Polymer Melts–Definitions and Physical Properties I*. 2013, Springer. p. 903-913.

34. S Costa and E Borowiak-Palen, *Raman study on doped multiwalled carbon nanotubes.* Acta Physica Polonica-Series A General Physics, 2009. **116**(1): p. 32.

35. SB Cronin, AK Swan, MS Ünlü, BB Goldberg, MS Dresselhaus, and M Tinkham, *Resonant Raman spectroscopy of individual metallic and semiconducting single-wall carbon nanotubes under uniaxial strain.* Physical review B, 2005. **72**(3): p. 035425.

36. Yongzheng Pan, Lin Li, Siew Hwa Chan, and Jianhong Zhao, *Correlation between dispersion state and electrical conductivity of MWCNTs/PP composites prepared by melt blending.* Composites Part A, 2010. **41**: p. 419-426.

37. K. Prashantha, J. Soulestin, M. F. Lacrampe, P. Krawczak, M. Claes, and G. Dupin, *Multi-walled carbon nanotube filled polypropylene nanocomposites based on masterbatch route: Improvement of dispersion and mechanical properties through PP-g-MA addition.* Express Polymer Letters, 2008. **2**(10): p. 735-745.

38. Kilwon Cho, Fengkui Li, and Jaeseung Choi, *Crystallization and melting behavior of polypropylene and maleated polypropylene blends.* Polymer, 1999. **40**(7): p. 1719-1729.

CHAPTER 3

MECHANICAL PROPERTIES AND CRYSTAL STRUCTURE OF PP/MWNT NANOCOMPOSITES

3.1 INTRODUCTION

This chapter focuses on the mechanical properties of PP/MWNT nanocomposites made by a combination of CNT functionalization, solution processing, followed by melt blending and injection molding. For comparison, studies have also been conducted using pristine MWNT, as well as MA-g-PP as a compatibilizer. A solution processing route has been used to manufacture master batches of MA-g-PP/f-MWNT and that of PP/f-MWNT (5 wt% f-MWNTs in polymers), as discussed in Chapter2. These master batches were subsequently diluted to a desired CNT concentration in PP via melt processing using a micro-compounder followed by injection molding of the final samples. Tensile, impact and thermal properties of the composites were investigated. These properties are compared with the properties obtained from control PP and PP/MWNT nanocomposites prepared by melt processing of pristine MWNT with PP. It has been shown that significant property improvements can be obtained at a relatively low CNT concentration of 1 wt. % by tailoring the interphase between the carbon nanotubes and the polymer matrix. Other experiments including high strain rate test, effect of additive and different PP formulations on the impact behavior, and the manufacturing of MWNT incorporated fibers are given in the Appendix B-F.

Key literature results of PP/CNT nanocomposites are summarized in Figure 1.13 and Table 1.3. Absolute property comparison of all the literature results is difficult, as sample history, polymer molecular weight, presence of additives such as stabilizers and nucleating agents are not always specified. However, when such information is specified, their effects are not always delineated. In terms of relative property improvements, with the presence of 0.5 to 5 wt. % CNTs (almost always MWNTs) in PP, impact strength improvement of 10% to 56% has been reported in the studies carried out over the last two decades. Incorporation of other fillers such as carbon black, talc, $CaCO_3$, etc. can also increase impact strength and tensile properties, however much higher loadings (typically 10 to 20 wt.% filler loading) are required and less than 100% increase in impact strength have been achieved [1, 2]. Another polymer phase, such as low density polyethylene (LDPE), ethylene/propylene copolymers and polyisobutylene also result in increased impact strength. 2 wt. % second polymer phase has been shown to increase the impact strength by as much as 70% [3]. However, this second polymer phase results in lower tensile and flexural properties. Incorporation of α type nucleating agent (4000 ppm of polymer) resulted in 65 % and 8 % increase in impact strength and tensile modulus, respectively [4].

3.2 EXPERIMENTAL

For the materials, MWNT functionalization and master batch preparation, please refer to Chapter 2.2.

3.2.1 Manufacture of nanocomposites

Master batches of MA-g-PP/f-MWNT and PP/f-MWNT were diluted using a PP homopolymer to prepare the corresponding nanocomposites. As-received PP powder was dried in a vacuum oven at 80 °C for about four hours prior to its use in melt processing. The CNT concentrations in the nanocomposites was 0.001, 0.005, 0.01, 0.1, 0.3, 0.5 and 1 wt. %. Mixing of master batch powder with PP powder was carried out manually using mortar and pestle. Samples with the aforementioned CNT concentrations were also prepared from pristine CNTs (referred to as p-MWNT) by manually mixing them using a mortar and pestle with the as-received PP. Various physical mixtures were melt blended using a micro compounder followed by injection molding. In addition, a control sample (no CNT present) was made for comparison to the PP/f-MWNT master batch processing conditions. PP powder was solution processed by dissolving it in the butanol-xylene mixture followed by solvent evaporation as was done for PP/f-MWNT master batch processing. For comparison, as received PP powder, along with 1.9 and 19 wt. % of the solution-processed PP were melt compounded and injection molded via the same protocol used for the various nanocomposites. 1.9 and 19 wt. % of solution processed PP in the control samples corresponds to the amount of solution-processed PP in the 0.1 and 1 wt. % CNT containing corresponding nanocomposites, respectively.

Dry blended PP/CNT mixtures were fed to the 15 cc micro-compounder (Xplore^{TM} Instruments, Netherlands). Compounding conditions for all the samples were kept the same. The temperatures for the three heating zones of the barrel were set at 185, 215, and 215 °C (Figure 3.1). The melt temperature was recorded by a thermocouple located after the third heating zone and before the die, and in both cases it was recorded as 200 °C. The micro-

compounder was operated in recirculation mode for three minutes at 200 rpm. At the end of three minutes of recirculation, the melt was transferred to the melt transfer device through a die with diameter of 3 mm. 12 cc melt transfer device was kept preheated to 200 °C. Subsequently, the melt transfer device was placed in the Xplore^{TM} micro injection molding device. The mold was pre-heated at 80 °C. The pressure used for injection molding was 7.5 bar. Duration of injection molding cycles, feed-hold-release were 5-20-5 sec, respectively. In this work, in order to study the properties changes due to MWNTs and not as a result of synergistic effect with other additives, the thermal stabilizers were not added to PP. The safe residence time during processing at 200 °C was determined by TGA under air, where the neat PP without stabilizers showed no weight loss at 200 °C for 5 minutes (Figure 3.2). TGA data clearly shows that the compounding and injection molding conditions used in this work were not causing PP degradation. Dog-bone shaped samples were prepared for tensile testing. Dimension of the tensile specimens are 63.5 × 3.27 × 3.33 mm. Rectangular bars were prepared for impact and heat deflection temperature testing. Dimensions of rectangular bars are 63.5 × 12.7 × 3.33 mm (Figure 3.3 and 3.4).

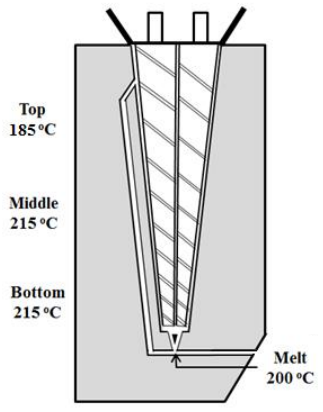

Figure 3.1. Schematic of the micro-compounder.

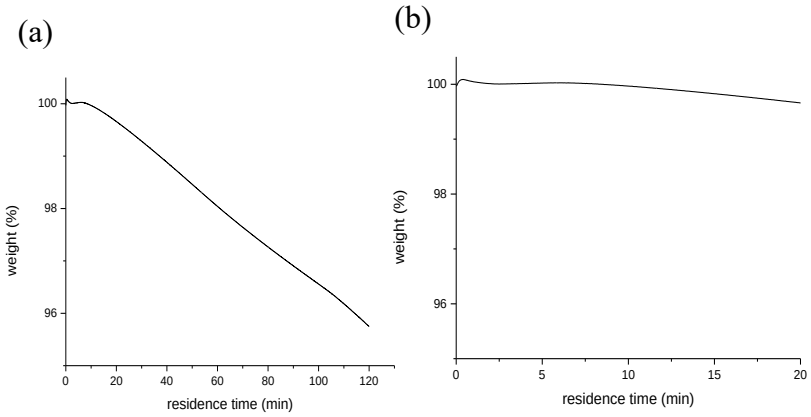

Figure 3.2. TGA under air at 200 °C of neat PP. Figure (b) shows the residual weight (%) from 0 to 20 minutes.

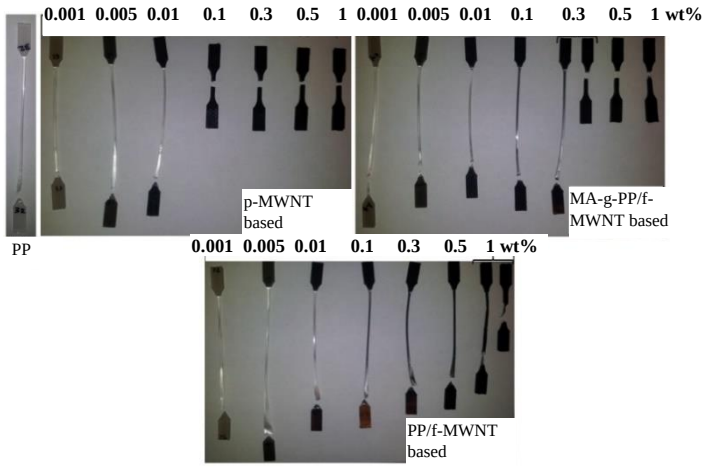

Figure 3.3. Photographs of various samples after tensile tests.

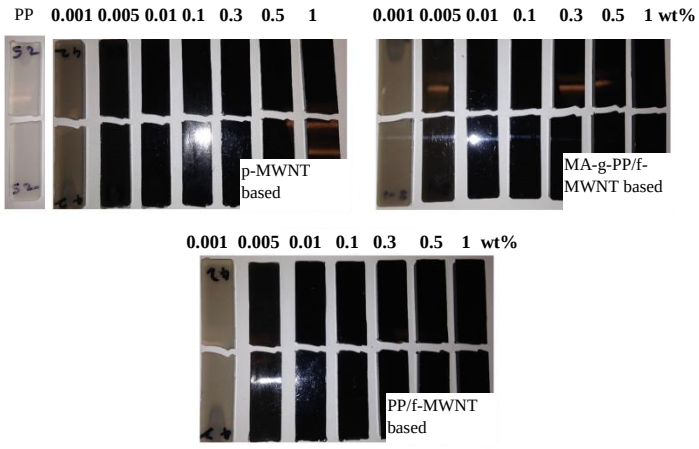

Figure 3.4. Photographs of various samples after impact tests.

3.2.2 Characterization

Izod impact testing was carried out on notched samples according to the ASTM D256 standard. Tensile testing was carried out according to the ASTM D638 standard using a 10 mm gauge length. Rate of crosshead displacement was 25.4 mm/min (strain rate

of 1 min^{-1}). Tensile tests were conducted using an Instron 5567 electro-mechanical test frame. Extension was measured using extensometer 2630-101, in the strain range of 0.1 to 0.4%. To determine the statistical significance of the CNTs effect on properties, Student's *t*-test was performed on the data using JMP™11 software from SAS at 95% confidence limit. Heat deflection temperature (HDT) of the nanocomposites was measured on rectangular specimens. These specimens were similar to the ones used for impact testing. A TA Instruments dynamic mechanical analyzer (DMA) Q800 was used to study the heat deflection temperature. ASTM D648 standard was followed for these tests using three-point bending test geometry. To obtain the HDT, static force of 0.85 N (0.45 MPa as recommended in ASTM standard D648) was applied to the sample and temperature was increased from 30 to 150 °C at the rate of 2 °C/min. The HDT reported here corresponds to the deflection of 244 μm (0.2% strain as recommended in ASTM D648 standard). In each case, a minimum of five samples were tested for impact, as well as for tensile tests, while a minimum of two samples were tested for the HDT.

A polarized optical microscope (Leica, DM 2500P) equipped with Linkam LTS420 heating stage was used to study the crystallization behavior. For this purpose, thin and small pieces of the injection molded samples were heated on glass plates covered with microscope cover slips. Samples were heated to 200 °C for five minutes and then cooled to 135 °C at a rate of 20 °C/min, and held at this temperature to monitor the crystallization behavior over a period of time. WAXD (wide angle X-Ray diffraction) was performed using Rigaku MicroMax-002 beam generator (Cu Kα $\boldsymbol{\lambda}$= 0.1542 nm, operating voltage and current 45 kV and 0.65 mA, respectively) equipped with R-axis IV++ detector. Percentage of b-crystals (K_β) in the tensile and impact specimens of nanocomposites prepared via MA-

g-PP/f-MWNT master batch. The relative amount of the β crystals in the crystalline phase is evaluated based on equation (2) in Chapter 1 [5]:

Isothermal crystallization studies were carried out using TA Instrument Q100 differential scanning calorimeter (DSC). Samples were heated to 220 °C at a heating rate of 10 °C/min and held at 220 °C for five minutes. These samples were then cooled at a rate of 100 °C/min to 135 °C and then held at that temperature for crystallization. The crystallization half-time, t1/2 is defined as the time at which the extent of crystallization is 50% of total crystallization. The crystallization half-time can be calculated from the total crystallinity [6],

$$(X_t) = \int_0^t (\mathrm{d}H_c/\mathrm{d}t)\mathrm{d}t \,/\, \int_0^\infty (\mathrm{d}H_c/\mathrm{d}t)\mathrm{d}t. \quad (1)$$

Here, t is the crystallization time and $\mathrm{d}H_c \,/\, \mathrm{d}t$ is the heat evolution rate during the crystallization process. For non-isothermal crystallization study, samples were heated in DSC at 2.5 °C/min from room temperature to 220 °C and then cooled at the same rate to room temperature and then heated again at 2.5 °C/min to 220 °C. The crystallization temperature (T_c) was derived from the cooling cycle.

Impact-fractured surfaces of the PP/MWNT nanocomposite containing 1 wt. % MWNT were investigated by SEM using Zeiss Ultra 60 FE-SEM at an accelerating voltage of 2 kV. A thin layer of gold was sputter coated onto these samples before imaging. SEM studies were also conducted on etched surfaces. For etching, impact fractured specimens were placed in a vial containing a 60:40 mixture of orthophosphoric acid (H_3PO_4) and sulphuric acid (H_2SO_4) with approximately 0.5 wt. % potassium permanganate ($KMnO_4$) [7]. Etching was carried out in the vials in the ultrasonic bath for two hours at room temperature. After the etching treatment, samples were repeatedly washed in deionized

water followed by washing in acetone. These samples were then dried in oven for one hour at 40 °C.

Rheological behavior was measured on an ARES rheometer (TA Instruments, USA) in the linear viscoelastic regime at a strain of 5%. A dynamic frequency sweep test was performed at 200 °C in the range of 0.1 to 500 rad/s using parallel-plate geometry (plate diameter 25 mm and the gap between the plates is 1 mm). Raman spectra (Horiba Explora One, λ = 785 nm) were collected to determine CNT orientation using parallel (VV) and crossed (VH) polarizers, with the sample (Figure 3.5) axis rotated in 10° increments from 0 to 90°. The equation below was used to determine CNT orientation, f_{CNT}. This equation was simultaneously solved for three variables (r, <P200> = f_{CNT}, and <P400>) [8].

$$R(\theta) = \frac{I_{VH}(\theta)}{I_{VV}(\theta)}$$

$$= \frac{(1-r)^2[-56 - 40\langle P_{200}\rangle + (105\cos 4\theta - 9)\langle P_{400}\rangle]}{[-56(8r^2+4r+3) + 40(4r^2-r-3)(1+3\cos 2\theta)\langle P_{200}\rangle - 3(r-1)^2(9+20\cos 2\theta+35\cos 4\theta)\langle P_{400}\rangle]} \quad (2)$$

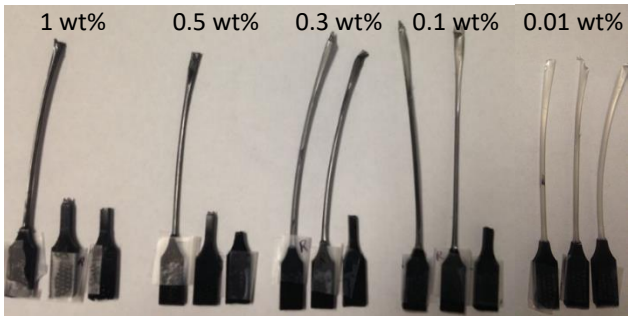

Figure 3.5. PP/MWNT nanocomposites prepared from PP/f-MWNT master batch (left), MA-g-PP/f-MWNT master batch (middle) and p-MWNT (right) used for Raman study at different MWNT concentration.

3.3 RESULTS AND DISCUSSION

3.3.1 Tensile and impact strength of nanocomposites

Figure 3.6 shows the impact strength of various samples as a function of MWNT loading and the corresponding data is given in Table G1 in Appendix G. At 0.01 wt. % p-MWNT loading, impact strength increased by 13.8%, and the *p*-value test shows that this increase was statistically significant. However, further increase in p-MWNT loading to 0.5 wt. %, decreases the impact strength of the nanocomposites to the level of the control PP, and at 1 wt. % p-MWNT, the impact strength value is lower than that of the control PP. This observation is similar to the observation made by several other investigators studying PP/CNT nanocomposites by melt processing, where a 56% and 47% increase in impact strength was observed at 1 wt. % and 0.6 wt.% CNT loading, respectively, followed by an impact strength decrease at higher CNT concentrations [9, 10]. Impact strength for MA-g-PP/f-MWNT master batch based nanocomposites showed statistically significant differences at f-MWNT concentrations of 0.3 wt. % or higher. At 0.5 and 1 wt. % f-MWNT, impact strength values were 3.95 and 4.03 kJ/m^2, and these represent an increase of 65% and 69%, respectively, over that of the control PP sample. PP/f-MWNT master batch containing samples, showed statistically significant differences at or above 0.1 wt. % f-MWNTs, and at 1 wt. % f-MWNT, impact strength was 6.04 kJ/m^2. This is an increase of 152% over the control PP sample. To the best of our knowledge, this is the highest percentage improvement in the impact strength of PP with CNT at room temperature reported in the literature to date. At higher f-MWNT concentration (2 wt. %), this value slightly dropped to 5.37 ± 1.23 (KJ/m^2).

The tensile modulus values are presented in Figure 3.7 and Table G2 in Appendix G. Tensile modulus of the PP/p-MWNT composites increased gradually up to 0.5 wt. % MWNT content in the composite. At 0.5 wt. % p-MWNT content, tensile modulus of the composite increased by 24% as compared to that of the control PP sample, which is the highest increase among all the nanocomposites samples analyzed in the current study. An increase in p-MWNT loading to 1 wt. % had no further effect on the tensile modulus. In the MA-g-PP/f-MWNT master batch based samples, at low f-MWNT loadings (0.001 to 0.1 wt. %), tensile moduli of the nanocomposites are comparable to that of the control samples. An approximate increase of 10% in the tensile modulus is observed for the nanocomposites containing 0.3 wt. % f-MWNT as compared to that of the control samples. However, no further enhancement in the tensile modulus was observed for the nanocomposites containing up to 1 wt. % f-MWNT. In PP/f-MWNT master batch based nanocomposites, an increase of 8% and 13% in the tensile modulus is observed at 0.001 and 0.01 wt. % f-MWNT loading, respectively, as compared to that of the control PP sample. With further increase in f-MWNT loading up to 1 wt. %, the modulus values decreased. Among all three types of nanocomposites, PP/f-MWNT master batch based nanocomposites showed the highest tensile modulus at low MWNT loadings of 0.001 and 0.01 wt. %. On the other hand, PP/p-MWNT composites exhibited the highest tensile modulus in the MWNT concentration range of 0.3 to 1 wt. %, compared to the other two categories (MA-g-PP/f-MWNT and PP/f-MWNT based) of samples.

Yield stress data is presented in Figure 3.8 and Table G3 in Appendix G. For the p-MWNT based nanocomposites, yield stress increased gradually with the increase in MWNT concentration and reached the highest value (among the three types of composites

in the current study) of 44.4 MPa at 1 wt. % MWNT loading. This is and 18% increase over the control PP. A statistically significant difference in yield stress was observed at as low as 0.1 wt. % for p-MWNT, at 0.3 wt. % for MA-g-PP/f-MWNT based samples, and only at 1 wt. % for PP/f-MWNT based sample. At 0.5 wt. % CNT, the yield stress of MA-g-PP/f-MWNT based nanocomposite increased by 8% as compared to that of the control PP. For the PP/f-MWNT based nanocomposite, the increase in yield stress compared to that of the control PP is 5% at 1 wt. % CNT loading.

Strain to failure data are given in Figure 3.9 and Table G4 in Appendix G. The control PP sample shows ductile behavior with the strain to failure value of 329%. In p-MWNT based nanocomposites, strain to failure drops to 12.5% at 1 wt. % p-MWNT loading. It decreases with statistically significant differences to below 218% even with p-MWNT loading in the range of 0.001 to 0.01 wt. %. At 0.1 wt. % p-MWNT, strain to failure decreased to 17.7%. On the other hand, for MA-g-PP/f-MWNT based nanocomposites, good to excellent strain to failure was retained even at 0.3 wt. % f-MWNT. However, in going from 0.3 wt. % to 0.5 wt. % f-MWNT, strain to failure decreased from 226% to 16.8%. PP/f-MWNT based nanocomposite samples exhibited the best ductile behavior when comparing the three categories of nanocomposite samples reported in this study. The strain to failure of 1 wt. % CNT containing PP/f-MWNT based nanocomposite is 113% compared to 12.5% and 19.9% for p-MWNT based and MA-g-PP/f-MWNT based nanocomposites, respectively.

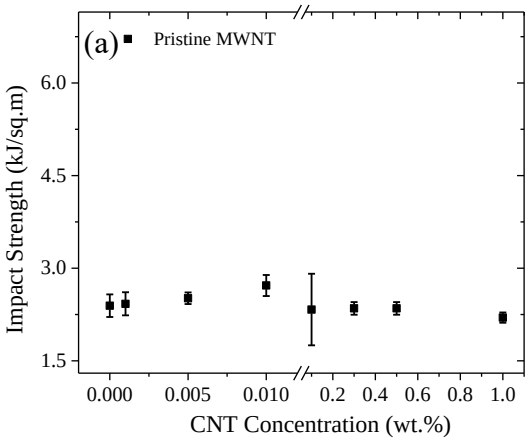

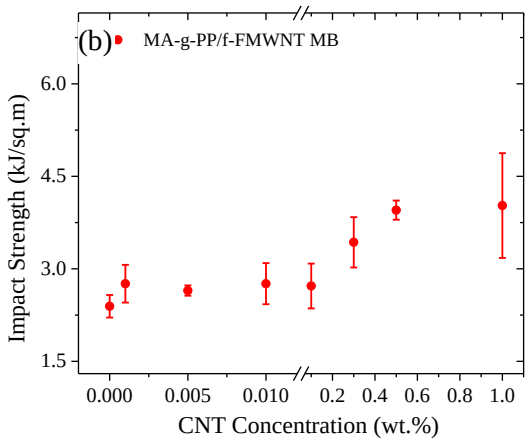

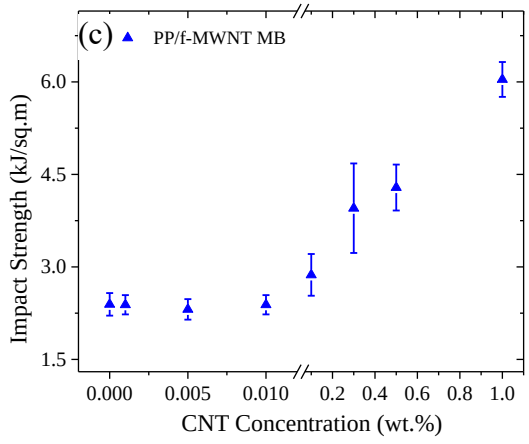

Figure 3.6. Notched Izod impact strength of PP/MWNT nanocomposites prepared from (a) p-MWNT, (b) MA-g-PP/f-MWNT master batch and (c) PP/f-MWNT master batch.

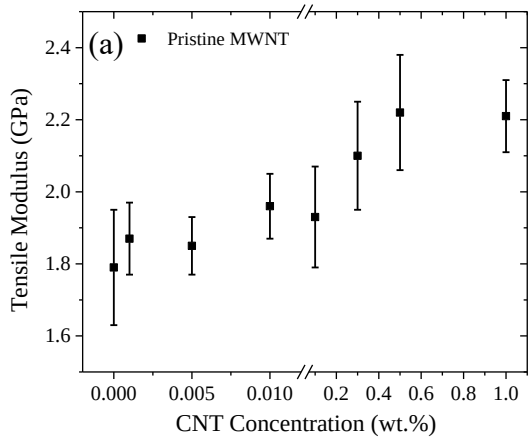

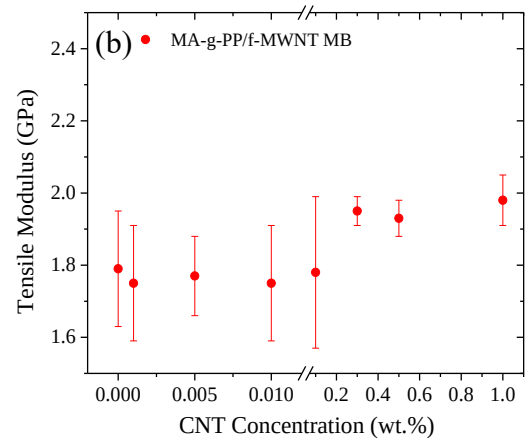

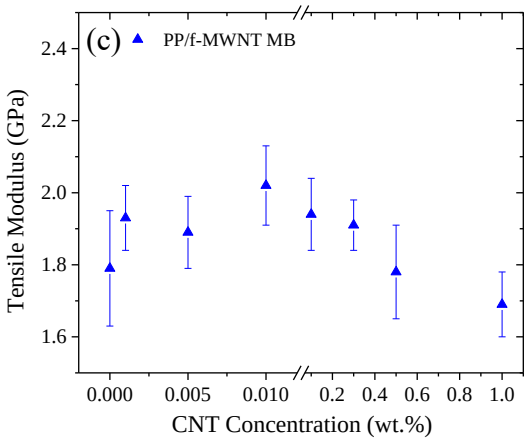

Figure 3.7. Tensile modulus of PP/MWNT nanocomposites prepared from (a) p-MWNT, (b) MA-g-PP/f-MWNT master batch and (c) PP/f-MWNT master batch.

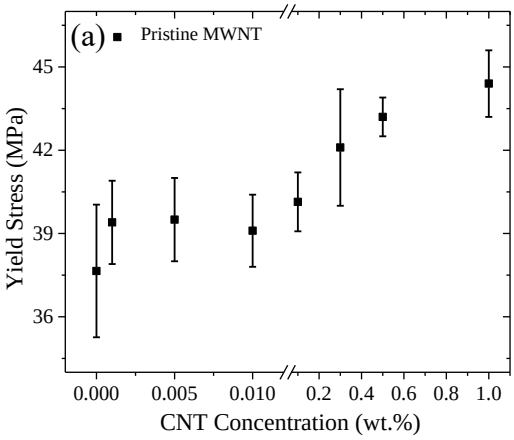

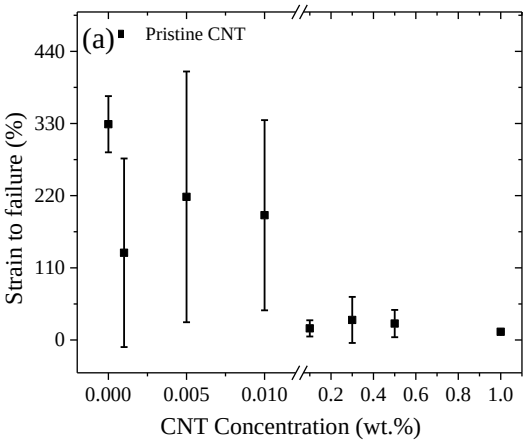

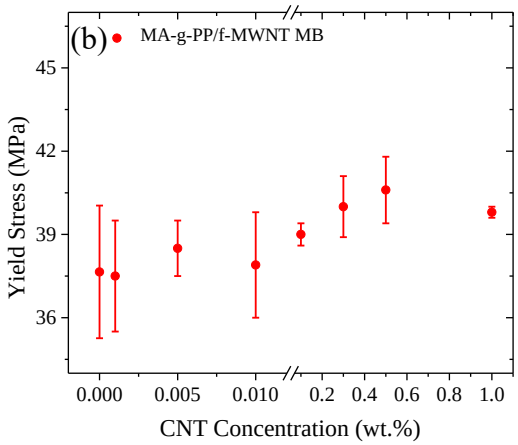

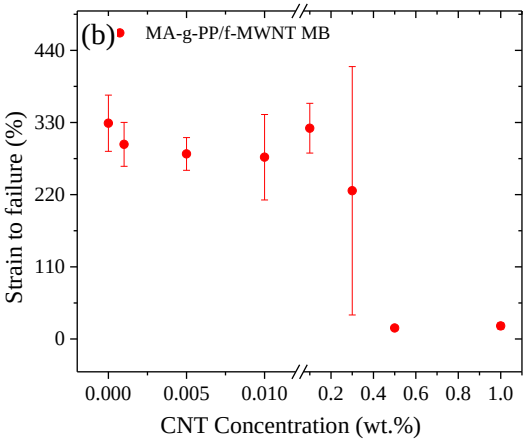

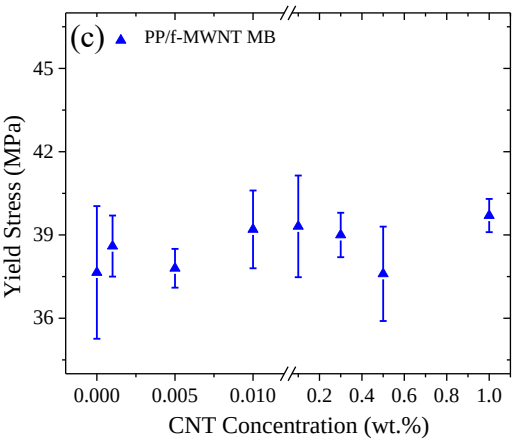

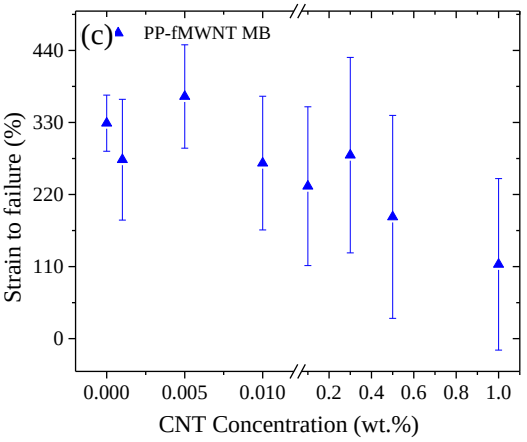

Figure 3.8. Yield stress of PP/MWNT nanocomposites prepared from (a) p-MWNT, (b) MA-g-PP/f-MWNT master batch and (c) PP/f-MWNT master batch.

Figure 3.9. Strain to failure of PP/MWNT nanocomposites prepared from (a) p-MWNT, (b) MA-g-PP/f-MWNT master batch and (c) PP/f-MWNT master batch.

3.3.2 CNT dispersion in the nanocomposites

In order to understand the changes in mechanical properties, the structure, morphology, and crystallization behavior of the samples were studied. Based on Izod impact strength testing of the samples, no nanotube pull-out was observed, and all nanotubes appear to be broken due to fracture (Figure 3.10 and Figures G2 to G4 in Appendix G). At 1 wt. % MWNT concentration, both optical and scanning electron microscopy images show that the MWNT dispersion was relatively poor within p-MWNT sample (Figure 3.11, Figure 3.12, Figure 3.13, and Figure G4 in Appendix G). While many individual p-MWNTs were observed (Figure 3.10), these samples also contained large (up to about 100 μm in size) p-MWNT aggregates (Figure 3.13). On the other hand, MA-g-PP/f-MWNT and PP/f-MWNT composite samples predominantly contained individual CNTs (Figure 3.10, Figure G2, and Figure G3 in Appendix G). However, some pockets of 0.5 to 1 μm sized f-MWNT aggregates were observed in the case of the MA-g-PP/f-MWNT master batch based samples (Figure G3 in Appendix G), and few larger aggregates (2 to 10 μm) were observed in PP/f-MWNT based samples (Figure 3.14). From the SEM images, at 1 wt. % CNT loading, the average distance between the CNTs was found to be about 400 nm in the two master batch based samples, while this distance was larger (~700 nm) in p-MWNT containing samples, due to the presence of more frequent and larger CNT aggregated regions in the latter case (Figure 3.10, Figure G2 to Figure G4 in Appendix G). At 1 wt. % CNTs of 12 nm diameter, the theoretical distance between CNTs should be about 170 nm [11]. The difference between the experimentally observed average distances between CNTs even in the best case reported here (MA-g-PP and PP master batch based systems) and its theoretically predicted value assuming uniform CNT dispersion, also

suggests that further room for improvement remains regarding both the dispersion and sample properties.

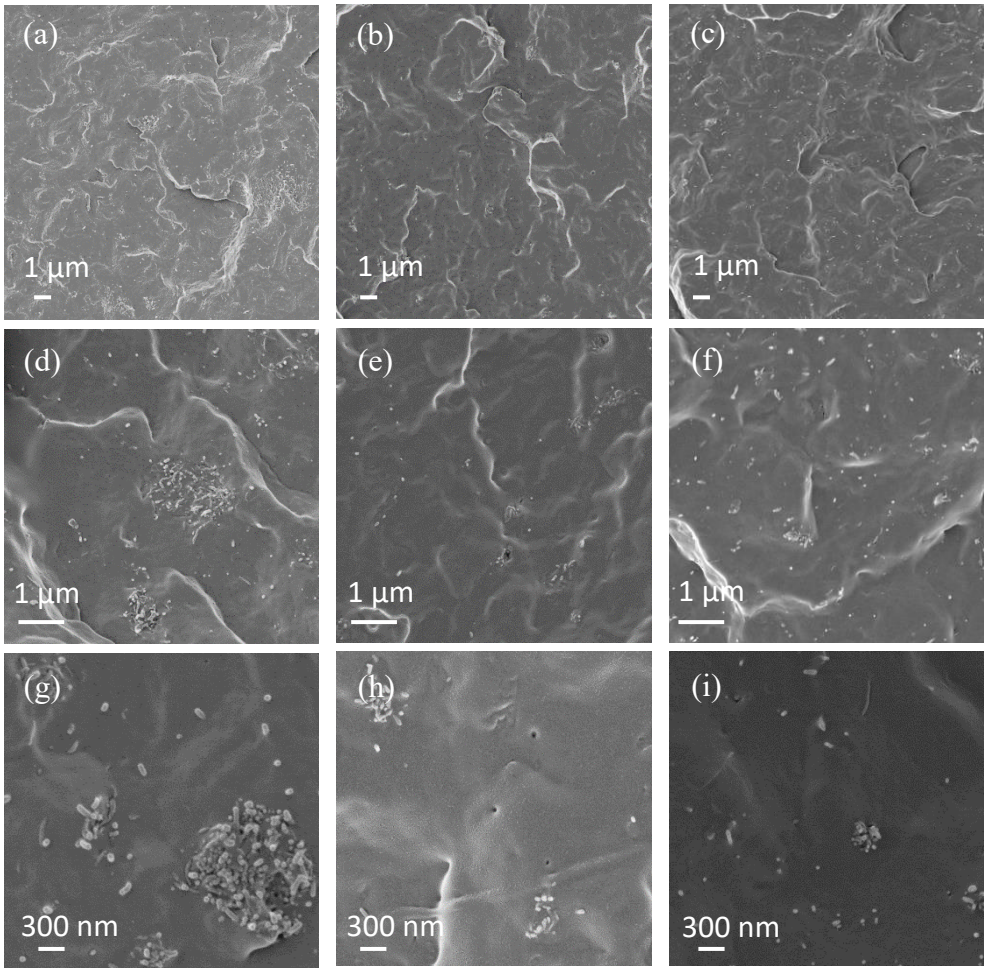

Figure 3.10. SEM images of PP/MWNT (1 wt.%) nanocomposites impact-fractured surface prepared from (a,d,g) p-MWNT, (b,e,h) MA-g-PP/f-MWNT master batch, and (c,f,i) PP/f-MWNT master batch before etching.

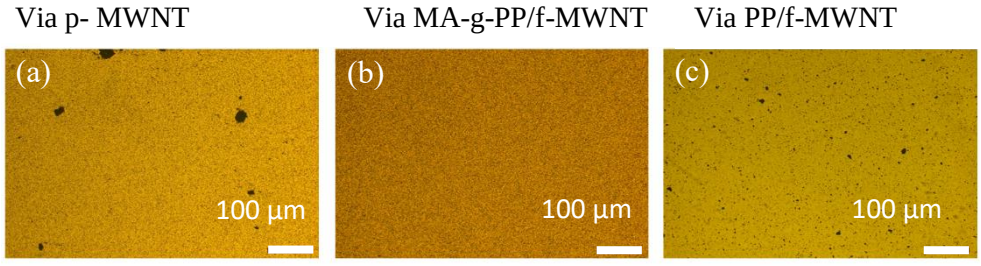

Figure 3.11. (a-c) Optical micrographs at 1 wt. % MWNT showing dispersion quality in the three types of nanocomposites.

PP/MWNT nanocomposite via p-MWNT

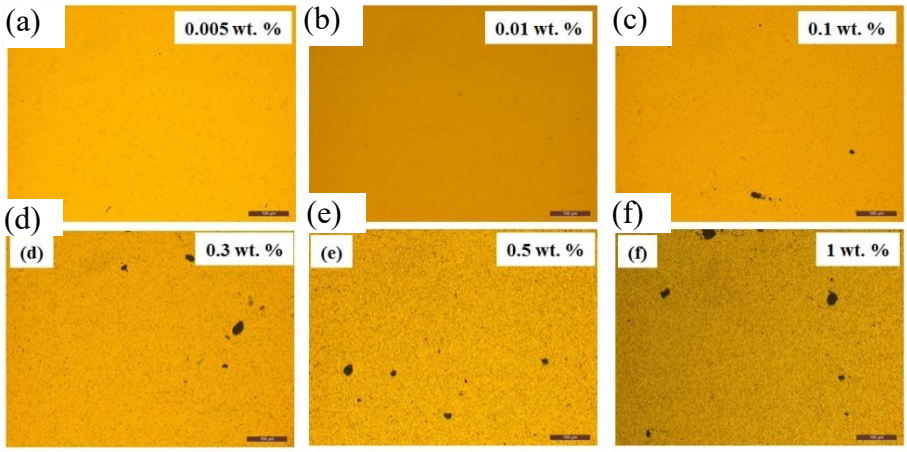

Figure 3.12. Optical micrographs of nanocomposites via p-MWNT at different MWNT concentrations. Scale bar represents 100 μm.

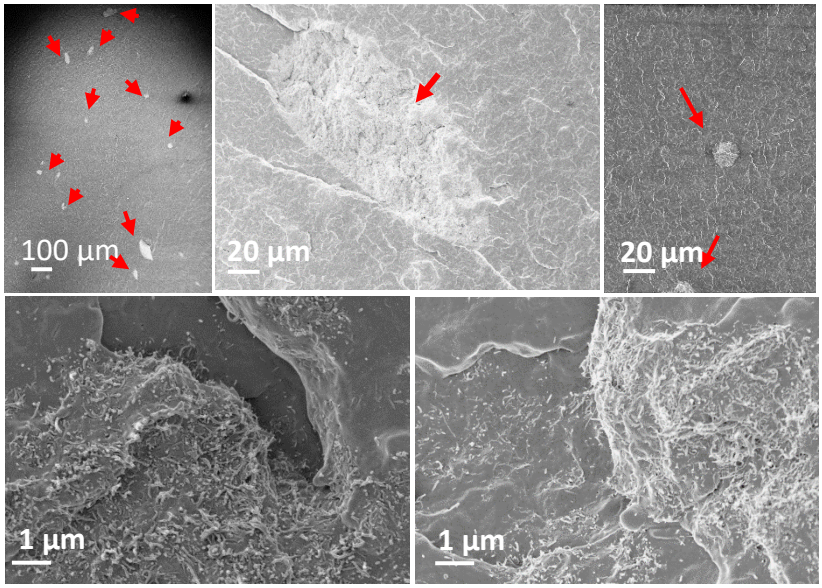

Figure 3.13. SEM images of fractured surfaces of PP/p-MWNT nanocomposites at 1 wt. % p-MWNT after impact test. These images show the presence of individual nanotubes as well as nanotube aggregates of various dimensions (from few μm to over 100 μm).

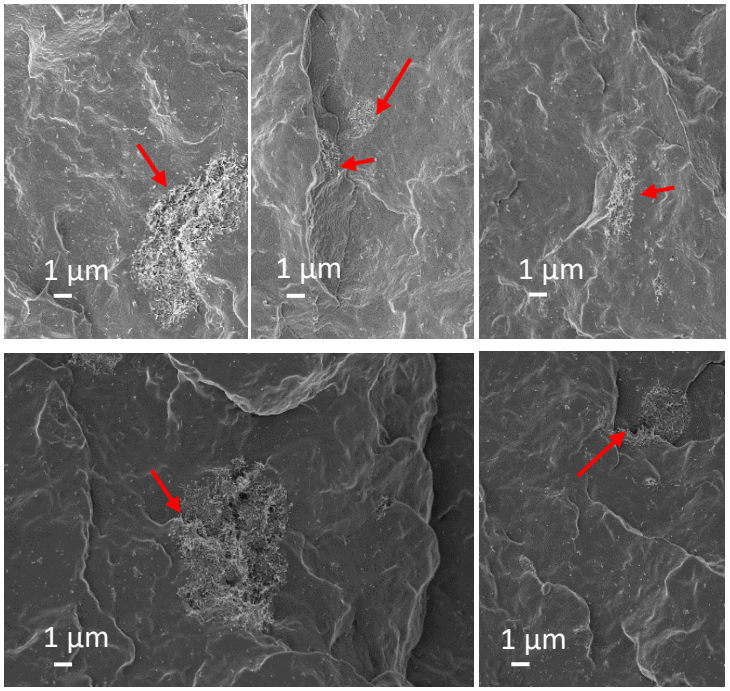

Figure 3.14. SEM images of fractured surfaces of PP/f-MWNT nanocomposites processed via PP/f-MWNT master batch at 1 wt. % f-MWNT after impact test. f-MWNT aggregates of 2 to 10 µm can be seen in these images.

3.3.3 Presence of β crystals in the MA-g-PP containing nanocomposite

Impact strength of polymers is known to increase with a decrease in spherulite size [12-15]. While spherulite size was not quantitatively determined in this study, polarized optical microscopy (Figure 3.15) can be used to qualitatively understand spherulite size. Based on this analysis it is observed that the smallest spherulite size was obtained for the p-MWNT containing samples and that control PP had the largest spherulite size. The spherulite size of MA-g-PP/f-MWNT and PP/f-MWNT master batch containing samples were within the range of these two extremes. The crystallization times as determined using polarized optical microscopy (POM) and DSC and the results support the spherulite size trends, as expected. In other words, samples exhibiting large spherulite size have long crystallization times and vice versa.

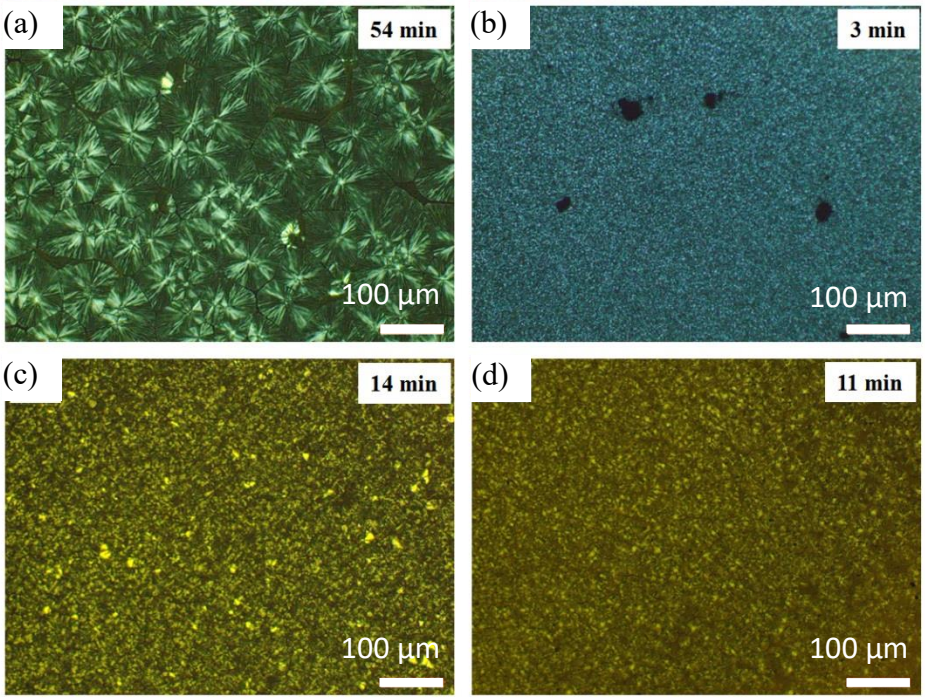

Figure 3.15. Polarized optical micrographs (POM) under cross-polars of (a) PP and PP/MWNT (1 wt.%) nanocomposites containing (b) p-MWNT, (c) MA-g-PP/f-MWNT master batch and (d) PP/f-MWNT master batch. The samples were melted at 200°C for 5 minutes, followed by cooling at 20 °C/min to 135 °C. Samples were held at 135 °C and photographed when no further spherulitic growth was observed. Time when no further spherulitic growth occurred is indicated on the optical micrographs.

The presence of β crystals has been shown to positively affect the impact strength of polypropylene [16-18]. While α crystals of PP exhibited higher modulus due to their interconnected lamellar network, β crystals are tougher because they slide with respect to one another in the interlamellar amorphous zones during shear deformation [19]. Previously it has been reported that maleic anhydride grafted propylene–butadiene copolymer (MPPB) results in the formation of β crystals [20]. In the current study, β crystals were observed in MA-g-PP containing sample, but they were not observed in the control PP, p-MWNT, and PP/f-MWNT based samples. This information has been ascertained from WAXD (Figure 3.16 and Figure 3.17), DSC (Figure 3.18), SEM (Figure 3.19), and optical microscopy (Figure 3.20) analysis. WAXD studies showed that that MA-

g-PP/f-MWNT master batch based nanocomposites contain β crystal peak at 2θ = 16.1° [7] (Figure 3.16 and 3.17), when MA-g-PP concentration is above 9.5 wt. % (9.5 wt. % MA-g-PP corresponds to the master batch based nanocomposite containing 0.5 wt. % f-MWNT). Below this concentration, β crystals were not observed. From the SEM images (Figure 3.19) it was found that β-phase lamellae grow radially outwards without interconnecting cross-hatched lamellar network, whereas α-phase spherulites contain both tangential and radial lamellae [7]. The POM images (Figure 3.20) for 0.5 and 1 wt. % f-MWNT containing MA-g-PP/f-MWNT nanocomposites show β-phase crystals which are optically distinguishable due to high brightness within the less bright spherulites from α crystals [7]. In DSC (Figure 3.18d), the 1st heating cycle from the 1 wt. % f-MWNT nanocomposite shows two endothermic peaks at ~147 and ~164 °C. The former is attributed to the melting of β-phase and the latter is attributed to the melting of α-phase [16]. It is worth noting that this β endothermic peak was observed when the DSC sample was taken from the center of the impact specimen, and when the DSC sample was taken from the end of the impact specimen (Figure 3.18a), then only melting corresponding to α-phase was observed. This observation suggests that small differences in the processing parameter window become important for the formation of β crystals, along with the presence of pristine (α-phase) MA-g-PP polymer. Also, after removing the processing history (first heating cycle), the two DSC samples (center and end portion of the injection molded bar as shown in Figure 3.18) during second heating cycle showed identical melting endotherms corresponding to α-phase (Figure 3.18c and Figure 3.18d). This further confirms the importance of precisely controlling the processing parameters toward the development of β crystals.

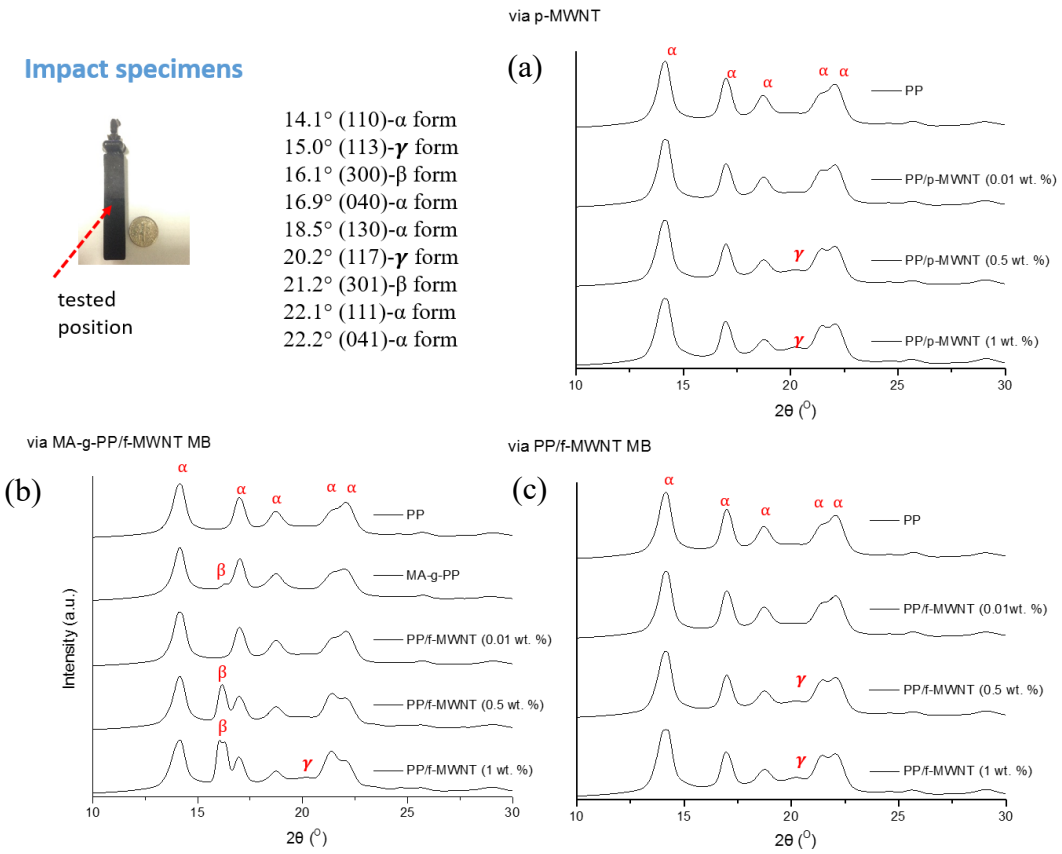

Figure 3.16. WAXD plots of injection molded bars. WAXD was done in the transmission geometry in the center of the bar as shown in the top left figure. Specimens prepared via (a) p-MWNT, (b) MA-g-PP/f-MWNT master batch and (c) PP/f-MWNT master batch. WAXD of control PP bars are also shown in figures (a), (b), and (c), and WAXD of only MA-g-PP (powder) is shown in figure (b). Nanocomposite samples prepared using MA-g-PP/f-MWNT master batch show the presence of β–crystals at 0.5 wt. % and 1 wt. % f-MWNT (figure b).

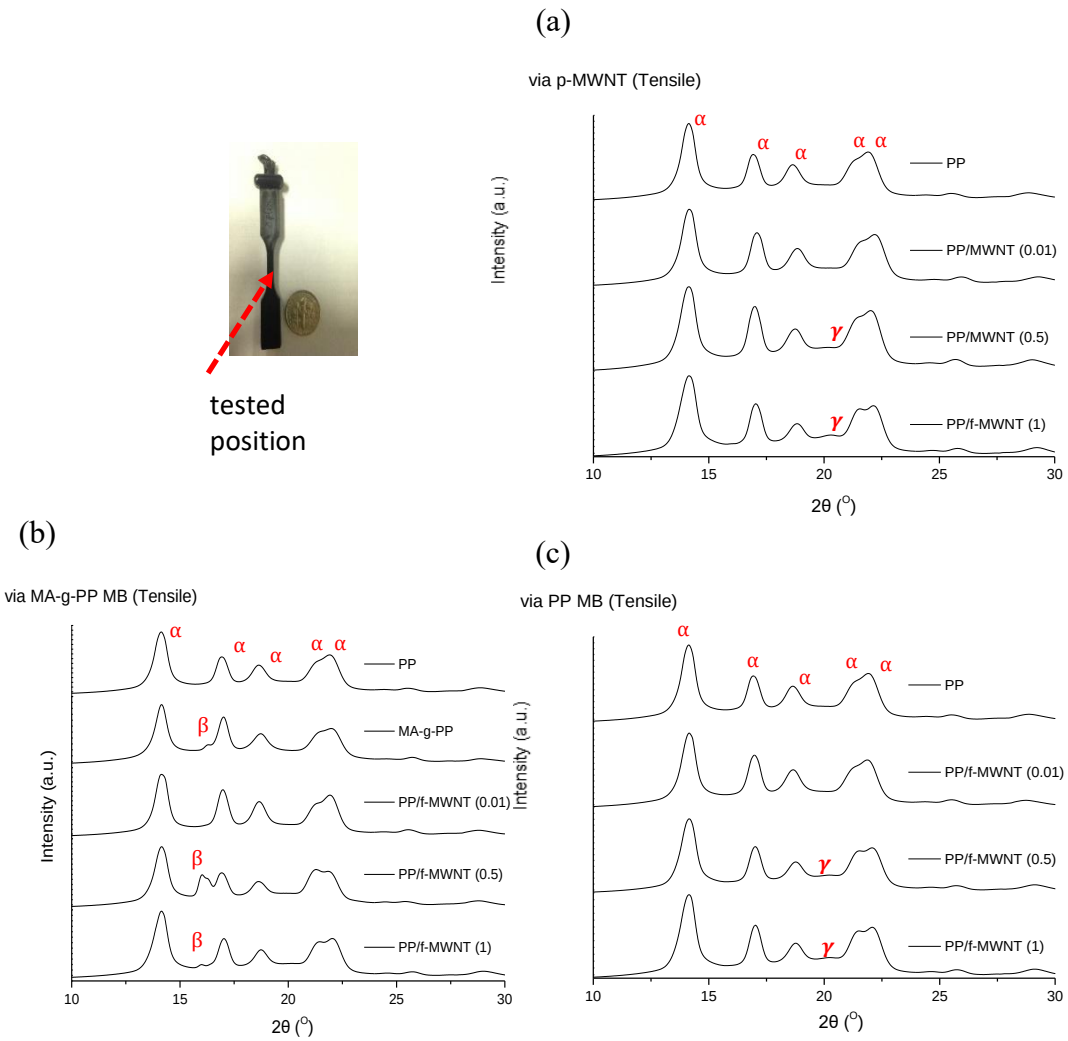

Figure 3.17. WAXD plots of PP/MWNT nanocomposite tensile specimens prepared via (a) p-MWNT, (b) MA-g-PP/f-MWNT master batch and (c) PP/f-MWNT master batch. Nanocomposite samples prepared via MA-g-PP/f-MWNT master batch route show the presence of β–crystal in the 0.5 wt. % and 1 wt. % MWNT containing samples. However, at 1 wt. % MWNTs, the amount of β–crystals are relatively insignificant. WAXD of MA-g-PP (powder) is also shown in the middle figure.

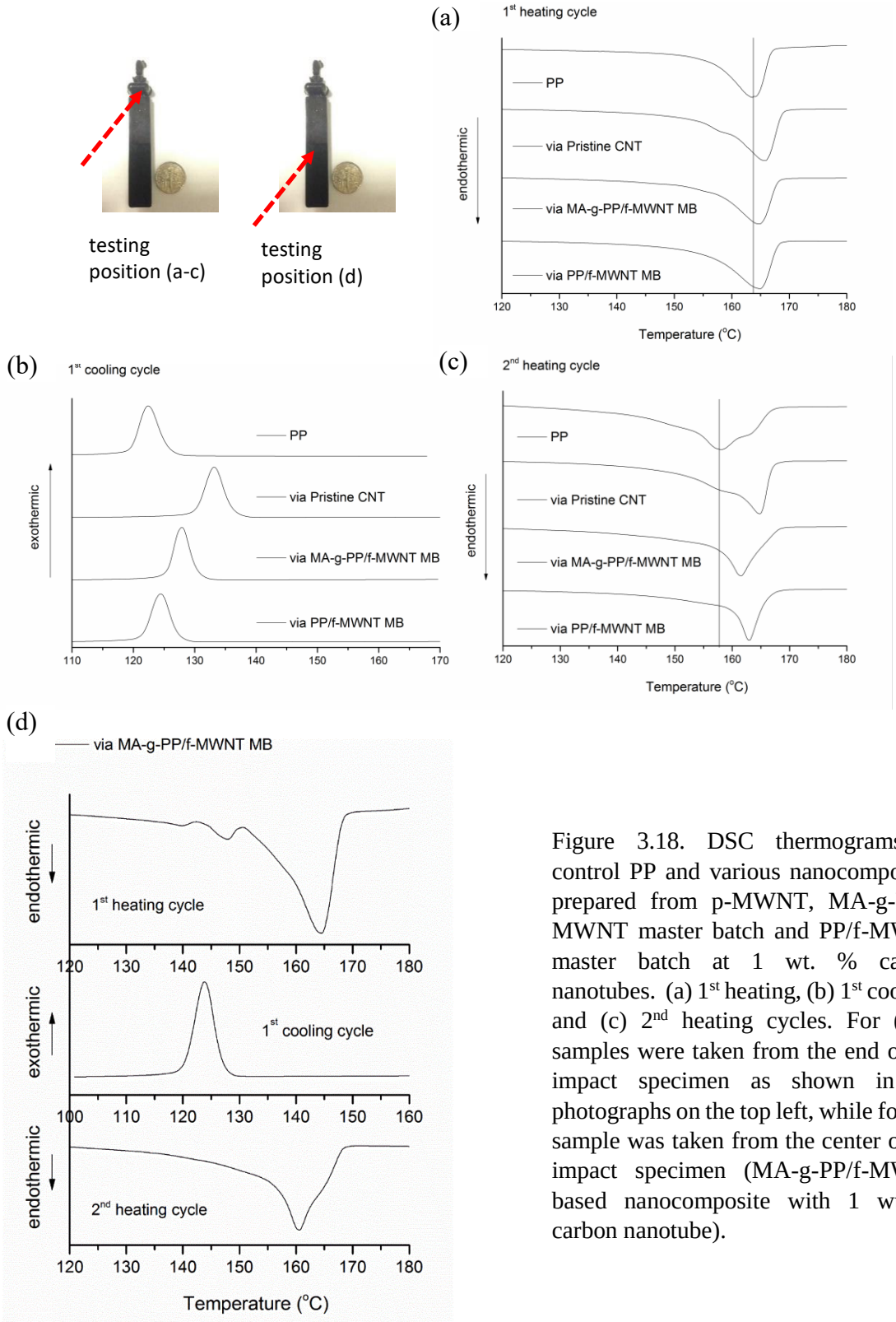

Figure 3.18. DSC thermograms of control PP and various nanocomposites prepared from p-MWNT, MA-g-PP/f-MWNT master batch and PP/f-MWNT master batch at 1 wt. % carbon nanotubes. (a) 1st heating, (b) 1st cooling, and (c) 2nd heating cycles. For (a-c), samples were taken from the end of the impact specimen as shown in the photographs on the top left, while for (d), sample was taken from the center of the impact specimen (MA-g-PP/f-MWNT based nanocomposite with 1 wt. % carbon nanotube).

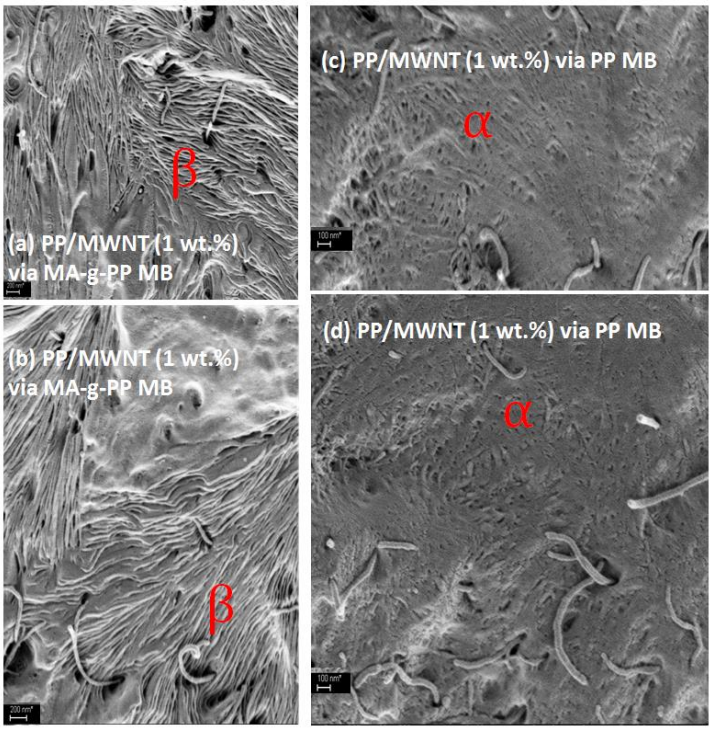

Figure 3.19. SEM images showing the lamellar morphology of the PP/MWNT nanocomposites prepared via (a,b) MA-g-PP/f-MWNT master batch and (c,d) via PP/f-MWNT master batch. Nanocomposites prepared via (a,b) MA-g-PP/f-MWNT master batch showed radial lamella of β-crystals [7], whereas those prepared via (c,d) PP/f-MWNT master batch showed both radial and tangential lamella of α-crystals [21]. SEM samples were prepared from the impact tested specimen's after surface etching.

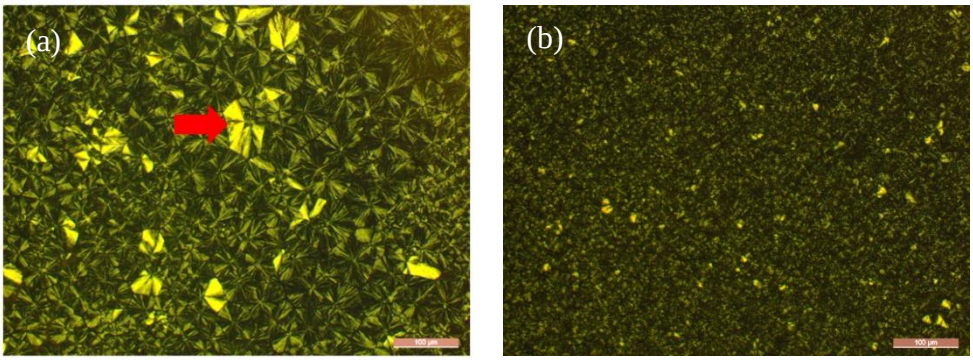

Figure 3.20. Polarized optical micrographs under cross-polars of PP/f-MWNT nanocomposites containing MA-g-PP/f-MWNT master batch at (a) 0.5 wt. % MWNT concentration and (b) 1 wt. % concentration. Bright spherulites (shown by red arrow) are the indication of β-crystals [7]. Spherulites with relatively low brightness consists of alpha crystals. The samples were melted at 200°C for 5 minutes, followed by cooling at 20 °C/min to 135 °C. Then samples were photographed at 135 °C when no further spherulitic growth could be observed. Scale bar represents 100 μm.

3.3.4 Effect of solution processed PP and PP/f-MWNT interphase on impact strength

Impact strength improvements in MA-g-PP/f-MWNT containing samples at least in part, can be attributed to the presence of β crystals. However, the largest improvement in impact strength was observed in PP/f-MWNT based samples that contained no β crystals and these samples exhibited spherulite size somewhat larger than that for p-MWNT containing samples. 1 wt. % CNT samples based on PP/f-MWNT master batch have tensile strength and modulus values statistically comparable, while the impact strength is 152% higher than that for the control PP. Tensile testing was done at a relatively low strain rate of 2.54/min, while significantly higher strain rates are realized in Izod notched impact testing (1.8×10^4/min). CNTs in PP/f-MWNTs master batch are coated with PP, which is then embedded in the PP matrix. On the other hand, CNTs in MA-g-PP/f-MWNTs master batch are coated with MA-g-PP, while p-MWNTs have no coating. PP interacts with p-MWNTs as seen from the high crystal nucleation rates and low crystallization times for the PP/p-MWNT system (Figure 3.15 and Table 3.1). However, it appears that the most coherent PP/CNT interface is present in the PP/f-MWNT containing samples. During solution master batch processing, entanglements are minimized both in PP and CNTs [22, 23]. This provides the opportunity for long length PP molecules to interact with CNTs. On the other hand, during melt blending of PP with p-MWNT, due to higher degree of entanglements, both in PP and in CNTs, the length of the interface would be relatively small, as compared to the interface length in PP/f-MWNT master batch based sample. The high impact strength of PP/f-MWNT master batch containing sample is attributed to this long and coherent interface coupled with small spherulite size, while relatively low impact strength of p-MWNT is attributed to CNT aggregates [24]. The higher molecular weight

of PP as compared to that of the MA-g-PP, is also likely to be responsible for differences in impact strength between PP/f-MWNT and MA-g-PP/f-MWNT master batch based samples.

Table 3.1. Crystallization temperature (T_c) based on DSC at heating and subsequent cooling rates of 2.5 °C/min, and isothermal DSC data of crystallization half-time $t_{1/2}$ (min) at 135 °C.

Materials	MWNT concentration (wt. %)	T_c (°C)	Half-time, $t_{1/2}$ (min) at 135 °C
Control PP	-	122.0	> 90
Nanocomposites via p-MWNT	0.01	126.5	11.8
	0.1	126.6	8.8
	0.3	127.4	4.4
	0.5	129.0	---
	1	132.9	1.5
Nanocomposites via MA-g-PP/f-MWNT master batch	0.005	120.0	---
	0.01	120.8	29.6
	0.1	122.0	21.1
	0.3	122.7	24.4
	0.5	122.3	---
	1	124.4	16.3
Nanocomposites via PP/f-MWNT master batch	0.005	121.8	---
	0.01	123.0	16.0
	0.1	125.7	6.9
	0.3	130.0	3.3
	0.5	127.6	---
	1	127.4	7.0

The role of the presence of solution-processed PP on the impact strength also needs to be understood, as 1 wt. % MWNT containing samples prepared from the PP/f-MWNT master batch contains high concentration (19 wt. %) of solution processed PP. The dilute solution processed PP is expected to have fewer entanglements than melt-processed PP, and this may affect crystallization which in turn will affect the mechanical properties.

Therefore, PP was processed from dilute solutions similar to the PP/f-MWNT master batch, except no f-MWNTs were used. PP/solution-processed PP (19 wt. %) mixtures were melt compounded and injection molded using the same process parameters as was used for various nanocomposites. PP/solution-processed PP (19 wt. %) samples exhibited a higher nucleation rate (Figure 3.21) and lower crystallization temperature as compared to that of the control PP (Table 3.2). This influence of solution-processed PP is similar to the effect of plasticizers on the nucleation rate and crystallization temperature of polymers [25-28]. WAXD results of PP/solution-processed PP are presented in Figure 3.22 and Table 3.3. Higher PP orientation (lower FWHM of (040) crystal peak) in the PP/solution-processed PP (19 wt. %) sample than in the control PP is attributed to the less entangled solution processed PP chains (Table 3.3). The impact strength of PP/solution processed PP was 55% higher than that for the control PP (Table 3.4), while the impact strength of 1 wt. % CNT containing sample based on PP/f-MWNT master batch was 152% higher. This data clearly shows that solution-processed PP affects both crystallization as well as impact behavior. However, the effect of PP/f-MWNT master batch based sample on the impact strength is significantly higher than that observed by using the same amount of solution processed PP as present in 1 wt. % CNT containing sample based on PP/f-MWNT master batch (impact strength increase of 55% with solution-processed PP versus 152% increase with PP/f-MWNT master batch at 1 wt. % CNT). This helps in distinguishing the contribution of solution-processed PP from that of the PP coated f-MWNTs.

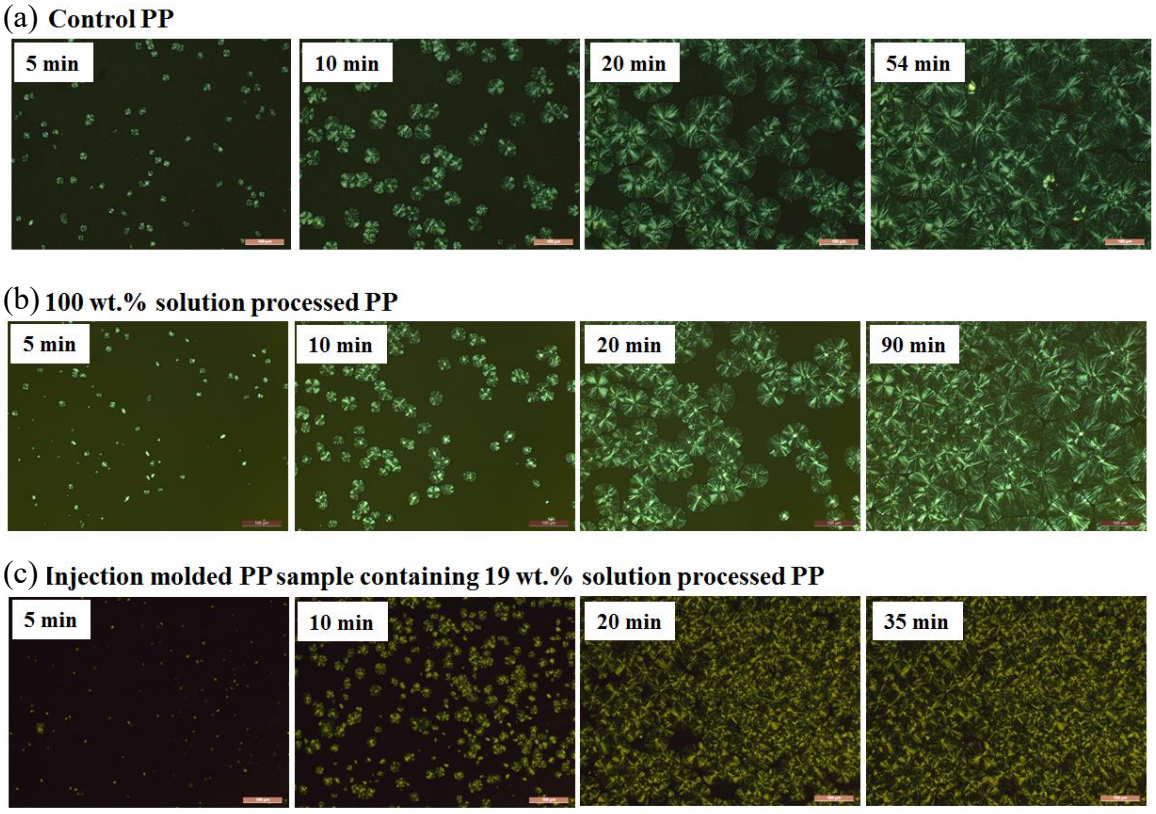

Figure 3.21. Polarized optical micrographs under cross-polars of (a) control PP, (b) solution processed PP and (c) 19 wt. % solution processed PP in the injection molded PP sample. The samples were melted at 200°C for 5 minutes, followed by a cooling at 20 °C/min to 135 °C. Then samples were photographed at different holding times at 135 °C as indicated on the images. Most right micrograph in each sample was taken at a time when no further spherulitic growth was observed. Scale bar represents 100 μm. Samples (a) and (c) are injection molded, while sample (b) was powder.

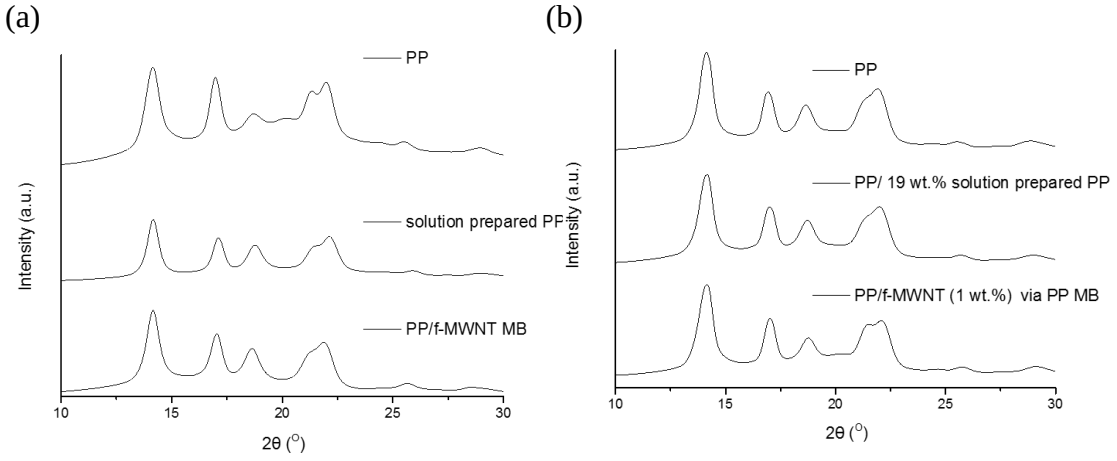

Figure 3.22. WAXD plots of (a) PP powder, solution processed PP powder, and PP/f-MWNT master batch. (b) Injection molded control PP tensile specimen, PP/19 wt. % solution processed PP tensile specimen and 1 wt. % CNT containing nanocomposite based on PP/f-MWNT master batch.

Table 3.2. DSC study of the injection molded samples.

Materials	T_c (°C)[1]	FWHM of T_c (°C) [1]	T_p (°C)[2]	Crystallinity (%)[3]	Crystallinity (%)[2]
PP	122.0	3.7	158.0	54	51
PP/ 19 wt.% solution processed PP	118.7	4.3	159.2	54	50
PP/MWNT (1 wt.%) via PP/f-MWNT	127.4	3.6	162.9	48	53.6

[1] from 1st cooling cycle
[2] from 2nd heating cycle
[3] from 1st heating cycle

Table 3.3. Structural information of injection molded samples as calculated from Figure 3.22.

	Crystallinity (%)	Crystal size (nm)	FWHM of (040)
PP	69	11.3	54.6
PP/ 19 wt.% solution processed PP	71	11.2	50.0
PP/MWNT (1 wt.%) via PP/f-MWNT	72	10.9	50.5

Table 3.4. Notched Izod impact strength of PP/MWNT nanocomposites prepared from PP/f-MWNT master batch and PP/solution processed PP (SpPP). The corresponding SpPP concentration in 0.1 wt. % and 1 wt. % PP/f-MWNT nanocomposites are 1.9 and 19 wt. %, respectively.

Impact strength (kJ/m^2)				
PP/f-MWNT nanocomposite via PP/f-MWNT master batch		f-MWNT wt. %		
		0	0.1	1
	Average	2.39	2.87	6.04
	SD	0.18	0.34	0.28
PP/solution processed PP (SpPP)		SpPP wt. %		
		0	1.9	19
	Average	2.39	3.23	3.73
	SD	0.18	0.11	0.67

3.3.5 Impact fracture surfaces under SEM

The photographs of the fractured surfaces of the impact tested control PP and 1 wt. % CNT containing samples are given in Figure 3.23. 1 wt. % CNT containing sample based on PP/f-MWNT master batch showed very rough fracture surface, while control PP and the other two types of nanocomposites (p-MWNT and MA-g-PP/f-MWNT master batch based systems) exhibited relatively smooth fracture surfaces. These differences in fracture surfaces clearly show that crack propagation has higher resistance in PP/f-MWNT based samples than all the other samples. To gain a better understanding of the fracture behavior under impact, fracture surfaces were also imaged using scanning electron microscopy. Imaging was done on both un-etched and etched surfaces.

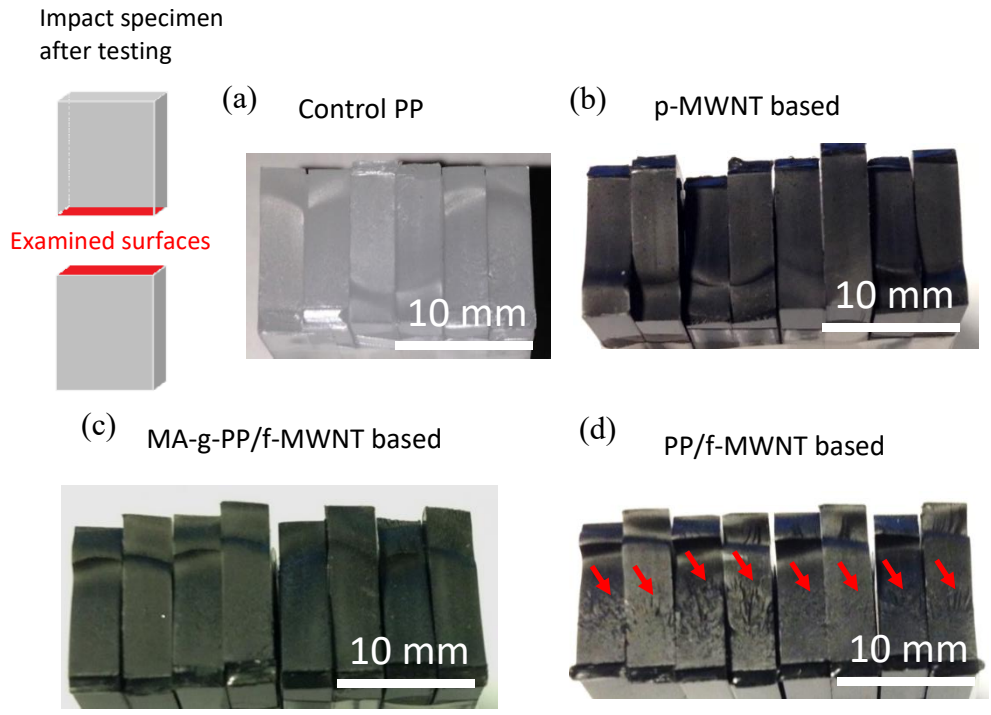

Figure 3.23. Photographs of the fractured surfaces of the impact tested samples prepared from (a) control PP and 1 wt. % MWNT containing nanocomposites via (b) p-MWNT, (c) MA-g-PP/f-MWNT master batch and (d) PP/f-MWNT master batch. Two consecutive pieces are obtained from the same sample. Red arrows show the presence of significant surface roughness in the PP/f-MWNT master batch based samples.

Under SEM observation at relatively low magnification, the entire impact-fracture surface of the p-MWNT based nanocomposite is relatively smooth as compared to the two master batch based samples (Figure 3.24). In the center region across the crack propagating direction, relatively rough features were clearly observed (Figure 3.23) in the PP/f-MWNT master batch based sample along with the broken nanotubes on the surface (Figure 3.24d and 3.24e). During acid etching of the impact-fractured surfaces, the amorphous PP regions were removed. SEM images of the etched samples are shown in Figure 3.25 and Figures G5 to G7 in Appendix G. The topography of the etched samples also shows that PP/f-MWNT master batch based samples still exhibits the roughest surface among the three types of nanocomposites (Figure 3.26). In PP/f-MWNT based nanocomposite, the pull-out lengths of the nanotubes are comparable to those before etching (Figure 3.27a and 3.27d). This indicates that CNTs are well-bonded in the matrix due to the strong PP/CNT interface. On the other hand, MA-g-PP is etched and washed away showing a relatively weak interaction between interfacial MA-g-PP and the matrix PP (Figure 3.25 and Figure G6 in Appendix G). The MWNT aggregates exhibit the worst interaction with the polymer are completely exposed to the surface in the p-MWNT based nanocomposite (Figure 3.25 and Figure G7 in Appendix G). PP/f-MWNT master batch based sample is more solvent resistant than MA-g-PP/f-MWNT based and PP/p-MWNT samples. In Figure 3.27, a significant difference in the interphase morphology in the etched nanocomposite samples can be seen. That is, longer lengths of CNTs are revealed in the latter two cases than for PP/f-MWNT based samples. Even upon etching, most of the nanotubes in the PP/f-MWNT based sample remains bonded with the polymer matrix,

while more CNT surfaces are visible in the MA-g-PP/f-MWNT based samples and in PP/p-MWNTs.

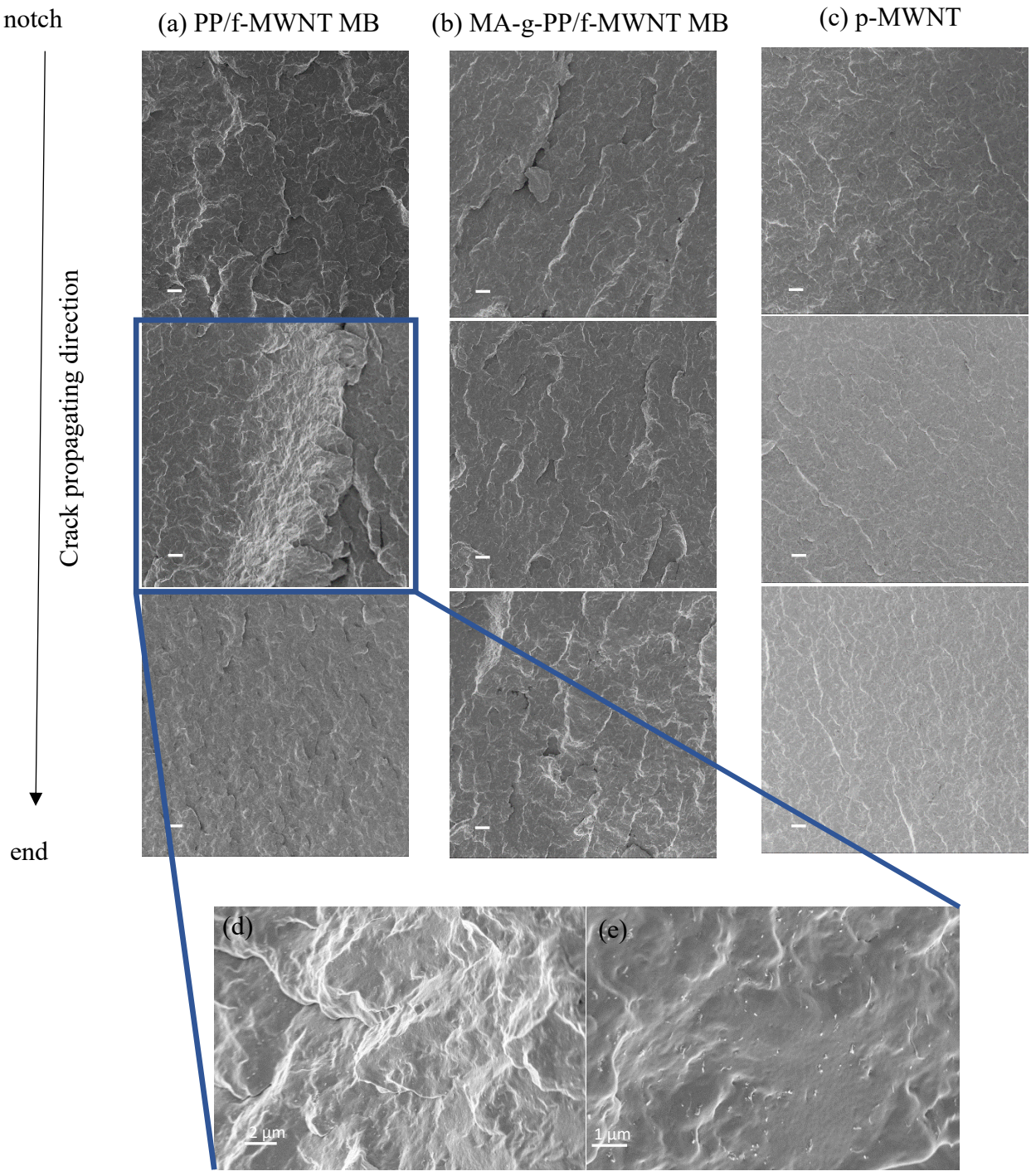

Figure 3.24. SEM images of PP/MWNT nanocomposites impact-fractured surface prepared from (a,d,e) PP/f-MWNT master batch (b) MA-g-PP/f-MWNT master batch and (c) p-MWNT. Scale bars represent 10 µm if not mentioned.

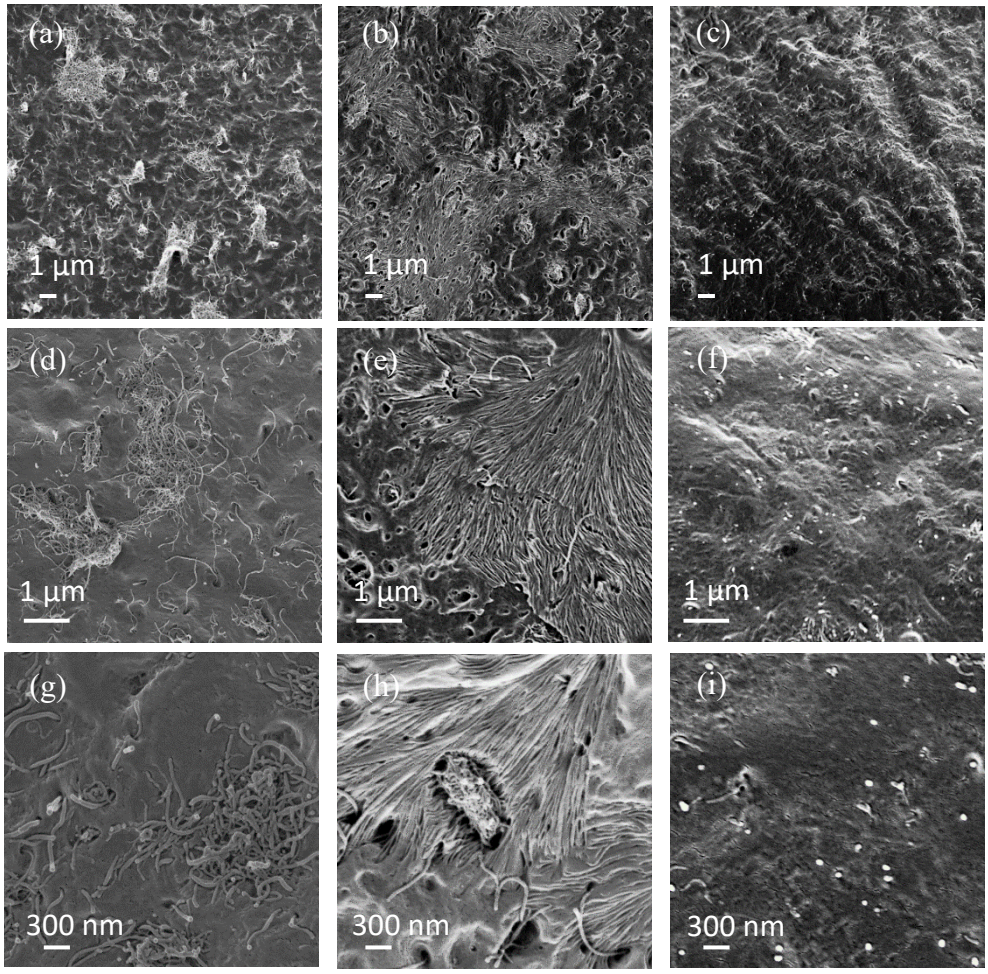

Figure 3.25. SEM images of PP/MWNT (1 wt.%) nanocomposites impact-fractured surfaces from (a,d,g) p-MWNT, (b,e,h) MA-g-PP/f-MWNT master batch and (c,f,i) PP/f-MWNT master batch after acid etching. Significant lengths of nanotubes were exposed in p-MWNT and MA-g-PP/f-MWNT based samples (figures d, g, e, and h), however such exposed nanotubes were not observed in PP/f-MWNT based samples.

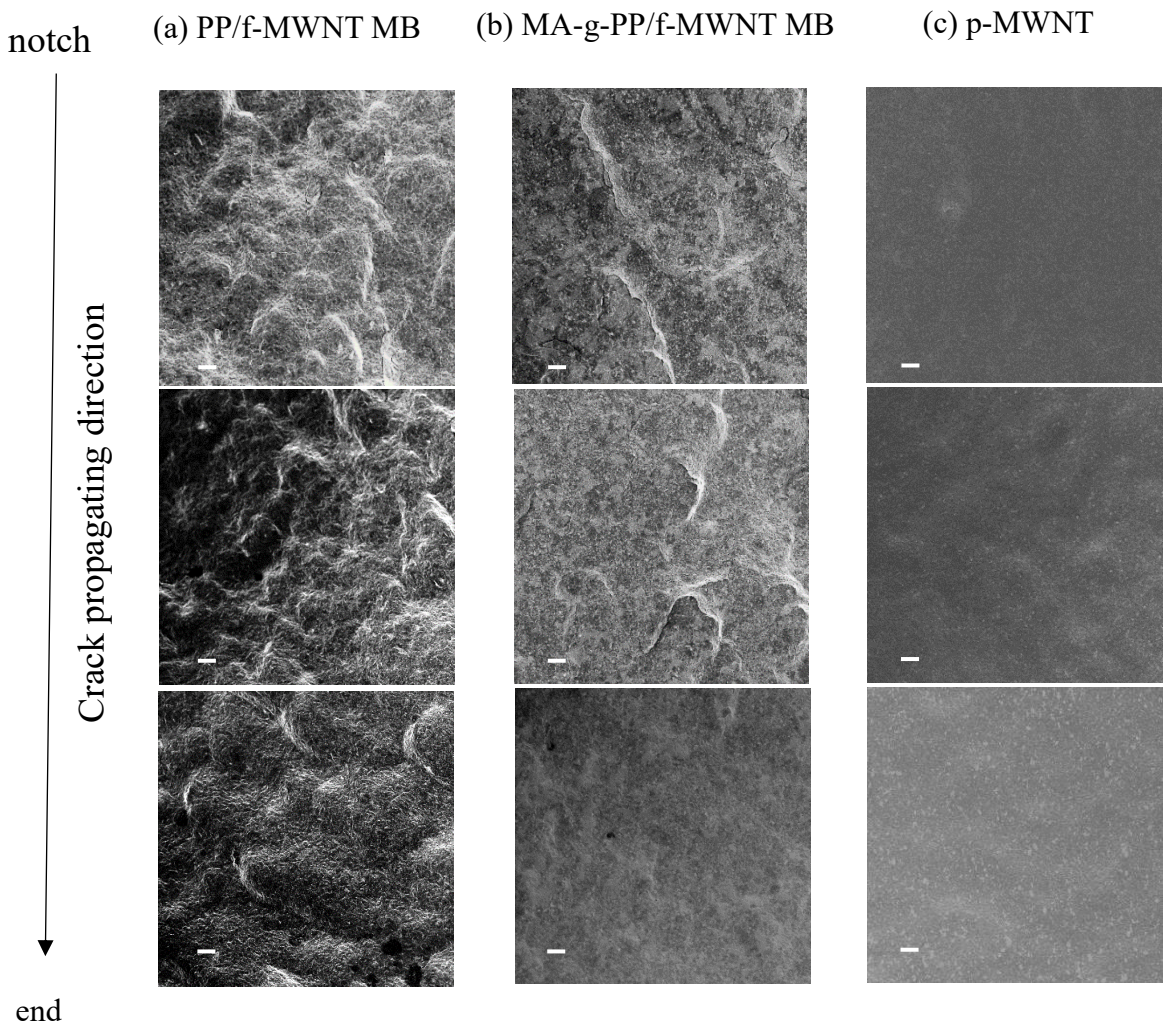

Figure 3.26. SEM images of PP/MWNT nanocomposites (at 1 wt. % CNT) impact-fractured surface prepared from (a) PP/f-MWNT master batch (b) MA-g-PP/f-MWNT master batch and (c) p-MWNT after acid etching. Scale bars represent 10 μm.

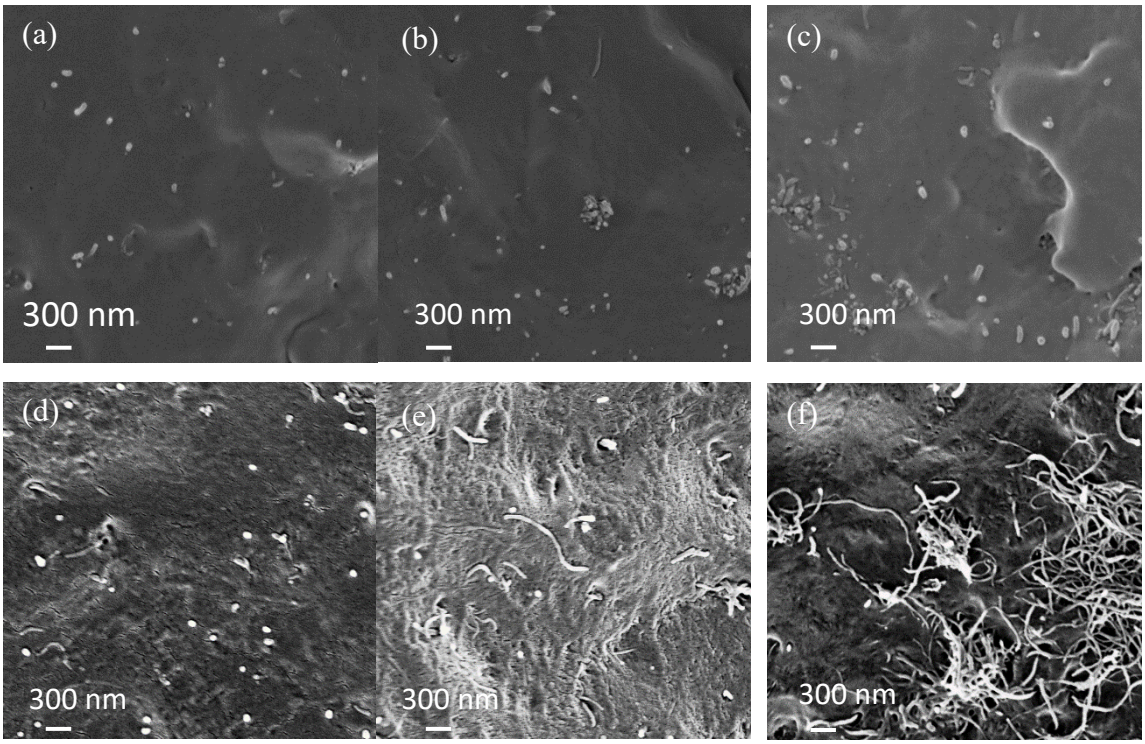

Figure 3.27. SEM images of PP/MWNT nanocomposites impact-fractured surface prepared from (a,b and d.e) PP/f-MWNT master batch and (c,f) p-MWNT. Figures (a, b, and c) are on un-etched samples, while figures (d, e, and f) were taken on etched samples. More of the CNTs are revealed in the etched samples from PP/p-MWNT then from PP/f-MWNT based samples. This suggests significant difference in the interphase morphology in the two nanocomposites. PP/f-MWNT master batch based sample is more solvent resistant than PP/p-MWNT.

The spherulitic boundary is typically considered to be the weak point and is often the initiating point for mechanical failure. Two strategies are often used to improve the fracture toughness of polypropylene. These strategies are reducing the spherulite size [12-15] and strengthening the spherulite boundaries [29]. The former is easily achieved through the introduction of nucleating agents such as sodium benzoate [30], while the latter has been approached through creating inter-spherulitic links and tie molecules at spherulite boundaries as well as in the interlamellar regions with the help of a multiblock copolymer of isotactic and atactic polypropylene (iPPaPP) or a random ethylene-propylene copolymer. The copolymer regions are unable to crystallize (and isotactic PP segments crystallize) and

hence these non-crystallizing regions migrate to the boundary sites and thus become connecting chains between adjacent spherulites [29].

In the PP/CNT nanocomposite, some of the CNTs that do not nucleate PP crystallization will be excluded from PP crystals [31], and these CNTs become the connecting links between spherulites and in between interlamellar amorphous regions. In Figure 3.28, individual f-MWNTs are observed at the spherulite boundaries (Figure 3.28a and b) as well as inside the spherulites (Figure 3.28d) within the PP/f-MWNT master batch based samples, and in MA-g-PP/f-MWNT based nanocomposite (Figure G6 in Appendix G). Thus, the highest impact strength in PP/f-MWNT based samples among the three categories of nanocomposites reported here suggests that the PP/f-MWNT based samples exhibit the strongest interfacial bond between these three nanocomposites. This interphase

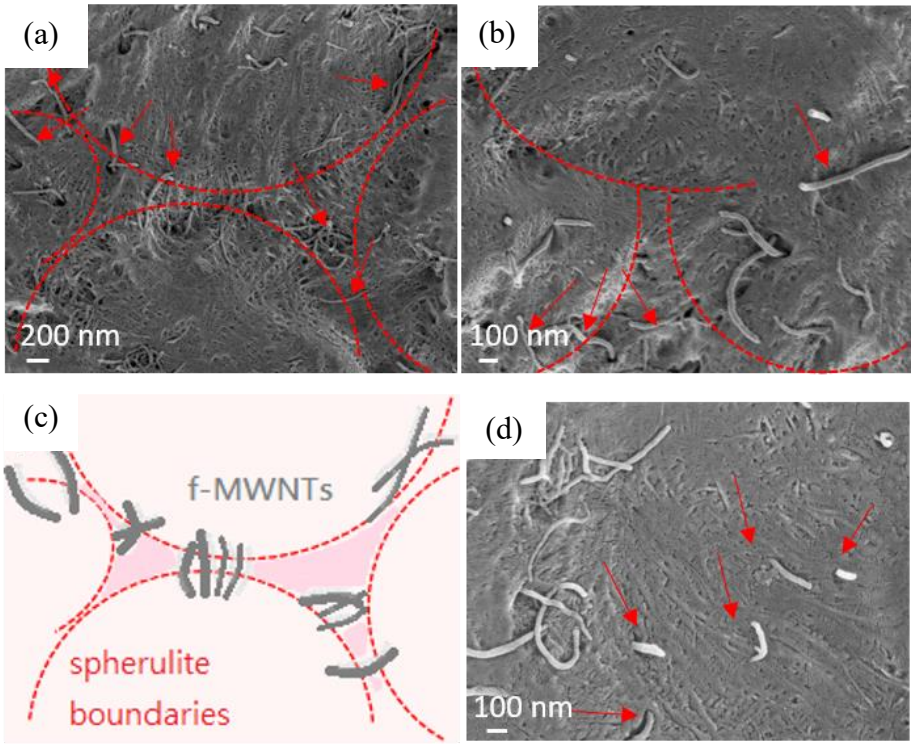

Figure 3.28. SEM images (a, b, c, d) of PP/MWNT (1 wt. %) nanocomposites impact-fractured surfaces prepared from PP/f-MWNT master batch. (c) is schematic of (a) showing CNTs connecting spherulites.

effect combined with the reduced spherulite size because of the nucleating ability of f-MWNTs, are believed to be the main toughening mechanisms in the PP/f-MWNT master batch based nanocomposites at high f-MWNT loadings (0.3 to 1 wt. %).

3.3.6 Crystal structure (crystal size and orientation) of PP in the presence of MWNTs

WAXD data on selected samples are given in Figure 3.16, Figure 3.17, and Table 3.5 and Table 3.6. The formation of β crystals in the injection molded tensile specimens was not as significant as in the injection molded impact bars in MA-g-PP/f-MWNT master batch based nanocomposites (Table 3.5). This is most likely due to the differences in the processing history encountered in the two cases during injection molding. Transformation from β crystal to α crystal under shear force has been reported in the literature [32, 33]. γ crystals [34] were also observed in the three types of nanocomposites at relatively high CNT loadings, but no γ crystals were observed in the neat PP.

Table 3.5. Percentage of β-crystals (K_β) in the tensile and impact specimens of nanocomposites prepared via MA-g-PP/f-MWNT master batch.

MWNT concentration (wt. %)	K_β	
	Tensile specimen	Impact specimen
0.5	20	27
1	5	33

Table 3.6. Structural information of PP/MWNT nanocomposites (tensile specimens) prepared from p-MWNT, MA-g-PP/f-MWNT master batch and PP/f-MWNT master batch.

MWNT concentration (wt. %)	Nanocomposites via p-MWNT			Nanocomposites via MA-g-PP/f-MWNT master batch			Nanocomposites via PP/f-MWNT master batch		
	X_c (%)[1]	L_{PP} (nm)[2]	f_{PP} [3]	X_c (%)[1]	L_{PP} (nm)[2]	f_{PP} [3]	X_c (%)[1]	L_{PP} (nm)[2]	f_{PP} [3]
0	69	11.3	54.6	69	11.3	54.6	69	11.3	54.6
0.01	68	11.3	52.1	68	12	56.6	69	11.1	52.6
0.5	71	10.7	50.3	73	11.1	50	72	11	51.2
1	72	10.2	45.2	73	10.9	43.3	72	10.9	50.5

[1] X_c: crystallinity from integrated radial scans.
[2] L_{PP}: crystal size of (110) at 2θ~ 14.1° according to Scherrer's equation with K = 0.9.
[3] f_{PP}: FWHM of (040) at 2θ ~16.9.

The polymer orientation data along the flow direction during injection molding is also given in Table 3.6. As the MWNT concentration increased, the polymer chains became more aligned in all three nanocomposites. The degree of alignment is related to the melt viscosity at 300 s^{-1} (correspond to the calculated shear rate at the exit of the melt transfer device to the mold). For this reason, the MA-g-PP/f-MWNT based sample has the lowest viscosity and the highest polymer orientation followed by p-MWNT and then the PP/f-MWNT based sample, which has the highest viscosity and lowest polymer orientation (Figure 3.29 and Table 3.6). MA-g-PP containing sample is expected to have lower viscosity due to its lower molecular weight than PP. Better dispersion as well as interaction of f-MWNT in the PP/f-MWNT based sample resulted in higher viscosity and lower polymer orientation as compared to the p-MWNT and MA-g-PP/f-MWNT based nanocomposites.

(a) FWHM of (040) WAXD peak on impact specimen

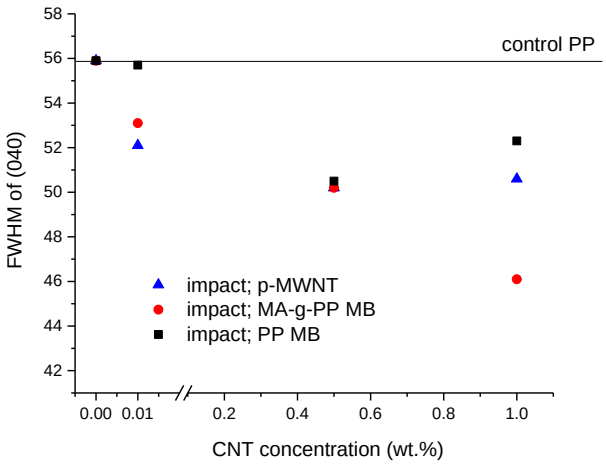

(b) FWHM of (040) WAXD peak on tensile specimen

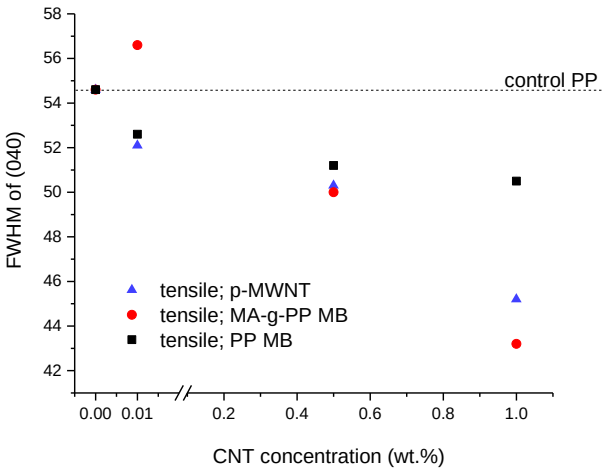

(c) Viscosity (at 300 s^{-1}) of the PP and PP/MWNT nanocomposites

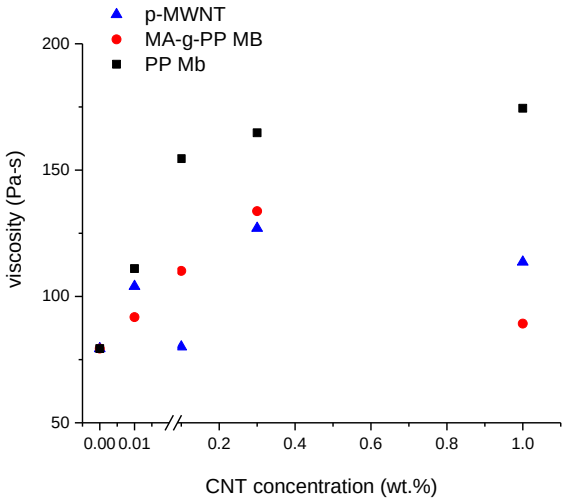

Figure 3.29. Full width at half maximum (FWHM) of the (040) WAXD peak of the (a) impact and (b) tensile samples prepared from PP and PP/MWNT nanocomposites at different MWNT concentrations. (c) Viscosity of the PP and PP/MWNT nanocomposite discs at different MWNT concentration at 300 s^{-1}. This shear rate of 300 s^{-1} corresponds to the calculated shear rate at the exit of the melt transfer device to the mold of the injection molding machine).

The data in Table 3.5 shows that there is modest increase in crystallinity from 69% in the control PP to 72-73% in the three nanocomposites at 1 wt. % CNT, and at the same time there is a modest decrease in crystal size (for the (110) plane) decreases from 11.3 nm to 10.2-10.9 nm in the three nanocomposites at the same CNT concentration.

3.3.7 MWNT orientation in the nanocomposites

MWNTs align along the drawing direction during the tensile test. The orientation of MWNTs (f_{CNT}) after tensile testing (Figure 3.5) is given in Table 3.7. The CNT orientation was determined using Raman spectroscopy following the method described in reference [35]. At 1 wt. % MWNT concentration, there is practically no MWNTs orientation developed during tensile testing. The strain to failure values for these two Raman tested samples (p-MWNT and MA-g-PP/f-MWNT based composites) was low (11 and 22%). However, the PP/f-MWNT based sample (at 1 wt. % CNT) with a strain of 283% also did not exhibit any CNT orientation. At low CNT concentration of 0.01 wt. %, there was reasonably good CNT orientation (in range of 0.3 to 0.42) in all three nanocomposites at strain values in the range of 285% to 335%. At CNT concentrations between 0.01 and 1 wt. %, intermediate level of CNT orientation values were observed, and reasonably good CNT orientation was observed at up to 0.5 wt. % CNT in PP/f-MWNT master batch based samples, while good CNT orientation was observed at up to 0.3 wt. % CNT in MA-g-PP/f-MWNT based samples, and good CNT orientation was observed only at 0.01 wt. % in the case of p-MWNT. This data provides further support for good interaction between CNTs and PP in the case of PP/f-MWNT based samples, as compared to the other two types of nanocomposites.

Table 3.7. f_{CNT} of PP/MWNT nanocomposites.

MWNT concentration (wt. %)	via p-MWNT	via MA-g-PP/f-MWNT master batch	via PP/f-MWNT master batch
0.01	0.42 [285%]	0.3 [335%]	0.35 [292%]
0.1	0.03 [8%]	0.18 [283%]	0.24 [302%]
0.3	0.07 [16%]	0.23 [350%]	0.23 [350%]
0.5	≅0 [15%]	0.04 [18%]	0.19 [281%]
1	≅0 [11%]	≅0 [22%]	≅0 [283%]

3.3.8 Heat Deflection Temperature (HDT)

Incorporation of MWNT also results in higher HDT as compared to the control PP (Figure 3.30 and Table 3.8). Higher HDT value is attributed to the ability of the material to retain stiffness at higher temperature. In Figure 3.31, HDT is plotted against tensile modulus at room temperature. Linear dependence is found in MA-g-PP/f-MWNT master batch and p-MWNT based samples but not in the PP/f-MWNT based samples. Among the three types of nanocomposites, the MA-g-PP/f-MWNT master batch based sample has the lowest increase in HDT. This is most likely a result of the presence of β crystals, which

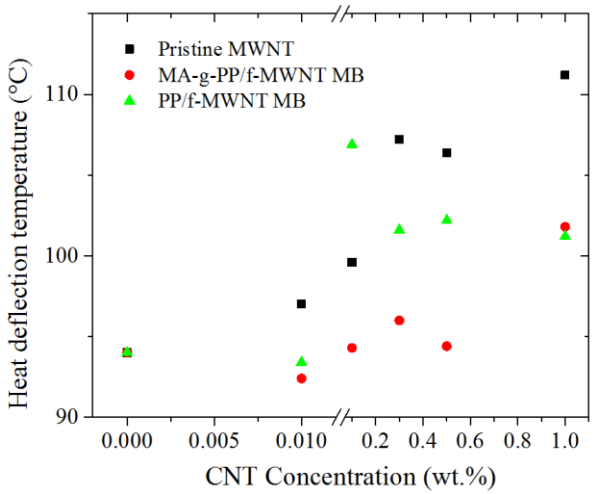

Figure 3.30. Heat deflection temperature of PP/MWNT nanocomposites prepared from p-MWNT, MA-g-PP/f-MWNT master batch, and PP/f-MWNT master batch.

have lower melting point than α crystals. HDT of the PP/f-MWNT master batch based sample reached a maximum of 106.9 °C at 0.1 wt. % CNT and then decreased to 101 °C at 1 wt. % CNT. This decrease is presumably due to the presence of the solution processed PP. It is worth noting that although the 1 wt. % CNT containing PP/f-MWNT based nanocomposite has comparable tensile modulus to that of the control PP at room temperature, the former has 7 °C higher HDT than the control PP. Among all the

nanocomposites, the highest HDT of 111.2 °C is achieved at 1 wt. % p-MWNT. This is an increase of 17.2 °C as compared to the control PP.

Table 3.8. Heat deflection temperature (HDT) of PP/MWNT nanocomposites prepared from p-MWNT, MA-g-PP/f-MWNT master batch and PP/f-MWNT master batch.

MWNT concentration (wt. %)	HDT (° C) of nanocomposites		
	Via p-MWNT	Via MA-g-PP/f-MWNT master batch	Via PP/f-MWNT master batch
0	94	94	94
0.01	97	92.4	93.4
0.1	99.6	94.3	106.9
0.3	107.2	96	101.6
0.5	106.4	94.4	102.2
1	111.2	101.8	101.2

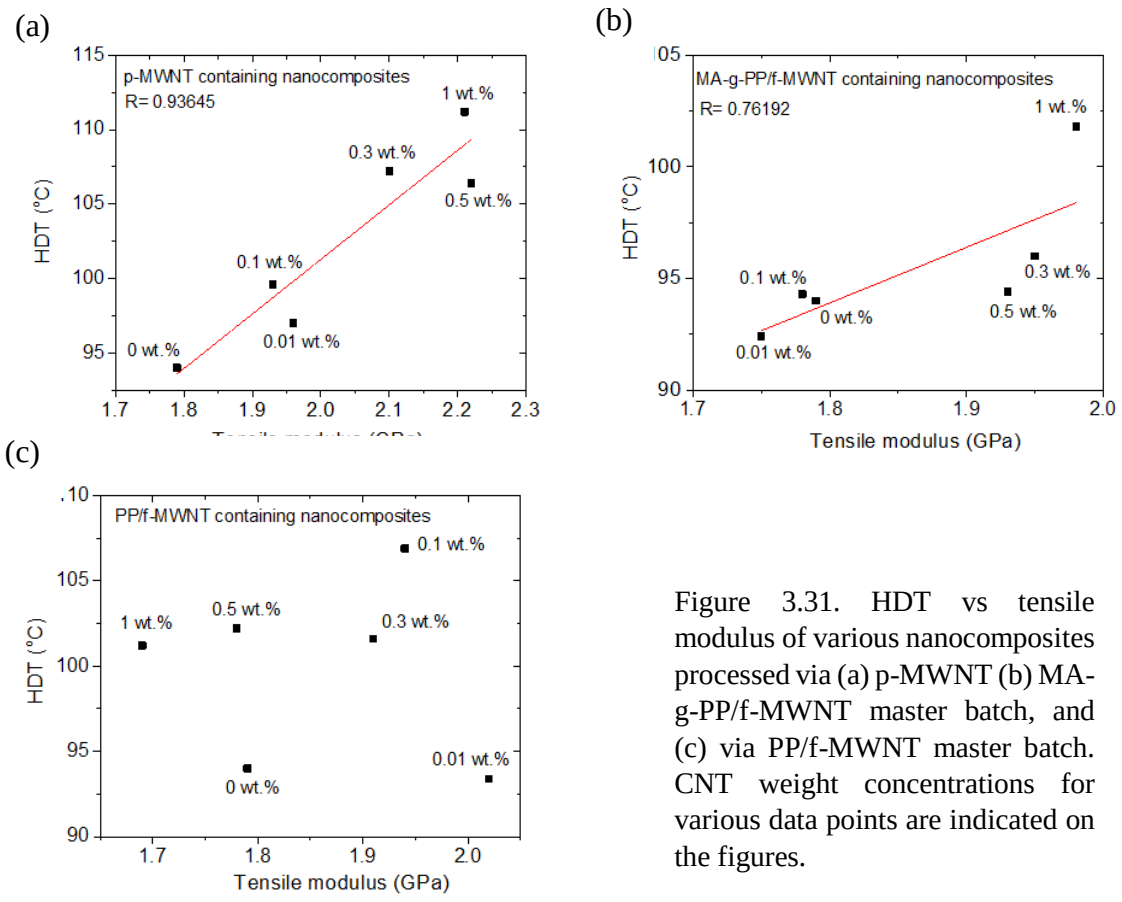

Figure 3.31. HDT vs tensile modulus of various nanocomposites processed via (a) p-MWNT (b) MA-g-PP/f-MWNT master batch, and (c) via PP/f-MWNT master batch. CNT weight concentrations for various data points are indicated on the figures.

3.4 CONCLUSIONS

Polypropylene/CNT nanocomposites were prepared by a combination of solution processing and melt blending approaches. Both functionalized and pristine carbon nanotubes were used in this study. MA-g-PP was used as a compatibilizer between f-MWNT and PP. Dispersion quality was notably improved in the solution processed master batch based samples. In all cases, CNTs acted as nucleating agents for polymer crystallization. As a result, at 1 wt. % carbon nanotube, crystallization time at 135 °C decreased by two orders of magnitude in the case of p-MWNT, and by an order of magnitude in the case of PP/f-MWNT and MA-g-PP/f-MWNT master batch based systems. MA-g-PP/f-MWNT based samples exhibited significant presence of β crystals, while no β crystals were observed in the PP/f-MWNT based samples or in PP/p-MWNT samples. Pristine MWNT containing samples exhibited highest improvement in modulus and tensile strength, but strain to failure decreased substantially at a relatively low CNT concentration. MA-g-PP/f-MWNT based samples exhibited an improvement in impact strength (69% increase at 1 wt. % f-MWNT), while also maintaining good modulus and yield stress values. The best impact strength was achieved with PP/f-MWNT master batch based samples, where at 1 wt. % f-MWNT, impact strength increased by 152%, while maintaining good tensile modulus, yield stress and strain to failure. Heat deflection temperature also increased in all cases. Further property improvements are expected by elimination of the CNT aggregates observed in the current study. This study shows that by tailoring the interface between polymer and the CNTs, nanocomposites with significant property improvements can be produced from polymers at very low CNT concentrations.

3.5 REFERENCES

1. Anatoliy Goldman, *Stiff and impact resistant compositions containing poly (propylene) or poly (ethylene/propylene) and calcium carbonate for closures*. 2003, Google Patents.

2. *Anti-impact modified PP/HDPE (Polypropylene/High Density Polyethylene) plastics for automotive interior parts and preparation method thereof* Google Patent, 2013.

3. Jr Jeremiah P Lehane, *Impact strength of blends of polyethylene and polypropylene*. 1964, Google Patents.

4. Petar Doshev, *Polypropylene copolymers with specific crystal nucleation* Google Patent, 2011.

5. A Turner Jones, Jean M Aizlewood, and DR Beckett, *Crystalline forms of isotactic polypropylene.* Die Makromolekulare Chemie, 1964. **75**(1): p. 134-158.

6. Yongsok Seo, Jinho Kim, Kwang Ung Kim, and Young Chul Kim, *Study of the crystallization behaviors of polypropylene and maleic anhydride grafted polypropylene.* Polymer, 2000. **41**: p. 2639-2646.

7. D. R. Norton and A. Keller, *The spherulitic and lamellar morphology of melt-crystallized isotactic polypropylene.* Polymer, 1985. **26**(5): p. 704-716.

8. B. A. Newcomb, H. G. Chae, P. V. Gulgunje, K. Gupta, Y. D. Liu, D. E. Tsentalovich, M. Pasquali, and S. Kumar, *Stress transfer in polyacrylonitrile/carbon nanotube composite fibers.* Polymer, 2014. **55**(11): p. 2734-2743.

9. Xiao Yan, Zhang Xiaoqing, Cao Wen, Wang Ke, Tan Hong, Zhang Qin, Du Rongni, and Fu Qiang, *Dispersion and mechanical properties of polypropylene/multiwall carbon nanotubes composites obtained via dynamic packing injection molding.* Journal of Applied Polymer Science, 2007. **104**(3): p. 1880-1886.

10. M. Hemmati, G. H. Rahimi, A. B. Kaganj, S. Sepehri, and A. M. Rashidi, *Rheological and Mechanical Characterization of Multi-Walled Carbon Nanotubes/Polypropylene Nanocomposites.* Journal of Macromolecular Science: Physics, 2008. **47**(6): p. 1176-1187.

11. Young Ho Choi, *Polyacrylonitrile / carbon nanotube composite fibers [electronic resource]: effect of various processing parameters on fiber structure and properties / by Young Ho Choi*. 2010: Atlanta, Ga. : Georgia Institute of Technology, 2010.

12. S. M. Ohlberg, J. Roth, and R. A. V. Raff, *Relationship between impact strength and spherulite growth in linear polyethylene.* Journal of Applied Polymer Science, 1959. **1**(1): p. 114.

13. C. F. Hammer, T. A. Koch, and J. F. Whitney, *Fine structure of acetal resins and its effect on mechanical properties.* Journal of Applied Polymer Science, 1959. **1**(2): p. 169.

14. Leo Barish, *The study of cracking and fracturing of spherulitic isotactic polypropylene.* Journal of Applied Polymer Science, 1962. **6**(24): p. 617.

15. D. G. M. Wright, R. Dunk, D. Bouvart, and M. Autran, *The effect of crystallinity on the properties of injection moulded polypropylene and polyacetal.* Polymer, 1988. **29**(5): p. 793-796.

16. R. Y. Bao, J. Cao, Z. Y. Liu, W. Yang, B. H. Xie, and M. B. Yang, *Towards balanced strength and toughness improvement of isotactic polypropylene nanocomposites by surface functionalized graphene oxide.* Journal of materials chemistry a, 2014. **2**(9): p. 3190-3199.

17. T. Barany, A. Izer, and J. Karger-Kocsis, *Impact resistance of all-polypropylene composites composed of alpha and beta modifications.* Polymer Testing, 2009. **28**(2): p. 176-182.

18. P. Jacoby, *Beta nucleating masterbatch offers enhanced properties in polypropylene products.* Plastics, Additives and Compounding, 2007. **9**(3): p. 32-35.

19. D. G. Papageorgiou, K. Chrissafis, and D. N. Bikiaris, *β-Nucleated Polypropylene: Processing, Properties and Nanocomposites.* Polymer Reviews, 2015. **55**(4): p. 596-629.

20. Q. Cheng, H. J. Byrne, and Z. Lü, *Synthesis of a maleic anhydride grafted polypropylene-butadiene copolymer and its application in polypropylene/styrene-butadiene-styrene triblock copolymer/organophilic montmorillonite composites as a compatibilizer.* Journal of Applied Polymer Science, 2009. **114**(3): p. 1820-1827.

21. Shanju Zhang, Marilyn L. Minus, Lingbo Zhu, Ching-Ping Wong, and Satish Kumar, *Polymer transcrystallinity induced by carbon nanotubes.* Polymer, 2008. **49**: p. 1356-1364.

22. C. Sawatari, S. Shimogiri, and M. Matsuo, *Morphological properties of ultrahigh molecular weight polyethylene-polypropylene blend films produced by gelation/crystallization from solutions.* Macromolecules, 1987. **20**(5): p. 1033-1041.

23. Geon-Woong Lee, Sudhakar Jagannathan, Han Gi Chae, Marilyn L. Minus, and Satish Kumar, *Carbon nanotube dispersion and exfoliation in polypropylene and*

structure and properties of the resulting composites. Polymer, 2008. **49**: p. 1831-1840.

24. K. Prashantha, J. Soulestin, M. F. Lacrampe, P. Krawczak, G. Dupin, and M. Claes, *Masterbatch-based multi-walled carbon nanotube filled polypropylene nanocomposites: assessment of rheological and mechanical properties.* Composites Science and Technology, 2009. **69**(11): p. 1756-1763.

25. Qing-Xin Zhang, Zhong-Zhen Yu, Xiao-Lin Xie, and Yiu-Wing Mai, *Crystallization and impact energy of polypropylene/CaCO3 nanocomposites with nonionic modifier.* Polymer, 2004. **45**: p. 5985-5994.

26. Z. Kulinski and E. Piorkowska, *Crystallization, structure and properties of plasticized poly(l-lactide).* Polymer, 2005. **46**: p. 10290-10300.

27. Chien-Chia Chu, Kevin L. White, Peng Liu, Xi Zhang, and Hung-Jue Sue, *Electrical conductivity and thermal stability of polypropylene containing well-dispersed multi-walled carbon nanotubes disentangled with exfoliated nanoplatelets.* Carbon, 2012. **50**: p. 4711-4721.

28. Hanwen Xiao, Wei Lu, and Jen-Taut Yeh, *Effect of plasticizer on the crystallization behavior of poly (lactic acid).* Journal of applied polymer science, 2009. **113**(1): p. 112-121.

29. A. Lustiger, C. N. Marzinsky, and R. R. Mueller, *Spherulite boundary strengthening concept for toughening polypropylene.* Journal of Polymer Science, Part B (Polymer Physics), 1998. **36**(12): p. 2047-2056.

30. G. S. Jang, W. J. Cho, and C. S. Ha, *Crystallization behavior of polypropylene with or without sodium benzoate as a nucleating agent.* JOURNAL OF POLYMER SCIENCE PART B-POLYMER PHYSICS, 2001. **39**(10): p. 1001-1016.

31. Donghua Xu and Zhigang Wang, *Role of multi-wall carbon nanotube network in composites to crystallization of isotactic polypropylene matrix.* Polymer, 2008. **49**: p. 330-338.

32. J. X. Li and W. L. Cheung, *On the deformation mechanisms of β-polypropylene: 1. Effect of necking on β-phase PP crystals.* Polymer, 1998. **39**(26): p. 6935-6940.

33. J. Garbarczyk, T. Sterzynski, and D. Paukszta, *Influence of additives on the structure and properties of polymers. 4. Study of phase transition in isotactic polypropylene by synchrotron radiation.* Polymer communications Guildford, 1989. **30**(5): p. 153-157.

34. S. Valdo Meille and S. Brückner, *Non-parallel chains in crystalline γ-isotactic polypropylene.* Nature, 1989. **340**(6233): p. 455-457.

35. Bradley A. Newcomb, Han Gi Chae, Prabhakar V. Gulgunje, Kishor Gupta, Yaodong Liu, Dmitri E. Tsentalovich, Matteo Pasquali, and Satish Kumar, *Stress transfer in polyacrylonitrile/carbon nanotube composite fibers.* Polymer, 2014. **55**: p. 2734-2743.

CHAPTER 4

IMPACT FRACTURE BEHAVIOR AND STRESS TRANSFER STUDIES

4.1 INTRODUCTION

In this Chapter, the impact fracture behavior is investigated by SEM fractography and interfacial shear strength is determined using Raman spectroscopy. First, stress transfer efficacy of the PP/f-MWNT nanocomposite, in which the PP interphase was tailored by co-solvent solution process (Chapter 2), was compared with that of the PP/p-MWNT nanocomposite without interphase engineering. Next, the impact fracture behaviors of neat PP and PP/f-MWNT were studied and compared by SEM micrographs to identify possible toughening mechanisms in the nanocomposite. It is worth noting that although the interfacial shear strength was determined using the fiber samples, this data represents the general characteristic of polymer-CNT interaction in different types of interphases, and therefore, can be applicable to the injection molded samples.

Typically, the impact resistance of PP can be improved by more than 100 % through the incorporation of β-type crystalline phase [1-3] or copolymers [4, 5]. While oftentimes stiffness is sacrificed from these two approaches, an alternative route, e.g. addition of fillers such as exfoliated graphite [6], carbon black [7], $CaCO_3$ [8, 9], carbon fiber and glass fiber [10], requires relatively high loading of fillers (typically 5 to 20 % or even more) to achieve intermediate level (10 to 100 %) of improvement in impact strength. In our previous work, it was shown for the first time that the impact strength of PP can be increased by 152 %

using only 1 wt% of carbon nanotubes (CNTs) [11] (and Chapter 3). Unlike the epoxy/CNT system where 129 % increase of fracture toughness can be achieved by as low as 0.1 wt% CNTs incorporation [12], literature on PP/CNTs prior to this study show less than 55 % improvement (0.5 wt% CNTs) in impact strength due to CNT aggregation and poor load transfer between the matrix and CNTs [13, 14]. Having said that, one can still infer from both the ductile deformation of PP transcrystalline in vicinity of CNTs [15] and formation of the more-extended PP molecules at CNT surface (Chapter 8) that PP/CNT holds a great potential in realizing stiffness-toughness balance through nano-engineered interface/interphase.

The fracture toughing mechanism in PP composites includes promoted plastic deformation of the matrix polymer, involving crazing, fabrillation and microvoids [8, 16-23]. Also, pull-out, shear yielding and cavitation of reinforcement fillers also plays an important role [13, 14, 24]. For example, Saminathan et al. [17] proposed that the polymer fibrils**,** embedded with exfoliated or intercalated silicate sheets**,** arrested the crack propagation. In nanoclay [19], elastomer [22] and $CaCO_3$ core-elastomer shell nanoparticle [18] filled nanocomposites, the toughening of polymer was attributed to the formation of microvoids upon fracture. These nano-filler nucleated microvoids release the plastic constraint surrounding PP matrix, promoting large scale plastic deformation with consequent tearing of matrix ligaments between microvoids. Also, Yang et al. [24] suggested that the pull-out of cellulose nanofiber (CNF) and microfibrillated cellulose is the major toughening mechanism in the PP/CNF composite. Nevertheless, to-date there is no comprehensive understanding on the impact fracture mechanism of PP/CNTs nanocomposite.

The quest for fracture toughening mechanisms has led to the development of several analysis methods, including, fractography [8, 13, 14, 16-22, 24], J-integral [25], essential work of fracture [24, 26], four point bending test [27, 28] as well as the interfacial shear strength determination via atomic force microscopy (AFM) [29-31], Kelly Tyson model [32, 33], molecular simulation [34], and Raman spectroscopy [35-41]. Raman spectroscopy provides information about molecular vibration, translation and rotation motions. In the field of the CNT-based polymer nanocomposites [35-37, 39-41], it has been shown that the application of a mechanical strain to the material results in downshifted frequencies of the Raman bands (D ~ 1300 cm^{-1}, G ~ 1590 cm^{-1}, G' ~ 2580 cm^{-1}) which are directly related to the interatomic force constants (stretching and weakening of C-C bond) [41]. Correlating such shifts with the applied strain leads to the determination of local stress profiles in the embedded fibers and fillers, and therefore the efficacy of stress transfer.

4.2 EXPERIMENTAL

For the materials, MWNT functionalization and master batch preparation, please refer to Chapter 2.2. For manufacturing the nanocomposites, please refer to Chapter 3.2.

4.2.1 Preparation of fibers for stress transfer test

Melt spun fibers were prepared for the single filament deformation test using Raman spectroscopy. The spinning process is similar to the injection molding, except after the recirculation, the melt was extruded directly from a 250 μm capillary at a spin-draw ratio of 6.25. The collected fibers were further drawn at 120 °C in air at a draw ratio of 10.

4.2.2 Characterization

Raman spectra were collected (Horiba Explora One, λ= 785 nm) at a laser power of ~500 μW (1 % power), with 50 X objective, 1600 grating, and resolution of 0.4 cm^{-1}. Single filament deformation of PP/f-MWNT (0.1 wt%) and PP/p-MWNT (0.1 wt%) fiber was performed using a gauge length of 25.4 nm with 0.0125 mm step sizes (Thorlabs motored stage, MTS25-Z8). Downshift of the D-mode peak position was utilized to determine the interfacial shear strength of the PP/CNT nanocomposites.

The impact-fractured surfaces of PP and PP/MWNT nanocomposite containing 1 wt. % MWNT were investigated by scanning electron microscopy (SEM) using Zeiss Ultra 60 FE-SEM at an accelerating voltage of 2 kV. A thin layer of gold was sputter coated onto these samples before imaging.

4.3 RESULTS AND DISCUSSIONS

4.3.1 Preparation of fibers for stress transfer test

Figure 4.1 shows the impact fracture surfaces of neat PP, PP/f-MWNT and PP/p-MWNT nanocomposites at 1 wt% MWNT concentration with impact strengths of 2.39 ± 0.18 KJ/m^2, 6.04 ± 0.28 KJ/m^2, and 2.20 ± 0.08 KJ/m^2, respectively [11]. In the previous Chapter (Chapter 3), this 152 % increase of impact strength in PP/f-MWNT was attribute to two mechanisms. First, the nucleating ability of CNTs that reduces the spherulite sizes (Chapter 5) and thus, results in more tortuous crack propagation paths. Second, based on the SEM observations, CNTs act as connecting links between spherulites and in between interlamellar amorphous regions. This bridging effect, in contrast to CNT debonding and pull-out, allows for a larger energy dissipation during material failure. Upon crack propagation, because of the high flexibility of CNTs (strain to failure of 10 % or more [42]), the CNTs can extend over a distance on either side of the bridged crack, absorb fracture

energy and promote local plastic deformation. This process is generally unimportant in the traditional brittle fiber based composites [43], and most importantly, can only be achieved if the interfacial adhesion between CNTs and the matrix polymer is strong enough.

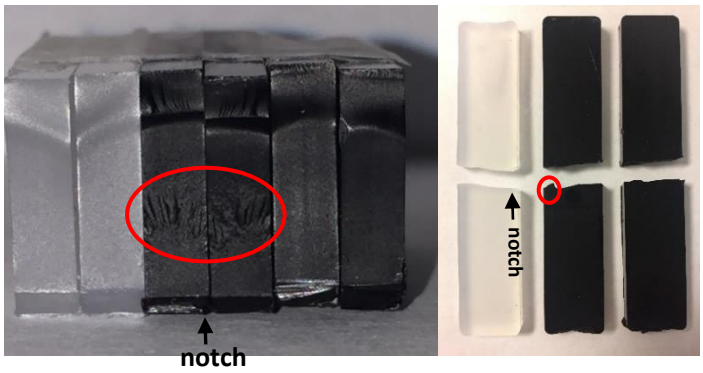

Figure 4.1. Fracture surfaces of impact fractured samples. From left to right: PP, PP/f-MWNT nanocomposite (1 wt%) and PP/p-MWNT nanocomposite (1 wt%).

To investigate and compare the interfacial shear strength (τ_i) between PP and MWNT in the PP/f-MWNT nanocomposite as well as the PP/p-MWNT nanocomposites, the strain-induced Raman D band shift in the CNTs was monitored. It is worth noting that fibers containing 0.1 wt% instead of 1 wt% MWNT were used for this purpose. It was observed in Chapter 3 and [11] that at 1 wt% MWNT loading, highly aggregated MWNTs were present in the PP/p-MWNT nanocomposite and there is no preferred MWNT orientation along the sample axis. 0.1 wt% MWNT concentration was chosen in this study to decouple the effect of MWNT dispersion and orientation differences between PP/f-MWNT and PP/p-MWNT such that the Raman band shifts reflects only the interface/interphase strength of the tailored (PP/f-MWNT) and untailored (PP/p-MWNT) systems.

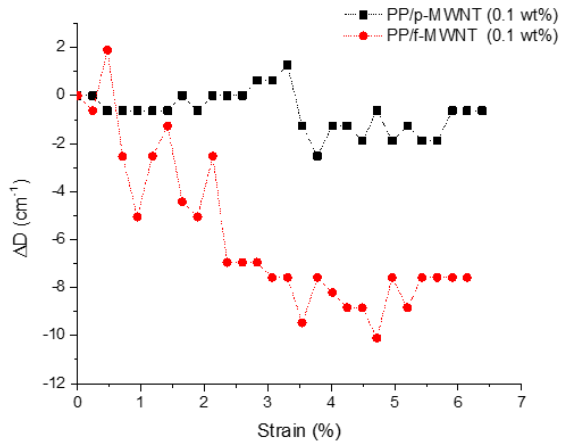

Figure 4.2. Change of Raman D band peak position (***Δ***D) as a function of stain for the PP/f-MWNT (0.1 wt%) fiber and the PP/p-MWNT (0.1 wt%) fiber.

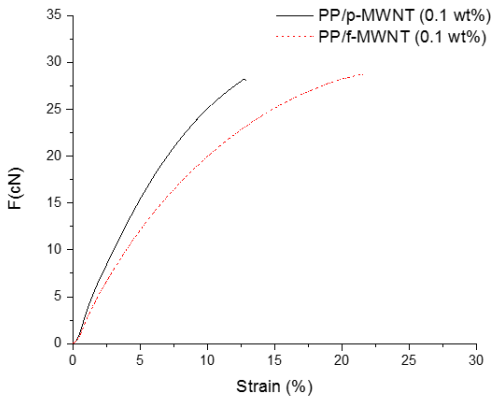

Figure 4.3. Force-strain curves for the PP/f-MWNT (0.1 wt%) fiber and PP/p-MWNT (0.1 wt%) fiber.

The strain-induced D band shifts for the PP/f-MWNT fiber and PP/p-MWNT fiber are shown in Figure 4.2. At low strain (< 2-3%), in the elastic regime (Figure 4.3), ***ΔD*** exhibits a gradual downshift in the case of PP/f-MWNT while ***ΔD*** remains mostly unchanged for PP/p-MWNT. At larger stain, in the plastic regime, the Raman response becomes insensitive to strain, that is, the maximum ***ΔD*** downshift (about 8-9 cm^{-1}) in PP/f-MWNT remains at the same level. This suggests good matrix-CNT interfacial adhesion. Considering CNTs remain elastic upto 13% strain [42, 44], such a plateu is unlikely due to the permenant deformation of CNTs. Instead, it implies that there is no interface failure and the mechanical load is continuously transfered from the polymer matrix to CNTs through the interface while straining the fiber. In contrast, the stress transfer between PP and p-MWNT in PP/p-MWNT is relatively ineffective since there is only about 1 cm^{-1} maximum ***ΔD*** shift. The Raman band shifts have been reported and correlated with stress transfer efficacy in various polymer-nanofiller systems, such as polyethylene/MWNT [36],

poly(ether ketone)/MWNT [37], polyacrylonitrile(PAN)/cellulose nanocrystal [38], poly(vinyl alcohol) (PVA)/single wall carbon nanotube [35, 39, 40], and PAN/few wall carbon nanotube [41]. For example, Newcomb et al. [41] has found an increase of maximum Raman G' band downshift of an as-spun PAN/CNT fiber from 3.1 cm^{-1} to 7.3 cm^{-1} after post spinning fiber drawing process. This was attributed to the improved interface due to the development of intimate contact between CNT and polymer during the drawing process. Also, both Liu [39] and Roy [40] suggested that an improved load transfer, therefore larger Raman band shifts, can be achieved between PVA and CNT through adequate functionalization via hydroxyl groups or biomolecule. Although direct comparison of Raman band shifts in the literatures is difficult owing to the use of different polymer and CNT types, based on the difference in maximum D band shift in our case (Figure 4.2), it is clear that PP/f-MWNT nanocomposite having a tailored interface/interphase possesses stronger matrix-CNT adhesion than the PP/p-MWNT nanocomposite.

As seen in Figure 4.2, the rate of stress transfer from the matrix to the nanotubes can also be derived from the slope in the elastic regime. The disparity between the two slopes reflects that the PP/f-MWNT exhibits significantly higher sensitivity to strain than PP/p-MWNT. Monitoring D band peak width allows for further insight into the stress transfer sensitivity from the polymer matrix to CNT. In Figure 4.4a, as PP/f-MWNT is strained, the stretching of C-C bond in the f-MWNTs is predominately in the portion that is along the straining direction, while the misoriented portion remains nearly un-stretched. Also, the stretching of the C-C bond in the f-MWNTs is uniformly distributed among the stretched portion. As the result, at 4% fiber strain, the D band exhibits a double peak

consisting of a peak remains at the similar location and another downshifted peak having narrower peak width with respect to that in the 0 % fiber strain spectrum. On the other hand, uneven straining of the C-C bond due to the differences in local interaction between the PP matrix and the CNTs was found in PP/p-MWNT. At 4 % fiber strain, the D band peak width increases compared to that of 0 % fiber strain. This result is expected since the interfacial interaction is not uniform along the CNT length in PP/p-MWNT, probably because of the weaker and uneven adhesion between PP and p-MWNT, and therefore, lower stress transfer sensitivity.

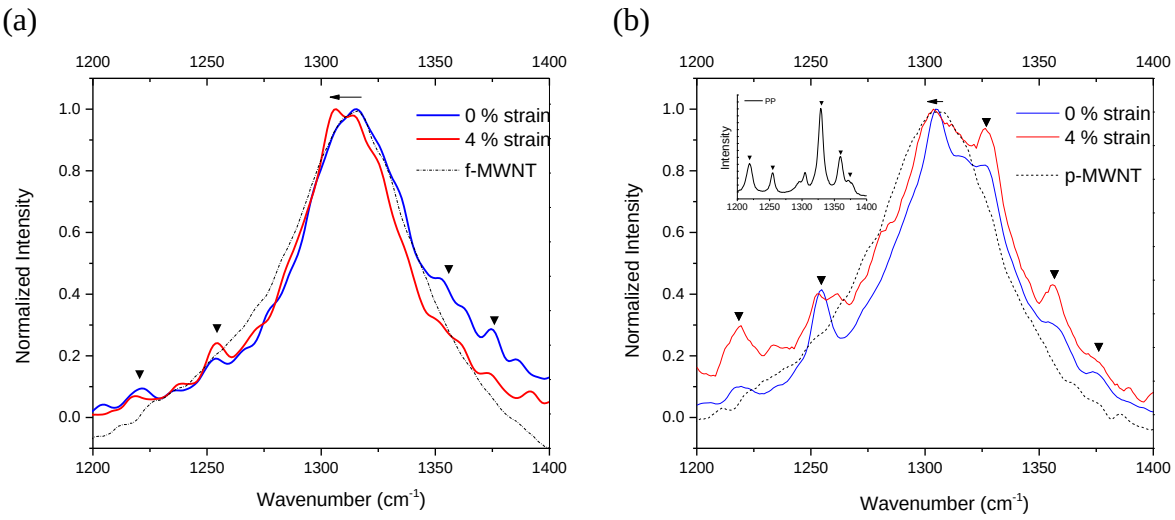

Figure 4.4. Raman D-mode spectra of the (a) PP/f-MWNT (0.1 wt%) fiber and (b) PP/p-MWNT (0.1 wt%) fiber at 0 % and 4 % filament strain.

The interfacial shear strength (τ_i) can be calculated using the modified shear lag equation [37, 41],

$$\tau_i = \frac{nE_{CNT}\varepsilon_i}{2}\tan h(ns) \quad (1)$$

where n^2 is defined as $\frac{2G_{13}}{\ln(R/r)E_{CNT}}$, E_{CNT} is the CNT effective modulus (Table 4.1),

$$\frac{1}{E_{CNT}} = \frac{1}{E_2} + \left(\frac{1}{G_{12}} - \frac{2\nu_{12}}{E_1} - \frac{2}{E_2}\right)\langle cos^2\theta\rangle + \left(\frac{1}{E_1} + \frac{1}{E_2} - \frac{1}{G_{12}} + \frac{2\nu_{12}}{E_1}\right)\langle cos^4\theta\rangle \quad (2)$$

ε_i is the elongation at the PP/f-MWNT or PP/p-MWNT interface, G_{13} is the PP shear modulus, which is estimated to be 0.675 GPa [11]. *s* is the ratio (*L/r*) where *L* is the length of the CNTs (4 μm) and *r* is the CNT diameter (12 nm), and the ratio (*R/r*) is defined by the spacing between neighboring CNTs divided by CNT radius. Downshift of the Raman D band peak position was used to determine ε_i, where $\varepsilon_i = \frac{-\Delta D_m}{S_{CNT}}$ and S_{CNT} is the shift rate of the D band peak position for individual CNT, S_{CNT} = -20.5 cm^{-1}/% [45]. $\boldsymbol{\Delta D_m}$ is the maximum D band peak shift which is approximately 8 cm^{-1} for PP/f-MWNT and 1 cm^{-1} for PP/p-MWNT (Fig. 2). Using the parameters in Table 4.1 and equation (2) and (3), the calculated τ_i for PP/f-MWNT and PP/p-MWNT is 17.8 MPa and 2.2 MPa, respectively. As mentioned earlier, the direct comparison of τ_i and its influence on mechanical performance between different systems are difficult since τ_i depends on various factors including the polymer and CNT types, CNT aspect ratio, CNT orientation and degree of aggregation in the matrix, covalent or non-covalent bonding of CNT to the matrix, etc. Only few literatures have reported the τ_i value in PP/MWNT (Table 4.2). Zare [32] fitted the experimental data using the Kelly-Tyson theory and obtained a τ_i value of 18.9 MPa. The MWNTs used in their work had not undergone any treatment and there was no further attempt to investigate the effect of CNT surface modification on τ_i. Although the strategy for improving τ_i in some of the thermoplastic polymer nanocomposites has been implemented, e.g. through hydrogen bonding formation between PVA and functionalized CNTs [35, 39], successful demonstration of engineering and improving the PP/CNT interfacial adhesion is relatively few in the literature.

Table 4.1. CNT orientation factors (fCNT), elastic constants and effective modulus (ECNT) along the nanocomposite fiber axis.

	PP/p-MWNT (0.1 wt%)	PP/f-MWNT (0.1 wt%)
f_{CNT}, $\langle P_{200} \rangle$	0.46	0.57
$\langle P_{400} \rangle$	0.3	0.34
$\langle cos^2\theta \rangle$	0.64	0.71
$\langle cos^4\theta \rangle$	0.53	0.60
E_1 (GPa)[1]	1060 [46]	
E_2 (GPa)[2]	50 [47]	
G_{12} (GPa)[3]	4 [46]	
v_{12} [4]	0.14 [48]	
E_{CNT} (GPa)	30.6	31.7

1 Longitudinal modulus of CNT 2 Transverse modulus of CNT 3 In-plane shear modulus of CNT
4 Poisson's ratio of CNT

Table 4.2. Interfacial shear strength (τ_i) values reported by various groups between carbon nanotube and matrix.

Matrix/CNT	Experimental Technique	τ_i
Polyethylene-butene/MWNT[1] [30]	AFM	47 MPa
Epoxy/MWNT [31]	AFM	35 - 380 MPa
Polyacrylonitrile/FWNT[2] [41]	Raman	15 - 44 MPa
polyvinyl alcohol/SWNT[3] [40]	Raman	188 MPa
Poly(ether ketone)/MWNT [37]	Raman	1 MPa
Poly(ether ketone)/FWNT [37]	Raman	8.4 – 14.2 MPa
Polyethylene/SWNT [34]	Molecular simulation	2.8 MPa
PP/MWNT [32]	Kelly-Tyson theory	18.9 MPa
Polystyrene/MWNT [32]	Kelly-Tyson theory	1.12 MPa
Polydicyclopentadiene/f-MWNT[4] [32]	Kelly-Tyson theory	51.9 MPa
Poly(ether ether ketone)/f-MWNT[4] [32]	Kelly-Tyson theory	1.13 MPa
Epoxy/f-MWNT[4] [32]	Kelly-Tyson theory	42.4 MPa

1 Multiwall carbon nanotube 2 Few-wall carbon nanotube 3 Single wall carbon nanotube
4 -COOH functionalized MWNT

Figure 4.5 depicts a proposed schematic of the PP/CNT interface/interphase in PP/f-MWNT and PP/p-MWNT nanocomposite. In PP/f-MWNT, f-MWNTs were firstly coated by the solution processed PP and then melt blended with neat PP (Chapter 2). In other word, the polymers around CNTs contain fewer entanglements which allow a better interaction between CNTs and PP (Chapter 2), promote surface crystallization, and therefore, result in a higher interfacial shear strength than that of PP/p-MWNT. On the other hand, in the PP/p-MWNT nanocomposite, p-MWNTs were simply melt blended with PP. Due to higher degree of entanglements in both PP and p-MWNTs, the development of the interphase would be relatively small, as compared to the PP/f-MWNT nanocomposite. In Chapter 3, it is shown that more CNTs were revealed at the acid etched impact fracture surface from PP/p-MWNT than from PP/f-MWNT, indicating stronger PP/CNT bonding in the latter [11]. Newcomb et al. [41] had also proposed a similar schematic to Figure 4.5 and attributed the high τ_i to the formation of ordered extended chain PAN around CNT. It is worth noting that the -COOH group on f-MWNT do not play a major role in enhancing PP/CNT adhesion. Based on Fourier transform infrared spectroscopy (FTIR), there is no interaction developed between the -COOH group and PP (Chapter 2).

As previously discussed, bridging effect of CNTs on a growing crack can not happen if the interfacial strength between the polymer matrix and the CNTs is weak. Since an effective load transfer in PP/f-MWNT nanocomposite has been demonstrated in Figure 4.2 and Figure 4.4, we further advance a hypothesis that the fracture toughing mechanism in PP/f-MWNT nanocomposite is the bridging effect of CNTs combined with the promoted plastic deformation of the PP matrix owing to good PP/CNT adhesion. Using the SEM fractography, we will show that CNTs, as stress concentrators under load, promote local

plastic deformation of surrounding PP matrix. One should note that, while it is well-understood that PP becomes more ductile when crystallizing into the β form, the incorporation of f-MWNTs or p-MWNTs in this work did not trigger the formation of β-type crystal [11].

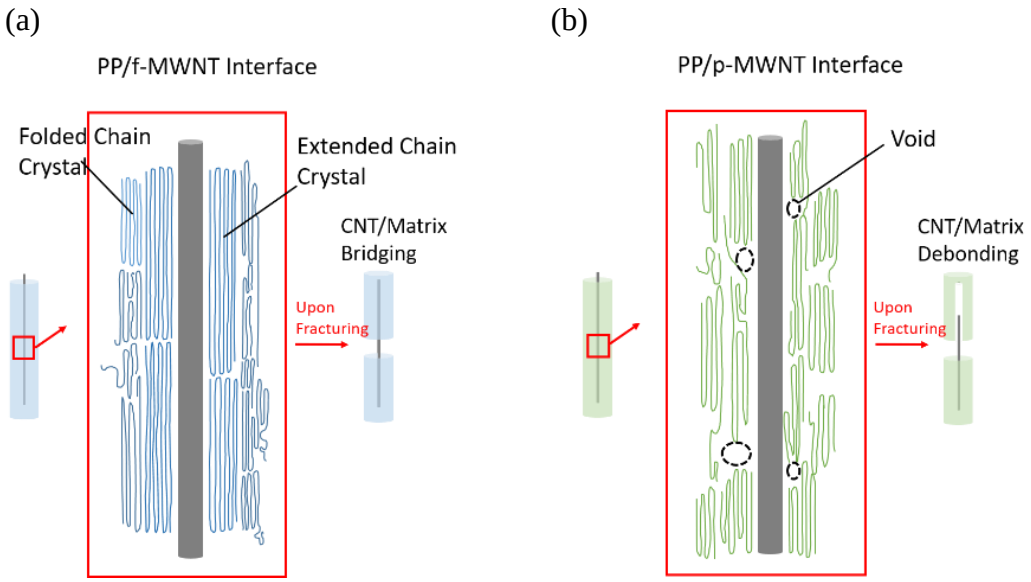

Figure 4.5. The schematic depicting the interface/interphase in PP/f-MWNT and PP/p-MWNT. In (a) PP/f-MWNT, the solution processed polymers render a highly ordered crystallization layer in vicinity of CNT, providing high degree of contact between PP and f-MWNT. In (b) PP/p-MWNT, the degree of contact between PP and p-MWNT is not very high, resulting a poorer interfacial shear strength. Upon sample fracturing, crack bridging happens in (a) while CNT/matrix debonding happens in (b) due to weak interfacial adhesion.

4.3.2 Fracture characteristics of the neat PP

Figure 4.6 presents the fracture surfaces of neat PP and PP/f-MWNT (1 wt%) nanocomposite impact tested at room temperature. Four primary zones can be defined as initiation (zone 1), slow propagation (zone 2), transition (zone 3) and fast propagation (zone 4). A parabolic ridge between zone 3 and 4 represents a stop-go crack front, or the stick-slip type propagation. This feature occurs when the speed of the crack is below a

critical value such that the crack stops (stick). When the stress build-up again, the crack will reinitiate and propagate (slip) [19].

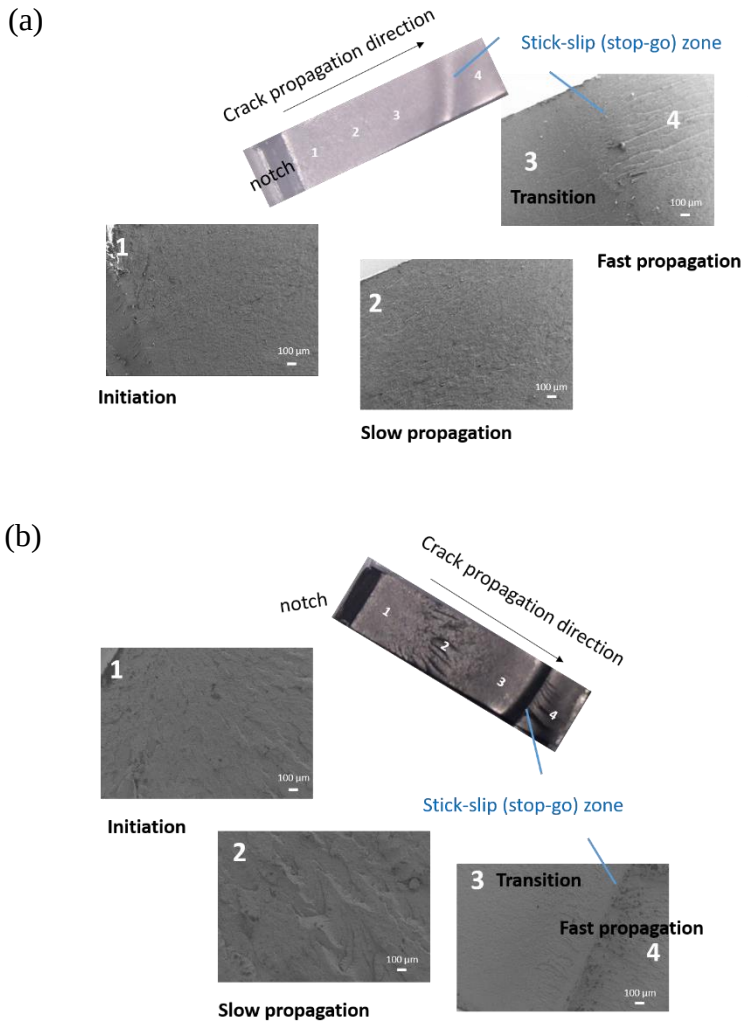

Figure 4.6. SEM micrographs of fracture surface of (a) neat PP and (b) PP/f-MWNT (1 wt%) nanocomposite impact tested at room temperature showing different zones: initiation (zone 1), slow propagation (zone 2), transition (zone 3), stick-slip zone, and fast propagation (zone 4).

In Figure 4.7, both the initiation and propagation zones have the cleavage brittle appearance. Also, the crack propagation paths can easily be identified. This is consistent with the smooth and flat fracture surface as shown in Figure 4.1. In thermoplastic polymer, the primary deformation mechanism is crazing, a localized plastic deformation consists of

the formation of fibrils and microvoids. This can be found in Figure 4.8. In between zone 3 and 4 where the crack propagation becomes slower and arrested, formation of fibrils along the crack propagation direction suggests that it is a highly sheared and stretched region involving tearing of materials (Figure 4.8). The craze type of feature was also reported by Misra et al. [19] and assigned to be a typical morphology in PP upon fracturing.

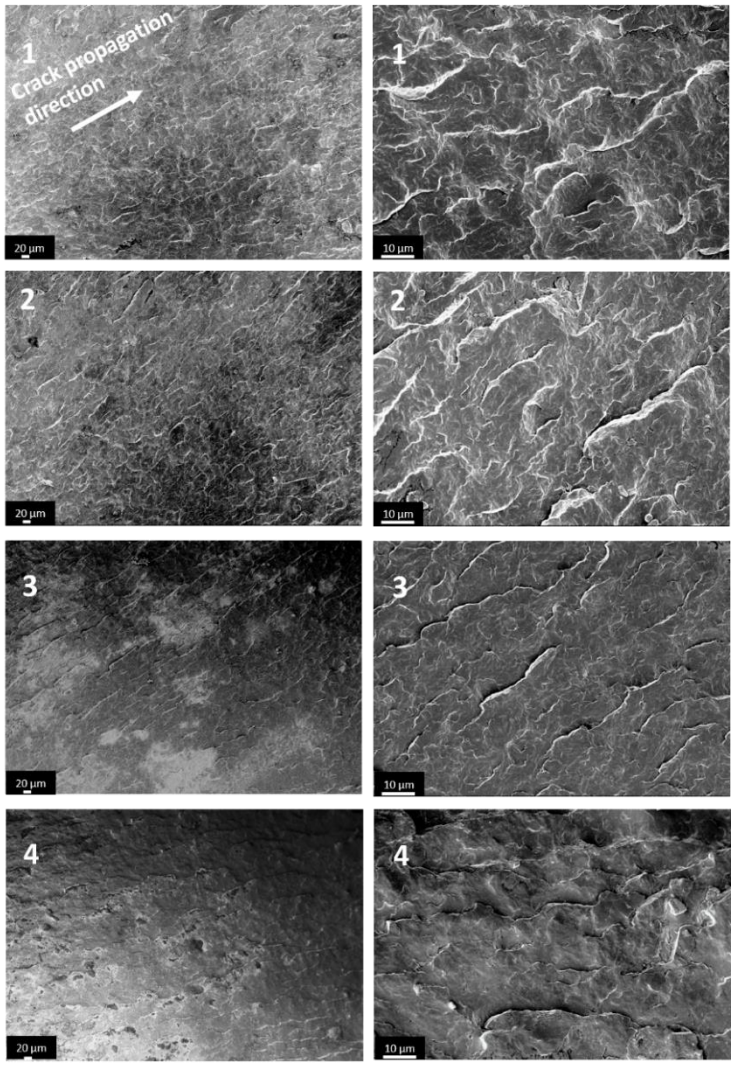

Figure 4.7. SEM micrographs of fracture surface of neat PP impact tested at room temperature showing different zones.

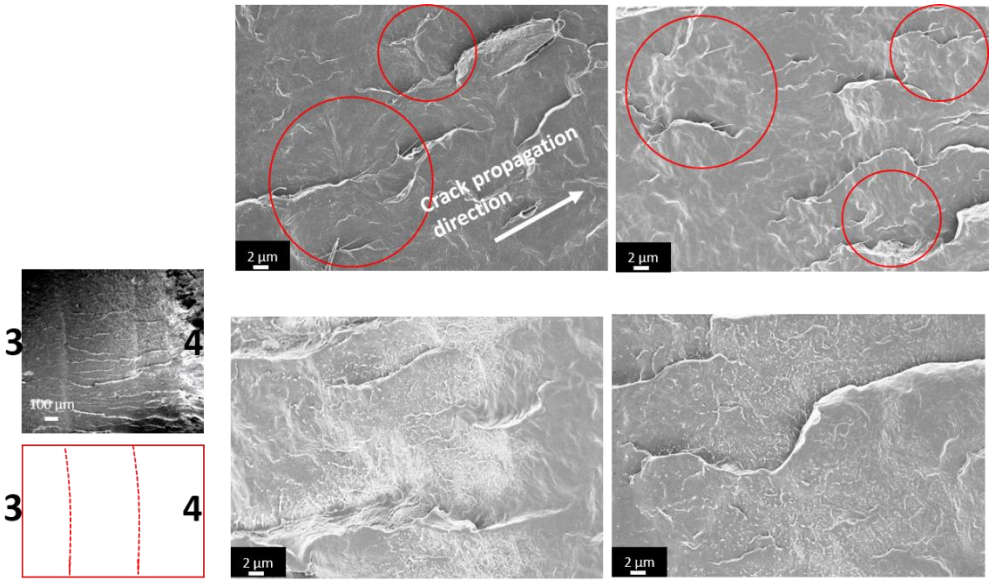

Figure 4.8. SEM micrographs between zone 3 and 4 of neat PP impact tested at room temperature showing fibrils along the crack propagation direction (top figures). Two markings perpendicular to the crack propagation direction having craze-like feature are shown in the bottom figures.

4.3.3 Fracture characteristics of the PP/f-MWNT nanocomposite

In contrast to neat PP, the overall macroscopic fracture surface of the PP/f-MWNT nanocomposite at room temperature appears to be relatively rough (Figure 4.1), i.e. more ductile-like. In a similar manner to neat PP, four primary zones were also defined from the PP/f-MWNT fracture surface (Figure 4.6). Microscopically, a major difference in PP/f-MWNT from neat PP is that cracks no longer propagate in a single direction but bifurcate and deflect (zone 1 and 3 in Figure 4.9). Also, the crack tip left residue chevron-shape markings at the shallow valleys (zone 2 in Figure 4.9 and Figure 4.10) implying some crack pinning/arresting mechanisms happening upon deformation. In the epoxy/graphene nanocomposite, Chandrasekaran et al. [49] reported that when the crack front met the surface of graphene sheet, it got deflected and went around the particle. The author suggested that this made the crack take a torturous path and accounted for the rough surfaces observed under SEM. In addition, because CNTs can act as stress concentrator

[13], microcracks (zone 2 in Figure 4.9 and Figure 4.10) were found nucleated by the high stresses in vicinity of the macroscopic crack tip. These microcracks then lower the stress experienced by the tip. Such shielding effect has also been observed in the rubber filled epoxy [50] where localized yielding (often referred as shear band) of the matrix material occurs between adjacent rubber particles in the plastic zone ahead of the crack tip. Furthermore, in Figure 4.10 and Figure 4.11, fibrils and CNTs were found bridging these microcracks which can be considered as a secondary effect of energy consumption action. Similar to what we have observed in neat PP (Figure 4.8), fibril formation also took place in the PP/f-MWNT (1 wt%) nanocomposite upon fracturing (Figure 4.12). However, fibrils were drawn not only along but also off-axis and even perpendicular to the crack propagation direction in PP/f-MWNT. This justifies a more complex in-plane stress profile around the crack tip as the result of microcrack initiation and the crack pinning/deflecting due to the presence of CNTs.

As we mentioned in the previous section, the major toughening mechanism in our PP/f-MWNT nanocomposite is the collective effects of CNT bridging and promoted matrix plastic deformation. Such effects are prevailing in the slow propagation zone (zone 2) and the stick-slip region as shown in Figure 4.13 and Figure 4.14. Rough fracture surface in these regions indicates improved crack propagation resistance as compared with neat PP. On the “ridge” surface where intense local plastic deformation happened, the presence of CNTs breakages (Figure 4.13a) and shear-to-ruptured fibrils (Figure 4.13b) indicate highly consumption of the fracture energy

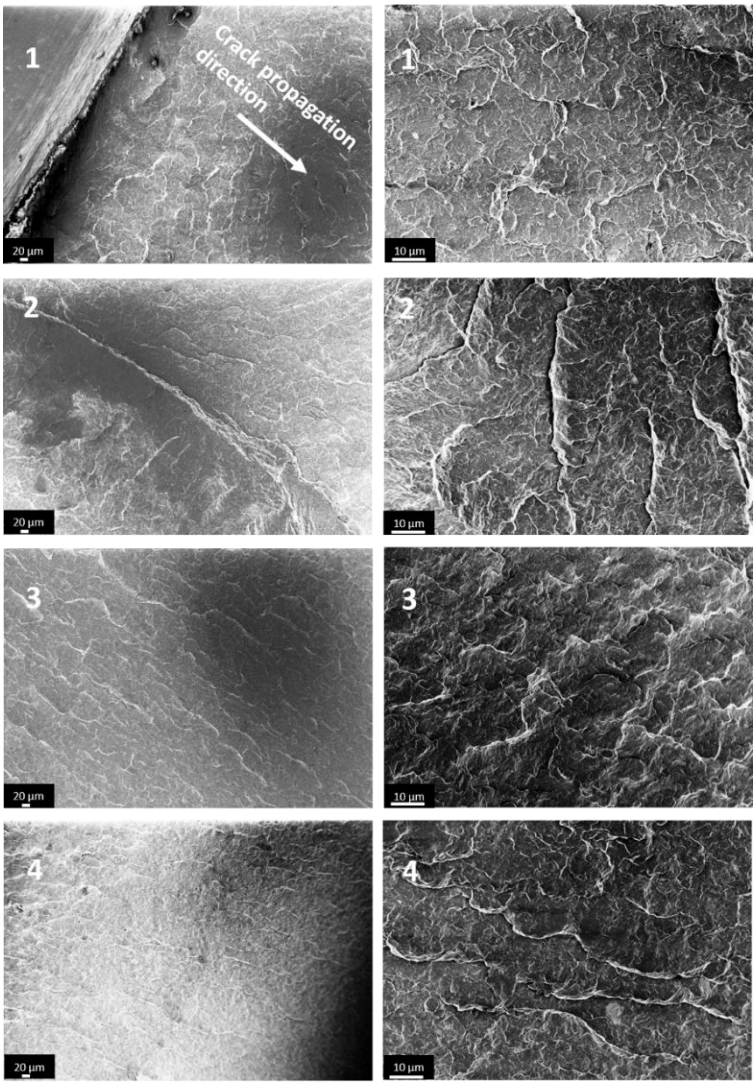

Figure 4.9. SEM micrographs of fracture surface of PP/f-MWNT (1 wt%) nanocomposite impact tested at room temperature showing different zones

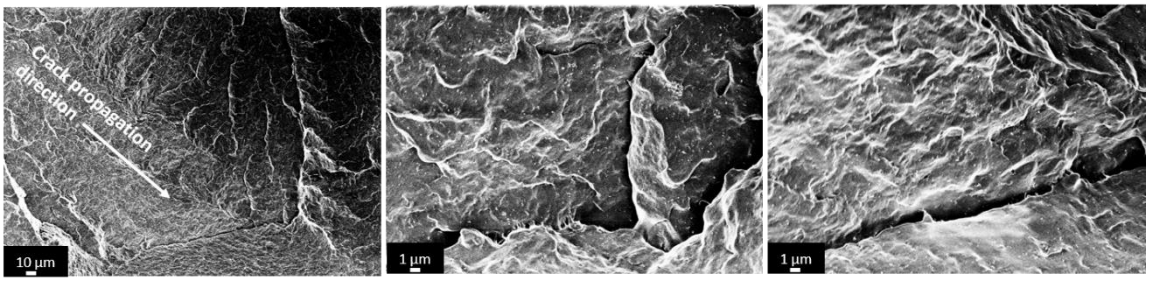

Figure 4.10. SEM micrographs at the slow propagation zone (zone 2) of PP/f-MWNT (1 wt%) nanocomposite impact tested at room temperature showing chevron-shape microcracks perpendicular to the crack propagation direction and the CNT bridging.

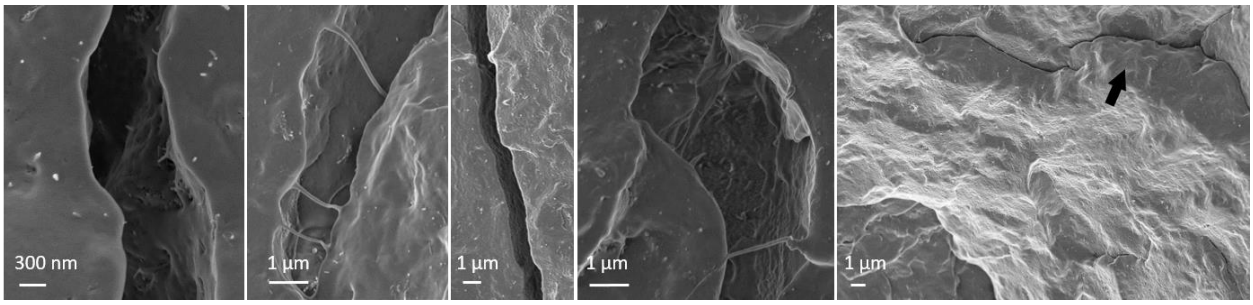

Figure 4.11. SEM micrographs of neat PP/f-MWNT (1 wt%) impact tested at room temperature showing CNTs bridged (micro)cracks.

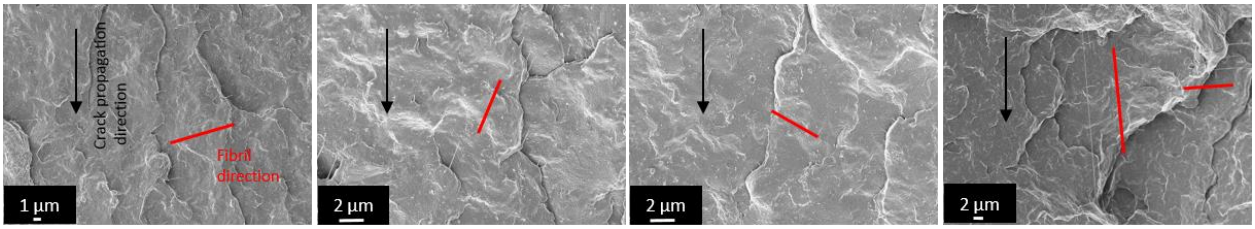

Figure 4.12. SEM micrographs of PP/f-MWNT (1 wt%) nanocomposite impact tested at room temperature showing fibrils perpendicular/along the crack propagation direction.

During impact test, the elements of the material (mostly the amorphous content) between spherulites were drawn down to fine points before the separation of polymer molecules, producing fibrillated fracture surfaces. The highly stretched material then shrinks producing an appearance presented in Figure 4.13b. In Chapter 3 and [11], CNTs were found connecting/bridging the spherulites boundaries, and perhaps, sustaining the interlamellar fibrils upon breakage. Sugimoto et al. [51] proposed that an increase of the fibril strength can sustain a higher fracture force and render the expansion of local plastic deformation until the critical stress level is reached, then causing the rupture of fibrils. Previous studies had demonstrated that such phenomenon can effectively slow down the crack propagation and improve the dissipation of external stress [8, 16, 20]. For example, similar shear-to-rupture fibrils morphology at the crack opening was reported by Lin. et al.

[8]. The author attributed the cause of intensive plastic deformation in PP happening at the crack initiation stage to the reinforced fibrils by $CaCO_3$ nanoparticles. Similarly, Deshmane et al. [20] suggested that the addition of nano-$CaCO_3$ (5 wt%) to polyethylene altered the mechanism of plastic deformation from crazing–tearing to fibrillation, releasing plastic constraint and encouraging plastic deformation of the matrix.

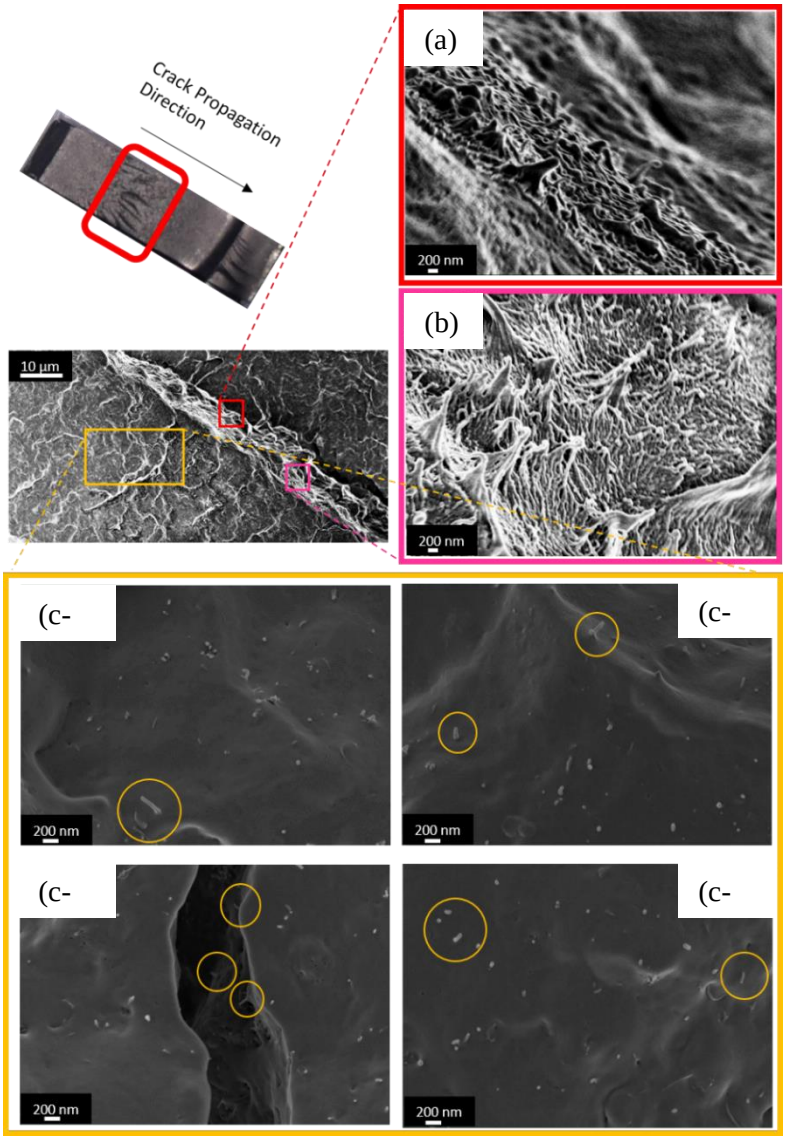

Figure 4.13. SEM micrographs at the slow propagation zone (zone 2) of PP/f-MWNT (1 wt%) nanocomposite impact tested at room temperature showing (a) polymer bonded CNTs, (b) extensive fibril formation at the "ridge" and (c) CNT breakages/pull-outs at the "terrace" of the impact fracture surface.

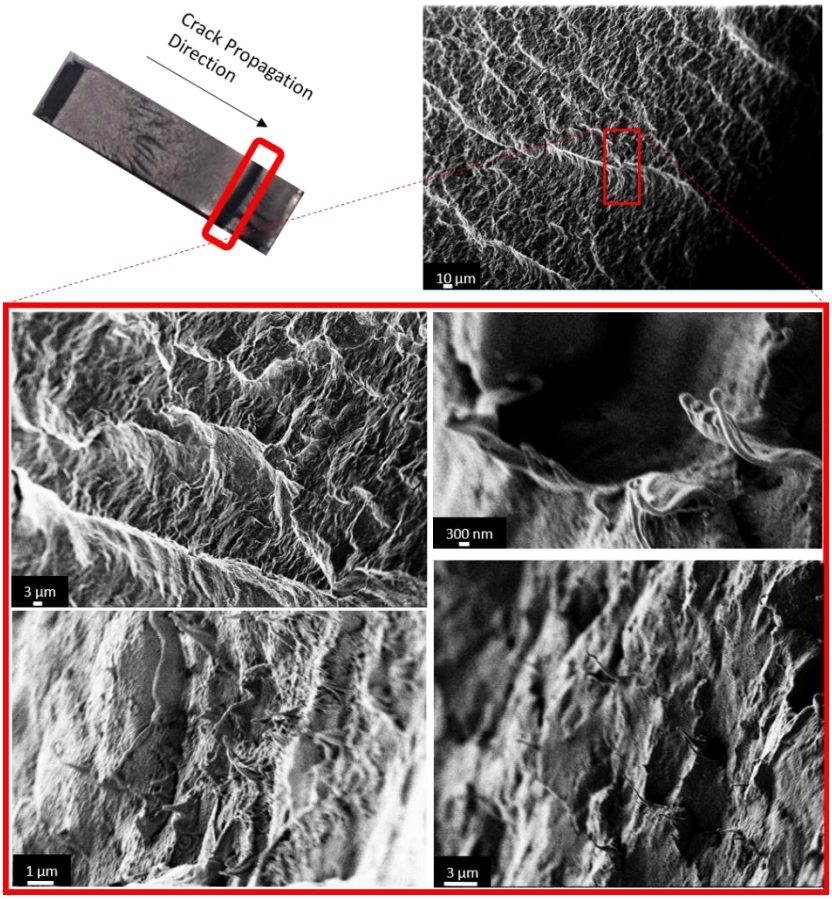

Figure 4.14. SEM micrographs at the stick-slip zone of PP/f-MWNT (1 wt%) nanocomposite impact tested at room temperature showing the intense plastic deformation (the "ridges") and the snapped fibrils.

More CNTs bridging/breakage can be seen in Figure 4.13c on the "terrace" surface. According to Greenfield and Wagner [52], if a filler is embedded more than ½ critical reinforcement length (l_c) beyond the fracture surface in both direction, it will break as the stress exceed its ultimate strength. Based on a rough approximation using 11-63 GPa as the ultimate tensile strength (σ_f) of MWNT [53] and 20 MPa as the interfacial shear strength, the equation $l_c = \frac{2\sigma_f t}{\tau_i}$ yields a l_c about 1.7 to 10 µm assuming 3.4 nm wall thickness t (10 walls). This is around the CNT length (4 µm in average) used in this work

suggesting a good chance of CNT breakage upon nanocomposite fracturing. Nevertheless, in Figure 4.13c, there are still some CNTs having relatively longer pull-out length at the fracture surface. Crack bridging of CNTs from the matrix is considered a major contribution to the toughening in epoxy based nanocomposites [12, 54-56] where the fracture toughness of epoxy can be increase by as much as 129 % using only 0.1 wt% MWNT [12]. However, in PP/CNT system from the literature, the potential of CNTs is not fully realized because of the presence of CNT aggregates at elevated CNT concentration. Herrera-Ramírez et al. [13] had achieved 55 % improvement of PP impact strength by diluting a CNT master batch (10 wt%) to 0.5 wt% through melt extrusion. While the author proposed that the high stress state around CNT agglomerates was released via the plastic deformation of neighboring polymers into fibrils, another mechanism that also accounts for energy dissipation, i.e. through the load transfer from matrix to the CNTs, is not as effective. This is possibly because of the weak bonding between the polymer and CNT agglomerates. Owing to the presence of larger CNT aggregates, there is no further increase of impact strength above 0.5 wt% [13]. In another work, Zhang et al. [14] ascribed 25% of impact strength improvement at 1 vol% CNTs to the enhanced load-carrying ability and the increased deformability of CNT-filled nanocomposite originated from nanotube breakage and pull-out. The effect of CNT concentration on impact behavior was not reported.

In PP/f-MWNT, a very interesting feature in the stick-slip zone where the crack stopped and reinitiated can be seen in Figure 4.1. Compared to neat PP and PP/p-MWNT, the PP/f-MWNT nanocomposite exhibits an abrupt protrusion similar to the ductile shear lip type of deformation in metal [57]. The microstructure details of this region are shown

in Figure 4.14. It is obvious that a large-scale plastic deformation accompanied with the extension of the PP matrix (i.e. presence of ridges) was triggered to release the plastic constraint in the matrix upon fracturing. This large-scale plastic deformation involves extensively drawing and rupture of fibrils (Figure 4.14) suggesting great consumption of impact energy. The contribution of promoted plastic deformation in PP/f-MWNT to the impact strength improvement can be verified by low temperature measurement. The notched specimens were immersed in liquid nitrogen for 40 minutes after which the Izod impact testing was carried out immediately. At such a temperature (about -190 °C) much lower than the glass transition temperature of PP (about 0 °C), the polymer exhibits only brittle characteristic, i.e. no plasticity. This is consistent with the SEM observations in Figure 4.15 and Figure 4.16. Compared with the fracture surface in Figure 4.13 and Figure 4.14, the low temperature tested specimen presents only the cleavage type brittle fracture without intensive ridges and fractured fibrils. It came as no surprise that the impact strength of the low temperature tested specimen reduces from 6.04 ± 0.28 KJ/m^2 (tested at room

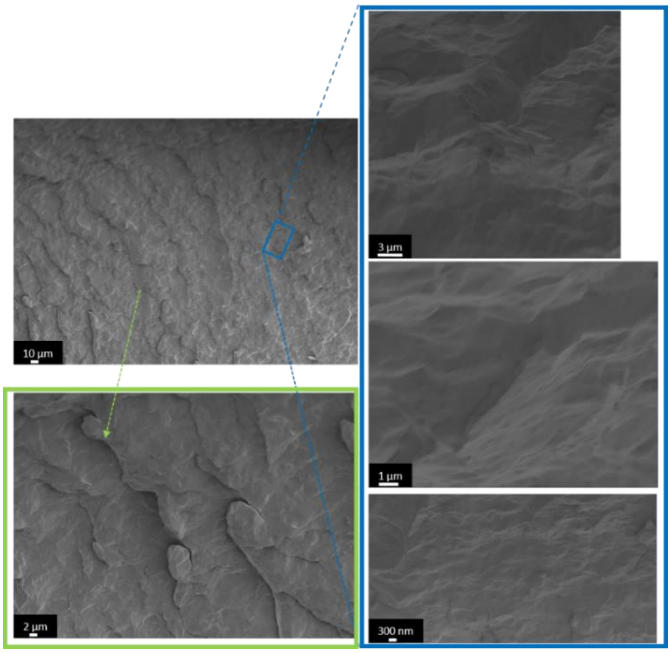

Figure 4.15. SEM micrographs at the stick-slip zone of PP/f-MWNT (1 wt%) nanocomposite impact tested at -190 °C.

temperature) to 4.01 ± 0.36 KJ/m^2 (the impact strength of neat PP went from 2.30 ± 0.11 KJ/m^2 to 2.61 ± 0.13 KJ/m^2). Therefore, it is evident that while reduced spherulite sizes and CNT breakage/pull-out contributes partly the impact strength improvement, the promoted local plastic deformation implemented by the load carrying ability of CNTs and strong matrix-CNT adhesion is also important.

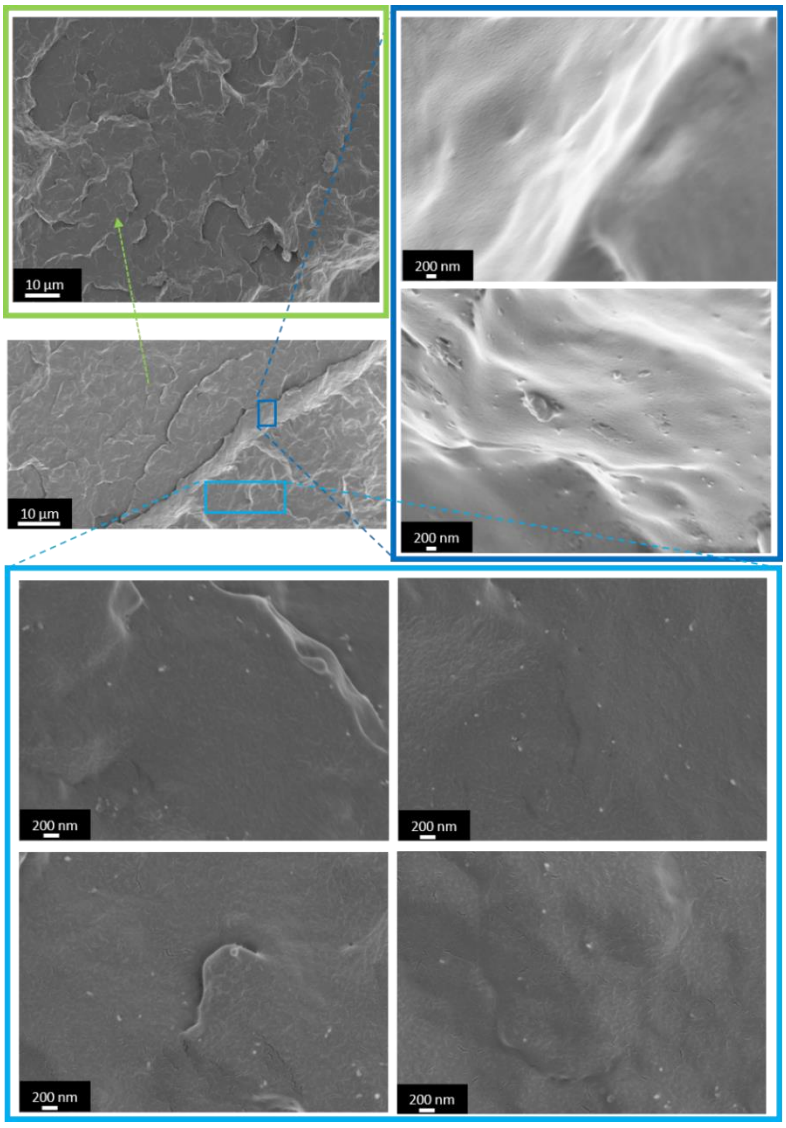

Figure 4.16. SEM micrographs at the slow propagation zone (zone 2) of PP/f-MWNT (1 wt%) nanocomposite impact tested at -190 °C.

4.4 CONCLUSIONS

The impact fracture mechanism of PP/f-MWNT nanocomposite was studied by SEM fractography and interfacial shear strength determination using Raman spectroscopy. Simply melt blending the PP and p-MWNT yielded interfacial shear strength (τ_i) of 2.2 MPa. With tailored interphase through solution processing, τ_i of the PP/f-MWNT nanocomposite improved to 17.8 MPa. This result suggests that better matrix-CNT adhesion can be achieved through interphase engineering.

The impact fracture surface of neat PP exhibits cleavage type brittle appearance with unidirectional crack propagation direction. In contrast, the fracture surface of PP/f-MWNT nanocomposite becomes rougher and consists of several microcracks, which are possibly nucleated by CNTs, to lower the constraint in the matrix. The cracks propagated in a more tortuous path than in neat PP due to the reduced spherulite size. Fibril formation that consumed the fracture energy can be observed both in-plane and out-of-plane. These fibrils were drawn not only along but also perpendicular to the crack propagation direction suggesting a more complex in-plane stress profile around the crack tip. Furthermore, shear-to-ruptured fibrils accompanied by the extension of PP matrix can be found at the slow crack propagation zone and the stick-slip region. The occurrence of such intense plastic deformation is attributed to the good matrix-CNT adhesion that allows effective load transfer at the CNT bridging cracks.

4.5 REFERENCES

1. SC Tjong, JS Shen, and RKY Li, *Mechanical behavior of injection molded β-crystalline phase polypropylene.* Polymer Engineering & Science, 1996. **36**(1): p. 100-105.

2. Shicheng Zhao, Zhi Cai, and Zhong Xin, *A highly active novel β-nucleating agent for isotactic polypropylene.* Polymer, 2008. **49**(11): p. 2745-2754.

3. Feng Luo, Chengzhen Geng, Ke Wang, Hua Deng, Feng Chen, Qiang Fu, and Bing Na, *New understanding in tuning toughness of β-polypropylene: the role of β-nucleated crystalline morphology.* Macromolecules, 2009. **42**(23): p. 9325-9331.

4. DE Mouzakis, D Mäder, R Mülhaupt, and J Karger-Kocsis, *Relationship between morphology and mechanical properties of polypropylene/ethene-co-butene binary blends with various butene contents.* Journal of materials science, 2000. **35**(5): p. 1219-1230.

5. SH Jafari and AK Gupta, *Impact strength and dynamic mechanical properties correlation in elastomer-modified polypropylene.* Journal of applied polymer science, 2000. **78**(5): p. 962-971.

6. Kyriaki Kalaitzidou, Hiroyuki Fukushima, and Lawrence T Drzal, *Mechanical properties and morphological characterization of exfoliated graphite–polypropylene nanocomposites.* Composites Part A: applied science and manufacturing, 2007. **38**(7): p. 1675-1682.

7. Zoran S Petrović, Bratislav Martinović, Vladimir Divjaković, and Jaroslava Budinski–Simendić, *Polypropylene–Carbon black interaction in conductive composites.* Journal of applied polymer science, 1993. **49**(9): p. 1659-1669.

8. Yong Lin, Haibin Chen, Chi-Ming Chan, and Jingshen Wu, *High impact toughness polypropylene/CaCO3 nanocomposites and the toughening mechanism.* Macromolecules, 2008. **41**(23): p. 9204-9213.

9. WCJ Zuiderduin, C Westzaan, J Huetink, and RJ Gaymans, *Toughening of polypropylene with calcium carbonate particles.* Polymer, 2003. **44**(1): p. 261-275.

10. SY Fu, B Lauke, E Mäder, X Hu, and CY Yue, *Fracture resistance of short-glass-fiber-reinforced and short-carbon-fiber-reinforced polypropylene under Charpy impact load and its dependence on processing.* Journal of Materials Processing Technology, 1999. **89**: p. 501-507.

11. Sushanta Ghoshal, Po-Hsiang Wang, Prabhakar Gulgunje, Nikhil Verghese, and Satish Kumar, *High impact strength polypropylene containing carbon nanotubes.* Polymer, 2016. **100**: p. 259-274.

12. Michael Shtein, Roey Nadiv, Noa Lachman, H Daniel Wagner, and Oren Regev, *Fracture behavior of nanotube–polymer composites: Insights on surface roughness and failure mechanism.* Composites Science and Technology, 2013. **87**: p. 157-163.

13. Luis C Herrera-Ramírez, Pere Castell, Miguel Castillo-Rodríguez, Ángel Fernández, and Roberto Guzman de Villoria, *The effect of a semi-industrial masterbatch process on the carbon nanotube agglomerates and its influence in the properties of thermoplastic carbon nanotube composites.* Journal of Polymer Science Part B: Polymer Physics, 2017. **55**(2): p. 189-197.

14. Hui Zhang and Zhong Zhang, *Impact behaviour of polypropylene filled with multi-walled carbon nanotubes.* European polymer journal, 2007. **43**(8): p. 3197-3207.

15. Shanju Zhang, Marilyn L Minus, Lingbo Zhu, Ching-Ping Wong, and Satish Kumar, *Polymer transcrystallinity induced by carbon nanotubes.* Polymer, 2008. **49**(5): p. 1356-1364.

16. Ilias Ali and Rabeh Elleithy, *Toughness of HDPE/CaCO3 microcomposites prepared from masterbatch by melt blend method.* Journal of Applied Polymer Science, 2011. **122**(5): p. 3303-3315.

17. K Saminathan, P Selvakumar, and Naresh Bhatnagar, *Fracture studies of polypropylene/nanoclay composite. Part II: Failure mechanism under fracture loads.* Polymer testing, 2008. **27**(4): p. 453-458.

18. Gang Yang, Liang Han, Haifeng Ding, Haiyan Wu, Ting Huang, Xiaoxi Li, and Yong Wang, *Fracture resistance improvement of polypropylene by joint action of core–shell particles and nucleating agent.* Materials Science and Engineering: A, 2011. **528**(3): p. 1382-1390.

19. Q Yuan and RDK Misra, *Impact fracture behavior of clay–reinforced polypropylene nanocomposites.* Polymer, 2006. **47**(12): p. 4421-4433.

20. C Deshmane, Q Yuan, and RDK Misra, *On the fracture characteristics of impact tested high density polyethylene–calcium carbonate nanocomposites.* Materials Science and Engineering: A, 2007. **452**: p. 592-601.

21. C Deshmane, Q Yuan, and RDK Misra, *High strength–toughness combination of melt intercalated nanoclay-reinforced thermoplastic olefins.* Materials Science and Engineering: A, 2007. **460**: p. 277-287.

22. SP Bao and SC Tjong, *Impact essential work of fracture of polypropylene/montmorillonite nanocomposites toughened with SEBS-g-MA elastomer.* Composites Part A: Applied Science and Manufacturing, 2007. **38**(2): p. 378-387.

23. M Bramuzzo, A Savadori, and D Bacci, *Polypropylene composites: fracture mechanics analysis of impact strength.* Polymer composites, 1985. **6**(1): p. 1-8.

24. Han-Seung Yang, Douglas J Gardner, and Jacques W Nader, *Morphological properties of impact fracture surfaces and essential work of fracture analysis of cellulose nanofibril-filled polypropylene composites.* Journal of Applied Polymer Science, 2013. **128**(5): p. 3064-3076.

25. JI Velasco, C Morhain, D Arencón, OO Santana, and M Ll Maspoch, *Low-rate fracture behaviour of magnesium hydroxide filled polypropylene block copolymer.* Polymer Bulletin, 1998. **41**(5): p. 615-622.

26. Mehrdad Khodabandelou, Mir Karim Razavi Aghjeh, and Majid Mehrabi Mazidi, *Fracture toughness and failure mechanisms in un-vulcanized and dynamically vulcanized PP/EPDM/MWCNT blend-nanocomposites.* RSC Advances, 2015. **5**(87): p. 70817-70831.

27. Jia Liu, Zachary J Thompson, Hung-Jue Sue, Frank S Bates, Marc A Hillmyer, Marv Dettloff, George Jacob, Nikhil Verghese, and Ha Pham, *Toughening of epoxies with block copolymer micelles of wormlike morphology.* Macromolecules, 2010. **43**(17): p. 7238-7243.

28. Jia Liu, Hung-Jue Sue, Zachary J Thompson, Frank S Bates, Marv Dettloff, George Jacob, Nikhil Verghese, and Ha Pham, *Nanocavitation in self-assembled amphiphilic block copolymer-modified epoxy.* Macromolecules, 2008. **41**(20): p. 7616-7624.

29. Asa H Barber, Sidney R Cohen, Shmuel Kenig, and H Daniel Wagner, *Interfacial fracture energy measurements for multi-walled carbon nanotubes pulled from a polymer matrix.* Composites Science and Technology, 2004. **64**(15): p. 2283-2289.

30. Asa H Barber, Sidney R Cohen, and H Daniel Wagner, *Measurement of carbon nanotube–polymer interfacial strength.* Applied Physics Letters, 2003. **82**(23): p. 4140-4142.

31. CA Cooper, RJ Young, and M Halsall, *Investigation into the deformation of carbon nanotubes and their composites through the use of Raman spectroscopy.* Composites Part A: Applied Science and Manufacturing, 2001. **32**(3): p. 401-411.

32. Yasser Zare, *Effects of interphase on tensile strength of polymer/CNT nanocomposites by Kelly–Tyson theory.* Mechanics of Materials, 2015. **85**: p. 1-6.

33. Jeffrey Luo, Huibin Chang, Amir A Bakhtiary Davijani, H Clive Liu, Po-Hsiang Wang, Robert J Moon, and Satish Kumar, *Influence of high loading of cellulose nanocrystals in polyacrylonitrile composite films.* Cellulose, 2017. **24**(4): p. 1745-1758.

34. SJV Frankland, A Caglar, DW Brenner, and M Griebel, *Molecular simulation of the influence of chemical cross-links on the shear strength of carbon nanotube–polymer interfaces.* The Journal of Physical Chemistry B, 2002. **106**(12): p. 3046-3048.

35. Noa Lachman, Christèle Bartholome, Pierre Miaudet, Maryse Maugey, Philippe Poulin, and H Daniel Wagner, *Raman response of carbon nanotube/PVA fibers under strain.* The Journal of Physical Chemistry C, 2009. **113**(12): p. 4751-4754.

36. SL Ruan, Ping Gao, Xin G Yang, and TX Yu, *Toughening high performance ultrahigh molecular weight polyethylene using multiwalled carbon nanotubes.* Polymer, 2003. **44**(19): p. 5643-5654.

37. Bradley A Newcomb, Han Gi Chae, Lindsey Thomson, Jeffrey Luo, Jong-Beom Baek, and Satish Kumar, *Reinforcement efficiency of carbon nanotubes and their effect on crystal-crystal slip in poly (ether ketone)/carbon nanotube composite fibers.* Composites Science and Technology, 2017.

38. Huibin Chang, Jeffrey Luo, H Clive Liu, Amir A Bakhtiary Davijani, Po-Hsiang Wang, and Satish Kumar, *Orientation and interfacial stress transfer of cellulose nanocrystal nanocomposite fibers.* Polymer, 2017.

39. Luqi Liu, Asa H Barber, Shahar Nuriel, and H Daniel Wagner, *Mechanical Properties of Functionalized Single-Walled Carbon-Nanotube/Poly (vinyl alcohol) Nanocomposites.* Advanced Functional Materials, 2005. **15**(6): p. 975-980.

40. Debdulal Roy, Sanjib Bhattacharyya, A Rachamim, A Plati, and Marie-Louise Saboungi, *Measurement of interfacial shear strength in single wall carbon nanotubes reinforced composite using Raman spectroscopy.* Journal of Applied Physics, 2010. **107**(4): p. 043501.

41. Bradley A Newcomb, Han Gi Chae, Prabhakar V Gulgunje, Kishor Gupta, Yaodong Liu, Dmitri E Tsentalovich, Matteo Pasquali, and Satish Kumar, *Stress transfer in polyacrylonitrile/carbon nanotube composite fibers.* Polymer, 2014. **55**(11): p. 2734-2743.

42. Chia-Chi Chang, I-Kai Hsu, Mehmet Aykol, Wei-Hsuan Hung, Chun-Chung Chen, and Stephen B Cronin, *A new lower limit for the ultimate breaking strain of carbon nanotubes.* ACS nano, 2010. **4**(9): p. 5095-5100.

43. Malte HG Wichmann, Karl Schulte, and H Daniel Wagner, *On nanocomposite toughness.* Composites Science and Technology, 2008. **68**(1): p. 329-331.

44. Keka Talukdar and Apurba Krishna Mitra, *Molecular dynamics simulation study on the mechanical properties and fracture behavior of single-wall carbon nanotubes*, in *Carbon Nanotubes-Synthesis, Characterization, Applications*. 2011, InTech.

45. SB Cronin, AK Swan, MS Ünlü, BB Goldberg, MS Dresselhaus, and M Tinkham, *Measuring the uniaxial strain of individual single-wall carbon nanotubes: resonance Raman spectra of atomic-force-microscope modified single-wall nanotubes.* Physical review letters, 2004. **93**(16): p. 167401.

46. Jean-Paul Salvetat, G Andrew D Briggs, Jean-Marc Bonard, Revathi R Bacsa, Andrzej J Kulik, Thomas Stöckli, Nancy A Burnham, and László Forró, *Elastic and shear moduli of single-walled carbon nanotube ropes.* Physical review letters, 1999. **82**(5): p. 944.

47. J-P Salvetat, J-M Bonard, NH Thomson, AJ Kulik, L Forro, W Benoit, and L Zuppiroli, *Mechanical properties of carbon nanotubes.* Applied Physics A, 1999. **69**(3): p. 255-260.

48. Lianxi Shen and Jackie Li, *Transversely isotropic elastic properties of multiwalled carbon nanotubes.* Physical Review B, 2005. **71**(3): p. 035412.

49. Swetha Chandrasekaran, Narumichi Sato, Folke Tölle, Rolf Mülhaupt, Bodo Fiedler, and Karl Schulte, *Fracture toughness and failure mechanism of graphene based epoxy composites.* Composites Science and Technology, 2014. **97**: p. 90-99.

50. HR Azimi, RA Pearson, and RW Hertzberg, *Fatigue of rubber-modified epoxies: effect of particle size and volume fraction.* Journal of materials science, 1996. **31**(14): p. 3777-3789.

51. Masataka Sugimoto, Masaru Ishikawa, and Kouichi Hatada, *Toughness of polypropylene.* Polymer, 1995. **36**(19): p. 3675-3682.

52. Israel Greenfeld and H Daniel Wagner, *Nanocomposite toughness, strength and stiffness: Role of filler geometry.* Nanocomposites, 2015. **1**(1): p. 3-17.

53. Min-Feng Yu, Oleg Lourie, Mark J Dyer, Katerina Moloni, Thomas F Kelly, and Rodney S Ruoff, *Strength and breaking mechanism of multiwalled carbon nanotubes under tensile load.* Science, 2000. **287**(5453): p. 637-640.

54. TH Hsieh, AJ Kinloch, AC Taylor, and IA Kinloch, *The effect of carbon nanotubes on the fracture toughness and fatigue performance of a thermosetting epoxy polymer.* Journal of Materials Science, 2011. **46**(23): p. 7525.

55. FH Gojny, MHG Wichmann, U Köpke, B Fiedler, and K Schulte, *Carbon nanotube-reinforced epoxy-composites: enhanced stiffness and fracture toughness at low nanotube content.* Composites science and technology, 2004. **64**(15): p. 2363-2371.

56. Wellington Marcos da Silva, Hélio Ribeiro, Juliana Cardoso Neves, Alexandre Rangel Sousa, and Glaura Goulart Silva, *Improved impact strength of epoxy by the addition of functionalized multiwalled carbon nanotubes and reactive diluent.* Journal of Applied Polymer Science, 2015. **132**(39).

57. MO Lai and WG Ferguson, *Relationship between the shear lip size and the fracture toughness.* Materials Science and Engineering, 1980. **45**(2): p. 183-188.

CHAPTER 5

EFFECT OF INTERFACIAL CHEMISTRY ON CRYTSALLIZATION OF POLYPOPYLENE/MULTIWALL CARBON NANOTUBE NANOCOMPOSITES

5.1 INTRODUCTION

In this chapter, the influence of three types of polymer/MWNT interfaces on the crystallization and melting behavior of the PP/MWNT nanocomposites was investigated. Through solution processing, PP or MA-g-PP was successfully coated non-covalently onto f-MWNT. The resulting PP/f-MWNT, MA-g-PP/f-MWNT master batches or untreated p-MWNT were melt micro-compounded with PP. In the first part of this chapter, dispersion quality, isothermal and non-isothermal crystallization studies of the three different types of nanocomposites at various MWNT concentrations are discussed. In the second part, crystal refinement and perfection as well as crystal size growth were realized through polymer self-seeding and templated growth. The proposed mechanism of the induced columnar crystalline interphase formation is also discussed.

In the semicrystalline polymer composites, crystallization can have a major influence on the structure and morphology of the derived composites and thereby on properties like thermal and gas barrier as well as the mechanical properties, e.g. tensile and impact strength. Also, from the manufacturing point of view, change of crystallization kinetics brings about the necessity of adjusting processing parameters during thermoforming, molding and fiber spinning, etc. in order to minimize and preferably

eliminate warpage and dimensional instabilities. For reasons outlined above, it is important to understand the crystallization phenomena.

In general, there are two mutually opposite effects of fillers on the crystallization behavior, namely: heterogeneous nucleation ability and crystal growth retardation, both of which are related to the filler concentration and dispersion quality. Various approaches have been adopted to modify the surface chemistry of fillers through polymer grafting or chemical functionalization in order to improve their dispersion quality [1-16]. The effect of these surface modifications on the crystallization and melting behavior as compared with their unmodified counterparts are summarized in Table 1 and Table 2. Various types of nano-fillers, includes CNT, reduced graphene oxide (rGO), cellulose nanocrystal (CNC), montmorillonite, etc, all result in up to 97% reduction in crystallization half time ($t_{1/2}$) or up to 18 °C increase in crystallization temperature (T_c). However, the equilibrium melting temperature (T_m^0) and melting peak maximum (T_p) of the resulting composites either decrease or show a small increase. Such observations demonstrate that the incorporation of the fillers in the composites, in most of the cases, increases the crystallization rate of the polymer, but has little or even negative influence on the crystalline structure. For example, the silane group grafted on MWNT improved its dispersion in the matrix but has a negative effect on the nucleation of polymers. While the reduction of $t_{1/2}$ is similar between the silane grafted MWNT and p-MWNT containing composites, more dramatic decrease of T_m^0 was found in the former which brought about 32 °C of reduction with 1 wt% MWNT loading [2].

5.2 EXPERIMENTAL

For the materials, MWNT functionalization and master batch preparation, please refer to Chapter 2.2. For manufacturing the nanocomposite, please refer to Chapter 3.2.

For the isothermal crystallization study (using TA Instrument DSC Q100), samples were heated to 220 °C at a heating rate of 10°C /min and held at 220 °C for 5 min. These samples were then cooled at a rate of 100 °C /min to 135 °C and then held at that temperature for crystallization. The crystallization half-time, $t_{1/2}$ is defined as the time at which the extent of crystallization is 50% of total crystallization (X_t). The crystallization half-time can be determined from the total crystallinity [17],

$$X_t = \int_0^t (\mathrm{d}H_c/\mathrm{d}t)\mathrm{d}t \,/\, \int_0^\infty (\mathrm{d}H_c/\mathrm{d}t)\mathrm{d}t. \quad (1)$$

Here, t is the crystallization time and $\mathrm{d}H_c \,/\, \mathrm{d}t$ is the heat evolution rate during the crystallization process. For non-isothermal crystallization study, samples were heated from room temperature at to 220 °C 2.5 °C/min and then cooled at the same rate to room temperature and then heated again to 220 °C. Crystallization temperatures (T_c) were derived from the first cooling cycle. Melting peak maximum (T_p) and all the melt endotherms presented in this work, if not specified, are from the second heating cycle. Polarized optical microscope (Leica, DM 2500P) equipped with Linkam LTS420 heating stage was used to study the crystallization behavior. For this purpose, thin pieces of samples were heated on a microscope glass cover slip covered with another cover slips. Samples were heated to 225 °C for 5 minutes and then cooled to 135 °C at a rate of 20 °C/min, and held at this temperature for monitoring crystallization behavior over a period of time.

5.3 RESULTS AND DISCUSSION

5.3.1 Non-isothermal and isothermal crystallization studies

Fig 5.1 provide a series of optical and SEM micrographs of PP/MWNT nanocomposites prepared via two types of f-MWNT based master batches and from p-MWNT at different MWNT concentrations. MA-g-PP/f-MWNT master batch containing samples showed the most homogeneous dispersion of MNWT through the matrix, indicating that the incorporation of MA-g-PP as a compatibilizer significantly improved the CNT dispersion quality. On the other hand, p-MWNT formed aggregates of up to tens of micrometers even at concentration as low as 0.01 wt % (Figure 5.1). Aggregates of much smaller size were found in the PP/f-MWNT master batch based samples showing an intermediate level of dispersion quality among the three types of nanocomposites.

In Chapter 3 and [18], β crystals were observed in MA-g-PP containing injection molded sample, but this was not observed in the control PP, *p*-MWNT, and PP/f-MWNT based samples. Even in the case of the MA-g-PP, after removing the processing history (first heating cycle in DSC), only melting corresponding to α-phase was observed which lead to the conclusion that the presence of β crystals was a joint effect of processing parameters (i.e. shear and temperature) and the incorporation of MA-g-PP. In this chapter, the sample processing history was always removed by the first heating cycle imposed on the sample in DSC and the second melting endotherm was used to study the effect of interfacial chemistry on crystallization in three different systems.

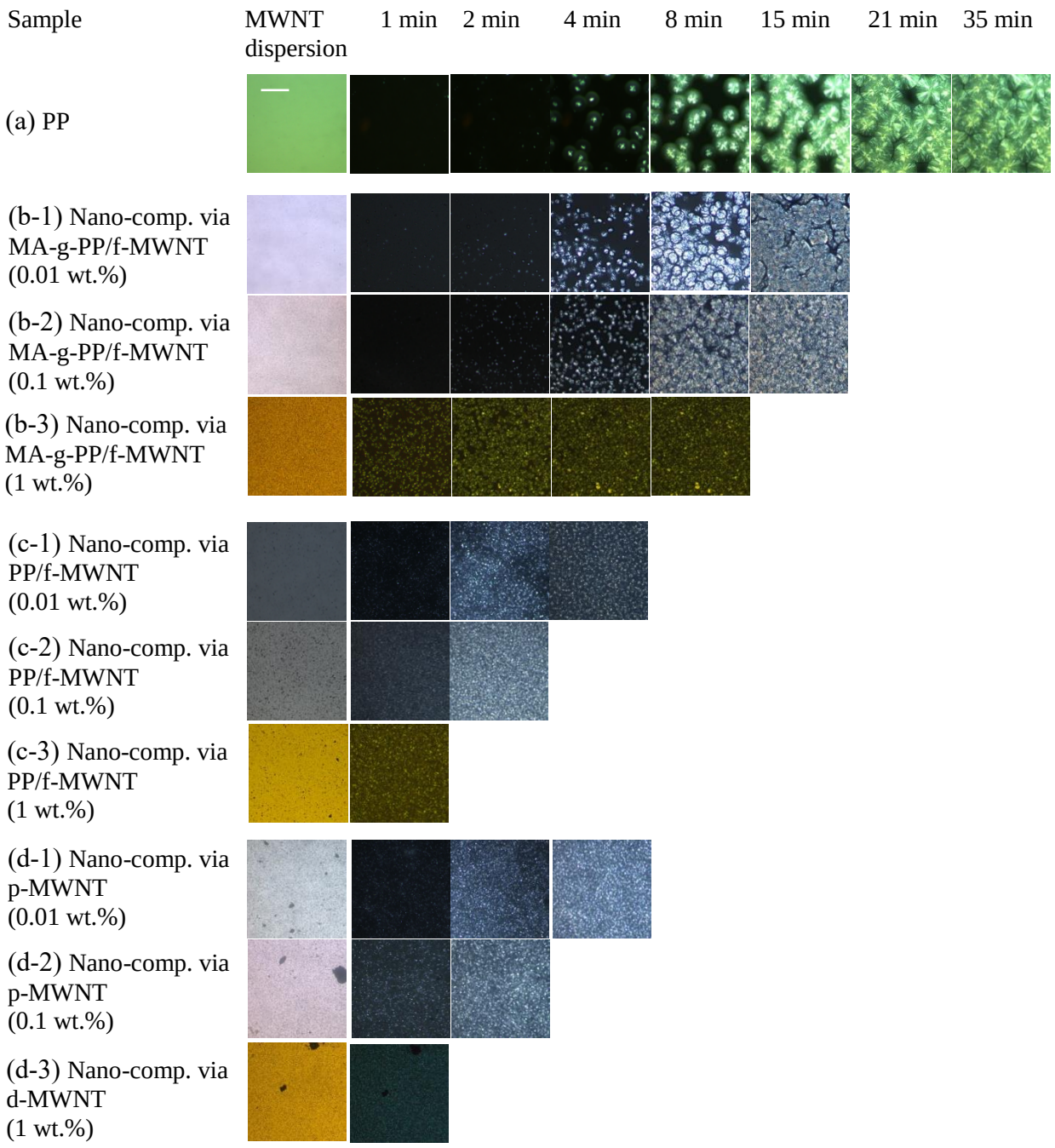

Figure 5.1. POM under cross-polar of (a) PP and (b-d) PP/MWNT nanocomposite at different concentrations (0.01 0.1, and 1 wt%) via (b) MA-g-PP/f-MWNT master batch (c) PP/f-MWNT master batch and (d) p-MWNT. The samples were melted at 225 °C for 5 minutes, followed by a cooling at 20 °C /min to 135 °C. Scale bar represents 100 µm.

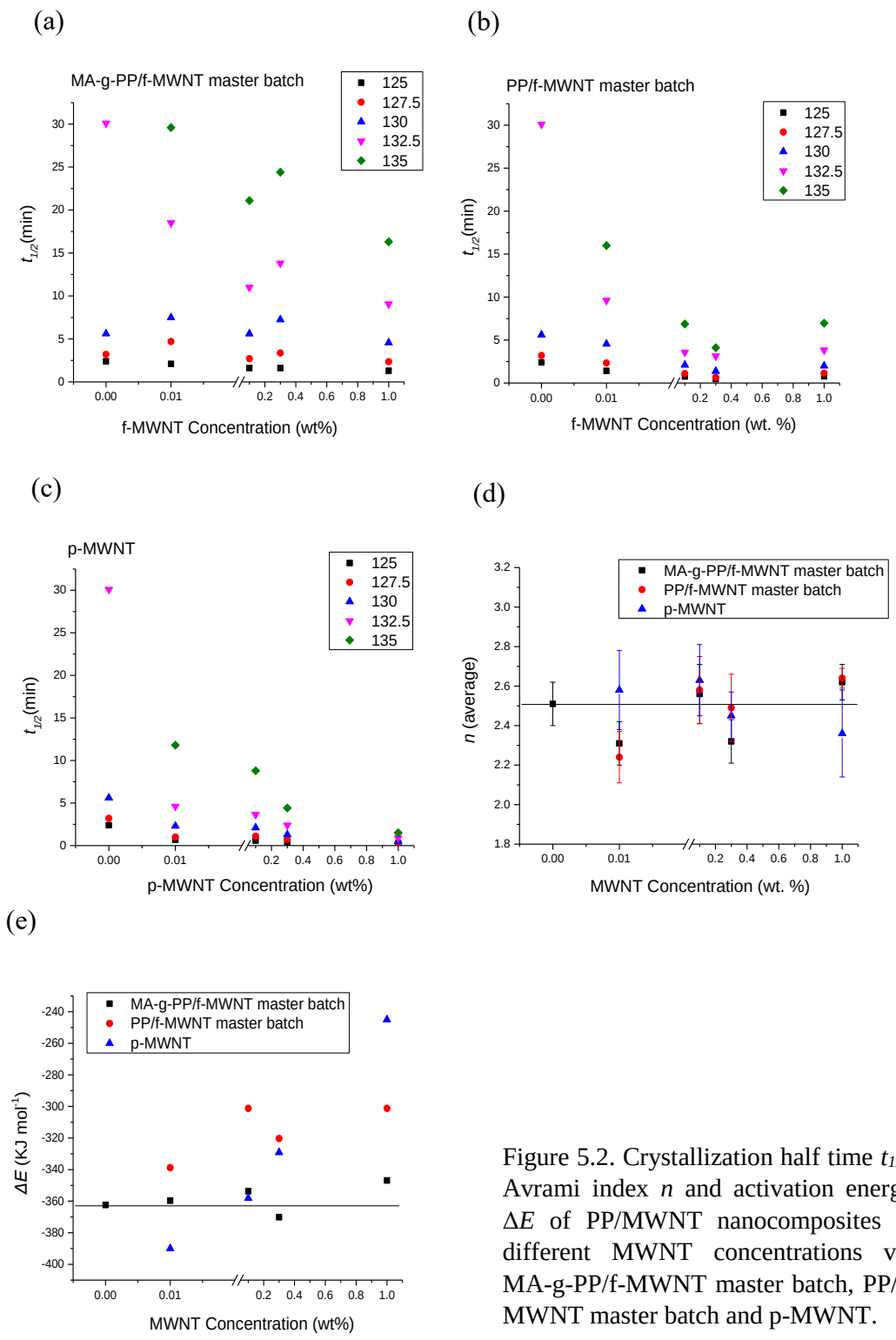

Figure 5.2. Crystallization half time $t_{1/2}$, Avrami index n and activation energy ΔE of PP/MWNT nanocomposites at different MWNT concentrations via MA-g-PP/f-MWNT master batch, PP/f-MWNT master batch and p-MWNT.

In order to understand the effect of different PP/MWNT interfaces on the crystallization behavior of the nanocomposites, isothermal crystallization studies were carried out at various temperatures. Crystallization half time ($t_{1/2}$) for neat PP was much longer at high temperature, e.g. $t_{1/2}$ is 1.25 minutes at 122.5 °C and 30.1 minutes at 132.5 °C. With 0.01 wt% loading of MWNT, $t_{1/2}$ at 132.5 °C decreased to 18.5 minutes, 9.6 minutes, and 4.6 minutes for MA-g-PP/f-MWNT, PP/f-MWNT, and p-MWNT containing samples, respectively. Further increase in crystallization rate was observed at higher MWNT loading (Figure 5.2a-c and Tables 5.1 to 5.3). The most pronounced improvement on $t_{1/2}$ was found for the p-MWNT based nanocomposites despite their relatively poor dispersion, followed by PP/f-MWNT and then the MA-g-PP/f-MWNT master batch based samples. Crystallization half time of p-MWNT based nanocomposites was lower than the f-MWNT based samples suggesting a better nucleation ability of p-MWNT than f-MWNT. $t_{1/2}$ of p-MWNT containing nanocomposites then progressively decreased as MWNT concentration increased to 1 wt%. On the other hand, the nucleation effect of the MA-g-PP/f-MWNT based sample leveled off above 0.1 wt%. Functional groups on the MWNT surface are considered obstacles that disturb polymer chain folding during crystallization [19]. Also, the presence of less crystallizable MA-g-PP at the interface between f-MWNT and matrix PP hindered the crystallization of PP (Chapter 2).

Table 5.1. Various parameters for PP and MA-g-PP/f-MWNT master batch containing PP/f MWNT nanocomposites from Avrami equation.

	T_c (°C)	n	n (aver.)	k (min^{-1})	K' (min^{-1})	$t_{1/2}$ (min)	ΔE (KJ mol^{-1})
PP	120	2.50	2.51	2.034	2.028	0.65	-362.4
	122.5	2.43		0.403	0.400	1.25	
	125	2.65		0.069	0.066	2.39	
	127.5	2.43		0.041	0.040	3.2	
	130	2.65		0.007	0.007	5.61	
	132.5	2.40		$2*10^{-5}$	0.001	30.1	
PP/f-MWNT (0.01 wt. %) via MA-g-PP/f-MWNT master batch	125	2.19	2.31	0.136	0.143	2.1	-359.7
	127.5	2.22		0.022	0.022	4.7	
	130	2.39		0.006	0.006	7.5	
	132.5	2.46		$5.2*10^{-4}$	$5.4*10^{-4}$	18.5	
	135	2.31		$2.7*10^{-4}$	$4.1*10^{-4}$	29.6	
PP/f-MWNT (0.1 wt. %) via MA-g-PP/f-MWNT master batch	125	2.68	2.56	0.193	0.186	1.61	-353.7
	127.5	2.62		0.051	0.048	2.7	
	130	2.40		0.011	0.012	5.6	
	132.5	2.72		0.001	0.001	11	
	135	2.38		$4.7*10^{-4}$	$6.1*10^{-4}$	21.1	
PP/f-MWNT (0.3 wt. %) via MA-g-PP/f-MWNT master batch	125	2.17	2.32	0.247	0.148	1.61	-370.1
	127.5	2.27		0.044	0.021	3.36	
	130	2.37		0.006	0.006	7.25	
	132.5	2.47		0.001	$5.4*10^{-4}$	13.8	
	135	2.35		$3.8*10^{-4}$	$3.9*10^{-4}$	24.4	
PP/f-MWNT (1 wt. %) via MA-g-PP/f-MWNT master batch	125	2.48	2.62	0.369	0.337	1.29	-346.9
	127.5	2.64		0.072	0.080	2.35	
	130	2.74		0.011	0.009	4.57	
	132.5	2.63		0.002	0.002	9.06	
	135	2.63		$4.4*10^{-4}$	$5.4*10^{-4}$	16.31	

Among the three investigated systems, PP/f-MWNT master batch containing nanocomposites obtained the balance between dispersion quality and crystallization rate. While the preservation of pristine graphitic structure is important, the amount of MWNT surfaces available as heterogeneous nucleating sites plays an important role on the crystallization behavior.

Table 5.2. Various parameters for PP/f-MWNT master batch containing PP/f-MWNT nanocomposites from Avrami equation.

	T_c (°C)	n	n (aver.)	k (min^{-1})	k' (min^{-1})	$t_{1/2}$ (min)	ΔE (KJ mol^{-1})
PP/f-MWNT (0.01 wt. %) via MA-g-PP/f-MWNT master batch	125	2.31	2.24	0.313	0.299	1.41	-338.8
	127.5	2.38		0.092	0.119	2.33	
	130	2.25		0.023	0.026	4.55	
	132.5	2.02		0.007	0.009	9.6	
	135	2.26		0.001	0.001	16	
PP/f-MWNT (0.1 wt. %) via PP/f-MWNT master batch	125	2.76	2.58	1.480	1.401	0.76	-301.2
	127.5	2.75		0.533	0.539	1.1	
	130	2.60		0.101	0.119	2.1	
	132.5	2.37		0.034	0.051	3.57	
	135	2.43		0.006	0.009	6.87	
PP/f-MWNT (0.3 wt. %) via PP/f-MWNT master batch	125	2.42	2.49	4.540	4.553	0.46	-320.3
	127.5	2.36		1.848	2.155	0.66	
	130	2.33		0.329	0.342	1.38	
	132.5	2.61		0.035	0.036	3.13	
	135	2.73		0.015	0.015	4.10	
PP/f-MWNT (1 wt. %) via PP/f-MWNT master batch	125	2.65	2.64	1.338	1.404	0.78	-301.2
	127.5	2.65		0.479	0.481	1.15	
	130	2.73		0.104	0.107	2.00	
	132.5	2.60		0.021	0.234	3.83	
	135	2.60		0.004	0.006	6.96	

Table 5.3. Various parameters for p-MWNT containing PP/p-MWNT nanocomposites from Avrami equation.

	T_c (°C)	n	n (aver.)	k (min^{-1})	K' (min^{-1})	$t_{1/2}$ (min)	ΔE (KJ mol^{-1})
PP/p-MWNT (0.01 wt. %) Via p-MWNT	125	2.53	2.58	1.84	1.81	0.68	-390.0
	127.5	2.76		0.69	0.59	1.0	
	130	2.54		0.083	0.094	2.3	
	132.5	2.28		0.021	0.031	4.6	
	135	2.82		$6.5*10^{-4}$	$7.1*10^{-4}$	11.8	
PP/p-MWNT (0.1 wt. %) Via p-MWNT	125	2.68	2.63	2.99	2.96	0.58	-358.1
	127.5	2.87		0.52	0.50	1.1	
	130	2.60		0.10	0.10	2.1	
	132.5	2.67		0.022	0.022	3.63	
	135	2.35		0.004	0.007	8.8	
PP/p-MWNT (0.3 wt. %) Via p-MWNT	125	2.30	2.45	6.42	6.51	0.38	-329.1
	127.5	2.37		1.46	1.78	0.73	
	130	2.53		0.36	0.36	1.29	
	132.5	2.62		0.07	0.07	2.39	
	135	2.43		0.018	0.016	4.42	
PP/p-MWNT (1 wt. %) Via p-MWNT	125	2.20	2.36	15.8	16.9	0.24	-245.0
	127.5	2.17		5.70	8.99	0.38	
	130	2.27		3.50	3.53	0.49	
	132.5	2.47		0.90	0.89	0.90	
	135	2.72		0.23	0.22	1.51	

Among the three investigated systems, PP/f-MWNT master batch containing nanocomposites obtained the balance between dispersion quality and crystallization rate. While the preservation of pristine graphitic structure is important, the amount of MWNT surfaces available as heterogeneous nucleating sites plays an important role on the crystallization behavior. As a consequence, at the intermediate MWNT loading level of 0.1 and 0.3 wt%, $t_{1/2}$ values were comparable between PP/f-MWNT and p-MWNT based nanocomposites, where improved MWNT dispersion compensated the negative effect of MWNT functional groups on crystallization in PP/f-MWNT system. However, when the concentration further increased to 1 wt%, $t_{1/2}$ was 3.83 minute and 0.9 minute for PP/f-MWNT and p-MWNT based nanocomposite at 132.5 °C, respectively. This further confirms the importance of pristine graphitic surfaces for PP crystallization nucleation and growth. Unlike p-MWNT based nanocomposites, where continuous decrease of $t_{1/2}$ was observed with increasing MWNT loading, $t_{1/2}$ of the PP/f-MWNT based sample reached a minimum at 0.3 wt% (crystallization rate reached its maximum) and went up at 1 wt%. This implies some degree of nucleation saturation [13]. More importantly, while the nucleation density did increase with increased f-MWNT loading, the reduction of polymer mobility became a counter force on accelerating crystallization process. The reason that the increase in $t_{1/2}$ at higher filler loading was observed in PP/f-MWNT but not in p-MWNT based sample could be as follows. First, the geometrical confinement, or the average MWNT-MWNT distance, that restrained the polymer diffusion is stronger in the former due to the better MWNT dispersion. Second, the functional groups on f-MWNT prevents them from being effective nucleating agents. As a result, the cost of introducing more fillers in the system at high f-MWNT loading exceeds the benefit leading to an increase of $t_{1/2}$.

The crystallization kinetics of the nanocomposites under isothermal conditions were analyzed by using Avrami equation assuming constant nucleation rate of nuclei that undergo free growth [4, 20]. The general form of the equation is:

$$1 - X_t = \exp(-kt^n) \quad (2)$$

Taking the logarithm on both sides, Eq. (2) is written as:

$$\log[-\ln(1 - X_t)] = n\ log\ t + \log k \quad (3)$$

Where X_t is the relative crystalline volume fraction at crystallization time *t*, and it is defined by Eq. (1). *n* is Avrami index and it is a complex exponent which is related to the dimensionality of the growing crystals and time dependence of nucleation [20, 21]; *k* is the Avrami rate constant or crystallization rate constant involving both nucleation and growth process. Eq. (3) is used to generate the so-called Avrami plots shown in Fig. S2. The fitting was performed not considering the deviations from linearity due to the onset of secondary crystallization at longer *t* that can not be described by Avrami equation [3, 22]. The reported *n* and *k* values are summarized in Tables 5.1 to 5.3. An alternative way to calculate *k* from $t_{1/2}$ (designated as *k'* in Tables 5.1 to 5.3) is given as [3]:

$$k' = \ln 2 \Big/ t_{1/2}^n \quad (4)$$

The values of *k* obtained by two different methods are in good agreement with each other (Tables 5.1 to 5.3). The overall crystallization rate *k* decreased greatly with increasing crystallization temperature, and it was higher for the nanocomposite samples than for the neat PP sample which is consistent with the $t_{1/2}$ observations. At 0.01 wt% MWNT concentration, *k* showed no significant difference from neat PP for MA-g-PP/f-MWNT based nanocomposite while it increased by roughly five times and twenty times for PP/f-MWNT and p-MWNT based nanocomposite, respectively, within the investigated

temperature range (125 to 135 °C). At higher MWNT concentration of 0.3 to 1 wt%, there was about five times higher *k* compared with the neat PP for MA-g-PP/f-MWNT based sample and fifty, and two hundred times for PP/f-MWNT based and p-MWNT based nanocomposites, respectively.

The Avrami index *n* is in between 2 to 3 for both neat PP and PP/f-MWNT nanocomposites (Tables 5.1-5.3, Figure 2d) which is similar to the reported values of iPP (isotactic PP) and their nanocomposites in the literature [1-3, 5, 7, 15, 23]. For polymers, the ideal Avrami index is expected to be 3 and 4 for heterogeneous and homogenous nucleation, respectively for the three dimensional growth [4, 20]. Zhao et al. [4] commented that the experimental value of *n* might be smaller depending on the experimental conditions. Similar reason for this discrepancy was put forward by Lorenzo et al. [20] who stressed that the insufficient cooling rate to the crystallization temperature can potentially lead to an experimental error.

The activation energy of the crystallization, ΔE can be derived from the following equation [24]:

$$\frac{1}{n}(ln\ k) = A_0 - \frac{\Delta E}{RT} \tag{5}$$

The negative sign of ΔE in this study (Tables 5.1-5.3, Figure 5.2e) is due to the isothermal crystallization behavior was investigated within the temperature range where lower crystallization temperature has higher crystallization rate. Difference of ΔE between the PP/f-MWNT master batch containing samples and that of neat PP was relatively moderate which seems to level off at a plateau value. This is again due to the nucleation saturation and growth retardation in the f-MWNT containing nanocomposites at high f-MWNT loading. MA-g-PP/f-MWNT master batch was the most ineffective nucleating

agent among the three types of nanocomposites in the sense that ΔE remained at the similar level to that of the neat PP. In p-MWNT containing nanocomposites, the absolute value of ΔE decreased substantially as MWNT concentration increased. This again suggests that the addition of p-MWNT into the PP matrix causes more heterogeneous nucleation and thereby results in less temperature dependence of crystallization rate [6, 24] than f-MWNT.

Table 5.4. T_c, T_p, FWHM of T_c and crystallinity of PP/MWNT nanocomposites at different MWNT concentration. DSC tests were conducted with heating and cooling rate of 2.5 °C/min. Crystallinity was determined from 2nd heating cycle.

Materials	Concentration (wt %)	T_c (°C)	FWHM of T_c (°C)	T_p (°C)	Crystallinity (%)
PP	-	122	3.7	158	51
PP/f-MWNT via MA-g-PP/f-MWNT master batch	0.005	120	4.46	159.3	51
	0.01	120.8	4.2	159.3	51.7
	0.1	122	3.7	160.7	50.5
	0.3	122.7	3.7	162.3	52
	0.5	122.3	3.7	161.0	50.6
	1	124.4	3.5	161.6	49.3
PP/f-MWNT via PP/f-MWNT master batch	0.005	121.8	4.4	158.7	50
	0.01	123	4	161	53
	0.1	125.7	3.5	163	53.3
	0.3	130	3.3	164.8	54.0
	0.5	127.6	3.7	163.9	53.8
	1	127.4	3.6	162.9	53.6
PP/p-MWNT via p-MWNT	0.005	125.4	2.7	160.6	50.4
	0.01	126.5	2.8	162	53.4
	0.1	126.6	2.6	162	55.8
	0.3	127.4	3.1	162.8	53.5
	0.5	129.5	3.5	164.1	51
	1	132.9	3.5	164.9	52.6

According to Hoffman nucleation model [25], the melting temperature of the polymer crystal is determined by its lamella thickness which is inversely proportioned to the supercooling below equilibrium melting point T_m^0. That is, the crystal formed at higher

temperature (less super cooling, $\Delta T = T_m^0 - T_c$) should have larger lamella thickness and thereby higher melting point [25]. The addition of MWNTs provides interface for heterogeneous nucleation that allowed crystals to grow at higher crystallization temperature (higher T_c) due to the reduced thermodynamic driving force needed. In Table 5.4, the increase in T_c in the p-MWNT containing nanocomposite was the most prominent among the three types of nanocomposites which is consistent with the observation from the isothermal crystallization experiments. The melting peak maximum of the nanocomposite samples in most cases showed a positive correlation to T_c as expected (Figure 5.3). The exception occurred at the MA-g-PP/f-MWNT master batch containing samples at f-MWNT loading above 0.3 wt% where the influence of less crystallizable MA-g-PP at the interface became noticeable. As for the PP/f-MWNT master batch containing sample, T_c (and T_p) reached maximum value at 0.3 wt% f-MWNT and decreased at higher loadings. As discussed earlier, the nucleation saturation, as well as the reduced polymer mobility at high f-MWNT loading is likely to be the reason for this behavior. Moreover, the interfacial PP, i.e. the polymer in the master batch, has gone through solution processing, and may have fewer entanglements than the matrix PP. Melt compounding this solution processed PP with neat PP resulted in lower T_c as compared with neat PP (Figure 5.4). As the master batch concentration increases in the nanocomposite, the influence of this interfacial solution processed PP becomes not negligible and thus the lowering of T_c (and T_p) was observed by several degrees celsius.

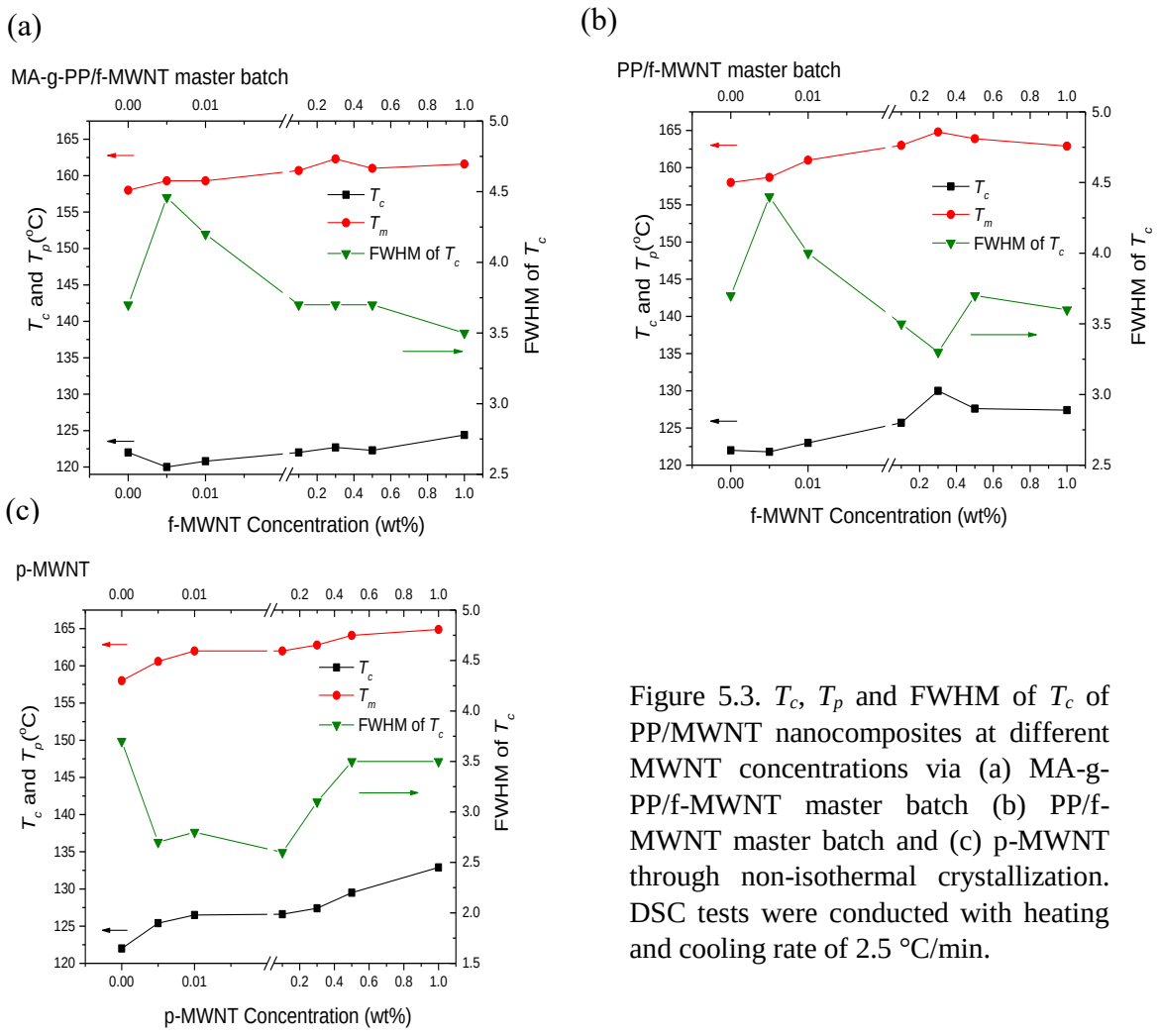

Figure 5.3. T_c, T_p and FWHM of T_c of PP/MWNT nanocomposites at different MWNT concentrations via (a) MA-g-PP/f-MWNT master batch (b) PP/f-MWNT master batch and (c) p-MWNT through non-isothermal crystallization. DSC tests were conducted with heating and cooling rate of 2.5 °C/min.

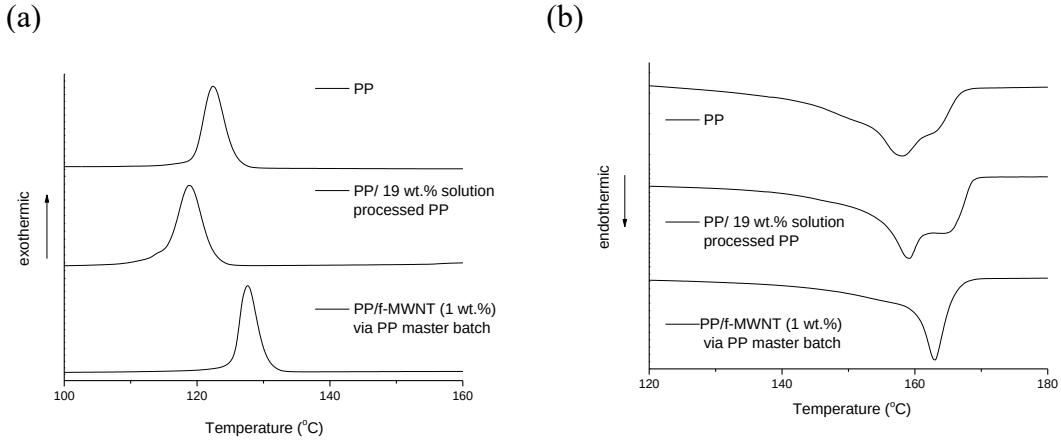

Figure 5.4. DSC of control PP, PP/19 wt% solution processed PP and 1 wt% f-MWNT nanocomposite based on PP/f-MWNT master batch. (a) is from the 1st cooling cycles and (b) is from the 2nd heating cycle. DSC tests were conducted with heating and cooling rates of 2.5 °C/min. Solution processed PP was prepared by dissolving PP powder in butanol-xylene mixture followed by solvent evaporation as was done for PP/f-MWNT master batch processing, except in this case nanotubes were not used.

Unlike the apparent increase of T_c, the change of T_p due to the incorporation of fillers is relatively moderate (Table 1.5 in Chapter 1) indicating that despite promoting crystallization nucleation, the fillers normally have limited influence on the morphology of PP in the perspective of lamella thickness or crystal perfection [26]. Most of the literature reported about 2 °C increase, and in several studies even reduction in T_p was reported in PP based nanocomposites. It is worth noting that in one study, 5 °C and 8 °C increase in T_p was observed for pristine multiwall and single wall nanotube loaded PP nanocomposites, respectively [13]. There are two distinct characteristics in this work compared with the others. First, the latex mixing technology introduced by the author resulted in good nanotube dispersion in the polymer matrix. Second, the nanotubes used in the study had not gone through any treatments thus retaining the pristine graphitic structure. Both characteristics minimize the disturbance of fillers on the polymer crystallization process as compared to a system with aggregates of fillers or unfavorable interfaces, e.g. monomer or polymer grafting on fillers, that can not provide an effective template for crystallization. In our work, significant increase of T_p (nearly 7 °C) was observed in the PP/f-MWNT containing sample with only 0.3 wt% f-MWNT loading. As the solution processed polymers in the master batch had fewer entanglements than the raw PP, they had better opportunity to interact with f-MWNTs and formed a coherent interface that could template the crystallization of the matrix polymers with higher crystal perfection. Effect of solution processing was also reported by Xie et. Al. [27] where about 5 °C higher T_p was found when polyethylene (PE) was crystallized from solution than from melt in the presence of MWNT. The author attributed this to the better chain regularity and larger crystal lamella in the former.

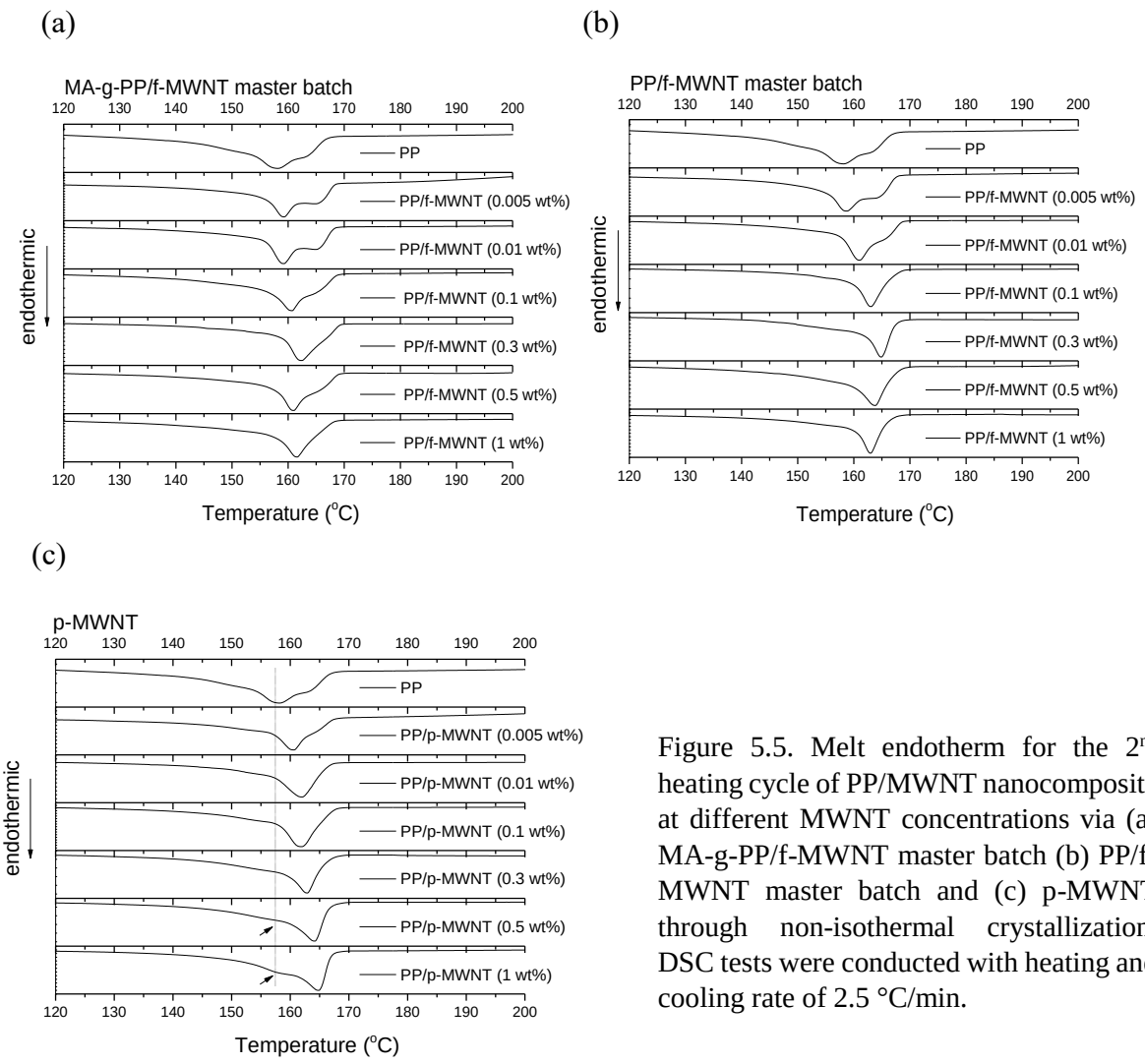

Figure 5.5. Melt endotherm for the 2nd heating cycle of PP/MWNT nanocomposite at different MWNT concentrations via (a) MA-g-PP/f-MWNT master batch (b) PP/f-MWNT master batch and (c) p-MWNT through non-isothermal crystallization. DSC tests were conducted with heating and cooling rate of 2.5 °C/min.

Narrower crystallization and melting peaks represent narrower crystal size distribution [28, 29]. In the MA-g-PP/f-MWNT and PP/f-MWNT based nanocomposites, the narrowest FWHM of T_c was observed at the f-MWNT concentration where the crystallization rate was the fastest, i.e. at 1 wt% and 0.3 wt% in the case of MA-g-PP/f-MWNT and PP/f-MWNT, respectively (Figure 5. 3). Considering a homogenous distribution of f-MWNT in the polymer matrix, it is not surprising that the crystal size distribution is inversely proportional to the crystallization rate assuming crystallization is

via heterogeneous nucleation. On the other hand, FWHM of T_c of the p-MWNT based sample was narrower when p-MWNT concentration was between 0.005 wt% and 0.1 wt% than at the higher p-MWNT concentration. Similar observation can also be found in the melt endotherm of p-MWNT containing nanocomposites (Figure 5.5). Above 0.5 wt% p-MWNT, a shoulder peak corresponds to the melting point of neat PP around 158 °C which is about 7 °C lower than T_p, suggesting that some of the PP was not effected by p-MWNT during crystallization owing to poor MWNT dispersion. Although the crystallization rate continuously increased with increase in p-MWNT concentration, inhomogeneous distribution of MWNT resulted in discrepancy in the crystallization behavior of matrix PP which is revealed by both broadening of melt endotherm and broadening FWHM of T_c. It is worth noting that while about 7 °C higher T_p was observed in both p-MWNT (1 wt%) and PP/f-MWNT (0.3 wt%) containing nanocomposite, a single and sharp peak observed in the PP/f-MWNT based sample demonstrated that the crystallization of matrix polymers was uniformly modified by well dispersed f-MWNT through a longer interphase than via p-MWNT. This refinement and perfection of the PP crystals can also be seen from the equilibrium melting temperature (T_m^0) of PP, determined by linear Hoffman-Weeks plots (Figure 5.6), which increased by about 5 °C in the PP/f-MWNT based nanocomposites while exhibited no significant change in the presence of 1 wt% p-MWNT. On the other hand, at MWNT concentration as low as 0.01 wt% where the difference of MWNT dispersion quality between the three types of nanocomposite is smaller as compared to that at a higher MWNT loading, the p-MWNT based sample has narrowest FWHM of T_c (Figure 5.3) and largest upshift of a sharp melting peak than the two f-MWNT master batch based samples (Figure 5.5).

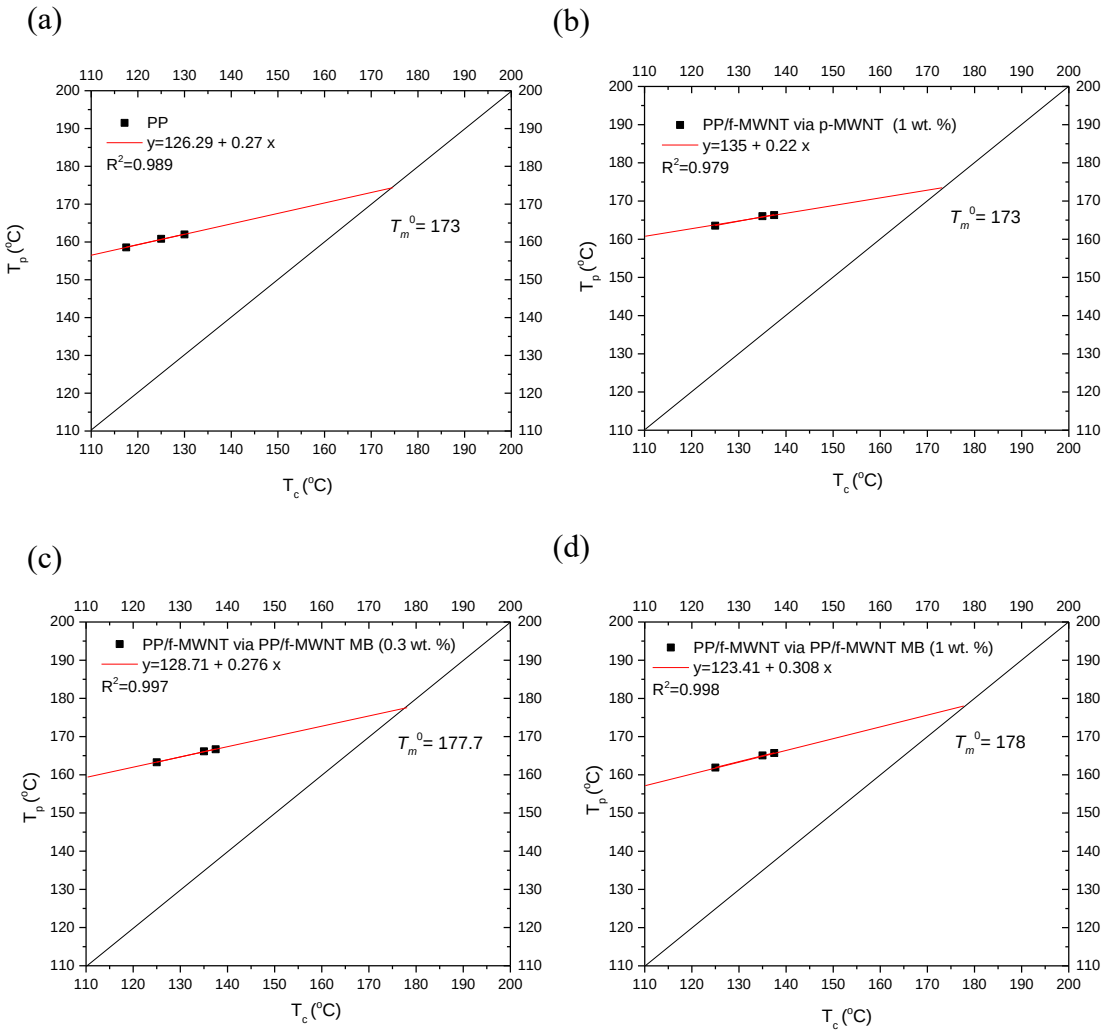

Figure 5.6. Linear Hoffam-Weeks analysis to obtain T_m^0 for (a) PP, (b) PP/p-MWNT nanocomposite (1 wt% p-MWNT) via p-MWNT, (c) PP/f-MWNT nanocomposite (0.3 wt% f-MWNT) via PP/f-MWNT master batch and (d) PP/f-MWNT nanocomposite (1 wt% f-MWNT) via PP/f-MWNT master batch.

Figure 5.7 shows the melt endotherm of PP and PP/MWNT nanocomposites with 1 wt% MWNT loading at various cooling and heating rates. The melt endotherm of the neat PP crystallized at 2.5 °C/min cooling rate (Figure 5.5 and Figure 5.7a-1) presented a shoulder at ~164 °C, which is higher than T_p (158 °C). Shoulder at similar temperature range was also apparent in the f-MWNT based nanocomposite samples below 0.01 wt% f-

MWNT loading (Figure 5.5). While the upshift of T_p can be attributed to the larger lamella thickness or higher crystalline perfection of PP resulting from the presence of CNT during crystallization [13], the shoulder peak higher than T_p is most likely the melting of the crystal lamellae that have gone through recrystallization process during heating. When heated slowly, less stable crystals may melt and recrystallize on the existing more perfect crystalline lamellae that are still present in the sample [13].

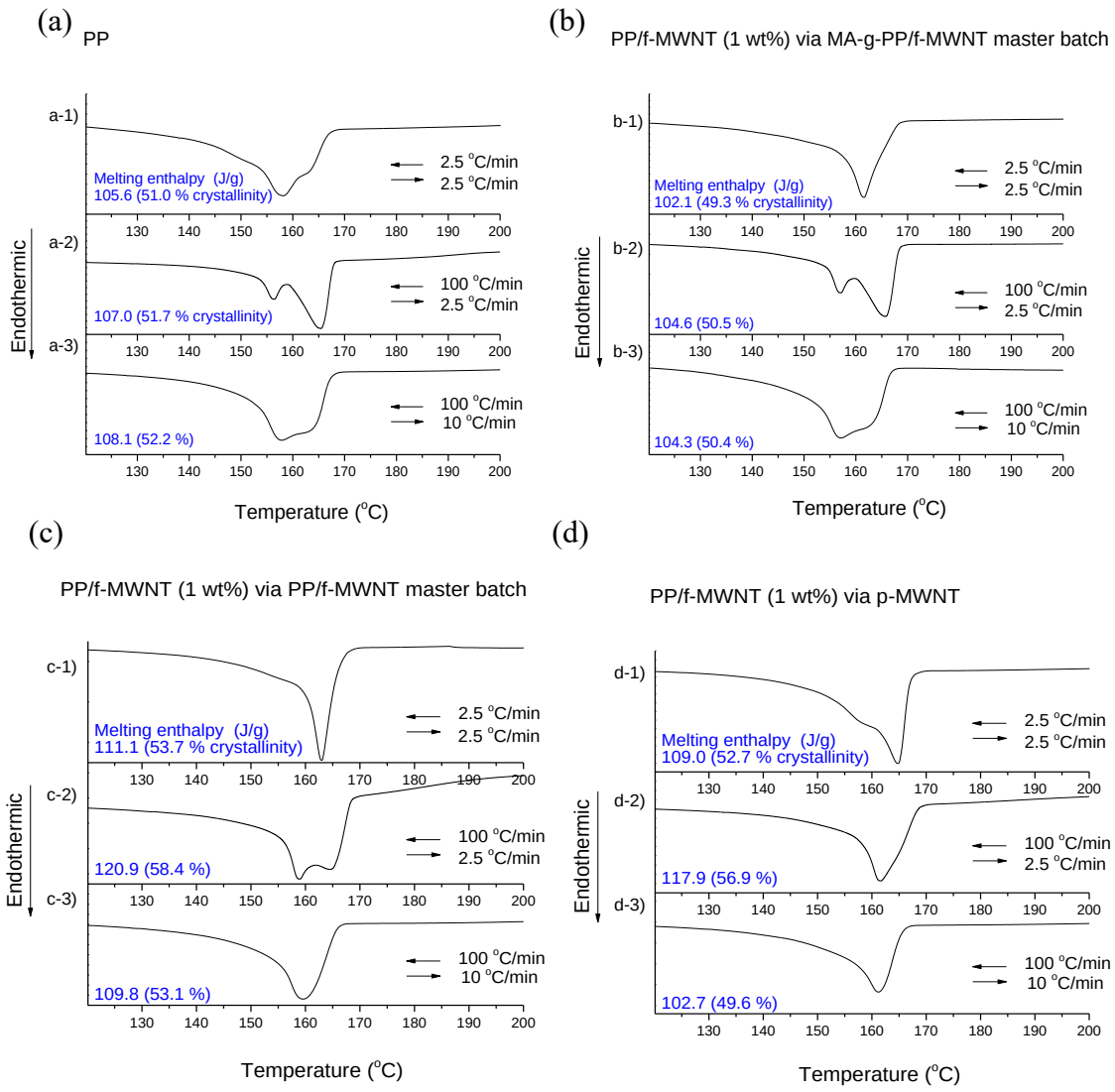

Figure 5.7. Melt endotherm for the 2nd heating cycle of (a) PP and PP/MWNT nanocomposite (1 wt%) via (b) MA-g-PP/f-MWNT master batch (c) PP/f-MWNT master batch and (d) p-MWNT. Cooling (1st cycle) and heating (2nd cycle) rate of DSC tests are indicated by the left arrow and right arrow, respectively.

The crystalline lamella thickness has also been demonstrated to increase upon recrystallization and thereby explaining the higher melting temperature [30, 31]. Crystals that formed through faster cooling rate have lower initial degree of crystalline perfection which may accentuate the occurrence of recrystallization. This is confirmed by the observation in Figure 5.7 a-2, b-2, and c-2, i.e., the recrystallization of the less perfect crystals resulted in apparent melting peak at about 165 °C as compared with the shoulder in Figure 5.7a-1 and the absence of this peak in Figure 5.7b-1 and c-1. On the other hand, because the reordering of polymer chains is more difficult upon fast heating than slow heating, the recrystallization process should be suppressed as the heating rate increased from 2.5 °C/min to 10 °C/min. This can be seen in Figure 5.7a-3 and b-3, where the peak assigned for melting crystals that formed upon recrystallization in Figure 5.7a-2 and b-2 reduced its intensity and disappeared in Figure 5.7c-3. The occurrence of recrystallization was greatly restricted in the p-MWNT containing nanocomposite (Figure 5.7d-2 and d-3) and was relatively moderate in the PP/f-MWNT than in the MA-g-PP/f-MWNT based sample. Increased melt viscosity in the presence of MWNT (Chapter 6), which is more pronounced in the case of p-MWNT and PP/f-MWNT, indicates impeded segmental motion and thereby suppression of recrystallization.

5.3.2 Columnar crystalline polymer coated MWNTs

Recrystallization process triggers crystal refinement and perfection during melting. These more perfect crystals created during recrystallization, are not retained upon complete melting. Partial melting of the sample with subsequent quenching and crystallization at a lower temperature was thus conducted to investigate the self-seeding or templating effect of the highly refined crystals that do not melt at a selective temperature before complete

melting. The morphology of the resulting crystal lamellae can be studied under SEM and the melting behavior (degree of crystal perfection, lamella thickness, and size distribution, etc.) can be investigated via DSC. The detail temperature profiles used in the DSC experiment for this purpose are shown in Figure. 5.8 and 5.9 for PP and PP/f-MWNT master batch (5 wt% f-MWNT), respectively.

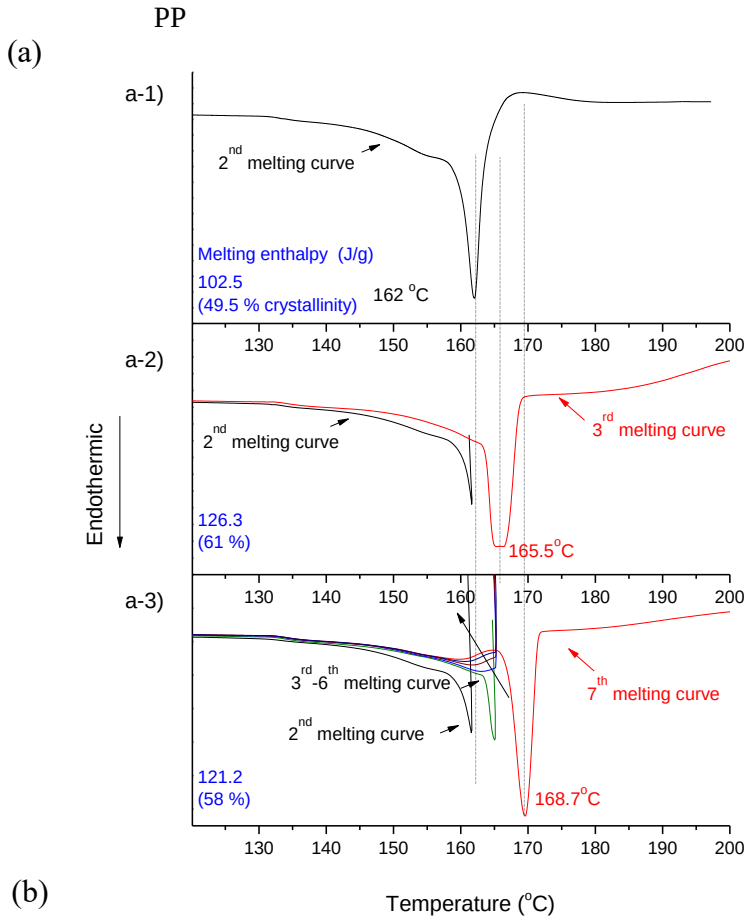

Figure 5.8. Melt endotherms of PP through various self-seeding thermal cycles as shown in (b). DSC tests were conducted with heating and cooling rates of 2.5 °C/min.

(a) PP/f-MWNT master batch (5wt% f-MWNT)

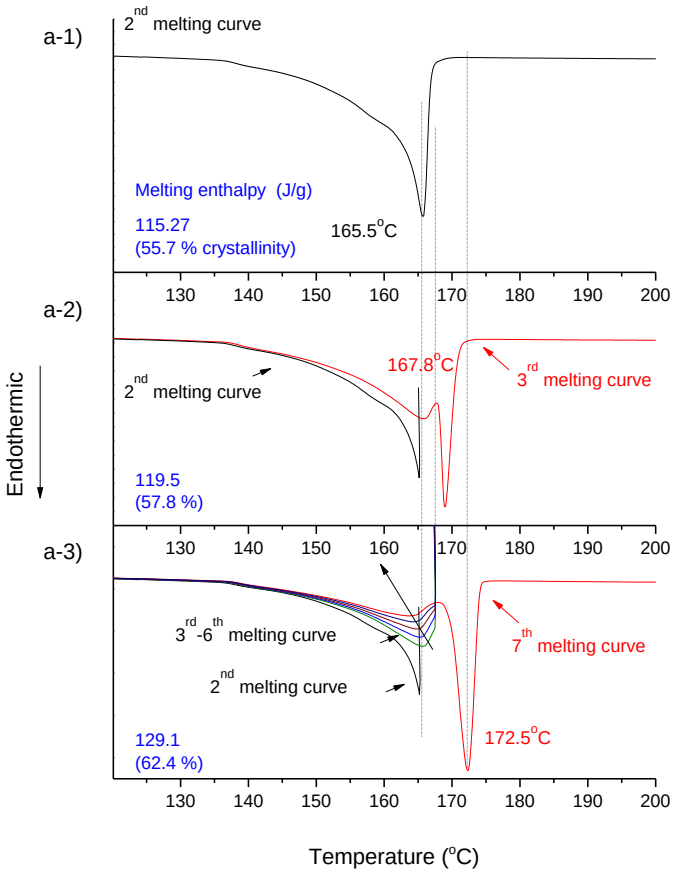

(b)

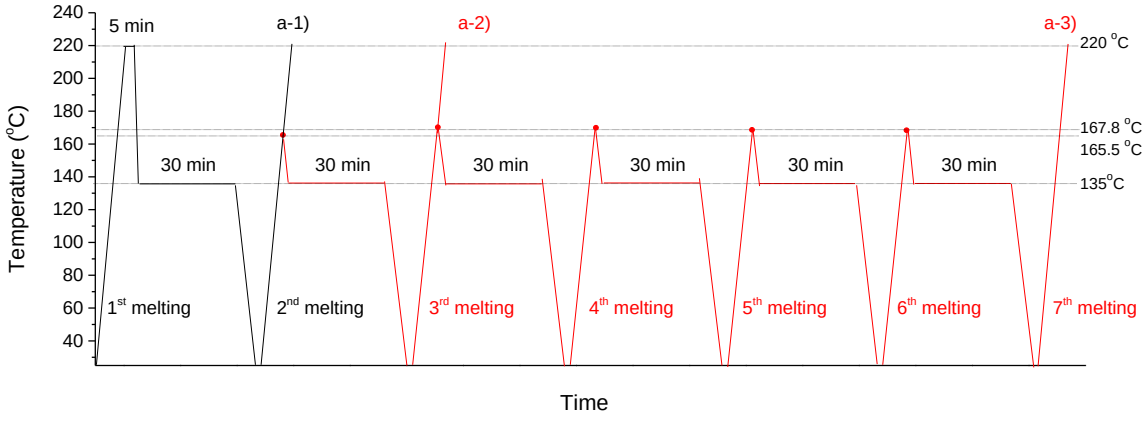

Figure 5.9. Melt endotherms of PP/f-MWNT master batch through various self-seeding thermal cycles as shown in b). DSC tests were conducted with heating and cooling rates of 2.5 °C/min.

Different isothermal crystallization temperature was chosen, i.e. 130 °C for neat PP and 135 °C for the master batch and nanocomposites, to ensure comparable test condition, i.e. similar $t_{1/2}$, since the incorporation of MWNT allows PP to crystallize at higher temperature than the neat PP and this should not be overlooked when comparing the crystallization behavior of the two. First self-seeding temperature, a temperature at which the sample is partially melted, was determined by the peak melting temperature of the sample crystallized from 130 °C (or 135 °C in MWNT containing samples), is 162 °C for neat PP and 165.5 °C for MWNT containing samples (Figure 8a-1 and Fig 5.9a-1). The second self-seeding temperature is determined from the melt endotherm of the sample after one complete self-seeding cycle (i.e., 1st heating for removing thermal history, 1st cooling for isothermal crystallization, 2nd heating for first self-seeding followed by 2nd cooling to the isothermal crystallization temperature). From the 3rd melting endotherm (i.e., the melting of the sample after one self-seeding cycle), the second self-seeding temperature was chosen to be 165.5 °C for PP and 167.8 °C (between two melting peaks) for PP/f-MWNT master batch (Figure 5.8 a-2 and Figure 5.9a-2).

After one self-seeding cycle, both the samples contain crystals that have 4 °C higher melting temperature (Figure 5.8a-2 and Figure 5.9a-2) than the crystals from samples that have only gone through isothermal crystallization (Figure 5.8a-1 and Figure 5.9a-1). That is, the crystals which have higher melting point than the first self-seeding temperature serves as templates for subsequent polymer crystallization when the sample was cooled to given isothermal crystallization temperature. From Figure 5.8a-2 and Figure 5.9a-2 it is apparent that the resulting crystals, with a good portion, have grown from these templates and possess high regularity thereby melted at higher temperature. A schematic

describing the self-seeding process is given in Figure 5.10. Further refinement of the crystals can be achieved through repeatedly conducting the self-seeding process multiple times as shown in the schematic in Figure 5.10 In other words, by repeated melting of the less perfect crystals below the second self-seeding temperature while keeping the more perfect ones as seeds, the crystals that grow on these pre-existing templates became larger in size and higher in ratio with respect to the total crystalline population. Figure 5.8a-3 and Figure 5.9a-3 showed the melting of samples underwent total of five self-seeding cycles which corresponds to the seventh melting curve as annotated in these figures. The melt endotherm of both PP and PP/f-MWNT master batch exhibited about 7 °C peak shift compared to their counterparts that have not gone through any self-seeding cycle, i.e. increased from 162 °C to 168.7 °C in the neat PP sample and from 165.5 to 172.5 °C in the PP/f-MWNT master batch based sample. Gradual reduction of the less perfect crystalline portion can also be seen in Figure 5.8a-3 and Figure 5.9a-3 as the sample goes through more self-seeding cycles (from 2^{nd} melting curve to 6^{th} melting curve). The final melt endotherm consisted of a broad peak below the second self-seeding temperature above which a major strong sharp peak attests the occurrence of templated crystal growth. From another perspective, the incorporation of f-MWNT and the self-seeding/templating crystallization jointly increase the melting temperature of PP by 10.5 °C (from 162 °C to 172. 5 °C). Typically, the thicker lamellae with high melting point can be obtained through prolonged crystallization time at a low super-cooling temperatures. For example, Maiti et al. [32] obtained PP lamellae with a high melting temperature of 180.8 °C via PP crystallization at 166 °C for six months. With the combination of shear (22.5 s^{-1}) and pressure (200 MPa) Yang, et al. [33] successfully crystallized a small portion of PP with

melting point of 179. 5 °C which is 16 °C higher than the PP crystallized under quiescent condition. While keeping the time required for the completion of crystallization relatively short, our approach affords a new method to considerably modify the melting behavior of matrix PP.

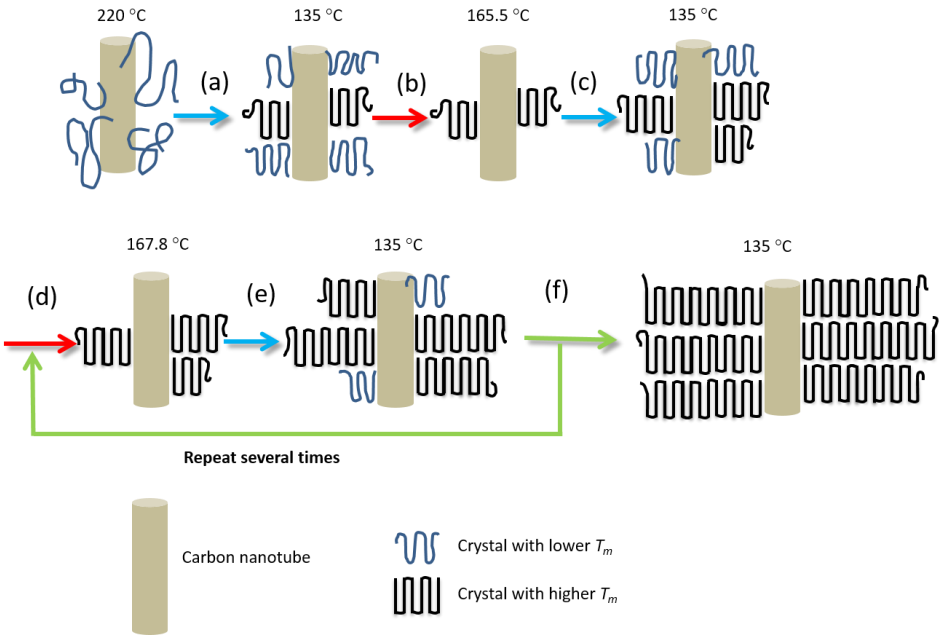

Figure 5.10. Schematic of the formation process of highly perfect columnar crystals surrounding f-MWNTs. During isothermal crystallization at 135 °C (a), crystals that nucleated at f-MWNT exhibited both relatively high and low T_m due to difference in crystal perfection. After quenching to room temperature and re-heating to 165.5 °C (b) crystals with lower T_m were melted, leaving more perfect crystals that have higher T_m as "seeds". When again isothermally crystallized at 135 °C (c), templated crystal growth happened at these "seeds" while crystals with both higher and lower perfection also nucleated on f-MWNT surface. After repeatedly heating to the second self-seeding temperature, i.e. 167.8 °C in this example (d), and followed by isothermal crystallization (e), the highly perfect crystals surrounding f-MWNTs can be achieved (f).

The role of MWNT in the self-seeding and templated growth scheme is to provide seeds with higher crystalline perfection to start with. This can be inferred based on a higher crystallinity (55.7 % versus 49.5 %) and higher peak melting temperature (165.5 °C versus 162 °C) in the PP/f-MWNT master batch than neat PP from Figure 5.8a-1 and Figure 5.9a-1. As a consequence, the resulting crystalline lamellae that have gone through five cycles of self-seeding process also possess higher crystallinity (62.4 % versus 58 %) and higher peak melting temperature (172.5 °C versus 168.7 °C) in the PP/f-MWNT master batch than in the neat PP as shown in Figure 5.8a-3 and Figure 5.9a-3. From Figure 5.11 and Table 5.5, the increase in crystal size as samples went through the self-seeding treatments verifies the hypothesis of templated crystal growth in the schematic (Figure 5.10). Larger crystal size in PP/f-MWNT master batch than in neat PP (24.6 nm versus 21.2 nm) is also in agreement with higher peak melting temperature in the former [34]. The morphology of the templated polymers on the f-MWNT interface was investigated by SEM where the columnar layers of crystalline PP were found surrounding f-MWNT that resulted in noticeable change in the PP/f-MWNT diameter from 25 ± 5 nm to 64 ± 10 nm (Figure 5.12). Such type of columnar layer of polymer crystalline lamellae growing perpendicular to the long axis of fillers has been reported in PP/CNT fiber [35, 36], PP/ramie fiber [37], PP/glass fiber [38], PP/carbon fiber [39], PP/graphene oxide fiber [36, 40], etc., and is often referred to as the transcrystalline interphase. However, it is the first time that this type of columnar crystalline interphase has been created through designed heat treatment and crystallization cycles.

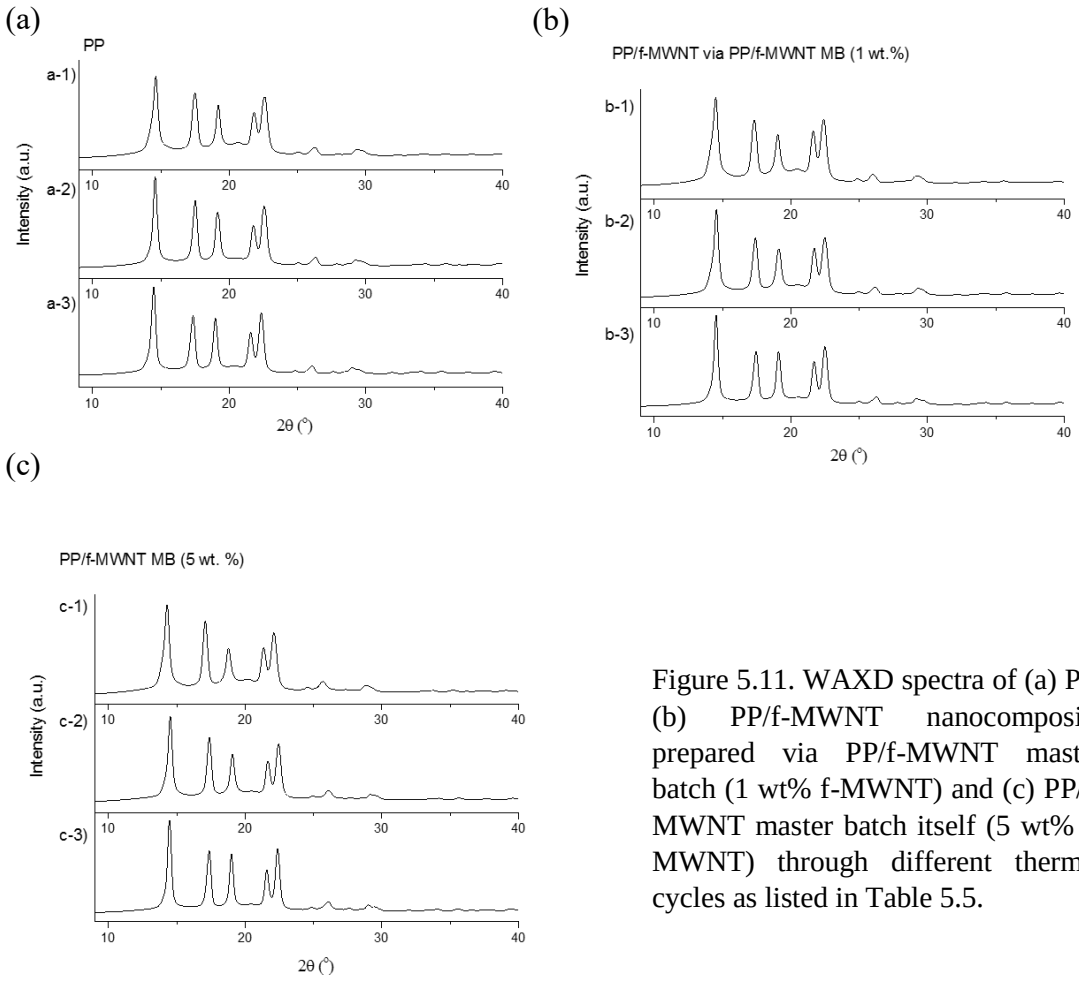

Figure 5.11. WAXD spectra of (a) PP, (b) PP/f-MWNT nanocomposite prepared via PP/f-MWNT master batch (1 wt% f-MWNT) and (c) PP/f-MWNT master batch itself (5 wt% f-MWNT) through different thermal cycles as listed in Table 5.5.

Table 5.5. WAXD results of PP and PP/f-MWNT nanocomposite prepared via PP/f-MWNT master batch (1 wt% f-MWNT) and PP/f-MWNT master batch itself (5 wt% f-MWNT) through different thermal cycles. Crystal size of (110) was determined by the Scherrer's equation.

Materials	Figure	Thermal treatment profile	Crystal size of (110) (nm)	Crystallinity (%)
PP	Figure 5.11, a-1)	Figure 5.8, a-1)	16.5	70
	Figure 5.11, a-2)	Figure 5.8, a-2)	22.8	75
	Figure 5.11, a-3)	Figure 5.8, a-3)	21.2	75
PP/f-MWNT via PP/f-MWNT master batch (1 wt%)	Figure 5.11, b-1)	Figure 5.15, a-1)	15.1	72
	Figure 5.11 b-2)	Figure 5.15, a-2)	18.3	75
	Figure 5.11, b-3)	Figure 5.15, a-3)	23.4	75
PP/f-MWNT via PP/f-MWNT master batch (5 wt%)	Figure 5.11, c-1)	Figure 5.9, a-1)	17.6	71
	Figure 5.11, c-2)	Figure 5.9, a-2)	21.8	74
	Figure 5.11, c-3)	Figure 5.9, a-3)	24.6	77

The interfacial strength between the filler and the matrix in a composite is an important factor in determining their mechanical properties. A number of studies have attempted to manipulate such interface or interphase through interfacial crystallization. Zhang, et al. [41] reported CNT fiber based nanocomposites prepared by polyethylene crystallization from both solution and melt. Both hybrid shish-kebab nanostructures and transcrystalline lamellae around nanotubes were observed along with improved mechanical properties. In another work, interfacial crystallization of poly(vinyl alcohol) on single wall carbon nanotube from solution resulted in extended-chain crystalline layer which appeared to increase load transfer between the polymer and the carbon nanotube [42]. Based on the above-mentioned studies, it is believed that the self-seeding and templated crystallization approach developed in this work has a potential to help understand the effect of interphase on the mechanical properties of nanocomposite containing well dispersed fillers. Also, the ability to increase crystallinity, crystal size, and lamella thickness of the matrix polymer via such approach should not be limited to PP but would be applicable to other semicrystalline polymers.

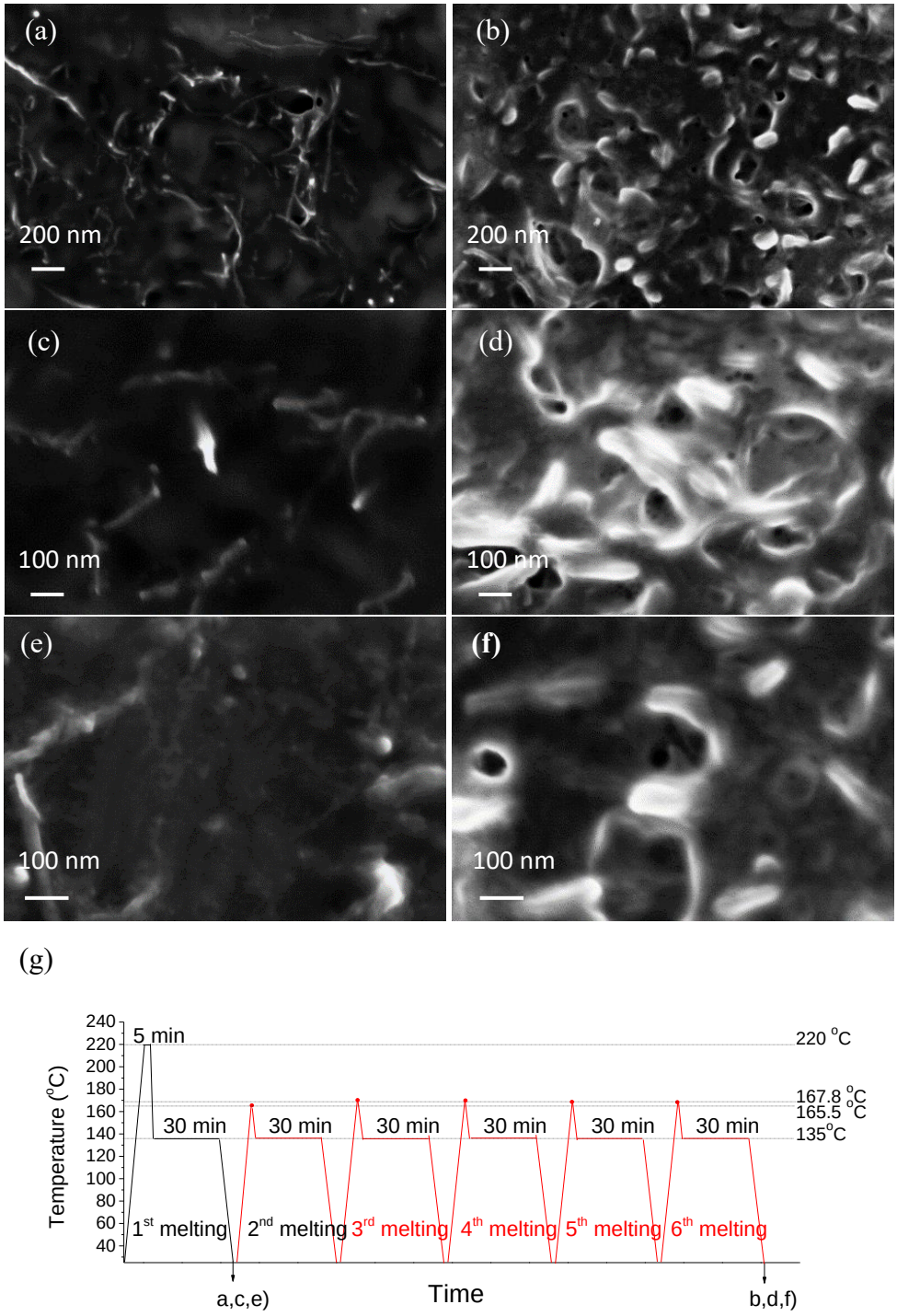

Figure 5.12. SEM images of (a, c, e) PP/f-MWNT master batch that was first heated to 220 °C for 5 minutes followed by isothermal crystallization at 135 °C for 30 minutes and then quenched to room temperature. In (b,d,f), the sample first underwent the same treatment as the sample in (a, c, e) and then followed the temperature profile shown in (g). Average diameter of f-MWNTs in (a,c,e) and (b,d,f) is 25 ± 5 nm and 64 ± 10 nm, respectively.

The parallel experiments on self-seeding and templated crystallization were also conducted in the PP/MWNT nanocomposites prepared via PP/f-MWNT, MA-g-PP/f-MWNT master batches, and p-MWNT. In Figure 5.13a and Table 5.6, the area under the high melting temperature peak became larger as f-MWNT concentration in the nanocomposite increased from 0.3 wt% to 1 wt% Comparison of the ability to induce templated crystal growth between difference types of interfaces is shown in Figure 5.13b and Table 5.7. The MA-g-PP/f-MWNT based nanocomposite did not result in as much elevation of melting temperature as seen in other samples. The incapability of promoting prefect crystal growth may be due to the less crystallizable MA-g-PP in the vicinity of f-MWNT which did not serve as best template for PP crystallization. Smaller area under the major melting peak in p-MWNT containing sample than in the PP/f-MWNT also pointed to the importance of MWNT dispersion quality in providing more perfect lamellar seeds for templated polymer crystal growth.

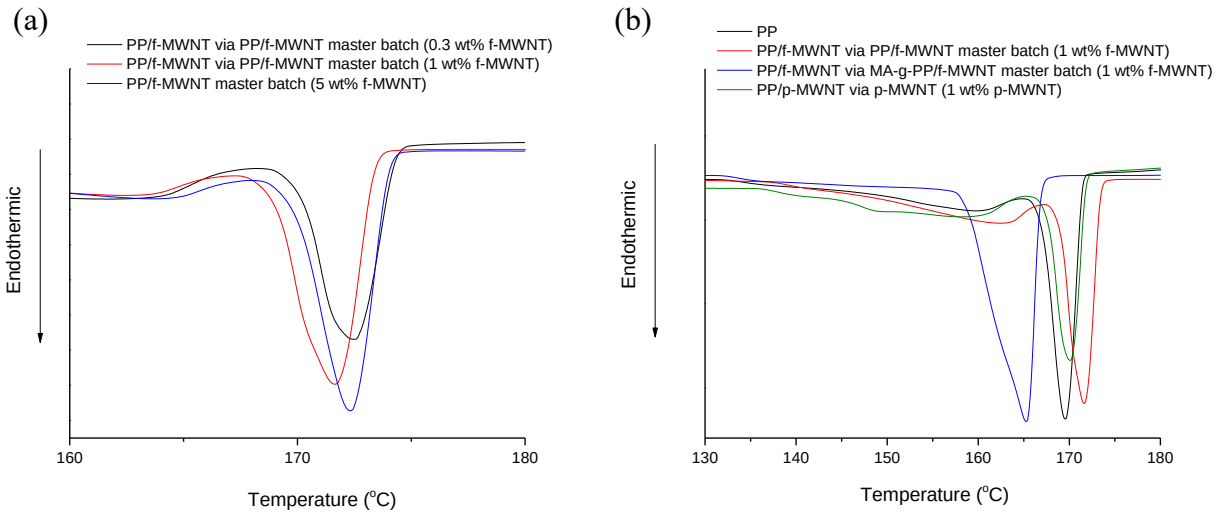

Figure 5.13. Melt endotherm of (a) PP/f-MWNT nanocomposites at different f-MWNT concentration via PP/f-MWNT master batch and (b) PP and PP/MWNT nanocomposite via different types of master batch at 1 wt% MWNT concentration after five cycles of self-seeding and templated crystal growth. The detailed heating and cooling profiles in each sample was provided in Figures 5.14-5.17.

Table 5.6. Melting peak position and melting enthalpy of PP/f-MWNT nanocomposites at different f-MWNT concentration via PP/f-MWNT master batch after five cycles of self-seeding and templated crystal growth.

Materials	Peak position	Melting enthalpy (J/g)
PP/f-MWNT via PP/f-MWNT master batch (0.3 wt%)	172.5 °C	35.4
PP/f-MWNT via PP/f-MWNT master batch (1 wt%)	171.7 °C	43.5
PP/f-MWNT master batch (5 wt%)	172.5 °C	42.5

Table 5.7. Melting peak position and melting enthalpy of PP and PP/MWNT nanocomposite via different types of master batch at 1 wt% MWNT concentration after five cycles of self-seeding and templated crystal growth.

Materials	Peak position	Melting enthalpy (J/g)
PP	168.7 °C	39.8
PP/f-MWNT via PP/f-MWNT master batch (1 wt%)	171.7 °C	43.5
PP/f-MWNT via MA-g-PP/f-MWNT master batch (1 wt%)	165.3 °C	79.3
PP/p-MWNT via p-MWNT (1 wt%)	171.2 °C	35.6

(a) PP/f-MWNT (0.3 wt%) via PP/f-MWNT master batch

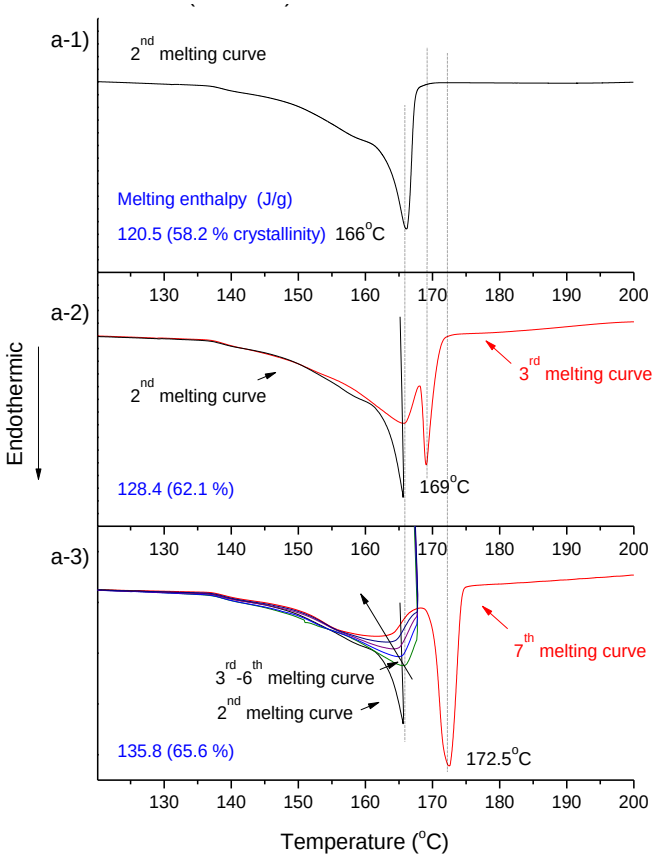

(b)

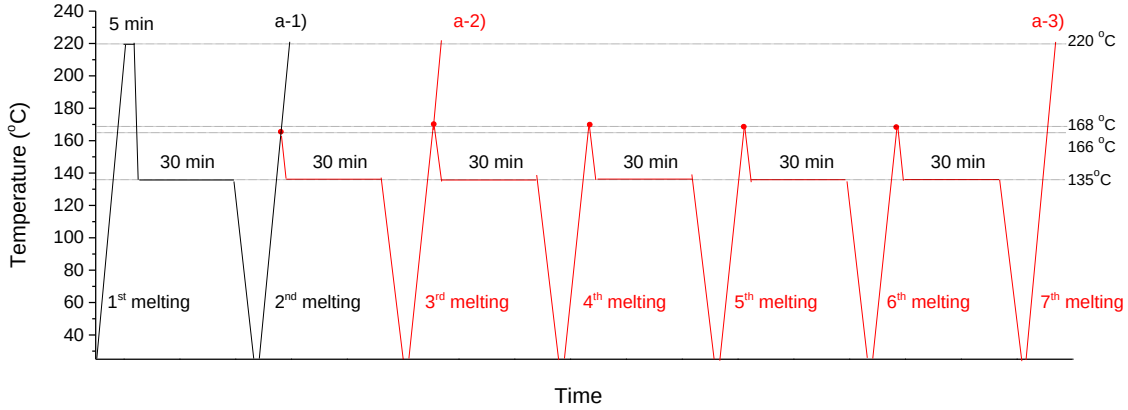

Figure 5.14. Melt endotherm of PP/f-MWNT nanocomposite prepared via PP/f-MWNT master batch (0.3 wt%) through different thermal cycles as shown in b). DSC tests were conducted with heating and cooling rate of 2.5 °C/min.

(a)

PP/f-MWNT (1 wt%) via PP/f-MWNT master batch

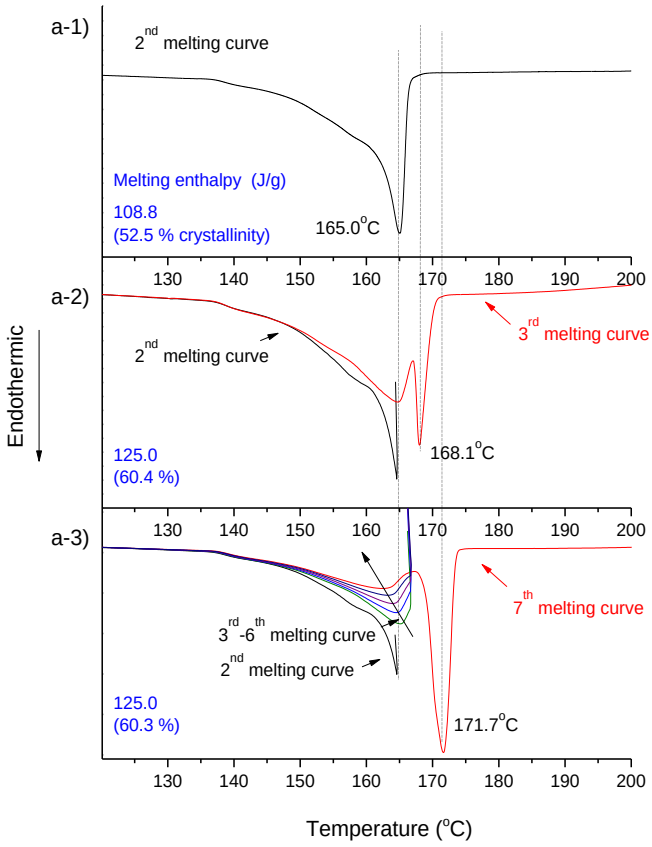

(b)

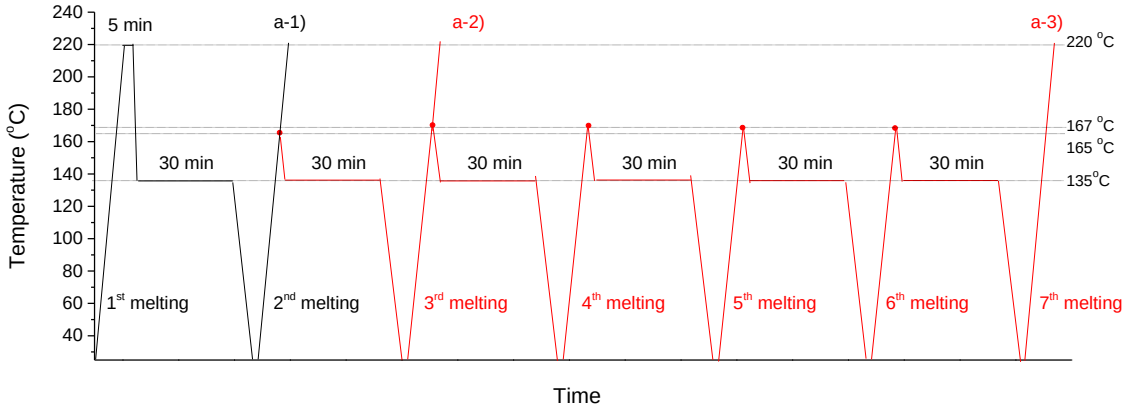

Figure 5.15. Melt endotherm of PP/f-MWNT nanocomposite prepared via PP/f-MWNT master batch (1 wt%) through different thermal cycles as shown in b). DSC tests were conducted with heating and cooling rate of 2.5 °C/min.

(a)

PP/f-MWNT (1 wt%) via MA-g-PP/f-MWNT master batch

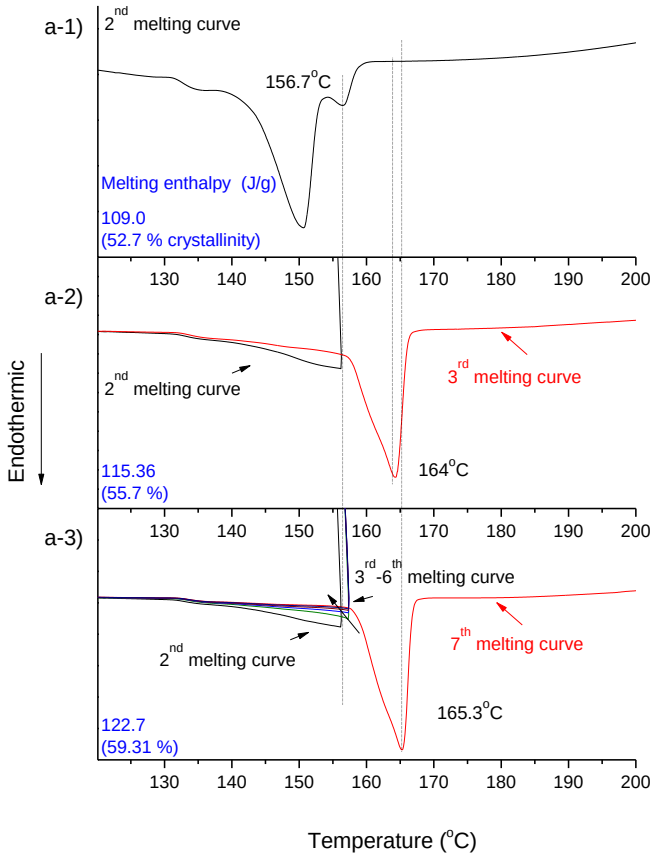

(b)

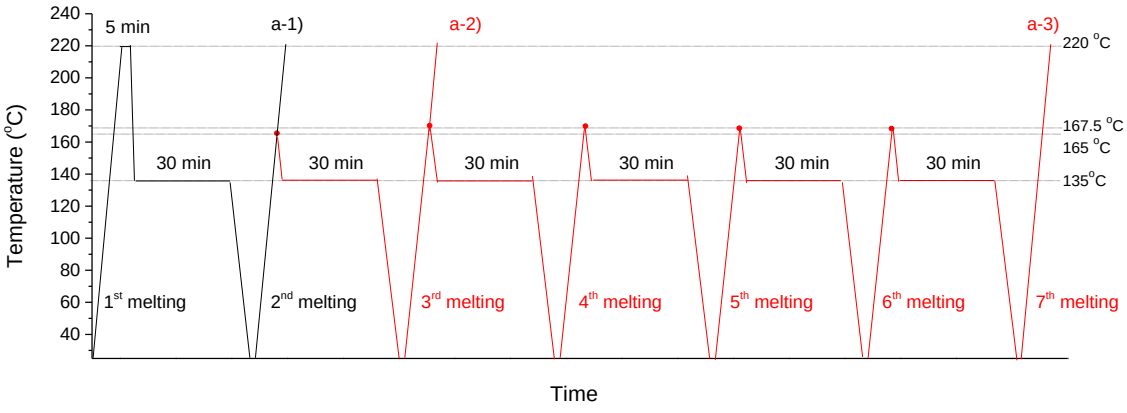

Figure 5.16. Melt endotherm of PP/f-MWNT nanocomposite prepared via MA-g-PP/f-MWNT master batch (1 wt%) through different thermal cycles as shown in b). DSC tests were conducted with heating and cooling rate of 2.5 °C/min.

(a)

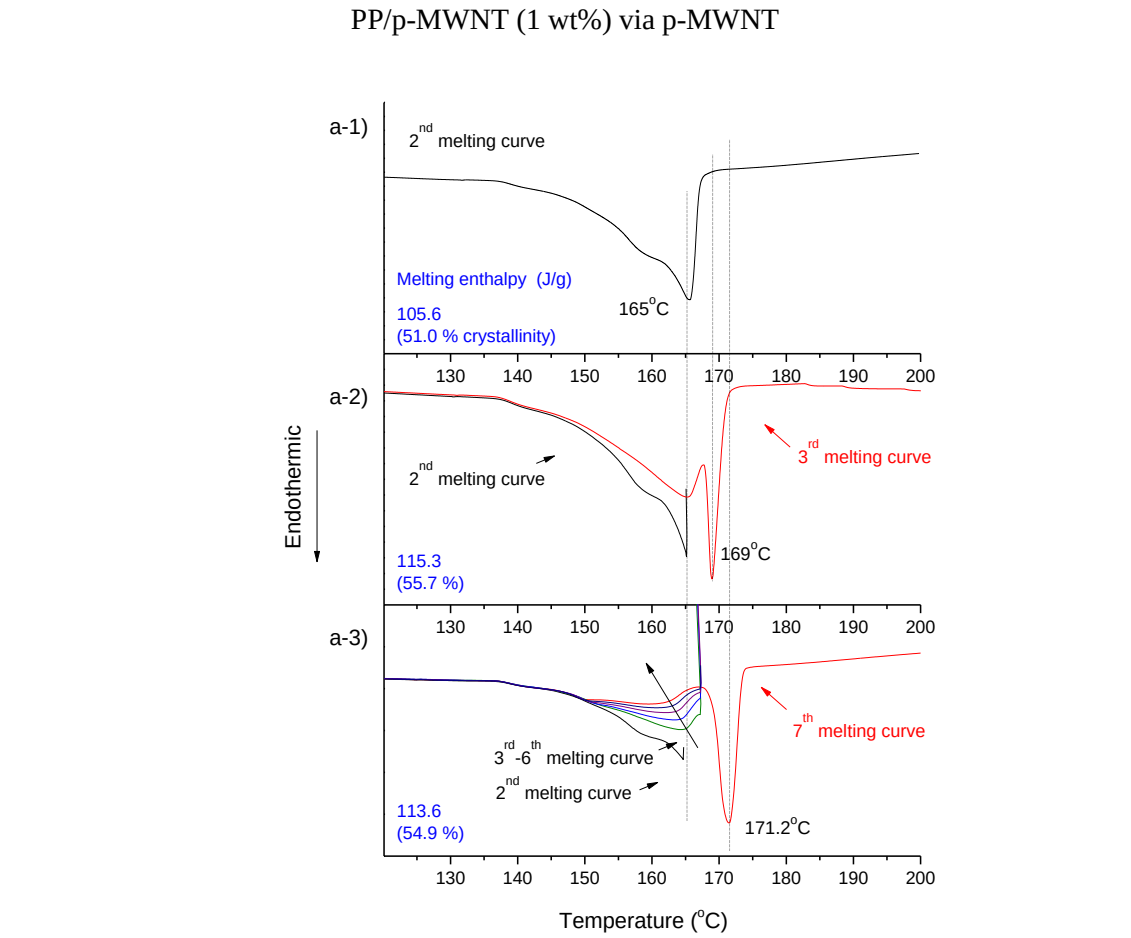

(b)

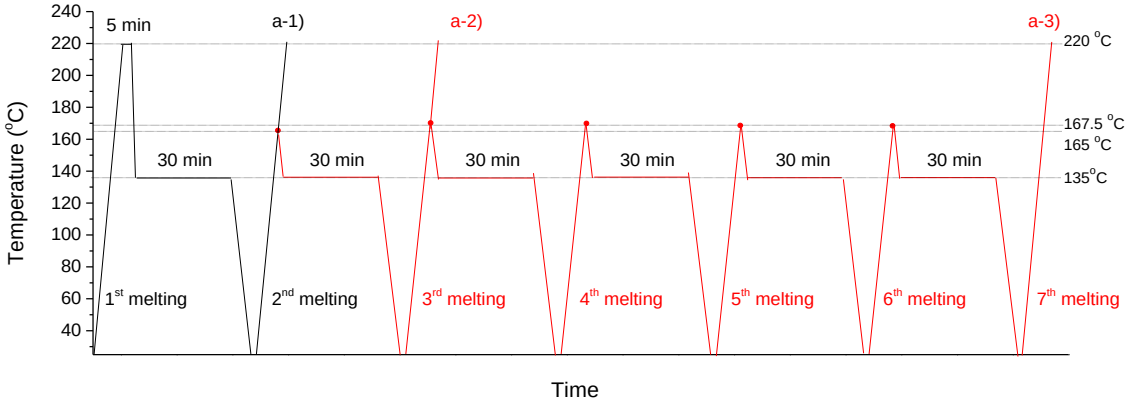

Figure 5.17. Melt endotherm of PP/p-MWNT nanocomposite prepared via p-MWNT (1 wt%) through different thermal cycles as shown in b). DSC tests were conducted with heating and cooling rate of 2.5 °C/min.

Figure 5.18 provides a visualization of the polymer self-seeding process. In the POM experiment, the set temperature of the heating stage for isothermal crystallization and self-seeding was chosen to be 5 °C higher than the experimental condition used in DSC. This is because the sample was placed on the cover slip instead of directly contacting the heating stage so some discrepancy between the temperature experienced by the sample and the set temperature of the heating stage was expected. When the sample was heated to the self-seeding temperature after isothermal crystallization at 140 °C, there were still some nuclei observable in the POM image that were not completely melted (step b in Figure 5.18). As the sample was quenched from the self-seeding temperature (step c in Figure 5.18), onset of crystallization was found shifted to a higher temperature such that more observable nuclei were presented in the POM image at 150 °C upon cooling. Consequently, the crystallization of the self-seeded polymers finished much earlier than the crystallization from unseeded melt (5 min versus 12 min). The resulting crystalline phase was completely melted when the set temperature of the heating stage reached 180 °C. The observation from the POM experiment is in good agreement with the proposed scheme of self-seeded and templated crystal growth shown in Figure 5.10.

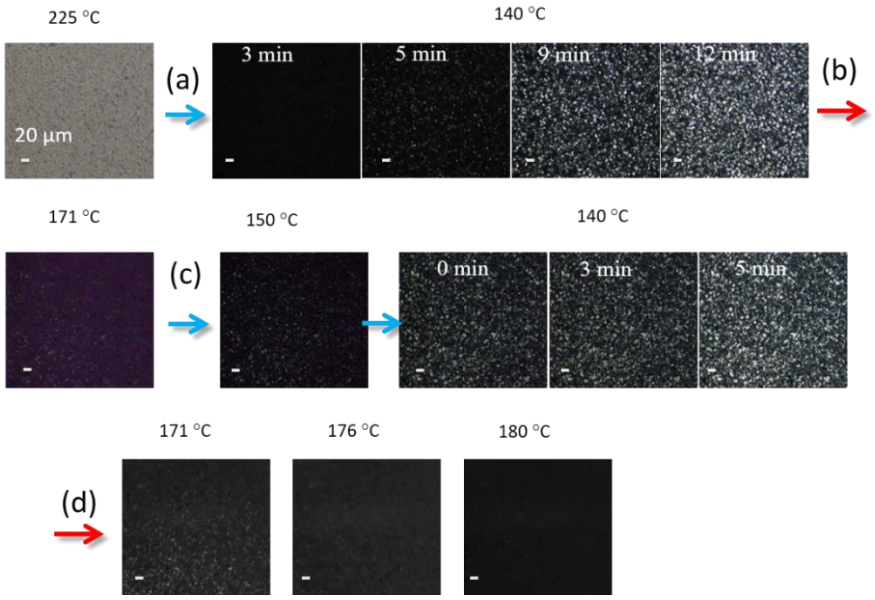

Figure 5.18. POM images of PP/f-MWNT nanocomposite prepared via PP/f-MWNT master batch at 1 wt% f-MWNT concentration. The sample was first heated to 225 °C for 5 minutes and isothermally crystallized at 140 °C. After fully crystallized, the sample was quenched to room temperature and then heated to 171 °C at 10 °C/min heating rate, followed by immediately quenching to 140 °C. Again, after being fully crystallized at 140 °C, the sample was firstly quench to room temperature and then heated to 180 °C at 10 °C/min heating rate.

5.4 CONCLUSIONS

The influence of three types of polymer/MWNT interfaces, namely matrix PP with PP/f-MWNT, MA-g-PP/f-MWNT or p-MWNT, on the crystallization and melting behavior of the PP/MWNT nanocomposites was investigated. Solution based master batches where PP or MA-g-PP was non-covalently coated onto f-MWNTs, and p-MWNTs without polymer coating were used for nanocomposite preparation. The nucleation ability was the highest for p-MWNT containing samples at all MWNT concentration despite their relatively poor dispersion compared with the f-MWNT based nanocomposites. On the other hand, MA-g-PP/f-MWNT containing nanocomposite exhibited the best f-MWNT dispersion. However, the presence of MA-g-PP in vicinity of f-MWNTs limited the

nucleation and growth of PP. As for the PP/f-MWNT based samples, although not being as efficient as the p-MWNT, the f-MWNTs had better dispersion in the matrix. This results in a comparable crystallization rate to the p-MWNT containing sample between 0.1 to 0.3 wt% MWNT concentrations. An increase in T_p after non-isothermal crystallization indicated a higher degree of crystal perfection in the presence of MWNTs in all cases. Within the three types of samples, relatively sharp melt endotherm in the PP/f-MWNT master batch containing sample pointed at a more homogenous crystal distribution which was not the case in p-MWNT based sample due to poor dispersion and in MA-g-PP/f-MWNT based sample due to the presence of less crystallizable MA-g-PP. Among all, nanocomposite comprised 0.3 wt% f-MWNT prepared from PP/f-MWNT master batch showed the optimum increase of crystal perfection (T_p increase by 6.8 °C as compared to the unfilled PP) along with a narrow crystal size distribution as determined by the FWHM of T_c. DSC study at various cooling and heating rates revealed partial and complete suppression of crystal refinement and perfection upon heating in PP/f-MWNT master batch based and p-MWNT based samples, respectively. The suppression can be attributed to the reduced polymer mobility in the vicinity of MWNTs. With the designed heating and cooling profile for polymer self-seeding and templated growth, a special morphology of columnar crystals surrounding f-MWNTs were observed under SEM. The span of this ordered crystalline layer was about 26 nm from the surface of f-MWNT. T_p of such polymer interphase was about 10 °C higher than the polymer that merely underwent isothermal crystallization in the unfilled PP sample. PP/f-MWNT master batch based nanocomposite has the greatest ability to induce this kind of ordered crystalline interphase compared to MA-g-PP/f-MWNT master batch and p-MWNT based ones. The mechanism of its

formation was proposed and supported by increased crystal size and the polarization optical microscopy observation. It is expected that the accelerated crystallization and the highly ordered polymer interphase surrounding f-MWNTs will bring about a synergistic effect on the physical properties of the polymer/CNT composite.

5.5 REFERENCES

1. Valerio Causin, Bing-Xing Yang, Carla Marega, Suat Hong Goh, and Antonio Marigo, *Nucleation, structure and lamellar morphology of isotactic polypropylene filled with polypropylene-grafted multiwalled carbon nanotubes.* European Polymer Journal, 2009. **45**(8): p. 2155-2163.

2. Zhen Zhou, Shifeng Wang, Lan Lu, Yong Zhang, and Yinxi Zhang, *Isothermal crystallization kinetics of polypropylene with silane functionalized multi-walled carbon nanotubes.* Journal of Polymer Science Part B: Polymer Physics, 2007. **45**(13): p. 1616-1624.

3. Pawan Verma and Veena Choudhary, *Polypropylene random copolymer/MWCNT nanocomposites: Isothermal crystallization kinetics, structural, and morphological interpretations.* Journal of Applied Polymer Science, 2015. **132**(13).

4. Songmei Zhao, Fenghua Chen, Yingjuan Huang, Jin-Yong Dong, and Charles C Han, *Crystallization behaviors in the isotactic polypropylene/graphene composites.* Polymer, 2014. **55**(16): p. 4125-4135.

5. Vahid Khoshkava, Hesam Ghasemi, and Musa R Kamal, *Effect of cellulose nanocrystals (CNC) on isothermal crystallization kinetics of polypropylene.* Thermochimica Acta, 2015. **608**: p. 30-39.

6. Manli Zhang, Yiqun Liu, Xiaohong Zhang, Jianming Gao, Fan Huang, Zhihai Song, Genshuan Wei, and Jinliang Qiao, *The effect of elastomeric nano-particles on the mechanical properties and crystallization behavior of polypropylene.* Polymer, 2002. **43**(19): p. 5133-5138.

7. Jisheng Ma, Shimin Zhang, Zongneng Qi, Ge Li, and Youliang Hu, *Crystallization behaviors of polypropylene/montmorillonite nanocomposites.* Journal of applied polymer science, 2002. **83**(9): p. 1978-1985.

8. Chien-Chia Chu, Kevin L White, Peng Liu, Xi Zhang, and Hung-Jue Sue, *Electrical conductivity and thermal stability of polypropylene containing well-dispersed multi-walled carbon nanotubes disentangled with exfoliated nanoplatelets.* Carbon, 2012. **50**(12): p. 4711-4721.

9. Bing-Xing Yang, Jia-Hua Shi, KP Pramoda, and Suat Hong Goh, *Enhancement of the mechanical properties of polypropylene using polypropylene-grafted multiwalled carbon nanotubes.* Composites Science and Technology, 2008. **68**(12): p. 2490-2497.

10. H Deng, E Bilotti, R Zhang, and T Peijs, *Effective reinforcement of carbon nanotubes in polypropylene matrices.* Journal of applied polymer science, 2010. **118**(1): p. 30-41.

11. Anton A Koval'chuk, Alexander N Shchegolikhin, Vitaliy G Shevchenko, Polina M Nedorezova, Alla N Klyamkina, and Alexander M Aladyshev, *Synthesis and properties of polypropylene/multiwall carbon nanotube composites.* Macromolecules, 2008. **41**(9): p. 3149-3156.

12. Parvathalu Kalakonda, Germano S Iannacchione, Michael Daly, Georgi Y Georgiev, Y Cabrera, R Judith, and Peggy Cebe, *Calorimetric study of nanocomposites of multiwalled carbon nanotubes and isotactic polypropylene polymer.* Journal of Applied Polymer Science, 2013. **130**(1): p. 587-594.

13. H. E. Miltner, C. E. Koning, B. Van Mele, N. Grossiord, K. Lu, and J. Loos, *Isotactic polypropylene/carbon nanotube composites prepared by latex technology. Thermal analysis of camon nanotube induced nucleation.* Macromolecules, 2008. **41**(15): p. 5753-5762.

14. Cristhian Garzon, Manfred Wilhelm, Mahdi Abbasi, and Humberto Palza, *Effect of Carbon-Based Particles on the Mechanical Behavior of Isotactic Poly (propylene) s.* Macromolecular Materials and Engineering, 2016.

15. L Valentini, J Biagiotti, MA López-Manchado, S Santucci, and JM Kenny, *Effects of carbon nanotubes on the crystallization behavior of polypropylene.* Polymer Engineering & Science, 2004. **44**(2): p. 303-311.

16. Shihong Chen, Xiangdong Wang, Xiuqing Ma, and Kuisheng Wang, *Morphology and properties of polypropylene/nano-CaCO3 composites prepared by supercritical carbon dioxide-assisted extrusion.* Journal of Materials Science, 2016. **51**(2): p. 708-718.

17. Yongsok Seo, Jinho Kim, Kwang Ung Kim, and Young Chul Kim, *Study of the crystallization behaviors of polypropylene and maleic anhydride grafted polypropylene.* Polymer, 2000. **41**: p. 2639-2646.

18. F. Xia, T. Mueller, Y. M. Lin, A. Valdes-Garcia, and P. Avouris, *Ultrafast graphene photodetector.* Nat Nanotechnol, 2009. **4**(12): p. 839-43.

19. Yuan-Ying Liang, Jia-Zhuang Xu, Xiang-Yang Liu, Gan-Ji Zhong, and Zhong-Ming Li, *Role of surface chemical groups on carbon nanotubes in nucleation for polymer crystallization: Interfacial interaction and steric effect.* Polymer, 2013. **54**(23): p. 6479-6488.

20. Arnaldo T Lorenzo, María Luisa Arnal, Julio Albuerne, and Alejandro J Müller, *DSC isothermal polymer crystallization kinetics measurements and the use of the Avrami equation to fit the data: guidelines to avoid common problems.* Polymer testing, 2007. **26**(2): p. 222-231.

21. Berlic, C., V. Barna, and B. Manolescu. *Invistigation of polymer nucleation process in n-dimensional space*. Digest Journal of Nanomaterials and Biostructures 10.4 (2015): 1365-1371.

22. Jian Li, Chixing Zhou, Gang Wang, Ying Tao, Qing Liu, and Yang Li, *Isothermal and nonisothermal crystallization kinetics of elastomeric polypropylene.* Polymer Testing, 2002. **21**(5): p. 583-589.

23. Brian P Grady, Francisco Pompeo, Robert L Shambaugh, and Daniel E Resasco, *Nucleation of polypropylene crystallization by single-walled carbon nanotubes.* The Journal of Physical Chemistry B, 2002. **106**(23): p. 5852-5858.

24. Mei-Jan Chu and Tzong-Ming Wu, *Isothermal crystallization kinetics of poly (lactic acid)/montmorillonite nanocomposites*, in *Experimental Analysis of Nano and Engineering Materials and Structures*. 2007, Springer. p. 827-828.

25. John D Hoffman and James J Weeks, *Melting process and the equilibrium melting temperature of polychlorotrifluoroethylene.* J Res Natl Bur Stand A, 1962. **66**(1): p. 13-28.

26. Weawkamol Leelapornpisit, Minh-Tan Ton-That, Florence Perrin-Sarazin, Kenneth C Cole, Johanne Denault, and Benoit Simard, *Effect of carbon nanotubes on the crystallization and properties of polypropylene.* Journal of Polymer Science Part B: Polymer Physics, 2005. **43**(18): p. 2445-2453.

27. X Xie, K Aloys, X Zhou, and F Zeng, *Ultrahigh Molecular mass Polyethylene/Carbon Nanotube CompositesCrystallization and melting properties.* Journal of thermal analysis and calorimetry, 2003. **74**(1): p. 317-323.

28. Geon-Woong Lee, Sudhakar Jagannathan, Han Gi Chae, Marilyn L. Minus, and Satish Kumar, *Carbon nanotube dispersion and exfoliation in polypropylene and structure and properties of the resulting composites.* Polymer, 2008. **49**: p. 1831-1840.

29. A. R. Bhattacharyya, T. V. Sreekumar, Liu Tao, S. Kumar, L. A. Ericson, R. H. Hauge, and R. E. Smalley, *Crystallization and orientation studies in polypropylene/single wall carbon nanotube composite.* Polymer, 2003. **44**(8): p. 2373-2377.

30. J Schmidtke, G Strobl, and T Thurn-Albrecht, *A four-state scheme for treating polymer crystallization and melting suggested by calorimetric and small angle X-ray scattering experiments on syndiotactic polypropylene.* Macromolecules, 1997. **30**(19): p. 5804-5821.

31. Gert Strobl, *Crystallization and melting of bulk polymers: new observations, conclusions and a thermodynamic scheme.* Progress in polymer science, 2006. **31**(4): p. 398-442.

32. Pralay Maiti, Masamichi Hikosaka, Koji Yamada, Akihiko Toda, and Fangming Gu, *Lamellar thickening in isotactic polypropylene with high tacticity crystallized at high temperature.* Macromolecules, 2000. **33**(24): p. 9069-9075.

33. Shu-Gui Yang, Zhengchi Zhang, Dong Zhou, Yan Wang, Jun Lei, Liangbin Li, and Zhong-Ming Li, *Flow and Pressure Jointly Induced Ultrahigh Melting Temperature Spherulites with Oriented Thick Lamellae in Isotactic Polypropylene.* Macromolecules, 2015. **48**(16): p. 5834-5844.

34. Koji Yamada, Masamichi Hikosaka, Akihiko Toda, Shinichi Yamazaki, and Katsuharu Tagashira, *Equilibrium melting temperature of isotactic polypropylene with high tacticity: 1. Determination by differential scanning calorimetry.* Macromolecules, 2003. **36**(13): p. 4790-4801.

35. Shanju Zhang, Marilyn L Minus, Lingbo Zhu, Ching-Ping Wong, and Satish Kumar, *Polymer transcrystallinity induced by carbon nanotubes.* Polymer, 2008. **49**(5): p. 1356-1364.

36. John P Abdou, Karina J Reynolds, Michaela R Pfau, Justin van Staden, Gregory A Braggin, Navid Tajaddod, Marilyn Minus, Víctor Reguero, Juan J Vilatela, and Shanju Zhang, *Interfacial Crystallization of Isotactic Polypropylene Surrounding Macroscopic Carbon Nanotube and Graphene Fibers.* Polymer, 2016.

37. Mi Zhou, Shuman Xu, Yuhan Li, Chao He, Tianxiang Jin, Ke Wang, Hua Deng, Qin Zhang, Feng Chen, and Qiang Fu, *Transcrystalline formation and properties of polypropylene on the surface of ramie fiber as induced by shear or dopamine modification.* Polymer, 2014. **55**(13): p. 3045-3053.

38. Kun Na, Han Soo Park, Hong Youn Won, Jong Kwan Lee, Kwang Hee Lee, Joo Young Nam, and Byung Suk Jin, *SALS study on transcrystallization and fiber orientation in glass fiber/polypropylene composites.* Macromolecular Research, 2006. **14**(5): p. 499-503.

39. Chang-Mou Wu, Ming Chen, and József Karger-Kocsis, *Transcrystallization in syndiotactic polypropylene induced by high-modulus carbon fibers.* Polymer Bulletin, 1998. **41**(2): p. 239-245.

40. John P Abdou, Gregory A Braggin, Yanqi Luo, Alexandra R Stevenson, Danielle Chun, and Shanju Zhang, *Graphene-Induced Oriented Interfacial Microstructures in Single Fiber Polymer Composites.* ACS applied materials & interfaces, 2015. **7**(24): p. 13620-13626.

41. Shanju Zhang, Wei Lin, Ching-Ping Wong, David G Bucknall, and Satish Kumar, *Nanocomposites of carbon nanotube fibers prepared by polymer crystallization.* ACS applied materials & interfaces, 2010. **2**(6): p. 1642-1647.

42. Marilyn L Minus, Han Gi Chae, and Satish Kumar, *Interfacial Crystallization in Gel-Spun Poly (Vinyl Alcohol)/Single-Wall Carbon Nanotube Composite Fibers.* Macromolecular Chemistry and Physics, 2009. **210**(21): p. 1799-1808.

CHAPTER 6

RHEOLOGICAL BEHAVIOR OF POLYPROPYLENE NANOCOMPOSITES WITH TAILORED POLYMER INTERPHASE

6.1 INTRODUCTION

In this chapter, the influence of three types of interfaces on the rheological behavior of PP/MWNT nanocomposites has been reported. Through solution processing, PP or MA-g-PP was successfully coated non-covalently onto f-MWNT. The resulting PP/f-MWNT, MA-g-PP/f-MWNT master batches or untreated p-MWNT were melt micro-compounded with PP. In previous chapters (Chapter 3 and Chapter 5), it has been demonstrated that the non-covalently modified MWNTs by PP brought about significant improvement not only in f-MWNT dispersion in PP but also in impact strength (152 % increase in impact strength at 1 wt% CNT loading) and crystal perfection (as demonstrated by 7 °C increase in peak melting temperature at 0.3 wt% MWNT loading). Here, we study the role of non-covalently coated polymer on the rheological properties of PP/f-MWNT nanocomposite melts. The nanotube concentration is between 0.01 wt% to 1 wt% since the main objective is to understand the interaction between MWNT and PP with different interface chemistries.

In general, the incorporation of CNTs renders strong restriction on polymer motion and material becomes more elastic [1-10]. Complex viscosity (η^*) increases and tan δ decreases at low shear rate, as CNT concentration increases. When CNT concentration increases above the rheological percolation threshold, shear thinning can be observed at low shear rate accompanied by a relatively low frequency dependence of the elastic

modulus (G'). Meanwhile, frequency at which tan δ = 1, signifying a liquid-solid transition, moves to a lower value [1-7]. This development of rheological percolation via filler-polymer or filler-filler network was reported to be around 1 to 2 wt% filler concentrations in various PP/CNT studies (Table 6.1) depending on CNT aspect ratio and dispersion state.

Although tailoring the CNT/polymer interphase has become an important subject for developing high performance nanocomposite, few studies have focused on the effect of CNT/PP interface chemistry at the molecular level on melt homogeneity, molecular relaxation, and the origin of enhancement in linear viscoelastic properties. Instead, many studies have focused on the influence of external stimuli such as shear, pressure, temperature, etc. on the rheological behavior of polymer/CNT nanocomposite melt. This includes, shear-induced CNTs structural evolution [11-16], shear-induced crystallization [17-20], time and temperature dependence of percolation threshold [4, 21-23], etc. For example, Wang. et al. found a synergic effect of CNTs and shear flow on PP crystallization [17]. Ke et al. studied the evolution of CNT agglomerate structure and thereby the change of electric conductivity under melt annealing [23].

Table 6.1. Onset of rheological percolations in PP/MWNT literature studies. (continued to the next page)

MWNT dimensions diameter/length	MWNT functionalization	Rheological percolation Threshold[1]	Method	Ref.
6-8 nm/50 μm	N/A[2]	1 wt%	Melt compounding	[1]
9.5 nm/1.5 μm	N/A	2-3 wt%	Melt compounding	[2]
Not specified	N/A	2 wt%[3]	Melt compounding	[3]
30-50 nm/10-20 μm	N/A	2 wt%	Melt compounding	[4]

8-15 nm/10-50 μm	N/A	2 wt%[4]	Melt compounding	[5]
30-50 nm/ not specified	N/A	1.5 to 2 wt%	Melt compounding and melt annealing at 200 °C for 120 min[5]	[6]
8-15 nm/10-50 μm	COOH	1.5 wt%[4]	Melt compounding	[5]
10-20 nm/450 nm	$(COOC_{18}H_{37})_n$	3.8-7.4 wt%	Solution mixing	[7]

[1] Non-terminal behavior at lower frequency ranges indicating by a frequency-independent G'
[2] Pristine MWNT was used
[3] Matrix polymer consisted of PP/MA-g-PP = 97:3
[4] Matrix polymer consisted of PP/MA-g-PP = 9:1
[5] Not percolated if the sample has not experience melt annealing

6.2 EXPERIMENTAL

For the materials, MWNT functionalization and master batch preparation, please refer to Chapter 2.2. For manufacturing the nanocomposites, please refer to Chapter 3.2.

Rheological behavior was measured on ARES rheometer (TA instruments, USA) in the linear viscoelastic regime at a strain of 5 %. Dynamic frequency sweep test was performed at 200 °C in the range of 0.1 to 500 rad/s using parallel-plate geometry (plate diameter 25 mm and the gap between the plates is 1 mm). Shear-induced crystallization for PP and PP/MWNT nanocomposites were measured by using the rheometer according to the following procedure. First, each sample was held at 200 °C for 5 minutes to remove the thermal history, and then the sample was cooled to the shearing temperature, 180 °C, at a cooling rate of 5 °C/min. At 180 °C, pre-shear (300 s^{-1} for 5 s, or 300 s^{-1} for 10 s, or 100 s^{-1} for 10 s) was applied to the sample, followed by quenching to the crystallization temperature of 140 °C at a cooling rate of 10 °C/min. The isothermal crystallization process at 140 °C was monitored by time sweep test with angular frequency of 1 rad/s and a strain

of 0.2 %. Crystallization time was defined when tan δ = 1. Linear viscoelastic properties under melt annealing at 200 °C were evaluated through frequency sweep experiments and the annealing time was 0, 45, 105, and 165 minutes. The parameter used for frequency sweep tests was the same as described above. There was no shearing applied to the samples except for the time during the measurements. Thus, the evolution of viscoelastic behaviors was considered only the effect of time (temperature) instead of the shear.

6.3 RESULTS AND DISCUSSION

6.3.1 Dynamic shear rheological properties

Figure 6.1 shows the dispersion state of MWNT in the three systems, namely, PP/f-MWNT nanocomposites prepared by diluting, 1. PP/f-MWNT master batch (5 wt% f-MWNT), 2. Ma-g-PP/f-MWNT master batch (5 wt% f-MWNT) with PP to the target f-MWNT concentrations via melt mixing, and 3. PP/p-MWNT nanocomposite was prepared through direct melt compounding of p-MWNT with PP. At 0.01 wt% MWNT, the dispersion quality is similar between PP/f-MWNT master batch based sample and the p-MWNT based sample. No apparent large MWNT aggregates was found at this concentration. Above 0.01 wt%, owing to the non-covalently coated polymers in the two master batch based samples, the f-MWNT dispersion in PP/f-MWNT is noticeably better than the PP/p-MWNT nanocomposite. Overall, the MA-g-PP/f-MWNT master batch based samples showed the best MWNT dispersion than the PP/f-MWNT and the p-MWNT based ones. This is not surprising since MA-g-PP is widely used as a compatibilizer for PP composites [24] and blends [25].

Rheology is a powerful tool for probing the molecular level motion and microstructure of the filled polymer systems because the linear viscoelastic response of the

nanocomposites are highly dependent on both the filler dispersion [6, 9, 10] and the interaction between fillers and polymers that altered because of other additives such as compatibilizer or filler-functionalization [15, 22, 26]. Ma et al. [15] reported that the acid treated MWNTs in epoxy resin with good dispersion exhibited lower complex viscosity and G' than that with poor dispersion state sample processed using untreated MWNT. On the other hand, through the incorporation of MA-g-PP (5 to 15 wt%) in PP/MWMT (3 wt% MWNT), Wu et al. [10] had found not only improvements in MWNT dispersion but also a noticeable increase in low-frequency G' and complex viscosity values. While in a similar study, Lee et al [3] observed gradual decrease in G' at low shear rate region when the MA-g-PP concentration increased from 1 to 5 wt%. Since the MWNT dispersion has been characterized to some extent in the three systems in our study (Figure 6.1), it is important to understand from the rheological perspective, how does the matrix PP interact with the non-covalently coated f-MWNTs, and hence the f-MWNT/polymer interphase. However, prior to this discussion, it must be established if the non-covalently coated polymers (PP or MA-g-PP) remains on the f-MWNT surface during the melt mixing with PP, or does this coated polymer gets fully removed from the f-MWNT surface, and dissolved with the rest of the PP matrix.

At 0.01 wt% CNT concentration, the complex viscosity (η^*) and G' in the PP/f-MWNT master batch based sample exhibited two to three times higher G' (in the whole frequency range) than the control PP (Figure 6.2) while there was no noticeable difference in η^* and G' in the case of p-MWNT at the same MWNT concentration (Figure 6.3).

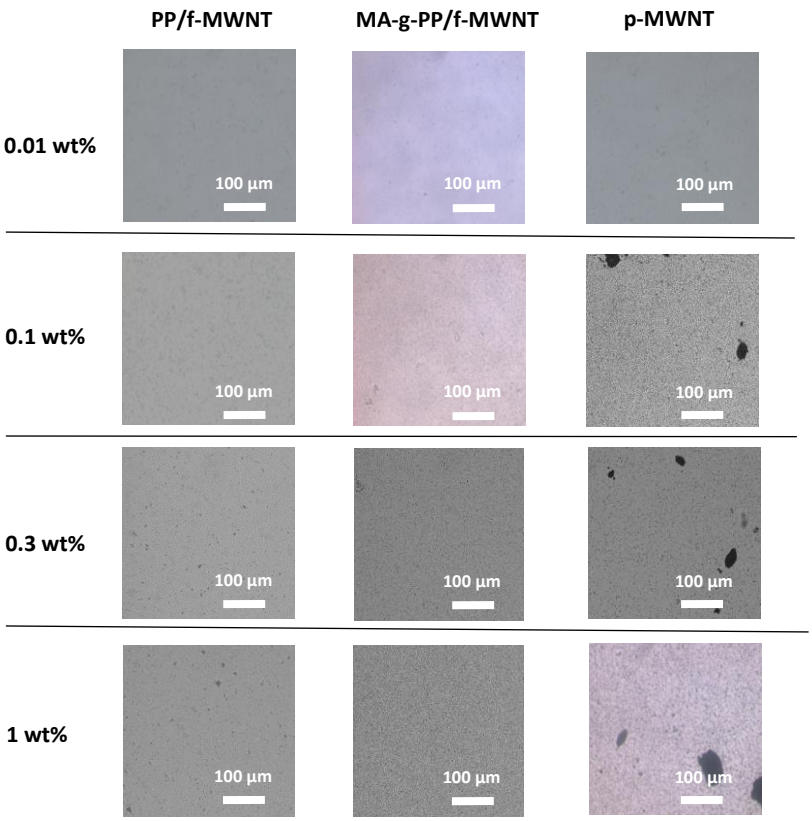

Figure 6.1. Optical micrograph of PP/MWNT nanocomposites at different MWNT concentrations via PP/f-MWNT master batch, MA-g-PP/f-MWNT master batch and p-MWNT.

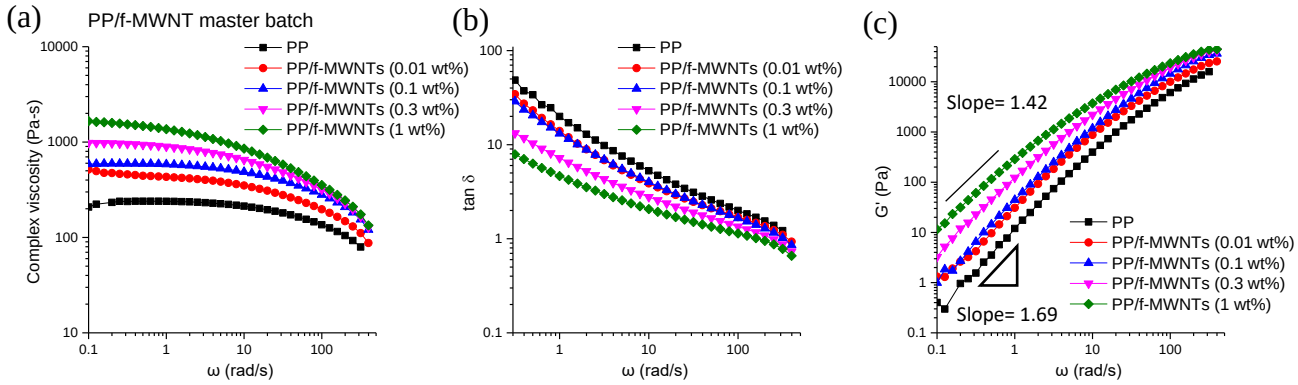

Figure 6.2. Complex viscosity, tan δ and G' as a function of frequency of PP and PP/f-MWNT nanocomposites at different f-MWNT concentrations via PP/f-MWNT master batch.

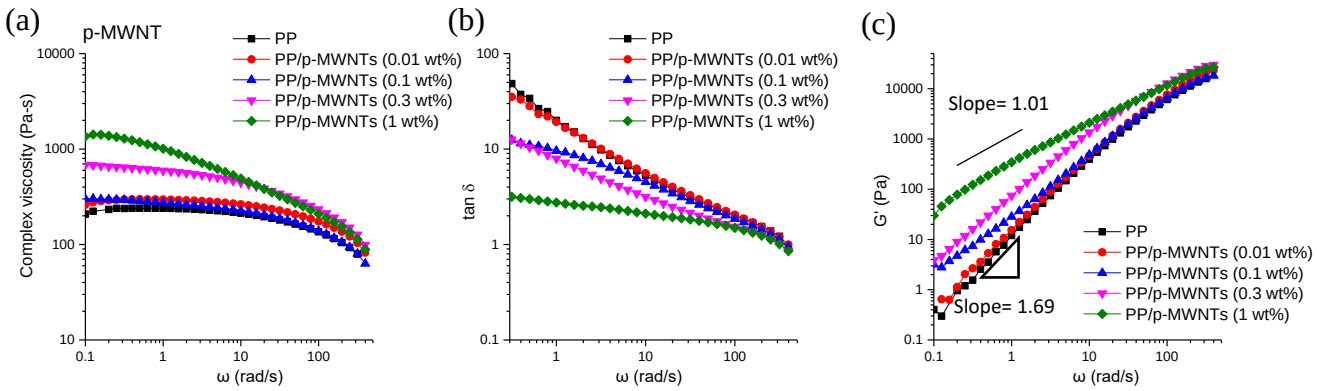

Figure 6.3. Complex viscosity, tan δ and G' as a function of frequency of PP and PP/p-MWNT nanocomposites at different p-MWNT concentrations via p-MWNT.

Since the dispersion quality of the two samples are similar under microscope, the PP-MWNT interaction can be a determining factor in viscoelastic response of the melt. The interfacial adhesion energy (W_a) between two phases can be used to evaluate the wettability of MWNT surface by the PP molecules, and W_a is given by [27]

$$W_a = \gamma_1(1 + cos\,\theta) = 2\sqrt{\gamma_1^d \gamma_2^d} + 2\sqrt{\gamma_1^p \gamma_2^p} \quad (1)$$

where $\boldsymbol{\gamma}$ represents the surface energy of the phase 1($\boldsymbol{\gamma}_1$) and phase 2($\boldsymbol{\gamma}_2$). θ is the contact angle between the two phases. $\boldsymbol{\gamma}^{\mathrm{d}}$ and $\boldsymbol{\gamma}^{\mathrm{p}}$ represent the dispersion and polar part of surface energy, which is 35.2 ± 0.18 and 7.0 ± 0.27 mJ/m^2 for p-MWNT [28], 28.8 ± 0.17 and 13.4 ± 0.24 mJ/m^2 for f-MWNT [28], 30.1 and 0 mJ/m^2 for isotactic PP [29], respectively. The calculated W_a between p-MWNT and iPP is larger (65.1 mJ/m^2) than that between f-MWNT and iPP (58.2 mJ/m^2) which indicates a weaker adsorption of iPP chains on f-MWNT than on p-MWNT due to the reduced dispersion part of surface energy after functionalization. While this calculation seems contradictory to the rheological behavior of the two 0.01 wt% MWNT loaded samples (via PP/f-MWNT master batch and by using

p-MWNT), it is worth noting that the polymers in the master batch have gone through relatively dilute solution processing, and thereby contains fewer entanglements than the PP in molten state. This enables the formation of a longer and stronger interphase between f-MWNT and solution processed PP than between p-MWNT and PP without solution processing. If that is the case, the non-covalently modified PP/f-MWNT interphase can exhibit higher W_a than PP/p-MWNT. As a consequence, it is likely that the solution processed PP, interact non-covalently with f-MWNT via CH-π interaction (Chapter 2), remains on the f-MWNT surface during melt processing.

These non-covalently coated polymers on f-MWNT also contributed to the distinct behavior of PP/f-MWNT interphase from that of the PP/p-MWNT interphase at high shear rate region in the frequency sweep tests (Figure 6.2 and Figure 6.3). At high shear rates, MWNTs tend to align along the shear direction and the short range dynamic motion of the polymer chains, which is normally independent of filler concentration [1, 4, 8, 10, 30], was investigated. This means G' and the tan δ of the neat PP and nanocomposites will come to a similar value as frequency increases. In PP/p-MWNT, the G' and tan δ behaviors were consistent with this trend (Figure 6.3b and c). However, in the PP/f-MWNT based nanocomposites, a clear deviation of G' and tan δ from the control PP at high shear rate was discovered. Such deviation justifies the presence of immobile PP interphase and it became more prominent with increasing f-MWNT concentration (Figure 6.2b and c).

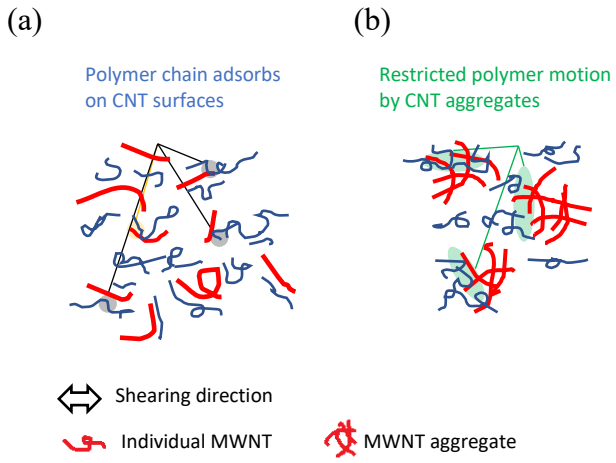

Figure 6.4. Resistance of polymer chain movement along the shearing direction due to (a) polymer-filler interaction and (b) physical blocking by MWNT aggregates. Both (a) and (b) contribute to the increase of melt viscosity.

At the low shear rate region, where the long range motion of polymer chains was impeded in the presence of CNTs, η^* of both PP/f-MWNT master batch and the p-MWNT based samples at 1 wt% MWNT loading increased by about one order of magnitude compared with that of the neat PP. However, the origin of this η^* and G' increase might be different between the two: one mechanism is referring to the filler-polymer interaction where the polymer chain segments adsorb on filler surfaces can be regarded as trapped entanglements between the bulk polymer and the filler [31] (Figure 6.4a). Another mechanism is the hydrodynamic effect which is related to the occupied space of the rigid filler particles [32]. The long range motion of polymer chains can also be restricted by the filler aggregates, making the viscosity higher than the unfilled polymer (Figure 6.4b). Based on the presence of PP/f-MWNT interphase as discussed previously and the optical images showing larger MWNT aggregations in PP/p-MWNT (Figure 6.1), the filler-polymer interaction mechanism might be the major contribution to the η^* and G' increase in the PP/f-MWNT master batch based nanocomposites, while the hydrodynamic effect is dominant in PP/p-MWNT.

Although the viscoelastic responses are similar between PP/f-MWNT and PP/p-MWNT at 1 wt% MWNT, on the perspective of η^* and G' in the terminal region, later we will show that the difference in melt homogeneity, which can be obtained from the slope of G' to G" log-log plot, reflected the difference in microstructure and MWNT dispersion quality in the two samples which ultimately result in very distinct mechanical property.

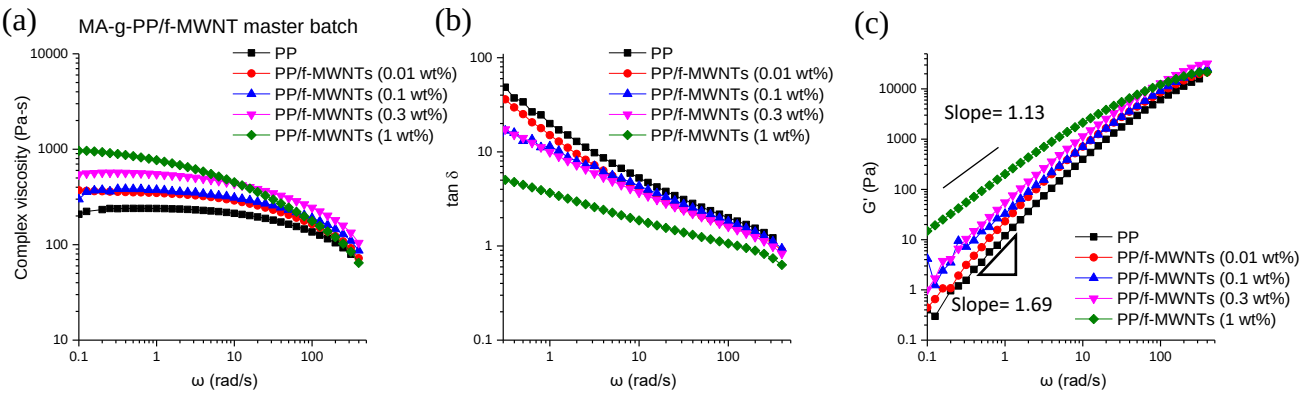

Figure 6.5. Complex viscosity, tan δ and G' as a function of frequency of PP and PP/f-MWNT nanocomposites at different f-MWNT concentrations via MA-g-PP/f-MWNT master batch.

The f-MWNT dispersion in the PP/f-MWNT nanocomposites became markedly better when the f-MWNTs were coated with MA-g-PP instead of PP (Figure 6.1). At 1 wt% f-MWNT, G' in the low shear rate region became less frequency dependents (slope change from 1.69 in neat PP to 1.13) (Figure 6.5). Also, G' in the MA-g-PP master batch based sample presented an abrupt increase from 0.3 wt% to 1 wt%, apart from a gradual change in PP/p-MWNT as p-MWNT concentration increased. This signifies an onset of rheological percolation network formation in the MA-g-PP/f-MWNT master batch based sample. The same slope in the PP/f-MWNT master batch based nanocomposite at 1 wt% was about 1.42 (Figure 6.2) showing fewer network forming. This is consistent with some literature findings which observed a lowering of rheological percolation threshold as CNT

dispersity increases [6, 30]. At high shear rate, η^* in the 1 wt% nanocomposite became lower than for the neat PP, implying a stronger shear thinning behavior in the presence of both MA-g-PP and f-MWNT. Better MWNT dispersion and lower molecular weight of MA-g-PP can both result in better polymer orientation and therefore lower viscosity.

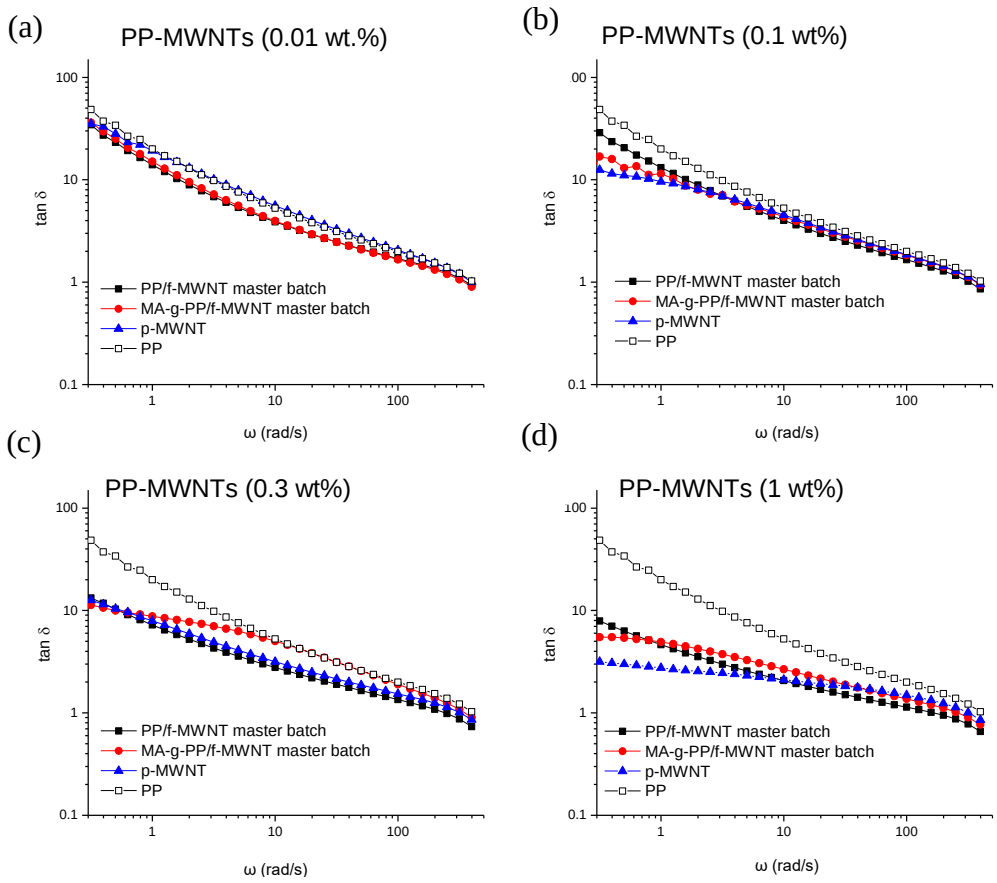

Figure 6.6. Tan δ behavior as a function of frequency of PP and PP/MWNT nanocomposites at different MWNT concentrations via PP/f-MWNT master batch, MA-g-PP/f-MWNT master batch and p-MWNT.

The loss modulus (G") and storage modulus (G') crossover as measured on an oscillatory rheometer has become useful for estimating melt strength (also referred as melt elasticity). The tan δ behavior of the three systems at different MWNT concentration was

given in Figure 6.6. As the MWNT concentration increased, all the nanocomposite samples showed an increased melt strength and reduced tan δ as compared with the neat PP despite the origin of this increase is different between the three systems, i.e. through filler-polymer interaction in the master batch based samples and through hydrodynamic effect in the p-MWNT filled samples. Typically, PP exhibits low melt strength because of it is a linear polymer, as compared with branched polymers. Excellent melt strength is particularly important for applications such as foaming, blow molding, thermoforming, etc [33]. However, the negative aspect of increased melt strength in polymer processing would be the occurrence of die swell and higher screw torque required for extrusion. The melt pressure records after three minutes of micro-compounding is given in Figure 6.7. Higher melt pressure requires higher screw torque for compounding. The PP/p-MWNT nanocomposites showed continuous increase in melt pressure with increase in p-MWNT concentration. This suggests increased difficulty in processing PP/p-MWNT at higher p-MWNT concentrations. On the other hand, in the two master batch based samples, the melt pressure first increased and then decreased to a level that was even lower than that observed for the neat PP above 0.5 wt% f-MWNT concentrations. This is attributed to the increased loading of solution processed polymers (PP or MA-g-PP) and to the presence of well dispersed f-MWNTs. Under continuous steady shear, it is easier to deform a fluid packet with less entangled polymer chains and aligned f-MWNTs along the flow direction, than one with a rigid and undispersed phase. While all three systems exhibited increased melt strength in the frequency sweep tests (Figure 6.6), the reason that only PP/p-MWNT system exhibited difficulty in processing can be explained as followed. In the frequency sweep test, an oscillating constant strain of 5 % was applied. The polymer chains responded within

the linear viscoelastic region. While in the micro-compounding, a continuous steady shear was applied in which the material deformed and "elongated" along the shear direction. The impeded polymer segments on MWNTs and the chain entanglements, which is responsible for the elastic behaviors, did not get disengaged or disentangled under small deformation during frequency sweep measurement. However, in the presence of continuous and steady shear, the interaction between polymers and MWNTs became lesser if both of them were stretched and aligned. This happened in the master batch based samples due to good f-MWNT dispersion and resulted in a lesser resistance of the flow (lower melt pressure) during compounding.

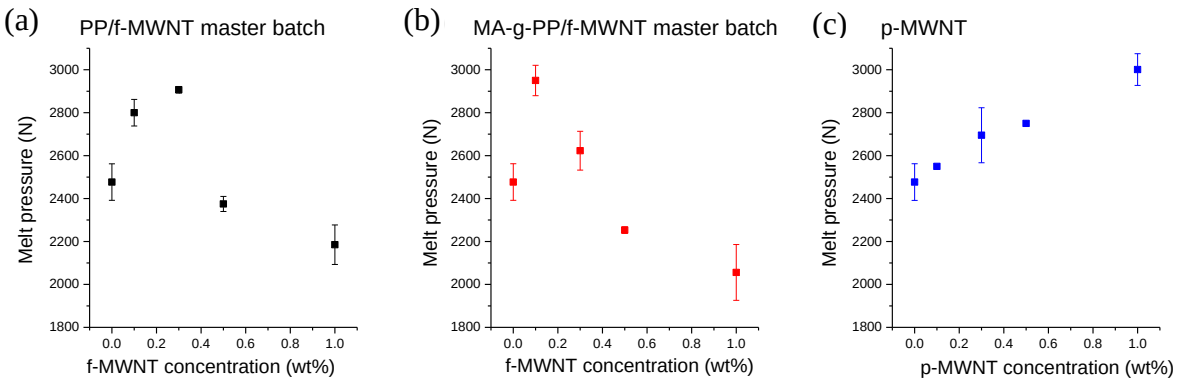

Figure 6.7. Melt pressure (N) after three minutes micro-compounding of PP and PP/MWNT nanocomposites at different MWNT concentrations via (a) PP/f-MWNT master batch, (b) MA-g-PP/f-MWNT master batch and (c) p-MWNT.

From Figure 6.7, it is evident that the polymer chains and f-WMNTs can be aligned along the shear direction and the presence of solution processed polymers which potentially contained fewer entanglements than the neat PP brought about lower melt pressure at high f-MWNT loadings. The effect of such polymer chain alignment during processing on the polymer orientation in the injection molded bars was shown in Figure 6.8a. The PP orientation was quantified by the full width half maximum of the PP (040) peak in the

WAXD azimuthal scan in our previous work [34]. In Figure 6.8a, the incorporation of MWNT resulted in lower (040) FWHM (i.e. higher PP orientation) than the neat PP in all three systems.

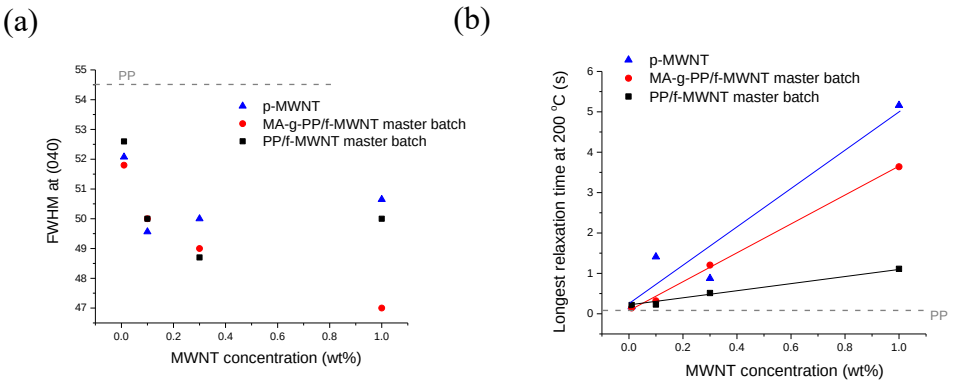

Figure 6.8. (a) FWHM at (040) representing polymer orientation and (b) longest relaxation time of PP and PP/MWNT nanocomposites at different MWNT concentrations via PP/f-MWNT master batch, MA-g-PP/f-MWNT master batch and p-MWNT.

It has been widely accepted that polymer chain segments are able to become locally aligned on the CNT surface followed by a templated crystal growth under shear [18, 20, 35-38]. Also, the restriction of polymer segmental motion imposed by the filler-polymer interaction prevents fast relaxation of the oriented polymer chains, once the shear has been removed [39, 40]. There are various experimental approaches for obtaining relaxation spectrum of the polymer chain [39, 41-43]. Highly entangled systems are characterized by a set of relaxation at longer times which are isolated from the more rapid process. The longest relaxation time, also referred to as the weight average relaxation time (τ_w), appears as a cutoff in the spectrum and characterizes the long-time behavior of the macromolecules in the terminal region [42, 44].

$$\tau_w = \eta_0 J_e^0 \quad (2)$$

where η_0 is the zero shear viscosity and J_e^0 is the plateau shear compliance. The experimentally determined longest relaxation time at 200 °C versus MWNT concentration in three different samples is given in Figure 6.8b. In all the three systems, the longest relaxation time increased with increasing MWNT concentration. The p-MWNT based nanocomposites showed a largest increase followed by MA-g-PP/f-MWNT and then PP/f-MWNT master batch based nanocomposites. On the other hand, polymer has highest orientation in the MA-g-PP/f-MWNT based samples at 1 wt% f-MWNT loading that exhibited a continuous drop of (040) FWHM as f-MWNT concentration increased (Figure 6.8a). In the PP/f-MWNT master batch and p-MWNT based nanocomposites, PP orientation first increased and then decreased above 0.3 wt% and 0.1 wt%, respectively. As MWNT concentration increases, poor MWNT dispersion and strong filler-polymer interaction acted as a counter force for chain alignment. This is, however, less predominate in the MA-g-PP/f-MWNT based nanocomposite due to better f-MWNT dispersion and lower molecular weight MA-g-PP.

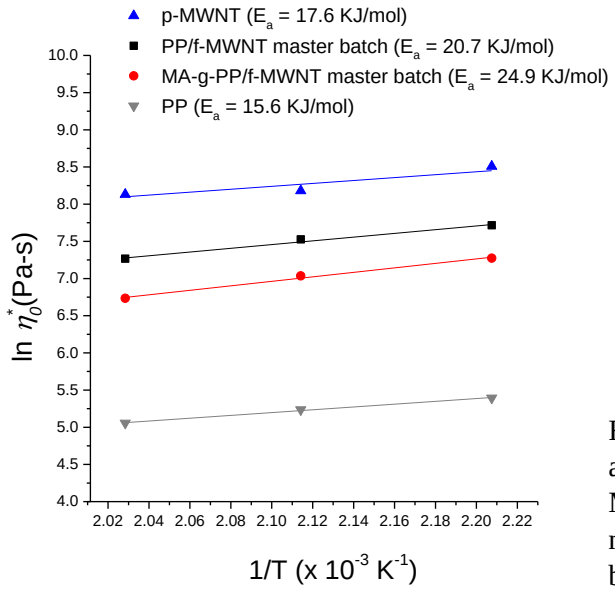

Figure 6.9. Activation energy (E_a) of PP and PP/MWNT nanocomposites at 1 wt% MWNT concentration via PP/f-MWNT master batch, MA-g-PP/f-MWNT master batch and p-MWNT.

The activation energy (E_a) of PP and PP/MWNT at 1 wt% MWNT is given in Figure 6.9. Higher activation energies of the melt in the nanocomposites than the neat PP supports the observed higher relaxation time in PP/MWNT because of the restricted polymer segmental motions. Interestingly, despite the highest relaxation time between the three systems, PP/p-MWNT has only slightly higher E_a than the neat PP (17.6 KJ/mol vs. 15.6 KJ/mol). This might be due to a broadened relaxation spectrum in PP/MWNT while the longest relaxation time captures only the slowest mode, which is, in the case of PP/p-MWNT, the trapped polymer chains in proximity to p-MWNT aggregates. The matrix polymers in PP/p-MWNT exhibited a similar relaxation behavior to the neat PP that dominated over the slow modes because of relatively fewer PP-CNT interfaces (poorer MWNT dispersion) as compared with the two master batch based samples.

In the case of homopolymer melt, the slope of G' versus G'' log-log plot decreases from its theoretical value of 2 as the level of heterogeneity within the melt increases. i.e. in the presence of entanglements, voids, and another polymer phase or fillers [41, 45]. The polymer melt inhomogeneity can increase due to the presence of molecular weight distribution, entanglements, voids, and due to the presence of fillers. The slope of G' versus G" log-log plot represents microscopic homogeneity of the melt through averaging over fast and slow relaxation modes. In Table 6.2, this slope is shown to be 1.6 in neat PP at 200 °C. The deviation from 2 might due to a distribution of molecular weight in the commercial polymers. Overall, the melt homogeneity decreased as MWNT concentration increased in all three systems. The PP/f-MWNT master batch based samples showed the highest melt homogeneity compared with the other two types of nanocomposites. The presence of MA-g-PP, though potentially reduced polymer entanglements because of the shorter MA-g-PP

chains, introduced incompatibility to the PP/MA-g-PP blend [46]. The slopes also reduced significantly in PP/p-MWNT especially at high p-MWNT loadings due to the presence of large p-MWNT aggregates. Such inhomogeneity in the melt can be preserved during processing steps (extrusion, molding, and fiber spinning, etc.) and be considered as defects in the structure. Thus, the mechanical properties of the tensile specimens may be affected by, but not limited to, the presence of inhomogeneity in the polymer melt. Literature has shown a markedly reduction of ductility (elongation at break) in PP/CNT nanocomposites due to either poor PP-CNT interaction or poor CNT dispersion [34, 47, 48]. Figure 6.10 correlated the slope of G' versus G'' log-log plot to elongation at break of the tensile specimen. Consistent with the observation of melt homogeneity, the PP/f-MWNT master batch based samples had best ductility among all three types of samples. Also, it seems like the samples became brittle when the slope fell below a certain level (about 1.45), Figure 6.10.

Table 6.2. Slope of G' to G" log-log plot at 200 °C in PP and PP/MWNT nanocomposites at different MWNT concentrations via PP/f-MWNT master batch, MA-g-PP/f-MWNT master batch and p-MWNT.

	0 wt%	0.01 wt%	0.1 wt%	0.3 wt%	1 wt%
PP/f-MWNT nanocomposite via PP/f-MWNT master batch	1.6	1.61	1.59	1.53	1.48
PP/f-MWNT nanocomposite via MA-g-PP/f-MWNT master batch	1.6	1.62	1.47	1.37	1.38
PP/p-MWNT nanocomposite	1.6	1.56	1.41	1.44	1.27

Table 6.3. Slope of G' to G" log-log plot at various temperature in PP and PP/MWNT nanocomposites at 1 wt% MWNT via PP/f-MWNT master batch, MA-g-PP/f-MWNT master batch and p-MWNT.

	180 °C	200 °C	220 °C
PP	1.62	1.6	1.62
PP/f-MWNT nanocomposite via PP/f-MWNT master batch	1.48	1.48	1.47
PP/f-MWNT nanocomposite via MA-g-PP/f-MWNT master batch	1.45	1.38	1.35
PP/p-MWNT nanocomposite	1.35	1.27	1.27

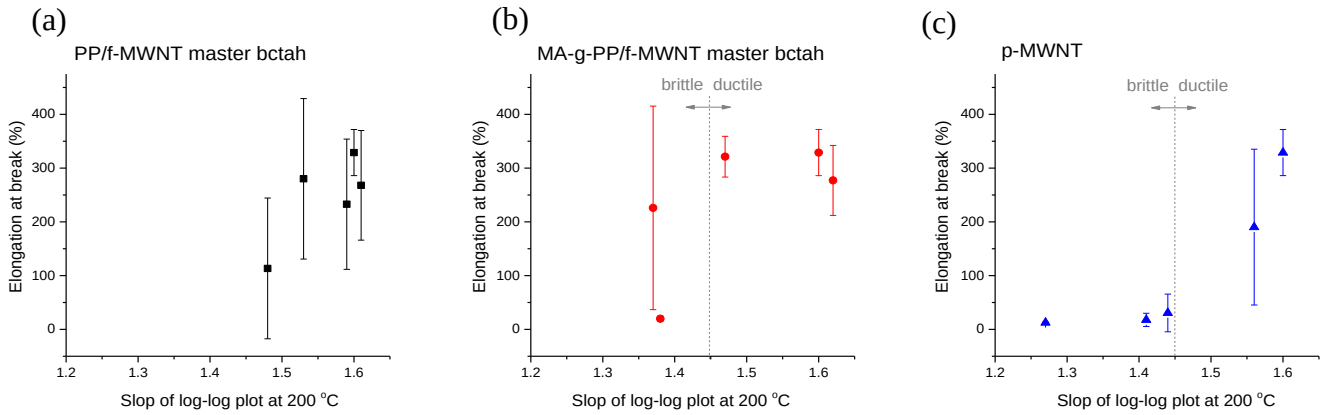

Figure 6.10. Elongation to break versus slope of G' to G" log-log plot of PP/MWNT nanocomposites at 1 wt% MWNT via (a) PP/f-MWNT master batch, (b) MA-g-PP/f-MWNT master batch, and (c) p-MWNT.

In Table 6.3, the slope of G' versus G'' log-log plot was given when the measurements were done at 180 °C, 200 °C, and 220 °C. There was no noticeable temperature dependent of the slope in PP and PP/f-MWNT master batch based samples. On the other hand, slightly lower melt homogeneity above 180 °C in p-MWNT and MA-g-PP/f-MWNT can result from accelerated phase separation due to higher polymer mobility.

6.3.2 Shear-induced crystallization (SIC)

Based on the previous discussion, we have seen shear aligning of polymer chains in the presence of MWNT during micro-compounding (Figure 6.7) and the preservation of such polymer orientation in the injection molded bar due to impeded chain motions by MWNT (Figure 6.8). Both phenomena are more prominent in the two master batch based systems compared with PP/p-MWNT. To further justify this difference and to understand how is the non-covalently coated polymer interphase interacted with the matrix PP, both under shear and in the quiescent state, two experiments (shear-induced crystallization and melt annealing) were conducted and discussed as follows.

Many authors have proposed that shear-induced crystallization (SIC) results from the effect of applied pre-shear on aligning and stretching polymer chains in the melt, which formed a thread-like structure (or row-nuclei) and hence accelerate the crystallization upon quenching to the crystallization temperature [17, 18, 49, 50]. The selection of shearing temperature, crystallization temperature, viscosity of the melt (η), shear rate ($\dot{\gamma}$) and time (t), and applied specific work (W), defined as

$$\mathrm{W} = \eta\dot{\gamma}^2 t \tag{3}$$

governs the shear-induced crystallization rate. While the synergistic effect of CNTs and shear flow on the crystallization rate has been reported [17, 18], the shearing temperature used in these two works were relatively low (about 145 °C) compared to the peak melting temperature of PP (about 160 °C) which may not be practical in the real-world practice.

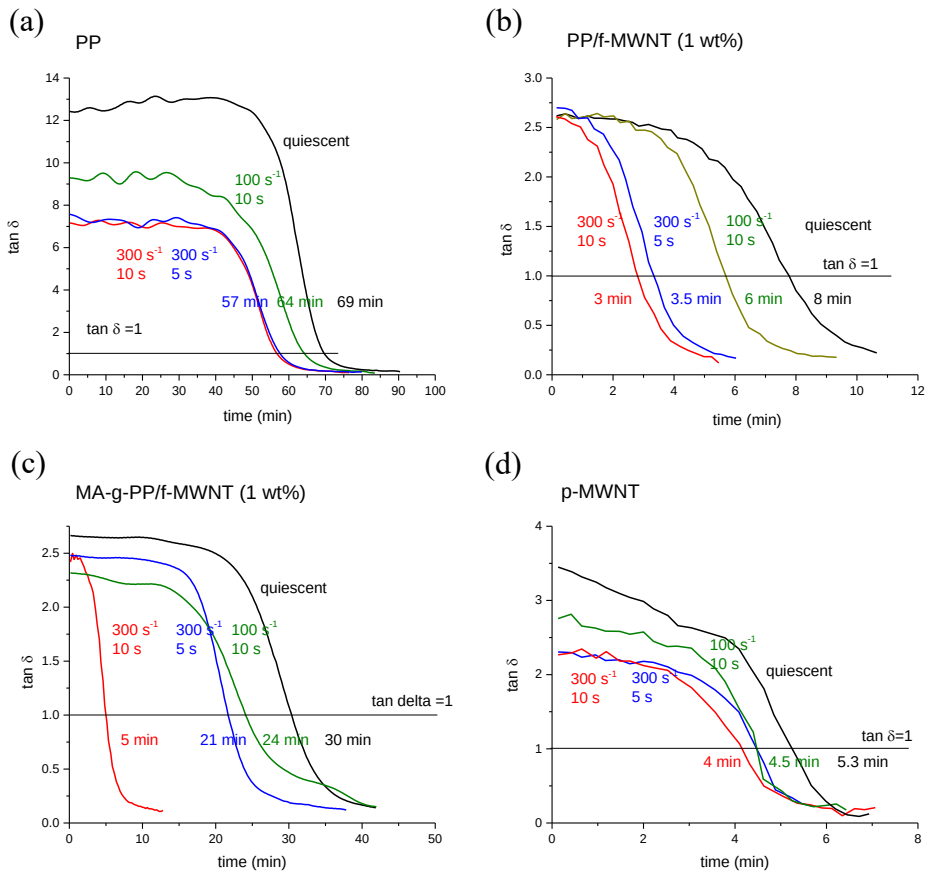

Figure 6.11. Shear-induced crystallization of (a) PP and PP/MWNT nanocomposites at 1 wt% MWNT concentration via (b) PP/f-MWNT master batch, (c) MA-g-PP/f-MWNT master batch and (d) p-MWNT. The pre-shear was applied at 180 °C while the crystallization took placed at 140 °C.

In the current study, pre-shear was applied at 180 °C and the effect of the non-covalent coated polymers on shear-induced crystallization is shown in Figure 6.11. Under quiescent crystallization (no applied pre-shear), the crystallization rate was the fastest in p-MWNT (5.3 min), followed by PP/f-MWNT master batch (8 min) and MA-g-PP/f-MWNT master batch (30 min) based nanocomposites (1 wt% MWNT), and then followed by neat PP (69 min). At 1 wt% MWNT, p-MWNT was found to be a more effective nucleation agent then f-MWNT due to the presence of the functional group in the latter [51]. However, under the effect of pre-shear applied at 180 °C, both master batch

based samples exhibited noticeable change of crystallization time while there was nearly no change in the case of neat PP and PP/p-MWNT (Figure 6.11). As a result, crystallization time of PP/f-MWNT and MA-g-PP/f-MWNT master batch based sample became comparable and even lower than that of PP/p-MWNT. It is worth noting that the amplitude of applied shear (100 or 300 s^{-1}) in this experiment was similar to the shear during conventional polymer processing.

Although it is not surprising that the master batch based samples showed stronger shear-induced crystallization than the p-MWNT based sample duo to better MWNT dispersion and more aligned polymer chains, the reason for the appearance of SIC even at 180 °C pre-shear is needed to be explained. Hypothetically, the initial molecular chain orientation induced by pre-shear can be stabilized at the f-MWNT surfaces for a long enough time before reaching crystallization temperature. In Fig. 12, a consecutive frequency sweep test at 180 °C was performed to verify this hypothesis. The pre-shear was applied prior to the third sweep, and it took about 15 minute to finish each sweep. In all samples, the curve of first and second sweep overlapped with each other indicating there was no structural change (change of CNT dispersion, CNT network formation, disentanglement of polymer chains) during and after the frequency sweep test. After the pre-shear (300 s^{-1} for 10 seconds) was applied to the sample, reduced complex viscosity was observed in all samples which was more significant in neat PP and MA-g-PP/f-MWNT based nanocomposite than the PP/f-MWNT and p-MWNT based ones. Stronger shear thinning in the presence of both MA-g-PP and f-MWNT has been shown previously in Figure 6.5. After the third sweep, which took about 15 minutes, the fourth sweep revealed whether the disentangled and oriented molecular chains by pre-shear were completely

relaxed or not. In Figure 6.12, the fourth sweep in the MA-g-PP/f-MWNT master batch based sample was the only one that had a viscosity curve close to the third sweep indicating partial relaxation of the aligned molecules. The neat PP and the PP/f-MWNT master batch based nanocomposite had a fourth curve close to the first/second curve while in the PP/p-MWNT, the fourth curve was nearly overlapped with the first/second curve showing the majority of aligned molecule had relaxed back to the condition before applying the pre-shear. This is consistent with the difference in the rate of SIC between the three types of PP/MWNT nanocomposites and confirmed our hypothesis that part of the shear aligned

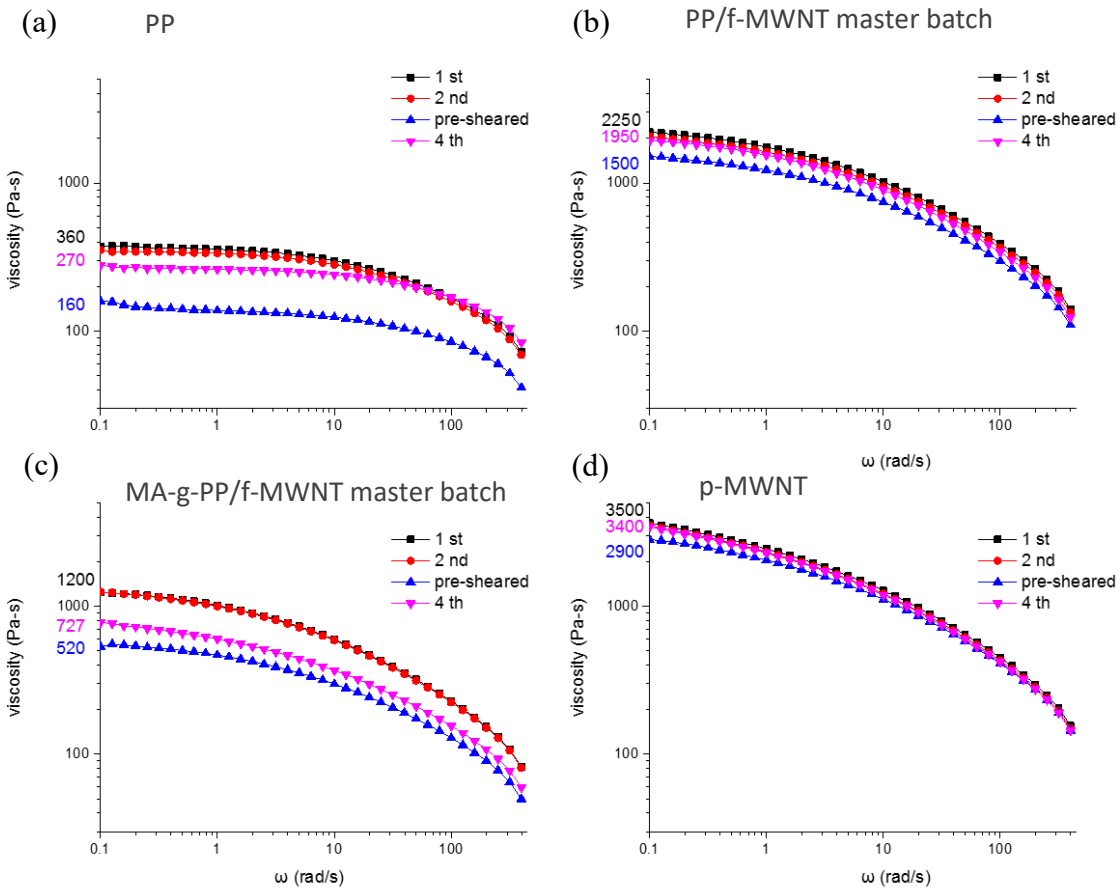

Figure 6.12. Consecutive frequency sweep tests of (a) PP and PP/MWNT nanocomposites at 1 wt% MWNT concentration via (b) PP/f-MWNT master batch, (c) MA-g-PP/f-MWNT master batch and (d) p-MWNT at 180 °C. Pre-shear (300 s^{-1}, 10s) was applied before the 3rd sweep.

polymer chains, predominantly those near the interphase, preserved their orientation upon quenching to the crystallization temperature and served as extra row-nuclei or a template for heterogeneous crystallization. When the shearing temperature increased to 200 °C, there was no observed SIC in the MA-g-PP/f-MWNT based nanocomposites (Figure 6.13). This may due to insufficient work (*W*) in aligning molecule as a result of the decreased viscosity at 200 °C and the loss of shearing memory during quenching from 200 °C to 140 °C.

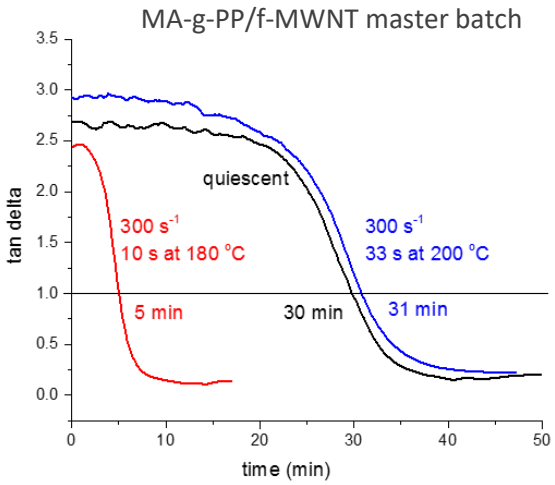

Figure 6. 13. Shear induced crystallization of PP/f-MWNT nanocomposites at 1 wt% f-MWNT concentration via MA-g-PP/f-MWNT master batch. The pre-shear was applied at 180 °C or 200 °C while the crystallization was taking placed at 140 °C.

6.3.2 Effect of melt annealing on the rheological behavior

The second experiment (melt annealing) revealed the effect of polymer interphase on the viscoelastic behavior of nanocomposite in the quiescent state. The frequency dependence of G' and G" for PP and PP/MWNT (1 wt% MWNT) before and after annealing at 200 °C is given in Figure 6.14. The neat PP G' and G" overlapped before and after annealing, and for PP/p-MWNT G' increased slightly at low frequency after annealing. In the two master batch based samples, G' increased by one to two orders of magnitude at low frequency after annealing, and also exhibited a distinct plateau in this low frequency

region. This appears to be solid-like viscoelastic behavior. More pronounced increase of G' in the PP/f-MWNT master batch case rather than in MA-g-PP/f-MWNT case (Figure 6.14) suggests deviation from terminal behavior ($G' \sim \omega^2$), and should be attributed to the formation of filler-polymer network, rather than filler-filler network. More specifically, if this is due to CNT-CNT networks, the effect should be stronger in the MA-g-PP/f-MWNT based sample since better f-MWNT dispersion facilitates the filler network formation [6].

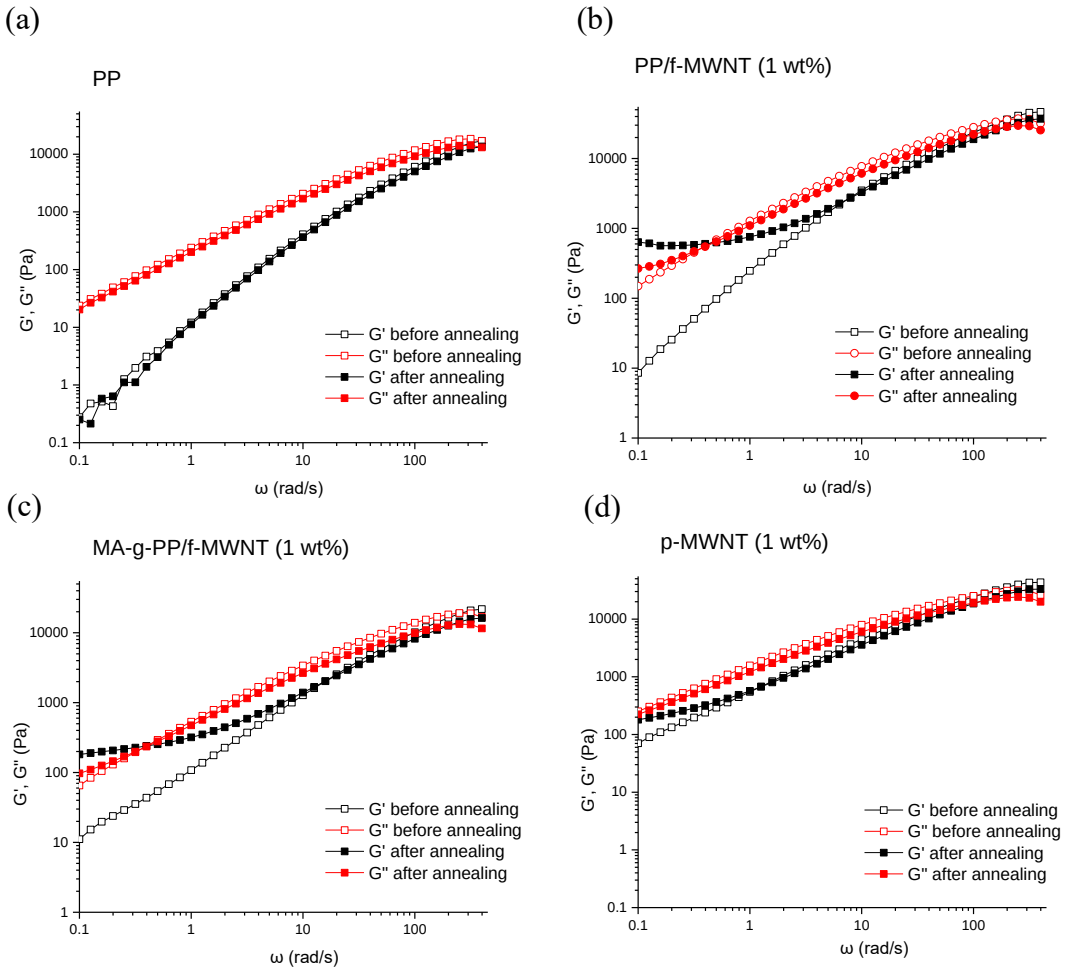

Figure 6.14. G' and G" before and after annealing at 200 °C for 165 minutes of (a) PP and PP/MWNT nanocomposites at 1 wt% MWNT concentration via (b) PP/f-MWNT master batch, (c) MA-g-PP/f-MWNT master batch and (d) p-MWNT.

In the nanocomposite melt, the effect of annealing at or above the melting temperature of the polymer on the filler dispersion state has been studied in many polymer/CNT systems [6, 8, 21, 23, 52]. Some of these studied the effect of melt annealing with oscillating shear [6, 8, 23] and some were not [21, 52]. While most of the works attributed the improvement of physical properties such as electrical conductivity and melt elasticity to the filler-filler network formation which requires relatively high CNT concentration, typically above 3 wt%, few have observed similar effect through polymer-filler interaction at lower CNT concentration, such as 1 wt% observed in the current study. As f-MWNT concentration decreased from 1 wt% to 0.1 wt%, the change of G' before and after annealing at 200 °C in the PP/f-MWNT based nanocomposite became less pronounced (Figure 6.15a).

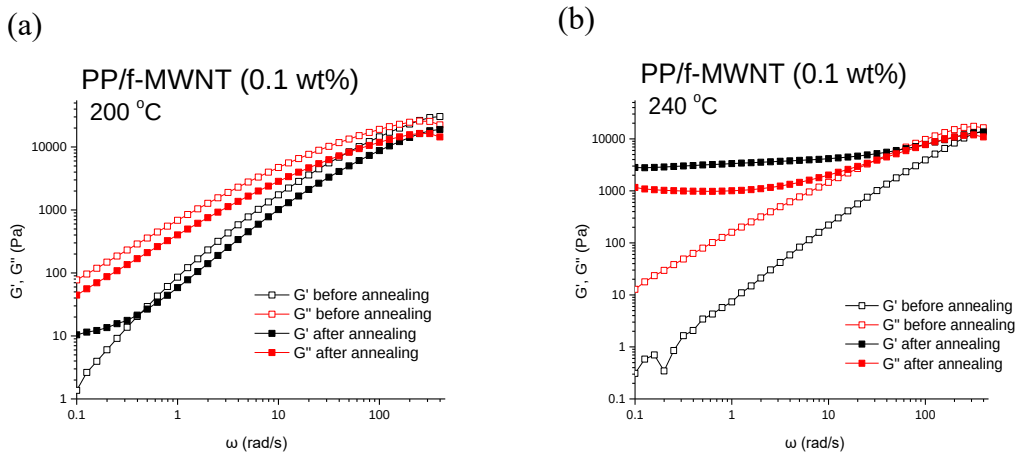

Figure 6.15. G' and G" before and after melt annealing for 165 minutes of PP/f-MWNT nanocomposites via PP/f-MWNT master batch at 0.1 wt% f-MWNT (a) under 200 °C, and (b) under 240 °C.

However, a dramatic increase in both G' and G" was observed after annealing at 240 °C even at 0.1 wt% f-MWNT (Figure 6.15b), which is below the percolation threshold for MWNTs used in this work (Table 6.1). This reconfirmed the observation of G'(G") jump during annealing was due to the polymer-filler network interaction, as opposed to the formation of a percolated MWNT network. Increased polymer-filler interaction has been also reported in other polymer composite systems. For example, Pötschke et al. found that rheological percolation threshold decreased from 5 to 0.5 wt% MWNT when the temperature increase from 170 to 280 °C in polycarbonate/MWNT [21]. Similarly, Fernandez et al. reported increased phenoxy chain mobility obstruction by organoclay because of a higher chain mobility as temperature increased [22]. As shown in Figure 6.13 and Figure 6.15a, G" and its frequency dependence do not change as significantly as G' upon annealing at 200 °C. This might due to the fact that G' is more sensitive to the solid-like network structure than G" at low frequencies [32].

Evolution of G' as a function of annealing time at 200 °C in PP and PP/MWNT is summarized in Figure 6.16 A proposed schematic suggested a formation of space-spanning network of PP and f-MWNTs which is connected by trapped/adsorbed chain segments near f-MWNT surface and the overlapped chain entanglements in the matrix. Better f-MWNT dispersion in the master batch based samples rendered more interaction between matrix polymers and f-MNWTs, where the non-covalently coated PP exhibited a stronger interaction than MA-g-PP owing to its higher molecular weight (longer chain). This schematic of polymer-filler network can be justified based on the following observations. First, the effect was stronger at an elevated temperature (Figure 6.15 and Figure 6.17). As the temperature increased, the polymer mobility increased accordingly and thereby the

chance for interacting with each other and with f-MWNTs was also increased. Second, there was no apparent change in the f-MWNT dispersion state before and after annealing under optical microscope (Figure 6.18). Thus, the contribution from filler-filler interaction can be ruled out. Third, the crystallization rate of the nanocomposite became lower after melt annealing (Figure 6.19). Similar observation in reduced crystallization rate was attributed to the depression of PP diffusion toward the crystal front due to an interpenetrating network formation [53]. The change of viscosity and tan δ over annealing time at 200 °C also showed an increase solid-like behavior at 0.1 rad/s in the master batch based sample as G' did (Figure 6.20-6.23).

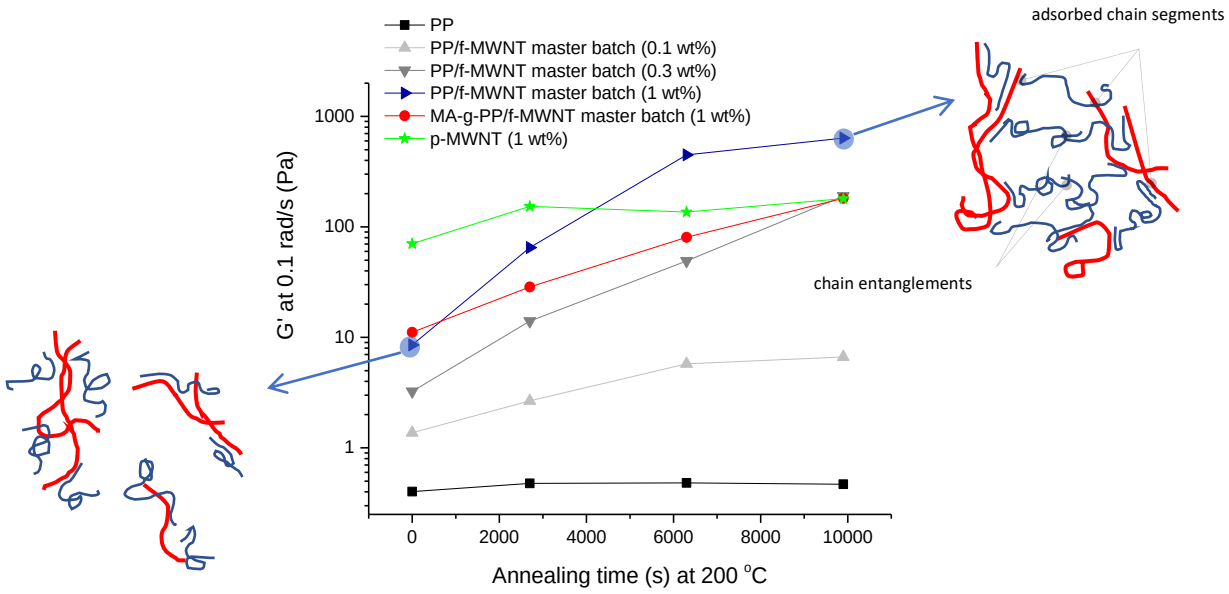

Figure 6.16. Change of G' during annealing at 200 °C in PP and PP/MWNT nanocomposites different MWNT concentrations via PP/f-MWNT master batch, MA-g-PP/f-MWNT master batch and p-MWNT.

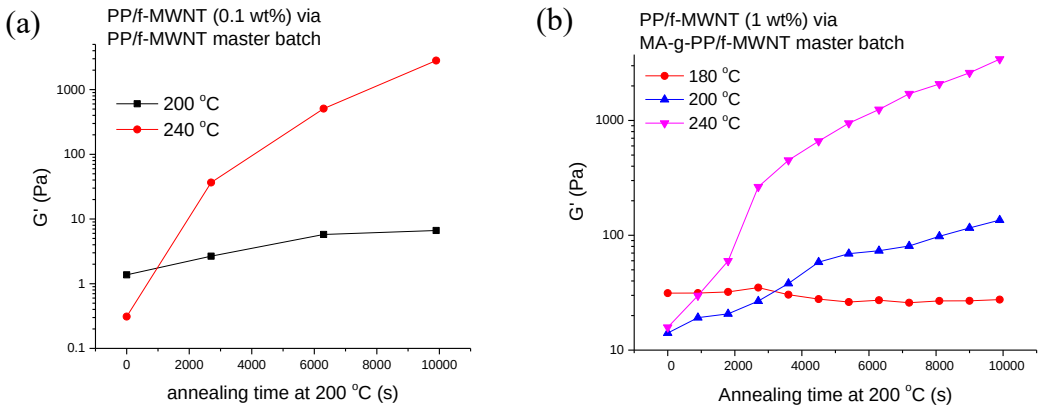

Figure 6.17. Change of G' during annealing (a) at 200 and 240 °C in PP/f-MWNT (0.1 wt%) via PP/f-MWNT master batch, and (b) at 180, 200 and 240 °C in PP/f-MWNT (1 wt%) via MA-g-PP/f-MWNT master batch.

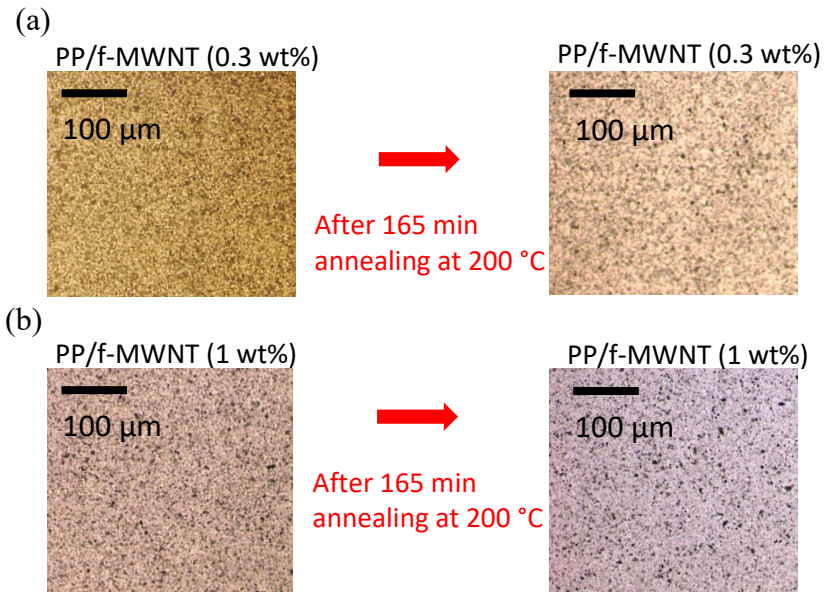

Figure 6.18. Optical image of (a) PP/f-MWNT (0.3 wt%) via PP/f-MWNT master batch, and (b) PP/f-MWNT (1 wt%) via PP/f-MWNT master batch, before and after annealing at 200 °C for 165 minutes.

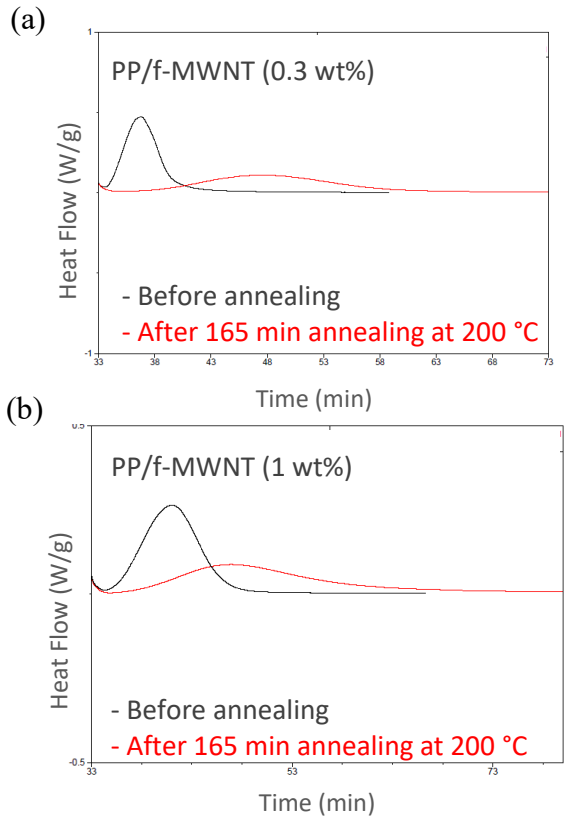

Figure 6.19. Heat flow vs. crystallization time during the isothermal crystallization process at 135 °C of (a) PP/f-MWNT (0.3 wt%) via PP/f-MWNT master batch, and (b)PP/f-MWNT (1 wt%) via PP/f-MWNT master batch, before and after annealing at 200 °C for 165 minutes.

Improved melt elasticity or melt strength can potentially broaden PP's application to blow molding, foam extrusion and similar processes, i.e. the structure can become strong enough to keep the extensional force without rupturing [54]. While this is conventionally accomplished through long-chain branching of PP [33, 55, 56], well-dispersed and distributed f-MWNTs in PP from this study affords a new approach in significant change in viscoelastic behavior through controlled annealing temperature and time (Figure 6.16 and Figure 6.17).

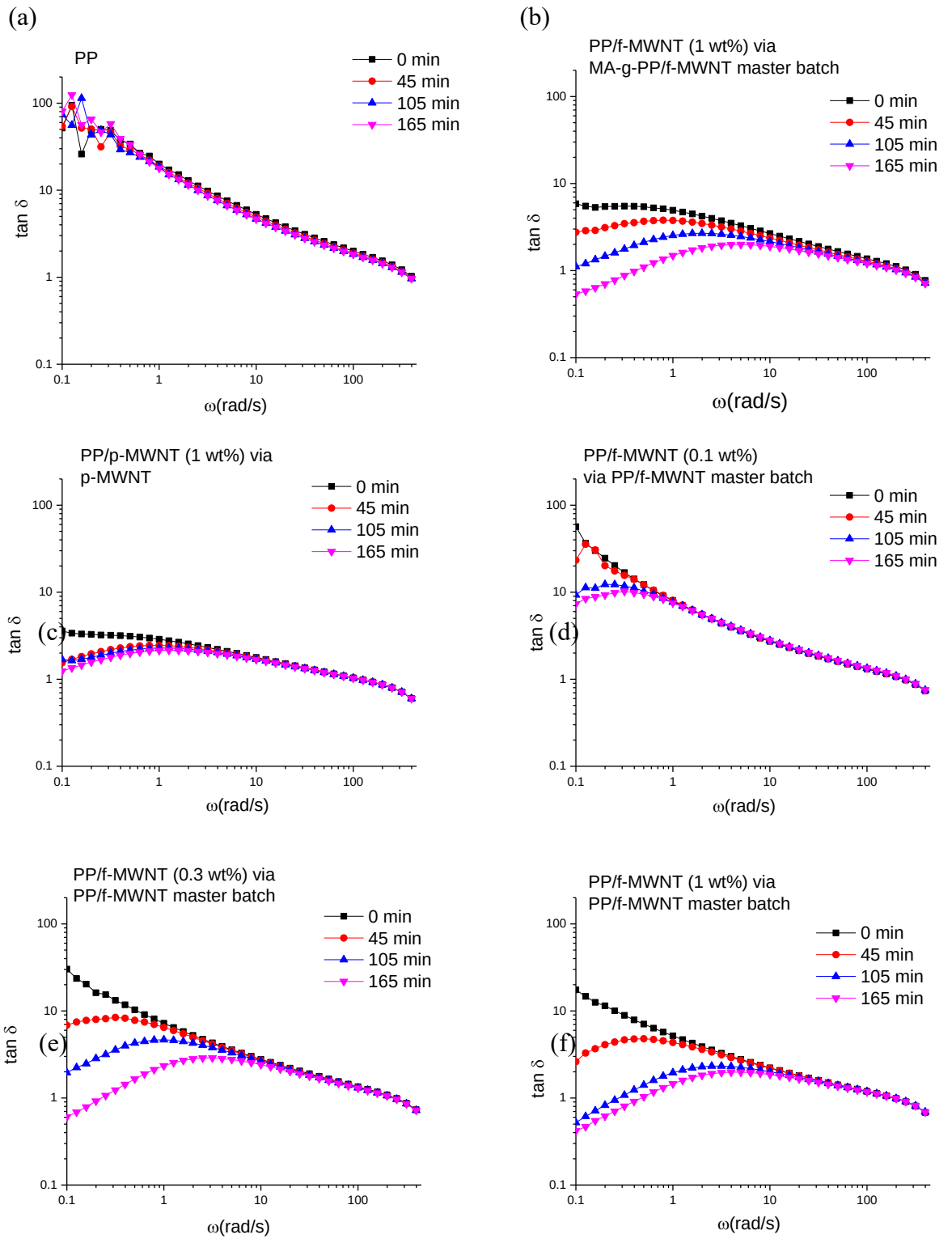

Figure 6.20. Tan δ as a function of frequency of PP and PP/MWNT nanocomposites at different MWNT concentrations via PP/f-MWNT, MA-g-PP/f-MWNT master batch, and p-MWNT after annealing at 200 °C at 0, 45, 105 and 165 minutes.

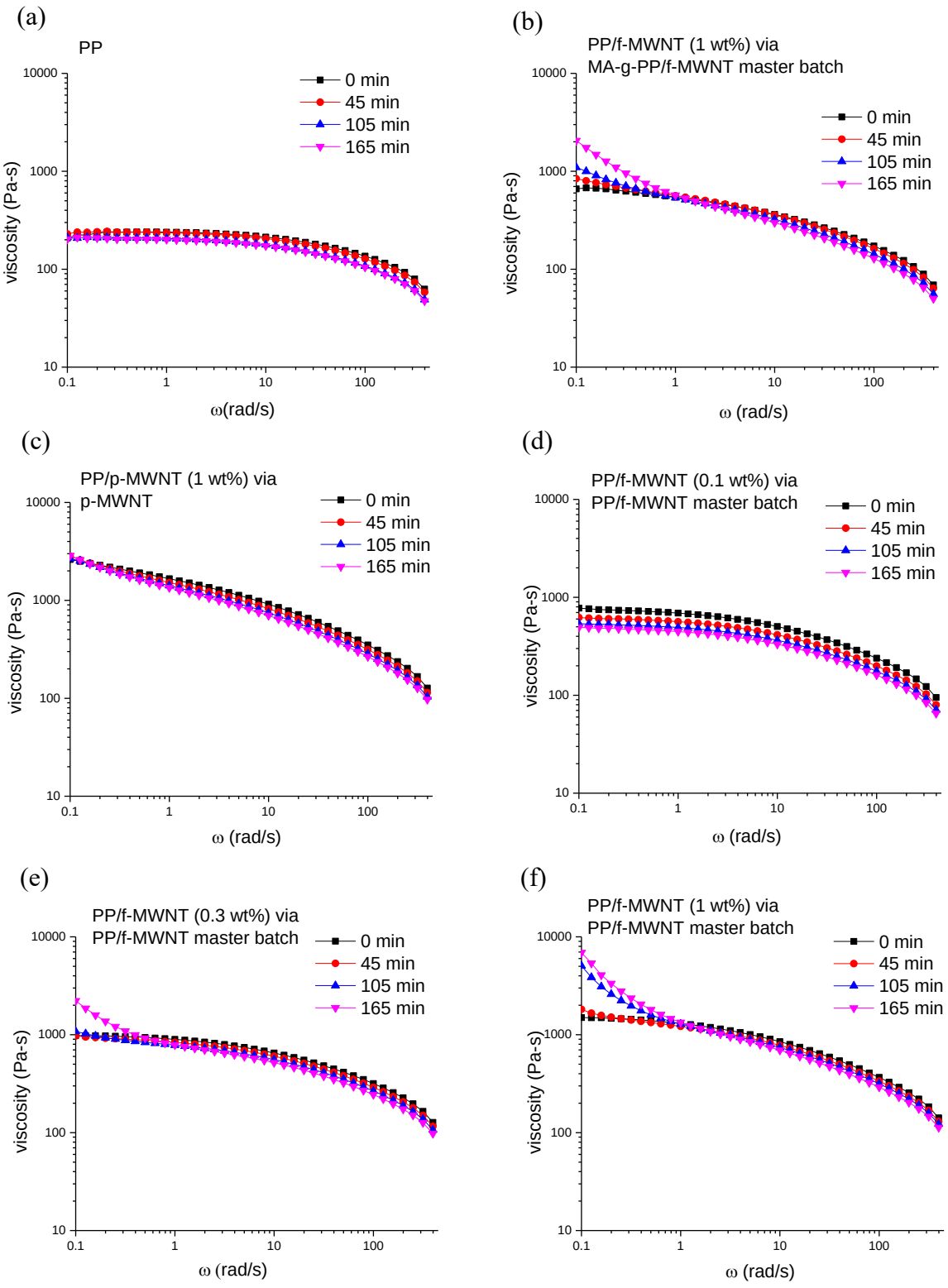

Figure 6.21. Viscosity as a function of frequency of PP and PP/MWNT nanocomposites at different MWNT concentrations via PP/f-MWNT, MA-g-PP/f-MWNT master batch, and p-MWNT after annealing at 200 °C at 0, 45, 105 and 165 minutes.

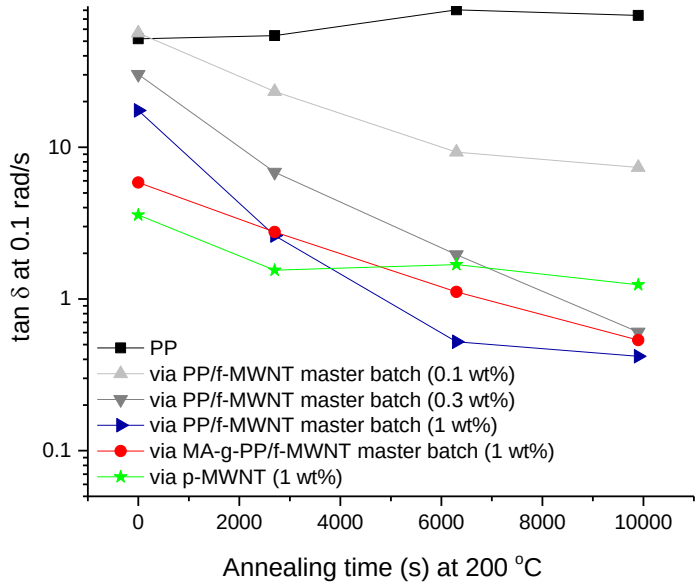

Figure 6.22. Change of tan δ during annealing at 200 °C in PP and PP/MWNT nanocomposites different MWNT concentrations via PP/f-MWNT master batch, MA-g-PP/f-MWNT master batch and p-MWNT.

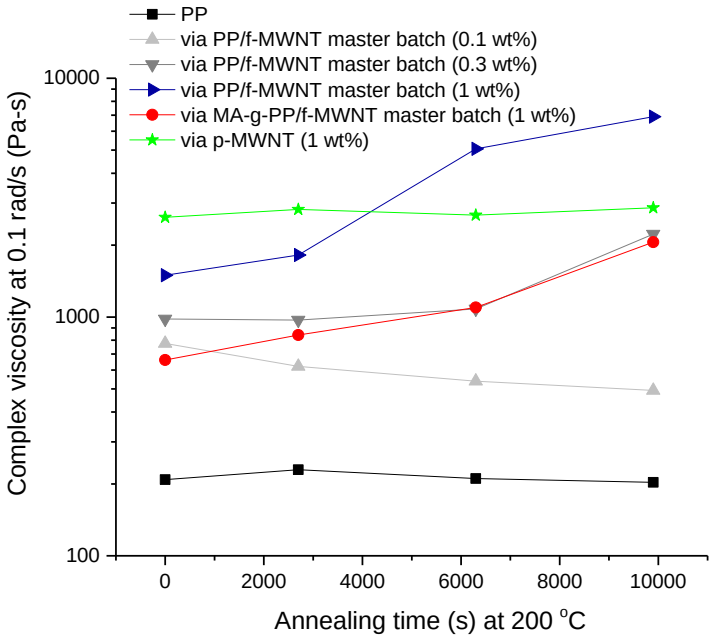

Figure 6.23. Change of Viscosity during annealing at 200 °C in PP and PP/MWNT nanocomposites with different MWNT concentration via PP/f-MWNT, MA-g-PP/f-MWNT master batch and p-MWNT.

Figure 6.24 provides the Cole-Cole plots of PP and PP/MWNT. It is accepted that, in Cole-Cole plot, a semi-circle is often obtained if the deformation behavior of the polymeric material can be described by a single relaxation or a narrow relaxation time distribution [57]. If more than one type of relaxation occurs, then the semi-circle will be distorted and a linear increment appears. Before annealing, the PP and PP/f-MWNT master batch based nanocomposite both showed a complete semi-circle, while the p-MWNT and MA-g-PP/f-MWNT master batch based sample showed a distorted line (open symbols in Figure 6.24). This is consistent to the melt homogeneity results (Table 6.2) obtained from the G' to G" log-log plot. The reduced slope of G' to G" log-log plot signifies the presence of inhomogeneity in the system, e.g. entanglements, CNT aggregated, and MA-g-PP, which brought about other relaxation modes. After annealing at 200 °C, the neat PP still exhibited a semi-circle while the curves of the two master batches based sample showed a significant upturn. Such upturn was also found in the long chain branched PP system [33]. Therefore, under melt annealing, the viscoelastic behavior of PP/MWNT can be altered significantly through modifying polymer interphase at f-MWNTs. This can potentially become an alternative approach to render foamability of the material.

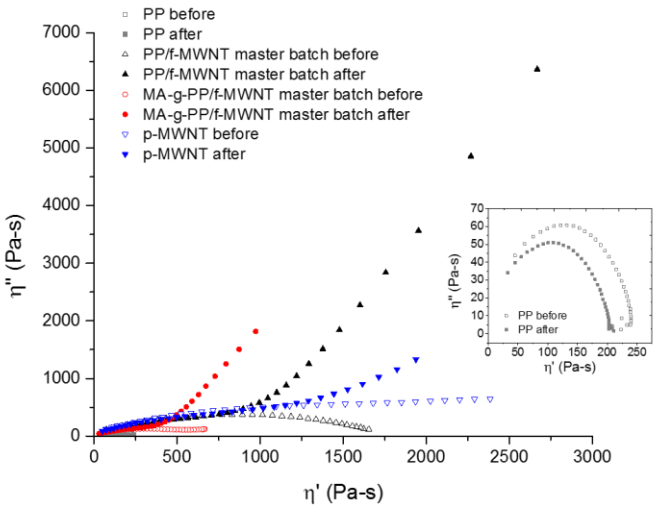

Figure 6. 24. Cole-Cole plot before and after annealing at 200 °C for 165 minutes in PP and PP/MWNT nanocomposites at 1 wt% MWNT concentration via PP/f-MWNT master batch, MA-g-PP/f-MWNT master batch and p-MWNT.

6.4 CONCLUSIONS

The p-MWNT and polymer coated f-MWNTs (namely, PP/f-MWNT master batch and MA-g-PP/f-MWNT master batch) were dispersed in PP using melt-compounding. The MA-g-PP coated f-MWNTs showed better dispersion and stronger shear thinning at high shear rate compared to the PP coated f-MWNTs based samples at the same CNT concentration. These non-covalently coated polymer layers were not completely detached from the f-MWNT surfaces during melt processing as confirmed by comparing the viscoelastic behavior of PP/f-MWNT and PP/p-MWNT nanocomposites. That is, when the effect of MWNT dispersion was decoupled (at 0.01 wt% MWNT), higher η^* and G' at high shear rate in the frequency sweep test, which was associated with retarded molecular motions, in PP/f-MWNT master batch based nanocomposites than in PP/p-MWNT. This justified the presence of PP interphase consisting of solution processed PP. At higher f-MWNT concentrations, the filler-polymer interaction at the interphase brought about further increases of η^* and G' at high shear rate. Also, due to the presence of the interphase, the shear-induced crystallization after shear at 180 °C and the significant increase of melt strength under melt annealing at 200 °C can only be realized in the two types of master batch (PP/f-MWNT and MA-g-PP/f-MWNT) based samples but not in neat PP or PP/p-MWNT. First, the crystallization time at 140 °C reduced from 30 minutes to 5 minutes and from 8 minutes to 3 minutes in MA-g-PP/f-MWNT and PP/f-MWNT based nanocomposites (1 wt%), respectively. Under the same conditions, the crystallization time in PP/p-MWNT only reduced from 5.3 minutes to 4 minutes. Increased polymer alignment under continuous shear and the preservation of shear memory in the two master batch based samples are attributed to this difference in crystallization times. This is consistent with the

observed lower melt pressure after micro-compounding and the higher polymer orientation from WAXD in the presence of polymer coated f-MWNTs. Second, under melt annealing at 200 °C, G' at 0.1 rad/s increased by two orders of magnitude in the PP/f-MWNT based nanocomposites (1 wt%) while there was only about two-fold increase in PP/p-MWNT. Similar effect can also be seen with only 0.1 wt% f-MWNT loading when annealing at 240 °C. The mechanism of increased melt strength was attributed to the formation of space-spanning network of PP and f-MWNTs which is connected by adsorbed or trapped chain segments near f-MWNT surfaces and overlapping chain entanglements in the matrix. The improved melt strength of PP, by adding polymer coated f-MWNTs, can potentially broaden its application in foaming and blow molding, etc.

The differences in the three investigated systems can also be found in processing and therefore structure and resultant mechanical property. The melt pressure recorded after melt-compounding increased as p-MWNT concentration in the nanocomposite increased, indicating greater processing difficulty in the presence of p-MWNT aggregates. On the other hand, melt pressure decreased with increasing f-MWNT concentration in the two types of master batch based nanocomposites. This at least in part can be attributed to well dispersed f-MWNTs and the presence of solution processed polymers that presumably contained fewer entanglements. The preservation of ductility in the injection molded bars in the PP/f-MWNT master batch based samples (even at 1 wt% f-MWNT) was attributed to the relatively high melt homogeneity as compared with MA-g-PP/f-MWNT and p-MWNT based nanocomposites.

6.5 REFERENCES

1. Jingjing Yang, Yaqiong Zhang, Zhigang Wang, and Peng Chen, *Influences of high aspect ratio carbon nanotube network on normal stress difference measurements and extrusion behaviors for isotactic polypropylene nanocomposite melts.* RSC Advances, 2014. **4**(3): p. 1246-1255.

2. K Prashantha, J Soulestin, MF Lacrampe, P Krawczak, G Dupin, and M Claes, *Masterbatch-based multi-walled carbon nanotube filled polypropylene nanocomposites: Assessment of rheological and mechanical properties.* Composites science and technology, 2009. **69**(11): p. 1756-1763.

3. Seung Hwan Lee, Myung Wook Kim, Sung Ho Kim, and Jae Ryoun Youn, *Rheological and electrical properties of polypropylene/MWCNT composites prepared with MWCNT masterbatch chips.* European polymer journal, 2008. **44**(6): p. 1620-1630.

4. Arrate Huegun, Mercedes Fernández, Juanjo Peña, María Eugenia Muñoz, and Antxon Santamaría, *Liquid-State and Solid-State Properties of Nanotube/Polypropylene Nanocomposites Elaborated via a Simple Procedure.* Nanomaterials, 2013. **3**(1): p. 173-191.

5. Yongzheng Pan, Xue Shuang Chan, and Lin Li, *Rheological Study on the Gel-like Behaviour of Carbon Nanotube/Polypropylene Composites: Effect of Interfacial Adhesion.* Nihon Reoroji Gakkaishi, 2013. **41**(3): p. 121-128.

6. Gennaro Gentile, Veronica Ambrogi, Pierfrancesco Cerruti, Rosa Di Maio, Giuseppe Nasti, and Cosimo Carfagna, *Pros and cons of melt annealing on the properties of MWCNT/polypropylene composites.* Polymer Degradation and Stability, 2014. **110**: p. 56-64.

7. Dong-Hua Xu, Zhi-Gang Wang, and Jack F Douglas, *Influence of carbon nanotube aspect ratio on normal stress differences in isotactic polypropylene nanocomposite melts.* Macromolecules, 2008. **41**(3): p. 815-825.

8. Wenlin Li, Yaqiong Zhang, Jingjing Yang, Jun Zhang, Yanhua Niu, and Zhigang Wang, *Thermal annealing induced enhancements of electrical conductivities and mechanism for multiwalled carbon nanotubes filled poly (ethylene-co-hexene) composites.* ACS applied materials & interfaces, 2012. **4**(12): p. 6468-6478.

9. Qinghua Zhang, Fang Fang, Xin Zhao, Yingzhi Li, Meifang Zhu, and Dajun Chen, *Use of dynamic rheological behavior to estimate the dispersion of carbon nanotubes in carbon nanotube/polymer composites.* The Journal of Physical Chemistry B, 2008. **112**(40): p. 12606-12611.

10. Defeng Wu, Yurong Sun, and Ming Zhang, *Kinetics study on melt compounding of carbon nanotube/polypropylene nanocomposites.* Journal of Polymer Science Part B: Polymer Physics, 2009. **47**(6): p. 608-618.

11. Ingo Alig, Tetyana Skipa, Dirk Lellinger, and Petra Pötschke, *Destruction and formation of a carbon nanotube network in polymer melts: rheology and conductivity spectroscopy.* Polymer, 2008. **49**(16): p. 3524-3532.

12. Semen B Kharchenko, Jack F Douglas, Jan Obrzut, Eric A Grulke, and Kalman B Migler, *Flow-induced properties of nanotube-filled polymer materials.* Nature materials, 2004. **3**(8): p. 564-568.

13. Jan Obrzut, Jack F Douglas, SB Kharchenko, and KB Migler, *Shear-induced conductor-insulator transition in melt-mixed polypropylene-carbon nanotube dispersions.* Physical Review B, 2007. **76**(19): p. 195420.

14. Hojjat Mahi and Denis Rodrigue, *Linear and non-linear viscoelastic properties of ethylene vinyl acetate/nano-crystalline cellulose composites.* Rheologica acta, 2012. **51**(2): p. 127-142.

15. Anson WK Ma, Malcolm R Mackley, and Francisco Chinesta, *The microstructure and rheology of carbon nanotube suspensions.* International Journal of Material Forming, 2008. **1**(2): p. 75-81.

16. Sonja Carolin Schulz, Jana Schlutter, and Wolfgang Bauhofer, *Influence of initial high shearing on electrical and rheological properties and formation of percolating agglomerates for MWCNT/epoxy suspensions.* Macromolecular Materials and Engineering, 2010. **295**(7): p. 613-617.

17. Junyang Wang, Jingjing Yang, Liang Deng, Huagao Fang, Yaqiong Zhang, and Zhigang Wang, *More dominant shear flow effect assisted by added carbon nanotubes on crystallization kinetics of isotactic polypropylene in nanocomposites.* ACS applied materials & interfaces, 2015. **7**(2): p. 1364-1375.

18. Yan-Hui Chen, Gan-Ji Zhong, Jun Lei, Zhong-Ming Li, and Benjamin S Hsiao, *In situ synchrotron X-ray scattering study on isotactic polypropylene crystallization under the coexistence of shear flow and carbon nanotubes.* Macromolecules, 2011. **44**(20): p. 8080-8092.

19. Gaurav Mago, Frank T Fisher, and Dilhan M Kalyon, *Effects of multiwalled carbon nanotubes on the shear-induced crystallization behavior of poly (butylene terephthalate).* Macromolecules, 2008. **41**(21): p. 8103-8113.

20. Yan-Hui Chen, Du-Fei Fang, Jun Lei, Liang-Bin Li, Benjamin S Hsiao, and Zhong-Ming Li, *Shear-Induced Precursor Relaxation-Dependent Growth Dynamics and Lamellar Orientation of β-Crystals in β-Nucleated Isotactic Polypropylene.* The Journal of Physical Chemistry B, 2015. **119**(17): p. 5716-5727.

21. Petra Pötschke, Mahmoud Abdel-Goad, Ingo Alig, Sergej Dudkin, and Dirk Lellinger, *Rheological and dielectrical characterization of melt mixed polycarbonate-multiwalled carbon nanotube composites.* Polymer, 2004. **45**(26): p. 8863-8870.

22. Ion Fernandez, Anton Santamaría, María Eugenia Muñoz, and Pere Castell, *A rheological analysis of interactions in phenoxy/organoclay nanocomposites.* European polymer journal, 2007. **43**(8): p. 3171-3176.

23. Kai Ke, Yu Wang, Yong Luo, Wei Yang, Bang-Hu Xie, and Ming-Bo Yang, *Evolution of agglomerate structure of carbon nanotubes in multi-walled carbon nanotubes/polymer composite melt: A rheo-electrical study.* Composites Part B: Engineering, 2012. **43**(8): p. 3281-3287.

24. Yongzheng Pan, Lin Li, Siew Hwa Chan, and Jianhong Zhao, *Correlation between dispersion state and electrical conductivity of MWCNTs/PP composites prepared by melt blending.* Composites Part A, 2010. **41**: p. 419-426.

25. GM Shashidhara, Devaraj Biswas, B Shubhalaksmi Pai, Ajay Kumar Kadiyala, GS Wasim Feroze, and M Ganesh, *Effect of PP-g-MAH compatibilizer content in polypropylene/nylon-6 blends.* Polymer bulletin, 2009. **63**(1): p. 147-157.

26. Young Seok Song and Jae Ryoun Youn, *Influence of dispersion states of carbon nanotubes on physical properties of epoxy nanocomposites.* Carbon, 2005. **43**(7): p. 1378-1385.

27. Athanase Dupré and Paul Dupré, *Théorie mécanique de la chaleur*. 1869: Gauthier-Villars.

28. Sang Chul Roh, Eun Yub Choi, Yeon Sik Choi, and CK Kim, *Characterization of the surface energies of functionalized multi-walled carbon nanotubes and their interfacial adhesion energies with various polymers.* Polymer, 2014. **55**(6): p. 1527-1536.

29. Arthur H Landrock and Sina Ebnesajjad, *Adhesives technology handbook*. 2008: William Andrew.

30. Xiang Gao, Avraam I Isayev, and Chao Yi, *Ultrasonic treatment of polycarbonate/carbon nanotubes composites.* Polymer, 2016. **84**: p. 209-222.

31. Yihu Song and Qiang Zheng, *Linear viscoelasticity of polymer melts filled with nano-sized fillers.* Polymer, 2010. **51**(14): p. 3262-3268.

32. Shilin Huang, Zhengying Liu, Chaolu Yin, Yu Wang, Yongjuan Gao, Chen Chen, and Mingbo Yang, *Enhancement effect of filler network on isotactic polypropylene/carbon black composite melts.* Colloid and Polymer Science, 2011. **289**(15-16): p. 1673-1681.

33. Shuzhao Li, Miaomiao Xiao, Dafu Wei, Huining Xiao, Fuzeng Hu, and Anna Zheng, *The melt grafting preparation and rheological characterization of long chain branching polypropylene.* Polymer, 2009. **50**(25): p. 6121-6128.

34. Sushanta Ghoshal, Po-Hsiang Wang, Prabhakar Gulgunje, Nikhil Verghese, and Satish Kumar, *High impact strength polypropylene containing carbon nanotubes.* Polymer, 2016. **100**: p. 259-274.

35. Han Gi Chae, Marilyn L Minus, and Satish Kumar, *Oriented and exfoliated single wall carbon nanotubes in polyacrylonitrile.* Polymer, 2006. **47**(10): p. 3494-3504.

36. Shanju Zhang, Wei Lin, Ching-Ping Wong, David G Bucknall, and Satish Kumar, *Nanocomposites of carbon nanotube fibers prepared by polymer crystallization.* ACS applied materials & interfaces, 2010. **2**(6): p. 1642-1647.

37. Marilyn L Minus, Han Gi Chae, and Satish Kumar, *Interfacial Crystallization in Gel-Spun Poly (Vinyl Alcohol)/Single-Wall Carbon Nanotube Composite Fibers.* Macromolecular Chemistry and Physics, 2009. **210**(21): p. 1799-1808.

38. Jinghui Yang, Chaoyu Wang, Ke Wang, Qin Zhang, Feng Chen, Rongni Du, and Qiang Fu, *Direct formation of nanohybrid shish-kebab in the injection molded bar of polyethylene/multiwalled carbon nanotubes composite.* Macromolecules, 2009. **42**(18): p. 7016-7023.

39. Kangsheng Liu, Efren Andablo-Reyes, Nilesh Patil, Daniel Hermida Merino, Sara Ronca, and Sanjay Rastogi, *Influence of reduced graphene oxide on the rheological response and chain orientation on shear deformation of high density polyethylene.* Polymer, 2016. **87**: p. 8-16.

40. Lingyu Li, Bing Li, Matthew A Hood, and Christopher Y Li, *Carbon nanotube induced polymer crystallization: The formation of nanohybrid shish–kebabs.* Polymer, 2009. **50**(4): p. 953-965.

41. Bradley A Newcomb, Prabhakar V Gulgunje, Yaodong Liu, Kishor Gupta, Manjeshwar G Kamath, Chandrani Pramanik, Sushanta Ghoshal, Han Gi Chae, and Satish Kumar, *Polyacrylonitrile solution homogeneity study by dynamic shear rheology and the effect on the carbon fiber tensile strength.* Polymer Engineering & Science, 2016. **56**(3): p. 361-370.

42. R Fulchiron, A Michel, V Verney, and JC Roustant, *Correlations between relaxation time spectrum and melt spinning behavior of polypropylene. 1: Calculation of the relaxation spectrum as a log-normal distribution and influence of the molecular parameters.* Polymer Engineering & Science, 1995. **35**(6): p. 513-517.

43. Aadil Elmoumni, H Henning Winter, Alan J Waddon, and Hitesh Fruitwala, *Correlation of material and processing time scales with structure development in*

isotactic polypropylene crystallization. Macromolecules, 2003. **36**(17): p. 6453-6461.

44. William W Graessley, *The entanglement concept in polymer rheology*, in *The Entanglement Concept in Polymer Rheology*. 1974, Springer. p. 1-179.

45. Chang Dae Han and Myung S Jhon, *Correlations of the first normal stress difference with shear stress and of the storage modulus with loss modulus for homopolymers.* Journal of applied polymer science, 1986. **32**(3): p. 3809-3840.

46. Kilwon Cho, Fengkui Li, and Jaeseung Choi, *Crystallization and melting behavior of polypropylene and maleated polypropylene blends.* Polymer, 1999. **40**(7): p. 1719-1729.

47. P. Liu, K. L. White, H. J. Sue, H. Sugiyama, J. Xi, T. Higuchi, T. Hoshino, R. Ishige, H. Jinnai, and A. Takahara, *Influence of trace amount of well-dispersed carbon nanotubes on structural development and tensile properties of polypropylene.* Macromolecules, 2013. **46**(2): p. 463-473.

48. Zuo-Jia Wang, Dong-Jun Kwon, Ga-Young Gu, Hak-Soo Kim, Dae-Sik Kim, Choon-Soo Lee, K. Lawrence DeVries, and Joung-Man Park, *Mechanical and interfacial evaluation of CNT/polypropylene composites and monitoring of damage using electrical resistance measurements.* Composites Science and Technology, 2013. **81**: p. 69-75.

49. Fawzi G Hamad, Ralph H Colby, and Scott T Milner, *Onset of Flow-Induced Crystallization Kinetics of Highly Isotactic Polypropylene.* Macromolecules, 2015. **48**(11): p. 3725-3738.

50. Fengmei Su, Weiming Zhou, Xiangyang Li, Youxin Ji, Kunpeng Cui, Zeming Qi, and Liangbin Li, *Flow-Induced Precursors of Isotactic Polypropylene: An in Situ Time and Space Resolved Study with Synchrotron Radiation Scanning X-ray Microdiffraction.* Macromolecules, 2014. **47**(13): p. 4408-4416.

51. P.V. Gulgunje P.-H. Wang, S. Ghoshal, N. Verghese, S. Kumar, *Effect of Interfacial Chemistry on Crystallization of Polypropylene /Multiwall Carbon Nanotube Nano Composites.* in preparation, 2017.

52. Yongzheng Pan, Henry Kuo Feng Cheng, Lin Li, Siew Hwa Chan, Jianhong Zhao, and Yang Kay Juay, *Annealing induced electrical conductivity jump of multi-walled carbon nanotube/polypropylene composites and influence of molecular weight of polypropylene.* Journal of Polymer Science Part B: Polymer Physics, 2010. **48**(21): p. 2238-2247.

53. Songmei Zhao, Fenghua Chen, Chuanzhuang Zhao, Yingjuan Huang, Jin-Yong Dong, and Charles C Han, *Interpenetrating network formation in isotactic polypropylene/graphene composites.* Polymer, 2013. **54**(14): p. 3680-3690.

54. GJ Nam, JH Yoo, and JW Lee, *Effect of long-chain branches of polypropylene on rheological properties and foam-extrusion performances.* Journal of Applied Polymer Science, 2005. **96**(5): p. 1793-1800.

55. Kun Wang, Shusheng Wang, Fei Wu, Yongyan Pang, Wei Liu, Wentao Zhai, and Wenge Zheng, *A new strategy for preparation of long-chain branched polypropylene via reactive extrusion with supercritical CO2 designed for an improved foaming approach.* Journal of Materials Science, 2016. **51**(5): p. 2705-2715.

56. AD Gotsis, BLF Zeevenhoven, and AH Hogt, *The effect of long chain branching on the processability of polypropylene in thermoforming.* Polymer Engineering & Science, 2004. **44**(5): p. 973-982.

57. Samaneh Abbasi, Pierre J Carreau, Abdessalem Derdouri, and Michel Moan, *Rheological properties and percolation in suspensions of multiwalled carbon nanotubes in polycarbonate.* Rheologica acta, 2009. **48**(9): p. 943-959.

CHAPTER 7

THERMAL, GAS AND MOISTURE BARRIER, AND ELECTROMAGNETIC INTERFERENCE SHIELDING PROPERTIES

7.1 INTRODUCTION

In the previous chapters, the PP coated functionalized MWNTs (f-MWNTs) have shown an improved MWNTs dispersion and adhesion between PP and MWNTs as compared to p-MWNT. Here, the thermal stability, moisture and gas barrier properties as well as electromagnetic interference (EMI) shielding effectiveness of the polypropylene (PP) nanocomposite containing 1 wt% polymer coated multiwall carbon nanotubes (MWNTs) were studied. The results were also compared to the PP/pristine MWNTs (p-MWNTs) nanocomposite in which pristine MWNT powders were simply melt-blended with neat PP. It is observed that even with thermally unstable -COOH group on f-MWNTs, the thermal stability of the PP/f-MWNTs nanocomposite shows a similar behavior to that of the PP/p-MWNT nanocomposite, both with about 95 °C higher temperature at maximum mass loss rate than that of the neat PP. Similarly, the introduction of hydrophilic -COOH group does not lower the oxygen barrier property of the neat PP as much as the p-MWNT nanocomposite does. Addition of 1 wt% polymer coated f-MWNTs has not yet effectively increased the dielectric constant and conductivity of the neat PP, neither the EMI shielding behavior.

The high intrinsic electrical conductivity makes CNTs an excellent candidate for high-performance EMI shielding materials at low filler concentration. Typically, about 1 to 5 wt% of CNTs is needed to form a conductive network that interacts with EM waves [1-7]. Such CNT network or clusters can also act as a physical barrier for molecular transport. While decrease of water permeability with increase in MWNT content was attributed to the increased stiffness of polymer chain in polyurethane/MWNT nanocomposite [8], an opposite result has been obtained as a consequence of reduced crystallinity after incorporating CNTs into polymer [9]. In this study, we will present and discuss the moisture and gas barrier behavior, thermal stability and electrical properties of the PP/f-MWNT (1 wt%) nanocomposite with engineered interface.

7.2 EXPERIMENTAL

For the materials, MWNT functionalization and master batch preparation, please refer to Chapter 2.2. For manufacturing the nanocomposite, please refer to Chapter 3.2. Sample containing stabilizers were also prepared using the same melt compounding protocol, where 300 ppm of calcium stearate, 1500 ppm of Irgafos 168, and 4000 ppm of Irganox 1010 were added to PP powder followed by micro compounding.

Thin film fabrication for permeability testing

To test nanocomposites for their oxygen and water barrier properties, ~100 µm-thick films were prepared by compression molding technique using Wabash hot press (Carver Model 4386, Carver Inc., Wabash, IN) (Figure 7.1). Hot-press steel platens (both top and bottom) were pre-heated to 200 °C. Two injection-molded discs were kept between two 0.015”-thick PTFE sheets. 100 µm (0.004 inch) PTFE shims were placed between

PTFE sheets to obtain films with length and thickness of 4.75” × 4.75” and 0.004”, respectively. The PTFE sheets were sandwiched between two steel plates of 6” × 6”. The above assembly was placed between the platens and then closed, such that the heated platens contact the steel plate without positive pressure. The set-up was left under such condition for 5 minutes. The pressure was then ramped to 5 MPa and held for 2 minutes. The pressure was released and the assembly was taken out followed by cooling under ambient condition for 5 minutes. The resulting film was peeled off the PTFE sheets. It should be noted that due to reduced flow at 200 °C, platen temperature was increased to 220 °C for PP/p-MWNT composites films.

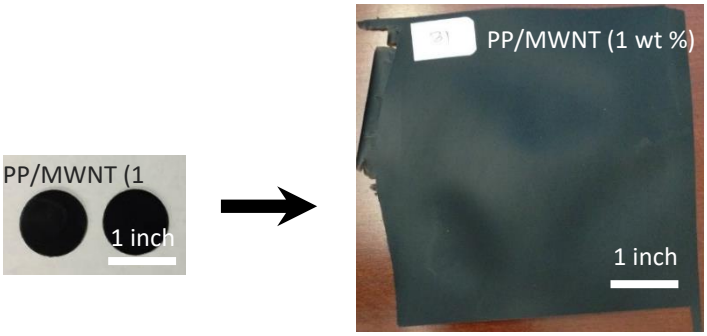

Figure 7.1. Thin fabricated film (right) for permeability testing from discs (left) made by injection molding.

Permeability testing

The gas and moisture permeability tests were done by Dr. Sergei I. Nazarenko’s group at the University of Southern Mississippi. Oxygen barrier of the control PP and PP/MWNT nanocomposite films were measured at 25°C, 0 % RH, and 1 atm partial oxygen pressure difference using a commercially manufactured diffusion apparatus, OX-TRAN® 2/21 ML (MOCON). This instrument employs a continuous-flow method (ASTM D3985-81 and ASTM F1249-01) with nitrogen as the carrier gas to measure oxygen flux, *J(t)*, through polymeric films. Mixture of oxygen (4 % molar fraction) and nitrogen was used to reduce exposure of high flux on the instrument sensors. The film specimens were

conditioned in the instrument under nitrogen flow over night prior to testing. Sample thickness was measured over at least 10 equally spaced spots over the sample testing area and averaged for obtaining the thickness used in the permeability calculations. The permeability coefficient, *P*, was calculated directly from the steady-state flux, J_∞, value as $P = J_\infty l / \Delta p$, where *l* is the film thickness and Δp is the oxygen partial pressure difference across the film. Each film was tested at least two times to obtain the permeability.

Water vapor transmission rates (WVTRs) were measured using a MOCON Permatran-W® 3/31. This instrument employs a continuous-flow method with nitrogen as the carrier gas and water vapor as the test gas. Calibration was performed using a film supplied by MOCON. Before testing, the specimens were conditioned for 3 hours at 100 % RH and 37.8 °C. A sample test area of 50 cm^2 was utilized. The nitrogen flow rate during the test was set to 100 cm^3/min. Measurements were carried out at 37.8 °C under 100 % RH and finished after values of WVTR reached a steady state. Multiple tests on the same films were conducted to obtain the transmission value.

Thermal degradation behavior

For studying thermal degradation, thermogravimetric analysis (TGA) study was carried out at a heating rate of 20 °C/min under nitrogen and under air using TA Instrument Q500.

Thin film fabrication for EMI shielding testing and EMI shielding testing protocol

EMI shielding effectiveness measurements was done by Keystone Compliance, LCC. About 80 µm-thick films (7" × 7") were prepared by compression molding technique following the similar procedure described in the earlier section, except that 50 µm PTFE

shims and steel plates of 8” × 8” were used. It should also be noted that thicker films ~80 µm was obtained than shim thickness (50 µm) due to incomplete filling of the mold. Also, it is noted that longer residence time was applied to PP/f-MWNT (two times longer than neat PP) due to observed difficulty in melt flow. EMI shielding test of the above fabricated films was carried out using Test Method MIL-STD-285 and MIL-STD-83528C within a frequency range of 30 MHz to 18 GHz by Keystone Compliance LLC, New Castle, PA (Figure 7.2).

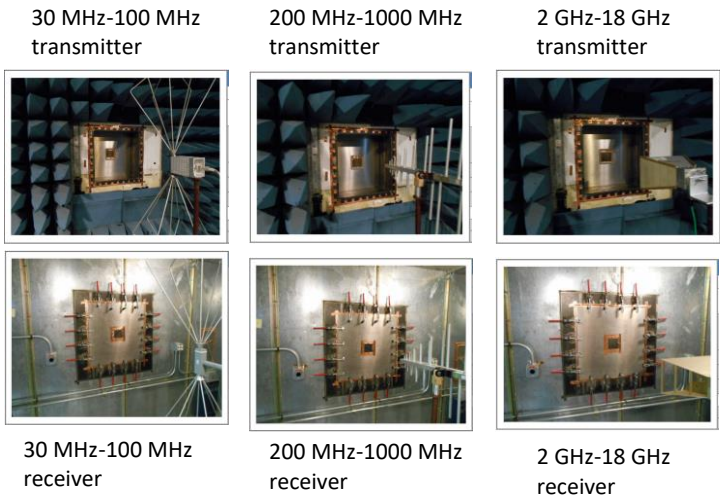

Figure 7.2. Transmitter and receiver for EMI shielding measurement.

7.3 RESULTS AND DISCUSSION

7.3.1 Gas and moisture barrier properties

Table 7.1 and Table 7.2 lists the oxygen and water vapor permeability of PP and PP/MWNT nanocomposites. The PP/f-MWNT nanocomposites show a slightly higher permeability (about 15 to 20 % higher) than the control PP samples. On the other hand, up to 55 % higher permeability in one of the two PP/p-MWNT samples than neat PP (8.28 vs.

5.1 to 5.5 cc·cm/m^2·day·atm) was observed. It is hypothesized that the presence of fillers, either organic or inorganic, in the polymer matrix constitutes solid barriers in the path when the gas molecules passing through the polymer. The efficiency of such barrier effect was predicted by Nielsen [10] who assumed that gas molecules travel through a tortuous pathway composed of rectangular platelets of width (L) and thickness (W), oriented in a direction that is perpendicular to the gas diffusion direction. The decrease in gas permeability can then be given by $\frac{P}{P_0} = \frac{1-\phi}{1+\frac{\alpha}{2}\phi}$, where P and P_0 represent gas permeability of polymers with and without nanoparticles, respectively. ϕ is the volume fraction of the nanoparticles and α = L (length)/W(width) is the aspect ratio of the platelets. Guo et al. has modified the Nielsen model for a system having evenly dispersed nanotubes with diameter (2R) perpendicular to the gas diffusion direction. The relative gas permeability equation of tubular additives is then: $\frac{P}{P_0} = \frac{1-\phi}{1+\frac{\pi^2-8}{16}\phi}$. It was found to have much smaller influence on the gas permeability, at the same loading than the platelets [11]. Having 1 wt% MWNTs in PP, i.e. about 0.45 vol%, the calculated $\frac{P}{P_0}$ is 0.995 (0.5 % reduction of permeability) for tubular fillers and 0.93 (7 % reduction in permeability) for platelets with α = 30. Although it seems like having a low filler concentration, especially in the case of tubular fillers, is almost ineffective for gas permeability, it is worth noting that as a nucleating agent [12], MWNTs nucleate smaller spherulites [13] than the neat PP and develop higher crystalline perfection in the PP/MWNT interphase region (Chapter 8). Both can contribute to a reduction of gas permeation rate. For example, reduction of O_2 permeability from 7 to 4.5 cc·cm/m^2·day·atm was reported by adding 1 wt% carbon back in PP [14]. The author attributed this to the difference in crystallinity: 62 % for neat PP and

67 % for the composite. While there is no reduction of crystallinity in our samples (Table 3), from 69 % to 72 % by adding 1 wt% MWNTs, a higher O_2 permeability in our nanocomposites can be due to the following: First, the presence of MWNT aggregates [13], about 2 to 10 μm in PP/f-MWNT and up to 100 μm in PP/p-MWNT (Chapter 3). Gas molecules can travel at a faster rate at the polymer-MWNT aggregate interfaces that produce voids or nanovoids [15, 16]. Second, a relatively smaller crystal size in the nanocomposites (11.3 nm in PP vs. 10.2 nm in PP/p-MWNT, and 10.9 nm in PP/f-MWNT) can also facilitate molecule transport [17].

Table 7.1. Oxygen permeability of PP and PP/MWNT nanocomposite films

Sample Type	O_2 transmission at 4 % ($cc/m^2 \cdot day$)	O_2 transmission at 100 % ($cc/m^2 \cdot day$)	Permeability ($cc \cdot cm/m^2 \cdot day \cdot atm$)	Average Permeability ($cc \cdot cm/m^2 \cdot day \cdot atm$)
Control PP	20.24 ± 0.80	506.1 ± 20.1	5.11 ± 0.20	5.21 ± 0.25
	23.67 ± 0.18	591.7 ± 4.4	5.50 ± 0.04	
	15.99 ± 0.44	399.6 ± 10.9	5.12 ± 0.14	
PP/f-MWNT (1 wt%) via PP/f-MWNT master batch	25.46 ± 0.91	636.6 ± 22.6	6.30 ± 0.22	6.13 ± 0.43
	24.58 ± 1.81	614.5 ± 45.3	5.96 ± 0.44	
PP/p-MWNT (1 wt%) via p-MWNT	26.43 ± 0.39	660.8 ± 9.8	6.34 ± 0.09	7.31 ± 1.07
	30.38 ± 0.83	759.4 ± 20.8	8.28 ± 0.23	

An important observation in our PP/f-MWNT nanocomposite compared to the literatures is that, oftentimes a much faster gas molecule transport rate was observed in the functionalized CNTs (f-CNTs) containing samples than the pristine CNTs (p-CNTs) containing samples. This is because that the acid treatment has made CNTs more hydrophilic by the formation of polar surface groups, and therefore, lower adhesion between hydrophobic PP and f-CNTs. For example, the O_2 transmission rate increases from

412.6 cc/m^2·day in neat PP to 517.7 cc/m^2·day in 3 wt% p-MWNT containing sample, and becomes 10008.2 cc/m^2·day in the PP/f-MWNT nanocomposite [18]. Similarly, almost two-fold higher O_2 permeability in 2.5 wt% PP/f-MWNT than in PP/p-MWNT nanocomposite was found [19]. However, this is not the case in our PP/f-MWNT nanocomposite, where a significant increase of gas molecules transport rate was not observed. Apart from good MWNT dispersion, much improved PP/f-MWNT adhesion in our solvent processed CNT master batch (Chapter 3) may account for the difference between this work and the literature.

Table 7.2. Moisture permeability of PP and PP/MWNT nanocomposite films

Sample Type	H_2O transmission at 100% RH (g/m^2·day)	Permeability (g·cm/m^2·day·atm)	Average Permeability (cc·cm/m^2·day·atm)
Control PP	2.00 ± 0.17	0.021 ± 0.002	0.0195 ± 0.002
	2.28 ± 0.06	0.018 ± 0.001	
PP/f-MWNT (1 wt%) via PP/f-MWNT master batch	1.99 ± 0.15	0.020 ± 0.001	0.02 ± 0.002
	2.07 ± 0.16	0.020 ± 0.002	
PP/p-MWNT (1 wt%) via p-MWNT	1.97 ± 0.09	0.019 ± 0.001	0.019 ± 0.0008
	1.76 ± 0.02	0.019 ± 0.0003	

Table 7.3. Crystallinity and crystal size of PP and PP/MWNT nanocomposites used for permeability study.

Sample Type	X_c (%)[1]	L_{PP} (nm)[2]
Control PP	69	11.3
PP/f-MWNT (1 wt%) via PP/f-MWNT master batch	72	10.9
PP/p-MWNT (1 wt%) via p-MWNT	72	10.2

[1] X_c: crystallinity from integrated radial scans.
[2] L_{PP}: crystal size of (110) at 2θ~ 14.1° according to Scherrer's equation with K = 0.9.

As PP itself exhibits hydrophobic characteristic and the crystallinity of the nanocomposites are not changed significantly with respect to the control PP sample, the water vapor permeability of PP is not affected after incorporating MWNTs (Table 7.2). In some hydrophilic polymers, such as polycaprolactone (PCL), 40 % reduction (from 1.51 to 0.92 g·mm/m^2·day·kPa) and 40 % reduction (from 2.1 to 1.25 % water uptake) of water vapor permeability have been observed using 0.5 wt% [20] and 1 wt% MWNTs [15], respectively. In PP/MWNT nanocomposites, Bounos et al. reported an unexpected result where the compression molded films exhibited no change of gas permeation (CH_4 and CO_2) after incorporation of 0.25 to 6 wt% maleic anhydride grafted polypropylene (MA-g-PP) functionalized MWNTs into neat PP. The water vapor permeability, on the other hand, increased by 27 times with 1 wt% functionalized MWNTs addition [16]. The mechanism of such selectivity in water transport over gas molecules is not well-understood yet, however, it brings up the attention that it is possible to tailor the molecular transport property through CNT-polymer interface engineering.

7.3.2 Thermal degradation behavior

Thermogravimetric analysis was carried out to study the thermal decomposition temperature of control PP and PP/MWNT (1 wt%) nanocomposites prepared from p-MWNT and the PP/f-MWNT master batch. The degradation behavior of the samples under air and nitrogen are shown in Figure 7.3 to Figure 7.5, and the $T_{99\%}$ ($T_{90\%}$) is defined as the temperature where 1 % (10 %) of the sample weight loss occurs. The onset weight loss temperature, T_{onset}, is calculated based on the point at which the tangents to the two different slopes of the TGA plot intersect. The temperature at maximum mass loss rate, T_{max}, is derived from the derivative weight loss curve. From Figure 7.3, the behavior of PP/f-

MWNT and PP/p-MWNT (1 wt%) nanocomposite is very similar, except that in the f-MWNT incorporated sample, the $T_{99\%}$ under nitrogen occurred much earlier (345 °C in neat PP, 422 °C in PP/p-MWNT and 290 °C in PP/f-MWNT) than in PP. Otherwise, the curves from the two nanocomposites overlap with each other and exhibit higher thermal decomposition temperatures than the neat polymer. Similar observation was reported in the amine functionalized MWNT/polymer system, in which the T_{max} of the f-MWNT (1 wt%) incorporated nanocomposite occurred in the same temperature range compared to that of the p-MWNT incorporated one [21]. From Figure 7.5, in the PP/f-MWNT nanocomposite, the early initial weight loss, i.e. before 350 °C under nitrogen, can be attributed to the loss of functional groups [22], the loss of the nanotubes catalyzed by the functional groups, and most importantly, to the accelerated polymer degradation in the presence of reactive -COOH groups [23]. The decomposition temperature of PP/f-MWNT under nitrogen was also studied by [24]. The authors found that as the extent of amino acid functionalization increased, T_{onset} of the nanocomposite decreased continuously by more than 20 °C due to the lower thermal stability of the functional group.

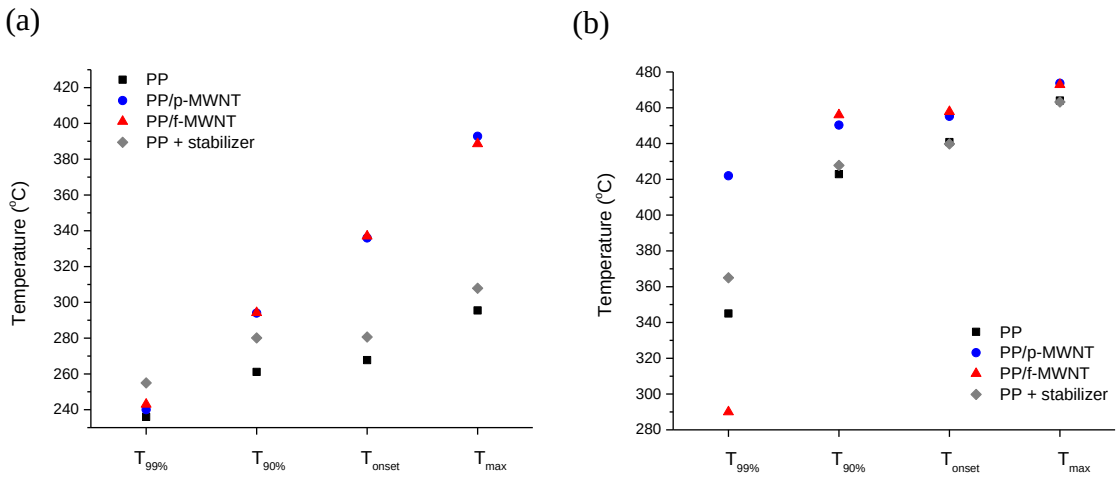

Figure 7.3. $T_{99\%}$, $T_{90\%}$, T_{onset}, and T_{max} of PP, PP/MWNT (1 wt%) nanocomposites and the PP with thermal stabilizer under (a) air and (b) nitrogen.

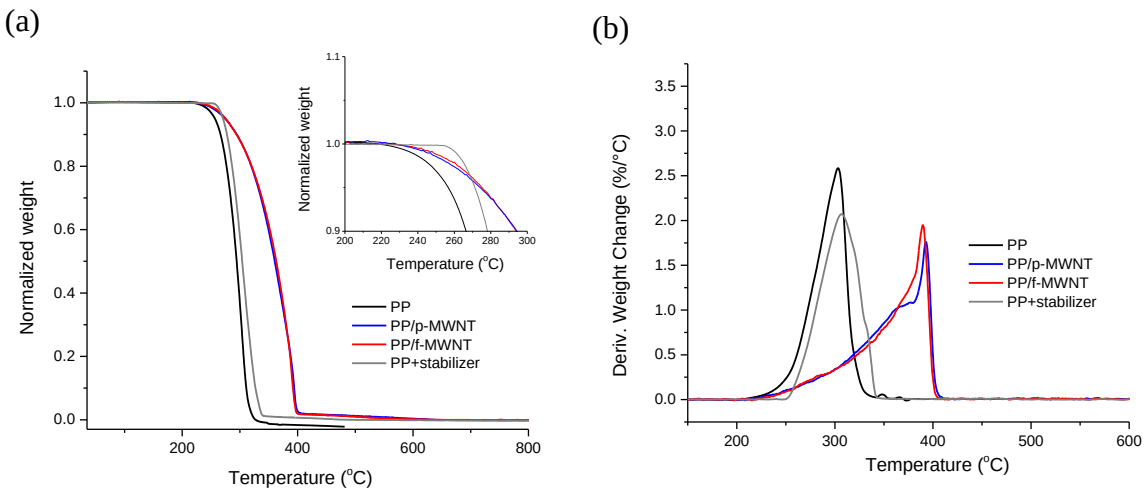

Figure 7.4. TGA (a) weight loss curves and (b) derivative weight loss curves as a function of temperature of PP, PP/MWNT (1 wt%) nanocomposites and the PP with thermal stabilizer under air.

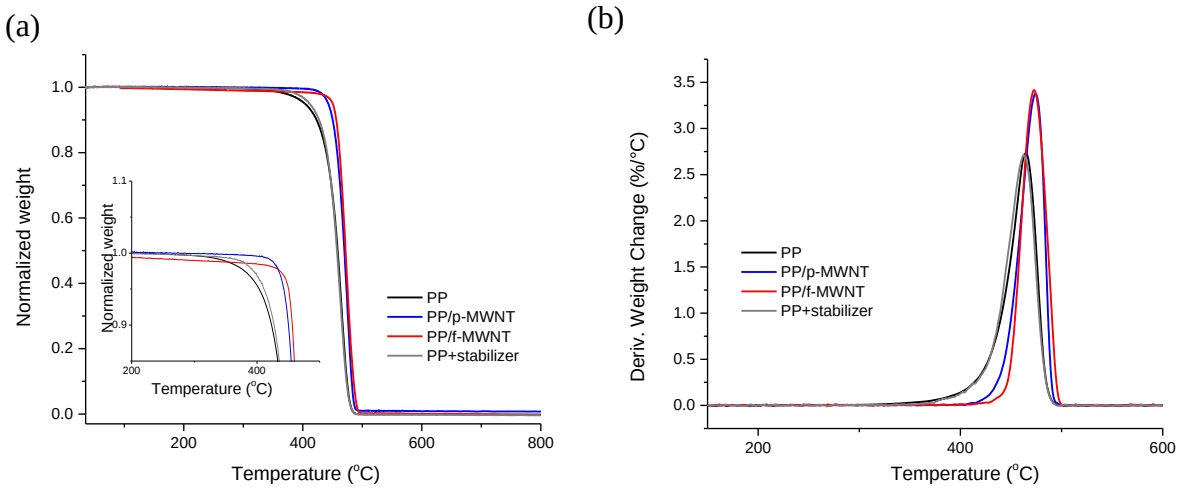

Figure 7.5. TGA (a) weight loss curves and (b) derivative weight loss curves as a function of temperature of PP, PP/MWNT (1 wt%) nanocomposites and the PP with thermal stabilizer under nitrogen.

Under air, PP/MWNT nanocomposites exhibit about 30 °C higher $T_{90\%}$, 70 °C higher T_{onset}, and 95 °C higher T_{max} compared to the neat PP (Figure 7.3). Under nitrogen, the difference between the nanocomposites and the neat polymer becomes smaller, where 30 °C increase in $T_{90\%}$, 15 °C increase in T_{onset}, and 10 °C increase in T_{max} were observed

(Figure 7.3). According to the literature studies, the increase in T_{max} ranges from 10 to 90 °C [25-30] under air and 10 to 60 °C [25, 26, 31-38] under nitrogen with the addition of 0.5 to 5 wt% MWNTs in PP. The CNT type, CNT purity, processing method of the nanocomposite, presence of compatibilizer, etc. are some possible causes that account for the decomposition temperature variation between different studies. Nevertheless, the increase in thermal stability of polymer-CNT composite can be attributed to some common factors. Firstly, the interfacial interaction between CNT and polymer hinders the thermal motion of macromolecules and increases the degradation activation energy [23, 39]. Secondly, the barrier effect of CNT network can potentially hinder the transport of decomposed polymer product from condensed phase to gas phase [23, 35]. Thirdly, CNTs demonstrate antioxidant effect due to its strong radical accepting ability that decelerates the degradation process [40]. Finally, the thermally conductive CNT network facilitates the heat dissipation within the nanocomposite and delays the polymer degradation [35]. Although Marosfői et al. proposed that at low temperature, CNTs can form a protective barrier that limits the permeation of O_2 and delays the degradation of PP under air [35], this is not likely the reason for the increased thermal stability in our nanocomposites since the O_2 permeability is either unchanged or lower than that for the neat PP in these samples as discussed in the previous section. While the thermal stability of the polymer-CNT nanocomposites could be explained by one of the above-mentioned effects or some combinations thereof, higher increase of PP decomposition temperature under air than under nitrogen in the presence of 1 wt% MWNTs might indicate that MWNTs are more effective in delaying the thermo-oxidation degradation under air (Figure 7.4 and Figure 7.5), which is in consistent with the literatures [21, 35]. Similarly, when compounding the

stabilizers into neat PP, the effect is more pronounced under air than under nitrogen: The TGA curve shifts about 20 °C to higher temperature compared to neat PP under air but remains almost un-shifted under nitrogen (Figure 7.4 and Figure 7.5). While both f-MWNT and p-MWNT increase the thermal stability of neat PP at the later stage of decomposition, i.e. after $T_{90\%}$ and T_{onset}, the incorporation of stabilizers is more effective in delaying the decomposition of PP at the earlier stage, i.e. around $T_{99\%}$.

7.3.3 Dielectric and electromagnetic (EMI) shielding properties

Figure 7.6 and Figure 7.7 show the resistivity and real part of permittivity (ε') as function of the frequency for neat PP and the PP/f-MWNT (1 wt%) nanocomposite. Generally, ε' is a measure of how much energy can be stored in the material upon the application of an external field. In the polymer nanocomposite, introduction of conductive particles contributes to the increase of ε' through the enhancement of interfacial polarization [41]. Oftentimes, the filler concentration under which such increase of ε' occurs is related to the electrical percolation of the polymer nanocomposite [1, 4, 42-45]. In the Figure 7.6, the resistivity of 1 wt% PP/f-MWNT nanocomposite is about the same as that of the neat PP, indicating that 1 wt% f-MWNT is still below the electrical percolation threshold. As a result, it is expected that both PP and PP/f-MWNT nanocomposite have a same ε value that is nearly frequency-independent between 0.1 to 1 MHz (Figure 7.7), representing the typical dielectric behavior of the neat PP [44-46].

The electrical percolation threshold of PP/CNTs nanocomposite has been reported in a broad range, between 0.1 wt% to more than 5 wt% [30, 47-61]. Among these, some studies have shown a value of 1 to 2 wt% [55, 56, 58-60], which is close to the CNTs loading in our system. However, even at 2 wt% f-MWNT addition, the resistivity and

permittivity of the PP are still not affected (Figure 7.8). There are several factors that contribute to the low conductivity in our PP/f-MWNT nanocomposite. Pan. et al. [60] discovered that even though the f-MWNT incorporated PP nanocomposites exhibited more homogeneous MWNTs distribution over the sample than the p-MWNT incorporated ones, significantly lower electrical conductivity was observed in the PP/f-MWNT nanocomposites than the PP/p-MWNTs nanocomposites having same MWNT loading (e.g. the percolation threshold is 5 wt% in the former and 1 to 2 wt% in the latter). The authors attributed this to the acid treatment that destroyed the nanotube surfaces and brought defects that reduce the intrinsic electrical conductivity of MWNTs. Marcelino et al. [62] demonstrated that the electrical conductivity of MWNTs reduced from 510 S/m to 431 S/m when the I_D (Raman D band intensity)/ I_G (Raman G band intensity) increased from 0.43 to 0.59. In our earlier study (Chapter 2), the I_D/I_G ratio was reported to be 1.69 ± 0.05 for p-MWNT and 2.32 ± 0.05 for the f-MWNT. It is possible that these nanotubes have a lower intrinsic conductivity, as indicated by low graphitic (I_G) percentage, which diminished even further due to functionalization. Also, 4 to 5 nm of polymer coating around the f-MNWTs prevents contact of the nanotubes, thus obstructs the formation of conductive pathway in the nanocomposite. This polymer coating was formed during the co-solvent based master batch preparation process as reported previously (Chapter 2). Similarly, Hayashida et al. [1] showed that the individual MWNTs were electrically isolated by the grafted poly (methyl methacrylate) chain. The volume resistivity of polymer-grafted MWNTs was as high as 1.3×10^{15} Ω cm even at 7.3 wt% of the MWNT. Finally, the length of f-MWNTs might be reduced during chemical oxidation and sonication. With shorter lengths, it becomes more difficult for nanotubes to form interconnected conductive networks.

Having the MWNT concentration fixed, some approaches can be used to enhance conductivity of a nanocomposite. For example, modifying the processing conditions, including temperature profile [63], screw profile and rotation speed [63], annealing of the polymer melt post mixing [64], and shear force during molding, etc. for achieving interconnected CNTs networks. The formation of CNT clusters into a CNT-rich and a CNT-poor phase can effectively improve the nanocomposite conductivity [64]. Also, the critical volume fraction of CNTs necessary to form the percolation network depends a lot on their orientation state [65-67]: ranges from below 1 vol% for a three-dimensional random distribution system to 21 vol% for an aligned arrangement [65]. Lastly, polymer nanocomposite foam with cellular morphology can reach 6 orders of magnitude higher electrical conductivity than their solid counterpart [42, 44, 68].

It is well-established that the EMI shielding effectiveness (SE) of a conductive composite is related to its conductivity [2, 5, 7]. The SE of a material is defined as $SE(\text{dB}) = -10\ \log_{10}(P_t/P_0)$, where P_t and P_0 are, the transmitted and incident electromagnetic power, respectively. From Figure 7.9, it is evident that SE of the neat PP and the PP/f-MWNT (1 wt%) nanocomposite have comparable values from 30 MHz to 18 GHz, which agrees with their similar dielectric and conductivity behavior from 10^{-1} to 10 MHz (Figure 7.6 and Figure 7.7).

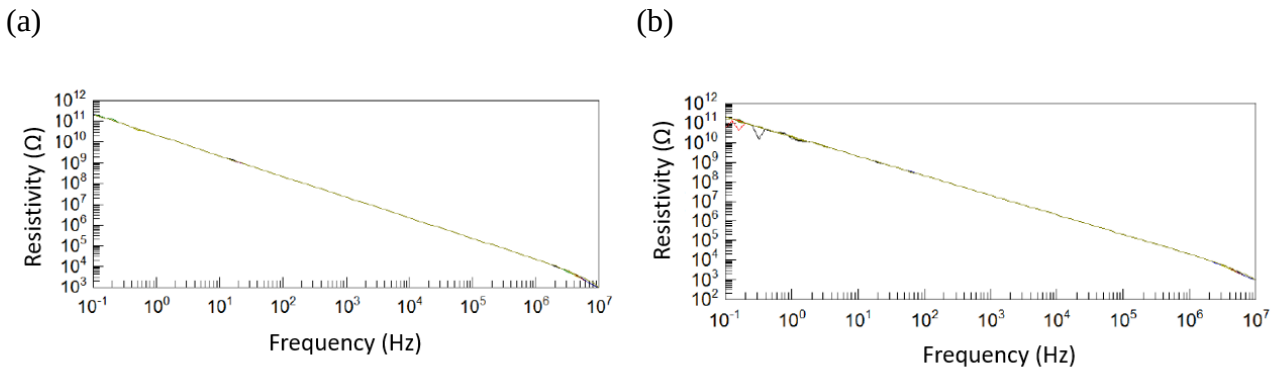

Figure 7.6. Frequency dependence of resistivity of (a) neat PP and (b) PP/f-MWNT (1 wt%) nanocomposite.

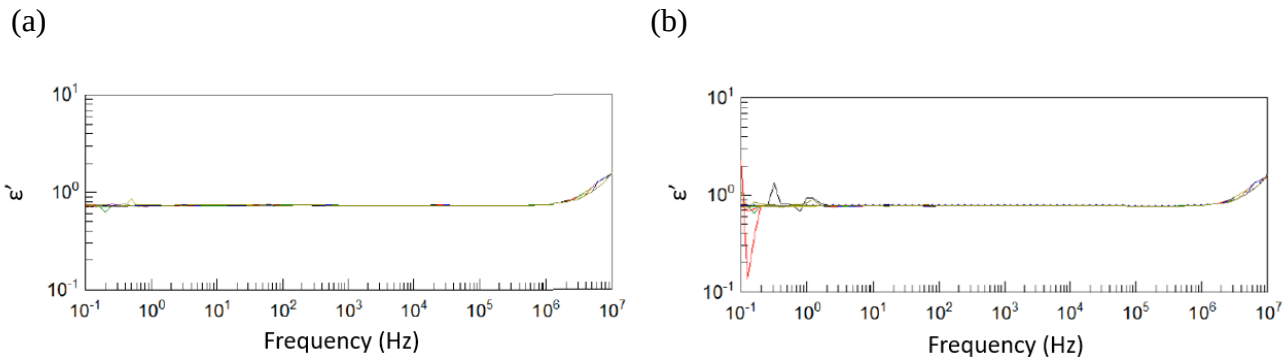

Figure 7.7. Frequency dependence of *ε'* of (a) neat PP and (b) PP/f-MWNT (1 wt%) nanocomposite.

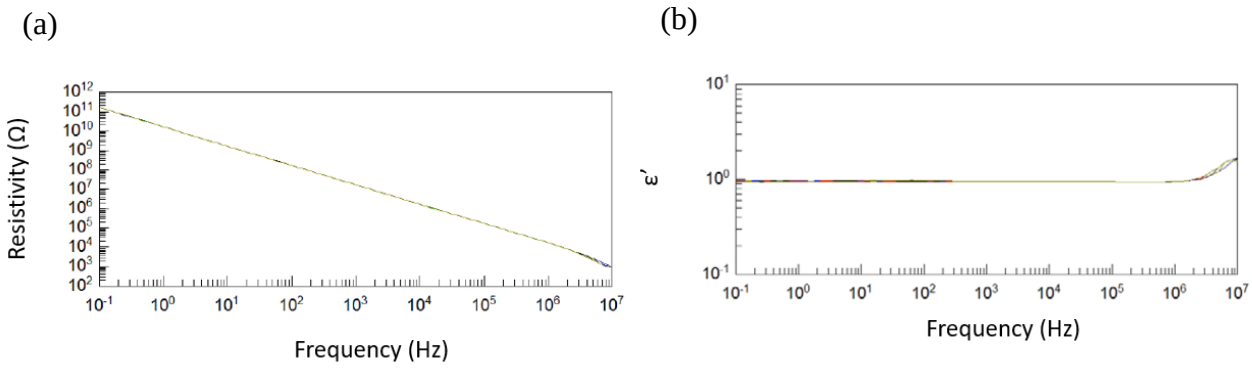

Figure 7.8. Frequency dependence of (a) resistivity and (b) *ε'* of PP/f-MWNT (2 wt%) nanocomposite.

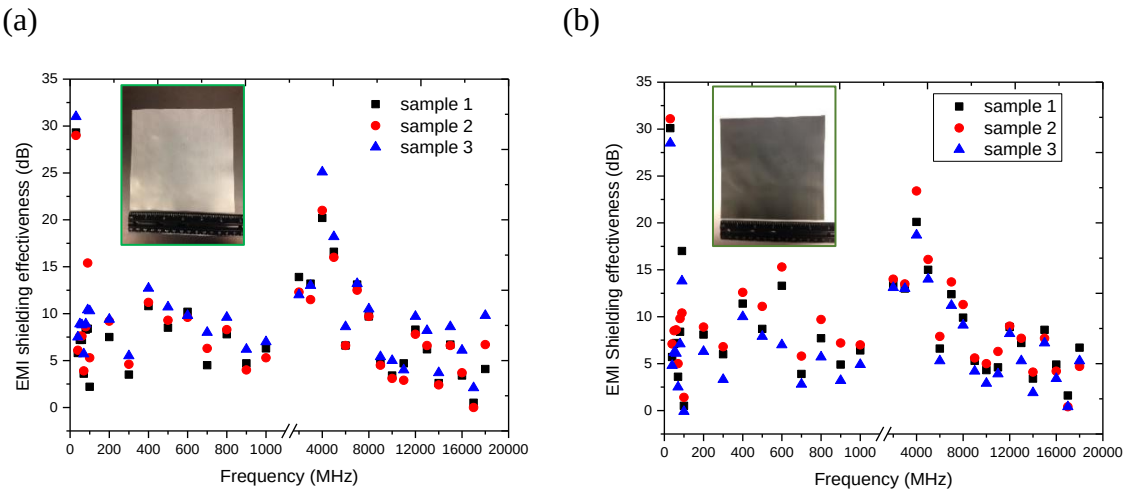

Figure 7.9. Frequency dependence of EMI shielding effectiveness (SE) of (a) neat PP and (b) PP/f-MWNT (1 wt%) nanocomposite.

7.4 CONCLUSIONS

The thermal stability, moisture and gas barrier properties as well as EMI shielding of the polypropylene (PP) nanocomposite containing 1 wt% polymer coated multiwall carbon nanotubes (MWNTs) were studied. The results show that even with thermally unstable -COOH group on f-MWNTs, the thermal stability of the PP/f-MWNTs nanocomposite has a similar behavior to that of the PP/p-MWNT nanocomposite, both show about 95 °C higher T_{max} than that of the neat PP under air. The increase of T_{max} was higher under air than under nitrogen indicating that MWNTs are more efficient in delaying the thermo-oxidative degradation of PP under air.

The introduction of -COOH group does not lower the oxygen barrier property of the neat PP as much as the p-MWNT nanocomposite does which is opposite to the literature findings. This might due to the improved PP-MWNT adhesion in the nanocomposite having polymer coated f-MWNTs. Owing to its hydrophobic nature, the PP and PP/MWNT

nanocomposites, either with f-MWNTs or p-MWNTs, does not show a distinct moisture barrier property.

Addition of 1 wt% polymer coated f-MWNTs has not yet effectively increased the dielectric constant and conductivity of the neat PP, neither the EMI shielding behavior. Both MWNT functionalization and polymer coating could potentially lead to the absence of electrically conductive network even under 2 wt% f-MWNT loading.

7.5 REFERENCES

1. Kenichi Hayashida and Yoriko Matsuoka, *Electromagnetic interference shielding properties of polymer-grafted carbon nanotube composites with high electrical resistance.* Carbon, 2015. **85**: p. 363-371.

2. Yonglai Yang, Mool C Gupta, Kenneth L Dudley, and Roland W Lawrence, *Novel carbon nanotube− polystyrene foam composites for electromagnetic interference shielding.* Nano letters, 2005. **5**(11): p. 2131-2134.

3. Jean-Michel Thomassin, Isabelle Huynen, Robert Jerome, and Christophe Detrembleur, *Functionalized polypropylenes as efficient dispersing agents for carbon nanotubes in a polypropylene matrix; application to electromagnetic interference (EMI) absorber materials.* Polymer, 2010. **51**(1): p. 115-121.

4. Mohammed H Al-Saleh, Walaa H Saadeh, and Uttandaraman Sundararaj, *EMI shielding effectiveness of carbon based nanostructured polymeric materials: a comparative study.* Carbon, 2013. **60**: p. 146-156.

5. Jia-Horng Lin, Zheng-Ian Lin, Yi-Jun Pan, Chien-Teng Hsieh, Chien-Lin Huang, and Ching-Wen Lou, *Thermoplastic polyvinyl alcohol/multiwalled carbon nanotube composites: preparation, mechanical properties, thermal properties, and electromagnetic shielding effectiveness.* Journal of Applied Polymer Science, 2016. **133**(21).

6. Ning Li, Yi Huang, Feng Du, Xiaobo He, Xiao Lin, Hongjun Gao, Yanfeng Ma, Feifei Li, Yongsheng Chen, and Peter C Eklund, *Electromagnetic interference (EMI) shielding of single-walled carbon nanotube epoxy composites.* Nano letters, 2006. **6**(6): p. 1141-1145.

7. Yan Li and Uttandaraman Sundararaj, *Comparative study on electrical properties of copper nanowire/polypropylene and carbon nanotube/polypropylene composites.* AIChE Journal, 2015. **61**(1): p. 296-303.

8. S Mondal and JL Hu, *Microstructure and water vapor transport properties of functionalized carbon nanotube-reinforced dense-segmented polyurethane composite membranes.* Polymer Engineering & Science, 2008. **48**(9): p. 1718-1724.

9. Jae-Hyun Choi, Jonggeon Jegal, and Woo Nyon Kim. *Modification of performances of various membranes using MWNTs as a modifier*. in *Macromolecular Symposia*. 2007. Wiley Online Library.

10. Lawrence E Nielsen, *Models for the permeability of filled polymer systems.* Journal of Macromolecular Science—Chemistry, 1967. **1**(5): p. 929-942.

11. Yichen Guo, Kai Yang, Xianghao Zuo, Yuan Xue, Clement Marmorat, Ying Liu, Chung-Chueh Chang, and Miriam H Rafailovich, *Effects of clay platelets and*

natural nanotubes on mechanical properties and gas permeability of Poly (lactic acid) nanocomposites. Polymer, 2016. **83**: p. 246-259.

12. P.V. Gulgunje P.-H. Wang, S. Ghoshal, N. Verghese, S. Kumar, *Effect of Interfacial Chemistry on Crystallization of Polypropylene /Multiwall Carbon Nanotube Nano Composites.* in preparation, 2017.

13. Sushanta Ghoshal, Po-Hsiang Wang, Prabhakar Gulgunje, Nikhil Verghese, and Satish Kumar, *High impact strength polypropylene containing carbon nanotubes.* Polymer, 2016. **100**: p. 259-274.

14. A Vassiliou, D Bikiaris, K Chrissafis, KM Paraskevopoulos, SY Stavrev, and A Docoslis, *Nanocomposites of isotactic polypropylene with carbon nanoparticles exhibiting enhanced stiffness, thermal stability and gas barrier properties.* Composites Science and Technology, 2008. **68**(3): p. 933-943.

15. MD Sanchez-Garcia, JM Lagaron, and SV Hoa, *Effect of addition of carbon nanofibers and carbon nanotubes on properties of thermoplastic biopolymers.* Composites science and technology, 2010. **70**(7): p. 1095-1105.

16. G Bounos, KS Andrikopoulos, H Moschopoulou, G Ch Lainioti, David Roilo, Riccardo Checchetto, T Ioannides, JK Kallitsis, and GA Voyiatzis, *Enhancing water vapor permeability in mixed matrix polypropylene membranes through carbon nanotubes dispersion.* Journal of Membrane Science, 2017. **524**: p. 576-584.

17. Kyriaki Kalaitzidou, Hiroyuki Fukushima, and Lawrence T Drzal, *Multifunctional polypropylene composites produced by incorporation of exfoliated graphite nanoplatelets.* Carbon, 2007. **45**(7): p. 1446-1452.

18. Alejandra J Monsiváis-Barrón, Jaime Bonilla-Rios, and Antonio Sánchez-Fernández, *Property Relationship in Organosilanes and Nanotubes Filled Polypropylene Hybrid Composites.* Materials, 2014. **7**(10): p. 7073-7092.

19. D Bikiaris, A Vassiliou, K Chrissafis, KM Paraskevopoulos, A Jannakoudakis, and A Docoslis, *Effect of acid treated multi-walled carbon nanotubes on the mechanical, permeability, thermal properties and thermo-oxidative stability of isotactic polypropylene.* Polymer Degradation and Stability, 2008. **93**(5): p. 952-967.

20. Ruhul A Khan, Dominic Dussault, Stephane Salmieri, Agnes Safrany, and Monique Lacroix, *Mechanical and barrier properties of carbon nanotube reinforced PCL-based composite films: Effect of gamma radiation.* Journal of Applied Polymer Science, 2013. **127**(5): p. 3962-3969.

21. Juan Li, Lifang Tong, Zhengping Fang, Aijuan Gu, and Zhongbin Xu, *Thermal degradation behavior of multi-walled carbon nanotubes/polyamide 6 composites.* Polymer degradation and stability, 2006. **91**(9): p. 2046-2052.

22. Yasunori Tsukahara, Tomohisa Yamauchi, Tadashi Kawamoto, and Yuji Wada, *Functionalization of multi-walled carbon nanotubes realized by microwave-driven chemistry inducing dispersibility in liquid media.* Bulletin of the Chemical Society of Japan, 2008. **81**(3): p. 387-392.

23. D Bikiaris, *Can nanoparticles really enhance thermal stability of polymers? Part II: an overview on thermal decomposition of polycondensation polymers.* Thermochimica Acta, 2011. **523**(1): p. 25-45.

24. Suchitra Parija and Arup R Bhattacharyya, *Multiwalled carbon nanotubes-based polypropylene composites: Influence of interfacial interaction on the crystallization behavior of polypropylene.* Polymer Engineering & Science, 2017. **57**(2): p. 183-196.

25. Takashi Kashiwagi, Eric Grulke, Jenny Hilding, Richard Harris, Walid Awad, and Jack Douglas, *Thermal degradation and flammability properties of poly (propylene)/carbon nanotube composites.* Macromolecular Rapid Communications, 2002. **23**(13): p. 761-765.

26. Huaili Qin, Shimin Zhang, Chungui Zhao, Meng Feng, Mingshu Yang, Zhongjun Shu, and Shousheng Yang, *Thermal stability and flammability of polypropylene/montmorillonite composites.* Polymer Degradation and Stability, 2004. **85**(2): p. 807-813.

27. Jiang Gong, Ran Niu, Xin Wen, Hongfan Yang, Jie Liu, Xuecheng Chen, Zhao-Yan Sun, Ewa Mijowska, and Tao Tang, *Correction: Synergistic effect of carbon fibers and carbon nanotubes on improving thermal stability and flame retardancy of polypropylene: a combination of a physical network and chemical crosslinking.* RSC Advances, 2015. **5**(52): p. 42054-42054.

28. Shenyuan Fu, Pingan Song, Haitang Yang, Yongming Jin, Fengzhu Lu, Jiewang Ye, and Qiang Wu, *Effects of carbon nanotubes and its functionalization on the thermal and flammability properties of polypropylene/wood flour composites.* Journal of materials science, 2010. **45**(13): p. 3520-3528.

29. Haiou Yu, Zhenjiang Zhang, Zhe Wang, Zhiwei Jiang, Jie Liu, Lu Wang, Dong Wan, and Tao Tang, *Double functions of chlorinated carbon nanotubes in its combination with Ni2O3 for reducing flammability of polypropylene.* The Journal of Physical Chemistry C, 2010. **114**(31): p. 13226-13233.

30. Chien-Chia Chu, Kevin L White, Peng Liu, Xi Zhang, and Hung-Jue Sue, *Electrical conductivity and thermal stability of polypropylene containing well-dispersed multi-walled carbon nanotubes disentangled with exfoliated nanoplatelets.* Carbon, 2012. **50**(12): p. 4711-4721.

31. Jun'ichi Masuda and John M Torkelson, *Dispersion and major property enhancements in polymer/multiwall carbon nanotube nanocomposites via solid-*

state shear pulverization followed by melt mixing. Macromolecules, 2008. **41**(16): p. 5974-5977.

32. Min-Kang Seo and Soo-Jin Park, *A Kinetic Study on the Thermal Degradation of Multi-Walled Carbon Nanotubes-Reinforced Poly (propylene) Composites.* Macromolecular Materials and Engineering, 2004. **289**(4): p. 368-374.

33. Abdolhosein Fereidoon, Mahmood Hemmati, Naser Kordani, Mohammad Kameli, Morteza Ghorbanzadeh Ahangari, and Narges Sharifi, *The effect of acid-treatment of carbon nanotubes on the thermal kinetics of isotactic polypropylene.* Journal of Macromolecular Science®, Part B: Physics, 2011. **50**(4): p. 665-678.

34. Sang Ho Park, Seung Goo Lee, and Seong Hun Kim, *Thermal decomposition behavior of carbon nanotube reinforced thermotropic liquid crystalline polymers.* Journal of Applied Polymer Science, 2011. **122**(3): p. 2060-2070.

35. B Marosfői, A Szabo, Gy Marosi, D Tabuani, Giovanni Camino, and S Pagliari, *Thermal and spectroscopic characterization of polypropylene-carbon nanotube composites.* Journal of thermal analysis and calorimetry, 2006. **86**(3): p. 669-673.

36. HKF Cheng, MF Chong, E Liu, K Zhou, and L Li, *Thermal decomposition kinetics of multiwalled carbon nanotube/polypropylene nanocomposites.* Journal of Thermal Analysis and Calorimetry, 2014. **117**(1): p. 63-71.

37. Jiawen Xiong, Zhen Zheng, Xiumin Qin, Ming Li, Huiqing Li, and Xinling Wang, *The thermal and mechanical properties of a polyurethane/multi-walled carbon nanotube composite.* Carbon, 2006. **44**(13): p. 2701-2707.

38. Tony McNally, Petra Pötschke, Peter Halley, Michael Murphy, Darren Martin, Steven EJ Bell, Gerard P Brennan, Daniel Bein, Patrick Lemoine, and John Paul Quinn, *Polyethylene multiwalled carbon nanotube composites.* Polymer, 2005. **46**(19): p. 8222-8232.

39. Milena Ginic-Markovic, Janis G Matisons, Raoul Cervini, George P Simon, and Peter M Fredericks, *Synthesis of new polyaniline/nanotube composites using ultrasonically initiated emulsion polymerization.* Chemistry of materials, 2006. **18**(26): p. 6258-6265.

40. PCP Watts, PK Fearon, WK Hsu, NC Billingham, HW Kroto, and DRM Walton, *Carbon nanotubes as polymer antioxidants.* Journal of Materials Chemistry, 2003. **13**(3): p. 491-495.

41. Jin-Young Kim, TaeYoung Kim, Ji Won Suk, Harry Chou, Ji-Hoon Jang, Jong Ho Lee, Iskandar N Kholmanov, Deji Akinwande, and Rodney S Ruoff, *Enhanced Dielectric Performance in Polymer Composite Films with Carbon Nanotube-Reduced Graphene Oxide Hybrid Filler.* Small, 2014. **10**(16): p. 3405-3411.

42. A Ameli, PU Jung, and CB Park, *Electrical properties and electromagnetic interference shielding effectiveness of polypropylene/carbon fiber composite foams.* Carbon, 2013. **60**: p. 379-391.

43. Petra Pötschke, Mahmoud Abdel-Goad, Ingo Alig, Sergej Dudkin, and Dirk Lellinger, *Rheological and dielectrical characterization of melt mixed polycarbonate-multiwalled carbon nanotube composites.* Polymer, 2004. **45**(26): p. 8863-8870.

44. A Ameli, M Nofar, CB Park, P Pötschke, and G Rizvi, *Polypropylene/carbon nanotube nano/microcellular structures with high dielectric permittivity, low dielectric loss, and low percolation threshold.* Carbon, 2014. **71**: p. 206-217.

45. Xiang Lin, Jie-Wei Tian, Peng-Hao Hu, Rohan Ambardekar, Glen Thompson, Zhi-Min Dang, and Phil Coates, *Improved dielectric performance of polypropylene/multiwalled carbon nanotube nanocomposites by solid-phase orientation.* Journal of Applied Polymer Science, 2016. **133**(3).

46. Ewa Markiewicz, Dominik Paukszta, and Sławomir Borysiak, *Acoustic and dielectric properties of polypropylene-lignocellulosic materials composites*, in *Polypropylene*. 2012, InTech.

47. Ingo Alig, Dirk Lellinger, Sergej M Dudkin, and Petra Pötschke, *Conductivity spectroscopy on melt processed polypropylene–multiwalled carbon nanotube composites: recovery after shear and crystallization.* Polymer, 2007. **48**(4): p. 1020-1029.

48. O Zetina-Hernández, S Duarte-Aranda, A May-Pat, G Canché-Escamilla, J Uribe-Calderon, PI Gonzalez-Chi, and F Avilés, *Coupled electro-mechanical properties of multiwall carbon nanotube/polypropylene composites for strain sensing applications.* Journal of materials science, 2013. **48**(21): p. 7587-7593.

49. Xi Zhang, Xingru Yan, Qingliang He, Huige Wei, Jun Long, Jiang Guo, Hongbo Gu, Jingfang Yu, Jingjing Liu, and Daowei Ding, *Electrically conductive polypropylene nanocomposites with negative permittivity at low carbon nanotube loading levels.* ACS applied materials & interfaces, 2015. **7**(11): p. 6125-6138.

50. Yuling Ma, Daming Wu, Ying Liu, Xiaofeng Li, Hui Qiao, and Zhong-Zhen Yu, *Electrically conductive and super-tough polypropylene/carbon nanotube nanocomposites prepared by melt compounding.* Composites Part B: Engineering, 2014. **56**: p. 384-391.

51. Beate Krause, Petra Pötschke, Evgeniy Ilin, and Mikhail Predtechenskiy, *Melt mixed SWCNT-polypropylene composites with very low electrical percolation.* Polymer, 2016. **98**: p. 45-50.

52. Henry Kuo Feng Cheng, Yongzheng Pan, Nanda Gopal Sahoo, Kahwei Chong, Lin Li, Siew Hwa Chan, and Jianhong Zhao, *Improvement in properties of multiwalled*

carbon nanotube/polypropylene nanocomposites through homogeneous dispersion with the aid of surfactants. Journal of Applied Polymer Science, 2012. **124**(2): p. 1117-1127.

53. Xing-Hua Li, Yadong He, Xiaofeng Li, Fei An, Dongzhi Yang, and Zhong-Zhen Yu, *Simultaneous enhancements in toughness and electrical conductivity of polypropylene/carbon nanotube nanocomposites by incorporation of electrically inert calcium carbonate nanoparticles.* Industrial & Engineering Chemistry Research, 2017. **56**(10): p. 2783-2788.

54. Luis C Herrera-Ramírez, Pere Castell, Miguel Castillo-Rodríguez, Ángel Fernández, and Roberto Guzman de Villoria, *The effect of a semi-industrial masterbatch process on the carbon nanotube agglomerates and its influence in the properties of thermoplastic carbon nanotube composites.* Journal of Polymer Science Part B: Polymer Physics, 2017. **55**(2): p. 189-197.

55. Min-Kang Seo, Jae-Rock Lee, and Soo-Jin Park, *Crystallization kinetics and interfacial behaviors of polypropylene composites reinforced with multi-walled carbon nanotubes.* Materials Science and Engineering: A, 2005. **404**(1): p. 79-84.

56. Michael Thomas Müller, Beate Krause, Bernd Kretzschmar, and Petra Pötschke, *Influence of feeding conditions in twin-screw extrusion of PP/MWCNT composites on electrical and mechanical properties.* Composites Science and Technology, 2011. **71**(13): p. 1535-1542.

57. Y Ngabonziza, J Li, and CF Barry, *Electrical conductivity and mechanical properties of multiwalled carbon nanotube-reinforced polypropylene nanocomposites.* Acta mechanica, 2011. **220**(1): p. 289-298.

58. Seung Hwan Lee, Myung Wook Kim, Sung Ho Kim, and Jae Ryoun Youn, *Rheological and electrical properties of polypropylene/MWCNT composites prepared with MWCNT masterbatch chips.* European polymer journal, 2008. **44**(6): p. 1620-1630.

59. E Logakis, E Pollatos, Ch Pandis, V Peoglos, I Zuburtikudis, CG Delides, A Vatalis, M Gjoka, E Syskakis, and K Viras, *Structure–property relationships in isotactic polypropylene/multi-walled carbon nanotubes nanocomposites.* Composites Science and Technology, 2010. **70**(2): p. 328-335.

60. Yongzheng Pan, Lin Li, Siew Hwa Chan, and Jianhong Zhao, *Correlation between dispersion state and electrical conductivity of MWCNTs/PP composites prepared by melt blending.* Composites Part A: Applied Science and Manufacturing, 2010. **41**(3): p. 419-426.

61. Sie Chin Tjong, GD Liang, and SP Bao, *Electrical behavior of polypropylene/multiwalled carbon nanotube nanocomposites with low percolation threshold.* Scripta Materialia, 2007. **57**(6): p. 461-464.

62. José Encarnación Moreno Marcelino, Enrique Vigueras Santiago, Gustavo Lopez-Tellez, and Susana Hernández López. *Chemical functionalization of carbon nanotubes and its effects on electrical conductivity*. in *Journal of Nano Research*. 2014. Trans Tech Publ.

63. Tobias Villmow, Petra Pötschke, Sven Pegel, Liane Häussler, and Bernd Kretzschmar, *Influence of twin-screw extrusion conditions on the dispersion of multi-walled carbon nanotubes in a poly (lactic acid) matrix.* Polymer, 2008. **49**(16): p. 3500-3509.

64. Ingo Alig, Tetyana Skipa, Dirk Lellinger, and Petra Pötschke, *Destruction and formation of a carbon nanotube network in polymer melts: rheology and conductivity spectroscopy.* Polymer, 2008. **49**(16): p. 3524-3532.

65. Stuart H Munson-McGee, *Estimation of the critical concentration in an anisotropic percolation network.* Physical Review B, 1991. **43**(4): p. 3331.

66. José Roberto Bautista-Quijano, Petra Pötschke, Harald Brünig, and Gert Heinrich, *Strain sensing, electrical and mechanical properties of polycarbonate/multiwall carbon nanotube monofilament fibers fabricated by melt spinning.* Polymer, 2016. **82**: p. 181-189.

67. Jinguang Kim and Younggon Son, *Effects of matrix viscosity, mixing method and annealing on the electrical conductivity of injection molded polycarbonate/MWCNT nanocomposites.* Polymer, 2016. **88**: p. 29-35.

68. A Ameli, Y Kazemi, S Wang, CB Park, and P Pötschke, *Process-microstructure-electrical conductivity relationships in injection-molded polypropylene/carbon nanotube nanocomposite foams.* Composites Part A: Applied Science and Manufacturing, 2017. **96**: p. 28-36.

CHAPTER 8

STRUCTURE AND RHEOLOGICAL BEHAVIOR OF POLYPROPYLENE INTERPHASE AT HIGH CARBON NANOTUBE CONCENTRATION

8.1 INTRODUCTION

In this chapter, the structure of the PP/CNT interphase was examined by converting the bulk polymer into interphase using high CNT loading: in the previous chapters, the MWNT concentration in the master batch is fixed at 5 wt%, here, 15 wt% and 30 wt% PP/f-MWNT master batches were prepared for investigating the interphase behavior. The structure, morphology, and physical and chemical stabilities of the interphase were studied. Also, the macroscopic rheological behavior, including shear viscosity and dynamic viscoelastic response, in the presence of interphase were also evaluated.

In order to improve the stress transfer in the master batch, controlling the structure development in the interphase region between polymer matrix and nanofillers is necessary. The interphase in the polymer/nanofiller system could be defined as: the interfacial region surrounding the nanofiller which comprises of physically or chemically bonded polymer chains with properties different than those of the bulk matrix. The extended chain conformation with good interfacial adhesion/wettability at the nanofiller surface is a favorable structure for fabricating strong master batch. Extended-chain polyethylene [1], polyvinyl alcohol [2, 3], and polyacrylonitrile [2, 4, 5] have been observed forming a tubular coating on carbon nanotubes (CNTs) through interfacial crystallization. However,

most of the morphological studies to-date on polypropylene (PP) interphase were carried out in a relatively macroscopic scale, i.e. transcrystallization on CNT fibers [2, 6], due to the difficulty in acquiring good CNT dispersion in PP. One exception is that Miltner et al. have studied the PP crystallization morphology from melt on the surface of CNTs and proposed the structure model of the transcrystalline PP layer using TEM and thermal analysis [7, 8]. While it has been demonstrated that the mechanical properties of PP can be improved significantly with small loading of CNT (below 1 wt% CNT) [9, 10], the understanding of the PP/CNT interphase is limited on the basis of theoretical calculation, e.g. finite element analysis [11], or shear lag model [12], etc. Although the adhesion between PP and CNT has been improved using dilute solution crystallization [13] and modified CNT surface topography [14], systematic studies of PP/CNT interphase formation and characterization are still lacking.

The presence of polymeric interphase in the nanocomposite has been verified and explained both theoretically and experimentally by various authors. Pukanszky et al. [15] developed a model to predict the nanocomposite yield stress with the particulate filler content, interphase thickness and interfacial strength. Sumita et al. [16] utilized dynamic mechanical analysis (DMA) measurements to identify the effective volume fraction of the 'immobilized matrix' associated with the interphase. Using the above two approaches, Rong et al. [17] concluded that the interphase thickness in the polymer grafted nanoparticle composites increases with the percentage grafting. If the miscibility between the grafted and matrix polymer is good, a thicker interphase would be beneficial to the interfacial adhesion and hence for the mechanical properties. Meanwhile, Miltner et al. [18] proposed that an excess contribution of the heat capacity in modulated differential scanning

calorimetry (MDSC) during isothermal crystallization is directly linked to the segmental mobility of the polymer chains in the interphase. Interphase thickness of PP master batch filled with $CaCO_3$ [19], clay [20], silicate [20], glass fiber [21], carbon nanotube [22] and graphite nanoplatelet [22] has been characterized to be in a range of 30 to 600 nm through atomic force microscopy (AFM) [21, 22] or theoretical modeling using experimental data [19, 20, 23].

Effect of interphase on the structure-property relationship in master batch has also been widely discussed in the literature. X-ray photoelectron spectroscopy (XPS) and Fourier transform infrared spectroscopy (FTIR) indicated that a dense interphase layer comprising polyamide 6 (PA 6) chains had formed on the silica during melt compounding and contributed to the 76 % increase of toughness at 5 wt% silica loading [24]. On the other hand, the immobilized amorphous interphase around the layered silicates retarded the crystallization process and the resulting crystallinity reduced from 30 % to 18 % in PA 6 at 60 wt% filler loading [25]. In contrast to the many studies that focus on the glass transition temperature (T_g)-polymer chain confinement effect in the nanocomposites [26-30] or in thin films [31], fewer studies have addressed the influence of restricted polymer motion at the interphase on crystalline structure (lamella and crystal size) [18, 25, 32] and on the flow behavior of semi-crystalline nanocomposites. To this end, the structure of the interphase in polypropylene (PP)/multiwall carbon nanotube (MWNT) nanocomposite was studied by thermal analysis, wide-angle X-ray diffraction and rheology in this chapter.

8.2 EXPERIMENTAL

For the materials, MWNT functionalization and master batch preparation, please refer to Chapter 2.2.

For DSC study (using TA Instrument DSC Q100), samples were heated from room temperature to 220 °C at 2.5 °C/minute and then cooled at the same rate to room temperature and then heated again to 220 °C. Crystallization temperature (T_c) was derived from the first cooling cycle. Melting peak maximum (T_p) and the melt endotherms were derived from the first and second melting cycles. Samples were also collected after finishing one complete melting and crystallization cycle in the DSC furnace for wide angle X-ray diffraction (WAXD), thermogravimetric analysis (TGA) and scanning electron microscopy (SEM) studies. WAXD was performed using Rigaku MicroMax-002 beam generator (Cu Kα $\boldsymbol{\lambda}$= 0.1542 nm, operating voltage and current 45 kV and 0.65 mA, respectively) equipped with R-axis IV++ detector. TGA was carried out at a heating rate of 20 °C/min under air and under nitrogen atmosphere using TA Instrument Q500. Scanning electron microscopy (SEM) was carried out using Zeiss Ultra 60 FE-SEM at an accelerating voltage of 2 kV. For etching, PP/f-MWNT samples were placed in a vial containing a 60:40 mixture of orthophosphoric acid (H_3PO_4) and sulphuric acid (H_2SO_4) with approximately ½ wt.% potassium permanganate ($KMnO_4$) [33]. Etching was carried out in the vials in the ultrasonic bath for 1 hour at room temperature. After the etching treatment, samples were repeatedly washed in deionized water followed by washing in acetone. These samples were then dried in oven for 1 hour at 40 ºC. Rheological behavior was analyzed using an ARES rheometer (TA instruments, USA) in the linear viscoelastic regime at a strain of 1 %. Dynamic frequency sweep tests were performed at 190°C, 200

°C, and 220 °C in the angular frequency range of 0.1 to 400 rad/s using parallel-plate geometry (plate diameter 7.9 mm and a gap setting of 0.5 mm). To prepare the rheology sample, the master batch powers were compression molded at 215 °C using Wabash hot press (Carver Model 4386, Carver Inc., Wabash, IN).

8.3 RESULTS AND DISCUSSION

8.3.1 Structure of interphase in PP/f-MWNT master batches

The optical micrograph of f-MWNT dispersion in PP in various master batches is shown in Figure 8.1. Given the relatively large fraction (30 wt%) of f-MWNT in PP, there are more dark regions with larger sizes than in the 5 wt% and 15 wt% samples. These dark regions represent high f-MWNT concentration regions and appear to be uniformly distributed in the master batch. Assuming individually dispersed f-MWNT arranged in a perfect periodic array, 30 wt% (16 vol%) f-MWNT in the master batch yields a spacing of 30 nm between nanotubes [34]. This spacing increases to about 170 nm when the master batch contains only 1 wt% (0.6 vol%) f-MWNT [34]. Based on Karevan et al. [22] who reported an about 30 nm interphase thickness in PP/CNT system from an average of five AFM measurements, it is reasonable to assume the interphase fraction increases markedly from 1 wt% to 30 wt% f-MWNT master batch. Although there are many other complications that exist in the real system, e.g. random nanotube orientation, nanotube diameter and length variations, presence of aggregates etc., this simplified calculation provides a rough, but useful, approximation of the extent of the possible interphase. Figure 8.2 shows schematic of PP crystals across f-MWNT surfaces. While it is well-understood that isotatic polypropylene crystallizes in the spherulite form [35], addition of carbon nanotube nucleates folded-chain lamella surrounding the nanotube surfaces [6, 8]. As CNT

concentration increases, it is possible that such crystalline interphase dominates over the formation of spherulite (Figure 8.2).

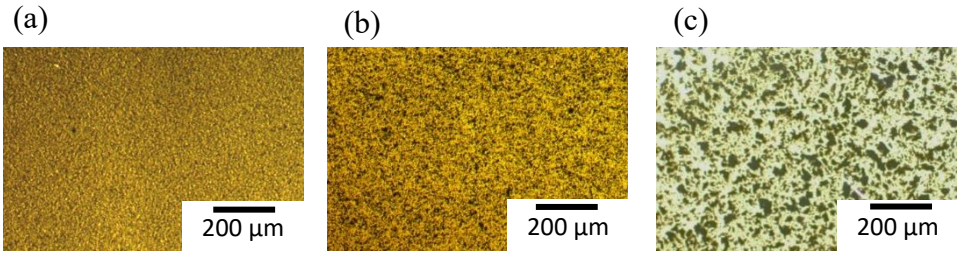

Figure 8.1. Optical images of PP/f-MWNT master batches at (a) 5 wt%, (b) 15 wt% and (c) 30 wt% f-MWNT concentration.

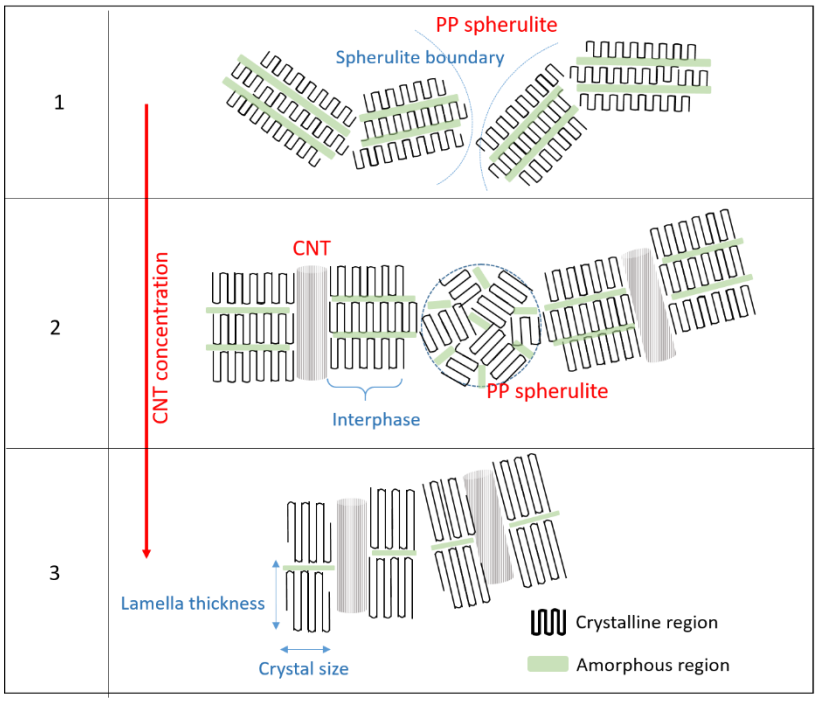

Figure 8.2. Schematic showing the effect of CNT on polypropylene crystallization and the interphase formation. As CNT concentration increases (from region 1 to 3), the crystallization of PP changes from spherulite to CNT nucleates folded-chain lamella.

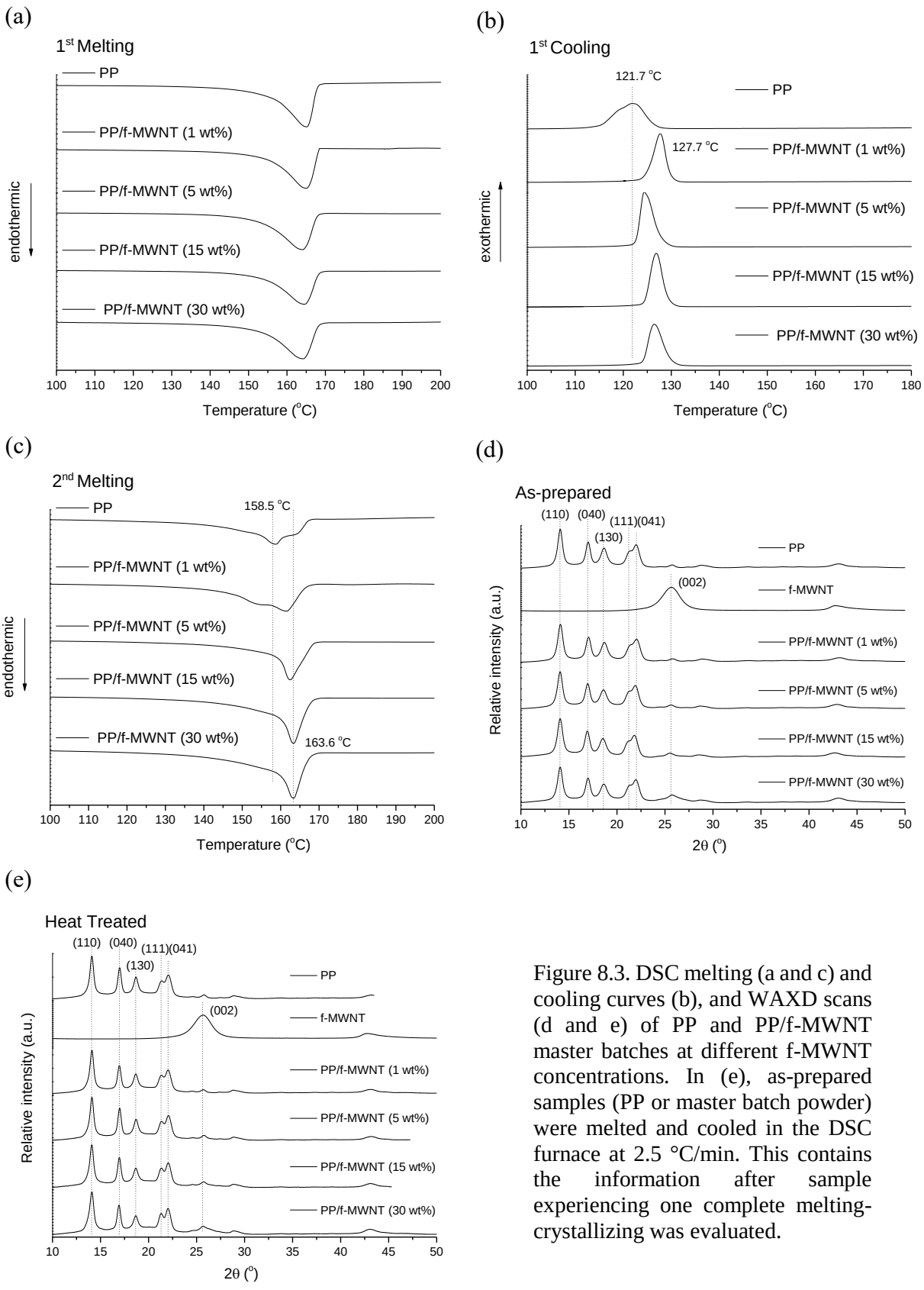

Figure 8.3. DSC melting (a and c) and cooling curves (b), and WAXD scans (d and e) of PP and PP/f-MWNT master batches at different f-MWNT concentrations. In (e), as-prepared samples (PP or master batch powder) were melted and cooled in the DSC furnace at 2.5 °C/min. This contains the information after sample experiencing one complete melting-crystallizing was evaluated.

The crystallization behavior of PP/f-MWNT master batch is given in Figure 8.3 and Table 8.1. With increased f-MWNT concentration (interphase fraction), increased crystallization temperature (T_c) and decreased FWHM of the crystallization peak as compared to that of the unfilled polymer were observed. Increased crystallization temperature suggests enhanced nucleation rate while a decreased FWHM of the crystallization peak suggests narrower crystal size distribution [36, 37]. Both indicates that f-MWNT acted as an effective nucleating agent for PP crystallization at the interface. While many have reported accelerated polymer crystallization in the presence of CNTs [6, 37-40], some have also observed a barrier effect that disturbs the crystal growth when the interphase consisted of amorphous or less-crystallizable material [25, 41].

Table 8.1. T_c, T_p, FWHM of T_c and crystallinity of PP and PP/f-MWNT master batches at different f-MWNT concentrations. DSC tests were conducted with heating and cooling rate of 2.5 °C/min.

	1st melting cycle		1st cooling cycle		2nd melting cycle	
	T_p†(°C)	Enthalpy of melting (J/g)	T_c (°C)	FWHM of T_c (°C)	T_p† (°C)	Enthalpy of melting (J/g)
PP	164.9	121.7	121.7	7.2	158.5	107.8
PP/f-MWNT master batch (1 wt%)	164.4	116.3	127.7	2.9	154.6/161.7	103.1
PP/f-MWNT master batch (5 wt%)	164.0	101.4	124.5	3.0	162.4	107.0
PP/f-MWNT master batch (15 wt%)	164.3	109.0	126.8	2.8	163.6	117.8
PP/f-MWNT master batch (30 wt%)	164.1	116.7	126.8	3.1	163.3	124.6

† Melting peak maximum

Table 8.2. Crystal size and crystallinity of PP and PP/f-MWNT master batches at different f-MWNT concentrations determined from WAXD data. (continue to next page)

	As-prepared[1]		Heat treated[2]	
	Crystallinity (%)	Crystal size (nm)	Crystallinity (%)	Crystal size (nm)
PP	67.1	13.5	64.1	17.1
PP/f-MWNT master batch (1 wt%)	62.0	12.7	67.8	17.0
PP/f-MWNT master batch (5 wt%)	67.5	12.9	70.5	17.1
PP/f-MWNT master batch (15 wt%)	68.8	12.4	69.7	16.1
PP/f-MWNT master batch (30 wt%)	68.2	11.8	70.9	14.0

1 As-prepared PP and master batches; Information about the sample right after solution processing was obtained.
2 As-prepared samples were melted and cooled in the DSC furnace at 2.5 °C/min; Information about the sample after experiencing one complete melting and crystallizing was obtained.

To understand the microstructure of the interphase, WAXD and melting endotherm from DSC were utilized to characterize lamellae dimensions (lamella thickness and crystal size). In Table 8.1 and Figure 8.3a-c, the first and second melting represent sample history corresponding to crystallization from butanol/xylene co-solvent system and from melt. Similarly, Table 8.2 and Figure 8.3d and e, provide information obtained from WAXD of the as-prepared samples after solution processing, and of the heat-treated samples that experienced one complete melting-crystallization cycle, like their second melting counterparts in the DSC experiment (Figure 8.3c). Based on the parameters in Table 8.1 and Table 8.2, there seems to be no apparent difference in melting peak maximum (T_p) of neat PP and the f-MWNT containing PP samples and a small reduction of melting enthalpy from the 1st melting cycle. Also, the crystallinity of as-prepared samples measured from WAXD are around 67-68 % except for the 1 wt% f-MWNT master batch where it was 62 %. On the other hand, from the 2nd melting cycle, a distinct change of T_p (5 °C increases in the 30 wt% master batch) and increase of melting enthalpy (about 16 % higher) with respect to the neat PP was observed. In the heat-treated samples, the crystallinity increases from 64 % to 68-70 % in WAXD when f-MWNT concentration increases. In other words, the interphase after one complete melting-crystallization from melt possesses a more perfect crystal formation, i.e. higher crystallinity and larger lamella thickness. At given melting temperature (T_m), the corresponding lamella thickness l_c can be evaluated based on Gibbs-Thomson equation: $T_m(l_c) \cong T_m^0(1 - \frac{2\,\sigma_e}{\Delta h l_c})$, where $T_m{}^0$ = 186.1 is the equilibrium melting point of PP, σ_e = 52.2 erg/cm^2 is the end surface free energy and $\boldsymbol{\Delta h}$ = 209.0 J/g denotes

the enthalpy of melting assuming 100 % crystallinity. The calculated l_c in neat PP, 5, and 30 wt% master batches are 3.3 nm, 3.9 nm and 4.1 nm, respectively. Although CNTs can act as an effective nucleating agent as mentioned earlier, most of the time the resulting crystals show a relatively moderate increase in T_m [39, 42-45] (and hence moderate increase in lamella thickness) from the literature. Normally there is only about 2 °C increase in T_m, compared with the increase in T_c where up to 15 °C can be achieved at same level of loading (20 wt% CNT in PP) [46]. According to the Hoffman nucleation model [47], the crystal formed at higher temperature (less super cooling ΔT, where $\Delta T = T_m^0 - T_c$) should have larger lamella thickness and therefore higher melting point. This failure in achieving ordered crystalline structure with larger lamella in PP/CNT can be attributed to poor CNT/polymer interaction and poor CNT dispersion that disturb the crystallization process as described in our previous works (Chapter 2 and Chapter 5). The formation of interphase containing higher crystalline perfection in this work can thus be ascribed to the following two reasons. Firstly, the co-solvent based master batch preparation process affords good CNT dispersion. Secondly, the interaction between f-MWNT and polypropylene is not disturbed given that they are bonded non-covalently instead of covalently [13].

The crystal size of the f-MWNT filled samples decreases as f-MWNT concentration increases (Table 8.2), which is also more pronounced in those samples after one melting-cooling cycle. The reduction of crystal sizes can be understood as the depletion of polymer between adjacent nanotubes during crystallization which becomes more apparent when two nanotubes are very close to each other, as the result of high CNT concentration. Interphase containing larger lamella thickness with reduced crystal size was also observed in the nanocarbon filled polyvinyl alcohol [32]. The author correlated this development of

lamellae microstructure with increased tensile modulus and yield strength [32] (up to about 200 % in both). It is worth noting that there was no β-form crystal induced by f-MWNTs in all our cases (Figure 8.3). This is different from what was observed on CNT fiber filled PP system by Abdou et al. [48].

The discrepancy of the interphase microstructure formation between solution crystallization in co-solvent and melt crystallization can be explained from the aspect of polymer mobility. The as-prepared PP and PP/f-MWNT samples were crystallized at 60 °C in xylene/butanol mixture. Normally PP dissolves in xylene at 100 °C. Although the selection of 60 °C affords stable f-MWNT dispersion that enables the adsorption of PP chains forming few layers of coating, the chain mobility may not be high enough to arrange itself into a more ordered form on f-MWNT surface. As a result, no obvious trend is shown in the structural parameters, except for the reducing crystal size, in the interphase as f-MWNT concentration increases when crystallizing from solution (1^{st} melting cycle in Table 8.1, and as-prepared sample in Table 8.2). On the contrary, larger lamella thickness, higher enthalpy of melting, and higher crystallinity were found in the interphase when the samples were melted and crystallized in the presence of f-MWNT (2^{nd} melting cycle in Table 8.1 and heat-treated sample in Table 8.2). Different interfacial morphological structures were also reported in polyacrylonitrile/CNTs under different processing conditions [4] (solution concentration, presence of shear force, etc.).

Given that higher crystallinity and higher enthalpy of melting were found in the high f-MWNT loadings samples, where higher amount of polymer is considered converted into the interphase (Table 8.1 and Table 8.2), acid etching of these master batches (5, 15 and 30 wt%) was carried out to further distinguish the interphase from bulk polymer. The

details of acid etching treatment are provided in the experimental section. The objective of acid treatment is to remove amorphous and less stable PP crystal (especially from the bulk) [33]. SEM images of the master batches before and after acid treatment are shown in Figure 8.4. Based on these images, it is evident that more PP was preserved in the PP/f-MWNT (15 wt% and 30 wt%) than in the 5 wt% master batch. To quantify the difference, the residual weight of the samples was determined from the weight difference before and after the treatment. There was about 47 % polymer remained after acid etching in the 5 wt% master batch while there was about 68 % and 72 % residual polymer in the 15 wt% and 30 wt% master batches, respectively. This result supports the argument that the interphase contains crystals with higher structural perfection and greater amount of PP is converted into interphase in the 15 and 30 wt% samples than in the 5 wt% sample.

Comparison of the derivative weight loss from TGA between the samples before and after acid treatment at 5 wt% f-MWNT confirmed that the interphase comprises of polymer with higher decomposition temperature (Figure 8.5a), i.e. higher thermal stability. Similar result has been reported in our previous work (Chapter 2), where the residual polymer after xylene wash at 70 °C also showed a upshift of maximum weight loss rate (T_{max}) in the derivative weight loss curve. For the 15 wt% and 30 wt% master batches, the derivative weight loss curve do not have a distinct difference before and after acid treatment (Figure 8.5b-c) suggesting that the thermal property of the two samples is dominated by the characteristic of the interphase.

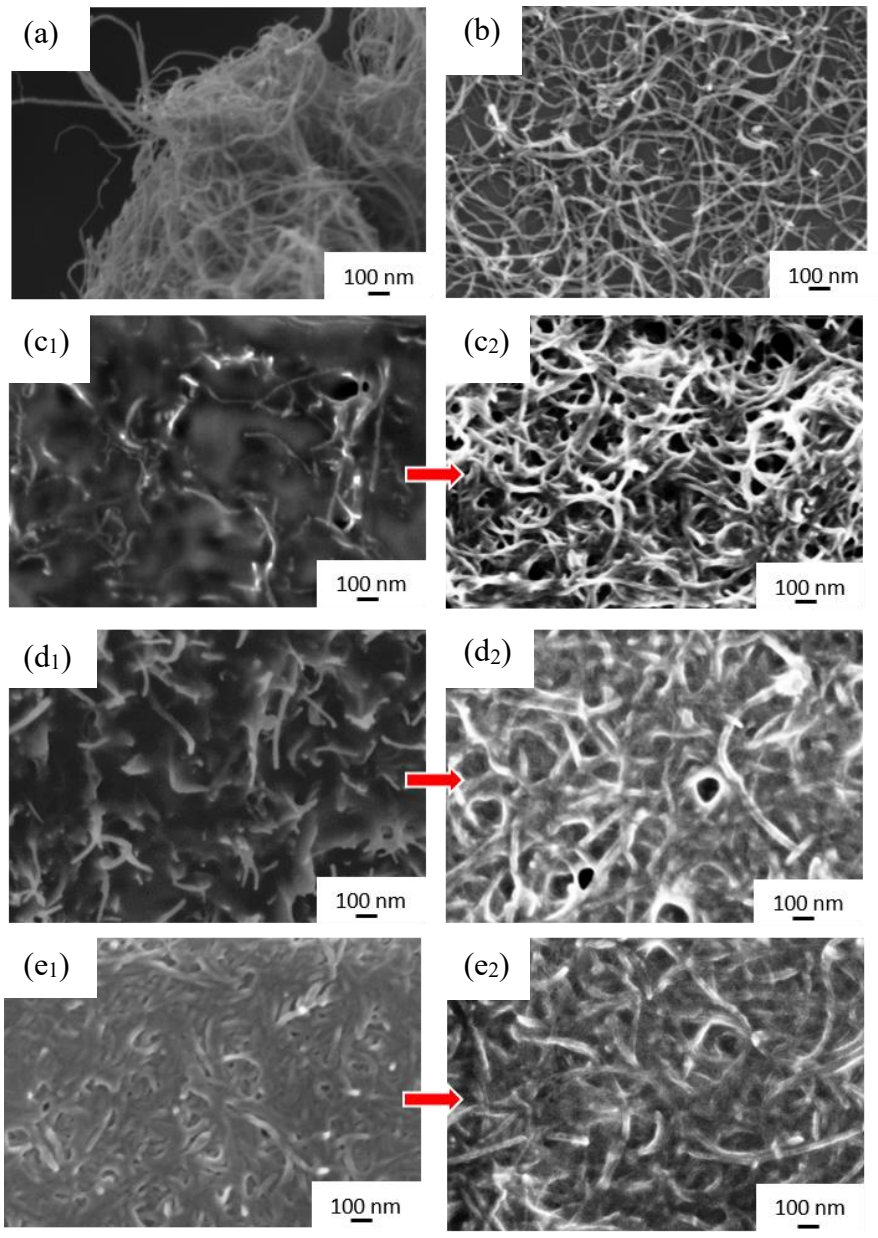

Figure 8.4. SEM images of (a) f-MWNT, (b) f-MWNT after bath sonication in butanol for 48 hours, PP/f-MWNT master batches at (c_1, c_2) 5 wt%, (d_1, d_2) 15 wt% and (e_1, e_2) 30 wt% f-MWNT concentration before (c_1, d_1, and e_1), and after (c_2, d_2, and e_2) acid treatment.

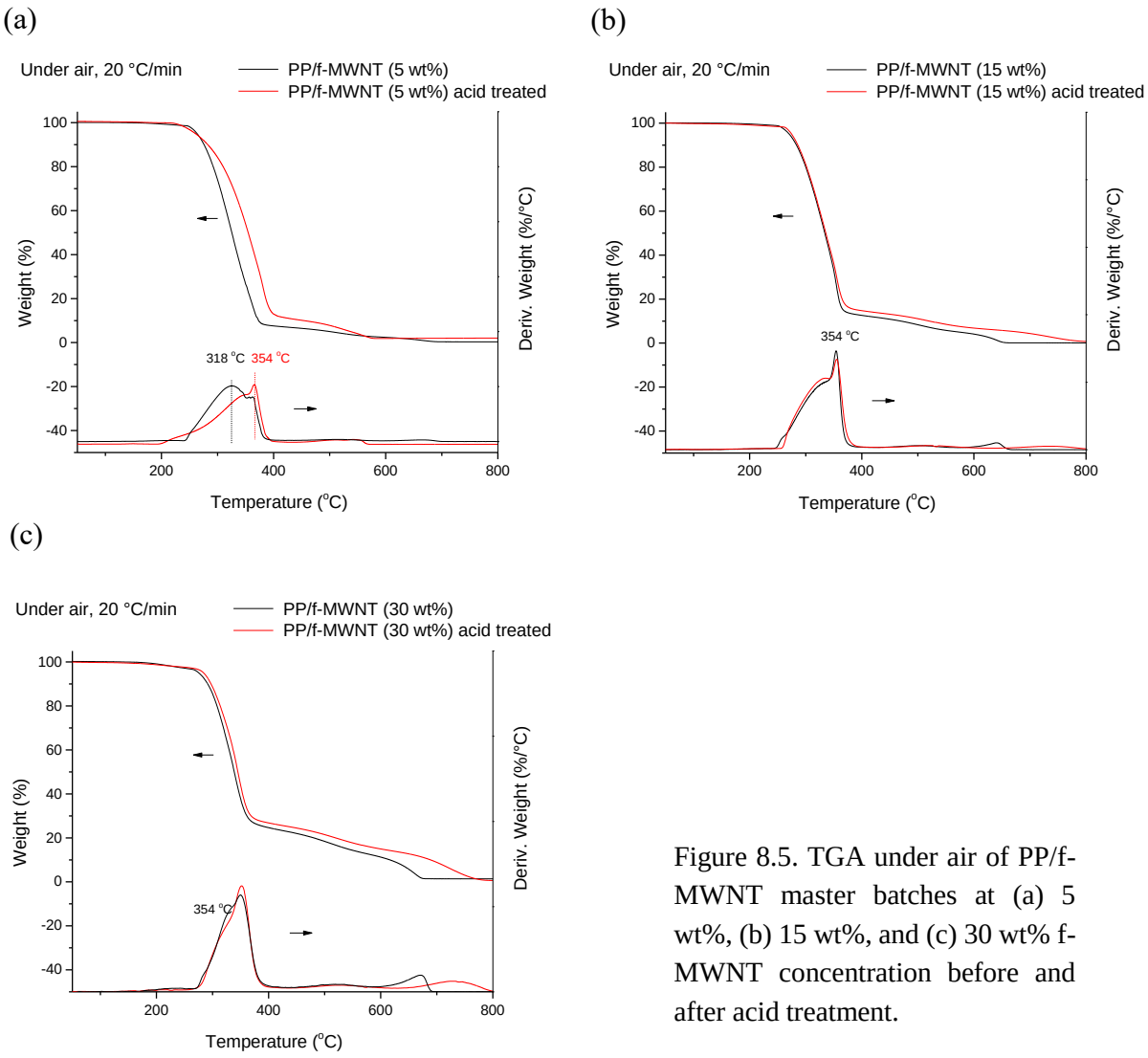

Figure 8.5. TGA under air of PP/f-MWNT master batches at (a) 5 wt%, (b) 15 wt%, and (c) 30 wt% f-MWNT concentration before and after acid treatment.

8.3.2 Bonded polymer at PP/f-MWNT interface

As previously mentioned, the nucleating and crystalline templating capability of CNTs successfully transform the PP at the interphase into a more ordered structure. Since the interphase is a gradual change of polymer dynamics and can become less effected when the polymer is away from CNT, it would be interesting to see how the strongly interacted or bonded polymers at the f-MWNT surface behave with respect to the loosely-bonded

polymers. There is about 4 to 5 nm thick polymer coating on f-MWNTs, based on Chapter 2, and this layer can also be seen in Figure 8.6. We consider that this 4 to 5 nm thick layer of PP strongly interacts with f-MWNT, and is referred as "bonded polymer" in Figure 8.7. On the other hand, the rest of PP is referred to as "non-bonded polymer". Note that the concept of bonded/non-bonded polymer is little different from the concept of interphase: if the non-bonded polymer crystallized onto the existing lamellae that nucleated from the CNTs, it will still be considered as the interphase. That is, the span of the interphase can be much longer than the thickness of bonded polymer on CNTs.

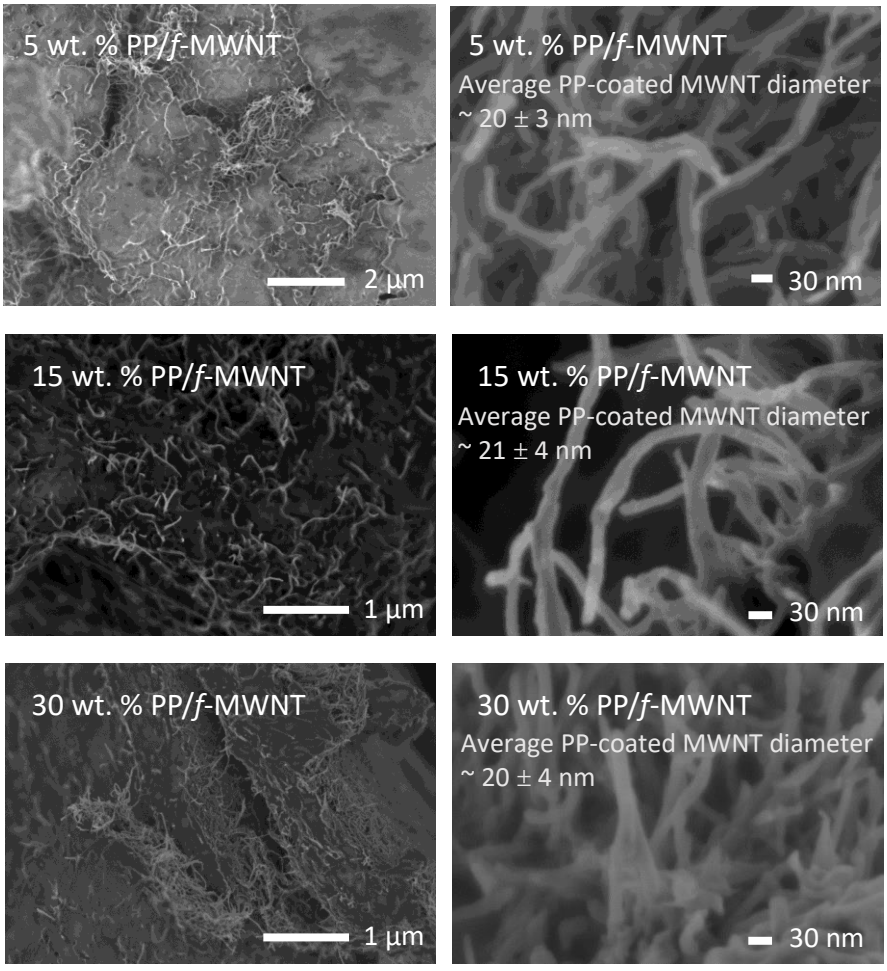

Figure 8.6. SEM images of PP/f-MWNT master batches (as prepared; without any treatment) at 5 wt%, 15 wt% and 30 wt% f-MWNT and the corresponding average PP coated f-MWNT diameters.

The distance between two adjacent CNTs assuming individually arranged in a perfect periodic array can be calculated from the following equation [34]:

$$CNT - CNT\ distance = D_{CNT}\sqrt{\frac{\pi(100 - f_m)\cdot\rho_{CNT} + f_m\cdot\rho_{PP}}{2\sqrt{3}\cdot f_m\cdot\rho_{PP}}}$$

Where D_{CNT} is the CNT diameter, f_m is the mass fraction of CNTs, and $\boldsymbol{\rho}$ is the density. Based on this equation, CNT to CNT distance in the 5 wt% and 30 wt% master batch, assuming CNT diameter of 12 nm and density of 2.1 g/cm^3, is about 78 nm and 30 nm, respectively.

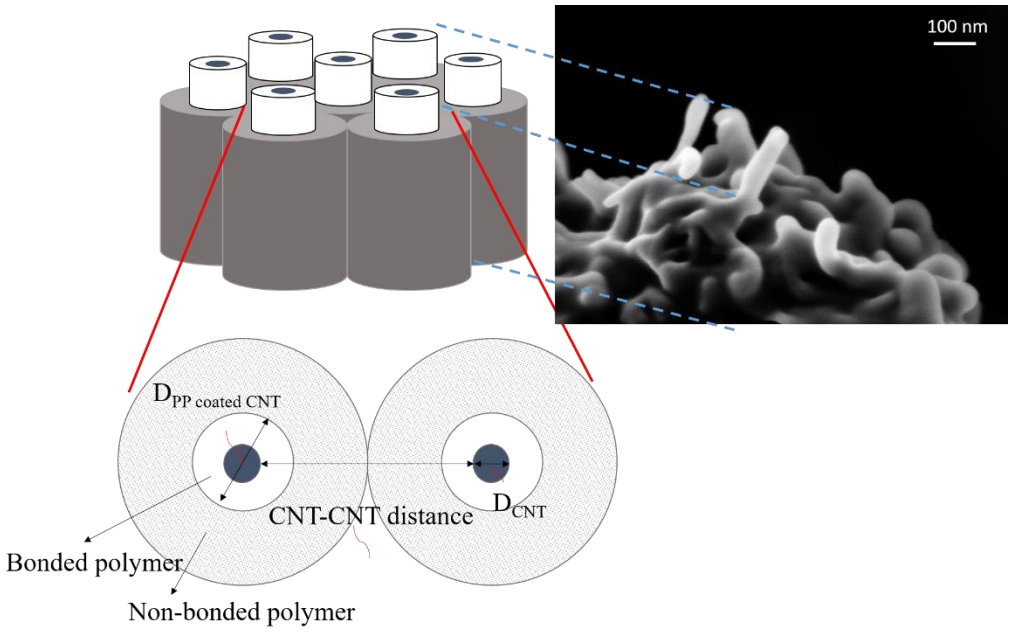

Figure 8.7. Schematic of CNT-CNT distance. and bonded and non-bonded polymer.

To characterize the structure of the bonded polymer on f-MWNT, as-prepared 30 wt% master batches was treated in xylene at 80 °C for 30 minutes. Figure 8.8a shows the SEM images of the resulting sample. The diameter of these coated f-MWNTs is measured using an image analysis software ImageJ. From average of 50 measurements, the diameter is 21.2 ± 5 nm, indicating 4 to 5 nm of polymer coating on f-MWNT (diameter of MWNT is 12 ± 3 nm). Assuming all f-MWNTs are arranged in an ordered array with homogeneously coated "bonded polymer" layer followed by the "non-bonded polymer" layer (schematic in Figure 8.7) and the latter is completely removed after treatment. Given the fact that about 74% of polymer was removed by the xylene treatment, a calculation based on the simplified model yields about 5 to 6 nm of the bonded polymer. This estimation is in good agreement with the measured coated f-MWNT diameter from SEM (Figure 8.8) and confirms that most of the non-bonded polymer were dissolved and washed away during xylene treatment leaving the bonded polymer at the CNT surface. Melt endotherm from second melting cycle shows a 4 °C higher T_p (From 163.3 °C to 167.3 °C) after xylene treatment in the 30 wt% master batch (Figure 8.9). The corresponding lamella thickness (based on DSC) increases from 4.1 nm to 5.0 nm implying a more extended polymer conformation in the interfacial bonded polymers than for the loosely or non-bonded polymers.

It is worth mentioning that the presence of γ-type PP was observed in the xylene treated sample from the WAXD scans (Figure 8.9b). γ-type i-PP is considered a rare type of crystal compared with α and β type i-PP. Normally γ-type crystal can be obtained through crystallizing under high pressure (e.g. 5000 atm) or by special synthesis (e.g. use of metallocene catalysts instead of Ziegler-Natta catalysts) [49]. Also, a very small fraction

of γ-type crystal was found in the injection molded PP/CNTs nanocomposites (above 0.3 wt% f-MWNT) as reported in Chapter 3.

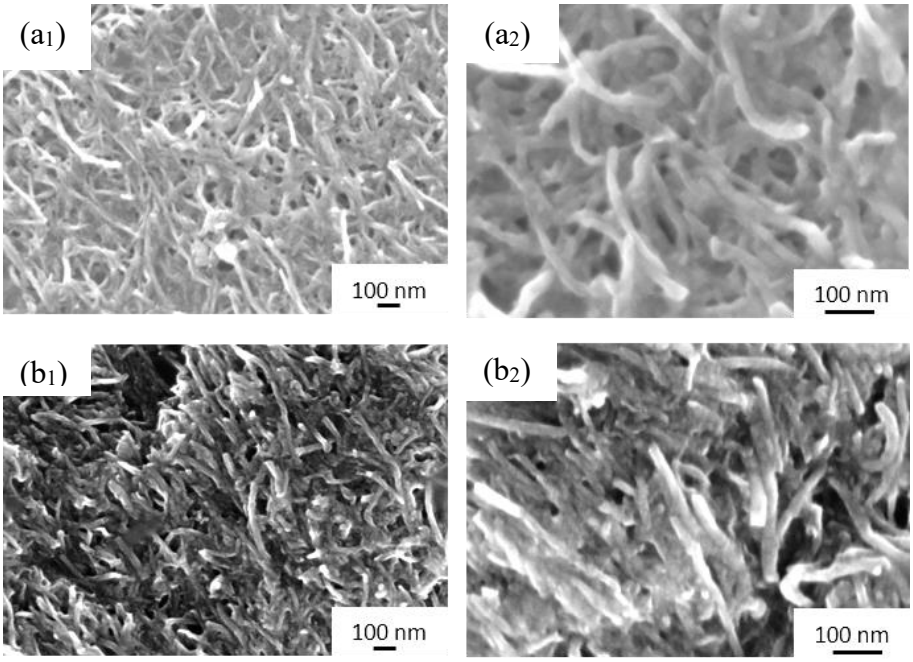

Figure 8.8. SEM images of PP/f-MWNT (30 wt%) master batch (a_1, a_2) after xylene treatment at 80 °C for 30 minutes revealing PP interphase and (b_1, b_2) repeatedly melting/re-crystallization processes forming columnar crystalline interphase.

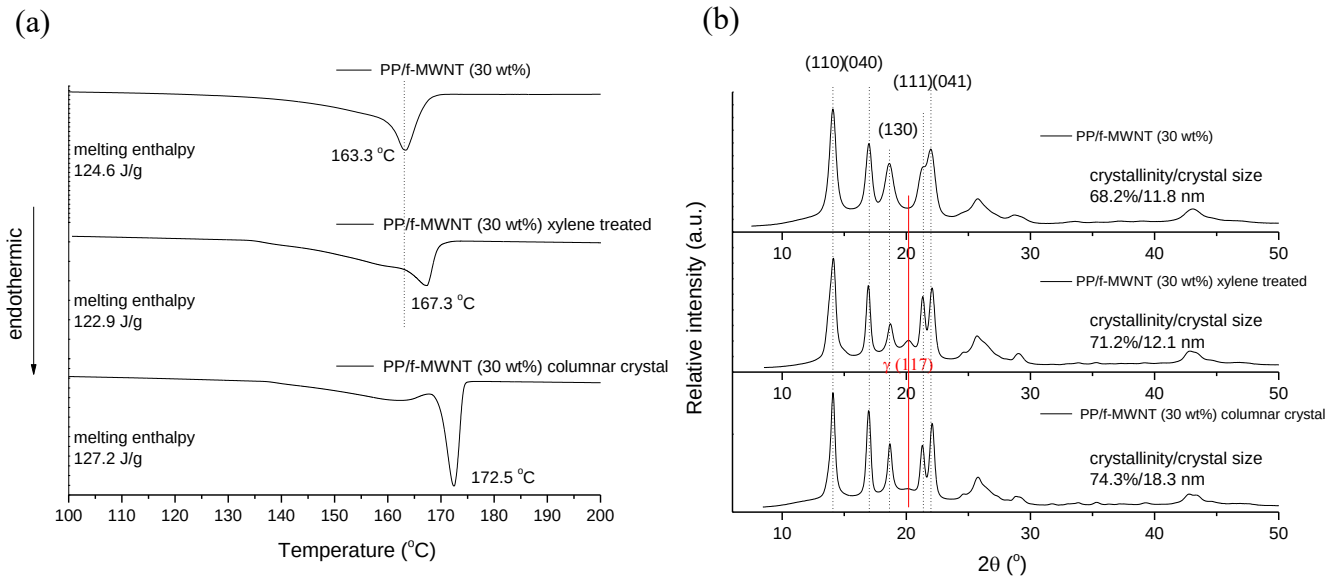

Figure 8.9. (a) DSC melting curve and (b) WAXD scans of PP/f-MWNT master batch before and after xylene treatment, or repeatedly melting/re-crystallization treatment.

8.3.3 Tailoring the interphase in PP/f-MWNT master batches

A designed heating and cooling profile was applied to the 30 wt% master batch. The details of this thermal treatment can be found in Chapter 5 (section 5.3.2). The objective of this experiment was to partially melt the crystal with smaller lamella thickness and leaving the more "perfect" crystals with more extended conformation (thus larger melting point) as templates for subsequent crystallization upon cooling. It is expected, that after such treatment, that the structure of the tubular coating on the f-MWNT can further be refined. In Figure 8.8b, a columnar crystalline interphase with average diameter of 23.8 ± 4 nm was observed. Similar morphology had also been observed in 5 wt% master batch using similar thermal treatment (Chapter 5.3.2). This observation demonstrates the successful of tailoring the interphase in PP/CNT master batch. Melt endotherm from second melting cycle exhibits a sharp peak at 172.5 °C which corresponds to the lamella thickness of 6.8 nm (Figure 8.9a). The DSC results along with the SEM images (Figure 8.8b and 8.9a) suggest that this columnar crystalline interphase contains uniform and highly extended lamella (lamella thickness of 6.8 nm as compared to that of 3.3 nm in the bulk polymer). Considering the similarity between MWNT and polymers, as suggested in some studies [50, 51], the presence of MWNT lowers the barrier of PP chain alignment. The resulting extended-chain conformation is considered more advantageous in stress transfer between polymer and CNT and possibly brings about significant improvement in mechanical properties of the nanocomposite. Microwave irradiation [52], for example, is one possible approach to locally raise the temperature at polymer/CNT interface for tailoring the interphase and inducing more refined crystal without disturbing the bulk property (such as loss of chain orientation due to entropic relaxation).

Based on the SEM image (Figure 8.8b), the columnar crystalline layer is about 6 nm thick. Using the same model as described before (Figure 8.3), this corresponds to about 27 % of the polymer to the total polymer volume. This ratio is consistent with that of area under the 172.5 °C peak to the whole melt endoderm (about 25 %) in Figure 8.9a. It should be noted that 25 % is not an upper limit of volume percentage polymer that can be tailored and converted into a more extended conformation in this PP/f-MWNT system utilizing thermal treatment. In Chapter 5, the columnar crystal had about 26 nm of thickness in the 5 wt% PP/f-MWNT which corresponds to nearly 50 % of the total volume. About 33 % of the area was found under the 172.5 °C peak to the whole melt endoderm (Figure 5.9 in Chapter 5). The limiting factor of volume percentage polymer which is tailored through thermal treatment might be the available material at the growing crystal front. When nanotubes are very close to each other (at high concentration), templated growing crystals from CNT surface soon meet with each other and compete for the material that has not yet crystallized. In a more diluted CNT case, such as 5 wt%, the CNT to CNT average distance is 78 nm compared to that of 30 nm in 30 wt% master batch. As a result, the growing columnar crystals have sufficient materials at the crystal front to form a longer interphase at lower MWNT concentration.

8.3.4 Thermal stability of the PP/f-MWNT master batches

The gradual change of polymer dynamics approaching the carbon nanotube surface causes the change in the degradation temperature of PP under air and nitrogen. Figure 8.10 shows the variation in the weight and derivative of the weight loss as a function of temperature in TGA experiments. Under air, the temperature of maximum weight loss rate (T_{max}) increases from 318 °C to about 354 °C in f-MWNT containing samples (from Figure

8.10c). There is a shoulder located around 318 °C in the 5 wt%, 15 wt%, and 30 wt% master batches indicating the decomposition of bulk polymer occurred prior to the polymer at the interphase region which is thermally more stable. Also, from Figure 8.10c and Table 8.3, the start of weight loss from derivative weight change increases from 207 °C in PP to 273 °C in PP/f-MWNT (30 wt%). Similarly, T_{max} increases from 439 °C to around 476 °C in PP/f-MWNT master batches under nitrogen (from Figure 8.10d). The start of weight loss first increases from 320 °C to around 425 °C in 1 wt% and 5 wt% samples and then decreases slightly to 400 °C in 15 wt% and 30 wt% samples (Figure 8.10d and Table 8.3). The reduction might be due to the reactive -COOH group on f-MWNT that accelerates the polymer degradation under nitrogen [53]. Increase in thermal stability of polymer-CNT composite can be attributed to number of factors. Firstly, the interfacial interaction between CNT and polymer restricts the thermal motion of macromolecules and increases the degradation activation energy [53, 54]. Secondly, the barrier effect of CNT network that hinders the transportation of degraded polymer product from condensed phase to gas phase [53, 55]. Thirdly, CNT demonstrates antioxidant effect due to its strong radical accepting ability that decelerates the degradation process [56]. Finally, the thermally conductive CNT networks facilitate the heat dissipation within the nanocomposite and delay the polymer degradation [55].

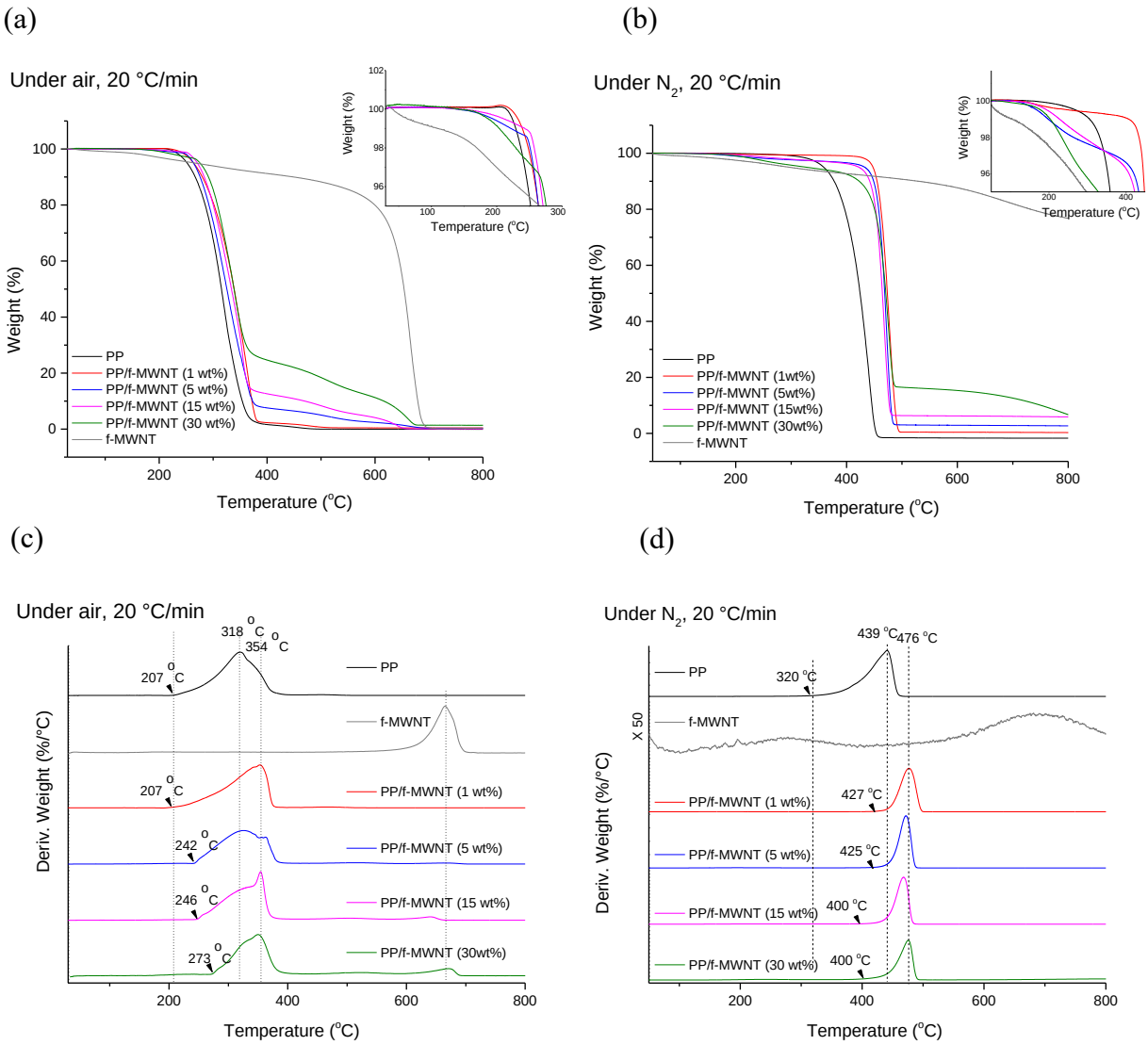

Figure 8.10. TGA under (a,c) air and (b,d) nitrogen of PP and PP/f-MWNT master batches at different f-MWNT concentrations.

Table 8.3. Start of weight loss of PP and PP/f-MWNT master batches at different f-MWNT concentrations determined from the derivative weight loss in TGA experiment.

	PP	PP/f-MWNT master batch (1 wt%)	PP/f-MWNT master batch (5 wt%)	PP/f-MWNT master batch (15 wt%)	PP/f-MWNT master batch (30 wt%)
Start of weight loss in air	207 °C	207 °C	242 °C	246 °C	273 °C
Start of weight loss in N_2	320 °C	427 °C	425 °C	400 °C	400 °C

The presence of interphase with higher thermal stability than the matrix bulk PP was further confirmed in Figure 8.11 and Table 8.4. Theoretical curves were obtained from the rule of mixture using neat PP and neat f-MWNT weight loss curves at a given ratio. It is obvious that the experimental curves shift to higher temperature than the curves obtained from rule of mixture both under air and under nitrogen. Under air, the difference of the start of weight loss between experimental and calculated curves increases from 5 °C in 1 wt% master batches to about 30-40 °C in master batches with higher f-MWNT loadings. Under nitrogen, this difference is about 80-100 °C in all master batches.

Table 8.4. Difference of the start of weight loss between curves from the rule of mixtures (using neat PP and neat f-MWNT at a given ratio) and their counterparts from the experimental data.

	PP/f-MWNT master batch (1 wt %)	PP/f-MWNT master batch (5 wt %)	PP/f-MWNT master batch (15 wt %)	PP/f-MWNT master batch (30 wt %)
ΔT (Start of weight loss in air)	5 °C	32 °C	38 °C	30 °C
ΔT (Start of weight loss in N_2)	107 °C	102 °C	97 °C	78 °C

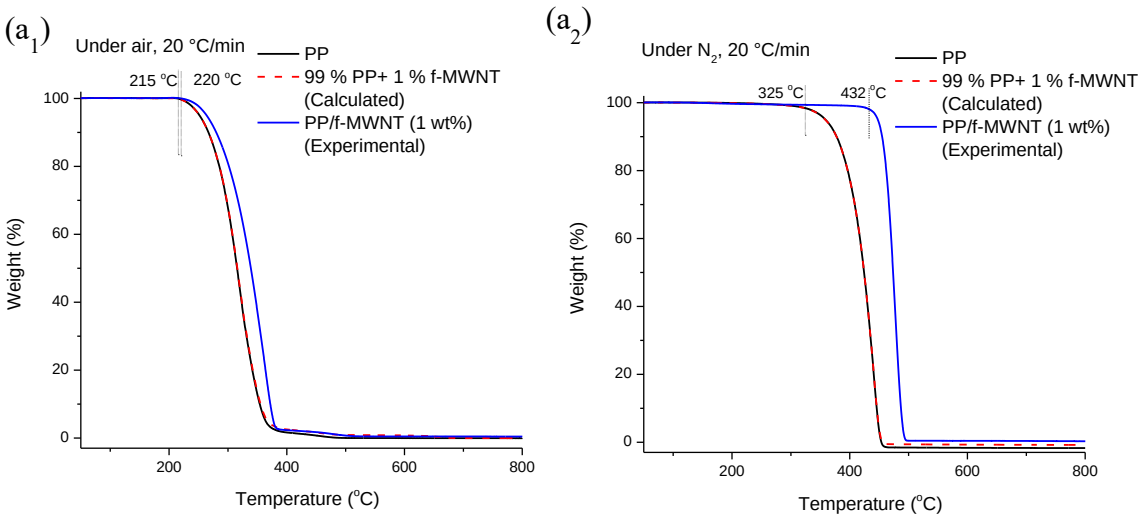

Figure 8.11. TGA under (a_1-d_1) air and (a_2-d_2) nitrogen of PP, PP/f-MWNT master batches at different f-MWNT concentrations (solid curves) and their counterparts calculated from the rule of mixture (dash curves, using neat PP and neat f-MWNT with a given f-MWNT wt%). The neat f-MWNT curve can be found in Figure 2.8. in Chapter 2. (continued to the next page)

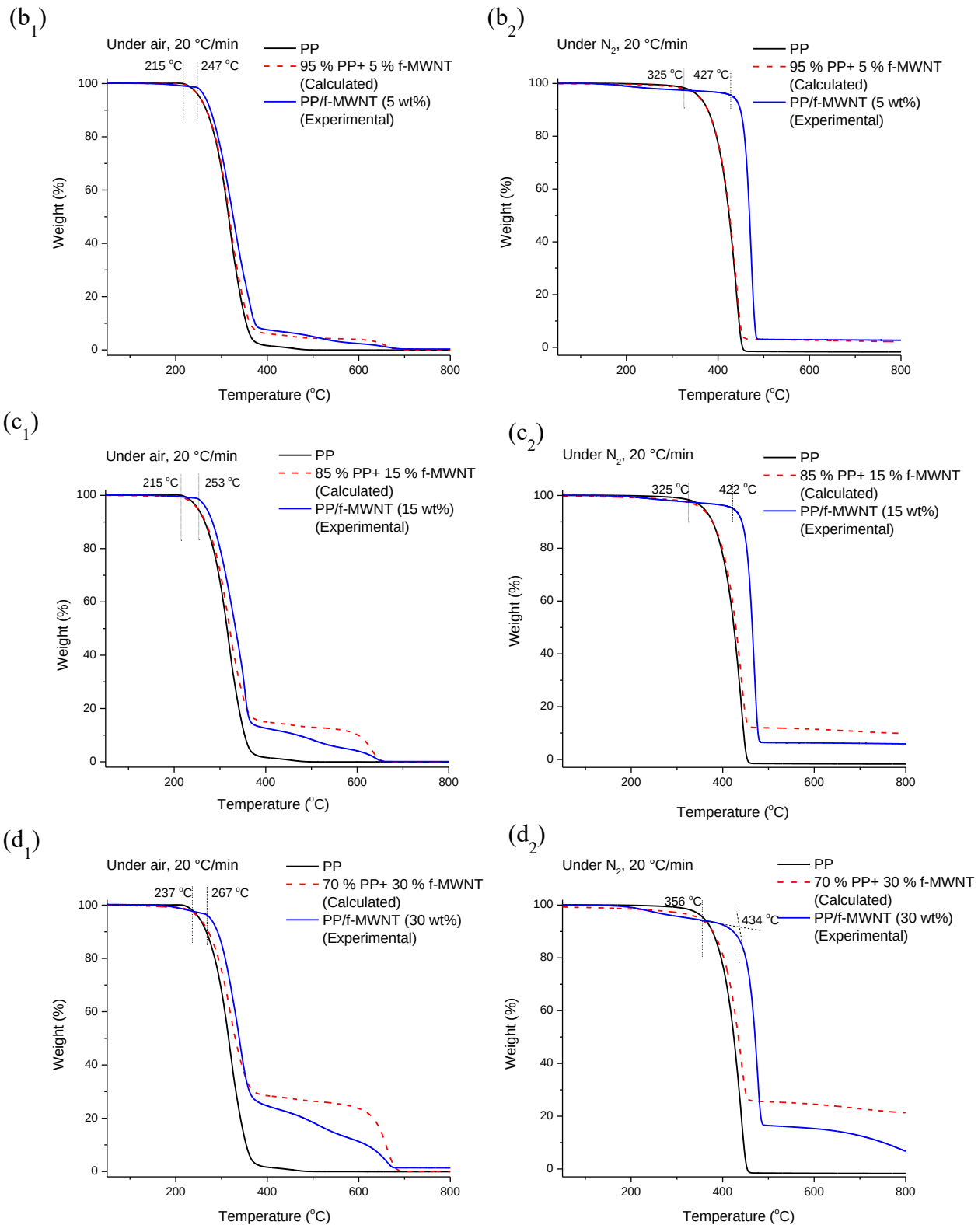

Figure 8.11. TGA under (a_1-d_1) air and (a_2-d_2) nitrogen of PP, PP/f-MWNT master batches at different f-MWNT concentrations (solid curves) and their counterparts calculated from the rule of mixture (dash curves, using neat PP and neat f-MWNT with a given f-MWNT wt%). The neat f-MWNT curve can be found in Figure 2.8. in Chapter 2. (continued from the previous page)

8.3.5 Rheological behavior of the PP/f-MWNT master batches

The rheological behavior of the PP/f-MWNT master batches was studied using dynamic frequency sweep tests, and the results are given in Figures 8.12 to 8.14. From Figure 8.12, the Newtonian plateau at low shear rate region in the neat PP disappears in the 1 wt% master batch, where the non-Newtonian behavior and the shear thinning phenomenon through the whole shear rate region studied were observed. This becomes more evident when the f-MWNT concentration increases to above 5 wt % (Figure 8.13). Also, at high f-MWNT concentration, the elastic modulus (G') deviates from the terminal behavior ($G' \sim \omega^2$) and becomes less dependent on the shear rate (slope of 0.11) signifying that the rheological behavior at low shear rate region is dominated by the interconnecting CNT network. From Figure 8.14, it is evident that above 5 wt%, G' is always larger than the G" in the studied frequency range. Moreover, G' exhibits a greater change than G" when temperature increases, especially under high f-MWNT loadings. In the system where elastic characteristic dominates over the viscous one, G' will be more sensitive to the structural change, such as the formation of polymer-filler or filler-filler network [78-81]. This is also observed in Chapter 6 (Figure 6.14 and 6.15) where G' showed a greater change than G" after annealing. In Figure 8.14, both G' and G" increase when temperature increases and since complex viscosity $\eta^* = \frac{(G'^2+G''^2)^{\frac{1}{2}}}{\dot{\gamma}}$, this abnormal increase of $\eta^*$with temperature will be discussed in the next section (section 8.3.6).

The restrained polymer segmental motion imposed by the filler-polymer interaction can be characterized through the relaxation spectrum. The longest relaxation time, also known as the weight average relaxation time (τ_w), illustrates the long-time behavior of the macromolecules in the terminal region (low shear rate region) [57, 58]: $\tau_w = \eta_0 J_e^0$, where

η_0 is the zero shear viscosity and J_e^0 is the plateau shear compliance. Based on this equation, the determined longest relaxation time at 190 °C, 200 °C and 220 °C versus f-MWNT concentration is given in Table 8.5. The relaxation time increases by two orders of magnitude in the PP/f-MWNT master batches implying restricted flow behavior owing to strong interaction between PP and f-MWNT.

At high shear rate, the effect of f-MWNT becomes insignificant due to the breakdown and alignment of the CNT network. This can be found in neat PP and the 1 wt%

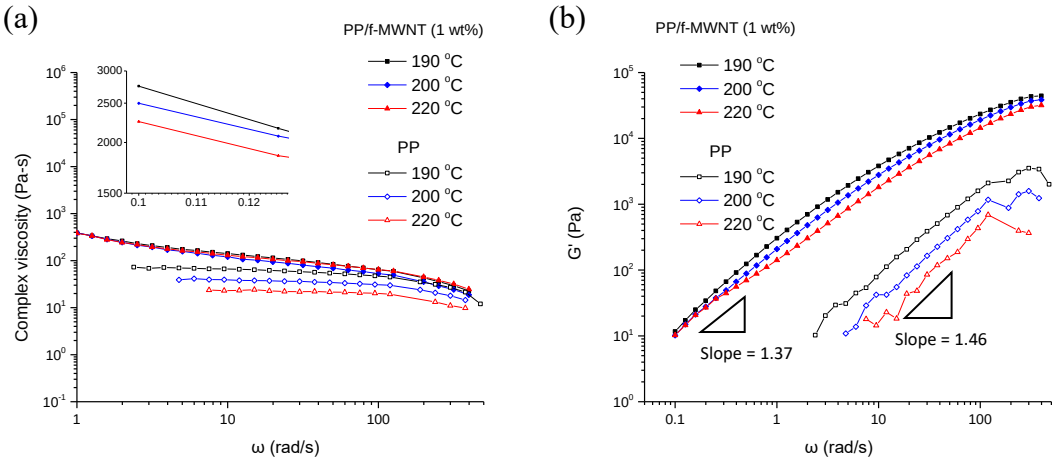

Figure 8.12. (a) Complex viscosity and (b) G' as a function of frequency of PP and PP/f-MWNT (1 wt%) master batch at 190, 200 and 220 °C.

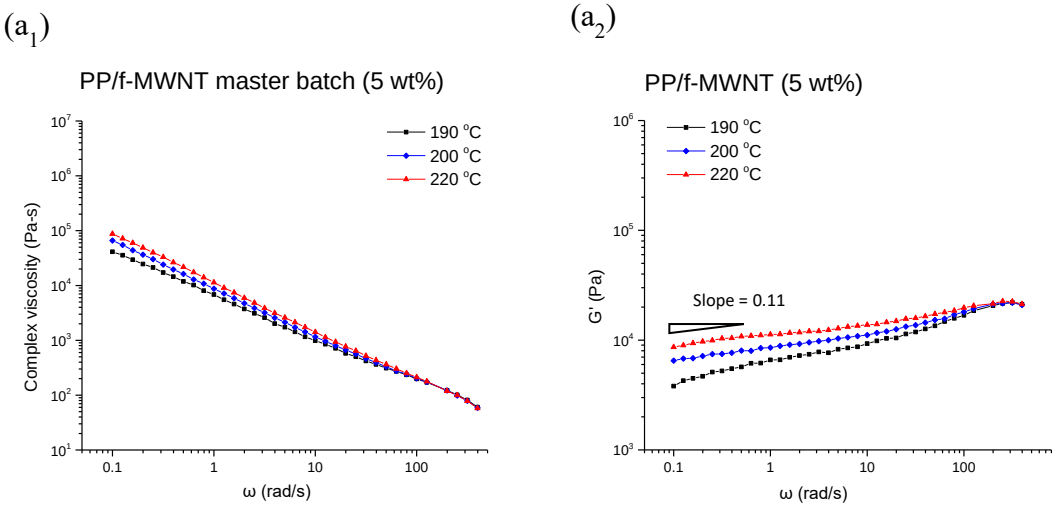

Figure 8.13. (a_1, b_1, and c_1) Complex viscosity and (a_2, b_2, and c_2) G' as a function of frequency of PP/f-MWNT master batches at 5 wt%, 15 wt%, and 30 wt% f-MWNT concentrations at 190, 200 and 220 °C. (continued to the previous page)

and 5 wt% master batches (Figure 8.12 and Figure 8.13a), where viscosity values converge to about 10 ~100 Pa-s at 300 - 400 rad/s. While at higher f-MWNT concentration (Figure 8.13b and 8.13c), the value increases to about 250 Pa-s (15 wt% master batch) and above 300 Pa-s (30 wt% master batch) due to the influence of CNT network as well as the confined polymer motion via filler-polymer interaction at the interphase (Chapter 6).

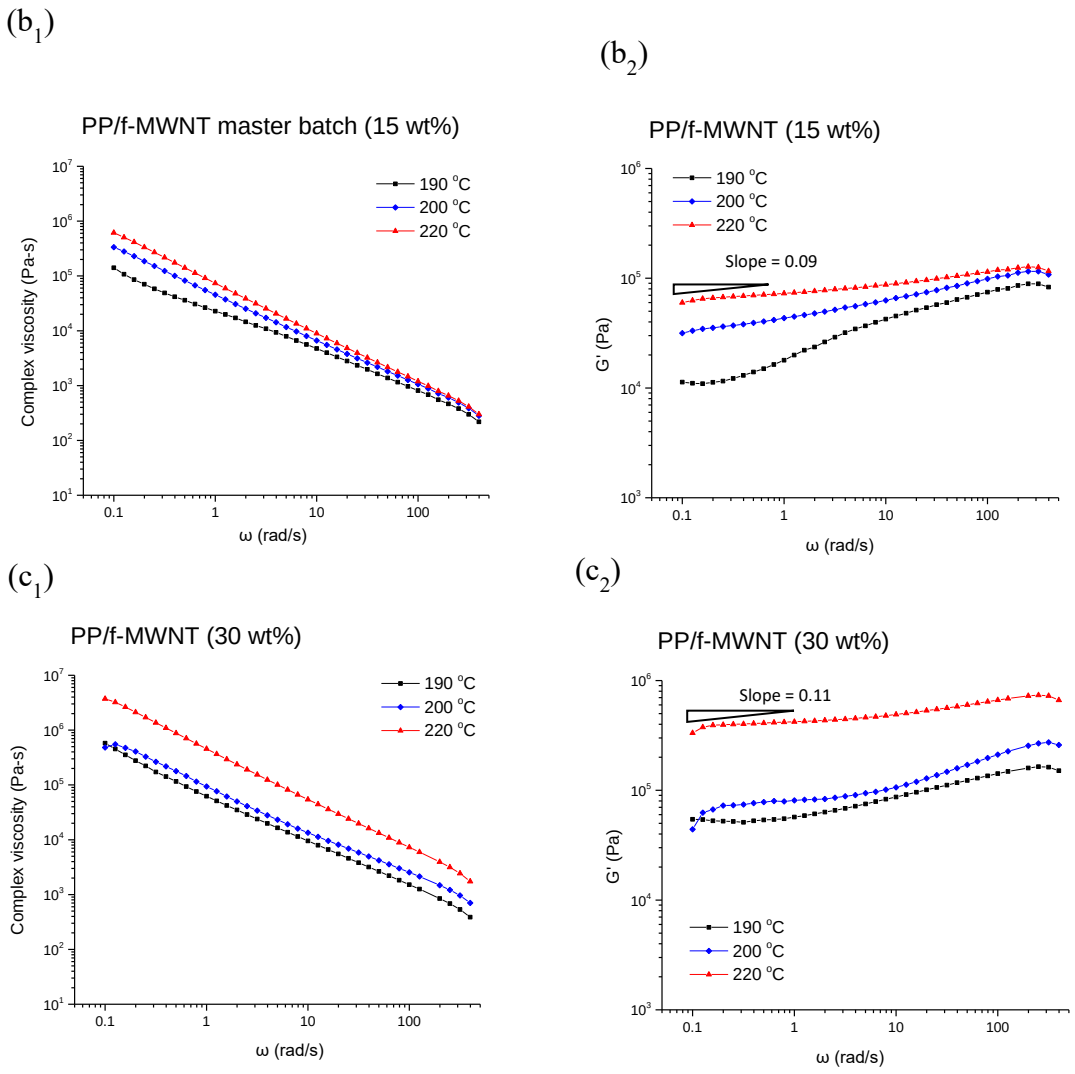

Figure 8.13. (a_1, b_1, and c_1) Complex viscosity and (a_2, b_2, and c_2) G' as a function of frequency of PP/f-MWNT master batches at 5 wt%, 15 wt% and 30 wt% f-MWNT concentrations at 190, 200 and 220 °C. (continued from the previous page)

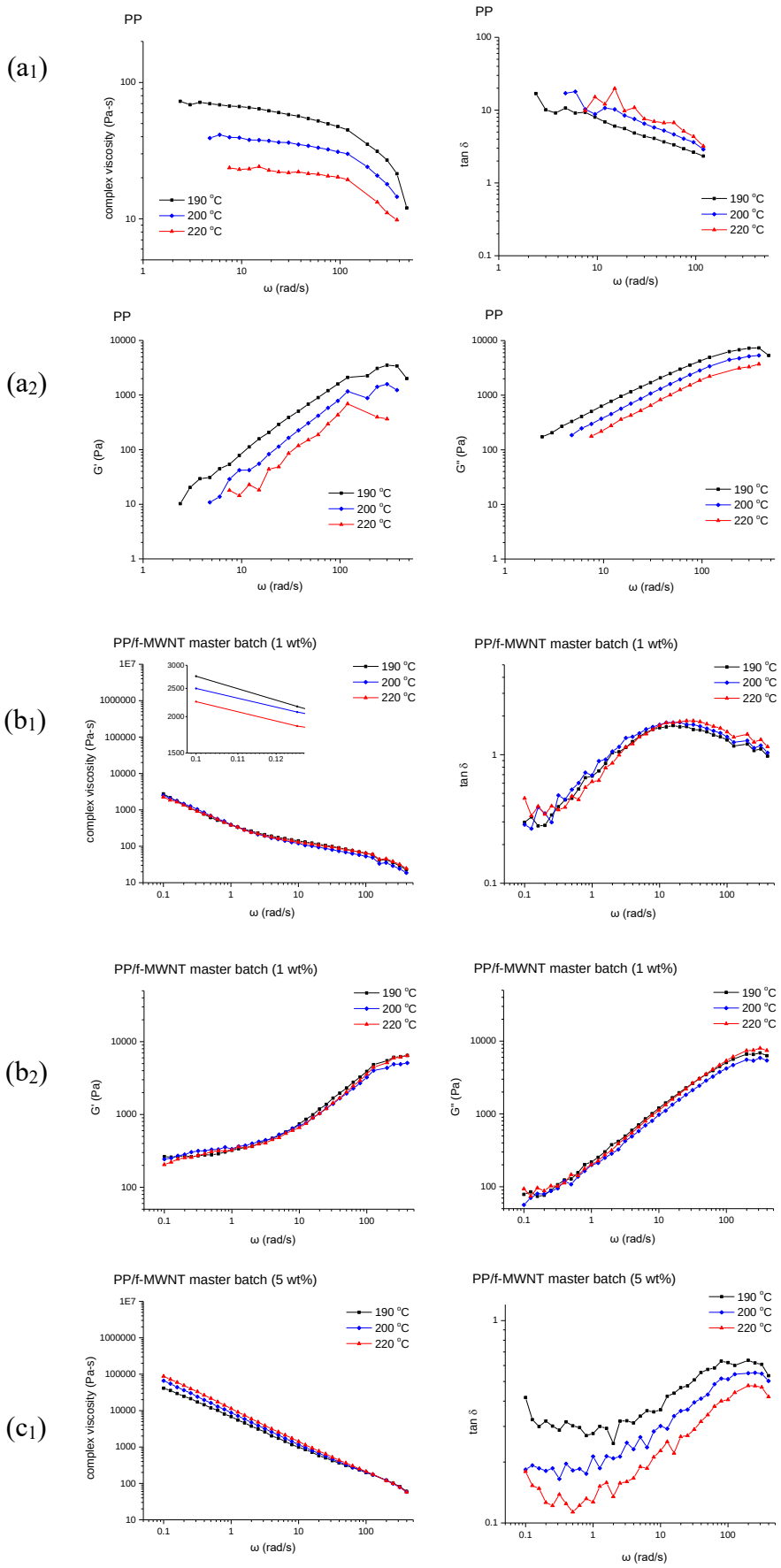

Figure 8.14. Complex viscosity, tan δ, G' and G" of (a) PP and PP/f-MWNT master batches at (b) 1 wt%, (c) 5 wt%, (d) 15 wt%, and (e) 30 wt% f-MWNT concentration at 190, 200 and 220 °C. (continued to the next page)

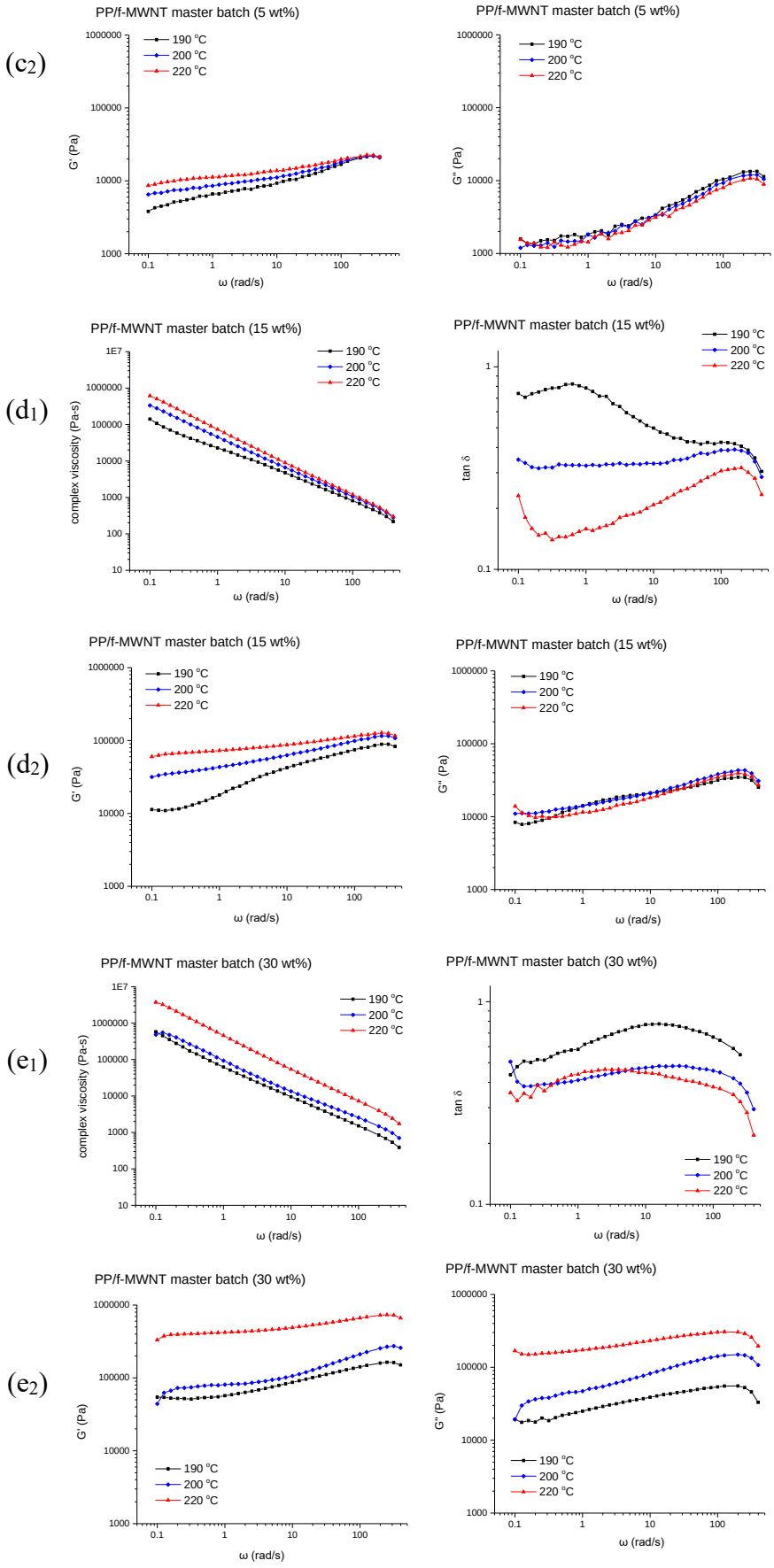

Figure 8.14. Complex viscosity, tan δ, G' and G" of (a) PP and PP/f-MWNT master batches at (b) 1 wt%, (c) 5 wt%, (d) 15 wt%, and (e) 30 wt% f-MWNT concentration at 190, 200 and 220 °C. (continued from the previous page)

Table 8.5. Longest relaxation time of PP and PP/f-MWNT master batches at different f-MWNT concentrations.

	190 °C	200 °C	220 °C
PP	0.1 s	0.04 s	0.02 s
PP/f-MWNT master batch (1 wt %)	34.8 s	33.0 s	31.4 s
PP/f-MWNT master batch (5 wt %)	30.1 s	33.8 s	34.0 s
PP/f-MWNT master batch (15 wt %)	28.8 s	34.2 s	33.5 s
PP/f-MWNT master batch (30 wt %)	35.9 s	42.8 s	94.1 s

In the case of homopolymer melt, the slope of G' versus G'' log-log plot decreases from its theoretical value of 2 as the level of heterogeneity within the melt increases. i.e. in the presence of chain entanglements, fillers and additives, or polymer interphases [59, 60]. In Table 8.6, this slope is shown to be 1.58 in neat PP and reduces to 1.18 in the 1 wt% master batch. A significant downshift in slope was observed in the master batch above 5 wt% concentration. Similar observation was reported by literature studies [61, 62], where the phenomenon was attributed to the microstructure change above the rheological percolation threshold. Formation of interphase that consists of polymer chains with impeded motion can also be a reason for such deviation.

Table 8.6. Slope of G' to G" log-log plot at 190 °C, 200 °C, and 220 °C of PP and PP/f-MWNT master batch at different f-MWNT concentrations.

	190 °C	200 °C	220 °C
PP	1.58	1.58	1.58
PP/f-MWNT master batch (1 wt %)	1.18	1.18	1.18
PP/f-MWNT master batch (5 wt %)	0.45	0.36	0.3
PP/f-MWNT master batch (15 wt %)	1.14	0.88	0.39
PP/f-MWNT master batch (30 wt %)	1.0	0.69	0.53

8.3.6 Abnormal rheological behavior as a function of temperature in PP/f-MWNT due to the interphase

The temperature (T) dependence of viscosity in polymer melt generally can be given by Arrhenius equation [63], $\eta_0(T) = A \exp(^{\Delta E}/_{RT})$, where η_0 is the zero-shear viscosity. $\boldsymbol{\Delta}$E is the flow activation energy which is a measure of the potential energy barrier to polymer segmental motion, and R is the gas constant. Normally, $\boldsymbol{\Delta}$E is a positive number, that is, the viscosity of polymer melt decreases as temperature increases [64, 65]. In Figure 8.13, an inverse temperature dependence of viscosity was observed in 5 wt% and more predominantly in 15 wt% as well as 30 wt% master batches. To understand the thermo-rheological behavior of the polymer melt, the so-called van Gurp-Palmen plot i.e., variation of phase angle (δ) with respect to complex modulus (G^*) was used. For a thermal-rheologically simple fluid, in which all the relaxation modes of the polymer have similar response to the temperature, the δ-$|G^*|$ curve has no temperature dependence. On the other hand, thermal-rheological complexity can be qualitatively characterized by a temperature dependence of the curves [66, 67]. The van Gurp-Palmen plots for both neat PP and PP/f-MWNT master batches (1 wt% and 30 wt%) measured at different temperatures are presented in Figure 8.15. The measured data from neat PP superimpose on a single curve indicating thermal-rheological simplicity. Similarly, the curves from 1 wt% master batch also follow a similar behavior. On the other hand, the δ-$|G^*|$ curves of 30 wt% master batch demonstrate a distinct split among the measured results shows the thermal-rheological complexity. Such complexity could arise from the difference of temperature dependence on polymer motion between the bulk polymer and the interphase.

We propose that this inverse temperature dependence of viscosity behavior is due to the presence of the interphase. When the temperature increases, polymer chains become more mobile and thus, interact with CNTs more readily. Once a single polymer chain has multiple segments adsorbed on the CNT surface, its motion becomes hindered. As a consequence, the restricted macromolecular motion at the interphase brings about an increase in viscosity. The theoretical ground of this hypothesis can be supported by several studies. First, the nanoscale surface roughness of CNTs likely results in an enhanced interlocking with the polymer chains and, consequently, better adhesion. Such an effect has been demonstrated by molecular dynamics studies that show altered polymer mobility due to geometrical constraints at filler-polymer interfaces. For example, through molecular dynamics simulation, Starr et al. found that the chains near (~ radius of gyration) the nanoparticle surface are elongated and flattened [68]. As a result of such constraint, polymer at the interphase can exhibit large shift in T_g of nearly 30 to 40 °C [26, 69]. Second, in some literature studies, an increased polymer-filler interaction has been observed with increasing temperature. For example, Pötschke et al. [70] has found a reduced percolation threshold from 5 to 0.5 wt% MWNT when the temperature increased from 170 to 280 ˚C in polycarbonate/MWNT melt. From the tan δ (G”/G’) curve, Fernandez, Ion, et al. [71] observed a suppression of polymer motion in the presence of organoclay as temperature increased. However, to the best of our knowledge, no one has reported an increased viscosity as temperature increases in the thermoplastic composite, neither with CNTs [70, 72-74] nor with other fillers [75-77], even above 15 wt% filler concentration.

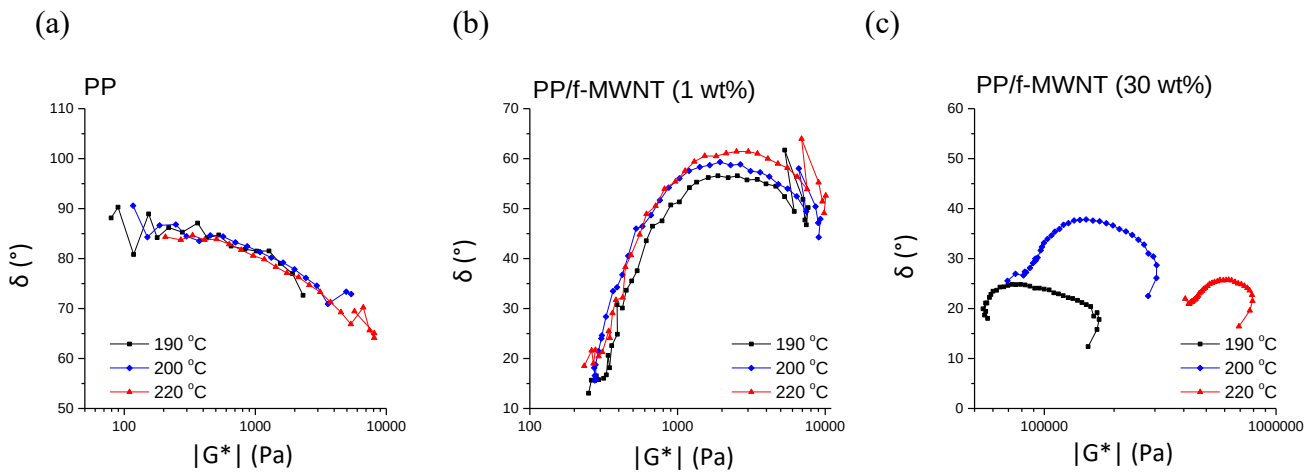

Figure 8.15. van Gurp-Palmen plots for (a) PP and PP/f-MWNT master batches at (b) 1 wt% and (c) 30 wt% f-MWNT concentrations.

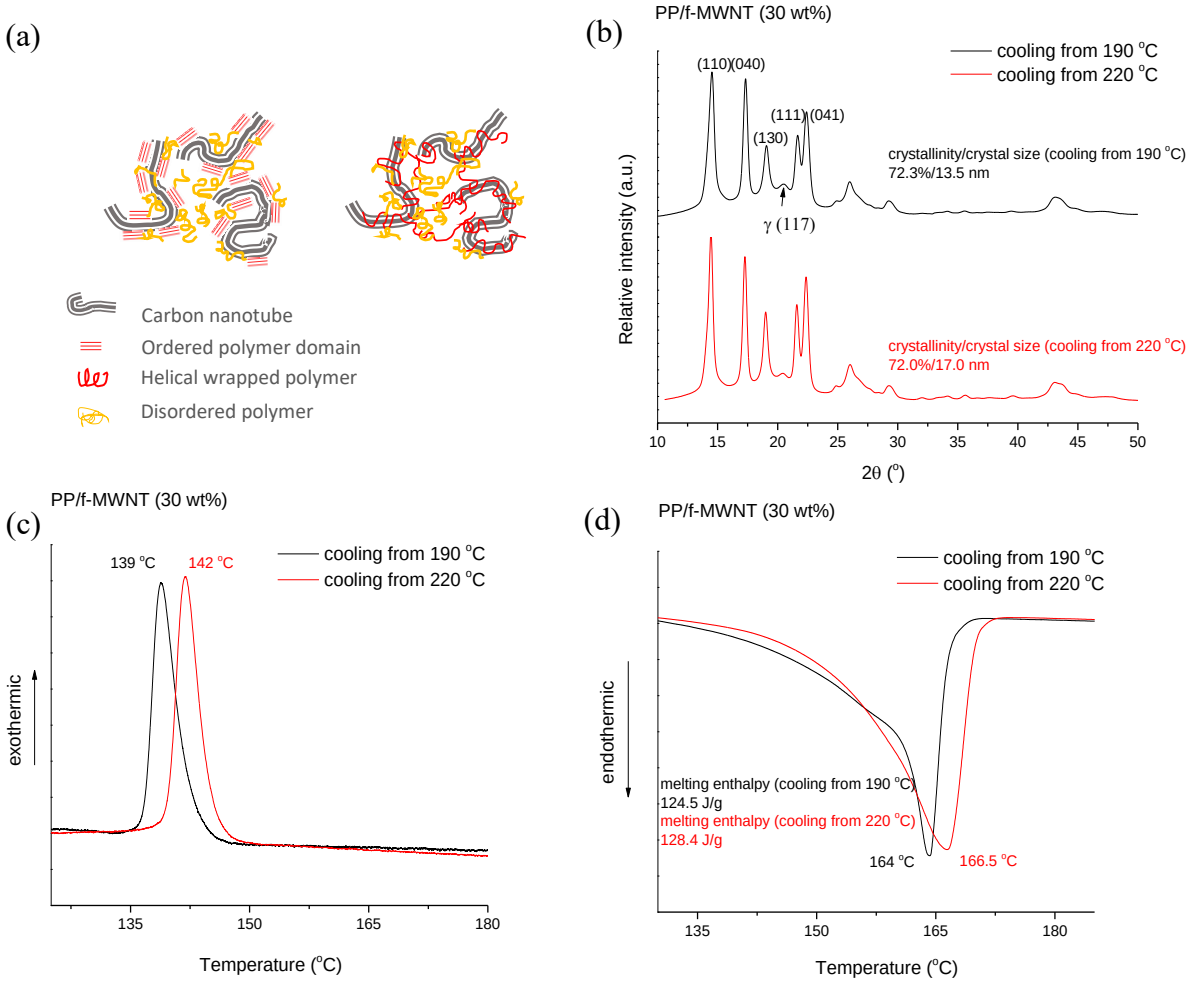

Figure 8.16. (a) Schematics showing two possible polymer morphologies at melt state in the presence of CNTs. (b) WAXD scan, and DSC (c) 1st cooling, (d) 2nd melting curves of PP/f-MWNT (30 wt%) master batches melted and slowly cooled (0.1 °C/minute) from 190 °C and 220 °C.

The unique rheological behavior in our PP/f-MWNT system can be attributed to the good CNT dispersion and the good interaction between f-MWNT and PP. The polymer morphology in melt state as temperature increases, however, is not yet well-understood. In Figure 8.16a, two possible interphase morphologies are provided in the schematic. These polymer chains may interact with nanotubes in an ordered manner epitaxially or in a wrapped form. Either structure, if promoted at elevated temperature, can increase the viscosity in the master batch melt due to restricted polymer motion. To test this hypothesis,

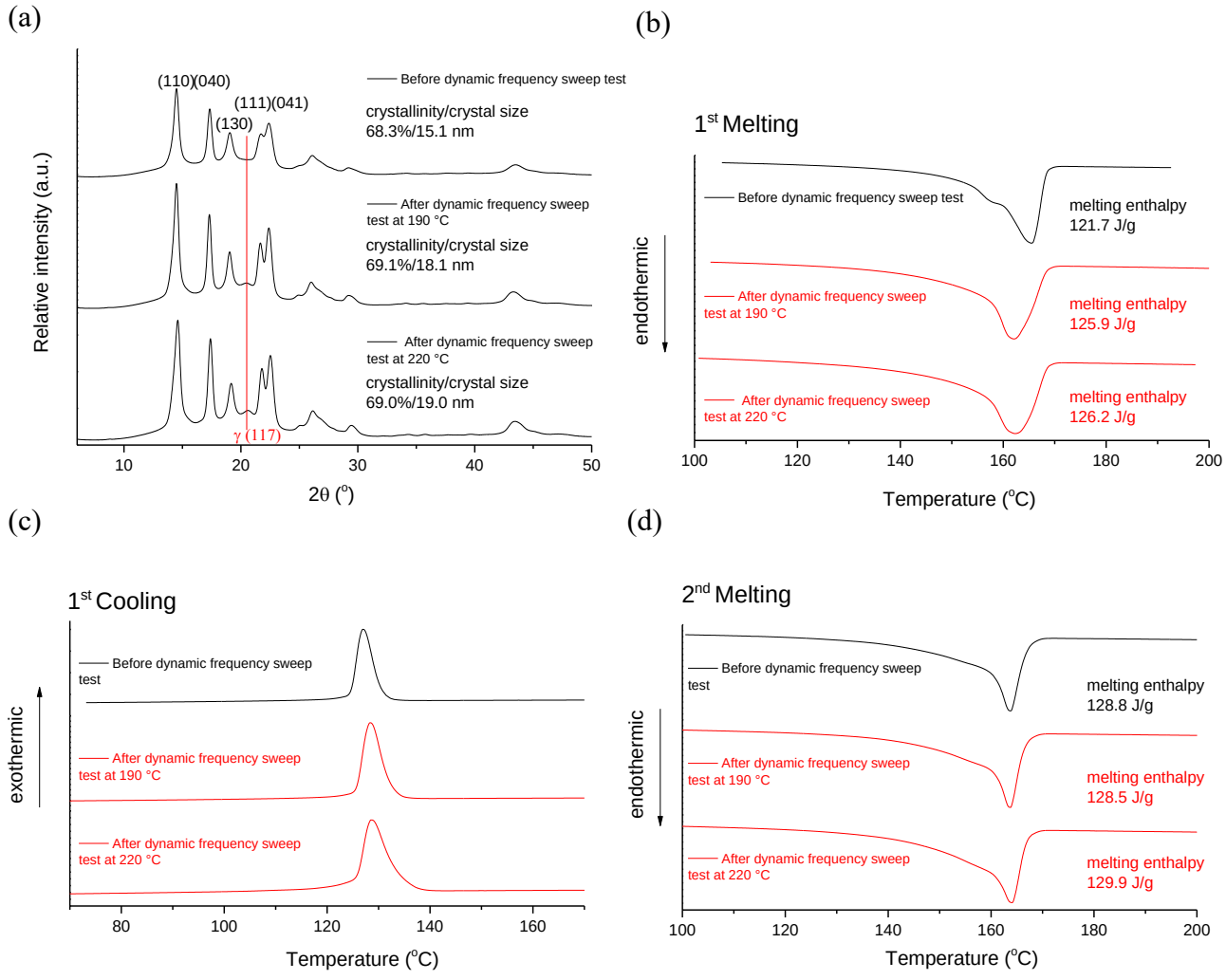

Figure 8.17. WAXD spectra and DSC melting and cooling curves of PP/f-MWNT (30 wt%) master batch before and after dynamic frequency sweep test at 190 and 220 °C.

two samples were removed from the rheometer right after the frequency sweep test at 190 °C and 220 °C. The structure of the two samples should be different, assuming the structure developed in the molten state can be preserved upon cooling. However, the structural parameters based on WAXD and DSC showed no significant difference between the two (Figure 8.17). As the thermal history of the samples can be lost during crystallization, especially at a high cooling rate, the loss of microstructure present at 220 °C/190°C will occur.

To preserve the morphology of the master batch at 220 °C (190 °C), another experiment was done in the DSC furnace where the samples were firstly heated to 220 °C (190 °C) and then slowly cooled down to room temperature at a rate of 0.1 °C/minute. From Figure 8.16, a more extended polymer (larger lamella thickness as indicated by higher T_p) and a longer interphase (larger crystal size) were observed in the sample that was cooled down from 220 °C. Also, this sample crystallized at a higher temperature than the sample that was cooled down from 190 °C indicating that there were more crystalline precursors in the former. Both observations suggest that the microstructure at 220 °C is more ordered such that a faster and templated crystal growth with higher melting point can be achieved. As a result, the inverse temperature dependence of viscosity is more likely due to the ordered interphase at high temperature that restricts the polymer flow. As f-MWNT concentration increases, the volume of interphase increases so the phenomenon becomes more apparent (Figure 8.13).

The implications of this abnormal rheological behavior on practical application can be inferred from the time-temperature superposition. Based on the time-temperature superposition, material that shows increased modulus (or viscosity) when temperature

increases should show increased modulus (or viscosity) over time as well. Unlike classical viscoelastic behavior (i.e. creep and stress relaxation), the PP/f-MWNT master batches with 5 to 30 wt% f-MWNT, which have demonstrated thermal-rheological complexity indicating a breakdown of the time-temperature equivalence, might exhibit phenomenal high fatigue life time and high fatigue strength.

8.4 CONCLUSIONS

In this study, the interphase of PP/f-MWNT was characterized through thermal analysis and WAXD. Based on the structural parameters, master batches at higher f-MWNT concentration, i.e. higher interphase fraction, exhibit increased melting peak maximum (up to 5 °C), increased enthalpy of melting (about 16 %), and higher crystallization temperature (up to 5 °C), as summarized in Figure 8.18. Such formation of ordered crystalline interphase was only observed in the sample after a complete melting and cooling cycle from melt, and was absent in the as-prepared sample crystalized from the xylene/butanol co-solvent at 60 °C. The structure of the bonded polymer layer, with the thickness about 4 to 5 nm, was also characterized by removing the bulk and loosely bonded polymer with xylene. DSC based calculation suggests a more extended conformation in the interfacial polymer layer with respect to the loosely bonded polymer, in which the lamella thickness is 5 nm and 4.1 nm, respectively. With a designed thermal treatment, the morphology of the interphase was successfully converted into an even more ordered crystalline structure with more extended polymer chain, where the lamella thickness increased to 6.8 nm, doubled to that of the bulk PP (3.3 nm). The thermal stability of the PP/f-MWNT master batches increases both under air and under nitrogen as determined from the increase of degradation temperature by about 30-40 °C, and 80-100 °C,

respectively. Finally, an abnormal temperature dependence of viscosity was found in 5, 15, and 30 wt % master batches, in which both viscosity and elastic modulus increase as temperature increases from 190 °C to 220 °C (Figure 8.18). This abnormal phenomenon was attributed to the formation of ordered interphase which can be facilitated by the promoted polymer-CNT interaction at higher temperature. This ordered interphase induced templated crystal growth such that a higher crystallization temperature as well as higher melting point of the resulting crystals were found when the sample was slowly cooled down from 220 °C with respect to that from 190 °C.

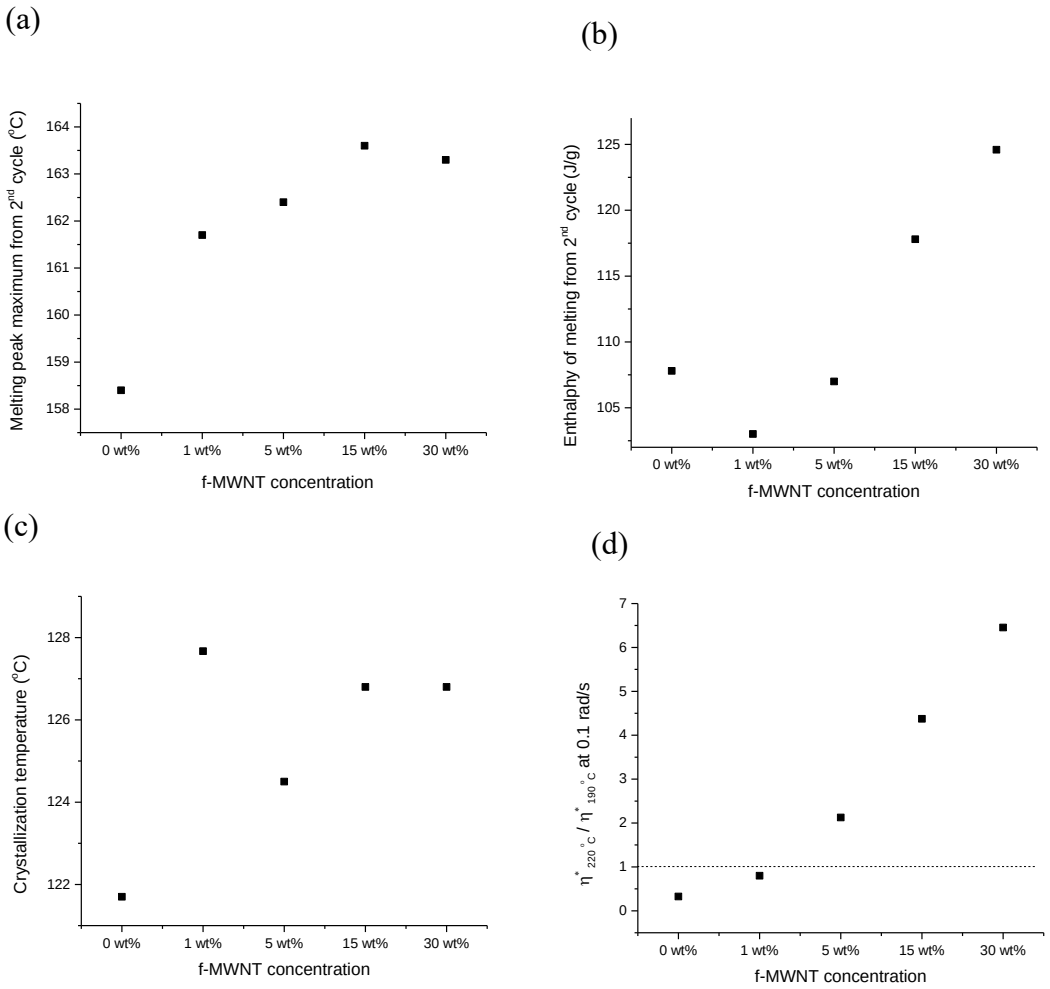

Figure 8.18 Comparison of thermal, rheological and structural parameters of PP and PP/f-MWNT master batches at different f-MWNT concentrations. (continued to the next page)

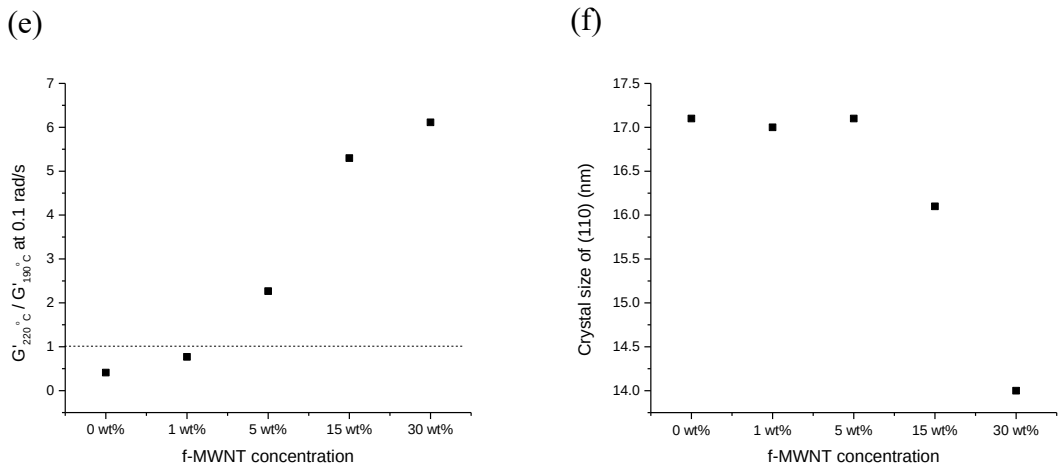

Figure 8.18 Comparison of thermal, rheological and structural parameters of PP and PP/f-MWNT master batches at different f-MWNT concentrations. (continued from the previous page)

8.5 REFERENCES

1. Marilyn L Minus, Han Gi Chae, and Satish Kumar, *Polyethylene crystallization nucleated by carbon nanotubes under shear.* ACS applied materials & interfaces, 2011. **4**(1): p. 326-330.

2. Yaodong Liu and Satish Kumar, *Polymer/carbon nanotube nano composite fibers–a review.* ACS applied materials & interfaces, 2014. **6**(9): p. 6069-6087.

3. Marilyn L Minus, Han Gi Chae, and Satish Kumar, *Single wall carbon nanotube templated oriented crystallization of poly (vinyl alcohol).* Polymer, 2006. **47**(11): p. 3705-3710.

4. Yiying Zhang, Kenan Song, Jiangsha Meng, and Marilyn L Minus, *Tailoring polyacrylonitrile interfacial morphological structure by crystallization in the presence of single-wall carbon nanotubes.* ACS applied materials & interfaces, 2013. **5**(3): p. 807-814.

5. Bradley A Newcomb, Lucille A Giannuzzi, Kevin M Lyons, Prabhakar V Gulgunje, Kishor Gupta, Yaodong Liu, Manjeshwar Kamath, Kenneth McDonald, Jaeyun Moon, and Bo Feng, *High resolution transmission electron microscopy study on polyacrylonitrile/carbon nanotube based carbon fibers and the effect of structure development on the thermal and electrical conductivities.* Carbon, 2015. **93**: p. 502-514.

6. Shanju Zhang, Marilyn L Minus, Lingbo Zhu, Ching-Ping Wong, and Satish Kumar, *Polymer transcrystallinity induced by carbon nanotubes.* Polymer, 2008. **49**(5): p. 1356-1364.

7. Hans E Miltner, Nadia Grossiord, Kangbo Lu, Joachim Loos, Cor E Koning, and Bruno Van Mele, *Isotactic polypropylene/carbon nanotube composites prepared by latex technology. Thermal analysis of carbon nanotube-induced nucleation.* Macromolecules, 2008. **41**(15): p. 5753-5762.

8. Kangbo Lu, Nadia Grossiord, Cor E Koning, Hans E Miltner, Bruno van Mele, and Joachim Loos, *Carbon nanotube/isotactic polypropylene composites prepared by latex technology: morphology analysis of CNT-induced nucleation.* Macromolecules, 2008. **41**(21): p. 8081-8085.

9. Sushanta Ghoshal, Po-Hsiang Wang, Prabhakar Gulgunje, Nikhil Verghese, and Satish Kumar, *High impact strength polypropylene containing carbon nanotubes.* Polymer, 2016. **100**: p. 259-274.

10. Peng Liu, Kevin L White, Hiroaki Sugiyama, Jiang Xi, Takeshi Higuchi, Taiki Hoshino, Ryohei Ishige, Hiroshi Jinnai, Atsushi Takahara, and Hung-Jue Sue, *Influence of trace amount of well-dispersed carbon nanotubes on structural*

development and tensile properties of polypropylene. Macromolecules, 2013. **46**(2): p. 463-473.

11. A Hernández-Pérez and F Avilés, *Modeling the influence of interphase on the elastic properties of carbon nanotube composites.* Computational Materials Science, 2010. **47**(4): p. 926-933.

12. A Haque and A Ramasetty, *Theoretical study of stress transfer in carbon nanotube reinforced polymer matrix composites.* Composite Structures, 2005. **71**(1): p. 68-77.

13. Po-Hsiang Wang, Sushanta Ghoshal, Prabhakar Gulgunje, Nikhil Verghese, and Satish Kumar, *Polypropylene nanocomposites with polymer coated multiwall carbon nanotubes.* Polymer, 2016. **100**: p. 244-258.

14. Nanying Ning, Wei Zhang, Yongsheng Zhao, Changyu Tang, Mingbo Yang, and Qiang Fu, *Facilitating the formation of nanohybrid shish kebab structure in helical polymer systems by using carbon nanotube bundles.* Polymer, 2012. **53**(20): p. 4553-4559.

15. B Pukánszky, B Turcsanyi, and F Tudos, *Effect of interfacial interaction on the tensile yield stress of polymer composites.* Interfaces in polymer, ceramic and metal matrix composites. Amsterdam: Elsevier, 1988: p. 467-77.

16. Masao Sumita, Hidetoshi Tsukihi, Keizo Miyasaka, and Kinzo Ishikawa, *Dynamic mechanical properties of polypropylene composites filled with ultrafine particles.* Journal of applied polymer science, 1984. **29**(5): p. 1523-1530.

17. Min Zhi Rong, Ming Qiu Zhang, Shun Long Pan, Björn Lehmann, and Klaus Friedrich, *Analysis of the interfacial interactions in polypropylene/silica nanocomposites.* Polymer International, 2004. **53**(2): p. 176-183.

18. Hans E Miltner, Guy Van Assche, András Pozsgay, Béla Pukánszky, and Bruno Van Mele, *Restricted chain segment mobility in poly (amide) 6/clay nanocomposites evidenced by quasi-isothermal crystallization.* Polymer, 2006. **47**(3): p. 826-835.

19. János Móczó, Erika Fekete, and Béla Pukánszky, *Acid-base interactions and interphase formation in particulate-filled polymers.* The Journal of Adhesion, 2002. **78**(10): p. 861-875.

20. Zita Dominkovics, József Hári, János Kovács, Erika Fekete, and Béla Pukánszky, *Estimation of interphase thickness and properties in PP/layered silicate nanocomposites.* European Polymer Journal, 2011. **47**(9): p. 1765-1774.

21. Shang-Lin Gao and Edith Mäder, *Characterisation of interphase nanoscale property variations in glass fibre reinforced polypropylene and epoxy resin*

composites. Composites Part A: applied science and manufacturing, 2002. **33**(4): p. 559-576.

22. Mehdi Karevan, Raghuram V Pucha, Md A Bhuiyan, and Kyriaki Kalaitzidou, *Effect of interphase modulus and nanofiller agglomeration on the tensile modulus of graphite nanoplatelets and carbon nanotube reinforced polypropylene nanocomposites.* Carbon letters, 2010. **11**(4): p. 325-331.

23. Wen-Yen Chiang, Wen-Der Yang, and Béla Pukánszky, *Polypropylene composites. III: Chemical modification of the interphase and its influence on the properties of PP/mica composites.* Polymer Engineering & Science, 1994. **34**(6): p. 485-492.

24. Haiwen Gu, Yangbo Guo, Siew Yee Wong, Chaobin He, Xu Li, and VPW Shim, *Effect of interphase and strain-rate on the tensile properties of polyamide 6 reinforced with functionalized silica nanoparticles.* Composites Science and Technology, 2013. **75**: p. 62-69.

25. Andreas Wurm, Mohamed Ismail, Bernd Kretzschmar, Doris Pospiech, and Christoph Schick, *Retarded crystallization in polyamide/layered silicates nanocomposites caused by an immobilized interphase.* Macromolecules, 2010. **43**(3): p. 1480-1487.

26. T Ramanathan, AA Abdala, S Stankovich, DA Dikin, M Herrera-Alonso, RD Piner, DH Adamson, HC Schniepp, XRRS Chen, and RS Ruoff, *Functionalized graphene sheets for polymer nanocomposites.* Nature nanotechnology, 2008. **3**(6): p. 327-331.

27. Rui-Juan Zhou and Thomas Burkhart, *Polypropylene/SiO2 nanocomposites filled with different nanosilicas: thermal and mechanical properties, morphology and interphase characterization.* Journal of materials science, 2011. **46**(5): p. 1228-1238.

28. LAS de A Prado, M Kwiatkowska, SS Funari, Z Roslaniec, G Broza, and K Schulte, *Studies on morphology and interphase of poly (butylene terephthalate)/carbon nanotubes nanocomposites.* Polymer Engineering & Science, 2010. **50**(8): p. 1571-1576.

29. T Ramanathan, H Liu, and LC Brinson, *Functionalized SWNT/polymer nanocomposites for dramatic property improvement.* Journal of Polymer Science Part B: Polymer Physics, 2005. **43**(17): p. 2269-2279.

30. Han Gi Chae, TV Sreekumar, Tetsuya Uchida, and Satish Kumar, *A comparison of reinforcement efficiency of various types of carbon nanotubes in polyacrylonitrile fiber.* Polymer, 2005. **46**(24): p. 10925-10935.

31. David S Fryer, Richard D Peters, Eui Jun Kim, Jeanne E Tomaszewski, Juan J de Pablo, Paul F Nealey, Chris C White, and Wen-li Wu, *Dependence of the glass transition temperature of polymer films on interfacial energy and thickness.* Macromolecules, 2001. **34**(16): p. 5627-5634.

32. Kenan Song, Yiying Zhang, and Marilyn L Minus, *Polymer Interphase Self-Reinforcement and Strengthening Mechanisms in Low-Loaded Nanocomposite Fibers.* Macromolecular Chemistry and Physics, 2015. **216**(12): p. 1313-1320.

33. D. R. Norton and A. Keller, *The spherulitic and lamellar morphology of melt-crystallized isotactic polypropylene.* Polymer, 1985. **26**(5): p. 704-716.

34. Young Ho Choi, *Polyacrylonitrile/carbon nanotube composite fibers: effect of various processing parameters on fiber structure and properties*. 2010, Georgia Institute of Technology.

35. DR Norton and A Keller, *The spherulitic and lamellar morphology of melt-crystallized isotactic polypropylene.* Polymer, 1985. **26**(5): p. 704-716.

36. Geon-Woong Lee, Sudhakar Jagannathan, Han Gi Chae, Marilyn L. Minus, and Satish Kumar, *Carbon nanotube dispersion and exfoliation in polypropylene and structure and properties of the resulting composites.* Polymer, 2008. **49**: p. 1831-1840.

37. A. R. Bhattacharyya, T. V. Sreekumar, Liu Tao, S. Kumar, L. A. Ericson, R. H. Hauge, and R. E. Smalley, *Crystallization and orientation studies in polypropylene/single wall carbon nanotube composite.* Polymer, 2003. **44**(8): p. 2373-2377.

38. H. E. Miltner, C. E. Koning, B. Van Mele, N. Grossiord, K. Lu, and J. Loos, *Isotactic polypropylene/carbon nanotube composites prepared by latex technology. Thermal analysis of camon nanotube induced nucleation.* Macromolecules, 2008. **41**(15): p. 5753-5762.

39. Anton A Koval'chuk, Alexander N Shchegolikhin, Vitaliy G Shevchenko, Polina M Nedorezova, Alla N Klyamkina, and Alexander M Aladyshev, *Synthesis and properties of polypropylene/multiwall carbon nanotube composites.* Macromolecules, 2008. **41**(9): p. 3149-3156.

40. Chien-Chia Chu, Kevin L. White, Peng Liu, Xi Zhang, and Hung-Jue Sue, *Electrical conductivity and thermal stability of polypropylene containing well-dispersed multi-walled carbon nanotubes disentangled with exfoliated nanoplatelets.* Carbon, 2012. **50**: p. 4711-4721.

41. Q. L. He, T. T. Yuan, X. R. Yan, D. W. Ding, Q. Wang, Z. P. Luo, T. D. Shen, S. Y. Wei, D. P. Cao, and Z. H. Guo, *Flame-Retardant Polypropylene/Multiwall Carbon Nanotube Nanocomposites: Effects of Surface Functionalization and Surfactant Molecular Weight.* MACROMOLECULAR CHEMISTRY AND PHYSICS, 2014. **215**(4): p. 327-340.

42. Chien-Chia Chu, Kevin L White, Peng Liu, Xi Zhang, and Hung-Jue Sue, *Electrical conductivity and thermal stability of polypropylene containing well-dispersed*

multi-walled carbon nanotubes disentangled with exfoliated nanoplatelets. Carbon, 2012. **50**(12): p. 4711-4721.

43. Bing-Xing Yang, Jia-Hua Shi, KP Pramoda, and Suat Hong Goh, *Enhancement of the mechanical properties of polypropylene using polypropylene-grafted multiwalled carbon nanotubes.* Composites Science and Technology, 2008. **68**(12): p. 2490-2497.

44. H Deng, E Bilotti, R Zhang, and T Peijs, *Effective reinforcement of carbon nanotubes in polypropylene matrices.* Journal of applied polymer science, 2010. **118**(1): p. 30-41.

45. Parvathalu Kalakonda, Germano S Iannacchione, Michael Daly, Georgi Y Georgiev, Y Cabrera, R Judith, and Peggy Cebe, *Calorimetric study of nanocomposites of multiwalled carbon nanotubes and isotactic polypropylene polymer.* Journal of Applied Polymer Science, 2013. **130**(1): p. 587-594.

46. Cristhian Garzon, Manfred Wilhelm, Mahdi Abbasi, and Humberto Palza, *Effect of Carbon-Based Particles on the Mechanical Behavior of Isotactic Poly (propylene) s.* Macromolecular Materials and Engineering, 2016.

47. John D Hoffman and James J Weeks, *Melting process and the equilibrium melting temperature of polychlorotrifluoroethylene.* J Res Natl Bur Stand A, 1962. **66**(1): p. 13-28.

48. John P Abdou, Karina J Reynolds, Michaela R Pfau, Justin van Staden, Gregory A Braggin, Navid Tajaddod, Marilyn Minus, Víctor Reguero, Juan J Vilatela, and Shanju Zhang, *Interfacial crystallization of isotactic polypropylene surrounding macroscopic carbon nanotube and graphene fibers.* Polymer, 2016. **91**: p. 136-145.

49. Ian L Hosier, Rufina G Alamo, and JS Lin, *Lamellar morphology of random metallocene propylene copolymers studied by atomic force microscopy.* Polymer, 2004. **45**(10): p. 3441-3455.

50. Shanju Zhang and Satish Kumar, *Carbon nanotubes as liquid crystals.* Small, 2008. **4**(9): p. 1270-1283.

51. Micah J Green, Natnael Behabtu, Matteo Pasquali, and W Wade Adams, *Nanotubes as polymers.* Polymer, 2009. **50**(21): p. 4979-4997.

52. Tongfei Wu, Yongzheng Pan, Erjia Liu, and Lin Li, *Carbon nanotube/polypropylene composite particles for microwave welding.* Journal of Applied Polymer Science, 2012. **126**(S2).

53. D Bikiaris, *Can nanoparticles really enhance thermal stability of polymers? Part II: an overview on thermal decomposition of polycondensation polymers.* Thermochimica Acta, 2011. **523**(1): p. 25-45.

54. Milena Ginic-Markovic, Janis G Matisons, Raoul Cervini, George P Simon, and Peter M Fredericks, *Synthesis of new polyaniline/nanotube composites using ultrasonically initiated emulsion polymerization.* Chemistry of materials, 2006. **18**(26): p. 6258-6265.

55. B Marosfői, A Szabo, Gy Marosi, D Tabuani, Giovanni Camino, and S Pagliari, *Thermal and spectroscopic characterization of polypropylene-carbon nanotube composites.* Journal of thermal analysis and calorimetry, 2006. **86**(3): p. 669-673.

56. PCP Watts, PK Fearon, WK Hsu, NC Billingham, HW Kroto, and DRM Walton, *Carbon nanotubes as polymer antioxidants.* Journal of Materials Chemistry, 2003. **13**(3): p. 491-495.

57. R Fulchiron, A Michel, V Verney, and JC Roustant, *Correlations between relaxation time spectrum and melt spinning behavior of polypropylene. 1: Calculation of the relaxation spectrum as a log-normal distribution and influence of the molecular parameters.* Polymer Engineering & Science, 1995. **35**(6): p. 513-517.

58. William W Graessley, *The entanglement concept in polymer rheology*, in *The Entanglement Concept in Polymer Rheology*. 1974, Springer. p. 1-179.

59. Bradley A Newcomb, Prabhakar V Gulgunje, Yaodong Liu, Kishor Gupta, Manjeshwar G Kamath, Chandrani Pramanik, Sushanta Ghoshal, Han Gi Chae, and Satish Kumar, *Polyacrylonitrile solution homogeneity study by dynamic shear rheology and the effect on the carbon fiber tensile strength.* Polymer Engineering & Science, 2016. **56**(3): p. 361-370.

60. Chang Dae Han and Myung S Jhon, *Correlations of the first normal stress difference with shear stress and of the storage modulus with loss modulus for homopolymers.* Journal of applied polymer science, 1986. **32**(3): p. 3809-3840.

61. Pawan Verma, Meenakshi Verma, Anju Gupta, Sampat Singh Chauhan, Rajender Singh Malik, and Veena Choudhary, *Multi walled carbon nanotubes induced viscoelastic response of polypropylene copolymer nanocomposites: Effect of filler loading on rheological percolation.* Polymer Testing, 2016. **55**: p. 1-9.

62. Petra Pötschke, TD Fornes, and DR Paul, *Rheological behavior of multiwalled carbon nanotube/polycarbonate composites.* Polymer, 2002. **43**(11): p. 3247-3255.

63. Samuel Glasstone, Keith James Laidler, and Henry Eyring, *The theory of rate processes: the kinetics of chemical reactions, viscosity, diffusion and electrochemical phenomena*. 1941: McGraw-Hill Book Company, Incorporated.

64. Sahil Gupta, Xuepei Yuan, TC Mike Chung, M Cakmak, and RA Weiss, *Influence of hydrogen bonding on the melt rheology of polypropylene.* Polymer, 2016. **107**: p. 223-232.

65. P.V. Gulgunje P.-H. Wang, S. Ghoshal, N. Verghese, S. Kumar, *Rheological Behavior of Polypropylene Nanocomposites with Tailored Polymer/Multiwall Carbon Nanotube Interface.* in preparation, 2017

66. Long Wang, Shota Ishihara, Megumi Ando, Atsushi Minato, Yuta Hikima, and Masahiro Ohshima, *Fabrication of High Expansion Microcellular Injection-Molded Polypropylene Foams by Adding Long-Chain Branches.* Industrial & Engineering Chemistry Research, 2016. **55**(46): p. 11970-11982.

67. Ute Keßner and Helmut Münstedt, *Thermorheology as a method to analyze long-chain branched polyethylenes.* Polymer, 2010. **51**(2): p. 507-513.

68. Francis W Starr, TB Schroder, and Sharon C Glotzer, *Molecular dynamics simulation of a polymer melt with a nanoscopic particle.* Macromolecules, 2002. **35**: p. 4481.

69. Thaliyil V Sreekumar, Tao Liu, Byung G Min, Huina Guo, Satish Kumar, Robert H Hauge, and Richard E Smalley, *Polyacrylonitrile single-walled carbon nanotube composite fibers.* Advanced Materials, 2004. **16**(1): p. 58-61.

70. Petra Pötschke, Mahmoud Abdel-Goad, Ingo Alig, Sergej Dudkin, and Dirk Lellinger, *Rheological and dielectrical characterization of melt mixed polycarbonate-multiwalled carbon nanotube composites.* Polymer, 2004. **45**(26): p. 8863-8870.

71. Ion Fernandez, Anton Santamaría, María Eugenia Muñoz, and Pere Castell, *A rheological analysis of interactions in phenoxy/organoclay nanocomposites.* European polymer journal, 2007. **43**(8): p. 3171-3176.

72. Samaneh Abbasi, Pierre J Carreau, Abdessalem Derdouri, and Michel Moan, *Rheological properties and percolation in suspensions of multiwalled carbon nanotubes in polycarbonate.* Rheologica acta, 2009. **48**(9): p. 943.

73. DS Bangarusampath, Holger Ruckdäschel, Volker Altstädt, Jan KW Sandler, Didier Garray, and Milo SP Shaffer, *Rheology and properties of melt-processed poly (ether ether ketone)/multi-wall carbon nanotube composites.* Polymer, 2009. **50**(24): p. 5803-5811.

74. R Zeiler, UA Handge, DJ Dijkstra, H Meyer, and V Altstädt, *Influence of molar mass and temperature on the dynamics of network formation in polycarbonate/carbon nanotubes composites in oscillatory shear flows.* Polymer, 2011. **52**(2): p. 430-442.

75. Alper Kiziltas, Behzad Nazari, Douglas J Gardner, and Douglas W Bousfield, *Polyamide 6–cellulose composites: Effect of cellulose composition on melt rheology and crystallization behavior.* Polymer Engineering & Science, 2014. **54**(4): p. 739-746.

76. Shu-Ying Gu, Jie Ren, and Qin-Feng Wang, *Rheology of poly (propylene)/clay nanocomposites.* Journal of Applied Polymer Science, 2004. **91**(4): p. 2427-2434.

77. Girish Galgali, C Ramesh, and Ashish Lele, *A rheological study on the kinetics of hybrid formation in polypropylene nanocomposites.* Macromolecules, 2001. **34**(4): p. 852-858.

78. Wenlin Li, Yaqiong Zhang, Jingjing Yang, Yanhua Niu and Zhigang Wang. *Thermal annealing induced enhancements of electrical conductivities and mechanism for multiwalled carbon nanotubes filled poly (ethylene-co-hexene) composites*. ACS applied materials & interfaces **4.12** (2012): 6468-6478.

79. Yongzheng Pan, Henry Kuo Feng Cheng, Lin Li, Siew Hwa Chan, Jianhong Zhao, and Yang Kay Juay. *Annealing induced electrical conductivity jump of multi-walled carbon nanotube/polypropylene composites and influence of molecular weight of polypropylene*. Journal of Polymer Science Part B: Polymer Physics 48.**21** (2010): 2238-2247.

80. Cipriano, B. H., Kota, A. K., Gershon, A. L., Laskowski, C. J., Kashiwagi, T., Bruck, H. A., & Raghavan, S. R. (2008). *Conductivity enhancement of carbon nanotube and nanofiber-based polymer nanocomposites by melt annealing*. Polymer, **49**(22), 4846-4851.

81. Shilin Huang, Zhengying Liu, Chaolu Yin, Yu Wang, Yongjuan Gao, Chen Chen, and Mingbo Yang. *Enhancement effect of filler network on isotactic polypropylene/carbon black composite melts*. Colloid and Polymer Science 289.15-**16** (2011): 1673-1681.

CHAPTER 9

CONCLUSIONS AND RECOMMENDATIONS

9.1 CONCLUSIONS

This research systematically investigates the polymer-CNT interaction when the interphase was tailored. Three types of interphases were studied:

1. The PP/f-MWNT system using co-solvent process

2. The MA-g-PP/f-MWNT system using co-solvent process

3. The PP/p-MWNT system using melt process

In the co-solvent process, dilute solution allows polymer chains to interact with f-MWNTs more effectively that reduces the entanglements of both the components, promoting the interphase formation. Mechanical, crystallization, and rheological properties of the resulting nanocomposites were examined to shed light on the interaction between PP and MWNTs in solid and in melt (Fig 9.1).

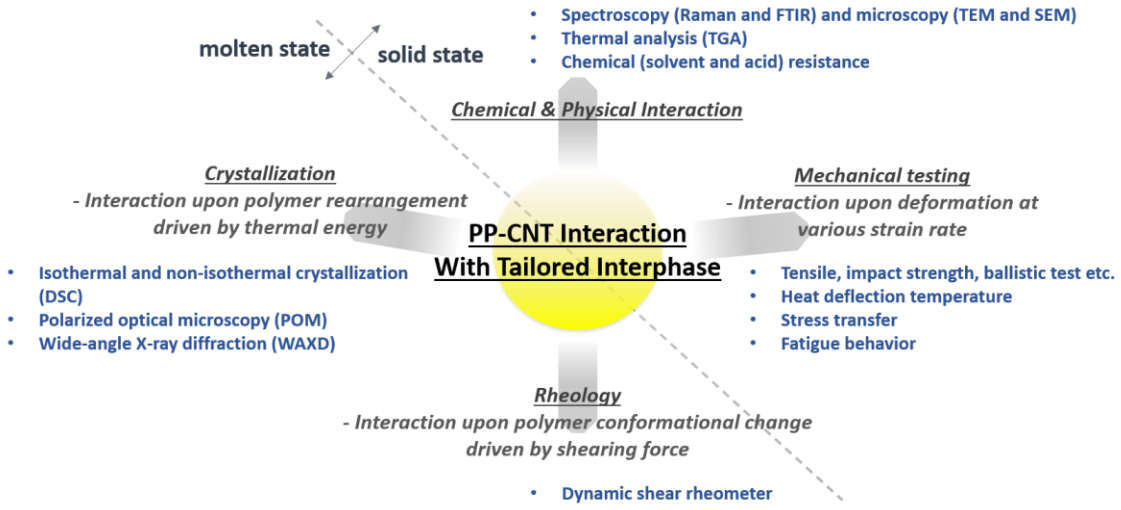

Figure 9.1. Methodology and scope of the thesis.

Key results and conclusions are summarized below. It is worth mentioning that although these conclusions are drawn based on this research, i.e. from the PP and CNT system, it is expected that some of the observations/suggestions can also be applied to other semi-crystalline polymers such as nylon, polyethylene (PE), polyethylene terephthalate (PET), poly(vinyl alcohol) etc. In addition, some of conclusions may also be applicable to amorphous polymer systems.

We hypothesized that tailored CNT/polymer interphase is needed for achieving high performance nanocomposites. To verify this hypothesis, a co-solvent process was developed to form a few layers of polymer coating on CNTs. The formation of this solution processed polymer interphase and the interaction between CNT and polymer were studied. Based on this study, following observations were made and conclusions were reached:

- As the polymer coating process took place during solvent removal, control over solvent evaporation rate and temperature is critical to achieve homogeneous polymer coating.
- From the SEM images, 4 to 5 nm thick layer of PP and MA-g-PP polymer coating is observed on the f-MWNT sidewall. From the TEM images, it can be seen that there is no gap between the polymers and the coated f-MWNTs, indicating good adhesion between the two.
- The CH_2-π interaction between PP and f-MWNTs, MA-g-PP and f-MWNTs, as well as the hydrogen bonding between MA-g-PP and f-MWNTs were verified using FTIR spectroscopy. Downshift of the Raman D band signal also confirmed the strained C-C bond on the f-MWNT in the presence of polymer sheath.
- Improved chemical stability of the polymer at the interphase was demonstrated by the solubility test using xylene or the acid etching. When higher amount of polymer is

converted into the interphase (presumably in the high concentration master batches), there were more residue polymers remained after acid etching. Since the purpose of acid treatment is to etch away amorphous and less perfect polymer crystals, this result indicates that polymer at the interphase has better crystalline perfection, then the polymer farther away (i.e. bulk polymer) from the interphase.

- From TGA study under air, PP at the interphase showed about 30 to 40 °C higher peak degradation temperature than the matrix PP.

The tailored interphase using solution processed polymer significantly changes the physical and chemical properties of the PP/MWNT nanocomposite, as compared to the system where the interphase is not engineered, i.e. simply melt blending of neat PP and MWNTs. From the processing point of view, the rheological and some of the crystallization behaviors are also improved compared to that of PP/p-MWNT.

For the mechanical properties, including tensile, impact strength, ballistic test, and the stress transfer behavior, it was shown that by tailoring the interphase between polymer and CNTs, nanocomposites can achieve good improvement at low CNT concentration. Specifically, some of the property improvements are listed below:

- At 1 wt% MWNT loading, although the best MWNT dispersion was achieved when the interphase consisted of MA-g-PP, the highest improvement of the impact strength was achieved in the PP/f-MWNT system compared to neat PP, i.e. 152 % improvement in PP/f-MWNT vs 70 % improvement in MA-g-PP/f-MWNT. On the other hand, no improvement in the impact strength of melt blended PP/p-MWNT system was achieved as compared to the control PP. This significant improvement in the PP/f-MWNT is due to: Firstly, the nucleating ability of CNTs that reduce the spherulite size, thus creating

more tortuous crack propagation paths. Secondly, CNTs act as connecting links between spherulites and in between interlamellar amorphous regions. Thirdly, it was found that the interfacial shear strength (τ_i) is 17.8 MPa in PP/f-MWNT and only 2.2 MPa in PP/p-MWNT, suggesting improved matrix-CNT adhesion in the former case.

- As fillers in the composites act as a stress concentrators under load, the fracture surface of PP/f-MWNT consists of microcracks under SEM, which were possibly nucleated by CNTs. These microcracks can potentially lower the stress constrains in the matrix. Many shear ruptured fibrils were observed, and this is due to the promoted plastic deformation and effective load transfer at the CNT bridged cracks.
- Presence of MA-g-PP deteriorates the interaction between CNT and matrix PP. After acid treatment, MA-g-PP was removed from the CNT surfaces, leaving holes between CNT and matrix PP.
- The impact strength of PP/f-MWNT was improved without a significant loss in polymer ductility. On the other hand, the specimen became brittle above 0.1 wt% and 0.5 wt% MWNT loading in the PP/p-MWNT and MA-g-PP/f-MWNT system, respectively.
- In the PP/f-MWNT system, when the strain rate increases from that of Izod impact test to that of ballistic test (one to two-order of magnitude higher strain rate), the kinetic energy absorbed by the specimen reduces from 152 % improvement to 40 % improvement.

For the crystallization behavior, CNT surface chemistry (functional groups) and the presence of MA-g-PP at the interface noticeably effect the crystallization of matrix PP. The melting point of the polymer increases in the presence of MWNTs. MWNTs can act as

nucleating agent, allowing polymer to crystallize at higher temperature which promotes polymer ordering and increases lamella thickness. The level of the above-mentioned effects is different in the three studied systems, as listed below:

- The crystallization nucleation ability is the highest for the PP/p-MWNT system, followed by PP/f-MWNT, then the MA-g-PP/f-MWNT.
- Smaller FWHM of the melting peak in PP/f-MWNT represented a more homogenous crystal size distribution than in PP/p-MWNT.
- PP at the interphase exhibits increased melting peak maximum (up to 5 °C higher than bulk PP) and enthalpy of melting (about 16 % than that for bulk PP), indicating more ordered crystalline in the interphase than in the bulk. DSC and WAXD studies also suggested that polymer at the CNT/PP interface has more extended chain conformation with respect to the loosely bonded polymer to the MWNTs.
- The crystal morphology at the interface can be modified through cyclic thermal treatment (repeated heating/cooling with a specified temperature profile) where more refined crystals act as templates for the subsequent PP crystal growth. This creates the columnar crystalline interphase having a distinct melting point, up to 10.5 °C higher than the bulk PP. From SEM images, this columnar interphase is about 26 nm thick. The cyclic thermal treatment can potentially improve the adhesion and interaction between polymer and CNTs through increasing crystal size at the interface.

For the rheological behavior, it was confirmed that the non-covalently coated polymer layers (in the PP/f-MWNT) remained on the f-MWNT surfaces during melt processing. Such interphase can promote chain alignment and preserve the polymer orientation more effectively than that of the PP/p-MWNT. Stronger interaction between

MWNT and the polymer melt (in the two co-solvent processed systems) can be concluded from the following observations:

- More evident shear-induced crystallization in PP/f-MWNT than in PP/p-MWNT
- More evident increase of melt strength (melt elasticity) during melt annealing at 200 °C in PP/f-MWMT than in PP/p-MWNT.

Melt homogeneity determined from the G' to G" log-log plot was found higher in the PP/f-MWNT than in the PP/p-MWNT. It is also found that the melt homogeneity correlated well with the ductile-brittle transition in the PP/MWNT specimens. One possible explanation can be that the inhomogeneity origins from chain entanglements, voids, CNT agglomerates etc. These inhomogeneities are likely to be preserved during processing steps and therefore result in loss of polymer ductility.

For the thermal, gas and moisture barrier properties, it was observed that even with thermally unstable -COOH group on f-MWNTs, the thermal stability of the PP/f-MWNT nanocomposite shows a similar behavior to that of the PP/p-MWNT nanocomposite, both with about 95 °C higher temperature at maximum mass loss rate than that of the neat PP. Also, the introduction of hydrophilic -COOH group does not lower the oxygen barrier property of the neat PP as much as the p-MWNT nanocomposite does. This might be due to the improved PP-MWNT adhesion in the PP/f-MWNT system.

Overall, this thesis study demonstrates that tailored CNT/polymer interphase is needed for achieving high performance nanocomposites and improving CNT/polymer interaction in both molten and solid state. As for how to effectively engineer the interphase, we provided at least three approaches: to process materials in solvents, or other media that can potentially reduce the entanglement of both polymer chains and CNTs; to refine

polymer crystals and increase crystal sizes at the interphase using repeated thermal treatment; to shear align and preserve the polymer ordering at the interphase from polymer melt.

9.2 RECOMMENDATIONS FOR FUTURE STUDY

Based on the concluding remarks summarized in Chapter 9.1, several future directions are given in this section:

1. Develop plans for solution processed PP/CNT master batch scale up to the pilot plant scale.

2. As we have seen in Chapter 2 and Chapter 8, the polymers at the interphase, especially the ~ 5 nm "bonded polymer" at the MWNT surfaces, exhibit better crystal ordering and therefore, better physical properties than the bulk materials. The change of polymer dynamics becomes less effective when the polymer is away from CNTs. There are about 95 to 97 vol% of polymers are considered "loosely bonded" or "non-bonded" to the MWNTs in the 5 wt% PP/f-MWNT master batch (assuming 4 to 5 nm of the polymer are "bonded polymers" using the model given in Figure 8.7). While the improvement of the nanocomposite's physical properties (in Chapter 3 to Chapter 7) are attributed to the tailored interphase between PP and the 5 wt% PP/f-MWNT master batch, it will be worth studying if one can first remove the 95 to 97 vol% "non-bonded" polymers in the master batch, leaving the 3 to 5 vol% "bonded polymer", and melt compound this with neat PP. It is hypothesized that the more ordered crystal from the "bonded polymers" can serve as a better template for the subsequent matrix PP growth than the "loosely bonded polymers" in the master batch (this is similar to the idea

introduced in Chapter 5 where the less-perfected crystals were melted at lower temperature, leaving the more perfect crystals as seeds for the subsequent crystal growth). Therefore, better stress transfer between the nanotube and the polymers can be expected because of the more ordered interphase. Also, one can consider first thermally treat the master batch to convert polymers into columnar crystals that have more perfect crystals (Chapter 5), and then melt compound this master batch with neat PP. During melt compounding, in order to keep the polymer morphology in the master batch consisting primary of the "bonded polymers" or the columnar crystals, one possible approach might be, firstly melt the neat PP at 200 °C under shearing, and then bring the melt temperature down to 180 °C to add the PP/CNT master batch.

3. The study in this thesis focused on the interphase development in semi-crystalline polymer. It would be interesting to see how does the amorphous polymer such as polycarbonate (PC) interacts with CNTs using the solution process. Unlike the interphase in the semi-crystalline polymers that can be modified and improved via crystallization, a tuning knob for the amorphous polymer can be its molecular weight. High molecular weight provides better interaction between polymer chains, however, as the molecular weight increases, viscosity of the polymer also increases which can potentially create difficulties in polymer chain alignment on the CNT surfaces. Dilute solution (to reduce viscosity), apply shearing and locally increase the temperature at polymer/CNT interface using microwave [1] or near infrared laser [2] are some possible directions for improving polymer ordering near CNTs.

4. PP and PE are not miscible with each other, and this creates an issue to recycle them at the same time. Recently the two immiscible polymers have been held together by adding "stitches" made of block copolymers of PP and PE [3, 4]. Given that the length of CNTs can typically be up to few microns, comparable or larger than the polymer blend domain sizes, and the fact that non-covalently PP coated f-MWNTs are effective nucleating agents (Chapter 5), a CNT coated with PP and PE at the same time can be used for compatibilization of the PP/PE blend. These CNTs locate at the domain boundaries can nucleate PP (or PE) crystals into the PP (or PE) domains and act as a "patch" at the interface (Figure 9.2). This idea has been proven using a non-covalently coated CNTs with the PMMA-PS triblock copolymers [5]. Since both PP and PE can be dissolved in xylene, the co-solvent process introduced in Chapter 3 can be modified to prepare the PP/PE/f-MWNT master batch. During the master batch preparation, the morphology and the crystallization competition (in solvent) in this ternary system can also be a research topic of interest.

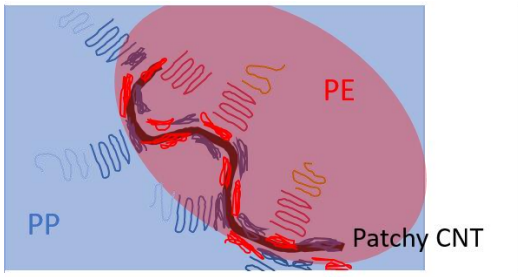

Figure 9.2. A "patchy" CNT with non-covalently bonded PP and PE bridging the blend interface.

5. From Chapter 6 and Chapter 8, increase of melt strength (or viscosity) both during melt annealing at 200 °C and at higher temperature (from 190 to 220 °C) indicate that the polymer at the molten state can interact with CNTs more effectively at the higher temperature. It was also shown in Chapter 8 that the information of such strong

interaction at high temperature was no longer preserved upon fast cooling (which typically happens during extrusion and various type of moldings). There was one successful experiment using very slow cooling rate (0.1 °C/min) that showed different structures (crystal size and melting temperature) when the two samples were fully cooled down and crystallized from two temperatures (190 and 220 °C), in Chapter 8 section 8.3.6. However, we are still not sure how the polymer chains change their configuration in the vicinity of CNTs as temperature increases, e.g. from 190 °C to 220 °C. Conducting X-ray diffraction (WAXD and SAXS) as a function of temperature might shed light on this question. Also, assuming the influence of CNTs (on the polymer morphology) reaches further into the matrix polymer as temperature increases, knowing how to preserve the structure developed at high temperature upon cooling, where the interphase is likely longer and has high polymer ordering, is important for practical application. This is possible to achieved, perhaps, when crystallizing under high pressure (hypothetically, specific volume of melt decreases and molecular diffusion becomes difficult [6]).

6. For the dielectric property, achieveing high permittivity and low dielectric loss is improtant in the application such as capacitor. Since the dielectric loss is induced by current leakage which becomes significant when forming a CNT percolating network, it is possible to suppress the dielectric loss by applying a layer of insulating sheath to prevent direct CNT contacts [7]. In this aspect, polymer coated pristine nanotube (p-MWNT) can be a promising candidate. The method we developed in Chapter 3 for polymer coating on f-MWNTs can be modified for this purpose. Different combination of co-solvents for dissolving polymer and dispersing p-MWNTs can be studied in order

to achieving good p-MWNT dispersion, therefore, higher percolation threshold. Appendix A provides an example of coating PP on p-MWNTs. CNTs with other polymers, e.g. PVDF, a most studied high-K polymer, can also be potential systems of interest.

7. Achieving high electrical conductivity and low thermal conductiviy is critical to increase the efficiency for producing thermoelectirc power (typically refer as the figure of merit). A reasonable approach is to achieve a conductivity path using conductive polymers (e.g. PEDOT:PSS, PPy, and PANI etc.) coated CNTs; in the meanwhile, thermoconductivity is low because phonons are scattered at the polymer-CNTs interface [8]. The thermoelectric property is expected to increase with a more homogenous polymer coating layer on CNTs, which is, typically achieved by polymerization or grafting of polymers. Solution processing (Chapter 3) along with repeatly thermal treatment (Chapter 5), might open up a new possibilty for tailoring the polymer coating homogeneity and improve the thermoelectric property in the CNTs contianing nanocomposites.

9.3 REFERENCES

1. Tongfei Wu, Yongzheng Pan, Erjia Liu, and Lin Li, *Carbon nanotube/polypropylene composite particles for microwave welding.* Journal of Applied Polymer Science, 2012. **126**(S2).

2. Byung Hak Lee, Jae Whan Cho, and Kyoung Hou Kim, *Crystallization, orientation, and mechanical properties of laser-heated photothermally drawn polypropylene/multi-walled carbon nanotube fibers.* European Polymer Journal, 2017. **91**: p. 70-80.

3. Costantino Creton, *Molecular stitches for enhanced recycling of packaging.* Science, 2017. **355**(6327): p. 797-798.

4. James M Eagan, Jun Xu, Rocco Di Girolamo, Christopher M Thurber, Christopher W Macosko, Anne M LaPointe, Frank S Bates, and Geoffrey W Coates, *Combining polyethylene and polypropylene: Enhanced performance with PE/iPP multiblock polymers.* Science, 2017. **355**(6327): p. 814-816.

5. Thomas Gegenhuber, Marina Krekhova, Judith Schöbel, André H Gröschel, and Holger Schmalz, *"Patchy" Carbon Nanotubes as Efficient Compatibilizers for Polymer Blends.* ACS Macro Letters, 2016. **5**(3): p. 306-310.

6. Shu-Gui Yang, Zhengchi Zhang, Dong Zhou, Yan Wang, Jun Lei, Liangbin Li, and Zhong-Ming Li, *Flow and Pressure Jointly Induced Ultrahigh Melting Temperature Spherulites with Oriented Thick Lamellae in Isotactic Polypropylene.* Macromolecules, 2015. **48**(16): p. 5834-5844.

7. Jiaming Zhu, Xiaoying Ji, Min Yin, Shaoyun Guo, and Jiabin Shen, *Poly (vinylidene fluoride) based percolative dielectrics with tunable coating of polydopamine on carbon nanotubes: Toward high permittivity and low dielectric loss.* Composites Science and Technology, 2017. **144**: p. 79-88.

8. Jian Zhou, Isaac Aguilar Ventura, and Gilles Lubineau, *Probing the role of poly (3, 4-ethylenedioxythiophene)/poly (styrenesulfonate)-coated multiwalled carbon nanotubes in the thermal and mechanical properties of polycarbonate nanocomposites.* Industrial & Engineering Chemistry Research, 2014. **53**(9): p. 3539-3549.

APPENDIX A: PP COATED PRISTINE MWNT MASTER BATCH

Experimental:

PP/p-MWNT master batch containing 5 wt% p-MWNTs was prepared following the steps below. i) p-MWNT was dispersed at 1 mg/dl in benzyl alcohol (anhydrous, 99.8%) using bath sonication at room temperature for 60 hours. ii) 38 mg PP was dissolved in 100 ml xylene at 120 °C. iii) the PP/xylene (120 °C) solution was added drop by drop to the p-MWNT/benzyl alcohol dispersion kept at about 65 °C, the ratio of benzyl alcohol to xylene is 2 to 1. This dispersion, maintained at 65 °C and kept under continuous stirring, was dried under vacuum at ~100 mbar for approximately 48 hours.

Results and discussion:

SEM images in Figure A1 showed no large CNT aggregates. Also, the average diameter of p-MWNT increased from 12 ± 3 nm to 20.7 ± 4.7 nm (from 40 measurements) indicating the presence of non-covalently coated PP on p-MWNTs. In DSC study, heating rate was 10 °C /min, and samples were heated from room temperature to 220 °C and then cooled and re-heated at the same rate. Crystallization temperature (T_c) and melting temperature (T_p) were derived from the 1st cooling cycle and the 2nd heating cycles, respectively. Increased crystallization temperature suggests enhanced nucleation rate. In Figure A2, the effect is more evident in PP/p-MWNT where 10 °C increase of T_c was observed. In contrast, only 4 °C increase in PP/f-MWNT as compared to the neat PP. T_p shifted from 160.5 °C to 162.3 °C and to 164.1 °C in PP/f-MWNT and PP/p-MWNT master

batch, respectively, suggesting that the later had higher crystal perfection and/or larger crystal.

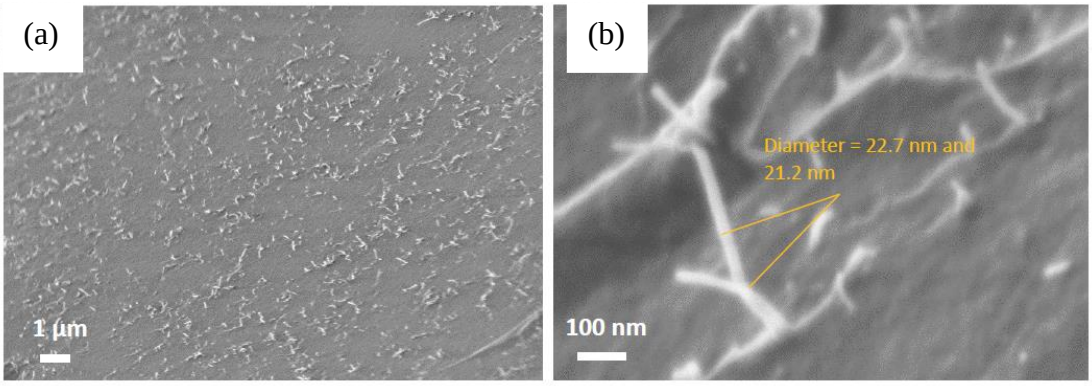

Figure A1. SEM images of PP/p-MWNT master batch (5 wt% p-MWNT). Diameter of the polymer coated CNTs were analyzed by software ImageJ.

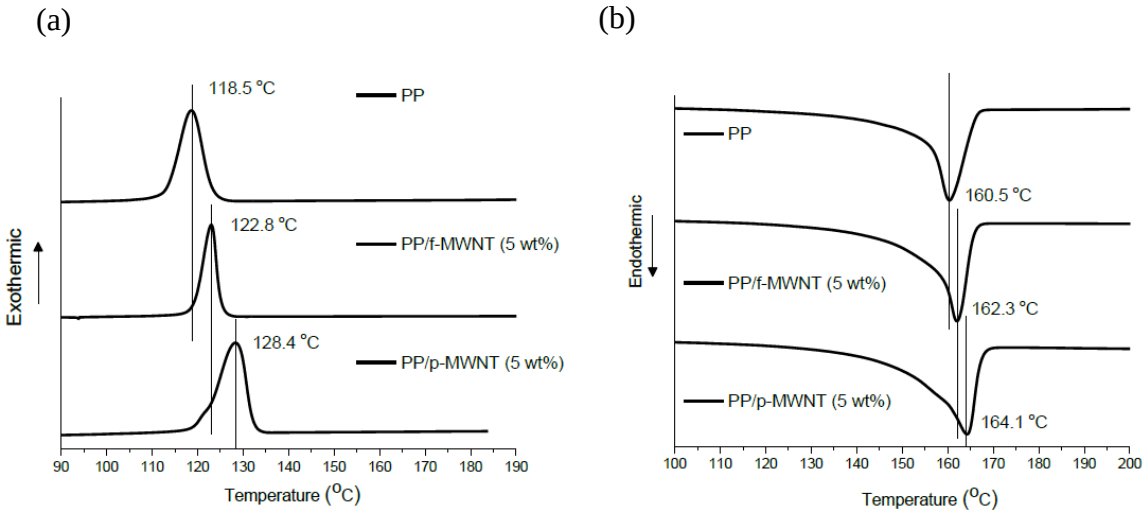

Figure A2. DSC of (a) first cooling cycles and (b) second heating cycles of PP, PP/f-MWNT and PP/p- MWNT master batch at 10 °C/min ramping rate. T_c and T_p were measured from 1st cooling cycle and 2nd heating cycle, respectively.

Background:

Chemical functionalization on CNT sidewall introduces defects and reduces the length of CNTs. As the result, mechanical strength [3], intrinsic electric [4] and thermal conductivity [5] of the nanotubes reduces even at 0.1 % of functionalized C-atom on CNT. Also, Hydroxyl functional groups can exhibit a more pronounced degradation because they act as Brønsted acidic sites that accelerated the degradation in polymer [6]. Therefore, pristine CNTs potentially have more advantages than the functionalized CNTs.

The adhesion energy (W_a) between polymer and CNT can be described using the following equation:

$$W_a = \boldsymbol{\gamma}_1(1 + \boldsymbol{cos}\,\boldsymbol{\theta}) = 2\sqrt{\boldsymbol{\gamma}_1^{\boldsymbol{d}}\boldsymbol{\gamma}_2^{\boldsymbol{d}}} + 2\sqrt{\boldsymbol{\gamma}_1^{\boldsymbol{p}}\boldsymbol{\gamma}_2^{\boldsymbol{p}}}$$

where $\boldsymbol{\gamma}$ represents the surface energy of the phase 1($\boldsymbol{\gamma}_1$) and phase 2($\boldsymbol{\gamma}_2$). θ is the contact angle between the two phases. $\boldsymbol{\gamma}^{\mathrm{d}}$ and $\boldsymbol{\gamma}^{\mathrm{p}}$ represent the dispersion and polar part of surface energy. Here, the polyolefin can be defined as phase 1 and CNT can be defined as phase 2. The surface energy of p-CNT and f-CNT can be found in the literatures [7], it is well established that the introduction of functional group and the increase of defect concentration on the surface of CNT raise its polar contribution of surface energy accompany by a reduction of the dispersion contribution. While in polyolefin such as polyethylene (PE) and polypropylene (PP) there is only dispersion contribution of surface energy due to their non-polar nature, the product of $\boldsymbol{\gamma}_1^{\boldsymbol{d}}$ and $\boldsymbol{\gamma}_2^{\boldsymbol{d}}$ is always higher, therefore higher W_a, when polyolefin is in contact with p-CNT than with f-CNT. Adhesion energy (W_a) has been shown correlated linearly with interfacial shear strength (IFSS) in the fiber-polymer matrix interface [8]. Similarly, nanocomposites filled with p-CNT should bring

about higher mechanical reinforcement as compared with f-CNT filled ones. For example, the contact angles and interfacial adhesion energies between MWNT and PE using a drop shape analysis method is given in Table A1 [7]. The values showed that the interfacial adhesion energy of PE with pristine MWNTs was greater than those functionalized MWNTs (by -COOH, -COCl and ethyl diamine) with PE. In another example, the $\boldsymbol{\gamma}^{d}$ and $\boldsymbol{\gamma}^{p}$ represent the dispersion and polar part of surface energy, which is 35.2 ± 0.18 and 7.0 ± 0.27 mJ/m^2 for pristine MWNT [7], 28.8 ± 0.17 and 13.4 ± 0.24 mJ/m^2 for -COOH functionalized MWNT [7], 30.1 and 0 mJ/m2 for isotactic PP [9], respectively. The calculated W_a between pristine MWNT and iPP is larger (65.1 mJ/m^2) than that between functionalized MWNT and iPP (58.2 mJ/m^2) which indicates a stronger interaction of iPP chains on p-MWNT than on f-MWNT.

Table A1. Contact angles and interfacial adhesion energies between MWNTs and PE [7].

	Contact angle (°)				Interfacial adhesion energy (mJ/m^2)			
	p-MWNT	MWNT-COOH	MWNT-COCl	MWNT-EDA	p-MWNT	MWNT-COOH	MWNT-COCl	MWNT-EDA
PE	13.1 ± 1.2	35.2 ± 3	34 ± 3.5	22.3 ± 2.3	72.6 ± 0.3	66.9 ± 1.7	67.3 ± 1.9	70.6 ± 1.0

EDA: ethyl diamine

REFERENCES

1. P.-H. Wang., et al., *Polypropylene nanocomposites with polymer coated multiwall carbon nanotubes.* Polymer, 2016. **100**: p. 244-258.

2. P.-H. Wang, S.G., N. Verghese, S. Kumar, Polymer Coated Multiwall Carbon Nanotubes. U.S. Provisional Application No. 62/323,146 filed on April 15, 2016.

3. Garg, A. and S.B. Sinnott, Effect of chemical functionalization on the mechanical properties of carbon nanotubes. Chemical Physics Letters, 1998. 295(4): p. 273-278.

4. Park, H., J. Zhao, and J.P. Lu, Effects of sidewall functionalization on conducting properties of single wall carbon nanotubes. Nano letters, 2006. 6(5): p. 916-919.

5. Shenogin, S., et al., Effect of chemical functionalization on thermal transport of carbon nanotube composites. Applied Physics Letters, 2004. 85(12): p. 2229-2231.

6. Bikiaris, D., Can nanoparticles really enhance thermal stability of polymers? Part II: an overview on thermal decomposition of polycondensation polymers. Thermochimica Acta, 2011. 523(1): p. 25-45.

7. Roh, S.C., et al., Characterization of the surface energies of functionalized multi-walled carbon nanotubes and their interfacial adhesion energies with various polymers. Polymer, 2014. 55(6): p. 1527-1536.

8. Nardin, M. and J. Schultz, Relationship between fibre-matrix adhesion and the interfacial shear strength in polymer-based composites. Composite Interfaces, 1993. 1(2): p. 177-192.

9. Landrock, A.H. and S. Ebnesajjad, Adhesives technology handbook. 2008: William Andrew.

APPENDIX B: FATIGUE AND J-R ANALYSIS (LITERATURE)

The fracture of most semicrystalline polymers, especially polyethylene (PE), polypropylene (PP), polyethylene terephthalate (PET), and nylon, oftentimes accompanies with large scale yielding that occurs at the crack tip which can be described by elastic-plastic fracture mechanics (EPFM) [1, 2]. The failure of glassy polymers such as PMMA [3] or PS [3], on the other hand, has been studied using linear-elastic fracture mechanics (LEFM) [1, 2]. In LEFM, the crack tip stress and displacement field is presented at a small elastic strain and can be uniquely characterized by K, the stress intensity factor. Irwin [4] showed that for an infinite sheet with a central crack of length $2c$ subjected to the fracture stress σ_B, the fracture toughness K_{IC} is simply given by $K_{\mathrm{IC}} = \sigma_B(\pi c)^{1/2}$. When the total work of fracture involves various forms of plastic deformation, such as crazing, fibrillation and microvoid formation, the EPFM approach must be used. These include, the *J*-integral [5-7], essential work of fracture [8-10] and crack opening displacement [11, 12]. The *J*-integral was originally defined by Rice [5] as a contour integral independent on the path and expresses the energy per unit area necessary to create new fracture surfaces. By knowing that the strain energy density $W = \int \sigma_{ij}\, \mathrm{d}\varepsilon_{ij}$ that relates to the stress and strain components σ_{ij} and ε_{ij} around the crack tip region and the surface traction vector T_i on the contour path moving through the displacement $\mathrm{d}u_i$, the *J*-integral can be defined as $J = \int W\, \mathrm{d}y - T_i \frac{\mathrm{d}u_i}{\mathrm{d}x}\, \mathrm{d}s$ [1]. Experimentally, the *J*-integral can be more simply determined from the decrease of potential energy U with crack length a, $J = -\frac{1}{B}\frac{\mathrm{d}U}{\mathrm{d}a}$, where B is the

specimen thickness. $\boldsymbol{\Delta}U$ can be obtain from the difference of area under load-displacement curves of two bodies with initial crack length a and (a + da) [1, 2]. The *J-R* resistance curve ($J - \boldsymbol{\Delta}a$) is then constructed through a set of identical specimens that are loaded to different levels of crack extensions ($\boldsymbol{\Delta}a$) prior to failure [2].

The *J*-integral and the *J-R* curve concepts have been applied to characterize the fracture toughness of PP composites. For example, Li et al. [13] found that the addition of $CaCO_3$ (20 wt%) led to change from brittle fracture in neat PP to ductile fracture. The fracture toughness at crack initiation (J_c) increased by about 90 %, which was attributed to the matrix/particle debonding that promoted the plastic yielding of the PP matrix. Similarly, with the addition of 2 to 40 vol% of talc, Velasco et al. [14] observed an increased crack resistance in the composites. However, the *J-R* curve for neat PP was not possible to be determined because catastrophic failure of the specimen happened prior to any stable crack growth ($\boldsymbol{\Delta}a$) larger than 0.1 mm. In another work, the addition of 40 wt% magnesium hydroxide, $Mg(OH)_2$, into PP impact copolymer reduced the J_c from 14.7 KJ/m^2 to 4.4 KJ/m^2 [15]. Nevertheless, the presence of the $Mg(OH)_2$ particles limited the plastic flow during fracture process such that the resistance to crack propagation (determined from the slope of the *J-R* curve) increased by 80%. Adding glass beads [16] or glass fibers [17] in PP also reduced its J_c. To the best of our knowledge, there is not yet a study on the fracture behavior of PP/carbon nanotube nanocomposite using *J-R* curve analysis.

The ability to maintain strength under cyclic stress is characterized by the fatigue resistance. There are two types of measurement to test the fatigue resistance of a given material. Firstly, the S-N curve reflects the life-to-failure at various stress levels, where S is the stress and N is the number of cycles to failure. According to ASTM test, the fatigue

strength, S_{Nf}, refers to as the value of stress at which failure occurs after N_f cycles; while the fatigue life, N_f, refers to as the number of stress cycles that a specimen sustains before failure at a specified stress level [18]. The second method to evaluate fatigue behavior is via the fatigue crack propagation rate (FCP), where $\frac{\mathrm{d}a}{\mathrm{d}N} = C(\Delta K)^m$. Here, C and m are constants that depend on the material, environment and stress ratio (ratio between maximum and minimum stress that alternatively applied to the sample), etc., and $\boldsymbol{\Delta K}$ is the range of the stress intensity factor during the fatigue cycle [19]. The observed increase of fatigue life in polymer/CNT nanocomposite is attributed to the delaying of crack initiation and growth through CNT pull-out, breakage, and bridging [20-25]. It was also shown in the epoxy/carbon fiber composite that the CNT coating on carbon fibers improved the fiber-matrix interface adhesion and increased the fatigue life with respect to the composite not having CNTs [26]. The effect of CNTs on fatigue has been most studied in epoxy using the S-N curve analysis [22-24] or FCP [20, 27]. With the help of dispersing agent (BYK-9077 consisting of block-copolymers with pigment affinic groups), up to 1550 % increase in fatigue life of epoxy was observed at 0.225 wt% CNTs incorporation [21]. An interesting result from Loos et al. showed that CNTs (0.3 wt%) only improved the fatigue life of the polyurethane nanocomposite at high cyclic stress, while the fatigue life remained unaffected at low stress level. This is contradicted with the rational because the CNT/matrix interface integrity should be better preserved and thus exhibit more effective nanotube pull-out and bridging at low stress [25]. There are relatively few works in the PP composites from the literature. With the addition of clay (5 wt%) [28] or $CaCO_3$ (20 to 40 wt%) [29], about 5 times increase of fatigue life was observed. About 2 to 3 times higher fatigue strength was reported by Peijs et al. [30, 31] in the PP/glass fiber composite. This

improvement was attributed to the stronger matrix-fiber adhesion due to the incorporation of maleic anhydride grafted PP (MA-g-PP) at the interface than the composite not having MA-g-PP.

REFERENCES

1. Ian M Ward and Dennis W Hadley, *An introduction to the mechanical properties of solid polymers*. 1993: John Wiley & Sons Ltd.; John Wiley & Sons, Inc.

2. David Arencón and José Ignacio Velasco, *Fracture toughness of polypropylene-based particulate composites.* Materials, 2009. **2**(4): p. 2046-2094.

3. JP Berry, *Determination of fracture surface energies by the cleavage technique.* Journal of Applied Physics, 1963. **34**(1): p. 62-68.

4. George R Irwin, *Analysis of stresses and strains near the end of a crack traversing a plate.* Journal of applied mechanics, 1957. **24**(3): p. 361-364.

5. James R Rice. *A path independent integral and the approximate analysis of strain concentration by notches and cracks*. 1968. ASME.

6. JA Begley and JD Landes, *The J integral as a fracture criterion*, in *Fracture Toughness: Part II*. 1972, ASTM International.

7. MKV Chan and JG Williams, *J-integral studies of crack initiation of a tough high density polyethylene.* International Journal of Fracture, 1993. **23**(2): p. 145-159.

8. KB Broberg, *Critical review of some theories in fracture mechanics.* International Journal of Fracture, 1968. **4**(1): p. 11-19.

9. Yiu-Wing Mai and Brian Cotterell, *On the essential work of ductile fracture in polymers.* International Journal of Fracture, 1986. **32**(2): p. 105-125.

10. Jingshen Wu and Yiu-Wing Mai, *The essential fracture work concept for toughness measurement of ductile polymers.* Polymer Engineering & Science, 1996. **36**(18): p. 2275-2288.

11. Norman Brown, J Donofrio, and X Lu, *The transition between ductile and slow-crack-growth failure in polyethylene.* Polymer, 1987. **28**(8): p. 1326-1330.

12. Xici Lu and Norman Brown, *The relationship of the initiation stage to the rate of slow crack growth in linear polyethylene.* Journal of materials science, 1986. **21**(7): p. 2423-2429.

13. Li Dongming, Zheng Wenge, and Qi Zongneng, *The J-integral fracture toughness of PP/CaCO3 composites.* Journal of materials science, 1994. **29**(14): p. 3754-3758.

14. JI Velasco, JA de Saja, and AB Martinez, *FRACTURE BEHAVIOUR OF UNTREATED AND SILANE-TREATED TALC-FILLED POLYPROPYLENE COMPOSITES.* Fatigue & Fracture of Engineering Materials & Structures, 1997. **20**(5): p. 659-670.

15. JI Velasco, C Morhain, D Arencón, OO Santana, and M Ll Maspoch, *Low-rate fracture behaviour of magnesium hydroxide filled polypropylene block copolymer.* Polymer Bulletin, 1998. **41**(5): p. 615-622.

16. D Arencon, JI Velasco, V Realinho, M Sanchez-Soto, and A Gordillo, *Fracture toughness of glass microsphere-filled polypropylene and polypropylene/poly (ethylene terephthalate-co-isophthalate) blend-matrix composites.* Journal of materials science, 2007. **42**(1): p. 19-29.

17. József Karger-Kocsis, *Structure and fracture mechanics of injection-molded composites.* Wiley Encyclopedia of Composites, 2012.

18. A ASTM, *Guide for Fatigue Testing and the Statistical Analysis of Fatigue Data.* ASTM STP, 1963(91-A).

19. Fernand Ellyin, *Fatigue damage, crack growth and life prediction*. 2012: Springer Science & Business Media.

20. W Zhang, RC Picu, and N Koratkar, *The effect of carbon nanotube dimensions and dispersion on the fatigue behavior of epoxy nanocomposites.* Nanotechnology, 2008. **19**(28): p. 285709.

21. MR Loos, J Yang, DL Feke, and I Manas-Zloczower, *Enhanced fatigue life of carbon nanotube-reinforced epoxy composites.* Polymer Engineering & Science, 2012. **52**(9): p. 1882-1887.

22. Christopher S Grimmer and CKH Dharan, *High-cycle fatigue of hybrid carbon nanotube/glass fiber/polymer composites.* Journal of Materials Science, 2008. **43**(13): p. 4487.

23. Daniel R Bortz, César Merino, and Ignacio Martin-Gullon, *Carbon nanofibers enhance the fracture toughness and fatigue performance of a structural epoxy system.* Composites Science and Technology, 2011. **71**(1): p. 31-38.

24. Ying Cao and Li Pan. *Fatigue of nanotube-reinforced carbon fiber epoxy composites*. in *Advanced Materials Research*. 2012. Trans Tech Publ.

25. MR Loos, J Yang, DL Feke, I Manas-Zloczower, S Unal, and U Younes, *Enhancement of fatigue life of polyurethane composites containing carbon nanotubes.* Composites Part B: Engineering, 2013. **44**(1): p. 740-744.

26. Davis C Daniel, Justin W Wilkerson, and Zhu Jiang, *Carbon nanotube fiber-reinforced polymer composites having improved fatigue durability and methods for production thereof*. 2009, Google Patents.

27. W Zhang, RC Picu, and N Koratkar, *Suppression of fatigue crack growth in carbon nanotube composites.* Applied Physics Letters, 2007. **91**(19): p. 193109.

28. Yuanxin Zhou, Vijay Rangari, Hassan Mahfuz, Shaik Jeelani, and PK Mallick, *Experimental study on thermal and mechanical behavior of polypropylene, talc/polypropylene and polypropylene/clay nanocomposites.* Materials Science and Engineering: A, 2005. **402**(1): p. 109-117.

29. SE Kultural and IB Eryurek, *Fatigue behavior of calcium carbonate filled polypropylene under high frequency loading.* Materials & design, 2007. **28**(3): p. 816-823.

30. M Van den Oever and T Peijs, *Continuous-glass-fibre-reinforced polypropylene composites II. Influence of maleic-anhydride modified polypropylene on fatigue behaviour.* Composites Part A: Applied Science and Manufacturing, 1998. **29**(3): p. 227-239.

31. E Kristofer Gamstedt, Lars A Berglund, and Ton Peijs, *Fatigue mechanisms in unidirectional glass-fibre-reinforced polypropylene.* Composites Science and Technology, 1999. **59**(5): p. 759-768.

APPENDIX C: IMPACT STRENGTH OF PP HAVING DIFFERENT FORMULATIONS

Description of the polymers:

The polymer used in this thesis study (Chapter 2 to Chapter 8) is the polypropylene homopolymer (09HG0090): According to SABIC, this grade is for general purpose application. Material is made using gas phase technology, and by using a Ziegler-Natta type catalyst. It has a melt flow index of 10 dg/min (MFI ISO 1133, 2.16 kg and T=230 °C). Material has a high isotacticity of approximately 97%, as measured with NMR. Polydispresity (M_w/M_n) is approximately 5. Material is the reactor powder and therefore not stabilized, and has no additives.

Apart from this polymer grade, another two grades of PP were also made into PP/f-MWNT master batches and melt compounded with neat PP, using the same method discussed in Chapters 2 and 3). The information based on the product data sheet of these two polymers are:

- SABIC® PP 578N, a homopolymer designed for injection molding, typically used in domestic appliances and furniture, even as replacement for talcum or talc filled compounds. The melt flow index is 25 dg/min (MFI ISO 1133, 2.16 kg and T=230 °C). This grade contains nucleating agent.
- SABIC® PP FPH50, a homopolymer designed for injection molding, typically used in thin wall packing applications both for food and non-food segments. The melt flow index is 50 dg/min (MFI ISO 1133, 2.16 kg and T=230 °C). This grade contains both a nucleating agent and an anti-static agent.

Results:

Experiment 1:

Here, 5 wt% f-MWNT master batch from PP (09HG0090) was used. The PP (578 N) was used as the bulk PP to make injection molded specimen containing 1 wt% f-MWNT. The results are given in Table C1. The PP/f-MWNT (1 wt%) nanocomposite showed about 34 % improvement in the impact strength over the control PP (578N).

Table C1. Impact strength of PP (578 N) based samples using PP (09HG0090) based master batch.

Test no.	Control PP (578 N)	PP/f-MWNT (1 wt% f-MWNT)
1	2.98 kJ/m^2	3.73 kJ/m^2
2	2.80 kJ/m^2	4.10 kJ/m^2
3	2.24 kJ/m^2	3.73 kJ/m^2
4	2.61 kJ/m^2	2.98 kJ/m^2
5	2.98 kJ/m^2	3.73 kJ/m^2
Average	2.72 kJ/m^2	3.65 kJ/m^2
SD	0.31 kJ/m^2	0.41 kJ/m^2

Experiment 2:

Here, 5 wt% f-MWNT master batch from PP (578 N) was used. The PP (578 N) was used as the bulk PP to make injection molded specimen containing 1 wt% f-MWNT. The results are given in Table C2. The PP/f-MWNT (1 wt%) nanocomposite showed about 120 % improvement in the impact strength over the control PP (578N).

Table C2. Impact strength of PP (578 N) based samples using PP (578 N) based master batch.

Test no.	Control PP (578 N)	PP/f-MWNT (1 wt% f-MWNT)
1	2.05 kJ/m^2	4.85 kJ/m^2
2	2.24 kJ/m^2	5.03 kJ/m^2
3	2.05 kJ/m^2	4.10 kJ/m^2
Average	2.11 kJ/m^2	4.66 kJ/m^2
SD	0.11 kJ/m^2	0.49 kJ/m^2

Experiment 3:

Here, 5 wt% master batch from PP (FPH50 N) was used. The PP (FPH50) was used as the bulk PP to make injection molded specimen containing 1 wt% f-MWNT. The results are given in Table C3. The PP/f-MWNT (1 wt%) nanocomposite showed about 105 to 130 % improvement in the impact strength over the control PP (FPH50).

Table C3. Impact strength of PP (FPH50 N) based samples using PP (FPH50 N) based master batch.

Trail 1		
Test no.	Control PP (FPH50)	PP/f-MWNT (1 wt% f-MWNT)
1	1.86 kJ/m^2	3.36
2	1.68 kJ/m^2	3.36 kJ/m^2
3	1.68 kJ/m^2	
4	1.49 kJ/m^2	
5	1.49 kJ/m^2	
Average	1.64 kJ/m^2	3.36 kJ/m^2
SD	0.16 kJ/m^2	0.00 kJ/m^2
Trail 2		
Test no.	Control PP (FPH50)	PP/f-MWNT (1 wt% f-MWNT)
1	1.49 kJ/m^2	2.98 kJ/m^2
2	1.12 kJ/m^2	2.98 kJ/m^2
3	1.12 kJ/m^2	2.24 kJ/m^2
4	1.30 kJ/m^2	2.61 kJ/m^2
5	0.93 kJ/m^2	
Average	1.18 kJ/m^2	2.70 kJ/m^2
SD	0.19 kJ/m^2	0.36 kJ/m^2

APPENDIX D: STUDIES OF PP WITH ADDITIVES (STABILIZERS)

Experimental:

In order to prepare stabilized PP pellets, Brabender KETSE 12/36 twin screw extruder (Figure D1) was used to compound stabilizers with PP powder. Screw diameter is 12 mm and L/D is 36. Temperatures of all the four extruder zones were 200 °C. The mixture of PP and stabilizer was prepared by manual mixing. Stabilizer contained three components, calcium stearate, Irgafos 168 and Irganox 1010. Recommended concentrations of these components in PP (suggested by SABIC) is 300, 1500 and 4000 ppm, respectively. The PP and stabilizers mixture was fed manually to TSE. Flow of nitrogen was maintained at feed section of TSE. Screw speed was maintained at 25 rpm. The extrudate was quenched by passing through a water trough and then fed to the pelletizer. The pellets were dried in vacuum oven at 80 °C for about 4 hours. These pellets are melt compounded and injection molded following the protocol in Chapter 3. Izod impact and tensile testing were also conducted following the method in Chapter 3.

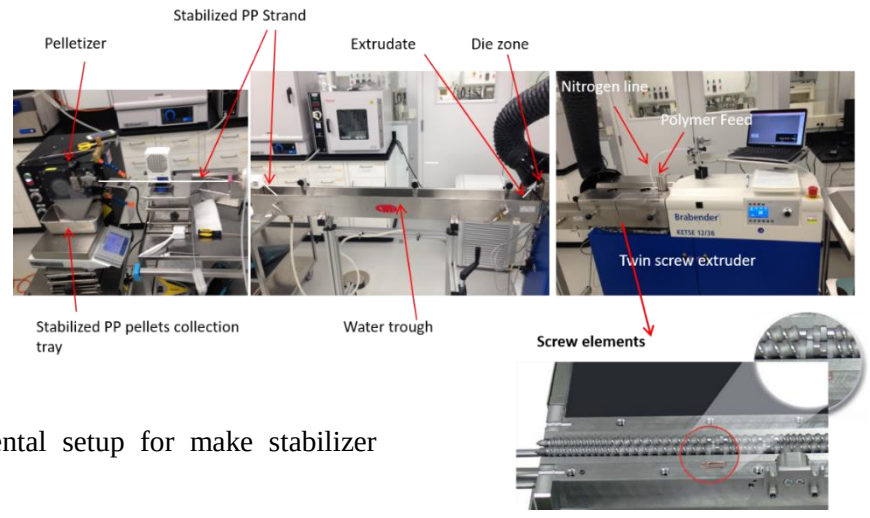

Figure D1. Experimental setup for make stabilizer containing PP pellets.

Results:

Impact strength

The impact strength of stabilizer containing samples, compared with samples without stabilizers are given in Figure D2. Key observations are listed below:

- Impact strength of stabilized PP sample is 34% higher than that of the control PP sample without stabilizer.
- Impact strength of 1 wt% p-MWNT containing stabilized PP sample is statistically similar to that of the stabilized PP.
- Impact strength of 0.1 wt% f-MWNT (PP/f-MWNT master batch) containing stabilized PP sample is 44% higher than that of 0.1 wt% f-MWNT containing PP sample without stabilizer.
- Impact strength of 0.1 wt% f-MWNT (PP/f-MWNT master batch) containing stabilized PP sample is 29% higher than that of stabilized PP sample.
- Impact strength of 1 wt% f-MWNT (PP/f-MWNT master batch) nanocomposite is statistically similar for the samples with and without stabilizer
- Further improvements are expected with high shear mixing using twin screw extruder (improving f-MWNT dispersion).

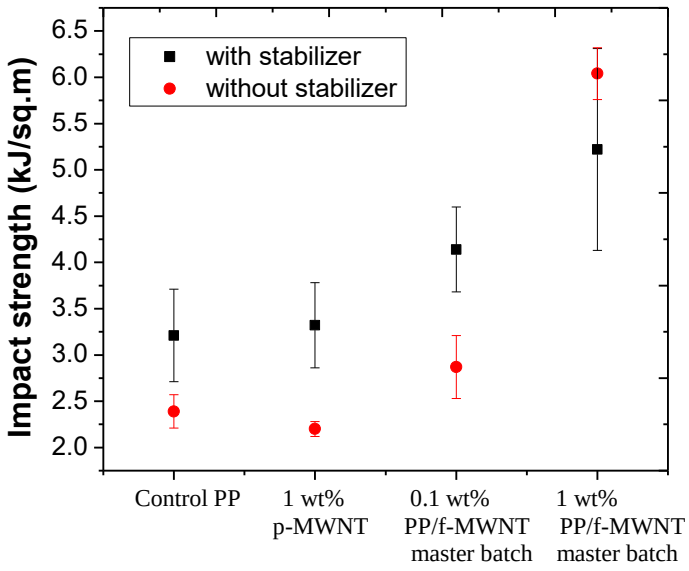

Figure D2. Impact strength of PP and PP/MWNT nanocomposites with and without stabilizers.

Tensile properties

The tensile properties of stabilizer containing samples, compared with samples without stabilizers are given in Figure D3. Key observations are listed below:

- Stabilized PP showed similar modulus and yield stress but 150% higher strain to failure as compared to unstabilized PP.
- p-MWNT containing stabilized PP samples showed similar modulus and 14% lower yield stress (p-value < 0.0001) than p-MWNT containing unstabilized PP. The p-MWNT containing samples exhibit brittle characteristic (low strain to failure) with and without stabilizers.
- Higher tensile modulus, and higher strain to failure of PP/f-MWNT containing stabilized samples as compared to their unstabilized counterparts.
- At 1 wt% f-MWNT, there is no significant loss in strain to failure in the stabilized samples.

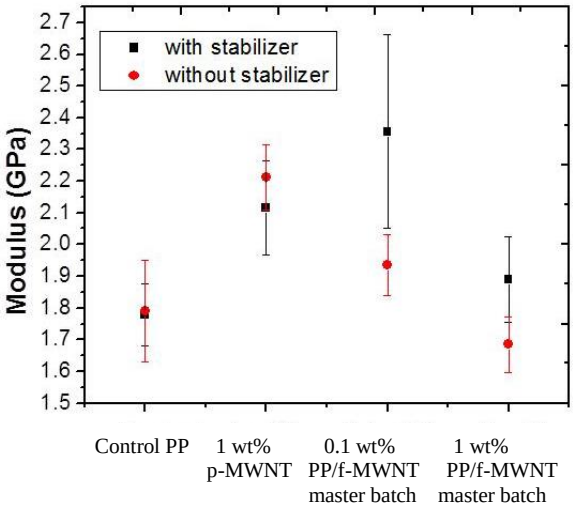

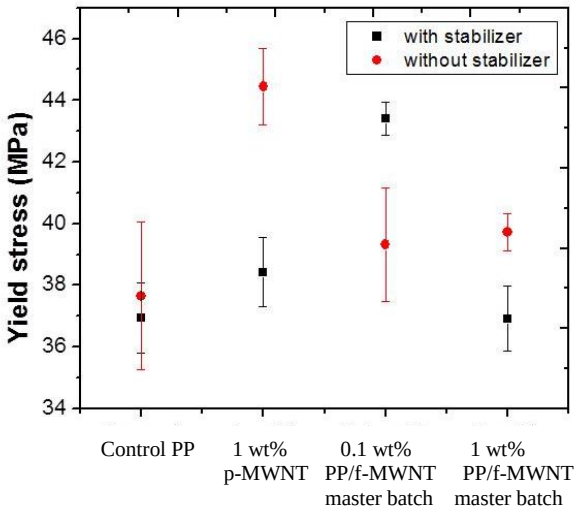

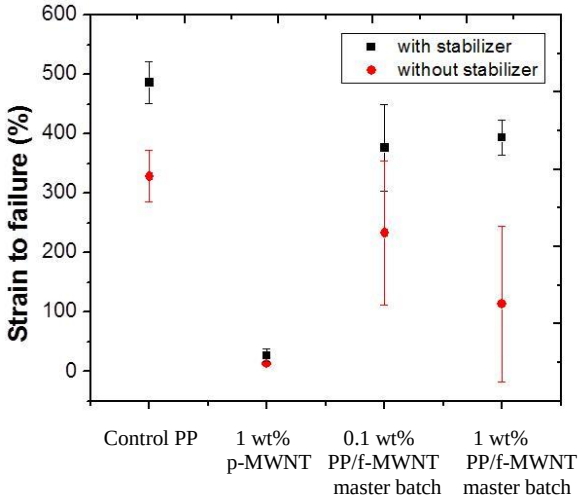

Figure D3. Tensile modulus, tensile strength and strain to failure of PP and PP/MWNT nanocomposites with and without stabilizers.

Crystallization behavior

Polarized optical microscopy (POM) images of PP and PP/f-MWNT nanocomposites (0.1 wt%) are shown in Figure D4. The full crystallization time is determined as the time when the full coverage of spherulite under was reached. Compared with samples without stabilizer (Chapter 5), these samples were crystallized in a faster rate: The full crystallization times reduced from 51 minutes, 3 minutes, and 15 minutes to 21 minutes, 2 minutes, and 13 minutes in neat PP, PP/f-MWNT master batch based nanocomposite, and MA-g-PP/f-MWNT master batch based nanocomposites, respectively.

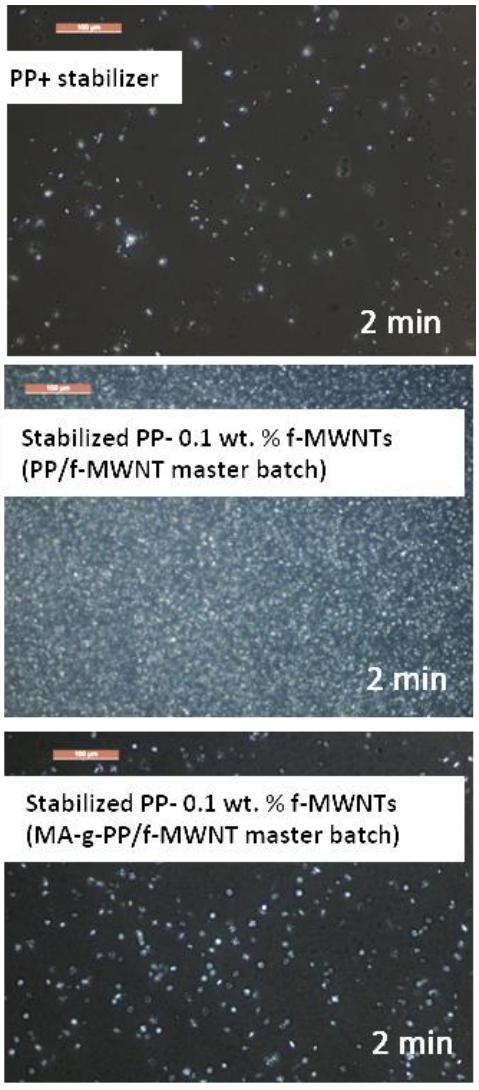

Figure D4. POM under cross polar of PP and PP/f-MWNT nanocomposites (0.1 wt%) containing stabilizers. The samples were melted at 225 °C for 5 minutes, followed by a cooling at 20 °C/minutes to 135 °C. Scale bar represents 100 μm. From the image, it is evident that the PP/f-MWNT based sample has faster crystallization rate than the other two samples.

Rheological behavior

Addition of stabilizer increases the complex viscosity and melt elasticity (reduced tan δ) of neat PP (Figure D5). There is no noticeable change in the rheological behavior between PP and the nanocomposites having 0.1 and 1 wt% f-MWNTs, after incorporating stabilizers. On the other hand, when there is no stabilizer in the system, i.e. in Chapter 6 section 6.3.1, complex viscosity increase from about 200 Pa-s to above 1000 Pa-s after adding 1 wt% f-MWNTs in PP.

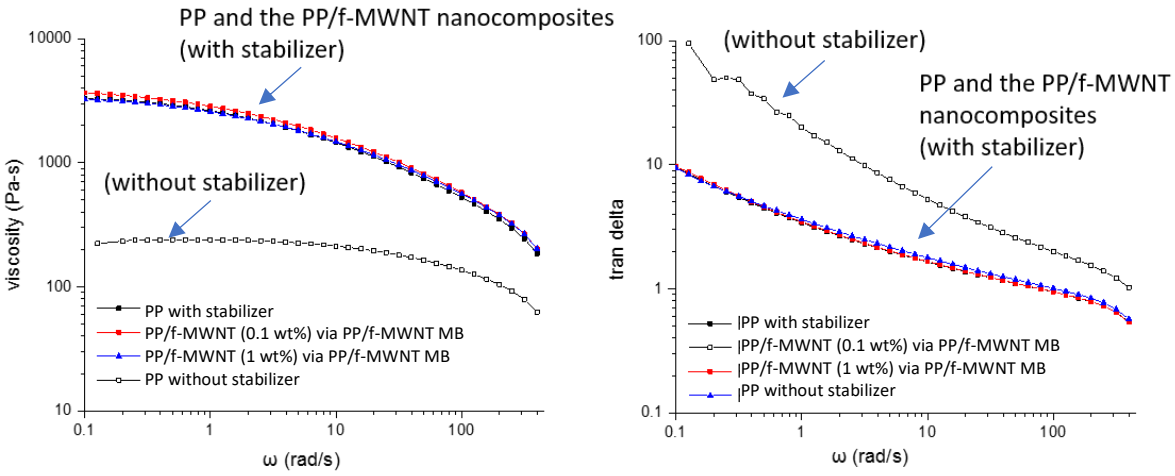

Figure D5. Complex viscosity and tan δ curve of PP and PP/f-MWNT nanocomposites (containing PP/f-MWNT master batch) with stabilizer. For comparison, PP without stabilizer was also plotted.

APPENDIX E: MANUFACTURING AND MECHANICAL PROPERTIES OF PP/MA-G-PP/f-MWNT FIBERS

Fibers were melt spun using control PP and 0.1 wt% f-MWNT (MA-g-PP/f-MWNT master batch based nanocomposite, the method for the preparation of master batch is given in Chapter 2).

Experiment set 1: Fiber spinning using one step melt processing (microcompounder)

In this of experiment, PP powders and MA-g-PP/f-MWNT master batch were manually mixed by mortar and pestle and then fed to 15 cc microcompounder. Temperature of three zones of the macromonomer barrel were set at 215 °C and the melt temperature measured before the die was 200 °C. Melt was recirculated in the microcompounder barrel for 30 min and then extruded using a 250 μm spinneret. For fiber spinning purposes, microcompounder was operated under controlled pressure mode at ~ 150 N.

For spinning the control PP fibers, take- up speed was 14 meters/min. After 30 minutes of recirculation at screw speed of 200 rpm, melt pressure was 1400 N at 200 rpm. After obtaining small quantity of fiber initially, subsequent attempts to take-up the fibers failed due to melt fracture.

For spinning PP/f-MWNT fibers (0.1 wt% f-MWNT), take up speed was 22 meters/min. It is to be noted that the difficulty observed in spinning fibers from control PP after 30 minutes of recirculation was not seen in the case of 0.1 wt% PP/f-MWNT fibers. After 30 minutes of recirculation at screw speed of 200 rpm, melt pressures were 2100 N at 200 rpm. 2 wt% MA-g-PP containing PP fibers were also melt spun using same

procedure as above. Take-up speed was 14 meters/min. Fibers were drawn using drawing set-up as shown in Figure E1. Drawing temperature was 120 °C. Hot draw ratio and the tensile properties of these three fibers are given in Table E1.

It can be seen from Table E1 that at similar post-spin draw ratio, tensile strength and modulus of PP/f-MWNT fiber is 17% and 30% higher, respectively, as compared to the control PP fiber (p values < 0.0001 for both properties). Smaller diameter of PP/f-MWNT fiber as compared to the control PP fiber is due to higher take-up speed (22 mpm in PP/f-MWNT v.s 14 mpm in PP) during fiber spinning. 2 wt% MA-g-PP containing fiber possesses statistically significantly lower (p value < 0.0001) tensile strength and tensile modulus as compared to control PP. The tensile strength and tensile modulus of PP/f-MWNT fiber is 38% and 61% higher than MA-g-PP containing PP fiber.

Table E1. Tensile properties of PP, PP/f-MWNT (0.1 wt% f-MWNT), and PP/MA-g-PP (2 wt% MA-g-PP) fibers (Experiment set 1).

Sample	Hot draw ratio	Diameter (μm)	Tensile Strength (GPa)	Tensile Modulus (GPa)	Strain to Failure (%)
Control PP	8	34.1 ± 3.30	0.46 ± 0.06	5.7 ± 1.1	17.5 ± 1.8
PP/f-MWNT (0.1 wt% f-MWNT)	8	25.3 ± 1.2	0.54 ± 0.04	7.4 ± 0.6	20.3 ±1.1
PP/MA-g-PP (2 wt% MA-g-PP)	6	31.9 ± 3.3	0.39 ±0.05	4.6 ± 0.8	59.3 ± 33.8

(a) (b)

Figure E1. Fiber spinning set up: (a) 15 cc microcompounder, and (b) fiber winding unit.

Experiment set 2: Fiber spinning using two step melt processing (microcompounder + Bradford spinning system)

In this set of experiment, firstly, melt compounding of PP and MA-g-PP/f-MWNT master batch (5 wt% f-MWNT) was conducted to achieve 0.1 wt% f-MWNT loading in PP using 15 cc microcompounder. Melt was recirculated in the microcompounder for 5 minutes. Screw rpm was 200 rpm during recirculation. Temperature of three zones of barrel were set at 215 °C and the melt temperature measured before the die was 200 °C. The melt was extruded from a 1 mm die, and then quenched by passing through DI water. For comparison purposes, PP powders were also pelletized under similar processing conditions. Pellets were dried under vacuum at 80 °C for 4 hours prior to spinning (using Bradford spinning system, where barrel (reservoir) diameter was 16 mm and the spinneret diameter was 250 μm. 20 μm screen filter was used in the spin pack. Flow rate was set at 0.08 cc/min (calculated from the ram speed that was set at 0.24 mm/min) and take-up speed was 10 meters/min. Fiber hot drawing was carried out using hot plate at 120 °C.

Table E2. Tensile properties of PP and 0.1 wt% PP/f-MWNT fibers (Experiment set 2).

Sample	Hot draw ratio	Diameter (μm)	Tensile Strength (GPa)	Tensile Modulus (GPa)	Strain to Failure (%)
Control PP	7.1	29.4 ± 3.9	0.61 ± 0.07	6.8 ± 1.2	50.1 ± 18.0
PP/f-MWNT (0.1 wt%)	7.1	27.0 ± 2.7	0.64 ± 0.05	7.5 ± 0.8	36.9 ±16.9

Table E2 shows the hot draw ratios achieved and the tensile properties of drawn fibers. Tensile modulus of PP/f-MWNT fiber was statistically similar to the control PP fiber. Table E3 lists the structural parameters of drawn fibers obtained from WAXD. Crystal size in the case of PP/f-MWNT fiber is larger than control PP fiber. Also, Figure

E2 shows the small angle XRD patterns of these fibers, where the as-spun fiber (fiber before hot drawing) exhibits oriented crystal lamella, presumably due to the presence of f-MWNTs.

Table E3. Structural parameters (WAXD) of drawn fibers

Sample	Control PP	PP/f-MWNT (0.1 wt%)
Crystallinity %	62.1	61.3
Orientation, FWHM of (040)	6.5°	6.8°
Crystal size (nm) (110) (2θ: 14°)	9.0	9.8
Crystal size (nm) (040) (2θ: 17.1°)	7.0	7.3

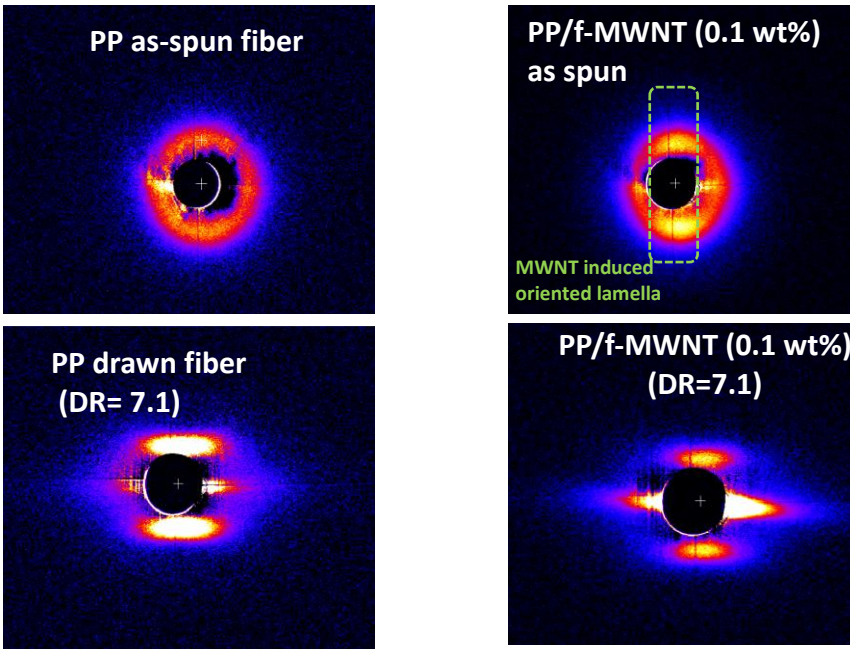

Figure E2. SAXS patterns of as-spun and drawn PP and PP/f-MWNT fibers. The lamella long period (L_B) was calculated from the 2θ from the SAXS scan using Bragg's Law. L_B equals to 9.5 nm and 16.0 nm from the as-spun and drawn PP fiber, respectively; L_B equals to 11.0 nm and 15.2 nm from the as-spun and drawn PP/f-MWNT fiber, respectively.

Figure E3 shows the strain in the drawn fibers as a function of stress at 155 °C during TMA tests. TMA400 was used for these tests. Heating rate was 5 °C/min in air. It is seen that PP/f-MWNT fibers exhibit ~35% reduction in shrinkage than control PP fibers at zero stress. Figure E4 shows that at 22 °C, there is no statistically difference in storage modulus between control PP fibers and the PP/f-MWNT fiber.

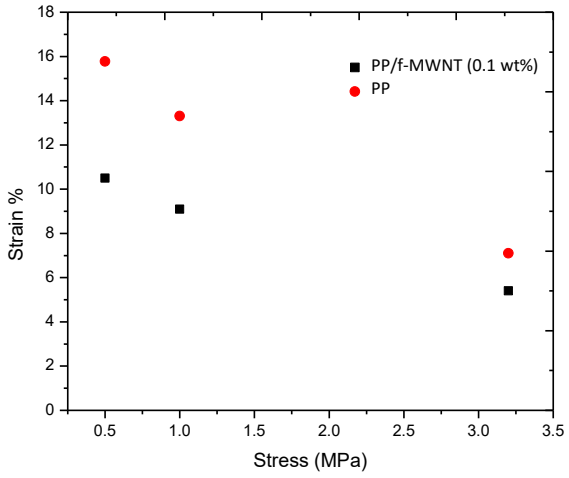

Figure E3. Thermal shrinkage under 0.5, 1, and 3.25 MPa applied stress of drawn PP and PP/f-MWNT fibers.

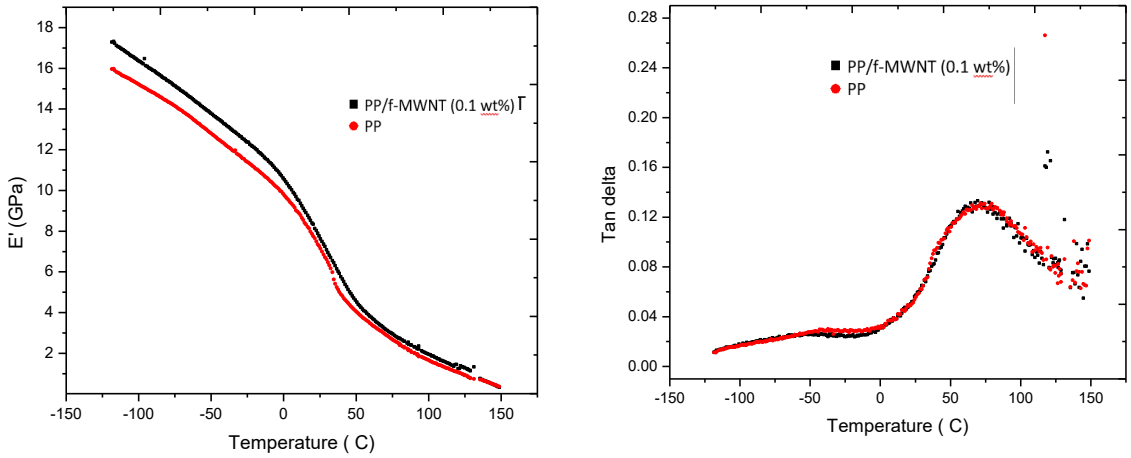

Figure E4. Dynamic mechanical behavior (1 Hz at a heating rate of 1 °C/min) of control PP and PP/f-MWNT fibers.

Summary:

- At same spin and hot draw ratio, f-MWNT containing samples possess higher tensile strength (up to 17%) and higher tensile modulus (up to 30%) than the control PP.
- MA-g-PP incorporated PP samples show lower tensile strength and modulus than control PP.
- At zero stress, thermal shrinkage of fiber with 0.1 wt% f-MWNT (PP/f-MA-g-PP master batch) is 35 % (under zero applied stress at 155 °C) lower than that in the control PP fiber.

APPENDIX F: HIGH STRAIN RATE IMPACT TEST

Introduction:

Notched Izod impact test results on the polypropylene (PP)/f-MWNT master batch based injection molded rectangular specimens showed that the impact strength increased by 150% than that of control PP when adding 1 wt% f-MWNTs (Chapter 3). The velocity of these tests is about 3 m/s. On the other hand, tensile tests wherein the strain rate is 0.00423 m/sec, there is no statistical difference in the tensile properties between control PP and PP/f-MWNT master batch based nanocomposites. Therefore, it was expected that the further higher strain rates impact testing (at velocities higher than 3 m/s) may result in even higher impact strength than observed in notched Izod impact tests.

Zamani et al.[1] reported the test results of high velocity impact testing on PP and PP/MWNT nanocomposites. Samples were prepared by injection molding. Sample size was square plate of size 120 mm X 120 mm X 2 mm. The projectile used was hemispherical tip hardened steel (Rc60) of dimensions, 25.6 mm (L) X 8.1 mm (diameter), shank length of 22.7 mm and weight was 11.34 g. Helium gas was used as propellant. Ballistic limit, V50, was determined from the highest impact velocity at which the projectile perforates the sample but is unable to go through and the lowest impact velocity with no residual velocity recordings. This definition is as per the standard MIL-STD-662F. In this work, V50 was found to be ~16 m/s for control PP and ~23 m/s for 1 wt% MWNT containing PP/MWNT nanocomposite. Thus, the ballistic limit increased by 43% in sample containing 1 wt% MWNT as compared to control PP sample.

[1] Zamani M. et al, Iran Polymer Journal 2012, 21, 887-894

Experimental:

Injection molded circular discs: diameter of 25.4 mm, thickness of 1.5 mm. The preparation of the sample can be found in Chapter 3.

Instrument used to conduct the impact tests at high velocity

Gas gun consisting of small diameter (bore diameter: 0.3") rifled barrel as shown in Figure F1. 3 mm diameter stainless steel balls weighing 0.13 g were used as the projectile. The sphere is mounted in sabot, which is assembly of four pieces of glass filled polycarbonate as shown in Figure F1. Sabot acts as a carrier of the projectile and the four pieces separate as soon as sabot exits the barrel, leaving only the projectile to continue with acquired velocity and hit the target. Sabots were purchased from Physics Applications Inc., Dayton, OH.

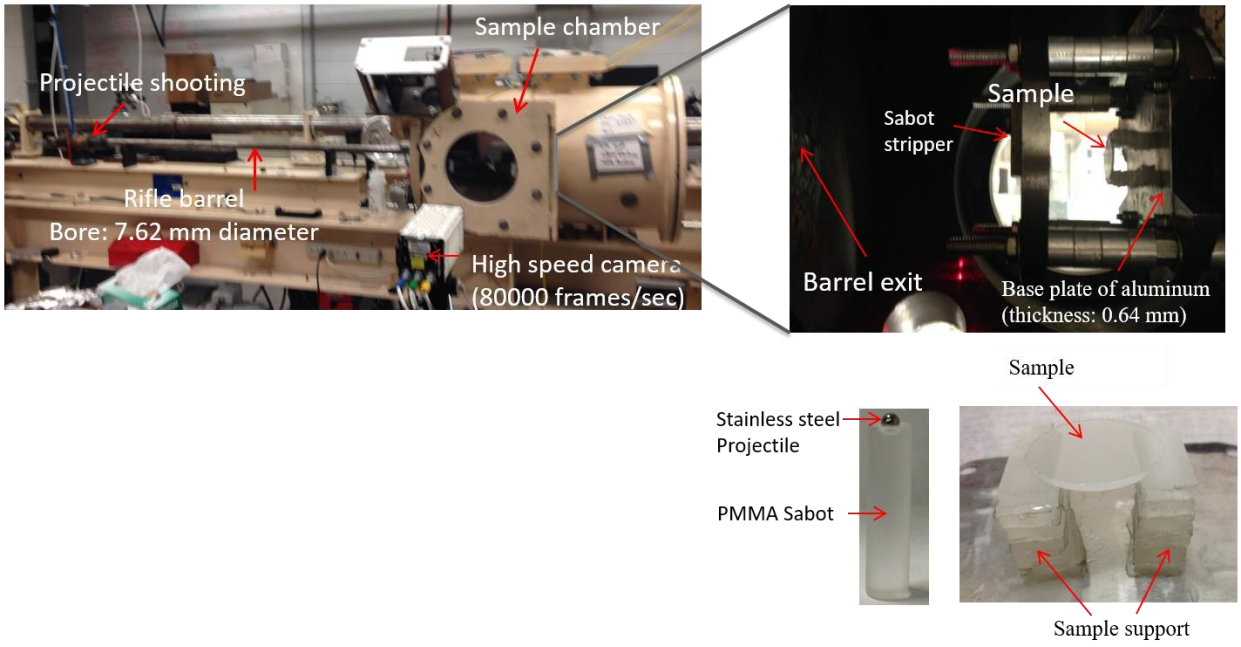

Figure F1. Gas gun of small diameter riffle barrel (Length: 6'); Sample mounted anvil inside the chamber (sabot stripper allows only the projectile to go through and hit the target).

Distance between sabot stripper and the sample as well as the distance between sabot stripper and aluminum support plate is measured. Upon keeping the sample with anvil inside the chamber, 5 mm hole of sabot stripper is aligned with respect to the barrel center. Currently, this alignement is being done with the help of a laser beam that is made to pass through the barrel and the center of the 5 mm hole. The distance between the exit of the barrel and laser 1 and laser 2 is measured by passing the governing rod through the barrel. As soon as the governing rod blocks the laser, it causes the voltage in a connected multimeter to drop and this distance is taken as the distance of laser from the barrel exit. Distance between barrel exit and sabot stripper is again measured by the governing rod.

On one side of the chamber, flash light is kept against the viewing window and on the other side, high speed camera is kept against the viewing window. This camera captures the images at rate of up to 80,000 frames/sec. During actual test, flash light and camera are activated based upon the time at which laser 1 is blocked by the projectile. To ensure proper activation mechanism of the flash light and camera, triggers are made by mannually blocking the lasers.

Typically, for high velocity tests (1000 m/s), vacuum of around 100 mtorr has to be reached before the test is conducted.

Results and Discussion:

Several attempts (sussessful and unssessful experiments) and the condition used are briefly descripted here. Test 1 to Test 12 are dedicated for the control PP trials; Test 12 to Test 14 are dedicated for the nanocomposites trials. The sucessful results are summarized in Table F1.

Tests conducted on control PP discs

Test 1:

Based on the work reported by Zamani, in order to reach the same kinetic energy corresponding to 15 m/s for the reported projectile, the velocity of the projectile in current tests was calculated to be ~200 m/s. At such low velocities, it was felt that there is no need to pull the vacuum inside the system. Hence first test was conducted in air. In order to reach the velocity of 213 m/s, air pressure required was calculated to be ~60 psi based on the models developed from earlier test results by Dr. Thadhani's group. However, at this pressure, the sabot did not move at all from its mounting position. Subsequently, pressurizing medium was changed to helium and pressurized to 500 psi. When fired at this pressure, the sabot moved but still remained inside the barrel. Subsequently, pressure of 1000 psi was used at which firing was successful. The predicted velocity was ~400 m/s. However, at these high speeds in the absence of vacuum, signal of laser 1 triggered prematurely and rest of the imaging system did not work appropriately. The projectile went through the PP sample and also passed through alumimum plate.

After realizing that the current set-up of sabot and the rifle barrel was only suitable for high velocity impact tests, it was decided to continue with the tests hoping that at least we could obtain the change in velocity of projectile before and after the impact on target to quantify the results.

Test 2:

After the system clean-up, sample mounting and all necessary measurements taken, vacuum was pulled to ~100 mtorr. Since 1000 psi could successfully fire the projectile in

test 1, pressure of 750 psi was attempted in this test. The test was successful, The projectile velocity before impact was 673 m/s. The velocity of projectile after impact was calculated based on the images captured by the camera and was calculated to be 680 m/s. Thus, projectile did not loose any energy by hitting the control PP sample. The frames captured in this test are shown in Figure F2.

Test 3:

After the system clean-up, sample mounting and all necessary measurements taken, vacuum was pulled to ~100 mtorr. Since 750 psi could successfully fire the projectile in test 2, pressure of 500 psi was attempted once again in this test. At 500 psi, pressure, the firing was successful. Projectile velocity before impact was 613 m/s. Due to misaligned sabot stripper, the projectile missed the target entirely. Sabot stripper was aligned again. Since the sample was intact in previous attempt, second test was conducted immediately afterwards to see if 300 psi pressure could fire the projectile successfully by pushing the sabot initially inside the barrel. However, firing was not successful. At 500 psi, firing was successful. But this time also, the sabot stripper was misaligned and projectile missed the target.

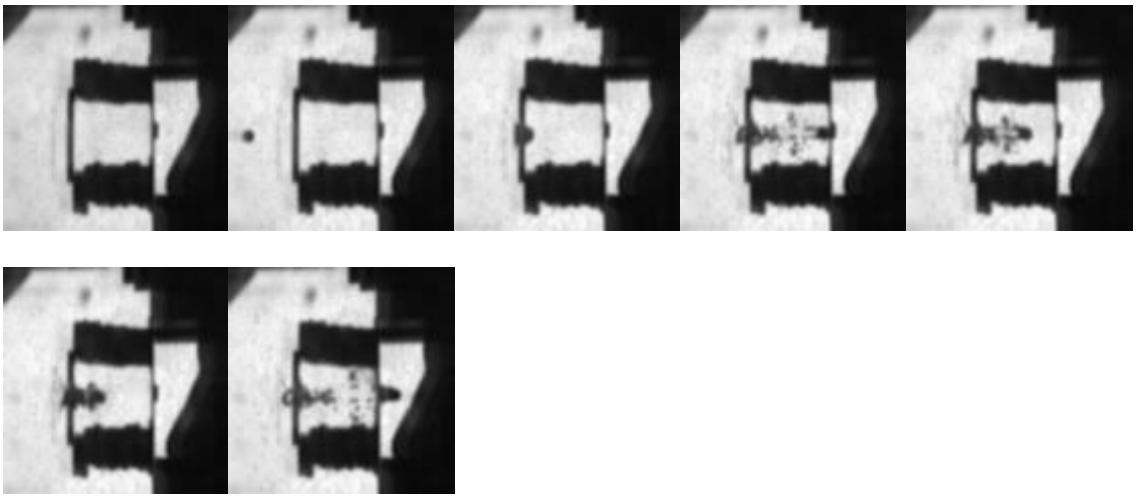

Figure F2. Progression of the impact event (Test 2).

Test 4:

Firing was attempted at pressures of 25, 50, 100, 150 psi. Firing was not successful at these pressures since the sabot could not escape the barrel. The pressure was increased to 250 psi. Under this condition, firing was successful. The projectile velocity recorded was 382 m/s and the projectile passed through control PP sample. Presumably, since the sample shattered into many pieces, there was no energy loss of the projectile before and after impact.

Test 5:

PMMA sabot was used for this test. The projectile was kept the same, i.e. stainless steel 3 mm diameter and mass of 0.13 g. Firing was attempted at pressure of 36 psi for target velocity of 140 m/s. Firing was successful. Speed of the projectile recorded by the system was 119 m/s. Velocities before and after impact were calculated based on the images captured by the video camera.

- Control PP sample shattered into pieces.

- Velocity of projectile before and after impact on sample was 115 m/s and 80 m/s, i.e. the velocity reduction of 30%.

Test 6:

To be able to attain lower velocities than 119 m/s, it was thought that using heavier sabot might help. Therefore, copper sabot was used for this test. The projectile was kept the same, i.e. stainless steel 3 mm diameter and mass of 0.13 g. Firing was attempted at 20 psi. Firing was successful. Velocity recorded was 35 m/s. However, projectile missed the target. Possibly, this is due to the misalignment of sabot stripper.

Test 7:

This attempt was carried out using copper sabot after proper alignment of sabot stripper. The projectile was kept the same, i.e. stainless steel 3 mm diameter and mass of 0.13 g. Firing was attempted at 9 psi. Firing was successful. Velocity recorded was 13 m/s. However, this time also projectile missed the target. Sabot and projectile fell down before hitting the sabot stripper. At this point, it was thought that due to heavier mass of copper sabot, as soon as sabot and projectile exit barrel, their path deviates from the expected trajectory.

Test 8:

Since copper sabot was not able to maintain the trajectory, PMMA sabot was used to attain lower velocities. Firing was attempted at 8 psi. Firing was successful. Velocity recorded was 25 m/s. However, this time projectile missed the target by following upward trajectory. Control PP sample shattered into pieces. Thus, it seems that even with PMMA sabot, at these lower velocities, maintaining desired trajectory is not achievable.

Test 9:

This test was conducted to repeat the successful test using PMMA sabot, i.e. test 5. Control PP sample was the target in this attempt. Firing was attempted at 36 psi. Firing was successful. Velocity recorded was 119 m/s. Unfortunately, video cameras did not capture the impact event.

Test 10 and Test 11:

The two tests was also conducted using PMMA sabot and SS projectile (0.13g). Control PP sample was the target in this attempt. Firing was attempted at 36 psi. Firing was successful. Velocity recorded was 118 m/s and 116 m/s.

- Control PP sample shattered.
- Velocity of the projectile after impact was 86 m/s in both tests.

Tests conducted on 1 wt% f-MWNT containing nanocomposites (PP-/f-MWNT master batch based)

Test 12:

This test was also conducted using PMMA sabot. 1wt% f-MWNT containing (PP/f-MWNT master batch based) sample was the target in this attempt. Firing was carried out at 36 psi. Firing was successful. Velocity recorded was 118 m/s. Projectile missed the target and the sample was intact.

Test 13:

After realigning the sabot stripper, this test was also conducted using PMMA sabot. Sample mounted in test 11, 1 wt% f-MWNT containing (PP/f-MWNT master batch based) sample was the target in this attempt. Firing was carried out at 36 psi. Firing was successful. Velocity recorded was 118 m/s.

- PP/f-MWNT sample shattered.
- Velocity of the projectile calculated from the images before and after impact was 119 and 73 m/s, respectively.

Test 14:

Similar to test 12 and 13, PMMA sabot was used. Firing was carried out at 36 psi. Firing was successful. Velocity recorded was 121 m/s.

- Velocity of the projectile calculated from the images before and after impact was 122 and 75 m/s, respectively.

Summary:

- At velocities of ~600 m/s, the velocity of projectile before and after impact was similar, indicating no energy absorption by the control PP sample.
- Based on the successful tests on control PP sample, the velocity of the projectile after impact reduced by 26 % to 30 % as compared to its velocity before impact (Table F1).
- Based on the successful tests on PP/f-MWNT (1wt% f-MWNT) nanocomposite sample, the velocity of the projectile after impact reduced by 39% and 40 % as compared to its velocity before impact (Table F1).

- The calculated energy absorbed by control PP and 1 wt% f-MWNT containing PP sample is around 0.37 to 0.43 J and 0.54 J to 0.57 J, respectively (Table F1).

Table F1: Results to the high strain rate tests.

Sample type		Control PP		PP/f-MWNT 1 wt % f-MWNT		
Test #		5	10	11	13	14
Velocity (m/s)	Before impact	115	118	116	119	122
	After impact	80	86	86	73	75
Reduction of velocity after impact		30 %	27 %	26 %	40 %	39 %
Reduction of energy after impact		0.43 J	0.40 J	0.37 J	0.54 J	0.57 J

APPENDIX G: SUPPLEMENTARY INFORMATION FOR CHAPTER 3

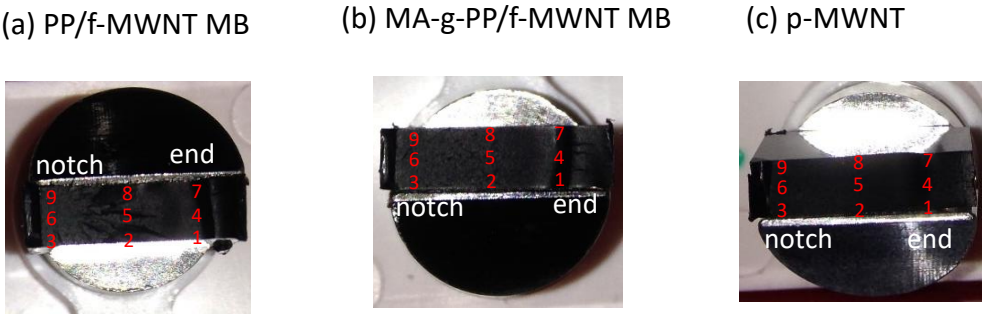

Figure G1. Photographs of the impact fractured specimens. Numbers (1 to 9) refer to regions from which SEM images were obtained as reported in Figures S3.2-S3.4 and Figure S3.5-3.7. This was done in an attempt to see if there are morphological differences in the fracture surfaces near the notch vs away from the notch in the three types of nano composites.

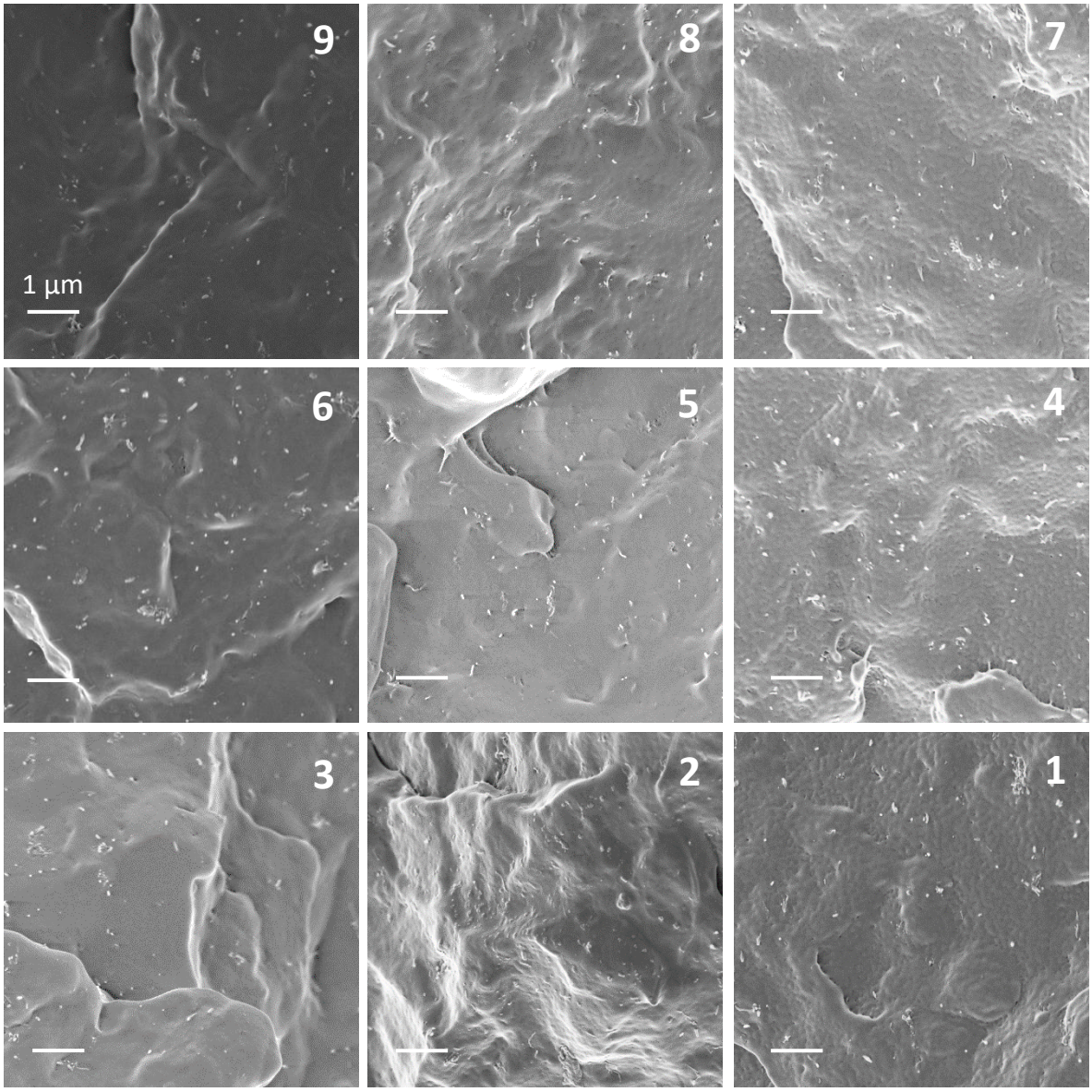

Figure G2. SEM mapping of PP/f-MWNT nanocomposite (at 1 wt. % CNT) impact-fractured surface prepared from PP/f-MWNT master batch. Scale bars represent 1 µm. Well dispersed f-MWNTs were broken instead of pulled out.

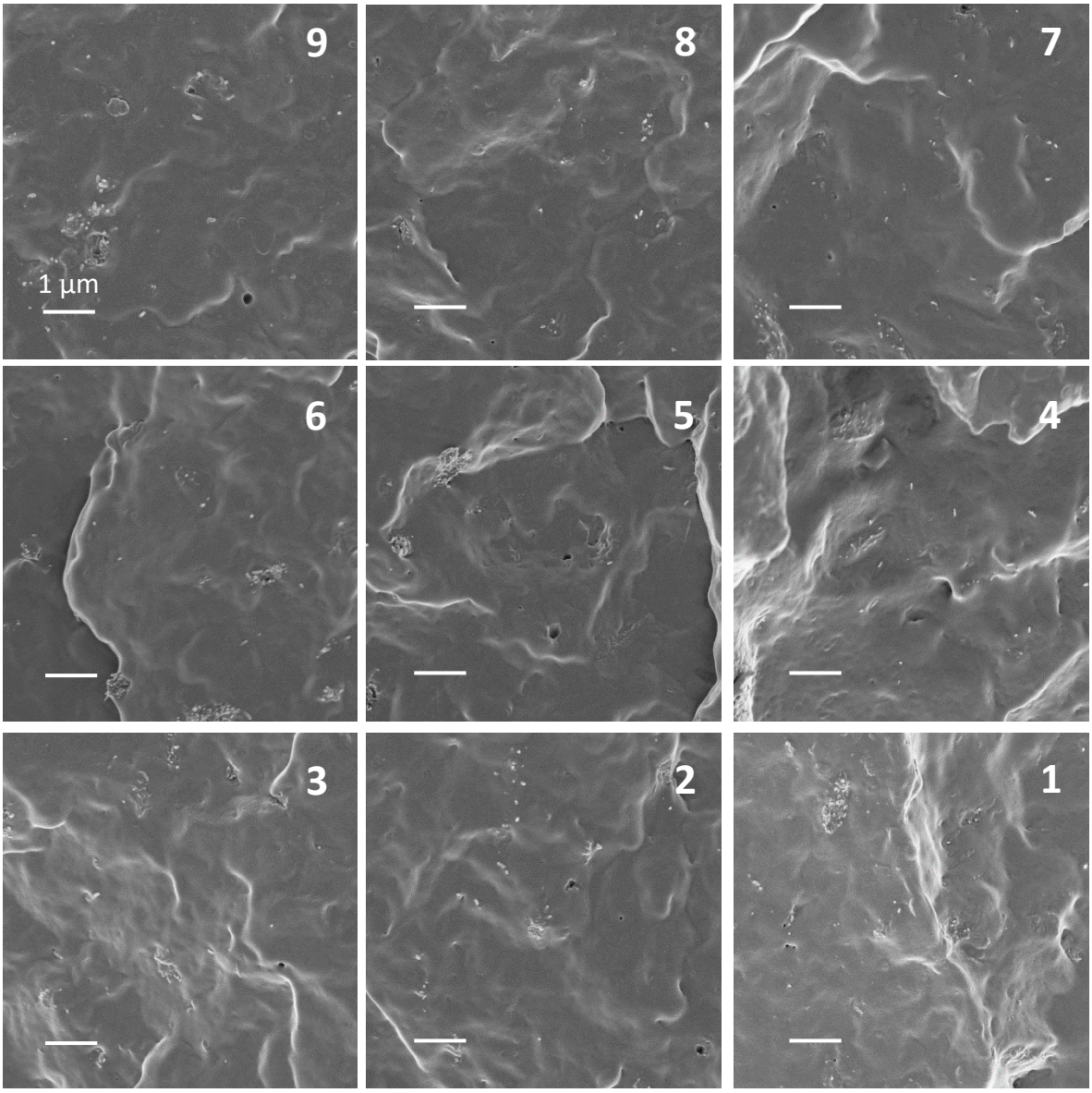

Figure G3. SEM mapping of PP/MWNT nanocomposites (at 1 wt. % CNT) impact-fractured surface prepared from MA-g-PP/f-MWNT master batch. Scale bars represent 1 µm. Small pocket of f-MWNTs (0.5 to 1 µm size) along with individual f-MWNTs are seen in these photographs.

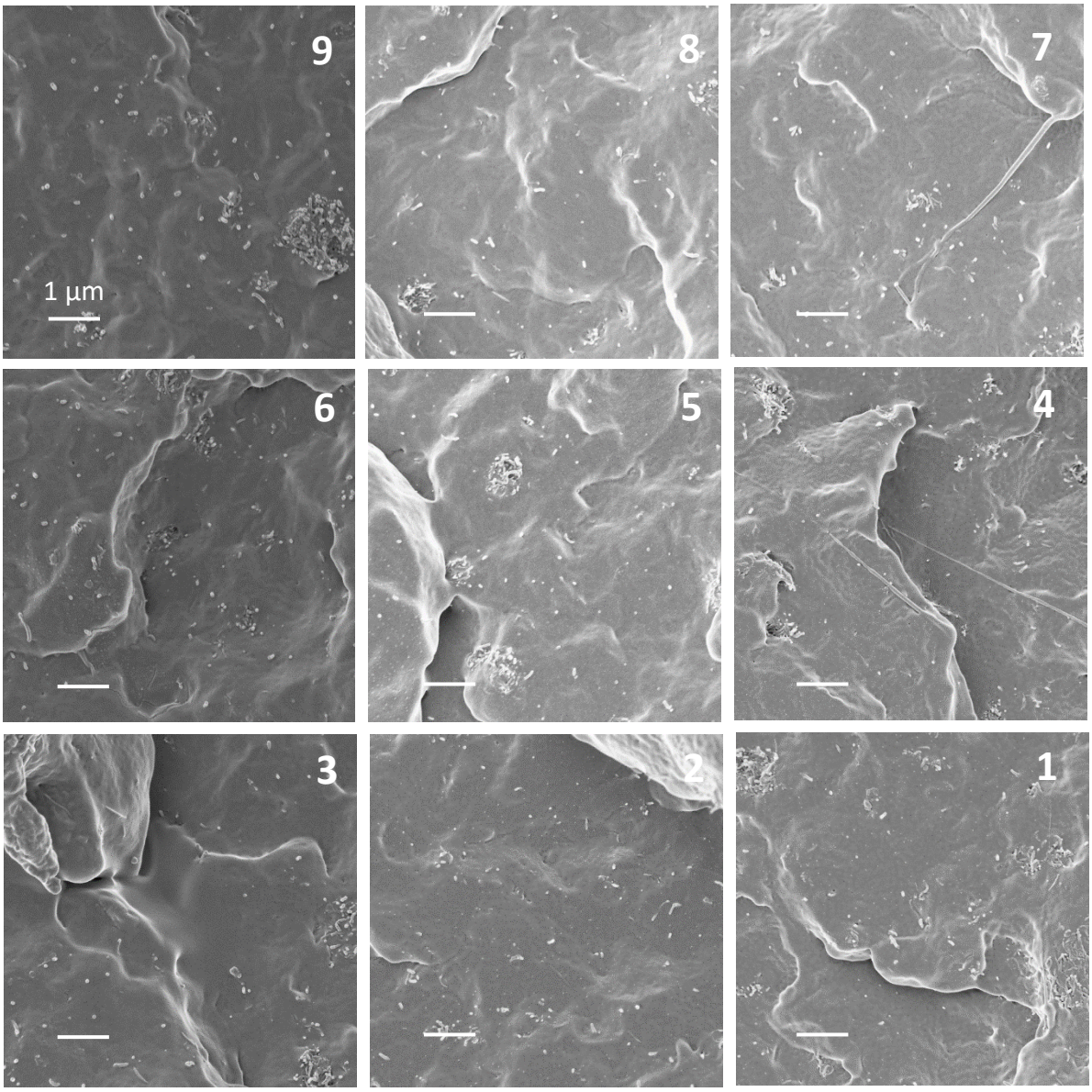

Figure G4. SEM mapping of PP/MWNT nanocomposites (at 1 wt. % CNT) impact-fractured surface prepared from p-MWNT. Scale bars represent 1 µm. Both individual p-MWNT and p-MWNT aggregates are observed.

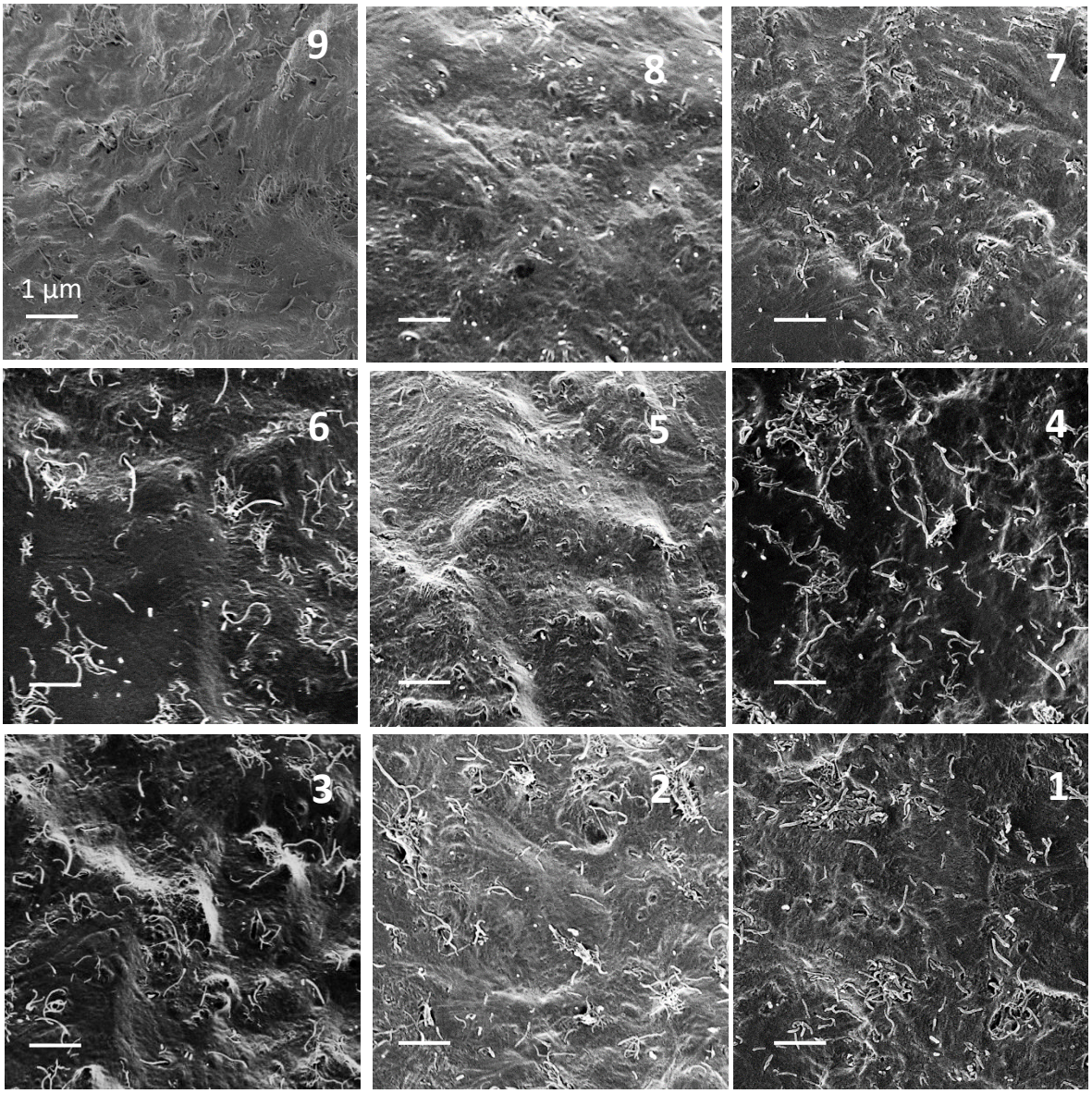

Figure G5. SEM mapping of PP/MWNT nanocomposites (at 1 wt. % CNT) impact-fractured surface prepared from PP/f-MWNT master batch after etching. Scale bars represent 1 µm.

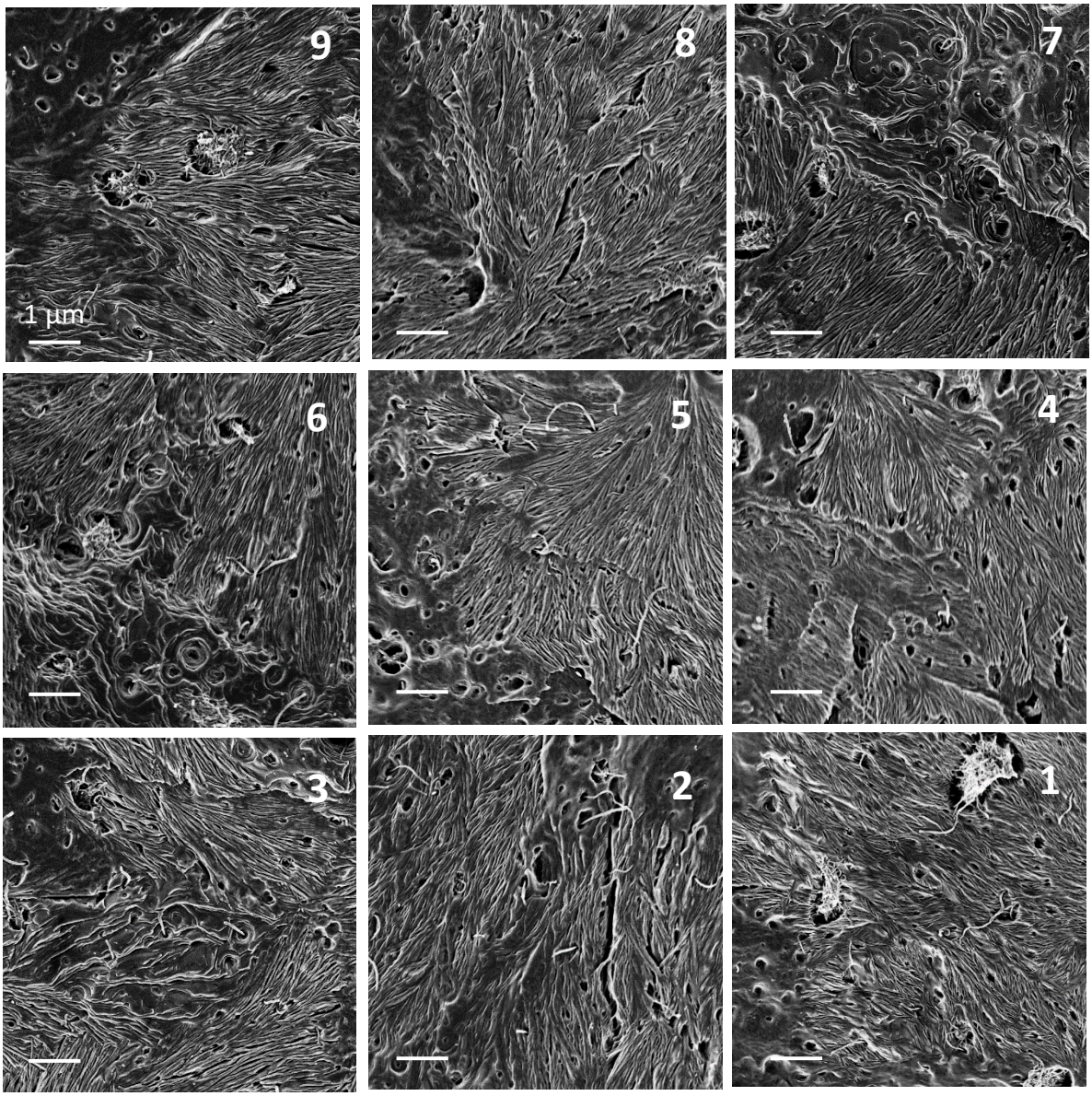

Figure G6. SEM mapping of PP/MWNT nanocomposites (at 1 wt. % CNT) impact-fractured surface prepared from MA-g-PP/f-MWNT master batch after etching. Scale bars represent 1 µm. Less crystalline MA-g-PP were etched and washed away leaving cavities on the sample surface.

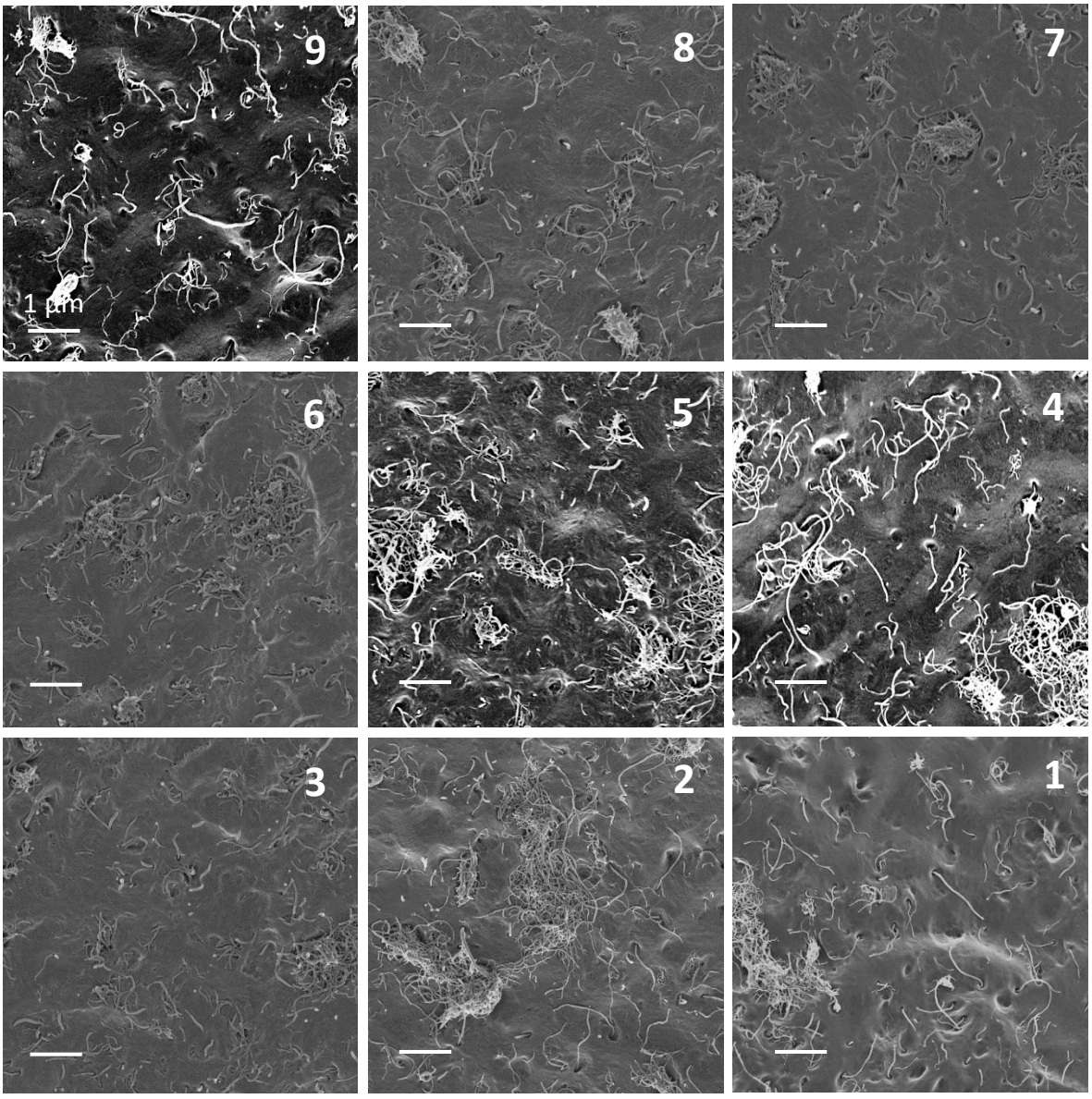

Figure G7. SEM mapping of PP/MWNT nanocomposites (at 1 wt. % CNT) impact-fractured surface prepared from p-MWNT after etching. Scale bars represent 1 μm. Many p-MWNT aggregates were observed, suggesting amorphous polymer in the vicinity of p-MWNT aggregates.

Table G1: Notched Izod impact strength data (a) and statistical significance of the data (b-d) of PP/MWNT nanocomposites prepared from p-MWNT, MA-g-PP/f-MWNT master batch and PP/f-MWNT master batch.

(a) Notched Izod impact strength of PP/MWNT nanocomposites

MWNT concentration (wt. %)	Nanocomposites via p-MWNT		Nanocomposites via MA-g-PP/f-MWNT master batch		Nanocomposites via PP/f-MWNT master batch	
	Impact strength (kJ/sq. m)	SD	Impact strength (kJ/sq. m)	SD	Impact strength (kJ/sq. m)	SD
0	2.39	0.18	2.39	0.18	2.39	0.18
0.001	2.42	0.19	2.76	0.31	2.39	0.16
0.005	2.51	0.09	2.65	0.08	2.31	0.17
0.01	2.72	0.17	2.76	0.33	2.39	0.16
0.1	2.33	0.58	2.72	0.36	2.87	0.34
0.3	2.34	0.10	3.43	0.41	3.95	0.73
0.5	2.34	0.10	3.95	0.16	4.29	0.37
1	2.20	0.08	4.03	0.85	6.04	0.28

(b) P-values showing the statistical significance of the impact strength data [Table S3.1(a)] of nanocomposites prepared via p-MWNT. P-value smaller than 0.05 is considered statistically significant.

MWNT concentration (wt. %)	0.001	0.005	0.01	0.1	0.3	0.5	1
0	1.00	0.53	0.04	0.53	0.59	0.59	0.12
0.001	X	0.53	0.04	0.53	0.59	0.59	0.12
0.005		X	0.14	0.23	0.25	0.25	0.03
0.01			X	0.01	0.01	0.01	0.001
0.1				X	0.90	0.90	0.40
0.3					X	1.00	0.30
0.5						X	0.30

(c) P-values showing the statistical significance of the impact strength data [Table S3.1(a)

of nanocomposites prepared via MA-g-PP/f-MWNT master batch P-value smaller than 0.05 is considered statistically significant. (continue to next page)

MWNT concentration (wt. %)	0.001	0.005	0.01	0.1	0.3	0.5	1
0	0.20	0.39	0.19	0.25	0.0004	<0.0001	<0.0001
0.001	X	0.67	0.99	0.89	0.0125	<0.0001	<0.0001
0.005		X	0.66	0.77	0.0042	<0.0001	<0.0001
0.01			X	0.88	0.0127	<0.0001	<0.0001
0.1				X	0.0088	<0.0001	<0.0001
0.3					X	0.05	0.0261

0.5						X	0.77

(d) P-values showing the statistical significance of the impact strength data [Table S3.1(a)] of nanocomposites prepared via PP/f-MWNT master batch. P-value smaller than 0.05 is considered statistically significant.

MWNT concentration (wt. %)	0.001	0.005	0.01	0.1	0.3	0.5	1
0	0.86	0.62	0.86	0.05	<0.0001	<0.0001	<0.0001
0.001	X	0.75	1.00	0.0352	<0.0001	<0.0001	<0.0001
0.005		X	0.75	0.0167	<0.0001	<0.0001	<0.0001
0.01			X	0.0352	<0.0001	<0.0001	<0.0001
0.1				X	<0.0001	<0.0001	<0.0001
0.3					X	0.1413	<0.0001
0.5						X	<0.0001

Table G2: Tensile modulus data (a) and statistical significance of the data (b-d) of PP/MWNT nanocomposites prepared from p-MWNT, MA-g-PP/f-MWNT master batch and PP/f-MWNT master batch.

(a) Tensile modulus of PP/MWNT nanocomposites

MWNT concentration (wt. %)	Nanocomposites via p-MWNT		Nanocomposites via MA-g-PP/f-MWNT master batch		Nanocomposites via PP/f-MWNT master batch	
	Tensile modulus (GPa)	SD	Tensile modulus (GPa)	SD	Tensile modulus (GPa)	SD
0	1.79	0.16	1.79	0.16	1.79	0.16
0.001	1.87	0.1	1.75	0.16	1.93	0.09
0.005	1.85	0.08	1.77	0.11	1.89	0.1
0.01	1.96	0.09	1.75	0.16	2.02	0.11
0.1	1.93	0.14	1.78	0.21	1.94	0.1
0.3	2.1	0.15	1.95	0.04	1.91	0.07
0.5	2.22	0.16	1.93	0.05	1.78	0.13
1	2.21	0.1	1.98	0.07	1.69	0.09

(b) P-values showing the statistical significance of the tensile modulus data [Table S3.2(a)] of nanocomposites prepared via p-MWNT. P-value smaller than 0.05 is considered statistically significant. (continue to next page)

MWNT concentration (wt. %)	0.001	0.005	0.01	0.1	0.3	0.5	1
0	0.30	0.45	0.0197	0.05	<0.0001	<0.0001	<0.0001
0.001	X	0.81	0.28	0.46	0.0106	0.0002	0.0002

0.005		X	0.19	0.34	0.0058	<0.0001	0.0001
0.01			X	0.73	0.12	0.0040	0.0054
0.1				X	0.06	0.0015	0.0021
0.3					X	0.15	0.19
0.5						X	0.91

(c) P-values showing the statistical significance of the tensile modulus data [Table S3.2(a)] of nanocomposites prepared via MA-g-PP/f-MWNT master batch. P-value smaller than 0.05 is considered statistically significant.

MWNT concentration (wt. %)	0.001	0.005	0.01	0.1	0.3	0.5	1
0	0.55	0.73	0.55	0.83	0.0359	0.06	0.0096
0.001	X	0.84	1.00	0.79	0.0332	0.05	0.0117
0.005		X	0.84	0.94	0.05	0.08	0.0194
0.01			X	0.79	0.0332	0.05	0.0117
0.1				X	0.08	0.12	0.0326
0.3					X	0.82	0.67
0.5						X	0.51

(d) P-values showing the statistical significance of the tensile modulus data [Table S3.2(a)] of nanocomposites prepared via PP/f-MWNT master batch. P-value smaller than 0.05 is considered statistically significant.

MWNT concentration (wt. %)	0.001	0.005	0.01	0.1	0.3	0.5	1
0	0.0329	0.12	0.0009	0.0283	0.07	0.82	0.09
0.001	X	0.63	0.29	0.96	0.78	0.06	0.0031
0.005		X	0.13	0.59	0.84	0.15	0.0113
0.01			X	0.32	0.18	0.0044	0.0001
0.1				X	0.74	0.05	0.0027
0.3					X	0.11	0.0067
0.5						X	0.24

Table G3: Yield stress data (a) and statistical significance of the data (b-d) of PP/MWNT nanocomposites prepared from p-MWNT, MA-g-PP/f-MWNT master batch and PP/f-MWNT master batch.

(a) Yield stress of PP/MWNT nanocomposites. (continue to next page)

MWNT concentration (wt. %)	Nanocomposites via p-MWNT		Nanocomposites via MA-g-PP/f-MWNT master batch		Nanocomposites via PP/f-MWNT master batch	
	Yield stress (MPa)	SD	Yield stress (MPa)	SD	Yield stress (MPa)	SD
0	37.7	2.4	37.7	2.4	37.7	2.4

0.001	39.4	1.5	37.5	2	38.6	1.1
0.005	39.5	1.5	38.5	1	37.8	0.7
0.01	39.1	1.3	37.9	1.9	39.2	1.4
0.1	40.1	1.1	39	0.4	39.3	1.8
0.3	42.1	2.1	40	1.1	39	0.8
0.5	43.2	0.7	40.6	1.2	37.6	1.7
1	44.4	1.2	39.8	0.2	39.7	0.6

(b) P-values showing the statistical significance of the yield stress data [Table S3.3(a)] of nanocomposites prepared via p-MWNT. P-value smaller than 0.05 is considered statistically significant.

MWNT concentration (wt. %)	0.001	0.005	0.01	0.1	0.3	0.5	1
0	0.06	0.06	0.12	0.0467	<0.0001	<0.0001	<0.0001
0.001	X	0.97	0.80	0.80	0.0280	0.0025	0.0001
0.005		X	0.77	0.83	0.0303	0.0028	0.0001
0.01			X	0.63	0.0152	0.0012	<0.0001
0.1				X	0.07	0.0081	0.0005
0.3					X	0.36	0.06
0.5						X	0.31

(c) P-values showing the statistical significance of the yield stress data [Table S3.3(a)] of nanocomposites prepared via MA-g-PP/f-MWNT master batch. P-value smaller than 0.05 is considered statistically significant.

MWNT concentration (wt. %)	0.001	0.005	0.01	0.1	0.3	0.5	1
0	0.90	0.33	0.84	0.19	0.0146	0.0027	0.0202
0.001	X	0.39	0.79	0.24	0.0398	0.0118	0.05
0.005		X	0.54	0.72	0.22	0.09	0.26
0.01			X	0.35	0.07	0.0225	0.08
0.1				X	0.42	0.20	0.47
0.3					X	0.61	0.91
0.5						X	0.54

(d) P-values showing the statistical significance of the yield stress data [Table S3.3(a)] of nanocomposites prepared via PP/f-MWNT master batch. P-value smaller than 0.05 is considered statistically significant. (continue to next page)

MWNT concentration (wt. %)	0.001	0.005	0.01	0.1	0.3	0.5	1
0	0.31	0.87	0.08	0.07	0.13	0.97	0.0252
0.001	X	0.50	0.55	0.51	0.68	0.41	0.30
0.005		X	0.20	0.18	0.28	0.87	0.09
0.01			X	0.95	0.85	0.16	0.67

0.1				X	0.79	0.14	0.72
0.3					X	0.22	0.54
0.5						X	0.07

Table G4: Strain to failure (STF) of PP/MWNT nanocomposites prepared from (a) p-MWNT, (b) MA-g-PP/f-MWNT master batch and (c) PP/f-MWNT master batch.

MWNT concentration (wt. %)	Nanocomposites via p-MWNT		Nanocomposites via MA-g-PP/f-MWNT master batch		Nanocomposites via PP/f-MWNT master batch	
	STF (%)	SD	STF (%)	SD	STF (%)	SD
0	328.9	42.9	328.9	42.9	328.9	42.9
0.001	133	143.7	296.7	33.4	273.2	92.2
0.005	218.2	191.1	282.1	25	369.7	78.9
0.01	190.2	144.9	277.1	65.1	268	102
0.1	17.7	12.3	321.3	37.9	232.8	121.2
0.3	30.6	35.1	226	189.3	280.1	149.2
0.5	25.1	20.8	16.8	2.9	185.9	154.9
1	12.5	1.1	19.9	4.7	113.4	130.9

(b) P-values showing the statistical significance of the strain to failure data [Table S3.4(a)] of nanocomposites prepared via p-MWNT. P-value smaller than 0.05 is considered statistically significant.

MWNT concentration (wt.%)	0.001	0.005	0.01	0.1	0.3	0.5	1
0	0.0002	0.0253	0.0058	<0.0001	<0.0001	<0.0001	<0.0001
0.001	X	0.15	0.33	0.05	0.08	0.07	0.0437
0.005		X	0.63	0.0013	0.0024	0.0018	0.0010
0.01			X	0.0048	0.0087	0.0068	0.0038
0.1				X	0.82	0.90	0.93
0.3					X	0.92	0.76
0.5						X	0.83

(c) P-values showing the statistical significance of the strain to failure data [Table S3.4(a)] of nanocomposites prepared via MA-g-PP/f-MWNT master batch. P-value smaller than 0.05 is considered statistically significant. (continue to next page)

MWNT concentration (wt. %)	0.001	0.005	0.01	0.1	0.3	0.5	1
0	0.38	0.20	0.16	0.83	0.0068	<0.0001	<0.0001
0.001	X	0.74	0.66	0.58	0.11	<0.0001	<0.0001
0.005		X	0.91	0.38	0.21	<0.0001	<0.0001
0.01			X	0.32	0.25	<0.0001	<0.0001
0.1				X	0.0354	<0.0001	<0.0001

0.3					X	<0.0001	<0.0001
0.5						X	0.94

(d) P-values showing the statistical significance of the strain to failure data [Table S3.4(a)] of nanocomposites prepared via PP/f-MWNT master batch. P-value smaller than 0.05 is considered statistically significant.

MWNT concentration (wt. %)	0.001	0.005	0.01	0.1	0.3	0.5	1
0	0.31	0.45	0.26	0.08	0.37	0.0110S	0.0003
0.001	X	0.15	0.93	0.54	0.91	0.19	0.0187
0.005		X	0.13	0.0422	0.18	0.0074	0.0003
0.01			X	0.59	0.85	0.22	0.0226
0.1				X	0.47	0.47	0.07
0.3					X	0.16	0.0144
0.5						X	0.27

APPENDIX H: PATENT REVIEW I: METHODS ABOUT DISPERSING CNTS IN VARIOUS POLYMER MATRICES

This review focuses on the recent inputs about dispersing CNTs in various polymer matrices, i.e. thermoplastic, thermoset and elastomers. General speaking, CNTs can be modified chemically (covalently) or physically (non-covalently) for improving their compatibility with organic solvent or polymers (Tables H1-H5). This includes: 1. Covalently functionalization and grafting of CNTs (with functional groups and/or alkyl chains and/or polymers). 2. Non-covalently wrapping or coating of polymer chains onto CNTs. 3. Introducing surfactants, coupling agents, compatibilizers, etc. Master batch dilution in which CNTs/polymer composite is prepared at higher concentration followed by mixing it with the same or another polymer can also improve CNTs dispersion in the nanocomposite. Mechanical dispersion involving high shear mixing in melt, ball milling, extrusion through twin-screw extruder and the modification thereof are not included in this review.

For covalently modification, the prior art consists of functionalization of CNTs followed by grafting of alkyl chains (C1 to C18) or amine or alkyl aryl amine having more than 9 carbon atom in length (up to 50) or ionic liquids with more complex structure (1-docosanyl-3-methylimidazolium and 1-docosanyl-3-methylimidazolium hexafluorophosphate). For non-covalently functionalization, polymer wrapping or coating is mostly achieved through π-π interaction between conjugated polymers/aromatic polymers and CNTs. Introducing small molecule surfactant or coupling agent that joins to

the polymer chain and non-covalently bonded to the carbon nanotube is another common approach. On the other hand, master batch dilution method can improve CNTs dispersion, the majority of works are either melt compounding un-treated CNTs directly with polymers or making master batch using another polymer that is different from the matrix polymer and this might create a barrier deteriorating the interaction between CNTs and the matrix polymer. What is missing in the field is an approach that modifies CNT non-covalently through polymer wrapping/coating where the polymer is the same as the matrix polymer to ensure good interaction and potentially template the matrix polymer through CNTs interfaces.

Table H1. Functionalized/grafted CNT (with functional groups and/or alkyl chains and/or polymers) to improve CNT dispersion in organic solvents (covalently). (continue to next page)

Title **Assignee/filed**					
Polymer 1 (matrix)	**Polymer 2 (in master batch (MB)/coated on CNTs)**	**CNT type**	**% components (CNT in composite/CNT in MB)**	**Method (1. master batch/ 2. composite)**	**Application (claim)**
Process for functionalizing carbon nanotubes under solvent-free conditions (US 7459137 B2) William Marsh Rice University, 2008/12/02					
Not applicable	Not applicable	Functionalized SWNT or MWNT	Not applicable	Mechanical mixing (ball milling, stirring, shaking, high shear mixing, twin-screw mixing, etc.)	Polymer composites, electronic applications, and sensor devices.
Pre-treatment method of carbon nanotube for carbon nanotube/polymer composite, manufacturing method for carbon nanotube/polymer composites and carbon nanotube/polymer composites using the carbon nanotube (WO 2008030038 A1) Ji-Woong Chung, Mi-Sun Han, Woo-Nyon Kim, Univ Korea Ind & Acad Coop, 2008/03/13					
Polycarbonate	Not applicable	Acid treated SWNT or MWNT	0.5-2 wt. %/ not applicable	Solution mixing	electrical conductivity and electromagnetic wave-shielding effect
Fabrication of polymer grafted carbon nanotubes/polypropylene composite bipolar plates for fuel cell (US 20100283174 A1) Yuan Ze University, 2010/11/11					
PP homopolymer or copolymer (with ethylene, butylene etc.)	Not applicable	MWNT, acyl chlorination-amidization	Not specified, 0.01-15 wt. % CNT in PP	Melt blended	proton exchange membrane fuel cell (PEMFC)
Solubilizing single-walled carbon nanotubes by direct reaction with amines and alkylaryl amines (US 6187823 B1)					

University of Kentucky Research Foundation, 2001/02/13					
Not applicable	Not applicable	amines and alkyl aryl amines grafted SWNT	Not applicable	Solution mixing	solubilizing single-walled carbon nanotubes in an organic solvent
Functionalized carbon nanostructures which are soluble in hydrocarbons and method for preparation (US 8841454 B2) Exxonmobil Research and Engineering Company, 2014/09/23					
Not applicable	Not applicable	Grafted CNTs (with ester or amide)	Not applicable	Solution mixing, drop-wise (reaction at 40-70 °C, 1-4 days)	CNT dispersion in organic solvents
Polyolefin nanocomposites with functional ionic liquids and carbon nanofillers (US 8211958 B2) The Research Foundation of State University Of New York, 2012/07/03					
Polyolefin	Not applicable	CNT grafted with 1-docosanyl-3-methylimidazolium or 1-docosanyl-3-methylimidazo-lium hexafluorophosphate	0.01-30 wt. %/ not applicable	Solution mixing	Fiber, film etc.
Polymers containing functionalized carbon nanotubes (US 20030089893 A1) Hyperion Catalysis International, 2003/05/15					
Not specified (polycarbonates, polyamides, polyesters, polyurethanes etc.)	Not applicable	Functionalized CNTs	0.25 to 20 wt. %/ not applicable	Polymerization resulting polymers grafted on CNTs	Not specified

Table H2. Polymer wrappings (non-covalently). (continue to next page)

Title **Assignee/filed**					
Polymer 1 (matrix)	**Polymer 2 (in master batch (MB)/coated on CNTs)**	**CNT type**	**% components (CNT in composite/CNT in MB)**	**Method (1. master batch/ 2. composite)**	**Application (claim)**
Polymer and method for using the polymer for noncovalently functionalizing nanotubes (US 7547472 B2) Zyvex Performance Materials, Inc., 2009/06/16 Polymer and method for using the polymer for solubilizing nanotubes (EP 1359121 A2) Zyvex Corporation, 2003/11/05					
Not applicable	Conjugated polymers: poly(aryleneethynylene); poly(phenylene ethynylene); and poly(3decylthiophene) etc.	SWNT or MWNT (functionalized)	Up to 5 wt. %	Solution mixing (non-covalently via π-stacking)	Not specified
Nanotubes and methods of dispersing and separating nanotubes (US 7247670 B2) General Electric Company, 2007/07/24					
Not applicable	Soluble polymers (including conjugated, polyfluorene polymers) in organic or aqueous solvent	Not specified	Not specified	Solution mixing: non-covalently through ionic interaction, π-stacking, hydrogen bonding,	Dispersing CNTs

				Van der Waals interaction etc.	
Composite materials containing carbon nanoparticles (US 7780875 B2) Cinvention Ag, 2010/08/24					
Not specified	PMMA, PS or other latex-forming polymers, polyvinyl acetate, or conducting polymers, etc.	Functionalized CNTs	Not specified	Encapsulation of CNT through dispersion, suspension, or emulsion polymerization, etc.	resistance to mechanical stress, electrical conductivity, impact strength or optical properties
Carbon nanotube coated with aromatic condensation polymer (US 7754328 B2) Teijin Limited, 2010/07/13					
Not applicable	Aromatic polyamides, aromatic polyesters, aromatic polyester carbonates, aromatic polycarbonates, semi-aromatic polyesters aromatic azoles	Acid treated CNTs	Not specified (0.01-100 wt. %)	Solution mixing	Not specified
Polymer-wrapped single wall carbon nanotubes (US 7264876 B2) William Marsh Rice University, 2007/09/04					
Not specified (including PMMA, PS, PP, PC, etc.)	Polyvinyl pirrolidone (PVP), polystyrene sulfonate (PSS), poly (1-vinyl pyrrolidone-co-vinyl acetate) (PVP/VA), etc.	SWNT	Not specified	Solution mixing/not specified	Electronic device

Table H3. Surfactant, coupling agent …etc. (non-covalently). (continue to next page)

Title **Assignee/filed**					
Polymer 1 (matrix)	**Polymer 2 (in master batch (MB)/coated on CNTs)**	**CNT type**	**% components (CNT in composite/CNT in MB)**	**Method (1. master batch/ 2. composite)**	**Application (claim)**
Dispersion method (WO 2008058589 A2) Byk Chemie Gmbh, 2008/05/22					
Not applicable	Polymeric dispersant (with polar groups)	Not specified (preferably not treated)	Not specified	In-situ polymerization	Dispersing CNTs
Carbon nanotube-filled composites (WO 2004001107 A2) Univ Oklahoma, 2003/12/31					
Not specified	Not applicable (surfactant and polymerization initiators are mixed with CNTs before combining with monomer/catalyst mixture)	SWNT	Not specified	In-situ polymerization	electrical resistivity of less than 10^5 Ω-cm
Method for preparing nanotube pre-composites, in particular made from carbon (EP 1995274 A1) Arkema France, 2008/11/26					
Not specified (including thermoplast	Plasticizers (in liquid/molten form or in solution)	Not specified	Up to 5 wt. %/not specified	Solution or melt mixing/not specified	Dispersion, mechanical, electrical conductivity, thermal

ic polymers)					conductivity of nanotubes in a polymer matrix.
Non-Covalent Bonding Agent for Carbon Nanotube Reinforced Polymer Composites (US 20070255002 A1) University of Florida Research Foundation, Inc, 2007/11/01					
rubber, polyester, polystyrene , latex, polyethylene, epoxies, polyacrylates	(planar pyrenyl group) bonding agent joined to the polymer chain and non-covalently bonded to the carbon nanotube	SWNT or MWNT	0.1-20 wt. %/ not applicable	Solution mixing	Not specified

Table H4. Master batch dilution. (continue to next page)

Title **Assignee/filed**					
Polymer 1 (matrix)	**Polymer 2 (in master batch (MB)/coated on CNTs)**	**CNT type**	**% components (CNT in composite/CNT in MB)**	**Method (1. master batch 2. composite)**	**Application (claim)**
Polymer materials containing dispersed carbon nanotubes (WO 2006106214 A1) Arkema France, 2006/10/12					
Not specified (including thermoplastic and thermoset, elastomers, etc.)	Block copolymer with at least one block miscible with Polymer 1	Preferably MWNT	0.1 to 80 wt. %/not specified	Melt mixing	Not specified
Polymer composition comprising carbon Nanotubes (WO 2013107875 A1) Total Research & Technology Feluy, 2013/07/25					
linear low density polyethylene (LLDPE)	High impact polystyrene (HIPS)	MWNT, non-functionalized	At most 1.9 wt. %/ Not applicable	Twin screw extrusion	Having a surface resistivity of at most 10^4 Ohm/sq
Carbon nanotube masterbatch, preparation thereof, and use in forming electrically conductive thermoplastic composition (WO 2012127357 A1) SABIC Innovative Plastics, 201209/27					
Not specified (polyester, polyolefin, polyimides etc.)	Wax (fatty alcohols, fatty acids, fatty acid salts, fatty acid amides etc.)	MWNT (< 30 nm), non-functionalized	2-20 wt. % of MB in composite /10-40 % CNT in MB	Melt blending (equipment not specified)	electrically conductive thermoplastic composition
Composites of poly (hydroxy carboxylic acid) and carbon nanotubes (US 9012534 B2) Total Research & Technology Feluy, 2015/04/21					
Polyolefin	Poly (hydroxyl carboxylic acid) e.g. PLA	SWNT or MWNT, non-functionalized	0.05 -3 wt. %/ not limited (preferably up to 5 wt. %)	solution processing, dry blending, melt blending/melt processing, wet blended	Better CNT dispersion in PP/PLA/CNT than in PP/CNT
Method for producing master batches containing nanoparticles (EP 2436720 A1) Rhein Chemie Rheinau GmbH, 2012/04/04					
Not applicable	Emulsion polymerized polymers/nature rubber	Not specified	Not applicable/10 wt. %	Mix the aqueous CNT dispersion with polymer latex	Master batch

Carbon nanotube reinforced polymer (WO 2009063008 A1) Stichting Dutch Polymer Inst, 2009/05/22					
Aqueous polymer latex including semi-crystalline polymers)	water soluble polymer	MWNT (~ 10 nm outer diameter)	Up to 5 wt. %/0.05-20 wt. %	Latex mixing (consisted of high shear mixing, sonication)	Improved conductivity

Table H5. Miscellaneous studies.

Title **Assignee/filed**					
Polymer 1 (matrix)	**Polymer 2 (in master batch (MB)/coated on CNTs)**	**CNT type**	**% components (CNT in composite/CNT in MB)**	**Method (1. master batch 2. composite)**	**Application (claim)**
Reinforced polymers (EP 1054036 A1) Fina Research S.A., 2000/11/22					
polyolefin, polyester, polyamide etc.	Not applicable	Not specified	Less than 50 wt. %/not applicable	In-situ polymerization/Fiber or sheet extrusion	Fiber
Single-wall carbon nanotube-polymer composites (US 6426134 B1) E. I. Du Pont De Nemours And Company, 2002/07/30					
Not specified (polyamides, polyesters, polyimides, or polyurethanes etc.)	Not applicable	Acid treated SWNT (carboxylic group functionalized)	Not specified	polymerization	Fiber, film etc.
Method for producing composite materials based on polymers and carbon nanotubes (cnts), and composite materials produced in this manner and the use thereof (WO 2011060839 A1) Bada Ag, 2011/05/26					
Thermoplastic	Not applicable	Not specified	0.001 to 30 wt. %/not applicable	Co-extrusion of dispersed CNT in liquid phase and polymer	Improved homogeneity, mechanical and electrical properties.
Composite materials comprising polar polymers and single-wall carbon nanotubes (US 6936653 B2) Carbon Nanotechnologies, Inc., 2005/08/30					
Polar polymer and non-polar polymers (polyolefin)	Not applicable	SWNT	0.01 wt. % to 20 wt. %/not applicable	Solution mixing	Conductivity enhancement
Well dispersed polymer nanocomposites via interfacial polymerization (US 20060122284 A1) William Marsh Rice University, 2006/06/08					
Monomer1 in polar solvent and monomer2 in non-polar solvent	Not applicable	Not specified (dissolved in polar or non-polar solvent)	Not applicable	Solution mixing	Not specified

REFERENCES

1 Tour, James M., and Christopher A. Dyke. "Process for functionalizing carbon nanotubes under solvent-free conditions." U.S. Patent No. 7,459,137. 2 Dec. 2008.

2 Ji-Woong Chung, Mi-Sun Han, Woo-Nyon Kim, Univ Korea Ind & Acad Coop. "Pre-treatment method of carbon nanotube for carbon nanotube/polymer composite, manufacturing method for carbon nanotube/polymer composites and carbon nanotube/polymer composites using the carbon nanotube" World Patent No. 2,008,030,038.1. Mar. 2008.

3 Ma, Chen-Chi Martin, et al. "Fabrication of polymer grafted carbon nanotubes/polypropylene composite bipolar plates for fuel cell." U.S. Patent Application 12/591,026.

4 University of Kentucky Research Foundation. "Solubilizing single-walled carbon nanotubes by direct reaction with amines and alkylaryl amines" U.S. Patent No. 6,187,823.1 Feb. 2001.

5 Habeeb, Jacob Joseph. "Functionalized carbon nanostructures which are soluble in hydrocarbons and method for preparation." U.S. Patent No. 8,841,454. 23 Sep. 2014.

6 Chu, Benjamin, et al. "Polyolefin nanocomposites with functional ionic liquids and carbon nanofillers." U.S. Patent No. 8,211,958. 3 Jul. 2012.

7 Niu, Chunming, and Lein Ngaw. "Polymers containing functionalized carbon nanotubes." U.S. Patent No. 8,980,136. 17 Mar. 2015.

8 Chen, Jian, and Haiying Liu. "Polymer and method for using the polymer for noncovalently functionalizing nanotubes." U.S. Patent No. 7,547,472. 16 Jun. 2009.

9 Chen, Jian, and Haiying Liu. "Polymer and method for using the polymer for solubilizing nanotubes." U.S. Patent No. 7,244,407. 17 Jul. 2007.

10 General Electric Company. "Nanotubes and methods of dispersing and separating nanotubes" U.S. Patent No. 7,247,670.2 Jul. 2007.

11 Asgari, Soheil. "Composite materials containing carbon nanoparticles." U.S. Patent No. 7,780,875. 24 Aug. 2010.

12 Chokai, Masayuki, et al. "Carbon nanotube coated with aromatic condensation polymer." U.S. Patent No. 7,754,328. 13 Jul. 2010.

13 Smalley, Richard E., et al. "Polymer-wrapped single wall carbon nanotubes." U.S. Patent No. 7,264,876. 4 Sep. 2007.

14 Byk Chemie Gmbh. "Dispersion method" World Patent No. 2,008,058,589.2 May. 2008.

15 Univ Oklahoma. “Carbon nanotube-filled composites” World Patent No. 2,004,001,107.2 Dec. 2003.

16 Arkema France. “Method for preparing nanotube pre-composites, in particular made from carbon” European Patent No. 1,995,274.1 Nov. 2008.

17 Alba, Nicolas. "Non-Covalent Bonding Agent for Carbon Nanotube Reinforced Polymer Composites." U.S. Patent Application 10/598,158.

18 El Bounia, Nour Eddine, et al. "Polymer materials containing dispersed carbon nanotubes." U.S. Patent No. 7,838,587. 23 Nov. 2010.

19 Rousseaux, Dimitri, et al. "Polymer composition comprising carbon nanotubes." U.S. Patent Application 14/372,675.

20 Bastiaens, Jos, and Arno Hagenaars. "Carbon nanotube masterbatch, preparation thereof, and use in forming electrically conductive thermoplastic composition." U.S. Patent No. 8,961,834. 24 Feb. 2015.

21 Debras, Guy, and Romain Luijkx. "Composites of poly (hydroxy carboxylic acid) and carbon nanotubes." U.S. Patent No. 9,012,534. 21 Apr. 2015.

22 Rhein Chemie Rheinau GmbH. “Method for producing master batches containing nanoparticles” European Patent No. 2,436,720.1 Apr. 2012.

23 Stichting Dutch Polymer Inst. “Carbon nanotube reinforced polymer” World Patent No. 2,009,063,008.1 May. 2009.

24 Fina Research S.A. “Reinforced polymers” European Patent No. 1,054,036.1 Nov. 2000.

25 E. I. Du Pont De Nemours And Company. “Single-wall carbon nanotube-polymer composites” U.S. Patent No. 6,426,134.1 Jul. 2002.

26 Bada Ag. “Method for producing composite materials based on polymers and carbon nanotubes (cnts), and composite materials produced in this manner and the use thereof” World Patent No. 2,011,060,839.1 May. 2011.

27 McElrath, Kenneth O., et al. "Composite materials comprising polar polymers and single-wall carbon nanotubes." U.S. Patent No. 6,936,653. 30 Aug. 2005.

28 Rodriguez-Macias, Fernando, and Enrique Barrera. "Well dispersed polymer nanocomposites via interfacial polymerization." U.S. Patent Application 11/294,883

APPENDIX I: PATENT REVIEW II: METHODS ABOUT IMPROVING IMPACT STRENGTH OF THERMOPLASTICS

This review focuses on common approaches to improve the impact strength of thermoplastics, especially of polypropylene (PP) (Tables I1-I5). This include: 1. Incorporation of organic or inorganic fillers such as carbon nanotubes (CNT), carbon black, clay, talc, mica, titanium dioxide (TiO_2), zinc oxide (ZnO), calcium carbonate ($CaCO_3$), etc. 2. Addition of another polymer phase, i.e. amorphous copolymers, rubbers, etc. 3. Addition of nucleation agent and the combination thereof.

Around 10-50 % increase of impact strength can be achieved through 0.5 – 10 wt. % of CNT incorporation to the polymer matrix. Tensile properties (tensile modulus and tensile strength) and flexural strength of the resulting nanocomposite are also improved to some extent (increases by 5-60 %). While the incorporation of other fillers such as carbon black, talc, $CaCO_3$, etc. can also enhance impact, tensile as well as flexural properties of the nanocomposites, it requires higher loadings (normally above 10 wt. %) to reach a comparable result than CNT. On the other hand, the introduction of another polymer phase, e.g. low density polyethylene (LDPE), ethylene/propylene copolymers and polyisobutylene which is commonly used for toughening PP, brings more pronounced effect (up to 24-folds increase of impact strength with 30 % of PP replaced by other polymers). However, mostly the tensile properties and flexural strength are compromised (decreases by 25-50 %). Small amount (0-4000 ppm) of α type nucleation agent in PP

results in around 65 % and 8 % increase of impact strength and tensile modulus, respectively

Table I1. Addition of carbon nanotube (CNT) incorporation. (continue to next page)

Title **Assignee/filed**					
Polymer 1 (matrix)	**Polymer 2 (copolymer, elastomer…etc.)**	**Filler type**	**% components**	**% change on Izod notched impact strength**	**Note**
Fabrication of polymer grafted carbon nanotubes/polypropylene composite bipolar plates for fuel cell (US 20100283174 A1) Yuan Ze University, 2010/11/11					
Homopolymer PP or copolymer propylene and ethylene, butylenes or hexalene	Not applicable	f-MWNT (acyl chlorination-amidization)	PP Graphite 50-95 wt.%; f-MWNT: 0.01 to 15 wt.% based on PP.	65.8 to 90 J/m (37 % increase with 8 wt. % f-MWNT in PP)	Flexural modulus increase by 60 %
Method for improving shock resistance of resin-based carbon fiber composite material (CN 101613944 B) 天津工业大学, 2011/02/09					
Epoxy/carbon fiber fabric	Not applicable	CNT (not specified)	0.5 to 10 wt.% of epoxy	16-18 % increase	
Carbon nanotube ultra-high molecular weight polyethylene composite, molded article including the same, and method of fabricating the molded article (US 20140329949 A1) Samsung Display Co., Ltd., 2014/11/06					
Ultrahigh molecular weight PE	Not applicable	CNT (8 to 15 nm/ 10-100 µm)	0.2 to 1 wt.% CNT 0.1 to 0.5 wt.% light stabilizer	13 % increase at 1 wt.% CNT loading	15 % of tensile strength increase
Thermoplastic resin composition for radar cover (WO 2015084110 A1) Lg Chem, Ltd., 2015/06/11					
Polyamide	Not applicable	CNT (not specified)	85-95 wt.% thermoplastic 1- 5 wt.% CNT 3-10 wt.% carbon black	78 % increase at 0.5 wt. % CNT loading	7 % of tensile strength decrease
Carbon nanotube masterbatch, preparation thereof, and use in forming electrically conductive thermoplastic composition (US 8961834 B2) Sabic Global Technologies B.V., 2015/02/24					
PPE and PA-6,6 PPE: Poly (2,6-dimethyl-1,4-phenylene ether)	Not applicable	CNT (20) in PA (80) (master batch) CNT (20) in PET (80) (master batch)	1.2 wt.% CNT	22 KJ/m^2 (no control sample value reported)	Melt blending

Fabrication of carbon nanotubes reinforced polymer composite bipolar plates for fuel cell (US 7883650 B2) National Tsing Hua University, 2011/02/08					
Vinyl ester resin	Not applicable	f-CNT (MA-POA grafted)	60 - 95 wt.% graphite to Graphite+ vinyl ester resin; 0.05 to 10 wt. % CNT to the vinyl ester resin	50 wt. % increase (70.73 to 105.94 J/M) between 1 wt.% pristine to grafted CNT	Flexural modulus increase by 14 %
Fabrication of carbon nanotubes reinforced semi-crystalline polymer composite bipolar plates for fuel cell (US 20100127428 A1) Yuan Ze University, 2010/05/27					
Homopolymer PP or copolymer propylene and ethylene	Not applicable	CNT (not specified)	PP Graphite 50-95 wt.%; f-MWNT 0.05 to 20 wt.% based on PP.	68.3 to 81.4 J/m (19.3 % increase with 1.6 wt. % MWNT in PP)	Max. 37.5 % increase of flexural strength
Polyolefin composition (US 8859670 B2) Georg Fischer Rohrleitungssysteme Ag, 2014/10/14					
PE and PP	Not applicable	CNT (pristine)	0-30 wt. % CNT	Increase by 50 % (claim without experimental result)	Elastic modulus, distortion resistance, chemical stability etc.

Table I2: Addition of other fillers (Talc, carbon black, $CaCO_3$, etc.). (continue to next page)

Title **Assignee/filed**					
Polymer 1 (matrix)	**Polymer 2 (copolymer, elastomer…etc.)**	**Filler type**	**% components**	**% change on Izod notched impact strength**	**Note**
Anti-impact modified PP/HDPE (Polypropylene/High Density Polyethylene) plastics for automotive interior parts and preparation method thereof (CN 103059416 A) 上海瀚氏模具成型有限公司, 2014/12/24					
PP + HDPE	hydrogenated styrene - butadiene - styrene block copolymer, (SBS); ethylene - octene copolymer (POE);	Talc, calcium silicate, glass fiber	100 part PP; 20-30 part HDPE; 1-5 part coupling agent; 15-40 part impact modifier(copolymer); 10-35 part modifying agent (fillers)	Maximum 90 % increase (6 to 11.5 KJ/m^2) when SBS and fillers were added	Flexural strength increase by 8 %
Impact-resistant conductive polyphenylene sulfide material and preparation method thereof (CN 104672902 A) 上海杰事杰新材料(集团)股份有限公司, 2015/06/03					
Conductive polyphenylene sulfide (PPS)	ethylene - acrylate - glycidyl methacrylate terpolymer	Carbon black	60 to 75 wt.% PPS; 0.5 to 1 wt. % lubricant; 0.5 to 0.8 wt. % epoxy; 8 to 15 wt. % toughening agent (terpolymer)	18- 25 KJ/m^2 (no control sample value)	extrusion

			0.5 to 2 wt. % coupling agent; 17 to 25 wt. % carbon black.		
Method for improving the impact strength of a plastics material (US 4186125 A) Skf Nova Ab, 1980/01/29					
Plastic	Not applicable	Metal particles	20 -50 wt. % filler	Not reported	
Polycarbonate composition with improved impact strength (WO 2012129276 A1) Sabic Innovative Plastics Ip B.V., 2012/09/27 Polycarbonate composition with improved impact strength (CN 103443178 A) Sabic Innovative Plastics Ip B.V., 2013/12/11					
Polycarbonate (PC), PC copolymer of BPA/PDMS	Not applicable	Talc, wollastonite, clay, mica, zinc sulfide, zinc oxide, or titanium dioxide	At least 3 wt. % filler	317 % increase (11.7 to 48.8 KJ/m^2) with 10 wt. % talc (and 0.3 wt. % H_3PO_3)	Tensile modulus increase by 38 %; tensile strength increase by 9 %; elongation increase by 131 %; flexural modulus increase by 39 %
Polyolefin compositions having improved impact strength (EP 0171513 A1) QUANTUM CHEMICAL CORPORATION (a Virginia corp.), 1986/02/19					
Polyolefin	Polyolefin (70-99.9)-ethylenically unsaturated carboxylic acids, acid anhydrides (30-0.1) copolymer	Group II metal carbonate	Up to 80 wt. % of filler	Decrease by 8 % with 30 wt. % $CaCO_3$ in HDPE	w/ and w/o compati-bilizers shows difference
High impact strength polyamides (US 5376712 A) The University Of Akron, 1994/12/27					
Polyamide	Rubbery polymer	Carbon black and silica	Not specified	22 % decrease with 4 wt. % silica loading (533 to 416 J/m)	37 % increase of flexural strength
Stiff and impact resistant compositions containing polypropylene or poly ethylene-propylene copolymer and calcium carbonate for closures (WO 2002004557 A2) Alcoa Closure Systems Int Inc, Anatoliy Goldman, 2002/01/17					
PP or PP/PE copolymer	Not applicable	$CaCO_3$ (2.5 to 3.5 µm)	25 to 35 wt.% of $CaCO_3$	72% increase at 15 wt. % loading (46 % increase at 25 wt. % loading)	extrusion

Table I3. Addition of another polymer phase, i.e. amorphous copolymers, rubbers, etc. (continue to next page)

Title **Assignee/filed**					
Polymer 1 (matrix)	**Polymer 2 (copolymer, elastomer…etc.)**	**Filler type**	**% components**	**% change on Izod notched impact strength**	**Note**
Impact-modified polypropylene composite (WO 2012177703 A1) Cryovac, Inc., 2012/12/27					
Polypropylene (PP)	Propylene-based elastomer	silicate platelets	PP: 65 to 97 wt. % Elastomer: 3 to 35 wt. % Filler: 0.1 to 20 wt. %	Increase by 196 % From 1.38 to 4.08 ft.lb from (90/5) to (75/20) (matrix wt. %/elastomer wt. %)	Modulus decrease by 35 %
PP (polypropylene) polymer material with high impact strength (CN 103540016 A) 青岛博玉特橡塑制品有限公司, 2014/01/29					
PP	Polypropylene block copolymer	Talc	PP: 40 to 60 parts Copolymer: 50 to 55 parts	Not reported	
Polypropylene Resin with Low Shrinkage, High Impact Strength, Stiffness and Scratch Resistance (US 20090137722 A1) Borealis Technology Oy, 2009/05/28					
PP (polymer A)	Ethylene-propylene copolymer (polymer B) and ethylene (polymer C)	Not applicable	Polymer A: less than 70 % Polymer B: more than 20 % Polymer C: less than 20 %	*Notched Charpy impact strength* Reaches 43.5 KJ/m^2 with (65/25/10) (wt. % A/ wt. % b/ wt. % c)	extrusion
Polypropylene compositions having improved impact strength containing polyethylene and ethylene-propylene copolymer (US 3256367 A) Union Carbide Corp, 1966/06/14					
PP and PE	Amorphous ethylene/propylene copolymers (preferred) and polyisobutylene	Not applicable	Not specified	2400 % increase From 0.4 to 10.0 (unit not reported) [from (100/0/0 to (70/15/15)E (wt. % PP/ wt. % PE/ wt. % copolymer)	Modulus decrease by 40 %
Impact strength of blends of polyethylene and polypropylene (US 3137672 A) Hercules Powder Co Ltd, 1964/06/16					

PP and PE	Ethylene/propylene copolymers	$CaCO_3$ and TiO_2	Not specified	70% increase From 2.4 to 4.1 (unit not reported) (2 wt. % of copolymer concentration)	
Polypropylene resin composition with good transparency and good impact strength (US 8779064 B2) Lg Chem, Ltd., 2014/07/15					
Propylene-alpha olefin random copolymer (A)	Propylene-alpha olefin elastic copolymer (B); ethylene-alpha olefin copolymer (C)	Not applicable	50-94 wt. % of A 5-49 wt. % of B 1-45 wt. % of C	1000 % increase From 5.1 to 56. 6 Kg/cm^2 from 100/0/0 to 80/14/6 (wt. % A/ wt. % b/ wt. % c)	Flexural modulus decrease by 25 %
Polypropylene blends having high impact strength and improved optical properties (US 4087485 A) Exxon Research & Engineering Co., 1978/05/02					
PP	Ethylene-propylene copolymer elastomer and LDPE	Not applicable	70 to 95 wt. % of PP 2 to 22 wt. % of elastomer 1 to 15 wt. % of LDPE	Not reported	
High impact strength thermoplastic composition containing polyvinyl acetal resin and butadiene elastomer (US 2684352 A) Us Rubber Co, 1954/07/20					
Polyvinyl acetal resin	Butadiene elastomer	Not applicable	Not specified	3500 % increase From 0.6 to 21.8 (unit not reported) (from 100/0 to 90/10 blend)	Flexural modulus decrease by 22 %
Impact strength modifiers for thermoplastic polyester and thermoplastic polyester resin composition containing the same (US 20100292390 A1) Lg Chem, Ltd., 2010/11/18					
Polyester	Rubber latex-vinyl monomer	Not applicable	50 – 95 wt. % polyester 5 – 50 wt. % copolymer	Not reported	
Polyolefin compositions with improved impact strength (US 5202380 A) Rohm And Haas Company, 1993/04/13					
Polyolefin	Acrylic core-shell polymer and a copolymeric compatibilizer	Not applicable	Not mentioned	0.34 to 0.52 ft-lb/in	

Table I4. Addition of nucleating agents.

Title **Assignee/filed**					
Polymer 1 (matrix)	**Polymer 2 (copolymer, elastomer…etc.)**	**Filler type**	**% components**	**% change on Izod notched impact strength**	**Note**
Polypropylene copolymers with specific crystal nucleation (EP 2526146 B1) Borealis AG, 2014/11/26					
Polypropylene (homopolymer and Impact copolymer)	Not applicable	α-type nucleating agent (four different nucleating agents were compared)	0-4000 ppm of nucleating agent	Maximum 116 % increase (7.85 to 16.98 KJ/m^2) in the case of copolymer; Maximum 65 % increase (2.45 to 4.04 KJ/m^2) in the case of homopolymer	small (8 %) modulus increase

Table I5. Miscellaneous studies (effect of dispersion, plasticizer, etc.). (continue to next page)

Title **Assignee/filed**					
Polymer 1 (matrix)	**Polymer 2 (copolymer, elastomer…etc.)**	**Filler type**	**% components**	**% change on impact strength**	**Note**
Method for improving the low temperature impact strength of polyblends of thermoplastic copolyesters and styrene acrylonitrile copolymers (EP 0444003 A1) Monsanto Company, 1991/08/28					
thermoplastic polyblend comprising PETG and SAN	Not applicable	dispersant (mono- and di-carboxylic acids containing 6 to 36 carbon atoms; alkali and alkaline-earth metal salts and amides of such acids; and aliphatic alcohols containing 6 to 36 carbon atoms)	0.05 to 0.2 wt. %	ASTM D-3763-85 Energy at max. from 0.95 (joule) to 1.08 – 18.17 (joule)	
Thermoplastic molding compositions with cold impact strength (US 4959403 A) Huels Aktiengesellschaft, 1990/09/25					
Polyamide (PA)	Not applicable	Plasticizer (ethyl p-hydroxybenzoate, octyl p-hydroxybenzoate, N-butyltoluenesulfonamide, N-octyltoluenesulfonamide, N-butylbenzenesulfonamide, or N-2-ethylhexylbenzenesulfonamide)	2 to 25 wt. %	Not reported	
Thermoplastic resin composition having high impact strength (US 3939112 A) Phillips Petroleum Company, 1976/02/17					
Polystyrene (A)-poly-1,3-butadiene or polyisoprene (B) Block copolymer	Not applicable	Extender oil	Not specified	1100 % increase (0.51 to 6.16 ft. lbs at 15 wt. % oil concentration)	Tensile strength/ elongation at

					break drops
Impact strength polypropylene (US 7659349 B2) Total Petrochemicals Research Feluy, 2010/02/09 Impact strength polypropylene (WO 2003042257 A1) Total Petrochemicals Research Feluy, 2003/05/22					
Degraded polypropylene (co)polymer modified with a linear dialkylperoxide in order to retain its impact strength and a process for its preparation.					

REFERENCES

1 Ma, Chen-Chi Martin, et al. "Fabrication of polymer grafted carbon nanotubes/polypropylene composite bipolar plates for fuel cell." U.S. Patent Application 12/591,026.

2 “Method for improving shock resistance of resin-based carbon fiber composite material,” CN 200910069674.

3 Bae, Jinwoo. "Carbon nanotube ultra-high molecular weight polyethylene composite, molded article including the same, and method of fabricating the molded article." U.S. Patent Application 14/056,606.

4 “Thermoplastic resin composition for radar cover”, EP20140844997.

5 Bastiaens, Jos, and Arno Hagenaars. "Carbon nanotube masterbatch, preparation thereof, and use in forming electrically conductive thermoplastic composition." U.S. Patent No. 8,961,834. 24 Feb. 2015.

6 Ma, Chen-Chi Martin, et al. "Fabrication of carbon nanotubes reinforced polymer composite bipolar plates for fuel cell." U.S. Patent Application 12/289,046.

7 Ma, Chen-Chi M., et al. "Fabrication of carbon nanotubes reinforced semi-crystalline polymer composite bipolar plates for fuel cell." U.S. Patent Application 12/458,649.

8 Schuessler, Stephan, Michaela Lendl, and Bernd Kretzschmar. "Polyolefin composition." U.S. Patent No. 8,859,670. 14 Oct. 2014.

9 “Anti-impact modified PP/HDPE (Polypropylene/High Density Polyethylene) plastics for automotive interior parts and preparation method thereof”, CN 201310023935.

10 “Impact-resistant conductive polyphenylene sulfide material and preparation method thereof”, CN 201310637782.

11 Lundgren, Bengt. "Method for improving the impact strength of a plastics material." U.S. Patent No. 4,186,125. 29 Jan. 1980.

12 Hao, Ning, Karin Irene Van De Wetering, and Amit S. Kulkarni. "Polycarbonate composition with improved impact strength." U.S. Patent Application 13/069,704.

13 Krigas, T. M., et al. "Polyolefin Compositions Having Improved Impact Strength." Patent NumberEP 0171513 (1986).

14 Needham, Donald G. "Thermoplastic resin composition having high impact strength." U.S. Patent No. 3,939,112. 17 Feb. 1976.

15 Nakajima, Nobuyuki. "High impact strength polyamides." U.S. Patent No. 5,376,712. 27 Dec. 1994.

16 Goldman, Anatoliy. "Stiff and impact resistant compositions containing poly (propylene) or poly (ethylene/propylene) and calcium carbonate for closures." U.S. Patent Application 10/361,342.

17 Campanelli, John R., and Michael L. Becraft. "Impact-Modified Polypropylene Composite." U.S. Patent Application 13/165,163.

18 “PP (polypropylene) polymer material with high impact strength”, CN 201310444205

19 Machl, Doris, Klaus Bernreitner, and Christelle Grein. "Polypropylene Resin with Low Shrinkage, High Impact Strength, Stiffness and Scratch Resistance." U.S. Patent Application 12/084,780.

20 Jayne, Jr William M. "Polypropylene compositions having improved impact strength containing polyethylene and ethylene-propylene copolymer." U.S. Patent No. 3,256,367. 14 Jun. 1966.

21 Lehane, Jr Jeremiah P. "Impact strength of blends of polyethylene and polypropylene." U.S. Patent No. 3,137,672. 16 Jun. 1964.

22 Kim, Yong-Jeon, et al. "Polypropylene resin composition with good transparence and good impact strength." U.S. Patent No. 8,779,064. 15 Jul. 2014.

23 Huff, Terrence. "Polypropylene blends having high impact strength and improved optical properties." U.S. Patent No. 4,087,485. 2 May 1978.

24 Fisk, Charles F. "High impact strength thermoplastic composition containing polyvinyl acetal resin and butadiene elastomer." U.S. Patent No. 2,684,352. 20 Jul. 1954.

25 Kim, Yoon-Ho, Geon-soo Kim, and Sang-il Nam. "Impact strength modifiers for thermoplastic polyester and thermoplastic polyester resin composition containing the same." U.S. Patent No. 8,252,867. 28 Aug. 2012.

26 Ilenda, Casmir S., David L. Dunkelberger, and Dennis J. Labanoski. "Polyolefin compositions with improved impact strength." U.S. Patent No. 4,997,884. 5 Mar. 1991.

27 “Polypropylene copolymers with specific crystal nucleation”, EP20110700437

28 “Method for improving the low temperature impact strength of polyblends of thermoplastic copolyesters and styrene acrylonitrile copolymers”, EP19910870026

29 Bartmann, Martin, et al. "Thermoplastic molding compositions with cold impact strength." U.S. Patent No. 4,959,403. 25 Sep. 1990.

30 Roegiers, Kristien. "Impact strength polypropylene." U.S. Patent Application 10/495,320